Doctoral Thesis

Electronic Structure of Quantum Dots: Response to the Environment and Externally Applied Fields

Author:
Carlos Segarra Ortí

Advisors:
Josep Planelles Fuster
Juan Ignacio Climente Plasencia

June 2016

Universitat Jaume I

Departament de Química Física i Analítica
Universitat Jaume I
Castelló de la Plana, Spain

Als meus pares

Els Doctors Josep Planelles Fuster i Juan Ignacio Climente Plasencia, del Departament de Química Física i Analítica de la Universitat Jaume I,

CERTIFIQUEN:

Que la memòria presentada pel llicenciat Carlos Segarra Ortí amb títol "Electronic Structure of Quantum Dots: Response to the Environment and Externally Applied Fields" ha estat realitzada sota la nostra direcció i constitueix la Tesi Doctoral de l'esmentat llicenciat. Autoritzem la presentació d'aquesta mitjançant el present escrit.

Castelló de la Plana, juny de 2016

Josep Planelles Fuster — Juan Ignacio Climente Plasencia

Agraïments

La present Tesi doctoral és el resultat final de quatre anys de treball i esforç en què he tingut la sort de comptar amb el suport de companys, familiars i amics que han compartit amb mi aquesta enriquidora experiència. Sens dubte, el treball que ací es mostra no haguera sigut possible sense la seua ajuda.

En primer lloc, voldria agrair a Josep Planelles i Juan Ignacio Climente el haver-me oferit la possibilitat de realitzar aquest projecte de Tesi sota la seua supervisió. Durant tot el temps que he tingut el plaer de treballar amb ells han mostrat un gran interès i una dedicació plena en proporcionar-me la millor formació investigadora tenint sempre present el que seria millor per al meu futur. De la mateixa manera, el meu agraïment és extensiu a la resta de membres del grup de Química Quàntica Fernando Rajadell, José Luis Movilla, Miquel Royo i Ana Ballester que d'una manera o altra han contribuït a la realització d'aquesta Tesi. En especial vull destacar a Ana B, amb qui vaig tindre la sort de compartir laboratori durant els primers anys de doctorat i que prompte es va convertir en una molt bona amiga.

D'altra banda, voldria mostrar també la meua gratitud als amics que han estat al meu costat en el dia a dia durant aquests anys i que han compartit amb mi molts bons moments dintre i fora de la universitat. En concret vull destacar a Ana M, David, Erica, Neus, Paula i, com no, a *chéritounet Loucou*. A més, cal mencionar a tots els membres del Departament de Química Física i Analítica, especialment a Merche per la seva predisposició a ajudar-me amb tota la paperassa i els tràmits burocràtics. Done també les gràcies a Sergio E. Ulloa per donar-me l'oportunitat de realitzar una estada breu en el seu grup de recerca en la Universitat d'Ohio (Estats Units), així com a tots els membres del grup per la seua acollida.

Finalment, voldria agrair de cor als meus pares el suport i la confiança incondicionals que m'han donat durant tota la meua vida. Perquè són els principals responsables de que haja arribat fins ací, els dedique aquesta Tesi.

Acronyms

1D one-dimensional

2D two-dimensional

3D three-dimensional

AB Aharonov-Bohm

CB conduction band

ch crystal-field split hole

DQD double quantum dot

DSOI Dresselhaus SOI

e-h electron-hole

EFA envelope function approximation

EMA effective mass approximation

hh heavy-hole

LED light emitting diode

lh light-hole

PL photoluminescence

QD quantum dot

QR quantum ring

RSOI Rashba SOI

so split-off

SOI spin-orbit interaction

TMDC transition metal dichalcogenide

VB valence band

WZ wurtzite

ZB zinc-blende

Contents

CHAPTER 1

Introduction

Over the last decades, big efforts have been dedicated to the fabrication of smaller and smaller technological devices. This miniaturization process has led to structures with sizes in the nanometer scale (from few nanometers to few hundred nanometers). A clear example is the size evolution of the silicon transistors that integrate computer chips, decreasing from few micrometers to around 10 nm in the last 50 years. The investigation of such small systems has given rise to a relatively new area of research called nanotechnology, which is remarkably multidisciplinary and of current interest. When charge carriers (electrons and holes) are confined into systems with such length scale, of the order of their de Broglie wavelength, they start obeying the laws of quantum mechanics and a classical approach no longer holds. This fact is a natural limitation for the traditional methods of device fabrication, but it also offers fascinating novel physical properties that makes these structures promising candidates for future applications in medicine, electronics, solar cells and batteries, among others.[1]

In particular, nanoelectronic devices formed by low-dimensional semiconductor nanostructures have been intensively investigated and various types of nanostructures have been developed. Based on the number of dimensions in which the carriers are confined, these can be classified into quantum dots (QDs) (confined in all three spatial dimensions), quantum wires (confined in two dimensions) and quantum wells (confined in only one dimension). Each one of them presents different features, but this Thesis will mainly focus on the study of zero-dimensional QDs. As a result of the quantum confinement in these systems, their energy states form a discrete energy spectrum, similar to that of atoms. Due to this analogous behavior, QDs are also known as *artificial atoms*.[2] However, both systems present important differences. Electrons in an atom are subject to the attractive centrosymmetric Coulomb potential of the nuclei, while electrons in a QD move freely inside the available space defined by the confining potential. Additionally, the population of electrons inside a QD can be controlled from zero up to tens or even hundreds, and this is not possible working with atoms. This experimental tunability is an enormous advantage for QDs compared to atoms, since it offers the possibility to modify their electronic and optical properties through changes in size, shape and composition. For example, the color of the light emitted by CdSe QDs can be controlled by simply changing their size.[3] Bigger dots (radius of 5-6 nm) emit longer wavelengths like red, while smaller dots (radius of 2-3 nm) emit shorter wavelengths like green. This high tunability of properties is the reason why QDs are suitable for a wide range of applications such as photovoltaic devices,[4] biosensors,[5] quantum computation,[6] light emitting diodes (LEDs),[7] lasers, display technologies,[8, 9] etc.

Since the synthesis of the first quasi-zero-dimensional QDs in the late 1980s, the growth techniques have been greatly improved and nowadays it is possible to obtain high-quality semiconductor QDs of many shapes, sizes and materials.[10, 11] There is a wide variety of techniques for their production but, for the sake of brevity, only the three main approaches will be briefly discussed here. The first method of obtaining QDs was reported by Reed *et al.* [12] in 1986, who produced square QDs with a side length of 250 nm by means of lithographic techniques. Starting from a structure of quantum wells, where carriers are confined in one direction, small columns are etched and, thus, their motion is further restricted in the in-plane direction. The main disadvantage of the etching technique is the defect formation and contamination of the dots. A variant that circumvents this problem is to laterally confine the carriers by patterning several electrodes over the surface of the quantum well.[13–15] The QDs fabricated this way are flat and can be created with almost arbitrary lateral shape. Their diameter is of the order of 10-100 nm. Another synthesis technique is the growth of self-organized QDs by the Stranski-Krastanov method.[16, 17] This process consists in the epitaxial crystallization of one material on top of a layer of another one (usually referred to as wetting layer) with significantly different lattice constant. The first deposited monolayers are highly strained and, when a critical thickness is exceeded, a breakdown takes place. This originates randomly distributed three-dimensional (3D) islands of regular shape and size, usually known as self-assembled QDs. Their shape is typically pyramids, truncated pyramids, flat lenses or rings with heights of the order of 25 nm and base widths of 20 nm. The biggest advantage of this method is its simplicity and the absence of edge defects. Lastly, it is also possible to fabricate QDs as colloidal semiconductor nanocrystals in glass dielectric matrices.[18] The first example of this method was carried out by Ekimov *et al.* [19], who created CuCl microcrystals in a solution of silicate glass. Colloidal QDs are nearly spherical in shape with small radii in the range of 1.2-10 nm. Such QDs can be further covered by a layer of another semiconductor material to form core-shell heterostructures that present altered properties in comparison to the uncovered ones. In light of the above, it is clear that the production method followed strongly determines the size and shape of the dots and, in turn, their properties. As for the materials used, typical dots are made of binary compounds of common zinc-blende (ZB) or wurtzite (WZ) semiconductors (PbS, PbSe, CdS, CdSe, InAs, GaAs, InP, GaN, InN and AlN) and their ternary and quaternary alloys. It is worth noting that QDs of some of these materials (e.g., GaAs and GaN) have been successfully synthesized in both crystal phases. Additionally, recent works have reported the fabrication of polytype QDs in which both ZB and WZ structures coexist within the same system.[20, 21] Moreover, since the discovery of graphene,[22] purely two-dimensional (2D) materials have been intensively studied and QDs made of graphene[23–25] and other related materials such as monoloyer transition metal dichalcogenides (TMDCs)[26–28] have also been fabricated. As can be seen, the diversity of semiconductor QDs is very rich and it is still growing.

In order to use QDs in real devices, a good understanding of their properties is needed from both experimental and theoretical points of view. As mentioned above, the optical and electronic properties of these structures are mainly governed by their shape, size and composition, i.e. by quantum confinement effects. Nevertheless, other factors that are intrinsic to the growth process, such as defects, impurities or crystal deformations to name a few, may also play an important role in their final performances. Therefore, it is crucial to identify and understand the phenomena that are relevant for each individual case under study, which will depend on the particular system and the application of interest. Then, based on this knowledge, QDs could be designed in order to enhance or diminish specific features. In addition to this, equally important is to have mechanisms to externally control and manipulate the system behavior in a reversible way. This is commonly done by switching on and off or changing the orientation of external electric and magnetic fields. Consequently, the effects of these fields in the conduction band (CB) and valence band (VB) of QDs must be also studied.

The aim of this Thesis is to theoretically investigate the electronic structure of semiconductor nanostructures. To this end, computational models are built to properly describe the CB and the VB of nanoscopic systems subject to various relevant phenomena. Particularly, we focus on QDs of different shape, dimensions, and composition to explore their behavior under external fields and interactions with the environment. Typical QDs are embedded into or grown on top of a different material, so that the lattice mismatch at the interface originates strain and this strain, in turn, gives rise to piezoelectricity. Here, the influence of these effects on the CB and VB electronic structure is explored, paying special attention to the role of the crystal phase, namely ZB, WZ or polytype crystal structure. Furthermore, the relaxation of the spin degree of freedom confined in QDs is also studied. Such spin scattering is mediated by the coupling of the spin states with acoustic phonons of the surrounding medium via the deformation and the piezoelectric potential mechanisms. For the relaxation to take place, the states involved in the transition need some spin admixture, which is produced by the spin-orbit interaction (SOI) in our case. By including all relevant sources of spin mixing (Rashba SOI (RSOI), Dresselhaus SOI (DSOI), and the coupling of light-hole (lh) and heavy-hole (hh) subbands) in a fully 3D model, it is shown that SOI is strongly anisotropic, which also translates into anisotropic spin relaxation. Additionally, the behavior of electrons and holes under externally applied fields is also investigated, focusing on the possibility of inducing ground state transitions and the emergence of the Aharonov-Bohm (AB) effect in quantum rings (QRs) as a consequence of their doubly-connected topology. Another topology-related effect is also analyzed in monolayer MoS_2, a truly 2D system in which edge states are formed owing to the marginal topological character of the MoS_2 material.

In the succeeding chapters we present the theoretical methods and the main findings of this Ph.D. Thesis together with a reasoned interpretation of the results. The remainder of this dissertation is structured as follows:

In chapter 2 we introduce the theoretical formalism used to model the electronic structure of the CB and the VB of semiconductor nanostructures.[1] To be specific, the description of electrons and holes in such systems is carried out by means of the k·p method within the effective mass approximation (EMA) and the envelope function approximation (EFA). Briefly, it consists in a semi-empirical continuum model based on perturbation theory that provides good estimates of the low-energy properties at a relatively low computational cost. The Hamiltonians employed to investigate structures made of ZB, WZ, and mixed crystal phases (polytypes) are presented. Besides being computationally low demanding, k·p methods are also ad-

[1] We note that the details of very specific simulations will be given in the corresponding chapters.

vantageous because they allow to take into account many phenomena by simply supplementing the base Hamiltonians with appropriate extra terms. In this respect, the basic aspects and the explicit Hamiltonians describing such phenomena are exposed, namely external electric and magnetic fields, SOI, strain, and piezoelectricity. For the latter two, the corresponding fields are calculated using the continuum theory of elasticity.

Chapter 3 is dedicated to study the effects of applying an external magnetic field in two different systems. First, the electronic structure of the VB in axially-symmetric GaN/AlN cubic QDs is investigated. A position-dependent six-band Hamiltonian in cylindrical coordinates is derived to explore the hole spin purity and the possibility of modulating the energy spectrum via magnetic fields to cause inversions of the ground state. In this way, optical properties such as light polarization could be easily tuned. Second, the response of nanostructures in the multi-particle regime pierced by axial magnetic fields is analyzed. In particular, the system considered is a flat hexagonal QR defined as the cross-section of a multishell nanowire. Remarkable signatures of the discrete geometry symmetry and of the correlation are found in the AB oscillation patterns, which allow to justify observations reported in recent magnetoconductance experiments.

In chapter 4 we describe the physics of the spin of carriers confined in zero-dimensional structures with various shapes, dimensions and crystallographic orientations. Special attention is paid to the SOI and its role in the spin relaxation of electrons and holes. Both RSOI and DSOI effects are taken into account in a fully 3D model, going beyond the commonly employed quasi-2D simplified description in which cubic DSOI terms are disregarded. Indeed, the importance of including all three spatial dimensions is confirmed in self-assembled dots and core-shell nanocrystals which are clearly not flat. Also, the high anisotropic character of the spin relaxation is shown by varying the aspect ratio of the QDs and by rotating the orientation of external magnetic fields. Such anisotropy leads to substantial spin relaxation suppressions, offering the possibility to obtain long-lived spins. Furthermore, for the VB the geometry regime at which the different sources of spin mixing, i.e. SOI or lh-hh coupling, prevail is identified. In addition, the intrinsic anisotropy of RSOI and DSOI is also demonstrated by studying the magnitude of the spin anticrossings in the energy spectra. All results are discussed in terms of the symmetry of the SOI Hamiltonians.

Chapter 5 deals with the influence of the environment on the properties of semiconductor QDs. Specifically, we account for the strain and piezoelectricity produced by the lattice mismatch between dot and surrounding materials. Interestingly, despite strain and piezoelectric fields can be undesirable for some applications, they offer the opportunity to fabricate strain-engineered QDs with improved performance.[29, 30] Two systems with different crystal structure are considered, core-shell WZ nanocrystals and polytype QDs, in order to assess the role of the crystal phase in these phenomena. It is known that the generated piezoelectric fields are usually weak in ZB structures, but they turn out to be crucial in WZ and even more in polytype systems, where spontaneous polarization is found to predominate. It is shown that the resulting polarization fields strongly affect the electron-hole (e-h) spatial separation, thus enabling a substantial exciton lifetime tunability.

Lastly, in chapter 6 we investigate atomically thin structures. In particular, the electronic structure of monolayer MoS_2 nanoribbons and QDs is analyzed. In such systems, states spatially localized near the edges and with energies lying in the band gap emerge, which play an important role in transport properties. The origin of these edge states is related to the marginal topological character of the system Hamiltonian.

The contents of the present report are based on the publications in which the author has contributed during the last four years. All of them have been published in international peer-reviewed journals. A copy of the works listed below can be found at the end of the present doctoral Thesis.

1. C. Segarra, J. I. Climente, and J. Planelles, *Valence band mixing of cubic GaN/AlN quantum dots*, J. Phys.: Condens. Matter **24**, 115801 (2012)
2. J. Planelles, J. I. Climente, and C. Segarra, *Electron spin relaxation in 3D quantum dots: geometrical suppression of Dresselhaus and Rashba spin-orbit interaction*, J. Phys. Chem. C **116**, 25143 (2012)
3. J. I. Climente, C. Segarra, and J. Planelles, *Spin-orbit-induced hole spin relaxation in InAs and GaAs quantum dots*, New J. Phys. **15**, 093009 (2013)
4. A. Ballester, C. Segarra, A. Bertoni, and J. Planelles, *Suppression of the Aharonov-Bohm effect in hexagonal quantum rings*, EPL **104**, 67004 (2013)
5. M. Royo, C. Segarra, A. Bertoni, G. Goldoni, and J. Planelles, *Aharonov-Bohm oscillations and electron gas transitions in hexagonal core-shell nanowires with an axial magnetic field*, Phys. Rev. B **91**, 115440 (2015)
6. C. Segarra, J. Planelles, and J. I. Climente, *Control of electron spin-orbit anisotropy in pyramidal InAs quantum dots*, Physica E **66**, 234 (2015)
7. C. Segarra, J. Planelles, J. I. Climente, and F. Rajadell, *Anisotropy*

of spin-orbit induced electron spin relaxation in [001] and [111] grown GaAs quantum dots, New J. Phys. **17**, 033014 (2015)

8. C. Segarra, J. I. Climente, F. Rajadell, and J. Planelles, *Hole spin relaxation in InAs/GaAs quantum dot molecules*, J. Phys.: Condens. Matter **27**, 415301 (2015)
9. C. Segarra, J. Planelles, and S. E. Ulloa, *Edge states in dichalcogenide nanoribbons and triangular quantum dots*, Phys. Rev. B **93**, 085312 (2016)
10. J. I. Climente, C. Segarra, F. Rajadell, and J. Planelles, *Electrons, holes, and excitons in GaAs polytype quantum dots*, J. Appl. Phys. **119**, 125705 (2016)
11. C. Segarra, J. I. Climente, A. Polovitsyn, F. Rajadell, I. Moreels, and J. Planelles, *Piezoelectric control of the exciton wave function in colloidal CdSe/CdS nanocrystals*, J. Phys. Chem. Lett. **7**, 2182 (2016)

CHAPTER 2

Theoretical framework

The aim of this chapter is to provide the theoretical background of the methods used throughout this Thesis for the calculation of the QD electronic structure. A brief discussion of the general aspects of the methods is presented here and whoever interested in further details is invited to consult dedicated books.[31–33] Nevertheless, when extra information is required for understanding a specific topic, this will be given in the corresponding chapter.

The models typically employed to study QDs can be classified into two categories: atomistic and continuum models. Atomistic models, e.g. empirical pseudopotential and tight-binding methods, take all atoms of the crystal and their interactions explicitly into account in order to describe the behavior of the system. These models are generally considered more accurate because they are based on more fundamental principles, but have the disadvantage of being computationally expensive (typical QDs are composed by 10^3-10^6 atoms) and the results are often hard to interpret. On the other hand, continuum models treat the systems as an ensemble of material domains whose properties are those of the bulk, thus ignoring the microscopic details. Although less accurate, these simpler models yield good estimates of the low-energy properties, offering more intuitive and computationally less demanding results.

Particularly, the approach taken for this Ph.D. project is the k·p method in the framework of the EMA and EFA. In spite of its simplicity, this continuum model has been successfully used to capture the main electronic and optical features of QDs at a reasonable computational cost. Additionally, it allows the implementation of phenomena such as externally applied fields or strain in a straightforward way.

2.1 The k·p method

The k·p method was originally developed in the 1950s for the calculation of the band structure of bulk semiconductors and adapted to study heterostructures subsequently. It is a perturbative method that takes advantage of the crystal symmetries to predict the band structure as a function of only a few empirical parameters, which are obtained from experiments or *ab initio* calculations.

2.1.1 General formulation of the k·p method

An electron moving in a crystal, i.e. in the periodic potential of the atomic nuclei, is governed by the following Schrödinger equation including spin-orbit:

$$\left(\frac{\mathbf{p}^2}{2m_0} + \frac{\hbar}{4m_0^2c^2}\mathbf{p}\cdot\left(\boldsymbol{\sigma}\times\boldsymbol{\nabla}V_{cr}(\mathbf{r})\right) + V_{cr}(\mathbf{r})\right)\psi(\mathbf{r}) = E\,\psi(\mathbf{r}), \tag{2.1}$$

where $V_{cr}(\mathbf{r}) = V_{cr}(\mathbf{r}+\mathbf{R})$ is the periodic potential, $\mathbf{p} = -i\hbar\boldsymbol{\nabla}$, m_0 is the free electron mass, c is the velocity of light in vacuum and $\boldsymbol{\sigma}$ stands for the vector of Pauli spin matrices.[1] Taking into account Bloch's theorem, the wave function of a particle in a periodic potential can be written as the product of a plane wave, $e^{i\mathbf{kr}}$, and a periodic function with the same periodicity as the potential, $u_{nk}(\mathbf{r}) = u_{nk}(\mathbf{r}+\mathbf{R})$. After substituting $\psi_{nk}(\mathbf{r}) = e^{i\mathbf{kr}}u_{nk}(\mathbf{r})$ into (2.1) and left multiplying by $e^{-i\mathbf{kr}}$ one obtains

$$\left[\frac{\mathbf{p}^2}{2m_0} + \frac{\hbar^2k^2}{2m_0} + \frac{\hbar}{4m_0^2c^2}\mathbf{p}\cdot(\boldsymbol{\sigma}\times\boldsymbol{\nabla}V_{cr}) + \frac{\hbar}{m_0}\mathbf{k}\cdot\boldsymbol{\pi} + V_{cr}\right]u_{nk} = E_{nk}\,u_{nk} \tag{2.2}$$

with

$$\boldsymbol{\pi} = \mathbf{p} + \frac{\hbar}{4m_0^2c^2}(\boldsymbol{\sigma}\times\boldsymbol{\nabla}V_{cr}). \tag{2.3}$$

The second term of $\boldsymbol{\pi}$, coming from the spin-orbit effect, has a small contribution and will be disregarded hereafter, so that $\boldsymbol{\pi} = \mathbf{p}$.

Equation (2.2) is the basic formulation of the k·p method, whose name comes from the appearance of the $\mathbf{k}\cdot\mathbf{p}$ factor[2]. It can be solved for a fixed wave vector $\mathbf{k} = \mathbf{k}_0$, yielding a complete and orthonormal set of eigenfunctions u_{nk_0}. For simplicity, $\mathbf{k} = 0$ is usually taken at the band extrema (the

[1] The components of $\boldsymbol{\sigma}$ are $\sigma_x = \begin{pmatrix}0&1\\1&0\end{pmatrix}, \sigma_y = \begin{pmatrix}0&-i\\i&0\end{pmatrix}$, and $\sigma_z = \begin{pmatrix}1&0\\0&-1\end{pmatrix}$.

[2] Note that $\mathbf{k}$ is a vector consisting of three real numbers with dimensions of inverse length, while $\mathbf{p}$ is a vector of operators.

Γ point in common semiconductors). Then, the band dispersion at finite $\mathbf{k}$ can be calculated by means of perturbation theory. To this end, equation (2.2) is rewritten as the sum of the Hamiltonian for $\mathbf{k} = 0$, H_0, plus the k-dependent terms as a perturbation, H'_k.

$$\Bigg(\underbrace{\frac{\mathbf{p}^2}{2m_0} + \frac{\hbar}{4m_0^2c^2}\mathbf{p}\cdot(\boldsymbol{\sigma}\times\boldsymbol{\nabla}V_{cr}) + V_{cr}}_{H_0} + \underbrace{\frac{\hbar^2k^2}{2m_0} + \frac{\hbar}{m_0}\mathbf{k}\cdot\mathbf{p}}_{H'_k}\Bigg)u_{nk} = E_{nk}\,u_{nk} \tag{2.4}$$

In practice, only a limited number of functions can be taken as basis set. As a result, the validity of the results is restricted to a small area in the vicinity of the Brillouin zone center. Nevertheless, the physics of semiconductors is mostly governed by the carriers in the extrema of the various energy bands and, thus, the k·p method suffices to capture their main properties.

The choice of the bands included in the model depends on how isolated the bands of interest are. Let us consider a situation where the investigated band is far from the other bands. In such a case, u_{nk} is mainly determined by u_{n0} and a basis set consisting of only this function can be used. This is true, as will become clear below, for the CB of most semiconductors. Applying second order non-degenerate perturbation theory to (2.4), the expressions for E_{nk} and u_{nk} are obtained

$$E_{nk} = E_{n0} + \frac{\hbar^2k^2}{2m_0} + \frac{\hbar^2}{m_0^2}\sum_{n'\neq n}\frac{|\langle u_{n0}\,|\mathbf{k}\cdot\mathbf{p}|\,u_{n'0}\rangle|^2}{E_{n0}-E_{n'0}} \tag{2.5}$$

and

$$u_{nk} = u_{n0} + \frac{\hbar}{m_0}\sum_{n'\neq n}\frac{\langle u_{n0}\,|\mathbf{k}\cdot\mathbf{p}|\,u_{n'0}\rangle}{E_{n0}-E_{n'0}}u_{n'0}. \tag{2.6}$$

Here, E_{n0} and the so-called optical matrix elements $P_{nn'} = \langle u_{n0}\,|\mathbf{k}\cdot\mathbf{p}|\,u_{n'0}\rangle$ are unknown parameters that need to be inferred from experiments. Equation (2.5) can be rewritten as

$$E_{nk} = E_{n0} + \frac{\hbar^2k^2}{2m^*} \tag{2.7}$$

where m^* is known as the effective mass of the band. This modified mass arises from the coupling of the considered band with other neighboring bands via the $\mathbf{k}\cdot\mathbf{p}$ term and has the following form:

$$\frac{1}{m^*} = \frac{1}{m_0} + \frac{2}{m_0^2k^2}\sum_{n'\neq n}\frac{|\langle u_{n0}\,|\mathbf{k}\cdot\mathbf{p}|\,u_{n'0}\rangle|^2}{E_{n0}-E_{n'0}}. \tag{2.8}$$

The values of the effective masses are deduced from experimental data and are tabulated for most materials. A comparison between equation (2.7) and the Hamiltonian of a free electron show that both expressions are identical except for the mass. Then, the motion of an electron in a crystal can be seen as the motion of a free electron whose mass has been modified by the action of the periodic potential. This one-band model showing a quadratic dispersion relation is also known as EMA and, despite its simplicity, it has been extensively used in literature with surprisingly good results in the description of the CB.

Contrary to the previous example, when studying the VB the bands of interest are commonly close in energy to other bands and they cannot be treated independently. In such a case, multiband models are necessary and the quasi-degenerate perturbation theory proposed by Löwdin [34] should be used. The $\mathbf{k}\cdot\mathbf{p}$ interaction between the few adjacent bands is explicitly taken into account, while the contribution from remote bands is introduced using the Löwdin perturbation theory. This approach results in a N-dimensional Hamiltonian containing additional terms of higher order in $\mathbf{k}$, with N being the number of bands included.

The separation between bands strongly depends on the material and its crystal structure. So, the model employed has to be selected based on the characteristics of the system under investigation. In sections 2.1.3 and 2.1.4 some typical cases will be discussed for ZB and WZ semiconductors. In general, single-band models for the CB and four- or six-band models for the VB are enough to obtain satisfactory results for most low-energy properties.

2.1.2 Envelope function approximation

The development of epitaxial growth techniques in the 1970s led to the fabrication of the first heterostructures with atomically sharp interfaces. In such systems, the carriers are confined due to the band misalignment of the constituting materials, as represented in figure 2.1.

The breaking of the translational invariance at the interface prevents the use of the k·p model in these nanostructures. Several alternative theories have been suggested to overcome this problem but, among them, the ones based on the EFA are especially relevant. Following Bastard's formalism,[35] the EFA assumes the interface to be abrupt, defect-free and without interdiffusion effects, so that each domain can be taken as a perfect bulk material. In addition, the materials are assumed to be perfectly matched and to present the same crystal structure. The latter allows one to take

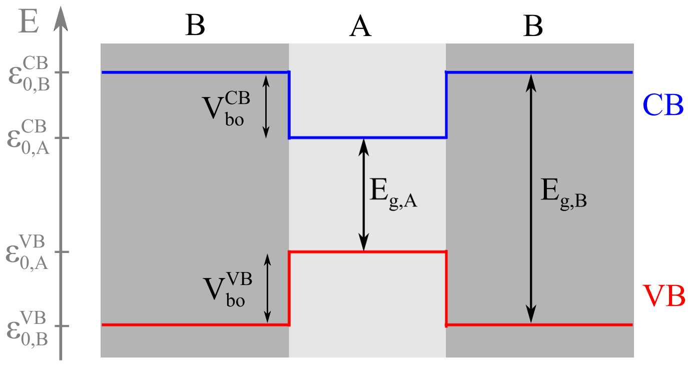

Figure 2.1: Sketch of the band edge profile along the z direction in a direct-gap heterostructure formed by two materials A and B. Band-edge energies ($\varepsilon_{0,A}^{CB}$, $\varepsilon_{0,B}^{CB}$, $\varepsilon_{0,A}^{VB}$ and $\varepsilon_{0,B}^{VB}$), band gaps ($E_{g,A}$ and $E_{g,B}$) and band offsets (V_{bo}^{CB} and V_{bo}^{VB}) are indicated for both CB and VB.

the periodic parts of the Bloch functions to be the same in both materials, $u_{nk}^A = u_{nk}^B = u_{nk}$. Then, the wave function can be expanded as

$$\psi_{nk}(\mathbf{r}) = \sum_n f_n^{(A,B)}(\mathbf{r})\, u_{nk_0}(\mathbf{r}), \tag{2.9}$$

where $f_n^{(A,B)}(\mathbf{r})$ is $f_n^A(\mathbf{r})$ or $f_n^B(\mathbf{r})$ depending on the region. This function varies slowly at the scale of the unit cell and it is usually referred to as envelope function.

For simplicity, a basis consisting of one band is used hereafter. Similarly to the derivation of the k·p method in the preceding section, equation (2.9) can be substituted into the Schrödinger equation (2.1) without spin-orbit and, after some algebraic manipulation[3], one gets

$$\left[-\frac{\hbar^2}{2m_0}\boldsymbol{\nabla}^2 + \varepsilon_{0,A} + V_{bo}(\mathbf{r})\right] f_n^{(A,B)}(\mathbf{r}) = E\, f_n^{(A,B)}(\mathbf{r}). \tag{2.10}$$

Here, $\varepsilon_{0,A}$ is the band energy of material A at $\mathbf{k} = 0$ and $V_{bo}(\mathbf{r})$ is a step-like function that takes $V_{bo}(\mathbf{r} \in A) = 0$ in layer A and $V_{bo}(\mathbf{r} \in B) = V_{bo}^{(CB,VB)}$ in layer B. Equation (2.10) is the second-order differential equation that governs the spatial behavior of the envelope function. This equation is solved after taking into account the appropriate boundary conditions. Typically, infinite barriers ($V = \infty$) at the outer edges and the continuity of the wave function derivative at the interface are imposed.

[3] The details of the derivation have been omitted for brevity, but can be easily found in books, e.g. see chapter 3 of Bastard's book.[35]

Just as the k·p method, this model can be further improved by perturbatively including the interaction with remote bands through the effective mass and by using several bands as basis in a multiband model. A comparison between both methods shows that the EFA Hamiltonian can be obtained from the k·p one by setting $\hbar\mathbf{k} \to -i\hbar\boldsymbol{\nabla}$ and adding a few terms. Hence, both models depend on the same set of parameters $P_{nn'}$. Consequently, due to the close similarity, EFA Hamiltonians are also known as k·p-EFA models.

The-one band model presented above is the simplest description of a heterostructure in which the presence of two materials is only taken into account through the band offset. Nevertheless, in such systems the effective mass m^* and the other band parameters become position dependent, so that $\mathbf{k}$ and m^* do not commute. This fact complicates the choice of the boundary condition at the interface. In fact, there has been much debate on the topic and several effective mass matching conditions have been proposed.[4]

The simplest model is the one based on BenDaniel-Duke boundary condition.[36] It considers a single parabolic and isotropic band and obtains a new Hamiltonian by changing the order of the differential operators in (2.10):

$$-\frac{\hbar^2}{2m^*}\boldsymbol{\nabla}^2 \quad \text{is replaced by} \quad -\frac{\hbar^2}{2}\boldsymbol{\nabla}\frac{1}{m^*(\mathbf{r})}\boldsymbol{\nabla}. \tag{2.11}$$

The new symmetrized Hamiltonian ensures the hermiticity and, thus, solutions with real eigenvalues and orthogonal eigenfunctions. The boundary condition is the continuity of $f_n(\mathbf{r})$ and $\frac{1}{m^*(\mathbf{r})}\frac{df_n}{d\mathbf{r}}$ at the interface. It is interesting to notice that the effective mass mismatch leads to a discontinuity in the derivative of the envelope function at the interface.

Similarly, the operator symmetrization approach has also been widely used in the description of holes in heterostructures. In such a case, a generic matrix element of a VB multiband model

$$\mathcal{H} = \sum_{ij}\mathcal{H}^{(2)}_{ij}k_ik_j + \sum_i \mathcal{H}^{(1)}_i k_i + \mathcal{H}^{(0)} \tag{2.12}$$

is rewritten for a variable mass system as

$$\mathcal{H} = \sum_{ij}k_i\mathcal{H}^{(2)}_{ij}k_j + \sum_i(\mathcal{H}^{(1)}_i k_i + k_i\mathcal{H}^{(1)}_i) + \mathcal{H}^{(0)}. \tag{2.13}$$

This reordering of the operators is, however, not strictly correct and may produce unrealistic results in some cases. As a consequence, in this Thesis

[4] A detailed discussion can be found in chapter 12 of Voon's book[31]

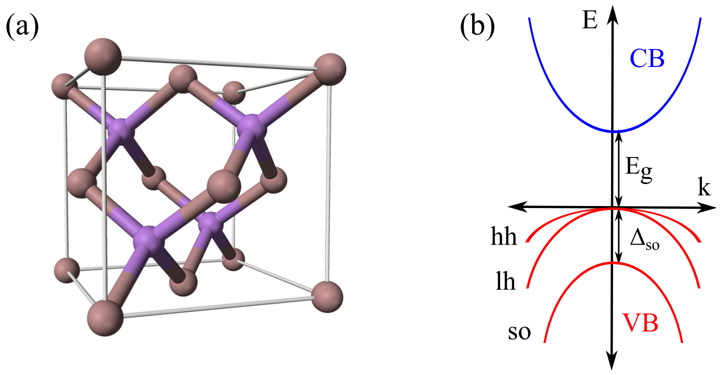

Figure 2.2: (a) Unit cell of ZB GaAs. Arsenic atoms are depicted in gray and gallium atoms in purple. (b) Schematic band dispersion of a ZB structure. The principal bands and their energy separations at the Γ point are indicated. For finite **k** the valence band is split in three subbands: hh, lh and split-off (so).

we follow the so-called Burt-Foreman model. Burt followed a completely different approach compared to Bastard's formalism. Instead of proposing an heuristic Hamiltonian and then search for valid solutions, he derived an exact envelope function theory from first-principles by first establishing constraints to the envelope function.[37–39] Later, Foreman used Burt's theory to derive an explicit multiband Hamiltonian and showed that this model gives reasonable results in particular cases where a symmetrized version of a conventional k·p model, namely the Luttinger-Kohn model, leads to nonphysical solutions.[40, 41]

2.1.3 Hamiltonians for zinc-blende structures

ZB is, together with WZ, one of the most common crystal structures in which binary semiconductors are grown. Examples are GaAs, InAs, CdTe and AlSb, to name a few. The crystal lattice consists of a face-centered cubic array of anions with cations occupying one half of the tetrahedral holes as figure 2.2(a) illustrates. This structure lacks inversion symmetry and corresponds to one of the piezoelectric crystal classes. Piezoelectric effects in QDs will be discussed in section 2.4.2.

Figure 2.2(b) shows the typical band dispersion for direct band gap ZB materials around the Γ point. Only four bands (eight with the spin degree of freedom) are depicted because other remote bands are far in energy and have negligible influence.

On one hand, the band gap E_g of the semiconductors studied in this Thesis is relatively large and allows the theoretical description of the CB in terms of a single-band model. The Hamiltonian reads

$$H = -\frac{\hbar^2}{2}\boldsymbol{\nabla}\frac{1}{m^*(\mathbf{r})}\boldsymbol{\nabla} + V(\mathbf{r}) \tag{2.14}$$

where a position-dependent effective mass $m^*(\mathbf{r})$ is assumed and $V(\mathbf{r})$ stands for the confining potential.

On the other hand, a multiband model is necessary to study the top of the VB. In the absence of spin-orbit the three valence subbands are degenerate, but spin-orbit lifts this degeneracy even for $\mathbf{k} = 0$. As shown in Fig. 2.2(b), the so subband becomes separated from the other two by the spin-orbit splitting Δ_{so}. Then, depending on the magnitude of Δ_{so}, a four- or six-band model should be employed.

From a microscopic point of view, the electronic bands are formed due to the hybridization of the valence s- and p-orbitals. In fact, the CB and the VB are mainly made of s- and p-orbitals, respectively. Thus, the most simple set of unperturbed basis functions are the Bloch functions: $|S\uparrow\rangle$, $|X\uparrow\rangle$, $|Y\uparrow\rangle$, $|Z\uparrow\rangle$, $|S\downarrow\rangle$, $|X\downarrow\rangle$, $|Y\downarrow\rangle$ and $|Z\downarrow\rangle$. However, it is more convenient to use a basis set made of a linear combination of the above functions that is adapted to the total angular momentum. This new basis set is[5]

$$\left|\frac{3}{2},+\frac{3}{2}\right\rangle = \frac{1}{\sqrt{2}}\left|(X+iY)\uparrow\right\rangle, \tag{2.15a}$$

$$\left|\frac{3}{2},+\frac{1}{2}\right\rangle = \frac{1}{\sqrt{6}}\left|(X+iY)\downarrow\right\rangle - \sqrt{\frac{2}{3}}\left|Z\uparrow\right\rangle, \tag{2.15b}$$

$$\left|\frac{3}{2},-\frac{1}{2}\right\rangle = -\frac{1}{\sqrt{6}}\left|(X-iY)\uparrow\right\rangle - \sqrt{\frac{2}{3}}\left|Z\downarrow\right\rangle, \tag{2.15c}$$

$$\left|\frac{3}{2},-\frac{3}{2}\right\rangle = \frac{1}{\sqrt{2}}\left|(X-iY)\downarrow\right\rangle, \tag{2.15d}$$

$$\left|\frac{1}{2},+\frac{1}{2}\right\rangle = \frac{1}{\sqrt{3}}\left|(X+iY)\downarrow\right\rangle + \frac{1}{\sqrt{3}}\left|Z\uparrow\right\rangle, \tag{2.15e}$$

$$\left|\frac{1}{2},-\frac{1}{2}\right\rangle = -\frac{1}{\sqrt{3}}\left|(X-iY)\uparrow\right\rangle + \frac{1}{\sqrt{3}}\left|Z\downarrow\right\rangle. \tag{2.15f}$$

[5]The definition of the basis set is not unique and Hamiltonians reported in literature may differ in the phase factors used. Here, we follow the standard basis generated with the angular momentum ladder operators. This is that employed in Voon's book.[31]

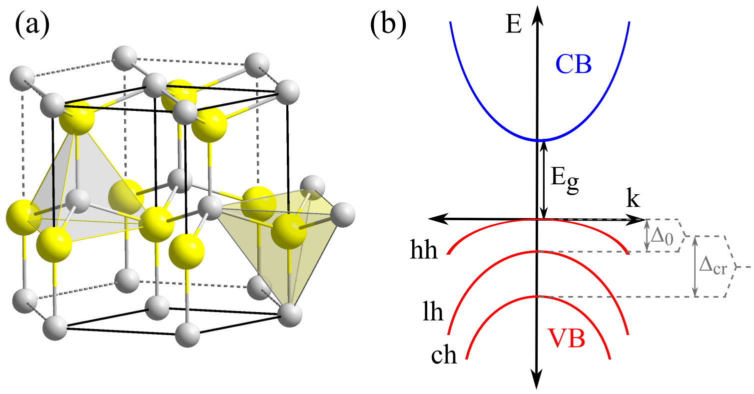

Figure 2.3: (a) Hexagonal structure of a WZ crystal, e.g. GaN. Gallium atoms are depicted in gray and nitrogen atoms in yellow. (b) Drawing of the band dispersion of a typical WZ semiconductor with $\Delta_{cr} > \Delta_0$. Band gap E_g, crystal-field splitting Δ_{cr} and spin-orbit splitting Δ_0 are indicated.

In this basis, the total angular momentum and it's projection J_z become diagonal in matrix representation.

Throughout the present dissertation, various multiband models are used to investigate the valence band of QDs. The choice of a particular method is based on the material, specifically the value of Δ_{so}, and the particular type of QD studied. In appendix A, all Hamiltonians used are collected together for ease of reference. The four-band Luttinger-Kohn Hamiltonian for constant mass calculations is given in appendix section A.1, and the six-band variable-mass Burt-Foreman one in section A.2.

2.1.4 Hamiltonians for wurtzite structures

WZ is the other typical crystal structure for binary semiconductors. Among the compounds that can take the WZ structure are CdS, CdSe, GaN, AlN, etc. It is constructed from two interpenetrating hexagonal-close-packed lattices, as represented in figure 2.3(a). WZ and ZB crystals are quite similar since their structure differ only in the second-nearest neighbors. Nevertheless, this difference causes WZ to have lower symmetry and this, in turn, results in two additional features compared to ZB materials: the emergence of the crystal-field splitting Δ_{cr} and spontaneous polarization (pyroelectricity). The latter will be accounted for in section 2.4.2.

Figure 2.3(b) displays the band structure of a common WZ semiconductor. Similarly to ZB, four spinless bands are taken into account to study the properties of WZ QDs. However, this selection is not as clear as for ZB because the separation of the CB lowest in energy from other conduction bands is rather small for some WZ materials.[42] In spite of this, a single-band parabolic Hamiltonian is used in the present Thesis due to the lack of effective mass parameters describing such a coupling.

With respect to the VB, it can be seen that, unlike ZB, the three (spin doubly degenerate) valence bands are split at $\mathbf{k} = 0$. In the absence of spin-orbit coupling, the hexagonal crystal field (Δ_{cr}) splits the p-like bands into two degenerate subbands and the crystal-field split hole (ch) subband. With the inclusion of spin-orbit coupling (Δ_0), the degenerate subband is further split into the hh and the lh subbands. In some works, the hh, lh and ch subbands are also referred to as A, B and C subbands, respectively. It is interesting to notice that the order of the lh and ch shown in figure 2.3(b) can be altered depending on the values of Δ_{cr} and Δ_0. Because of this, a six-band model is commonly used in WZ simulations.

Contrary to ZB, the lower symmetry of WZ does not allow to find a basis set that diagonalizes the Hamiltonian at $\mathbf{k} = 0$. The basis of Bloch functions considered here is[43]

$$|u_1\rangle = -\frac{1}{\sqrt{2}}|(X + i\,Y) \uparrow\rangle, \tag{2.16a}$$

$$|u_2\rangle = \frac{1}{\sqrt{2}}|(X - i\,Y) \uparrow\rangle, \tag{2.16b}$$

$$|u_3\rangle = |Z \uparrow\rangle, \tag{2.16c}$$

$$|u_4\rangle = \frac{1}{\sqrt{2}}|(X - i\,Y) \downarrow\rangle, \tag{2.16d}$$

$$|u_5\rangle = -\frac{1}{\sqrt{2}}|(X + i\,Y) \downarrow\rangle, \tag{2.16e}$$

$$|u_6\rangle = |Z \downarrow\rangle. \tag{2.16f}$$

Various authors have reported six-band models to study the WZ VB.[32, 43, 44] In this Thesis, a position-dependent Hamiltonian derived following Burt-Foreman operator ordering is used.[45] The matrix representation can be found in appendix A.2. This Hamiltonian depends on 6 mass parameters A_{1-6} and three energy splittings Δ_{1-3}, with $\Delta_1 = \Delta_{cr}$, and Δ_2 and Δ_3 being the spin-orbit matrix elements ($\Delta_2 = \Delta_3 = \Delta_{so}/3$ in the so-called quasi-cubic approximation).

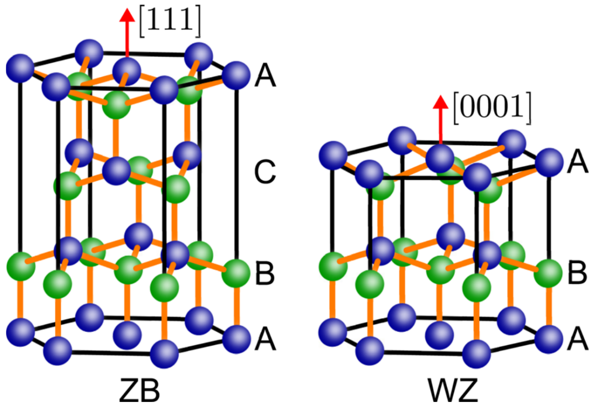

Figure 2.4: Crystal structures and their stacking sequence for (left) ZB in the [111] direction and (right) WZ in the [0001] direction. Reprinted with permission from [46]. Copyright 2012, AIP Publishing LLC.

2.1.5 Hamiltonians for polytypes

As mentioned above, WZ and ZB crystals present close similarities. This becomes evident when considering the ZB structure in the [111] direction and comparing it to WZ [0001]. In figure 2.4, it can be seen that both structures only differ in the stacking order of the layers: ABCABC for ZB while ABABAB for WZ. As a result, polytypical nanostructures consisting of ZB [111] and WZ [0001] phases of the same material have been successfully fabricated.[20, 21] These systems present typical characteristics of heterostructures formed by different materials because the band gap and the parameters also depend on the crystalline phase.

The theoretical study of these systems requires a model able to describe both crystal structures simultaneously. For the CB, this can be done by simply considering a different effective mass for each region in a position-dependent one-band Hamiltonian. For the VB, instead, this may seem a complicate task in view of the six-band Hamiltonians proposed for both structures in appendix A. However, Bir and Pikus realized in their book (see page 328 in [32]) that a transformation of the ZB Hamiltonian to the appropriate coordinate system[6] yields a new Hamiltonian which is similar

[6] In the new coordinate system, the z'-axis is along [111] direction and x'- and y'-axis are along $[11\bar{2}]$ and $[\bar{1}10]$ directions, respectively. To perform this transformation, the Hamiltonian is first rotated 45° along the z-axis and then 54.7° along the new y'-axis. This rotation procedure is well described in [47].

to the WZ one. This opens the possibility of constructing a general Hamiltonian for the whole system and then particularize it to the structure of each region by considering the pertinent parameters.

In order to compare both Hamiltonians systematically the Bloch basis functions of lower symmetry should be used, i.e. the basis set of WZ given in 2.16. In this basis, one gets a Hamiltonian for ZB that is formally identical to the standard WZ one, equation (A.4), but now two extra terms emerge:

$$\Delta K = 2\sqrt{2}\,\frac{\hbar^2}{2m_0}\,A_z k_- k_z, \tag{2.17a}$$

$$\Delta H = \frac{\hbar^2}{2m_0}\,A_z k_-^2. \tag{2.17b}$$

These terms are zero for WZ ($A_z = 0$) and allow the ZB Hamiltonian to regain the original isotropic symmetry. In addition to this, the following relations arise connecting the mass parameters and energy splittings of both structures:

$$\Delta_1 = 0, \tag{2.18a}$$

$$\Delta_2 = \Delta_3 = \Delta_{so}/3, \tag{2.18b}$$

$$A_1 = -\gamma_1 - 4\gamma_3, \tag{2.18c}$$

$$A_2 = -\gamma_1 + 2\gamma 3, \tag{2.18d}$$

$$A_3 = 6\gamma_3, \tag{2.18e}$$

$$A_4 = -3\gamma_3, \tag{2.18f}$$

$$A_5 = -\gamma_2 - 2\gamma_3, \tag{2.18g}$$

$$A_6 = -\sqrt{2}(2\gamma_2 + \gamma_3), \tag{2.18h}$$

$$A_z = \gamma_2 - \gamma_3. \tag{2.18i}$$

Taking into account (2.18) reduces the number of independent parameters from 9 in WZ to 4 in ZB, as expected from symmetry considerations.

The full six-band Hamiltonian derived to study polytypes can be consulted in appendix A.3.1. It is worth noting that all diagonal elements are over stabilized by $\Delta_{so}/3$ when using ZB parameters. Thus, equation (A.3.1) must be corrected by subtracting this amount in the ZB region.

For simplicity, the above discussion has considered a situation with constant mass. Nevertheless, since the parameters in the two phases are different, it is more appropriate to use a position-dependent Hamiltonian and, thus, this is the model employed in all the polytype calculations of this Thesis. Starting from the WZ variable-mass Hamiltonian, equation (A.4), and following the same procedure as before, a position-dependent Hamiltonian for polytype systems is constructed. See appendix A.3.2 to consult its full matrix form. As expected from Foreman [40], the resulting Hamiltonian presents some extra coefficients compared to (A.5).

2.2 Externally applied fields

Particle energy levels are modified in the presence of external fields. This paves the way for manipulating the properties of QDs and, thus, controlling devices by external means.

2.2.1 Electric field

An external homogeneous electric field pulls electrons and holes towards opposite directions, leading to lower e-h overlaps and the suppression of exciton recombination processes. In addition, it is also responsible for the quantum-confined Stark effect, which generates a redshift of the emitted/absorbed light.

Accounting for static electric fields $\mathbf{F}$ into k·p Hamiltonians is straightforward. An extra potential energy V_F needs to be added to the confining potential of the heterostructure

$$V_F(\mathbf{r}) = -e\,\mathbf{F}\cdot\mathbf{r} \tag{2.19}$$

where e is the particle charge, $e = -1$ for electrons and $e = 1$ for holes.

It is worth stressing that the presence of electric fields may also give rise to other phenomena in nanostructures, e.g. the Rashba SOI (see section 2.3.2).

2.2.2 Magnetic field

The application of magnetic fields to QDs originates shifts in the energy spectrum and lifts of spin degeneracies. The latter phenomenon is known as Zeeman effect and is the magnetic field analogous of the Stark effect.

The standard way of including a magnetic field $\mathbf{B}$ in the k·p-EFA formalism is via minimal coupling, i.e. by replacing the canonical momentum $\mathbf{p}$ by the kinetic momentum $-i\hbar\boldsymbol{\nabla} - e\mathbf{A}$ and adding the Zeeman term to the

Hamiltonian. Here, e is the particle charge and $\mathbf{A}$ is the vector potential defining the magnetic field $\mathbf{B} = \boldsymbol{\nabla} \times \mathbf{A}$. The choice of the vector potential is not unique and it is common practice to use a different version based on the symmetry of the problem.

In a one-band isotropic model describing the CB and with position-dependent effective mass, the resulting Hamiltonian is as follows:

$$H = \frac{1}{2}\left(-i\hbar\boldsymbol{\nabla} - e\mathbf{A}\right)\frac{1}{m^*(\mathbf{r})}\left(-i\hbar\boldsymbol{\nabla} - e\mathbf{A}\right) + V\left(\mathbf{r}\right) + \frac{g^*}{2}\mu_B\,\boldsymbol{\sigma}\cdot\mathbf{B} \tag{2.20}$$

The last term in (2.20) is the Zeeman splitting, where g^* is the effective Landé g-factor, $\mu_B = \frac{|e|\hbar}{2m_0}$ the Bohr magneton and $\boldsymbol{\sigma}$ is a vector whose components are the Pauli matrices.

As for the magnetic field implementation in multiband models, the minimal coupling approach first used by Luttinger [48] has been widely employed in literature, providing satisfactory results for many experimental evidences. However, this model has been unable to describe some particular observations, such as the photoluminescence (PL) magnetoresonances in QRs under axial magnetic fields.[49] In this regard, recent works have proposed a new approach which outperforms the Luttinger approximation.[50, 51] It consists in performing the same replacement, $\mathbf{p} \rightarrow -i\hbar\boldsymbol{\nabla} - e\mathbf{A}$, but now prior to applying the EFA. The Hamiltonian obtained, unlike the Luttinger model, has no off-diagonal terms depending on $\mathbf{B}$, thus reducing the coupling between hole subbands.

We particularize this approach for a ZB constant mass system under an axial magnetic field $\mathbf{B} = (0, 0, B_0)$ defined by the vector potential $\mathbf{A} = \frac{B_0}{2}(-y, x, 0)$. In this specific case, the six-band Hamiltonian supplementing the zero-field one (A.2), presents the following diagonal elements:

$$H_{11}^B = -\left(\gamma_1 + \gamma_2\right)\left[\frac{B_0^2\left(x^2+y^2\right)}{8} + \frac{B_0}{2}\left(xp_y - yp_x\right)\right] - \frac{3}{2}\kappa\,\mu_B B_0 \tag{2.21a}$$

$$H_{22}^B = -\left(\gamma_1 - \gamma_2\right)\left[\frac{B_0^2\left(x^2+y^2\right)}{8} + \frac{B_0}{2}\left(xp_y - yp_x\right)\right] - \frac{1}{2}\kappa\,\mu_B B_0 \tag{2.21b}$$

$$H_{33}^B = -\left(\gamma_1 - \gamma_2\right)\left[\frac{B_0^2\left(x^2+y^2\right)}{8} + \frac{B_0}{2}\left(xp_y - yp_x\right)\right] + \frac{1}{2}\kappa\,\mu_B B_0 \tag{2.21c}$$

$$H_{44}^B = -\left(\gamma_1 + \gamma_2\right)\left[\frac{B_0^2\left(x^2+y^2\right)}{8} + \frac{B_0}{2}\left(xp_y - yp_x\right)\right] + \frac{3}{2}\kappa\,\mu_B B_0 \tag{2.21d}$$

$$H_{55}^B = -\gamma_1\left[\frac{B_0^2\left(x^2+y^2\right)}{8} + \frac{B_0}{2}\left(xp_y - yp_x\right)\right] - \frac{1}{2}\kappa'\,\mu_B B_0 \tag{2.21e}$$

$$H_{66}^{B} = -\gamma_1 \left[\frac{B_0^2 \left(x^2+y^2\right)}{8} + \frac{B_0}{2}\left(xp_y - yp_x\right) \right] + \frac{1}{2}\kappa' \, \mu_B B_0 \tag{2.21f}$$

with κ and κ' standing for the hole effective g-factors and $\mu_B = \frac{|e|\hbar}{2m_0}$.

As can be seen in (2.20) and (2.21), the Zeeman energy splitting is mainly determined by the value of the effective g-factor. In bulk systems, the SOI causes the g-factor to deviate from the bare electron value $g \approx 2$ and effective g-factors g^* are inferred experimentally. In QD simulations it is common to use these bulk effective g-factors, although some works have pointed out the quenching of the SOI-induced deviation in QDs due to confinement.[52] In this respect, van Bree *et al.* [53] suggest to disregard the contribution from remote bands and simply consider the bare Landé g-factors: $g^* = 2$, $\kappa = 4/3$ and $\kappa' = 2/3$.

2.3 Spin-orbit interaction (SOI)

In this section, we will present a theoretical description of the SOI effects on the CB and the VB of ZB materials. The SOI in WZ semiconductors is omitted here since in the present Thesis the spin dynamics of these crystal structures is not investigated.

In atomic physics, the SOI is a well-known phenomenon originating from the coupling of the electron spin to its orbital momentum via the electric field generated by the nuclei. Similarly, the SOI in solids comes from the interaction between the spin and the average electric field of the lattice nuclei. The most relevant effect of SOI on the band structure of semiconductors is the degeneracy breaking of the three topmost VB subbands. In particular, in cubic semiconductors such as ZB or diamond crystal structures this causes the energy separation at the center of the Brillouin zone of the so band from the lh and hh ones, which remain degenerate. In addition to this, SOI is also responsible for the spin splitting of the bands in materials lacking inversion symmetry, e.g. ZB semiconductors, even in the absence of a magnetic field. As a result, the CB and the three VB are no longer doubly spin-degenerate. The latter effect is, however, relatively small and it does not significantly affect most electronic properties, thus justifying not including it in many studies. Nonetheless, it may play an important role when investigating the properties of the spin degree of freedom,[54–56] such as the spin dynamics we will deal with in chapter 4.

The models discussed in the previous sections take into account the band splitting of the VB through the SOI term in H_0, equation (2.4), but ignore the spin-orbit-induced spin splitting. In order to include this effect, the Hamiltonians need to be supplemented by extra terms coming from the SOI contribution in equation (2.3) that was initially disregarded. The expressions of these additional terms can be obtained by using both the theory of invariants or perturbation theory up to third or fourth order. For the sake of brevity, their derivation will not be presented here, but we invite the interested reader to consult Winkler's book [33] for a detailed presentation.

Next, we will briefly discuss the origin and introduce the Hamiltonians of the two main spin-orbit sources of spin splitting in ZB materials: DSOI and RSOI.

2.3.1 Dresselhaus SOI

The DSOI is an intrinsic property of some materials resulting from the absence of an inversion center in its crystal structure.[57] In such a case, the microscopic electric fields generated by the lattice atoms do not cancel each other, thus originating a net contribution to the SOI. This phenomenon is also known as bulk inversion asymmetry (BIA).

For the CB, there are no terms up to second order in k, so that the cubic contributions are the lowest-order terms that characterize DSOI. The corresponding Hamiltonian for electrons reads:[33]

$$H_{BIA}^{CB} = b_{41}^{CB} \left[\sigma_x k_x \left(k_z^2 - k_y^2\right) + \sigma_y k_y \left(k_x^2 - k_z^2\right) + \sigma_z k_z \left(k_y^2 - k_x^2\right)\right], \tag{2.22}$$

where b_{41}^{CB} is a material-dependent parameter.

On the other hand, the contribution of DSOI in the VB includes linear- and third-order-in-k terms and is given by:[33]

$$\begin{aligned} H_{BIA}^{VB} = & \frac{2}{\sqrt{3}} C_k \left[k_x \left\{J_x, J_y^2 - J_z^2\right\} + \mathrm{cp}\right] \\ & + b_{41}^{VB} \left[\left\{k_x, k_y^2 - k_z^2\right\} J_x + \mathrm{cp}\right] \\ & + b_{42} \left[\left\{k_x, k_y^2 - k_z^2\right\} J_x^3 + \mathrm{cp}\right] \\ & + b_{51} \left[\left\{k_x, k_y^2 + k_z^2\right\} \left\{J_x, J_y^2 - J_z^2\right\} + \mathrm{cp}\right] \\ & + b_{52} \left[k_x^3 \left\{J_x, J_y^2 - J_z^2\right\} + \mathrm{cp}\right], \end{aligned} \tag{2.23}$$

with C_k, b_{41}^{VB}, b_{42}, b_{51} and b_{52} being material-dependent coefficients, cp standing for cyclic permutations of the preceding terms, and $\{A, B\} = \frac{1}{2}(AB + BA)$.

The matrix form of Hamiltonians (2.22) and (2.23) can be found in appendix B.1.

2.3.2 Rashba SOI

Besides the bulk inversion asymmetry, a spin splitting can also be produced by the structure asymmetry generated by the confining potential of the heterostructure itself and/or an externally applied electric field.[58] Consequently, this effect is also referred to as structure inversion asymmetry (SIA). Unlike DSOI, RSOI is a combined effect of the microscopic electric fields of the nuclei and the macroscopic external field felt by the system. Both of them must be present in order to have RSOI.

The Hamiltonian for the CB is linear in k and presents the following form:

$$H_{SIA}^{CB} = r_{41}\boldsymbol{\sigma} \cdot (\mathbf{k} \times \mathbf{F}). \tag{2.24}$$

Here, r_{41} is a material-specific prefactor and $\mathbf{F}$ is an external electric field. Equation (2.24) points out that the magnitude of RSOI is proportional to both r_{41}, which is determined by the microscopic details of the lattice, and the macroscopic field. This fact is very important because it allows to tune the strength of this effect by changing the intensity of $\mathbf{F}$. The explicit matrix representation of (2.24) is given in appendix B.2.

As for the VB, the RSOI contribution has been disregarded in all simulations included in this dissertation since it is less efficient than DSOI for moderate electric fields. This has been checked by carrying out a series of preliminary calculations for the particular systems investigated.

2.4 Strain and polarization fields

Heterostructures composed of various semiconductors, e.g. self-assembled QDs and core-shell nanocrystals, may present crystal deformations at the heterointerface originating from the lattice mismatch of the constituent materials. The resulting displacement of the lattice nuclei from their original equilibrium positions generates strain fields which, in turn, produce changes in the band structure of the system. Additionally, in non-centrosymmetric crystal structures such as ZB and WZ, these strain fields lead to a piezoelectric polarization that also affects the QD electronic and optical properties.

In this section, the theoretical framework for the calculation of strain and polarization fields is presented for both ZB and WZ structures. Next, we explain how these effects are accounted for within k·p formalism.

2.4.1 Strain

Strain fields can be calculated using the continuum theory of elasticity established by Cauchy and Poisson in the 1820s.[59] The strain tensor $\epsilon_{ij}(\mathbf{r})$ arising from the displacement field $\mathbf{u}(\mathbf{r})$ is defined by

$$\epsilon_{ij}(\mathbf{r}) = \frac{1}{2}\left(\frac{\partial u_i(\mathbf{r})}{\partial x_j} + \frac{\partial u_j(\mathbf{r})}{\partial x_i}\right). \tag{2.25}$$

This strain can be related to the stress forces by using the generalized Hooke's law

$$\sigma_{ij}(\mathbf{r}) = C_{ijkl}\,\epsilon_{kl}(\mathbf{r}), \tag{2.26}$$

where σ_{ij} denotes the stress tensor and C_{ijkl} is the four-rank stiffness tensor.[7] The number of independent constants in C_{ijkl} is determined by the symmetry of the crystal structure. The volumetric elastic energy of the system is formulated as a function of these tensors as follows:[60]

$$U = \frac{1}{2}\sigma_{ij}\,\epsilon_{ij} = \frac{1}{2}C_{ijkl}\,\epsilon_{ij}\,\epsilon_{kl}. \tag{2.27}$$

In practice, the system is initially considered as the matrix material not strained and the QD compressed/expanded by an initial strain that is estimated from the lattice constants of the materials. Then, the system is allowed to relax to the equilibrium state and the strain and displacement fields are calculated by minimizing the elastic energy.

Strain in [001]-grown ZB structures

In cubic materials as ZB, strain is isotropic and the initial strain of the QD is calculated as

$$\epsilon^0_{xx} = \epsilon^0_{yy} = \epsilon^0_{zz} = \left(\frac{a_{QD} - a_m}{a_m}\right) \tag{2.28}$$

with a_m and a_{QD} denoting the lattice parameter of the matrix and the QD materials, respectively. Here, $\epsilon^0 > 0$ indicates expansion and $\epsilon^0 < 0$ compression of the QD.

Due to the high symmetry of cubic crystals only three elastic constants are independent. The stiffness tensor in Voigt notation ($C_{xxxx} = C_{11}$,

[7] Note that there is an implied sum over repeated indices (Einstein summation notation).

$C_{xxyy} = C_{12}$, and $C_{xyxy} = C_{44}$) is as follows: [61]

$$C_{ZB} = \begin{pmatrix} C_{11} & C_{12} & C_{12} & 0 & 0 & 0 \\ C_{12} & C_{11} & C_{12} & 0 & 0 & 0 \\ C_{12} & C_{12} & C_{11} & 0 & 0 & 0 \\ 0 & 0 & 0 & C_{44} & 0 & 0 \\ 0 & 0 & 0 & 0 & C_{44} & 0 \\ 0 & 0 & 0 & 0 & 0 & C_{44} \end{pmatrix}. \tag{2.29}$$

Substituting (2.29) into (2.27) one obtains the expression to compute the strain energy of cubic structures. It reads

$$\begin{aligned} U_{ZB} =& \frac{1}{2}\Big[C_{11}\left(\epsilon_{xx}^2 + \epsilon_{yy}^2 + \epsilon_{zz}^2\right) + 2\,C_{12}\left(\epsilon_{xx}\epsilon_{yy} + \epsilon_{xx}\epsilon_{zz} + \epsilon_{yy}\epsilon_{zz}\right) \\ &+ 4\,C_{44}\left(\epsilon_{xy}^2 + \epsilon_{xz}^2 + \epsilon_{yz}^2\right)\Big]. \end{aligned} \tag{2.30}$$

Strain in [0001]-grown WZ structures

WZ crystal structure is anisotropic and the unit cell is defined by two lattice constants: one in the z direction (c) and the other in the in-plane direction (a). Therefore, the initial strain will also depend on the direction, being

$$\epsilon_{xx}^0 = \epsilon_{yy}^0 = \left(\frac{a_{QD} - a_m}{a_m}\right) \qquad \text{and} \qquad \epsilon_{zz}^0 = \left(\frac{c_{QD} - c_m}{c_m}\right), \tag{2.31}$$

where a_{QD} and c_{QD} are the lattice parameters of the QD, and a_m and c_m are the ones of the matrix material.

WZ structures have lower symmetry and five different constants are required to define the stiffness tensor[61]

$$C_{WZ} = \begin{pmatrix} C_{11} & C_{12} & C_{13} & 0 & 0 & 0 \\ C_{12} & C_{11} & C_{13} & 0 & 0 & 0 \\ C_{13} & C_{13} & C_{33} & 0 & 0 & 0 \\ 0 & 0 & 0 & C_{44} & 0 & 0 \\ 0 & 0 & 0 & 0 & C_{44} & 0 \\ 0 & 0 & 0 & 0 & 0 & C_{66} \end{pmatrix}. \tag{2.32}$$

Here, $C_{xxxx} = C_{11}$, $C_{xxyy} = C_{12}$, $C_{zzzz} = C_{33}$, $C_{xxzz} = C_{13}$, $C_{xyxy} = C_{44}$, and $C_{66} = \frac{1}{2}\left(C_{11} - C_{12}\right)$.

Finally, the elastic energy in strained WZ systems is given by

$$\begin{aligned} U_{WZ} = &\frac{1}{2}\Big[C_{11}\left(\epsilon_{xx}^2+\epsilon_{yy}^2\right)+C_{33}\epsilon_{zz}^2+2\,C_{12}\epsilon_{xx}\epsilon_{yy}+2C_{13}\epsilon_{zz}\left(\epsilon_{xx}+\epsilon_{yy}\right) \\ &+4\,C_{44}\left(\epsilon_{xz}^2+\epsilon_{yz}^2\right)+2\,\left(C_{11}-C_{12}\right)\epsilon_{xy}^2\Big]. \end{aligned} \tag{2.33}$$

2.4.2 Piezoelectric polarization

The application of an external strain causes the displacement of the charged atomic nuclei from their original positions in the crystal. In semiconductor materials lacking a center of inversion this displacement produces an electric polarization. The magnitude of such polarization is, neglecting higher-order contributions, proportional to the strain field as:

$$P_i(\mathbf{r}) = e_{ijk}\,\epsilon_{jk}(\mathbf{r}), \tag{2.34}$$

with e_{ijk} being the piezoelectric tensor.

The charge density $\rho(\mathbf{r})$ arising from the polarization $\mathbf{P}(\mathbf{r})$ is given by

$$\rho(\mathbf{r}) = -\nabla\cdot\mathbf{P}(\mathbf{r}). \tag{2.35}$$

Then, the corresponding electrostatic potential $\phi_{pz}(\mathbf{r})$ generated by $\rho(\mathbf{r})$ is obtained by solving Poisson's equation

$$\varepsilon_0\nabla\left[\varepsilon_r(\mathbf{r})\cdot\nabla\phi_{pz}(\mathbf{r})\right] = -4\pi\rho(\mathbf{r}), \tag{2.36}$$

where ε_0 is the dielectric constant in vacuum and ε_r is the material-dependent dielectric tensor.

Piezoelectric polarization in [001]-grown ZB structures

For ZB crystals, only one independent coefficient does not vanish in the piezoelectric tensor e_{ijk}. It reads

$$e_{ZB} = \begin{pmatrix} 0 & 0 & 0 & e_{14} & 0 & 0 \\ 0 & 0 & 0 & 0 & e_{14} & 0 \\ 0 & 0 & 0 & 0 & 0 & e_{14} \end{pmatrix}, \tag{2.37}$$

and the resulting polarization after applying equation (2.34) is

$$\mathbf{P}(\mathbf{r}) = e_{14}\begin{pmatrix} \epsilon_{yz} \\ \epsilon_{xz} \\ \epsilon_{xy} \end{pmatrix}. \tag{2.38}$$

Piezoelectric polarization in [0001]-grown WZ structures

The piezoelectric tensor for WZ semiconductors depends on three non-vanishing coefficients:

$$e_{WZ} = \begin{pmatrix} 0 & 0 & 0 & 0 & e_{15} & 0 \\ 0 & 0 & 0 & e_{15} & 0 & 0 \\ e_{31} & e_{31} & e_{33} & 0 & 0 & 0 \end{pmatrix}. \tag{2.39}$$

In contrast to cubic ZB systems, WZ materials present an additional contribution to the total polarization, the so-called spontaneous polarization or pyroelectricity. It is present even without strain and originates from the inversion symmetry breaking along the c axis in the WZ lattice.[62] The spontaneous polarization in WZ systems is a constant vector in the z direction, $\mathbf{P}_{sp} = (0, 0, P_{sp})$, where P_{sp} is material dependent. Therefore, the total polarization $\mathbf{P}(\mathbf{r})$ coming from both contributions is given by

$$\mathbf{P}(\mathbf{r}) = \mathbf{P}_{pz}(\mathbf{r}) + \mathbf{P}_{sp}(\mathbf{r}) = \begin{pmatrix} e_{15}\epsilon_{xz} \\ e_{15}\epsilon_{yz} \\ e_{31}(\epsilon_{xx} + \epsilon_{yy}) + e_{33}\epsilon_{zz} + P_{sp} \end{pmatrix}. \tag{2.40}$$

2.4.3 k·p Hamiltonians including strain and polarization fields

As stated before, strain and polarization fields modify the energy band structure and, thus, these effects need to be incorporated into the k·p models discussed in previous sections.

With this aim in mind, we follow the approach taken by Bir and Pikus [32] who used group theory to calculate the strain effects on the band structure by employing deformation potentials.[8] Since the strain considered here is small, it may be treated as a perturbation. The additional Hamiltonian accounting for the strain contributions is derived up to first-order perturbation theory.

The resulting strain Hamiltonians H_ϵ using this procedure have the same form as their k·p Hamiltonians counterparts, but replacing $k_i k_j$ by ϵ_{ij} and the corresponding mass parameters by deformation potentials. This can be understood taking into account that the strain tensor is symmetric and, thus, its transformation properties are identical to $k_i k_j$. The explicit form

[8] Deformation potential theory was originally formulated by Bardeen and Shockley [63] and then generalized by Herring and Vogt [64].

of the CB and VB strain Hamiltonians for both ZB and WZ structures are collected in appendix C.

On the other hand, the implementation of the piezoelectric potential $\phi_{pz}(\mathbf{r})$ generated by the charge polarization is straightforward as it enters the Hamiltonian as a diagonal term.

$$H_{pz} = e\,\phi_{pz}(\mathbf{r})\,\mathcal{I}, \tag{2.41}$$

with $\mathcal{I}$ denoting the identity matrix and e the particle charge.

CHAPTER 3

Magnetic field effects in semiconductor structures

Zero-dimensional semiconductor nanostructures are systems with appealing optical and electronic properties for many applications. In most semiconductors, these properties are governed by the band-edge energies at the Γ point. The application of external fields modifies the system band structure, thus offering an easy way to manipulate the QD features.

In general, particles in QDs have lighter effective masses and are subject to weaker confinements compared to atoms. As a consequence, the effect of a magnetic field in these systems is much stronger and may exceed the confinement energies, resulting in the emergence of new effects not present in atoms for the magnetic field intensities accessible in the laboratory. This opens the possibility of externally controlling QDs by means of magnetic fields. To that end, this topic has been the subject of intense research during the last decades.[10, 65]

Furthermore, magnetic fields are also responsible for the manifestation of the AB effect, which was predicted by Aharonov and Bohm [66] in 1959. They showed that, contrary to classical mechanics, charged particles are affected by potentials even in the regions where all fields vanish. This was soon confirmed in the laboratory by interference experiments.[67] In the 1980s, the progress on the fabrication and detection techniques allowed the observation of such phenomenon also in nanoscale ring structures, thus raising anew the old AB effect. These nanostructures are doubly-connected quantum systems, usually called QRs, that show distinct properties compared to QDs, a singly-connected structure. Since then, much effort has been dedicated to understand the implications of the AB effect in QRs.[68, 69]

This chapter reviews three papers[1] focusing on the behavior of two different systems under an externally applied magnetic field. First, the electronic structure of GaN/AlN QDs with ZB crystal structure and its dependence on the magnetic field is studied. In particular, we pay special attention to factors influencing the spin mixing of the hole states and the circumstances that may lead to ground state transitions. The second half of this chapter deals with the AB effect in hexagonal core-shell systems. The AB periodic oscillations of the electron energy spectrum for single- and few-electron hexagonal QRs are investigated. We compare the results with the well-known case or circular QRs to emphasize the consequences of the symmetry lowering of the confinement potential.

3.1 Magnetic-field modulation of the hole ground state in cubic GaN/AlN QDs

GaN/AlN QDs present good properties for optoelectronic applications owing to the direct wide band gap of GaN and AlN (3.5 and 6.25 eV,[70] respectively) that has led to successfully use them in blue lasers and LEDs.[71, 72] Furthermore, these structures show strong particle confinement due to their large band offsets and large effective masses, and also weak SOI.[73] The former allows to use them at high temperatures, while the latter makes them promising candidates for spintronic applications.

Nitrides semiconductors are commonly grown in WZ phase, but under certain conditions cubic ZB GaN/AlN QDs can also be fabricated. The symmetry of hexagonal crystals originates strong piezoelectric and spontaneous polarization fields of several MV/cm in WZ heterostructures,[73] which heavily quenches the spin relaxation times. However, these built-in fields are negligible in ZB systems and much longer relaxation times are expected. Indeed, Lagarde *et al.* [74] studied the exciton spin dynamics of self-assembled GaN/AlN ZB QDs and showed that the linear polarization persists up to room temperature and the spin relaxation times (exceeding 10 ns) are two or three orders of magnitude longer than in WZ phase.

Both optical polarization and exciton spin dynamics are governed by the VB mixing.[43, 75, 76] In GaN, the admixture between the topmost valence subbands is expected to be important since the SOI is weak (the spin-orbit splitting Δ_0 is only 17 meV [70]) and the so subband is close in

[1] The full version of them can be found in pages 155, 163 and 169 of the present dissertation.

energy to the lh and hh ones. Nevertheless, confinement and magnetic fields are known to modify the band edge energies, so that VB mixing in QDs is surely also affected by these factors and calculations are required to assess their influence.

The system investigated is a self-assembled cubic GaN/AlN QD with cylindrical shape. The dependence of the VB mixing on the QD size and on an axial magnetic field are studied. In order to do that, taking into account that the mass parameters of GaN and AlN are quite different and their spin-orbit splitting Δ_0 small, a six-band position-dependent Hamiltonian is used. The explicit form of this Hamiltonian can be found in appendix A.1.2. Since the system studied has axial symmetry, such Hamiltonian can be simplified by using cylindrical coordinates instead of Cartesian ones. In addition, the axial approximation $\tilde{\gamma} = \frac{1}{2}(\gamma_2 + \gamma_3)$[77, 78] is applied, so that the Hamiltonian becomes cylindrically symmetric and the problem can be reduced to two-dimensions by analytically integrating the angular coordinate. In axially symmetric systems the total angular momentum, $F_z = m_z + J_z$, is well defined and the states can be labeled by their F_z. Here, m_z and J_z are the envelope and Bloch angular momentum, respectively. The resulting Hamiltonian $H_{BF}^{ZB}(F_z)$ in cylindrical coordinates is shown in appendix A.1.3.

Additionally, an uniform magnetic field applied along the [001] direction, $\mathbf{B} = (0, 0, B_0)$, is included by carrying out the replacement of the canonical momentum by the kinetic one before applying the EFA, following reference [50]. Such magnetic field is described by the vector potential in the symmetric gauge $\mathbf{A} = \frac{B_0}{2}(-y, x, 0)$. The total Hamiltonian reads

$$H(F_z) = H_{BF}^{ZB} + H^B + V(\rho, z)\,\mathcal{I}, \tag{3.1}$$

with ρ being the radius coordinate and $\mathcal{I}$ the identity matrix. H^B is the Hamiltonian including the magnetic field contributions. It has the following nonzero elements:

$$H_{11}^B = -\left(\gamma_1 + \gamma_2\right)\left[\frac{B_0^2\,\rho^2}{8} + \frac{B_0\left(F_z - \frac{1}{2}\right)}{2}\right] \tag{3.2a}$$

$$H_{22}^B = -\left(\gamma_1 - \gamma_2\right)\left[\frac{B_0^2\,\rho^2}{8} + \frac{B_0\left(F_z - \frac{1}{6}\right)}{2}\right] \tag{3.2b}$$

$$H_{33}^B = -\left(\gamma_1 - \gamma_2\right)\left[\frac{B_0^2\,\rho^2}{8} + \frac{B_0\left(F_z + \frac{1}{6}\right)}{2}\right] \tag{3.2c}$$

$$H_{44}^B = -\left(\gamma_1 + \gamma_2\right)\left[\frac{B_0^2\,\rho^2}{8} + \frac{B_0\left(F_z + \frac{1}{2}\right)}{2}\right] \tag{3.2d}$$

$$H_{55}^B = -\,\gamma_1\left[\frac{B_0^2\,\rho^2}{8} + \frac{B_0\left(F_z + \frac{1}{6}\right)}{2}\right] \tag{3.2e}$$

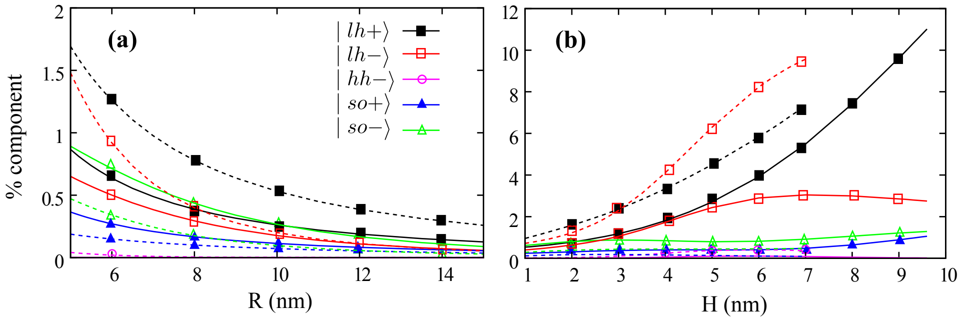

Figure 3.1: Composition of the minor hole subbands as a function of (a) the QD radius (fixed height $H = 1.5$ nm) and (b) the QD height (fixed radius $R = 6$ nm). In both panels, solid lines correspond to GaN/AlN QDs and dashed lines correspond to InGaAs/GaAs QDs.

$$H_{66}^B = -\gamma_1 \left[\frac{B_0^2 \rho^2}{8} + \frac{B_0 \left(F_z - \frac{1}{6}\right)}{2} \right] \tag{3.2f}$$

$$H_{25}^B = H_{52}^B = -\gamma_2 \frac{B_0}{3} \tag{3.2g}$$

$$H_{36}^B = H_{63}^B = \gamma_2 \frac{B_0}{3} \tag{3.2h}$$

Please note that (3.2) differ from (2.21) because the spin Zeeman splitting is disregarded here.

All simulations are carried out by numerically integrating (3.1). Both GaN/AlN and InGaAs/GaAs QDs are considered for comparison and the corresponding material parameters can be consulted in the published paper (see page 155).

3.1.1 Effect of the aspect ratio

First, we perform calculations for both materials varying the aspect ratio of the dots. Preliminary calculations for a typical-size QD ($R = 6\,nm$ and $H = 1.5\,nm$ [74, 79]) show that the hole ground state has $F_z = \pm 3/2$ symmetry and a major contribution of the $|hh+\rangle$ component. In order to analyze the VB mixing, the relative weight of each component within the spinor is calculated as $c_i = \frac{\langle f^{(i)}|f^{(i)}\rangle}{\sum_{j=1}^{6}\langle f^{(j)}|f^{(j)}\rangle}$, and the results for the minor components represented in figure 3.1. Solid lines are used for GaN/AlN QDs and dashed lines for InGaAs/GaAs QDs.

Table 3.1: Effective masses of hh, lh and so (times m_0)

	m^z_{hh}	m^z_{lh}	$m^\perp_{hh}$	$m^\perp_{lh}$	m_{so}
GaN	0.85	0.24	0.29	0.52	0.37
InGaAs	0.38	0.05	0.07	0.15	0.09

Two series of calculations are carried out: one varying the QD radius and the other varying the QD height. On one hand, figure 3.1(a) shows the results for variable radius and fixed height $H = 1.5\,\text{nm}$. It can be seen that the weight of the minor components decreases with R for both materials. On the other hand, the variation of the minor components contribution as a function of the QD height ($R = 6\,\text{nm}$) is depicted in figure 3.1(b). The behavior is now opposite and the weight increases with H.

These results can be understood taking into account the effective masses of the bands along the z ([001] axis) and the lateral directions. The concrete values are summarized in table 3.1. In QDs with vertical confinement much stronger than the horizontal one, such as the ones considered in figure 3.1(a) and figure 3.1(b) at smaller H, the lateral confinement can be disregarded. Since the kinetic energy in the z direction is larger for the lh and so bands ($m^z_{hh} > m^z_{lh}$), their energy separation from the hh ground state increases for smaller H and their coupling weakens. Consequently, lh and so components are less important the smaller the aspect ratio (H/2R) is, as shown in figure 3.1(a). Contrarily, as H increases the lateral confinement becomes more important and the weight of the lh band raises ($m^\perp_{hh} < m^\perp_{lh}$). In fact, in high enough QDs a ground state transition from $F_z = \pm 3/2$ symmetry to $F_z = \pm 1/2$ symmetry takes place. This is the situation in figure 3.1(b), where the curves have been truncated at the transition points. Now the ground state has dominant lh character and can be used to emit strongly linearly polarized light.[80]

It is also worth stressing the overall high spin purity obtained for both materials. This can be attributed to the fact that $|hh+\rangle$ is the only component of the $F_z = 3/2$ ground state whose envelope function has angular momentum $m_z = 0$, what stabilizes this component. In addition, a direct comparison between both materials in figure 3.1 reveals the smaller spin admixture for GaN/AlN. This high spin purity is in contrast to the initial predictions based on the much heavier effective masses and the smaller bulk spin-orbit splitting of GaN. It is, however, consistent with the long spin relaxation times observed in reference [74]. This surprising behavior can be explained considering the coupling terms in Hamiltonian A.3. For example, many of these terms are proportional to $\tilde{\gamma}$ and this parameter is much smaller in GaN, $\tilde{\gamma}_{GaN} = 0.925$, than in InGaAs, $\tilde{\gamma}_{InGaAs} = 4.51$, thus justifying the smaller VB mixing.

3.1.2 Magnetic field modulation

Typical QDs have an aspect ratio of about 1/8 [79] and present a ground state with $F_z = \pm 3/2$ symmetry that is relatively far in energy from other states. This fact, together with the large effective masses of GaN, impedes the manipulation of the electronic structure via magnetic fields. Nevertheless, the energy of the lh and hh bands is similar in dots with aspect ratio close to 1, so controlling the character of the hole ground state by using moderate magnetic fields should be possible in such dots.

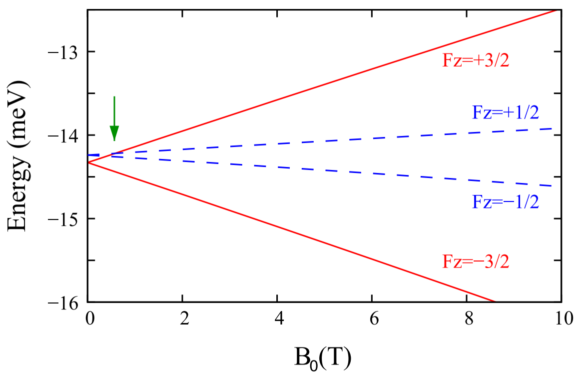

Figure 3.2: Magnetic-field-induced energy splitting of the lowest-lying hole states in a GaN/AlN QD with aspect ratio ≈ 1. The arrow indicates the ground state transition point, $B_0 \approx 0.6\,\mathrm{T}$.

Figure 3.2 illustrates the orbital Zeeman splitting of the topmost VB states in a GaN/AlN QD with aspect ratio approximately 1. Blue dashed lines correspond to $F_z = \pm 1/2$ states and red solid lines correspond to $F_z = \pm 3/2$ states, which present a major contribution of $|lh\rangle$ and $|hh\rangle$ components, respectively. In the absence of a magnetic field the states are degenerate, but for finite B_0 the degeneracy is broken and the states split. The magnitude of the splitting is proportional to the coefficients of the linear-in-B terms in equation (3.2): $(\gamma_1 + \gamma_2)/2$ for $|hh\pm\rangle$ and $(\gamma_1 - \gamma_2)/6$ for $|lh\pm\rangle$. Then, the splitting of $|hh+\rangle$ is larger and the ground state undergoes a transition from $F_z = +1/2$ to $F_z = +3/2$ at $B_0 \approx 0.6\,\mathrm{T}$[2]. As

[2]Note that hole states have negative energies.

a consequence, because $F_z = +1/2$ and $F_z = +3/2$ yield different optical polarizations, these results show that external magnetic fields can be used to modify the optical response of GaN/AlN QDs.

3.2 Aharonov-Bohm effect in systems with hexagonal symmetry

Nanowires are one-dimensional (1D) nanostructures in which carriers are confined laterally but move freely along the growth direction. Most nanowires made of III-V semiconductors present an hexagonal section when their diameter is less than 400 nm.[81–85] Taking this structure as starting point, core-multishell nanowires can be obtained after a few overcoating processes.[86, 87] Here, the electron motion can be further restricted in the radial direction by choosing the appropriate material sequence. Figure 3.3 shows an example of a multishell nanowire cross section in which a potential well is created by the misalignment of the CBs of the constituent materials. The electrons in the nanowire are then confined into a hexagonal prismatic tube surrounding the core. In addition, confinement in the growth direction can also be generated by cutting the nanowires or by modulating the materials in this direction, thus yielding hexagonal flat QRs.[88, 89]

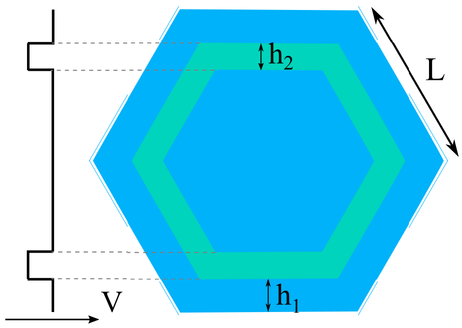

Figure 3.3: Drawing of a core-multishell nanowire cross section. Free electrons are confined into the hexagonal ring (green region). The band-edge profile showing the square-well-type confinement potential is indicated, as well as some geometry parameters.

Recent publications have shown that electrons in hexagonal QRs are not homogeneously distributed over the entire structure. They are mainly localized at the corners of the ring, giving rise to quasi-1D channels in the nanowires.[90, 91] Furthermore, in multi-particle systems the degree of localization is further enhanced as the number of electrons increases up to six.[92] This is a consequence of many-particle interactions, demonstrating the important role of correlation in these systems. The charge inhomogeneous localization constitutes a remarkable difference in comparison to circularly-symmetric systems which, in turn, may also result in distinct behavior and properties.

It is well established that when a magnetic field is axially applied to a ring or a tubular system the AB effect emerges. It manifests itself in the electronic spectra, magnetization, optical and transport properties of QRs.[69] For instance, the single-electron energy spectrum of a circular QRs shows an integer and periodic AB oscillation pattern.[93, 94] In nanowires, AB-like oscillations have also been observed in magnetotransport experiments performed on radial heterostructures.[95–97] Most theoretical works studying AB-related effects have considered systems with axial symmetry, but little is known about the implications of a symmetry lowering.

The aim of this section is to investigate the response of correlated hexagonal structures to an external axial magnetic field. In particular, we study AB-derived properties, e.g. ground-state energy and magnetoconductance oscillations, in single- and few-electron hexagonal QRs and core-multishell nanowires. The results are compared with the ones of their circular counterparts to explore the role of the hexagonal symmetry.

3.2.1 AB effect in hexagonal quantum rings

We first consider a flat hexagonal QR similar to that represented in figure 3.3 with $L = 66.5\,\text{nm}$, $h_1 = 13.5\,\text{nm}$ and $h_2 = 6.8\,\text{nm}$. The materials are GaAs for the ring and AlAs for the core and the outer shell. All parameters, namely effective masses, CB offset and dielectric constants, are taken from reference [92]. We carry out calculations of the low-energy spectrum for N interacting electrons, from $N = 1$ up to $N = 7$, in the low-density regime.

Single-particle energy spectrum

The position-dependent effective Hamiltonian describing a single electron under an external magnetic field reads

$$H_{sp} = \frac{1}{2}\left(\mathbf{p} + \mathbf{A}\right)\frac{1}{m^*(\mathbf{r})}\left(\mathbf{p} + \mathbf{A}\right) + V(\mathbf{r}) \tag{3.3}$$

where m^* is the isotropic effective mass and $\mathbf{A} = \frac{B}{2}(-y, x, 0)$ is the vector potential defining the magnetic field along the axial direction. Equation

(3.3) is numerically solved following the finite element method over a uniform, triangular mesh. A grid with the same symmetry of the system is used to guarantee high accuracy, specially in the description of the boundary conditions, and to avoid artificial asymmetries in the discretization.

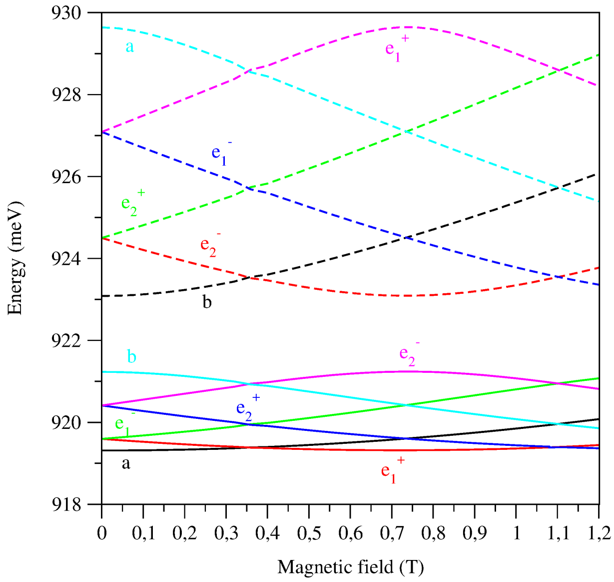

Figure 3.4: Single-electron energy spectrum as a function of the magnetic field intensity. The states are labeled and presented in different line styles according to the C_6 symmetry group.

Figure 3.4 shows the energy of the twelve lowest-lying states as a function of the magnetic field. Similarly to circular QRs, regular AB oscillations of the ground state energy are observed. However, for the hexagonal QRs the states are organized in groups of 6 orbitals each, separated by an energy gap of $\approx 2\,\text{meV}$. This is in clear contrast to the case of circular rings where all states form a single ensemble. The different behavior of the two structures can be justified from symmetry considerations. On one hand, systems with circular symmetry have an infinite number of irreducible representations (irreps), so that all states are associated to different irreps and can cross. On the other hand, orbitals in hexagonal QRs are associated to the six different irreps of the C_6 symmetry group. The states with different symmetry can cross while the states with the same symmetry anticross. As a result, groups of 6 orbitals with a different irrep each form a shell within which they cross, but that is spit from other shells. The states in figure 3.4 are labeled with their associated irreps to illustrate this.

Multi-particle energy spectra

Next, we examine the effect of populating the system with a few interacting electrons. To this purpose, a full configuration interaction (FCI) approach is used.[98] FCI is a variational method that takes into account all possible Slater determinants out of the one-electron basis set chosen. Then, an approximate solution for the multi-particle problem is obtained by exactly solving the Hamiltonian within this basis set. The many-electron Hamiltonian is as follows

$$H_{mp} = \sum_{i\sigma} \epsilon_i e^{\dagger}_{i\sigma} e_{i\sigma} + \frac{1}{2} \sum_{ijkl} \sum_{\sigma\sigma'} U_{ijkl} e^{\dagger}_{i\sigma} e^{\dagger}_{j\sigma'} e_{k\sigma'} e_{j\sigma} \tag{3.4}$$

with $e_{i\sigma}$ ($e^{\dagger}_{i\sigma}$) being the annihilation (creation) operator for an electron in the state i and spin σ. The few-electron states are obtained by exactly diagonalizing equation (3.4) using 24 single-particle spin-orbitals as basis, i.e. two shells of six orbitals.

In correlated systems the period and amplitude of the energy oscillations decrease with the electron population.[99–101] The oscillation period scales as $1/N$ and, hence, this phenomenon is known as the fractional AB effect.[102] In figure 3.5 the energy spectra for a QR populated with up to seven electrons are displayed. The energies are taken relative to the ground-state energy at zero magnetic field (see the horizontal red line in the graphs). We observe regular oscillations for both $N = 2$ and $N = 3$, the period of which is in perfect agreement with the fractional AB effect. In fact, the first crossing of the ground state in the single-particle case (figure 3.4) is at $B \approx 0.4\,\mathrm{T}$, and is reduced to $B \approx 0.2\,\mathrm{T}$ and $B \approx 0.13\,\mathrm{T}$ for $N = 2$ and $N = 3$, respectively. For $N = 4$, $N = 5$ and $N = 7$ the oscillations are not regular and the period clearly deviates from the behavior expected considering the fractional AB effect. The results for $N = 6$ deserve especial consideration since the ground state does not cross with other excited states in the range of magnetic fields under study. The AB effect is, thus, completely suppressed.

The above results can also be seen, and perhaps more clearly, in figure 3.6 where the corresponding magnetization, $M = \partial E/\partial B$, is represented. Here, the magnetization for different N has been offset for clarity. Figure 3.6 illustrates the loss of regularity in the oscillations period as N increases as well as the flat magnetization profile for $N = 6$.

The above-mentioned deviations in the oscillation period for larger N have already been found in previous calculations.[99, 101] This behavior

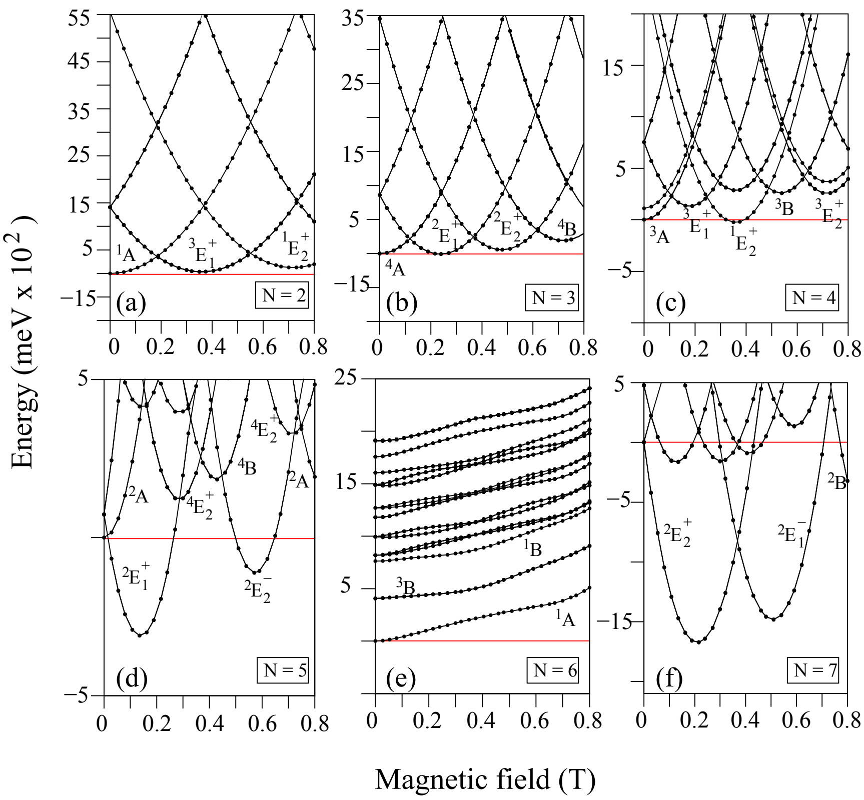

Figure 3.5: Energy of the lowest-lying states *vs.* the magnetic field intensity for systems containing from $N = 2$ up to $N = 7$ interacting electrons. The energy values are relative to the ground state energy at $B = 0$, indicated by a horizontal red line. The states are labeled according to the C_6 symmetry group and spin multiplicity.

can be justified in the framework of the empirical Hubbard model.[103] In this model it was concluded that the fractional AB oscillations emerge only for small values of $\alpha = Nt/UL$, where t is the tunneling integral, U is the repulsion integral and L is the number of sites along the QR where the states are localized. The value of α is inversely proportional to the number of electrons. Therefore, a low-density regime is needed to observe the fractional AB oscillations, explaining the deviations for larger N.

Conversely, the suppression of the AB effect in multi-particle systems has not been reported in literature. To understand this result, we repeat the calculations for $N = 6$ but introducing a scaling factor f to the electron-electron integrals. In this way we are able to determine the role of Coulomb interactions. Four series of calculations are carried out for $f = 0$, 0.1, 0.2

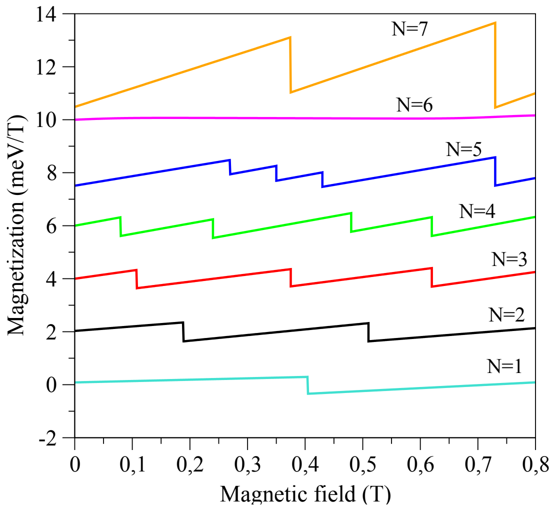

Figure 3.6: Magnetization profiles for a N-electron hexagonal QR with N varying from 1 to 7. For the sake of clarity, the results for each N have been offset by 2 meV/T.

and 0.5, and the results are summarized in figure 3.7. For a non-interacting system, figure 3.7(a), two different states with the same total symmetry and spin, ${}^1A$, cross at $B \approx 0.4\,\text{T}$. The configurations of these states are $a^2(e_1^+)^2(e_1^-)^2$ and $(e_1^+)^2a^2(e_2^+)^2$.[3] When the Coulomb interaction is activated the states with ${}^1A$ symmetry anticross. The magnitude of the anticrossing increases with f as can be easily seen by comparing panels (b), (c) and (d) of figure 3.7, thus causing the suppression of the AB oscillations.

It is worth mentioning that calculations for a three times smaller hexagonal QR have also been performed. The results obtained (not shown) reveal that the AB suppression is no longer present. This is because in this density regime the anticrossing is not big enough and the ${}^3B$ state (see figure 3.5) cross the ${}^1A$ ground state, originating a non-flat magnetization profile.

In summary, the AB suppression found for a hexagonal QR populated by six electrons is a symmetry-related effect that emerges in the high-correlation, low-density regime as a consequence of an anticrossing between the ground state and an excited state with the same symmetry.

[3] We use the standard Schoenflies notation with lower- and upper-case letters referring to the symmetry of orbitals and N-electron states, respectively.

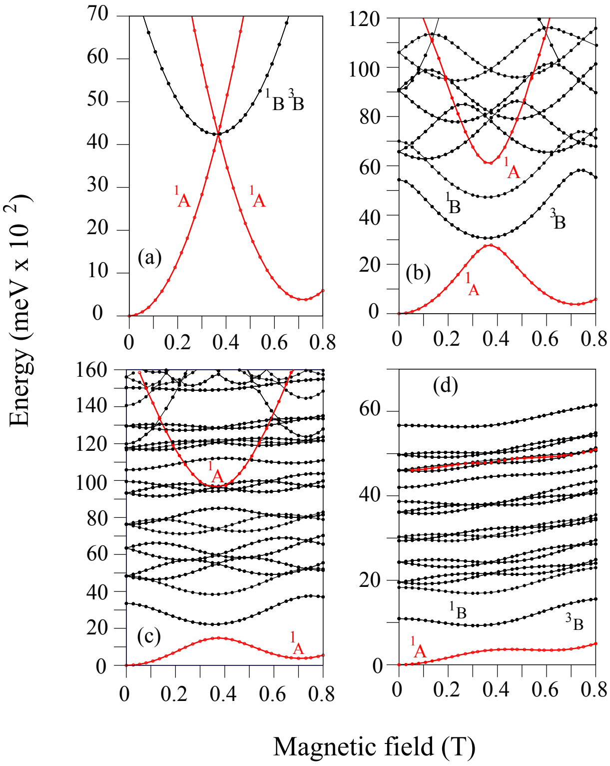

Figure 3.7: Same as figure 3.5(e) but for different weight of the electron-electron interaction integrals. This weight is modulated via an scaling factor f, which takes $f = 0$, 0.1, 0.2 and 0.5 in panels (a), (b), (c) and (d), respectively. The total symmetry of the main states is indicated and the ^1A ones are shown in red to improve their visibility.

3.2.2 AB magnetoconductance oscillations and electron gas transitions in hexagonal core-shell nanowires

In this section, we investigate the electronic states and magnetoconductance of a core-shell hexagonal nanowire pierced by an external magnetic field along the growth direction. The nanowire considered is infinitely long and its cross section has the same form as figure 3.3. Here, it is composed by a GaAs core with a minimal diameter of 100 nm, a InAs shell with thickness of 25 nm, and an external 30-nm-thick capping layer of SiO_2.

Simulations are carried out within the spin-density-functional theory following an iterative procedure. Although the system is 3D, the translational invariance along the z direction allows one to write the wave function as

$\Psi(x, y, z) = e^{ikz}\phi(x, y)$. If one further assumes the motion of the electrons in the longitudinal and transverse directions to be decoupled, the problem reduces from 3D to 2D. The effective Kohn-Sham Hamiltonian reads:

$$H = H_{sp}(\mathbf{r}) + V_Z^{\sigma}(\mathbf{r}) + V_H(\mathbf{r}) + V_{XC}^{\sigma}(\mathbf{r}), \tag{3.5}$$

where H_{sp} is the single-particle Hamiltonian under an external magnetic field presented in equation (3.3). $V_Z^{\sigma}(\mathbf{r})$ is the Zeeman splitting term, $V_H(\mathbf{r})$ is the Hartree potential energy and $V_{XC}^{\sigma}(\mathbf{r})$ is the exchange-correlation potential. Finally, $\sigma =\uparrow, \downarrow$ denotes the spin index of the electrons.

The Zeeman term is given by

$$V_Z^{\sigma}(\mathbf{r}) = g^* \mu_B B \eta_{\sigma} \tag{3.6}$$

with g^* standing for the effective g-factor, μ_B for the Bohr magneton and η_{σ}=+1/2(-1/2) for $\sigma =\uparrow(\downarrow)$.

The Hartree potential energy is calculated as $V_H(\mathbf{r}) = -e\,\phi(\mathbf{r})$ after obtaining the electrostatic potential $\phi(\mathbf{r})$ by means of the Poisson equation

$$\nabla \varepsilon_r(\mathbf{r}) \nabla \phi(\mathbf{r}) = \frac{e}{\varepsilon_0} \left[\rho(\mathbf{r}) - \rho_D(\mathbf{r})\right]. \tag{3.7}$$

Here, $\rho(\mathbf{r})$ is the total free-electron charge density calculated from the Kohn-Sham eigenstates of equation (3.5). $\rho_D(\mathbf{r})$ corresponds to the density of donors and ε_r to the material-dependent dielectric constant.

The last term in (3.5), the exchange-correlation potential $V_{XC}^{\sigma}(\mathbf{r})$, is defined as the functional derivative within the local-spin-density approximation (LSDA). The correlation functional used in all calculations is the one proposed by Perdew and Wang [104].

First, equation (3.5) is numerically integrated by using a finite-element scheme, and taking $V_H = 0$ and $V_{XC}^{\sigma} = 0$. From the spin eigenstates obtained we calculate the free-electron charge density and, using this density, the associated values of V_H and V_{XC}^{σ}. Such potentials are incorporated in equation (3.5) and the process is started over. These steps are repeated iteratively until the convergence criteria are achieved.

In the subsequent sections, two device configurations are investigated: gate-all-around and back-gate. The gate-all-around configuration consists in an electrode surrounding the entire structure, so that the energy can be modulated while preserving the hexagonal symmetry of the system. This type of gate is simulated by forcing the electrostatic potential, $\phi(\mathbf{r})$, in the Poisson equation (3.7) to be that of the gate voltage V_g at all nanowire edges.

For a back-gate configuration we assume two flat electrons sandwiching the nanowire. This situation is simulated by defining the electrostatic potential to be zero at the boundary corresponding to one electrode and V_g at the other. Unlike the all-around-gate case, the hexagonal symmetry is broken in this configuration.

For the simulations of the present section we consider the GaAs core to be doped with a homogeneous density of donors $\rho_D = 5 \times 10^{15}\,\mathrm{cm}^{-3}$. The Fermi energy E_F is taken 75 meV above the InAs CB edge and the temperature is set to $T = 1.8\,\mathrm{K}$. All material parameters can be consulted in table I of the published article (page 169).

Low-magnetic-field regime

First, we study the electronic structure of the hexagonal core-shell nanowire for low magnetic fields and zero gate voltage, $V_g = 0$. The results (not shown) are qualitatively the same as for the hexagonal QR of the previous section. That is, the electron density is mainly localized at the corners of the InAs shell, and the states in the energy spectrum are organized in groups of six, presenting AB oscillations as the magnetic field intensity increases, same as figure 3.4. Nevertheless, now the spin degree of freedom is taken into account and the Zeeman splitting included in the simulations. As a consequence, the spin-degenerate states at $B = 0$ split for finite fields and two magnetic spin-subbands are formed: one with spin-up ($\uparrow$-MSS) and the other with spin-down ($\downarrow$-MSS). Each one of them is composed by six states of the same spin and show AB oscillations.

Next, we explore the result of applying a gate-all-around voltage to tune the Fermi energy of the system. To this end, the total magnetoconductance G is calculated for various, both negative and positive, voltages. The value of G is obtained using the linear-response Landauer formula,[4]

$$G_\sigma = \frac{e^2}{h} \sum_n \int_{B_{n,\sigma}} -\frac{\partial f(E - E_F, T)}{\partial E} dE, \qquad (3.8)$$

where f is the Fermi occupation function, with E_F and T being the Fermi energy and the temperature, respectively. The integral in equation (3.8) is performed along each energy spin-subband $B_{n,\sigma}$. The magnetoconductance results obtained are shown in figure 3.8. Typical oscillations arising from

[4] This formula assumes a fully ballistic regime which is not exactly the experimental regime in InAs nanowires. However, this simplified formula can be used to get correct qualitative results.

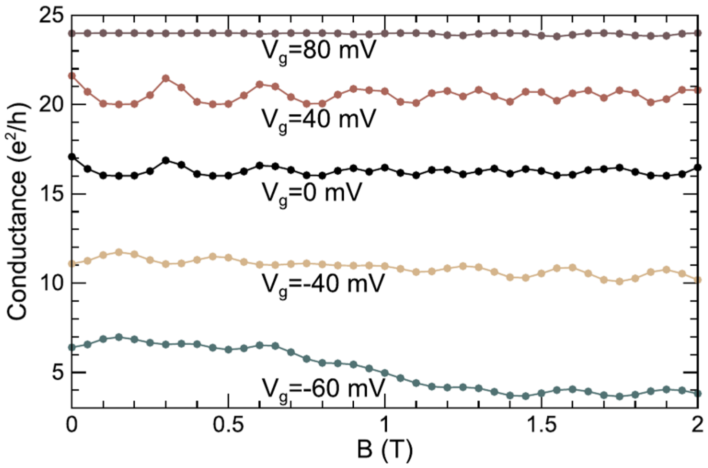

Figure 3.8: Total magnetoconductance for five gate-all-around voltages: $V_g = 80\,\mathrm{mV}$, $V_g = 40\,\mathrm{mV}$, $V_g = 0\,\mathrm{mV}$, $V_g = -40\,\mathrm{mV}$ and $V_g = -60\,\mathrm{mV}$.

the AB effect are observed for most V_g but are absent, for instance, at $V_g = 80\,\mathrm{mV}$, where the conductance is completely flat.

In order to get insight into this singular behavior, in figure 3.9 we represent the energy spectrum *vs.* the magnetic field for $V_g = -60\,\mathrm{mV}$, panel (a), and $V_g = 80\,\mathrm{mV}$, panel (b). By comparing both spectra, it can be seen that the gate voltage affects the width of the MSSs as well as the gaps separating them. For $V_g > 0$ the electron density is more localized at the corners of the InAs ring, see inset in figure 3.9(b). This is due to the larger electron-electron interaction, which is also responsible for the larger gaps between MSSs. Contrarily, for $V_g < 0$ the electron density is more delocalized, see inset in figure 3.9(a), and the gaps become smaller or even disappear. In addition to this, figure 3.9(b) also explains the flat magnetoconductance observed for $V_g = 80\,\mathrm{mV}$ in figure 3.8. The position of E_F exactly coincides with the energy gap between the second and third group of MSSs, so that it does not cross any MSS. As a result, the number of conducting channels is constant and so is the conductance profile. Since energy gaps between subbands increase with gate voltage, flat magnetoconductance profiles are more likely to be found at large positive V_g.

In light of the above results, one would expect to find flat magnetoconductances when sweeping V_g in transport experiments on hexagonal nanowires. However, typical profiles show flux periodic oscillations, [96, 97]

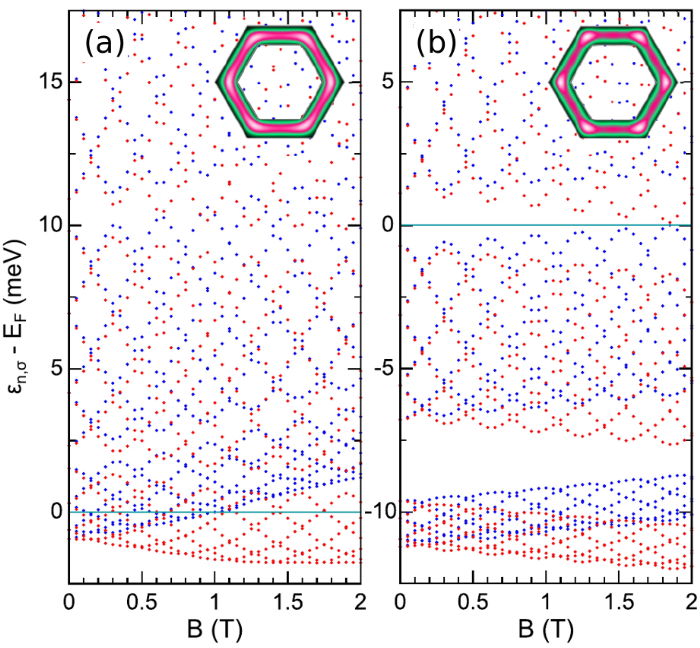

Figure 3.9: Energy spectrum as a function of the magnetic field for (a) $V_g = -60\,\mathrm{mV}$ and (b) $V_g = 80\,\mathrm{mV}$. Red and blue dots correspond to ↓-MSS and ↑-MSS, respectively. The horizontal black line represents the Fermi energy E_F. Insets in panels (a) and (b) show the electron density distribution at $B = 0$ for the nanowire cross section.

and a situation with constant G has never been observed experimentally. This may be due to the fact that the most common device configuration for manipulating the electron density is to use a back-gate, instead of a gate-all-around. The main difference between both configurations is the breaking of the hexagonal symmetry when a back-gate is used. We know from the previous section that the separation of the states in groups in the energy spectrum is a direct consequence of the hexagonal symmetry of the system. Therefore, a back-gate device is expected to present no significant gaps and a situation with constant G would not be possible, justifying the lack of flat profiles in experiments. Nonetheless, a back-gate voltage could also destroy the doubly-connected topology that originates the AB effect. In a such a case, AB oscillations should not emerge and one wonders why they are observed at all.

In order to understand the origin of the oscillations, we carry out the same calculations as in figures 3.8 and 3.9, but for a back-gate device. The total magnetoconductance profiles in figure 3.10 evidence that flux oscilla-

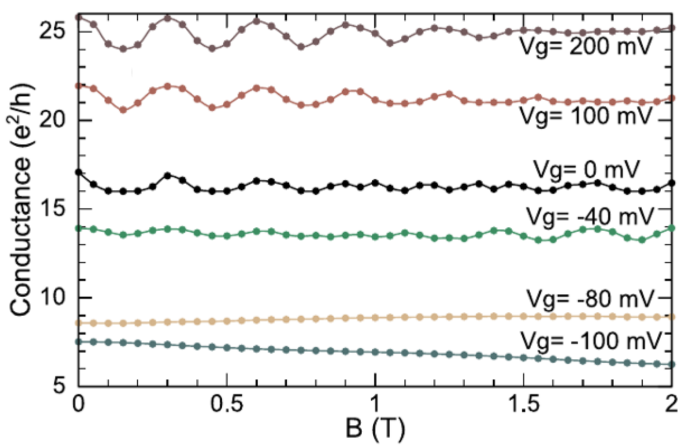

Figure 3.10: Same as figure 3.8 but for a back-gate configuration and different V_g.

tions take place for positive or slightly negative voltages but are absent for large enough negative values, $V_g = -80\,\mathrm{mV}$ and $V_g = -100\,\mathrm{mV}$. Again, this behavior can be explained looking at the energy spectra in figure 3.11. To illustrate both situations, we have chosen two V_g with different sign, $V_g = -80\,\mathrm{mV}$ in figure 3.11(a) and $V_g = 200\,\mathrm{mV}$ in figure 3.11(b). As shown in the insets, the back-gate voltage clearly reshapes the electron density distribution, which is pushed towards the top (bottom) half of the cross section for negative (positive) V_g. A comparison between both insets show that the doubly-connected topology is more robust for $V_g > 0$ since the electron density is more delocalized in panel (b) even though the voltage is stronger. As for the MSSs, for both V_g we see that states lower and higher in energy behave very differently. Lowest-lying states are more affected by the back-gate voltage and exhibit a quasi-linear dispersion with B, i.e. the doubly-connected topology is completely broken, while typical AB oscillations are present in more excited states. For $V_g = -80\,\mathrm{mV}$, the Fermi energy is in the region of states with linear dispersion and, thus, only states without doubly-connected topology are occupied. This justifies the flat magnetoconductance in figure 3.10 and the strongly localized electron density distribution in the inset of figure 3.11(a). In contrast, in 3.11(b) several states with doubly-connected topology are occupied, the electron density is more delocalized and the AB-like magnetoconductance oscillations persist. The latter is indeed the usual regime in magnetotransport experiments,[96, 97] what explains why only oscillating profiles have been reported in literature.

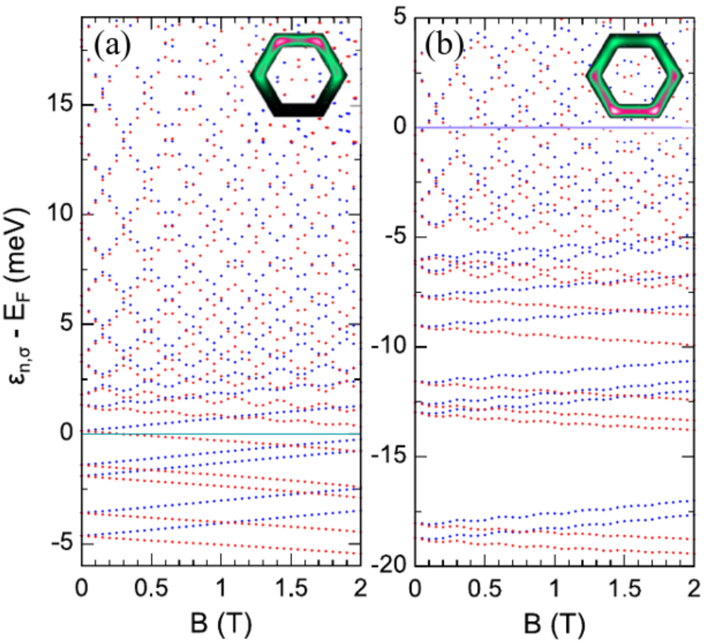

Figure 3.11: Same as figure 3.9 but for a back-gate device, and voltages (a) $V_g = -80\,\text{mV}$ and (b) $V_g = 200\,\text{mV}$.

High-magnetic-field regime

We next study the high-magnetic-field regime for the same hexagonal nanowire system. All simulations are performed considering the absence of external gates, i.e. $V_g = 0$. Figure 3.12 displays the MSSs up to $B = 20\,\text{T}$, where complete electron depletion occurs, and also the total electron density at selected fields. By comparing figures 3.12(b)-3.12(f), it is clear that as B increases the electron density undergoes a transition from being localized at the corners, panels (b) and (c), to a distribution with maximum density at the center of the facets, panels (e) and (f). This change in the electron density positioning is caused by the parabolic magnetic confinement. At low magnetic fields the confining potential originated from the materials band offset dominates, but at big enough fields the magnetic confinement becomes more important. The larger B is, the more the electrons are pushed to lower radius, i.e. at the center of the facets, giving rise to a corner-to-facet transition.

A signature of the aforementioned transition can be identified in the energy spectrum shown in figure 3.12(a). At zero magnetic field, the states are

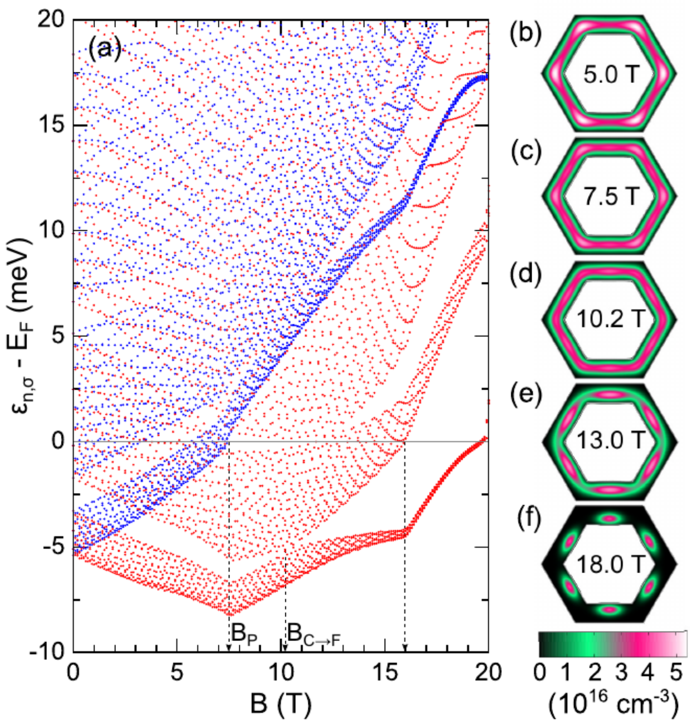

Figure 3.12: (a) MSSs for magnetic fields up to $B = 20\,\mathrm{T}$, where the complete electron depletion takes place. Dashed vertical lines are added to indicate the fields at which spin or charge transitions occur. (b)-(f) Electron density distribution at selected magnetic-field intensities.

organized in spin-degenerate MSSs. The lowest-lying MSS is composed by states whose electron density is localized at the corners, while the states of the second MSS have their electron density mostly localized at the system facets for orthogonality. As the magnetic field increases, the ↓-MSSs are stabilized and the ↑-MSSs destabilized due to the Zeeman effect. Besides this spin-splitting, we also see that the first two ↓-MSSs get closer in energy for larger B and eventually overlap at $B_{C\rightarrow F} \approx 10.2\,\mathrm{T}$. At this field, the electron density is equally distributed over the entire InAs ring and, therefore, $B_{C\rightarrow F} \approx 10.2\,\mathrm{T}$ can be identified as the transition point. For $B > B_{C\rightarrow F}$ the ↓-MSSs cross, and the lowest-lying states are now mainly localized at the facets of the hexagon. The same behavior is observed for the spin-up subbands, but they are already depopulated at this magnetic field and do not affect the electron density distribution.

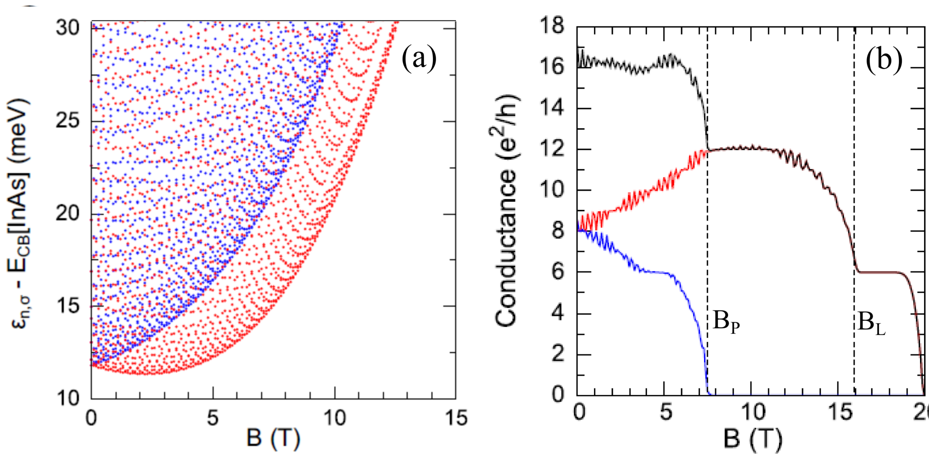

Figure 3.13: (a) Non-interacting MSSs with respect to the InAs CB edge. Both spin-up (blue) and spin-down (red) subbands are shown. (b) Total magnetoconductance $G = G_\downarrow + G_\uparrow$ (black) and spin-projected magnetoconductances $G_\downarrow$ (red) and $G_\uparrow$ (blue) as a function of the magnetic field B.

Figure 3.12(a) exhibits two additional transition points in the energy spectrum. They are characterized by noticeable changes in the slope of the MSSs and are indicated with dashed vertical lines in the graph. The first transition is found at $B_P \approx 7.5\,\mathrm{T}$, where the slope of the lowest-lying MSS changes sign from negative to positive. If one looks at figure 3.12(a) carefully, it can be observed that the transition coincides with the complete depletion of the last $\uparrow$-MSS with charge. Consequently, the system becomes completely polarized and B_P represents a transition to a ferromagnetic state. At fields higher than $B_{C\to F}$, the MSSs rearrange and tend to form Landau-like bands. When the magnetic field reaches $B_L \approx 16\,\mathrm{T}$, a second transition appears as an abrupt change in the subband slope. At this point, the first-excited $\downarrow$-MSS is fully depleted and only one subband remains below the Fermi energy. Finally, this subband becomes completely depopulated for magnetic fields higher than $B = 20\,\mathrm{T}$.

In order to asses the role of many-electron contributions we also carry out simulations using a non-interacting model, i.e. by setting $v_H = 0$ and $v^\sigma_{XC} = 0$ in Hamiltonian (3.5). The obtained energy spectrum, see figure 3.13(a), shows smooth MSSs with no visible changes in slope. The absence of abrupt transitions in this non-interacting system demonstrates their multi-particle origin. Moreover, additional calculations neglecting only the exchange-correlation potential $v^\sigma_{XC} = 0$ (not shown) present the same energy spectrum as figure 3.12(a). This indicates the minor role of this term, being the Hartree potential energy the term responsible for the presence of transitions.

Lastly, we explore the signatures of these spin and charge transitions in magnetoconductance experiments. The results are summarized in figure 3.13(b). Here, the total magnetoconductance curve exhibits a clear step-like form. At low magnetic fields, we observe regular oscillations as predicted previously for the low-magnetic-field regime. As the magnetic field is increased, the oscillations persist up to $B \approx 6\,\mathrm{T}$, but close to the first transition point the conductance is strongly reduced. The value of G drops from $G \approx 16\,\mathrm{e}^2/\mathrm{h}$ to $G \approx 12\,\mathrm{e}^2/\mathrm{h}$ at this point, and then remains constant with minimal oscillations up to $B \approx 12\,\mathrm{T}$. This plateau is generated because E_F is located between the second and third $\downarrow$-MSS, so there are no crossings. At $B > 12\,\mathrm{T}$, the conductance starts oscillating again as E_F merges the second $\downarrow$-MSS, and G experiences a progressive reduction until the second transition is reached. After this point we find another plateau for the same reason as before, that eventually drops to zero when the CB gets completely depleted.

Summing up, in the high-magnetic-field regime we have found various field-induced transitions, which can be related to the complete depletion of excited subbands. Such transitions can be identified in magnetoconductance experiments by an step-like behavior.

CHAPTER **4**

Spin-orbit-induced spin relaxation in semiconductor QDs

Advances in the fabrication techniques over the last few decades have enabled the isolation and control of individual spins in solid-state systems.[54] This has opened the possibility of developing a new generation of devices that exploit the spin of the electron rather than its charge, giving rise to new fields in condensed matter physics such as spin-based electronics (*spintronics*) and quantum computing.[6, 55, 105] These spin-based devices are of great interest for future applications due to the predicted improved properties compared to the conventional electronic ones. For instance, some of their advantages would be the increased data processing speed, decreased electric power consumption, and increased integration densities.[6]

The electron spin degree of freedom is a natural two-level system in which information can be encoded through a particular spin orientation (either up or down). This stored information can then be carried over space in transport processes since spins are attached to electrons. Furthermore, the spin orientation is known to survive for a relatively long time (of the order of nanoseconds), offering the opportunity to store and manipulate phase coherence over length and time scales much longer than in typical charge-based devices. All this makes the spin degree of freedom particularly attractive and several novel devices have been proposed.[105] For example, some spin-valves and magnetoresistive random-access memories (MRAM) are already commercially available, but many other technologies are still under development. Among the latter, two of them deserve a special mention: the spin field-effect transistor proposed by Datta and Das [106] and the spin quantum bit (*qubit*) proposed by Loss and DiVincenzo [107]. On one hand, a spin-based transistor is one of the leading candidates to substitute the traditional silicon ones when the length limit of 7 nm is reached in 4 or 5 years. These new transistors are believed to improve the energy efficiency of the current ones. On the other hand, the fabrication of a quantum computer has been subject to intense research over the last years since it is expected to be much faster due to the direct use of quantum superposition and entanglement. Many different systems are being pursued for physically implementing a quantum computer, e.g. trapped ions, photons, superconductor junctions, and QDs. In particular, we focus on spin qubits as they are promising candidates that fulfill all the requirements needed for quantum computing.[108] However, despite important advances have been achieved, the fabrication of these spin-based devices is still not possible. To this end, a deeper understanding of the fundamental spin physics and the coupling with the environment is necessary.

One of the greatest challenges in using the spin degree of freedom in real applications is controlling or removing quantum decoherence.[109, 110] In a solid, the electron spin is not completely decoupled from other degrees of freedom, thus limiting its lifetime to be finite. Fortunately, spins in QDs exhibit longer lifetimes than in delocalized systems since quantum confinement suppresses the main bulk decoherence mechanisms.[111, 112] The two main spin relaxation channels in III-V ZB semiconductor QDs are the hyperfine interaction and the SOI.[54, 56] The former takes place as a result of the coupling with the spin bath constituted by the spins of the nuclei. This mechanism is dominant when the energy separation between spin states is small, i.e. at relatively weak magnetic fields. Additionally, the hyperfine interaction mechanism is further diminished in the VB because of the p-like nature of the hole orbitals. On the other hand, for moderate and strong fields, when the energy splitting exceeds the nuclear magnetic field, the phonon-assisted relaxation due to SOI prevails. The magnetic field regime we are interested in corresponds to the second case, so only the SOI-induced spin relaxation is considered here. As already discussed in section 2.3, in semiconductors without inversion symmetry such as ZB and WZ structures, SOI in the CB is originated from bulk inversion asymmetry (DSOI) or structural inversion asymmetry (RSOI). Besides these two interactions, in the VB one has to consider the additional coupling between hh and lh subbands, which also results in spin mixing.

DSOI and RSOI Hamiltonians have different symmetries and present an anisotropic character.[33] Consequently, SOI-related effects are strongly affected by structural anisotropies, different crystallographic orientations as well as the directions along which external fields are applied. This can be exploited to externally control and manipulate the spin degree of freedom. Most previous theoretical works dealing with SOI-induced spin relaxation have considered quasi-2D systems where the lateral confinement has been modeled by a parabolic potential. Nevertheless, current synthetic methods are able to produce 3D QDs routinely and, thus, accounting for the 3D nature of SOI becomes essential to understand their properties.

In this chapter we present an overview of the results of five published works that deal with spin-orbit-related properties of single spins confined in ZB semiconductor QDs. A copy of these articles can be found at pages 179, 183, 193, 205 and 227 of the present dissertation. In particular, we focus on the role of three-dimensionality in the QD spin dynamics, paying special attention to the anisotropic behavior of SOI. First, the basic aspects of the theoretical procedure employed for computing the spin relaxation time are presented. Using this model, the spin dynamics of electrons and holes in spheroidal QDs under external fields is investigated. The study of this simple system allows one to understand the dependence of the spin relaxation on the QD geometry, laying the basis for the investigation of more complex systems where the 3D nature of the structures may be important, namely cuboidal QDs grown along different crystal directions, quantum dot molecules, and pyramidal QDs.

4.1 Theoretical formalism for the calculation of phonon-induced spin relaxation rates

In this section we present the expressions employed to estimate the spin relaxation rate of electrons and holes confined in ZB semiconductor QDs.

Any spin relaxation process needs both a source of spin admixture and a source of energy relaxation in order to take place. As stated above, the spin mixing in these systems is produced by SOI. The corresponding Hamiltonians are given in section 2.3. As for the source of energy relaxation, the dominant mechanism is determined by the transition energy ΔE_{fi}. We study the spin relaxation between Zeeman-split sublevels of lowest energy, i.e. the ground and the first-excited state. For moderate magnetic fields, the energy splitting of the two states is of the order or few meV. It is known that in transitions of this energy range the main scattering mechanism is mediated by the interaction of the carriers spin with the phonon bath.

Phonons are originated in the quantization of lattice vibrations and can be classified into acoustic and optical phonons. Since we restrict to low energies, short-wave optical phonons cannot participate in the spin relaxation processes investigated, so only acoustic phonons are included in our calculations. In addition, for low ΔE_{fi} the linear dispersion regime holds, $E_{\lambda q} = \hbar\omega_{q\lambda} = \hbar c_\lambda q$, where c_λ is the phonon velocity of the longitudinal ($\lambda = l$) or two transversal ($\lambda = t_1, t_2$) acoustic phonon modes and q is the phonon wave vector.

Vibrations of the bulk lattice (phonons) produce small displacements of the atoms from their equilibrium positions. These deviations lead to small shifts in the energy bands and also to the origin of additional electric fields that are responsible for the scattering processes. For ZB crystal structures, the two relevant scattering mechanisms at low temperature are the deformation potential and the piezoelectric potential.[113] Thus, the carrier-phonon Hamiltonian is as follows

$$H^\lambda_{c-ph} = e\,\phi^\lambda_{pz}\,\mathcal{I} + H^\lambda_{dp}, \tag{4.1}$$

where e is the particle charge, $\mathcal{I}$ is the identity matrix, and ϕ^λ_{pz} and H^λ_{dp} denote the piezoelectric and the deformation potential terms, respectively. To compute the spin relaxation, Hamiltonian (4.1) needs to be written in terms of the normal modes of vibration. The derivation and complete expressions of ϕ^λ_{pz} and H^λ_{dp} for both CB and VB are given in appendix D.

The transition rate between the initial occupied state ($|\Psi_i\rangle$) and the final unoccupied state ($|\Psi_f\rangle$), mediated by the carrier-phonon interaction, is calculated within time-dependent first-order perturbation theory, specifically the Fermi's golden rule:

$$\frac{1}{T_1} = \frac{2\pi}{\hbar}\sum_{\lambda,\mathbf{q}} \left|\langle\Psi_f|H^\lambda_{c-ph}\,|\Psi_i\rangle\right|^2 \delta(\Delta E_{fi} + E_{\lambda q}). \tag{4.2}$$

Here, H^λ_{c-ph} is the carrier-phonon coupling Hamiltonian (4.1), $E_{\lambda q} = \hbar c_\lambda q$, and $\Delta E_{fi} = E_f - E_i$. The sum is done over all directions of wave vector $\mathbf{q}$ and all possible decay channels. We assume bulk phonons, which is an appropriate model for embedded QDs. Calculations are carried out at zero temperature for the sake of simplicity, so that phonon absorption and multiphonon processes are negligible.[114]

4.2 Spin relaxation in 3D spheroidal QDs

We start investigating the spin relaxation rates between Zeeman-split sublevels in spheroidal QDs. This 3D system allows to easily tailor the QD shape in order to assess the effect of confinement on the SOI and, by extension, on the spin dynamics. Quantum confinement is known to influence the orbital motion of carriers which, in turn, affects its spin through SOI. Therefore, it is expected that the spin physics could be controlled by growing structures with specific geometries.

4.2.1 Electron spin relaxation

We first study the spin relaxation due to single-phonon emission in the CB. The spheroidal QDs are modeled using parabolic confinement potentials and are subject to an axial magnetic field defined by the vector potential in the symmetric gauge, $\mathbf{A} = \frac{B}{2}(-y, x, 0)$, and an electric field $\mathbf{F}$ with arbitrary direction. The electron Hamiltonian reads

$$H = \sum_{j=x,y,z} H_{HO}(j) - e\,\mathbf{F}\cdot\mathbf{r} + \frac{1}{2} g^* B\,\sigma_z + H_{SOI}, \tag{4.3}$$

where $e = -1$ is the electron charge and $H_{HO}(j)$ is the harmonic oscillator Hamiltonian

$$H_{HO}(j) = \frac{1}{2m^*}\,(k_j - e\,A_j)^2 + \frac{1}{2} m^* \omega_j^2\, j^2, \tag{4.4}$$

with ω_j standing for the frequency of the confining parabola and $k_j = -i\hbar d/dj$. The second term in equation (4.3) represents the electric field potential, equation (2.19). The third term accounts for the Zeeman splitting resulting from a magnetic field along the z direction (see section 2.2.2 for details). The last term is the SOI Hamiltonian $H_{SOI} = H^{CB}_{BIA} + H^{VB}_{SIA}$. Here, H^{CB}_{BIA} denotes the DSOI term, equation (2.22), and H^{VB}_{SIA} the RSOI term, equation (2.24).

Hamiltonian (4.3) is solved by rewriting all derivatives and coordinates in terms of harmonic oscillator ladder operators and then projecting it onto a basis formed by oscillator eigenstates $|\nu_x, \nu_y, \nu_z\rangle$. The spin relaxation is computed by means of the Fermi's golden rule as explained in the previous section. In particular, we consider In(Ga)As QDs in all calculations. The specific values of the corresponding parameters can be consulted in the published work, see page 183 of this Thesis.

The effect of the SOI in the electron spin dynamics is studied for each mechanism individually, namely DSOI and RSOI. The results are presented below.

Dresselhaus SOI

Figure 4.1(a) summarizes the results obtained for the spin relaxation rate as a function of the vertical confinement. Calculations are performed at $B = 1\,\mathrm{T}$ and $\mathbf{F} = 0$, considering various in-plane confinements ($\omega_\perp = \omega_x = \omega_y$) ranging from $\hbar\omega_\perp = 5\,\mathrm{meV}$ to $\hbar\omega_\perp = 40\,\mathrm{meV}$. Previous works in literature have reported an increasing dependence of $1/T_1$ with $\hbar\omega_z$ for quasi-2D systems.[33, 54] Indeed, this is the behavior we find for the QD with weakest lateral confinement, $\hbar\omega_\perp = 5\,\mathrm{meV}$, which can also be seen as quasi-2D ($\omega_z > \omega_\perp$). However, we observe from the other curves in figure 4.1(a) that for non-flat systems the behavior is richer. In all cases, the spin relaxation rate becomes minimum for $\omega_\perp = \omega_z$ and rapidly increases as the QD geometry deviates from a perfect sphere. In other words, the spin relaxation is suppressed when the system has spherical symmetry and it is enhanced when the symmetry is lowered. These results stress the importance of three-dimensionality when investigating the spin dynamics of QDs.

In order to understand the origin of the minimum in the spin relaxation curves, we calculate the degree of spin admixing of the states involved in the transition. Other factors, such as the density of phonons, are not important since they are independent of ω_z and remain constant during each calculation series. The spin purity of the ground state (solid line) is plotted in figure 4.1(b). We see that it becomes maximum for a spherical QD and decreases in prolate and oblate structures. This fact indicates that a minimum value of $1/T_1$ originates from a situation with maximum spin purity, i.e. where SOI is more hindered. Consequently, the dependence between spin relaxation rate and QD shape lies in the form of the SOI Hamiltonians for different system symmetries.

The spin admixture is determined by the σ_x and σ_y terms in H_{BIA}^{CB}, equation (2.22), since σ_z is diagonal in spin-space and does not flip spins. The mixing Hamiltonian is then approximated as

$$H_{BIA}^{mix} \approx b_{41}^{CB} \left[p_x(\langle p_y^2 \rangle - \langle p_z^2 \rangle)\sigma_x + p_y(\langle p_z^2 \rangle - \langle p_x^2 \rangle)\sigma_y \right]. \tag{4.5}$$

For a spherical QD we have $\langle k_x^2 \rangle = \langle k_y^2 \rangle = \langle k_z^2 \rangle$. In the absence of a magnetic field the kinetic and canonical momenta coincide, $\langle k_j^2 \rangle = \langle p_j^2 \rangle$, but for finite B this is not longer true since $p_j = k_j - eA_j$. In spite of this, in the limit of small fields, $B \to 0$, we can consider that $\langle p_\perp^2 \rangle \approx \langle p_z^2 \rangle$, so that equation (4.5) tends to vanish, thus justifying the profound minimum found in figure 4.1(a) when $\omega_z = \omega_\perp$.

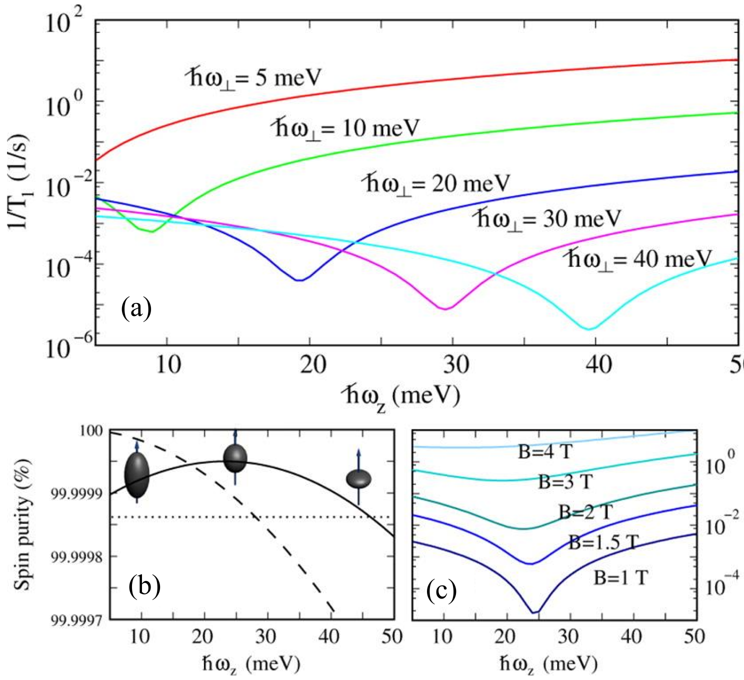

Figure 4.1: (a) Spin relaxation rate as a function of the vertical confinement $\hbar\omega_z$ with only DSOI included. Results for various in-plane confinements $\hbar\omega_\perp$ are presented. (b) Spin purity of the ground state for a QD with $\hbar\omega_\perp = 25\,\text{meV}$. Three levels of calculation have been considered: exact result (solid line), linear approximation (dashed line), and in-plane cubic approximation (dotted line). Insets show schematic drawings illustrating QDs with different vertical confinement. (c) $1/T_1$ *vs.* vertical confinement for increasing magnetic field and $\hbar\omega_\perp = 25\,\text{meV}$.

The above approximation, $\langle k_j^2 \rangle \approx \langle p_j^2 \rangle$, is only valid for relatively small magnetic fields. As B increases the canonical momentum $\langle p^2 \rangle$ becomes more anisotropic, so that the suppression of the spin admixture is progressively reduced. This is exactly the behavior observed in figure 4.1(c), where the $1/T_1$ minimum is gradually removed for increasing magnetic fields.

For the sake of completeness, we repeat the spin purity calculations for other commonly used approximations.[54] For oblate structures in the limit of $\langle k_z^2 \rangle \ll \langle k_\perp^2 \rangle$, equation (4.5) reduces to $H_{BIA}^{mix} \approx b_{41}^{CB} \langle p_z^2 \rangle (p_y \sigma_y - p_x \sigma_x)$ (linear approximation). The dashed line in figure 4.1(b) shows that this approximation provides a qualitatively correct estimate of the spin mixing for oblate QDs, albeit systematically overestimated. In the limit of quasi-1D prolate QDs, $\langle k_z^2\rangle \gg \langle k_\perp^2\rangle$, we have $H_{BIA}^{mix} \approx b_{41}^{CB}\langle p_\perp^2\rangle(p_x\sigma_x - p_y\sigma_y)$ (cubic approximation). As can be seen in figure 4.1(b), the spin mixing does not depend on ω_z in this approximation (dotted line), hence the calculated spin purity is constant and mostly underestimated. In light of these results, we can state that the interplay between 3D degrees of freedom is crucial and the full DSOI Hamiltonian must be considered.

Rashba SOI

We next investigate the spin relaxation rate in QDs with RSOI. In particular, we pay special attention to the quantum confinement anisotropy and the direction of the external electric field $\mathbf{F}$ as mechanisms to control the RSOI strength and, in turn, the spin dynamics in QDs. In this respect, previous publications have pointed out the possibility of modulating the RSOI in quasi-2D systems due to the confinement anisotropy.[115–117] Here, we extend the study to 3D QDs.

Figure 4.2(a) shows a contour plot of $1/T_1$ as a function of the vertical confinement ω_z and the polar angle θ of the electric field orientation. All calculations are carried out for QDs with in-plane confinement $\hbar\omega_\perp = 50\,\mathrm{meV}$ and under an axial magnetic field $B = 5\,\mathrm{T}$. In general, one can see that the maximum (minimum) spin relaxation is found when $\mathbf{F}$ points in the direction of strongest (weakest) confinement. To improve the readability of this plot and help extracting interesting information, four cross-sections are also included in figure 4.2(b-e). On one hand, we observe a decreasing behavior of $1/T_1$ with ω_z for $\mathbf{F} \perp \mathbf{B}$, figure 4.2(c), while it remains constant for $\mathbf{F} \parallel \mathbf{B}$, figure 4.2(b). On the other hand, the dependence of $1/T_1$ on the polar angle θ shows opposite behavior for the two vertical confinements considered. It increases for $\omega_z = 10\,\mathrm{meV}$, figure 4.2(d), and decreases for $\omega_z = 100\,\mathrm{meV}$, figure 4.2(e).

These results can be justified following the same strategy as for DSOI. Then, the spin relaxation rate is mainly determined by the strength of the RSOI, which can be understood by analyzing the terms in H_{SIA}^{CB}, equation (2.24), contributing to spin flips. The spin mixing part is as follows

$$H_{SIA}^{mix} = r_{41}\left[F_z(p_y\sigma_x - p_x\sigma_y) + F_x p_z\sigma_y - F_y p_z\sigma_x\right]. \tag{4.6}$$

The first term in (4.6) corresponds to figure 4.2(b) ($\mathbf{F} \parallel \mathbf{B}$). It is worth mentioning that this is the only term included in most studies on quasi-2D QDs.[54] This term does not depend on the vertical carrier motion, i.e. does not contain p_z, explaining the flat dependence with ω_z. Contrarily, the

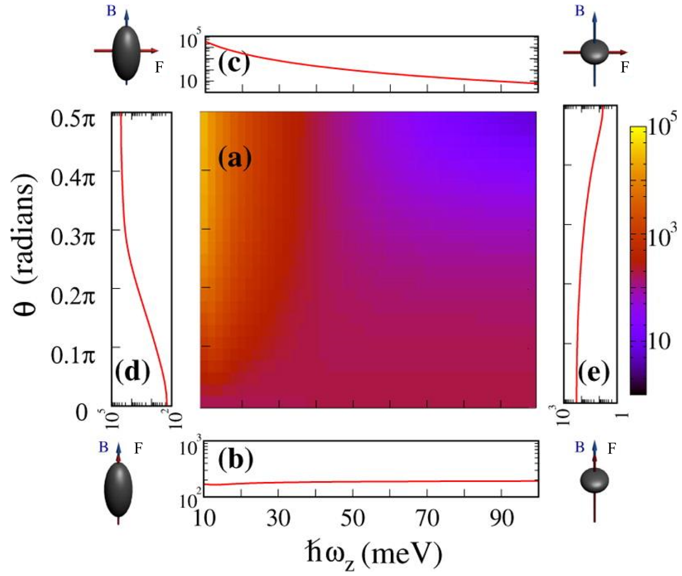

Figure 4.2: Spin relaxation rate in a QD with $\hbar\omega_\perp = 50\,\text{meV}$ in the presence of RSOI. All calculations are carried out for $\mathbf{F} = 30\,\text{kV/cm}$ and $B = 5\,\text{T}$. (a) Contour plot of $1/T_1$ as a function of vertical confinement and the orientation of the electric field. Panels (b) and (c) are cross sections for $\theta = 0$ and $\theta = \pi/2$, respectively. Panels (d) and (e) are cross sections for $\hbar\omega_z = 10\,\text{meV}$ and $\hbar\omega_z = 100\,\text{meV}$, respectively. The schematics at the corners illustrate the QD shape and the orientation of $\mathbf{B}$ and $\mathbf{F}$.

other two terms ($\mathbf{F} \perp \mathbf{B}$) do depend on the vertical confinement, justifying the high influence of ω_z on $1/T_1$ in figure 4.2(c). As for the opposite behavior observed in panels (d) and (e), we have to take into account the states that Hamiltonian (4.6) couples. One can see that all three terms couple the ground state $|0,0,0\rangle$ to excited states with a node in a direction perpendicular to the electric field. As $\mathbf{F}$ is tilted the dominant term changes and so does the excited states involved in the coupling. Thus, when $\mathbf{F}$ is perpendicular (parallel) to the direction of strongest confinement, H_{SIA}^{mix} couples the ground state with excited states of higher (lower) energy, hence the coupling is inhibited (enhanced) and so is the relaxation rate.

4.2.2 Hole spin relaxation

Here we extend the study on electron spin relaxation discussed in the previous section to the spin of holes. Several theoretical works have investigated the spin dynamics of single holes in quasi-2D QDs considering different sources of spin mixing, namely lh-hh coupling,[113, 118] cubic-in-k DSOI,[119] linear-in-k DSOI,[120] and the e-h exchange interaction together with strain in holes forming excitons.[121] In all these works, one spin mixing mechanism is assumed as dominant, while the others are neglected without any comparison between them. In order to shed light on this matter, we investigate the dependence of the hole spin lifetime on the QD geometry by considering simultaneously all relevant sources of spin admixing. In this way, it is possible to identify the dominant mechanisms in hole spin scattering processes and establish their regime of application. In addition, some of the aforementioned works report opposite results, [113, 118] or predict results not observed in experiments.[119] In this respect, we explicitly compare our results with those apparently controversial.

The Hamiltonian describing the hole states in 3D spheroidal QDs reads

$$H = H_{ZB}^{LK} + H_{BIA}^{VB} + V_{QD}\,\mathcal{I} + H_Z, \tag{4.7}$$

where $\mathcal{I}$ is the 4x4 identity matrix. H_{ZB}^{LK} is the four-band Luttinger-Kohn Hamiltonian,[122] whose matrix form is given in appendix A, section A.1.1. The second term in (4.7) corresponds to the DSOI Hamiltonian, equation (2.23).[33] It includes linear- and cubic-in-k terms, and its matrix representation can be found in section B.1.2. The RSOI is disregarded in this study because it is an extrinsic effect, and for holes it is less efficient than DSOI under moderate magnetic fields.[119] The third term denotes the confining potential, V_{QD}, modeling QDs with parabolic confinement:

$$V_{QD} = -\frac{1}{2} m_\perp^* \omega_\perp^2 (x^2 + y^2) - \frac{1}{2}\, m_z^* \omega_z^2 z^2, \tag{4.8}$$

with ω_j standing for the frequency of the confining parabola. Equation (4.8) simulate 3D spheroidal QDs with different aspect ratios. Finally, last term in (4.7) is the Hamiltonian describing the splitting of the hole states by an effective axial magnetic field:

$$H_Z = \frac{1}{2} \begin{pmatrix} \Delta & 0 & 0 & 0 \\ 0 & \frac{1}{3}\Delta & 0 & 0 \\ 0 & 0 & -\frac{1}{3}\Delta & 0 \\ 0 & 0 & 0 & -\Delta \end{pmatrix} \tag{4.9}$$

Here, Δ is the value of the energy splitting, which is three times larger for hh than for lh. The origin of this splitting could be the e-h exchange interaction or a Zeeman effect.

Equation (4.7) is solved following the same procedure as for the CB. Nevertheless, we now deal with a four-band model where each subband has different mass and, hence, also different oscillator frequency. Then, we rewrite all coordinates and derivatives of equation (4.7) in terms of the hh harmonic oscillator Hamiltonians. The resulting Hamiltonian is then projected onto the 1D hh eigenfunctions.

Hole spin lifetimes are calculated within the theoretical formalism exposed in section 4.1, i.e. the Fermi's golden rule. The specific expressions for a four-band VB model are given in appendix D. Simulations are carried out for InAs QDs embedded in a GaAs matrix. The material parameters compiled in table 1 of the published manuscript (see page 205).

Geometry and spin splitting dependence

We start investigating the role of the QD aspect ratio and the spin splitting magnitude on the hole spin lifetime, T_1^h. The results obtained are summarized in figure 4.3. For the sake of comparison, both hole (red solid line) and electron (blue dotted line) spin relaxation times are depicted. Calculations for electrons and holes are performed considering a QD with the same size, i.e. defining the confining parabola with the same force constants $m_j^{hh}(\omega_j^{hh})^2 = m_j^e(\omega_j^e)^2$ with $j = \perp, z$.

Figure 4.3(a) shows T_1 as a function of $\omega_\perp$ in InAs QDs with strong vertical confinement. One can see that T_1^e increases with the vertical confinement because DSOI is gradually suppressed as we get closer to a spherical QD ($\omega_\perp^e = \omega_z^e$), in agreement with the results of the preceding section. On the other hand, T_1^h has a non-monotonic behavior, presenting a minimum at $\hbar\omega_\perp^{hh} = 28\,\mathrm{meV}$. Previous works have reported an opposite dependence of T_1^h on $\omega_\perp^{hh}$: Woods *et al.* [118] predicted the hole spin lifetime to increase with the lateral confinement, while Lü *et al.* [113] predicted the opposite trend in a similar study. These apparently contradictory results are both compatible with figure 4.3(a), corresponding to the right and left side of the minimum.

We next study the dependence of the spin relaxation on the vertical confinement. In QDs with moderately strong lateral confinement, figure 4.3(b), which can be roughly seen as self-assembled QDs, electrons and holes present opposite behavior. T_1^e decreases with ω_z since the system becomes flatter, i.e. less spheric. The hole spin lifetime, instead, increases in general but a shallow minimum can be observed at $\hbar\omega_z = 14\,\mathrm{meV}$, showing that different trends for T_1^h are also possible when varying ω_z. In figure 4.3(c) we consider structures with weak lateral confinement, which are comparable to electrostatic QDs. Electrons present the same qualitative behavior

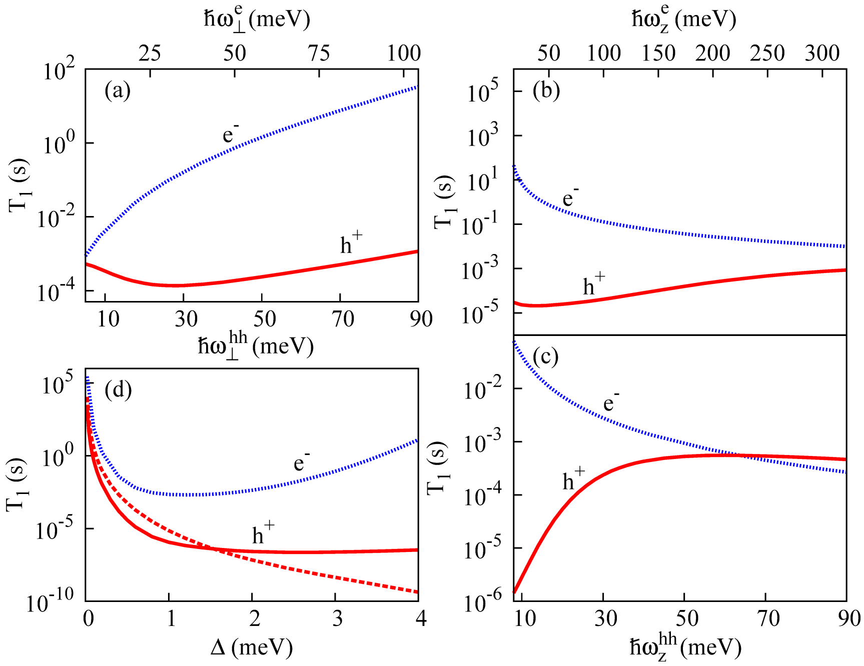

Figure 4.3: Hole (red solid line) and electron (blue dotted line) spin relaxation time as a function of (a) lateral confinement, (b-c) vertical confinement, and (d) energy splitting Δ. (a) $\hbar\omega_z^{hh} = 50\,\text{meV}$, $\hbar\omega_z^e = 179\,\text{meV}$, $\Delta = 0.4\,\text{meV}$. (b) $\hbar\omega_\perp^{hh} = 20\,\text{meV}$, $\hbar\omega_\perp^e = 23.2\,\text{meV}$, $\Delta = 0.4\,\text{meV}$. (c) $\hbar\omega_\perp^{hh} = 5\,\text{meV}$, $\hbar\omega_\perp^e = 5.8\,\text{meV}$, $\Delta = 0.4\,\text{meV}$. (d) $\hbar\omega_\perp^{hh} = 20\,\text{meV}$ and $\hbar\omega_z^{hh} = 50\,\text{meV}$; $\hbar\omega_\perp^e = 23.2\,\text{meV}$ and $\hbar\omega_z^e = 179\,\text{meV}$; $\hbar\omega_\perp^{hh} = 40\,\text{meV}$ and $\hbar\omega_z^{hh} = 5\,\text{meV}$ (red dashed line).

as before, while the minimum of T_1^h is now absent since it is shifted towards smaller ω_z. Remarkably, we find that the spin lifetime of holes may exceed that of electrons in flat enough QDs. This result corroborates the prediction of Bulaev and Loss [119], who reported the possibility of having $T_1^h > T_1^e$ in gated structures. For self-assembled QDs, instead, T_1^h is one order of magnitude shorter than T_1^e, what also goes along with experimental observations.[123]

The electron spin relaxation is known to be maximum when the phonon wavelength is similar to the carrier wave function extension, but it decreases for smaller or larger spin splitting energy Δ. Figure 4.3(d) displays T_1 as a function of Δ for a self-assembled-like QD. For electrons a minimum is found ($\Delta \approx 1\,\text{meV}$), as expected. However, T_1^h becomes constant for $\Delta > 1.5\,\text{meV}$. This different behavior can be understood from their distinct effective masses which, despite considering QDs of the same size, result in unlike characteristic oscillator lengths. As a result, a larger Δ is needed for T_1^h to increase again. We also run simulations for a nanorod-like structure (red dashed line), for comparison. In this case, the plateau in T_1^h disappears and the relaxation is sensitive to Δ for all the range under study.

Mechanisms of spin admixture

As we have seen for electrons in the preceding section, in most cases the spin relaxation is mainly determined by the degree of spin admixing. Therefore, it is crucial to establish which mechanisms are dominant in order to understand the dependence of spin lifetimes on system geometry. To this aim, we repeat all calculations depicted in figure 4.3 but now taking into account each source of mixing individually. Notice that henceforth only the spin of holes is considered, so the hh superscript is dropped. The results for the spin relaxation rate, $1/T_1$, are summarized in figure 4.4.

The two relevant spin-mixing mechanisms for the VB are the lh-hh coupling originating from the Luttinger-Kohn Hamiltonian H_{ZB}^{LK}, and the DSOI, which can be further divided into its various terms. Then, the simulations are performed including the diagonal terms of H_{ZB}^{LK} plus different combinations of the off-diagonal H_{ZB}^{LK} Hamiltonian and some DSOI terms, as shown in figure 4.4.

We analyze first the influence of the lateral confinement on the spin relaxation main mechanisms, figure 4.4(a). It is found that lh-hh coupling is more important than DSOI alone for large $\omega_\perp$. However, both contributions are comparable for moderate lateral confinement (self-assembled-like QDs), and H_{BIA} becomes dominant for weak laterally confined structures (e.g. gated dots). As for the contribution of the different H_{BIA}^{VB} terms, figure 4.4(a) reveals that $H_{b_{41}}$ is the most relevant one. In fact, by only considering the lh-hh coupling and the $H_{b_{41}}$ term (green dotted line) we almost recover the spin relaxation rate obtained employing the full Hamiltonian (black line). In contrast, the linear-in-k term H_{C_k} has a negligible influence, oppositely to reference [120] where it has been proposed as the dominant SOI term.

The behavior when changing the vertical confinement is in agreement with that seen in figure 4.4(a). In QDs with moderate lateral confinement, figure 4.4(b), lh-hh coupling dominates for all ω_z under study, but for weak lateral confinement, figure 4.4(c), the strength of both mechanisms is comparable. Indeed, a transition from a dominant H_L to a dominant H_{BIA} situation takes place as ω_z decreases. Interestingly, H_{BIA} provides a lower bound to $1/T_1$ that is responsible for the origin of a plateau for $\omega_z > 40\,\text{meV}$.

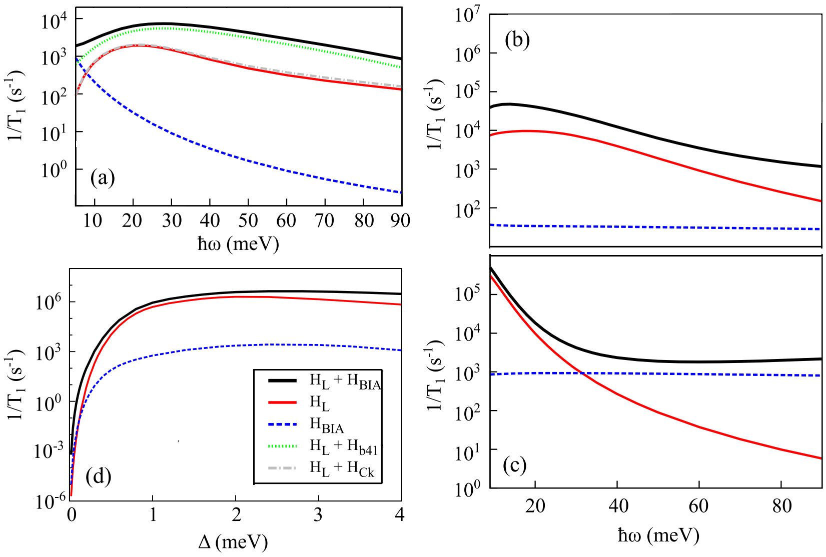

Figure 4.4: Same as figure 4.3, but considering the most relevant mechanisms of spin admixture individually. That is, the diagonal terms of H_{ZB}^{LK} plus: off-diagonal H_{ZB}^{LK} terms only, H_L (red solid line); all DSOI terms, H_{BIA} (blue dashed line); off-diagonal H_{ZB}^{LK} terms and b_{41}^{VB} DSOI term, $H_{b_{41}}$ (green dotted line); off-diagonal H_{ZB}^{LK} terms and C_k DSOI term, H_{C_k} (gray dash-dotted line); and full Hamiltonian $H_L + H_{BIA}$ (thick black line). Only the spin relaxation of holes is included. Note that here we represent the spin relaxation rate $1/T_1$, while in figure 4.3 we represent the spin lifetime T_1.

The influence of the spin splitting Δ on the mechanisms of spin admixture is explored in figure 4.4(d). The lh-hh coupling has a dominant contribution for most Δ, but H_{BIA} becomes equally important when $\Delta \to 0$. For such small energy splitting, the hole-phonon coupling becomes very inefficient and the relaxation rate decreases rapidly. The presence of DSOI, however, originates a small zero-field spin splitting that becomes significant for $\Delta \approx 0$, thus causing H_{BIA} to prevail.

In summary, in this section we have shown the substantial effect of the geometry anisotropy on the spin relaxation of both electrons and holes by changing the aspect ratio of spheroidal QDs. In addition, we have found that accounting for the 3D nature of the structures is crucial for a proper description of the SOI. In the subsequent sections, we also study SOI-induced effects in more complex systems in which three-dimensionality is expected to play and important role.

4.3 Electron spin-relaxation anisotropy in [001] and [111] grown QDs

In the preceding section we have shown the anisotropy of the spin-orbit-induced spin relaxation by changing the aspect ratio of 3D spheroidal QDs with circular lateral confinement. Other theoretical works investigating also QDs with circular symmetry have reported an in-plane spin relaxation anisotropy with the magnetic field orientation due to the interplay between RSOI and DSOI.[124, 125] In those studies, the spin lifetime becomes maximum (minimum) when the magnetic field is along the [110] ([$1\bar{1}0$]) crystallographic direction. Such anisotropic angular dependence has been confirmed experimentally by Scarlino *et al.* [126], but the singular points of the T_1 curve obtained are deviated from the theoretical angles. This fact is ascribed to the elongated geometry of the QDs in the experiments, what goes along with some theoretical works that have pointed out that deviations from the in-plane circular symmetry affect the spin relaxation anisotropy.[127–129] It is also worth noting that all the aforementioned theoretical works have considered 2D models ignoring the contribution of cubic DSOI terms. Nonetheless, we have already seen above the important role of these terms on the SOI anisotropy in 3D QDs, so that one can also expect them to have a relevant influence on the in-plane spin relaxation anisotropy.

Here we study the in-plane electron spin relaxation anisotropy including all terms of RSOI and DSOI in a fully 3D model. The spin relaxation rate is monitored by modifying the orientation of the externally applied electric **F** and magnetic **B** fields, see figure 4.5. In particular, we consider cuboidal GaAs QDs with different heights and base shapes in order to gain insight into the role of three-dimensionality and QD elongation. Additionally, we investigate QDs with various crystallographic orientations, particularly QDs rotated around the z axis and QDs grown along the [111] crystal direction. The latter are particularly interesting for optical spin preparation.[130] In fact, the spin relaxation has already been extensively discussed in [111] quantum wells,[131–133] but it is still poorly understood in zero-dimensional structures.

The Hamiltonian describing the electronic states of such systems is as follows:

$$H = \frac{\mathbf{p}^2}{2m^*} + V_{QD} - e\,\mathbf{F}\,\mathbf{r} + H_Z + H^{CB}_{BIA} + H^{CB}_{SIA}, \tag{4.10}$$

with $\mathbf{p} = -i\hbar\boldsymbol{\nabla} - e\,\mathbf{A}$, and V_{QD} standing for the confining potential. The vector potential employed to define the in-plane magnetic field is $\mathbf{A} =$

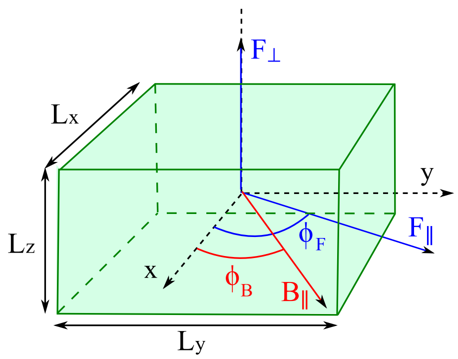

Figure 4.5: Schematic representation of the cuboidal GaAs QD. The parameters defining the system dimensions and the orientation of the external electric and magnetic fields are indicated.

$z\, B(\sin\phi_B, -\cos\phi_B, 0)$. The third term in (4.10) is the electric field potential, equation (2.19), with $e = -1$ for electrons. The fourth term H_Z is the Zeeman splitting, equation (2.20). Finally, last two terms in (4.10) H_{BIA}^{CB} and H_{SIA}^{CB} correspond to the DSOI, equation (2.22), and the RSOI, equation (2.24), respectively.

Hamiltonian (4.10) is only valid for ZB QDs grown along the [001] crystal direction. In order to study systems grown along other directions, new expressions need to be derived. To this purpose, we consider the confinement potential to be fixed in space and perform a rotation of the crystalline structure. In this way, we guarantee the accuracy of the calculations since the mesh always fits the cuboidal geometry in the same way independently of the QD orientation. A rotation of the crystalline structure causes changes in the internal coordinates and, thus, changes in the Hamiltonian. Next, we analyze how the different terms in equation (4.10) are affected by rotations. Since the mass of the CB is isotropic, the kinetic energy term has spheric symmetry and is invariant under rotations. The confinement potential and the external fields are not rotated, so their corresponding terms remain also unaltered. As for the Zeeman term, we need to take into account that the dot product of two vectors defined with respect to the same coordinate system is invariant as long as they rotate simultaneously. This is indeed the case of the magnetic field and the spin in H_Z. However, H_{BIA}^{CB} and H_{SIA}^{CB} do change when the crystalline structure is rotated and the expressions introduced in section 2.3 must be recalculated.

First, we obtain the SOI Hamiltonians corresponding to an in-plane rotation θ_z around the z axis. The resulting Hamiltonians read:

$$H_{SIA}^{[001]}(\theta_z) = r_{41} F_z (\sigma_x p_y - \sigma_y p_x), \tag{4.11}$$

and

$$H_{BIA}^{[001]}(\theta_z) = b_{41}^{CB} \cos 2\theta_z \Big[\sigma_x p_x \left(p_y^2 - p_z^2\right) + \sigma_y p_y \left(p_z^2 - p_x^2\right) + \sigma_z p_z \left(p_x^2 - p_y^2\right)\Big] + \\ b_{41}^{CB} \sin 2\theta_z \Big[p_z^2(\sigma_y p_x + \sigma_x p_y) - 2\sigma_z p_x p_y p_z + \frac{1}{2}(p_x^2 - p_y^2)(\sigma_x p_y - \sigma_y p_x)\Big]. \tag{4.12}$$

Note that we have restricted ourselves to an axially applied electric field F_z and, in such a case, the Rashba Hamiltonian (4.11) is independent of θ_z.

We consider next QDs grown along the [111] direction. This orientation is reached by rotating the crystalline structure by the following Euler angles: $\theta = \arccos(1/\sqrt{3})$, $\phi = 45$ and $\alpha = -45$. The rotated SOI Hamiltonians have the following form:

$$H_{SIA}^{[111]} = \frac{r_{41}\, F_z}{\sqrt{3}} \left[\sigma_z(p_y - p_x) - \sigma_y(p_x + p_z) + \sigma_x(p_y + p_z)\right], \tag{4.13}$$

and

$$H_{BIA}^{[111]} = \frac{b_{41}^{CB}}{2\sqrt{3}} \Big[(p_x^2 + p_y^2 - 4p_z^2)(p_x\sigma_y - p_y\sigma_x) + p_z(p_x^2 - p_y^2)(\sigma_x + \sigma_y) + \\ 2p_x p_y p_z(\sigma_x - \sigma_y) - \sigma_z p_x^2(p_x + 3p_y) + \sigma_z p_y^2(p_y + 3p_x)\Big]. \tag{4.14}$$

Once the electron states have been calculated, the spin relaxation rate between Zeeman-split sublevels is estimated using the Fermi's golden rule as explained in section 4.1.

The eigenvalue problem is solved numerically using a finite-difference scheme. Accounting for the SOI terms, which present third-order derivatives and are small in magnitude, requires high precision in the simulations. In general, higher precision can be achieved by increasing either the number of mesh points or the number of points in the discretization of the derivatives. In our particular case, after a series of convergence tests, we have found that a seven-point stencil central difference scheme and a number of 42875 mesh points provides an appropriate description of the system at a reasonable computational cost.

All calculations are carried out, unless otherwise stated, considering an in-plane magnetic field $B_{\parallel} = 1\,\mathrm{T}$ and an axial electric field $F_z = 10\,\mathrm{kV/cm}$. The material parameters used are those of GaAs. For specific values see the published paper in page 193.

4.3.1 Effect of the QD geometry

First, we explore the influence of the QD shape on the electron spin relaxation. To this aim, we consider QDs with square ($L_x = L_y = 80\,\text{nm}$) or rectangular ($L_x = 70\,\text{nm}$ and $L_y = 90\,\text{nm}$) base and with several heights ranging from $L_z = 10\,\text{nm}$ to $L_z = 40\,\text{nm}$. The spin relaxation rate is calculated for varying in-plane magnetic field orientation, as represented in figure 4.6(a) for three values of the magnetic field angle ϕ_B.

We note that, after a series of preliminary calculations, it is seen that the spin relaxation is much slower when mediated by RSOI than by DSOI. This is because our structure does not present any potential gradient, so the relatively weak external electric field is the only factor breaking the inversion symmetry of the system. Because of this, in figure 4.6 and hereafter the two spin-orbit couplings are only taken into account individually.

When only RSOI is included, figure 4.6(b), the angular dependence is completely flat for QDs with square base (solid line), but shows a clear anisotropic behavior in rectangular dots (dashed line). In this case, $1/T_1$ is maximum (minimum) when the magnetic field is oriented along the direction of weaker (stronger) confinement. In both cases, the spin relaxation rate is independent of the QD height within the calculated range, $L_z = 10-40\,\text{nm}$.

On the other hand, for DSOI, figures 4.6(c) and 4.6(d), the spin relaxation is remarkably different for short and tall QDs, evidencing that accounting for the three-dimensionality of the dots is critical to properly investigate the spin relaxation. In square dots with $L_z = 10\,\text{nm}$, figure 4.6(c), the relaxation rate does not significantly change with the magnetic field orientation. Contrarily, the $1/T_1$ curves for larger QDs, $L_z = 20, 30, 40\,\text{nm}$, exhibit striking minima at $\phi_B = 45$ and $\phi_B = 135$. The same calculations but for a rectangular QD are shown in figure 4.6(d). Now the relaxation rate varies smoothly for all heights investigated and the sharp minima are removed. The results for different L_z show an opposite trend, when $B_{\|}$ is along the direction of weaker confinement $\phi_B = 90$ the relaxation is maximum (minimum) for tall (short) QDs. This behavior is inverted for $\phi_B = 0$.

In order to understand the results found in figure 4.6(b) we need to analyze the degree of spin admixing of the states involved in the transition. A perturbative analysis[1] shows that the spin mixing originates from the coupling between the ground state ψ_{000} and the excited states ψ_{100} and ψ_{010}, where the three numbers in the subscript represent in this order the number

[1] The details are omitted here for brevity but the reader can find them in the publication (see page 193).

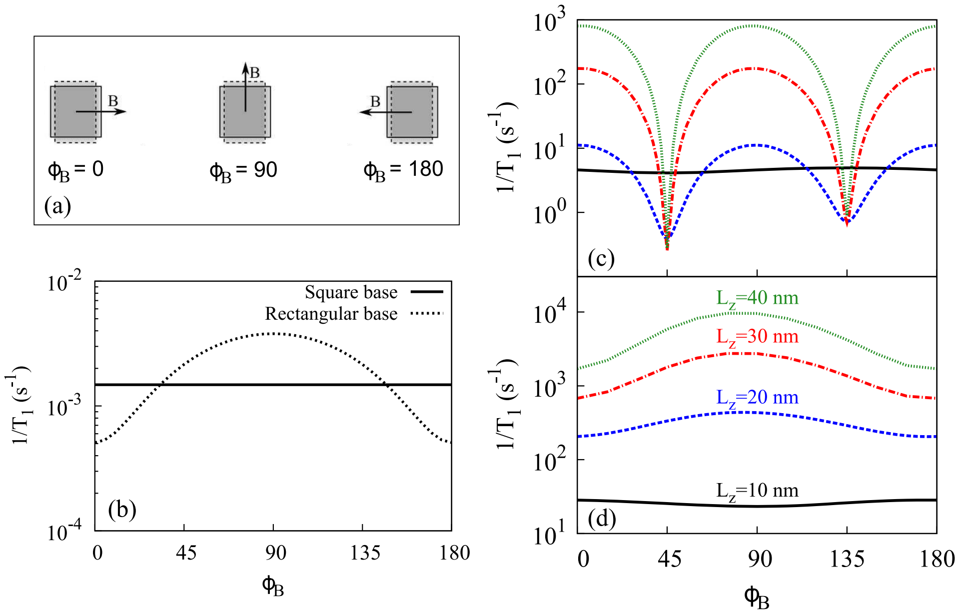

Figure 4.6: (a) Schematic drawing of the QD base (squared or rectangular) showing the relative orientation of the magnetic field for three specific angles $\phi_B = 0, 90, 180$. (b) Electron spin relaxation rate as a function of the magnetic field orientation considering only RSOI. QDs of 10 nm height with square (solid line) and rectangular (dashed line) base are considered. (c) $1/T_1$ versus ϕ_B in QDs with square base when only DSOI is taken into account. Various dot heights are studied: $L_z = 10\,\text{nm}$ (black solid line), $L_z = 20\,\text{nm}$ (blue dashed line), $L_z = 30\,\text{nm}$ (red dash-dotted line), and $L_z = 40\,\text{nm}$ (green dotted line). (d) Same as in panel (c), but for a rectangular base QD.

of nodes in the x, y and z direction. The specific excited state that couples with the ground state is determined by the magnetic field orientation. Then, square QDs, where both in-plane directions are equivalent, give rise to an isotropic behavior. For dots with rectangular base, instead, the excited state with a node in the direction of weaker confinement becomes closer in energy, justifying the spin relaxation anisotropy seen for varying ϕ_B.

To analyze the case of DSOI we split Hamiltonian (2.22) as $H^{CB}_{BIA} = H_z + H_{xy}$, with $H_z = b^{CB}_{41}\, p_z^2 (p_y\, \sigma_y - p_x\, \sigma_x)$ and $H_{xy} = H_x + H_y = b^{CB}_{41}\, [p_x^2 (p_z\, \sigma_z - p_y\, \sigma_y) + p_y^2 (p_x\, \sigma_x - p_z\, \sigma_z)]$, and perform calculations considering them individually (not shown). For QDs with $L_z = 10\,\text{nm}$ H_z dominates, as expected for quasi-2D systems. Then, the flat $1/T_1$ dependence for square QDs and the minimum at $\phi_B = 90$ for rectangular ones can be justified following the same perturbative study for H_z as for RSOI. As the dot height is increased, H_{xy} soon takes over H_z as the dominant contribution. The individual H_x and H_y terms show opposite behavior. H_x presents maximum (minimum) $1/T_1$ for $\phi_B = 90$ ($\phi_B = 0$) and H_y for $\phi_B = 0$ ($\phi_B = 90$), independently of the base shape. In rectangular QD, the different confinement strength in each in-plane direction determines which term, H_x or H_y, predominates, so the spin relaxation exhibits its dependence with ϕ_B. For square QDs, H_x and H_y cancel each other out at $\phi_B = 45$ and $\phi_B = 135$, originating the minima found in figure 4.6(c) at these angles.

4.3.2 In-plane rotation of the QD

In this section, we investigate the effect of rotating the QD confinement potential with respect to the crystalline structure on the spin dynamics. The rotation angle θ_z is defined between the x axis of the dot and the [100] crystal direction, as represented in the inset of figure 4.7(a). The QDs considered are the same as the ones with square base in section 4.3.1 with heights $L_z = 10\,\text{nm}$ and $L_z = 20\,\text{nm}$.[2] The in-plane magnetic field is kept still at $\phi_B = 0$ in all cases.

The spin relaxation versus θ_z when only RSOI is taken into account is shown in figure 4.7(a). The results are exactly the same for both dot heights. As expected from equation (4.12), which does not depend on θ_z, the magnitude of $1/T_1$ remains unaltered with the system rotation.

Conversely, for pure DSOI the spin relaxation rate as a function of the rotation angle presents an anisotropy with a 45° periodicity, showing profound minima at $\theta_z = 0, 45, 90$, see figure 4.7(b). At these particular angles, the value of the relaxation rate drops approximately five orders of magnitude. This behavior can be explained from the form of the Hamiltonian (4.14) if one notices that half of the terms depend on $\sin 2\theta_z$ and the other half on $\cos 2\theta_z$. Consequently, for $\theta_z = 0, 90$ the first part of (4.14) vanishes and for $\theta_z = 45, 135$ the second one, thus originating the quenching of the spin mixing and, by extension, of the relaxation rate.

It is interesting to note that the suppression of the spin relaxation at specific rotation angles is caused by H_{xy}, while H_z is completely flat, see the inset of figure 4.7(b). This fact stresses the important role of cubic DSOI terms in the SOI anisotropy even in flat structures, $L_z = 10\,\text{nm}$.

[2] Rectangular QDs show the same qualitative trends and are omitted here for the sake of brevity.

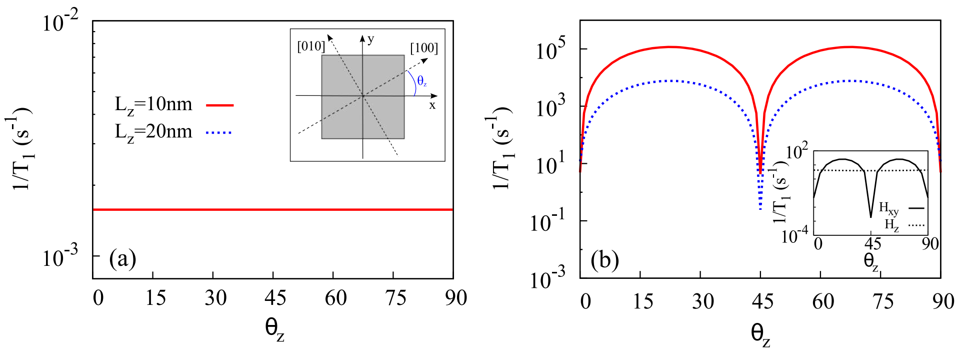

Figure 4.7: Spin dynamics as a function of the QD orientation for (a) pure RSOI and (b) pure DSOI in QDs with square base. Two dot heights are studied: $L_z = 10\,\mathrm{nm}$ (red solid line) and $L_z = 20\,\mathrm{nm}$ (blue dotted line). The magnetic field is directed along the x axis ($\phi_B = 0$) in all calculations. The inset in panel (a) depicts an illustration of the system in which the rotation angle θ_z is defined. The inset in panel (b) shows $1/T_1$ when the DSOI Hamiltonian is split into H_{xy} (solid line) and H_z (dashed line) for the dot with $L_z = 10\,\mathrm{nm}$.

Once we have studied the influence of geometry and in-plane QD orientation on the spin relaxation anisotropy, we are in a position to make sense of the results reported in the experiments of Scarlino *et al.* [126]. They measured the spin lifetime for rotating in-plane magnetic field and found a 180° periodicity with a small deviation of the extrema from the theoretical [110] direction. The periodicity was ascribed to the QD elongation assuming RSOI and DSOI to have the same weight, and the deviation from [110] to the misalignment of the dot principal axes with respect to the crystallographic main directions as well as to the RSOI to DSOI strength ratio. These two last factors are unknown in the experimental setup.

We investigate the effect of QD base elongation and in-plane rotation in the angle at which the relaxation rate becomes minimum, ϕ_B^{min}. The cubic DSOI terms that were ignored in their analysis, are taken into account here. In addition, the coefficient r_{41} has been changed to make RSOI as strong as the linear DSOI term H_z, i.e. $r_{41} = b_{41}^{CB}\langle p_z^2\rangle/F_z$.

Figure 4.8 illustrates ϕ_B^{min} versus the QD orientation θ_z. Calculations are carried out for dots with $L_x = 80\,\mathrm{nm}$ and $L_y = 80, 90, 110, 150\,\mathrm{nm}$. The results for a strongly elongated QD (green dotted line) shows that ϕ_B^{min} takes place when $B_{\parallel}$ points approximately along [110], which is consistent with the results of Scarlino *et al.* [126]. We attribute the small deviations observed to the cubic DSOI terms. As the elongation is reduced, these

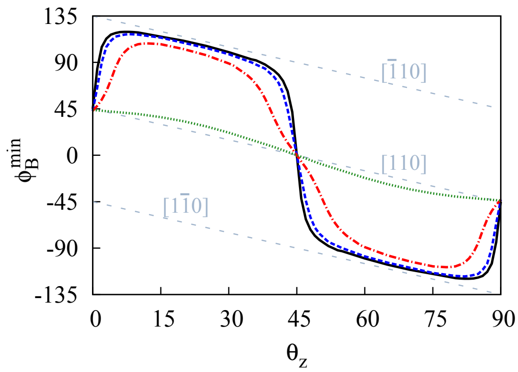

Figure 4.8: Magnetic field angle at which the $1/T_1$ curve presents a minimum as a function of the in-plane dot orientation θ_z. QDs with $L_x = 80\,\text{nm}$, variable L_y and $L_z = 10\,\text{nm}$ are considered. The L_y studied are: $L_y = 80\,\text{nm}$ (black solid line), $L_y = 90\,\text{nm}$ (blue dashed line), $L_y = 110\,\text{nm}$ (red dash-dotted line), and $L_y = 150\,\text{nm}$ (green dotted line). The values of ϕ_B corresponding to characteristic crystal directions [110], [1$\bar{1}$0] and [$\bar{1}$10] are indicated as gray dashed lines for reference.

deviations become much larger and the behavior with θ_z richer. In this case, the minimum relaxation is found when the magnetic field is along [110] only for $\theta_z = 0, 45, 90$, and rapidly deviates for other orientations. As can be seen in figure 4.8, for $0 < \theta_z < 45$ it is found when $B_\parallel$ is along [$\bar{1}$10] and for $45 < \theta_z < 90$ when is along [1$\bar{1}$0]. This behavior can be understood considering the inset of figure 4.7(b). When $\theta_z = 0, 45, 90$ the linear DSOI term H_z dominates, while H_{xy} takes over for any other θ_z. Then, the assumption of RSOI and H_z of similar strength to interpret the deviations of the electron spin relaxation is no longer valid. This stresses the important role of DSOI cubic terms in SOI anisotropy if the QDs are not strongly elongated.

4.3.3 [111] grown QDs

Lastly, we explore the spin dynamics as a function of the in-plane magnetic field orientation in the same square QD system as in section 4.3.1,[3] but now considering the dot is grown in the [111] crystal direction. The results for three different QD heights, $L_z = 10, 20, 30\,\text{nm}$, are depicted in figure 4.9.

[3]Rectangular dots yield the same qualitative behavior, the only difference is that the minima is slightly shifted for pure DSOI.

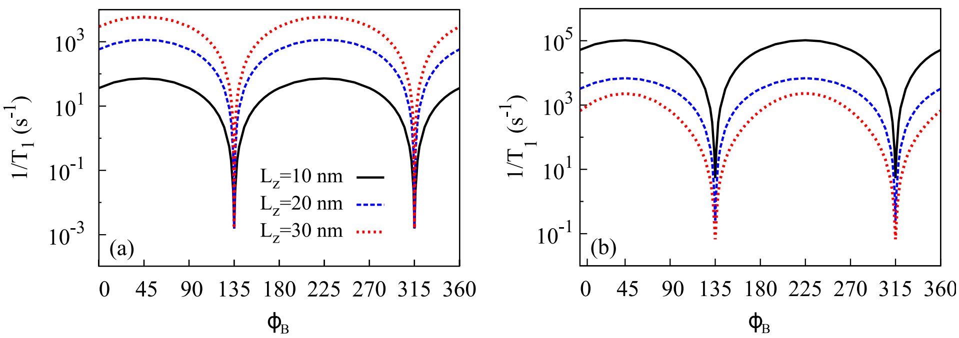

Figure 4.9: $1/T_1$ versus ϕ_B in square QDs grown along the [111] crystallographic direction. Simulations considering (a) pure RSOI and (b) pure DSOI are presented for three dot heights: $L_z = 10\,\text{nm}$ (black solid line), $L_z = 20\,\text{nm}$ (blue dashed line), and $L_z = 30\,\text{nm}$ (red dotted line).

Overall, a moderate increase in the spin relaxation rate is found in [111] grown QDs, figure 4.9, in comparison to [001] QDs, figure 4.6. Interestingly, both spin mixing mechanisms show the same angular dependence. That is, a periodicity of 180° with sharp minima at $\phi_B = 135$ and $\phi_B = 315$. The qualitative trend is the same for the three QD heights studied, with the only difference that $1/T_1$ increases for RSOI while it decreases for DSOI. Therefore, since the difference in magnitude is relatively small, the dominant coupling depends on the height of the QD.

The identical dependence observed for both SOIs is due to the formal equivalences between $H_{SIA}^{[111]}$ and $H_{BIA}^{[111]}$, as already discussed in literature for quantum wells.[131, 134] As for the strong suppression of the spin relaxation at $\phi_B = 135$ and $\phi_B = 315$, it can be justified if one notices that at these specific angles the canonical momenta $p_x = -i\hbar\, d/dx + zB \sin\phi_B$ and $p_y = -i\hbar\, d/dy - zB\cos\phi_B$ are exactly equal in magnitude since $L_x = L_y$. As a result, the first term in equation (4.13) and several terms in equation (4.14) cancel out, giving rise to a sharp decrease in $1/T_1$.

4.4 Hole spin relaxation in InAs/GaAs quantum dot molecules

Quantum dot molecules are ensembles of two QDs which are close enough to couple via tunneling. The coherent tunneling leads to the formation of

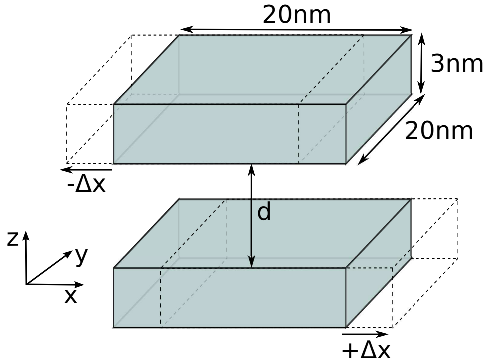

Figure 4.10: Drawing of the DQD cuboidal system. The dimensions of the QDs and the variables corresponding to interdot barrier thickness, d, and the shift in opposite directions along the x direction, Δ_x, are indicated. Dashed lines represent the DQD with misalignment.

states delocalized over the entire system that are truly molecular in nature, analogously to the hydrogen molecule. In general, they present the same properties as the constituent single QDs, but with the important advantage of being more versatile. That is, the localization of the wave function can be tuned by modifying the intensity of an externally applied electric field.[135–138] Therefore, one can change from an atomic-like state that is confined in one QD for large electric fields, to a fully molecular-like state when the energy of the QDs is modulated to be the same in both of them.[138] This clearly offers an additional control mechanism that might be very useful in the development of applications. For instance, quantum dot molecules have been suggested as a way to use independent optical transitions for spin preparation, manipulation and readout,[139] as well as in multiple qubit architectures.[140]

In particular, in this section we discuss the hole spin relaxation in a vertically coupled double quantum dot (DQD) formed by two identical InAs cuboidal dots embedded in a GaAs matrix, see drawing in figure 4.10. We consider systems with various relative positions of the individual QDs in order to assess the effect of different tunneling regimes and dots misalignments. The parameters that control the geometry of the structure are the interdot separation, d, and the offset along the x direction, Δ_x. It is obvious that to properly describe such a system, a 3D model is indispensable.

The four-band Hamiltonian describing the hole states in a DQD under an external electric field $\mathbf{F} = (0, 0, F_z)$ and a magnetic field $\mathbf{B} = (0, 0, B_0)$, both applied along the growth direction, reads:

$$H = H_{ZB}^{LK} + H_B + (V_{QD} + e\, F_z\, z)\,\mathcal{I} + H_{BIA}^{VB}, \tag{4.15}$$

where H_{ZB}^{LK} is the Luttinger-Kohn Hamiltonian, equation (A.1). H_B stands for the terms coming from the implementation of the magnetic field obeying the procedure introduced in section 2.2.2 for the VB. The third and fourth terms in (4.15) are the confining potential V_{QD} and the electric field potential (see section 2.2.1), respectively. Finally, the last term in the Hamiltonian stands for the DSOI, equation (2.23). Note that RSOI is disregarded here because preliminary calculations (not included) showed its negligible influence. This is due to the minimal asymmetry of the system in the growth direction under resonant electric fields.

The hole spin relaxation rate between Zeeman-split sublevels is computed by means of the Fermi's golden rule following the procedure described in section 4.1. Both lh-hh coupling and DSOI sources of spin admixing are taken into account in the scattering processes mediated by acoustic phonons.

The multi-band Hamiltonian (4.15) is integrated numerically by using the finite differences method. A 5-point stencil central difference scheme is employed since a series of convergence tests yielded the desired accuracy while maintaining a reasonable computational cost. On account of using a constant-mass model, all parameters used in the simulations correspond to InAs, except for the ones defining the phonons where parameters of the GaAs matrix are considered, as we assume bulk phonons.

We investigate the dependence of the spin relaxation on the electric field strength F_z in a DQD with strong tunneling, $d = 3\,\mathrm{nm}$. Figure 4.11 illustrates the energy spectrum and hole spin lifetime in DQDs with two different relative positions of the constituent dots: aligned (left panels) and misaligned (right panels). The displacement of the QDs takes place along the x direction by an offset $\Delta_x = 3.3\,\mathrm{nm}$ as represented in figure 4.10, which is relatively big but still realistic.[141] The investigated transition between the spin-split sublevels of the ground state is indicated by orange arrows in the energy spectra.[4] The wave function of these sublevels present hh character, as expected of flat systems. Therefore, the transition takes place from states with $J_z = +3/2$ ($\Uparrow$ in figure 4.11 insets) to states with $J_z = -3/2$ ($\Downarrow$). All calculations are performed considering an uniform axial magnetic field $B_0 = 2\,\mathrm{T}$.

To begin with, we focus on the energy spectra (top panels in figure 4.11). For both alignments, we observe a clear anticrossing at $F_z = 0$ between the

[4] Notice that the VB has negative energies, so that the ground state corresponds to the state with lowest absolute value of energy.

two lowest-lying states. The origin of this anticrossing lies in the change of localization of the wave function when varying F_z. As represented in the insets of figures 4.11(a) and 4.11(b), for large negative F_z the wave function is mainly localized at the bottom (top) QD for the ground (first-excited) state, while the situation is inverted for positive F_z. We see that the magnitude of this charge transfer anticrossing is smaller in the misaligned case as a consequence of the weaker tunneling between the dots.[141] It is also worth mentioning that, since the two QDs are identical in size, in the absence of an external electric field the dots are in resonance and the wave function is equally delocalized over the entire structure, i.e. we have molecular-like states.

As for the hole spin relaxation (bottom panels), two series of calculations are carried out: one taking into account only the Luttinger-Kohn Hamiltonian H_{ZB}^{LK} (black solid line), and the other including also the contribution of DSOI (blue dashed line). For both alignments the dependence of the relaxation time with the electric field is similar. When only the lh-hh spin mixing is considered, the spin relaxation time is maximum for molecular states, $F_z = 0$, and decreases as the states become more atomic-like at finite F_z. When the DSOI mechanism of spin mixing is added to the model, T_1 is obviously diminished. The lifetime reduction is about one order of magnitude for molecular states and somewhat less for finite F_z. In addition, now the T_1 curve at $F_z = 0$ is smoothed, becoming almost flat. With regard to the misalignment, we observe two main effects: an overall reduction of about one order of magnitude for both situations studied, H_L and H_{BIA}, and a faster decrease of T_1 with F_z for H_L. Both differences are also attributed to the fact that the molecular states disappear at smaller electric fields due to the weaker tunneling.

To justify the above results we need to analyze the degree of spin mixing in each situation. Other factors influencing T_1, such as the density of phonons, are not relevant since all calculations are performed at the same magnetic field. The strength of the SOI is related to the symmetry of the system. In general, a lowering in symmetry implies the activation of new mixing channels and, thus, an enhancement of the scattering mechanisms.[33] The symmetry of the system for the most relevant situations is indicated in figures 4.11(c) and 4.11(d) taking into account the ZB crystal structure, the confining potential and the presence of an axial magnetic field. An aligned homonuclear DQD considering only lh-hh mixing (H_L) has C_{4h} symmetry. The inclusion of an electric field breaks the parity symmetry in z, reducing the system symmetry to C_4, which justifies the decrease in T_1 with F_z. If we include the DSOI instead, the descent in symmetry is more important (C_2) and, consequently, the hole spin relaxation quenching is larger. Finally,

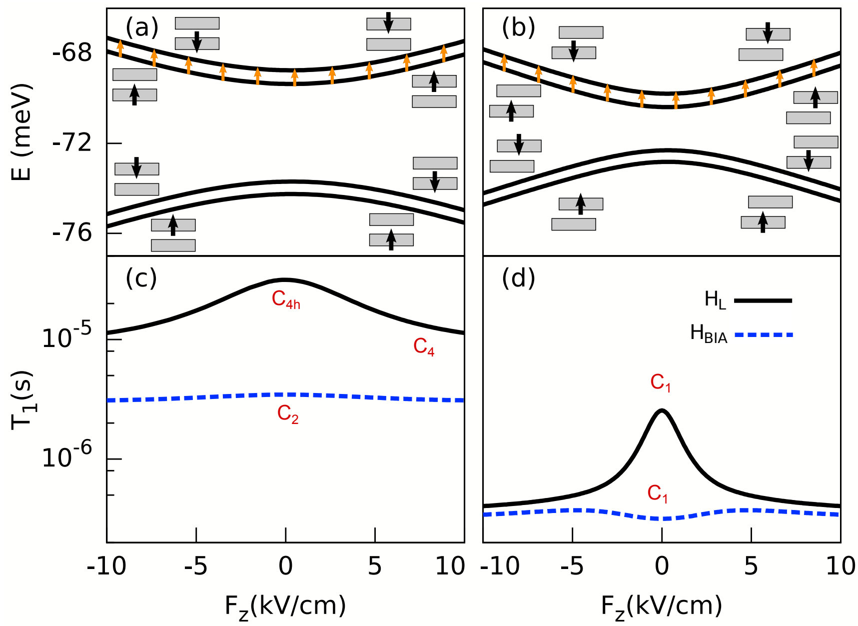

Figure 4.11: (a-b) Hole energy spectra and (c-d) hole spin lifetimes as a function of the electric field intensity F_z for a InAs/GaAs DQD in the strong tunneling regime, $d = 3\,\text{nm}$. Top panels include orange arrows indicating the investigated transition, and insets showing the localization of the wave function and its dominant component: $J_z = +3/2$ ($\Uparrow$) or $J_z = -3/2$ ($\Downarrow$). Bottom panels illustrate T_1 calculated by considering: only H_{ZB}^{LK} (black solid line H_L), i.e. lh-hh coupling, or both H_{ZB}^{LK} and DSOI Hamiltonian H_{BIA}^{VB} (blue dashed line H_{BIA}). Labels denoting the symmetry point group have also been added. Lastly, left (right) panels correspond to aligned (misaligned) QDs.

adding an external electric field to the H_{BIA} case does not further reduce the system symmetry and a flat dependence is obtained. On the other hand, in the DQD with misalignment the combination of the confining potential and the magnetic field lifts all symmetries, group C_1. This explains the reduction in the hole spin lifetime by one order of magnitude or more compared to the aligned case. Introducing an electric field or the DSOI to the model cannot reduce the symmetry further, but it improves the efficiency of the scattering by opening new channels of mixing, thus making T_1 even shorter.

Calculations for a DQD with weaker tunneling, $d = 9\,\text{nm}$, have been also carried out. The complete results are not included here for brevity, since they are qualitatively the same as the ones for strong tunneling, but can be found in the article (page 227). The hole spin lifetimes are of the same order of magnitude as those in figure 4.11 and also exhibit maximum T_1 for molecular states, $F_z = 0$. Nevertheless, the range of electric fields presenting enhanced lifetimes is now much narrower due to the weaker tunneling.

4.5 Control of electron spin-orbit anisotropy in pyramidal QDs

To close this chapter we investigate another experimental signature of SOI in semiconductor QDs, particularly the emergence of spin anticrossings in the energy spectrum. The magnitude of the gap opened at the anticrossing is known to be proportional to the SOI intensity,[142–144] offering the possibility to study the intrinsic anisotropy of RSOI and DSOI.

In relation to this, a experimental work by Takahashi *et al.* [116] reported a strong in-plane SOI anisotropy in InAs self-assembled QDs by measuring the size of the anticrossings as an external magnetic field is rotated. They found a dependence on the magnetic field azimuthal angle ϕ that fits the form of an absolute cosine function with an offset ϕ_0, i.e. $f(\phi) \propto |\cos(\phi - \phi_0)|$. In the same publication it was suggested that the origin of this offset might be a consequence of the QD elongated pyramidal geometry along with the contribution of only RSOI. Subsequently, a theoretical study by Nowak *et al.* [145] proposed an alternative origin. They attributed the offset to the combined action of both RSOI and DSOI in elongated QDs, and not solely to RSOI. The model they used consists in a cuboidal QD in which the confinement potential is taken as separable, $V(\mathbf{r}) = V_x(x) + V_y(y) + V_z(z)$. All results discussed throughout the preceding sections of this chapter have pointed out the crucial role of the geometry on the SOI strength, hence one wonders if using a simplified cuboidal system is enough to describe the behavior of realistic pyramidal QDs.

In view of the above, we investigate here the dependence of the anticrossing energy, E_{AC}, on the in-plane magnetic field orientation, ϕ, in a QD with similar geometry to the one used in the experiments of reference [116]. It consists in an uncapped InAs pyramidal QD grown on top of a GaAs wetting layer. Uncapped dots are usually oxidized on the surface, so the tip may acquire an insulating character and, thus, a truncated structure offers a more realistic description than a pyramidal one.[146] In addition, the base of the QD is rectangular with the longer side along the [100] crystallographic direction. A schematic drawing of the QD modeled is depicted in figure 4.12(a) together with all system dimensions.

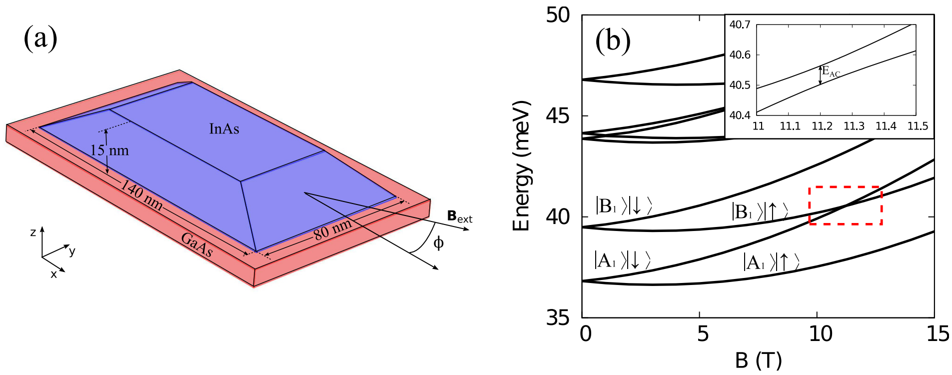

Figure 4.12: (a) Schematic representation of the uncapped pyramidal InAs QD grown on top of a GaAs wetting layer. The specific dimensions of the modeled geometry are indicated as well as the orientation of the magnetic field. The truncated pyramid is defined as having the upper base 0.6 times the size of the lower one. (b) Energy spectrum as a function of the magnetic field strength ($\phi = 0$) in the absence of SOI. The orbitals are labeled with its symmetry and spin orientation for $B = 0$ and no SOI. The inset is a zoom-in of the region marked by the red dashed box when both SOIs are activated.

The electronic states of such a system in the presence of an axial electric field and an in-plane magnetic field are described by employing the following constant-mass 3D Hamiltonian:

$$H = \frac{\mathbf{p}^2}{2m^*} + V(\mathbf{r}) - e\,\mathbf{F}\,\mathbf{r} + H_Z + H_{SIA}^{CB} + H_{BIA}^{CB}, \tag{4.16}$$

where $\mathbf{p} = -i\,\hbar\boldsymbol{\nabla} - e\,\mathbf{A}$ and $e = -1$. The in-plane magnetic field $\mathbf{B} = B(\cos\phi, \sin\phi, 0)$ is defined by the vector potential $\mathbf{A} = z\,B(\sin\phi, \cos\phi, 0)$, with ϕ being the azimuthal angle with respect to the x axis as represented in figure 4.12(a). The terms in equation (4.16) are, in this order, the kinetic energy (equation (2.20)), the confining potential, the external electric field (equation (2.19)), the Zeeman splitting (equation (2.20)), the RSOI Hamiltonian (equation (2.24)), and the DSOI Hamiltonian (equation (2.22)).

Hamiltonian (4.16) is solved using a finite-difference method on a regular 3D grid. Simulations are carried out taking the experimental effective g-factor instead of the bulk one, which is consistent with the observed g-factor reduction due to confinement. The axial electric field is estimated to be $F_z \approx -15\,\mathrm{kV/cm}$ from the supplemental material of [116]. In addition, unless otherwise stated we assume the QD to have a composition of 66 % In, accounting for the diffusion of Ga atoms from the wetting layer into

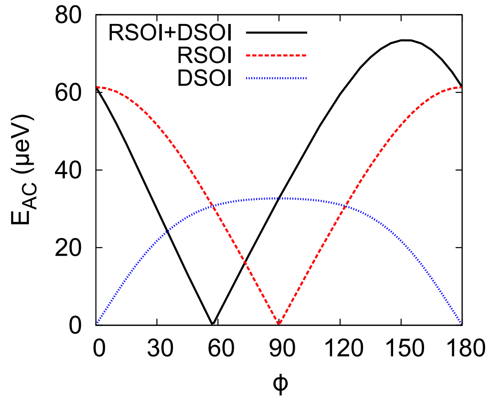

Figure 4.13: Anticrossing energy E_{AC} *vs.* magnetic field azimuthal angle ϕ. Calculations are performed including only RSOI (red dashed line), only DSOI (blue dotted line), and both RSOI and DSOI (black solid line).

the QD. Similar alloy compositions have been found experimentally in InAs self-assembled QDs.[147, 148] Consequently, the system parameters are calculated as the linear interpolation from the pure InAs and GaAs material parameters.

4.5.1 Angular dependence of the SOI

As mentioned above, we analyze the anticrossing energy E_{AC} for varying magnetic field orientation ϕ. We consider the intersection of states marked by a red dashed box in figure 4.12(b), where the energy spectrum in the absence of SOI is shown. We see that no avoided crossing between the states emerges. This is due to the different symmetry of the states involved, which are labeled in the plot according to their orbital symmetry (C_{2v} point group) and spin orientation at $B = 0$. Nevertheless, when the SOI is included the symmetry is reduced and an anticrossing appears, see inset in figure 4.12(b). The size of the opened gap is defined as the anticrossing energy E_{AC}.

In figure 4.13, we summarize the dependence of the spin anticrossing energy on ϕ when DSOI and RSOI are considered individually and also simultaneously. The results clearly evidence the strong anisotropy of the two SOI mechanisms. When only RSOI is taken into account, E_{AC} is maximum (minimum) for a magnetic field oriented along the x axis, $\phi = 0$ (y axis, $\phi = 90$). If only DSOI is considered, instead, the behavior is the opposite. Including both couplings at the same time gives rise to a curve with similar form to the ones obtained for the individual cases, but the singular points are no longer found for **B** pointing toward the main axes of the QD. The anticrossing energy vanishes exactly at the point where the two individual curves cross, indicating that the two terms cancel each other out. Based on this fact and after analyzing figure 4.13 carefully, it can be inferred that the curve including both terms can be derived from the absolute value of the addition or subtraction of the curves for the individual SOI mechanisms. The angular dependence of E_{AC} can be fitted well using the absolute value of a cosine function with an offset ϕ_0, i.e. $E_{AC} \propto \cos(\phi - \phi_0)$. Since the minimum of the function is determined by the crossing of the individual curves, the magnitude of ϕ_0 depends on the relative strength of the RSOI and DSOI contributions.

These results demonstrate the need of considering both SOIs for the offset ϕ_0 to exist. This is qualitatively the same behavior found by Nowak *et al.* [145], thus confirming the validity of their simplified cuboidal model in explaining the origin of the offset.

4.5.2 Effect of the QD composition and height

From the point of view of taking advantage of the SOI anisotropy in the development of spin-based applications, knowing under which circumstances the SOI vanish is of vital importance. For instance, it may be useful in spin control protocols and also in hindering spin decoherence mechanisms. In this regard, we investigate how the E_{AC} dependence is affected by two factors, namely the diffusion of the matrix material into the QD and the dot height.

Diffusion effects are generally relevant in InAs/GaAs self-assembled QD islands, leading to important variations in their composition.[147, 148] In figure 4.14(a), we consider four $In_xGa_{1-x}As$ alloys with a uniform concentration ranging from 50 % In to 100 % In. We observe that when the diffusion of Ga atoms becomes more important, the maximum in E_{AC} decreases and the angle at which SOI vanish is moved towards lower values. This behavior can be justified taking into account the values of the SOI coefficients. On one hand, the DSOI coefficients are similar for both materials, so its strength does not vary noticeably when changing the alloy composition. On the other hand, the InAs RSOI parameter is approximately 23 times higher than the GaAs one. As a consequence, increasing the Ga content results in weaker RSOI, thus shifting the angle where the anticrossing disappears towards the DSOI limit, $\phi = 0$.

Next, various QD heights are investigated in figure 4.14(b): $L_z = 10$, 15, 20 nm. A clear modulation of the overall SOI strength and the ϕ_0 value with

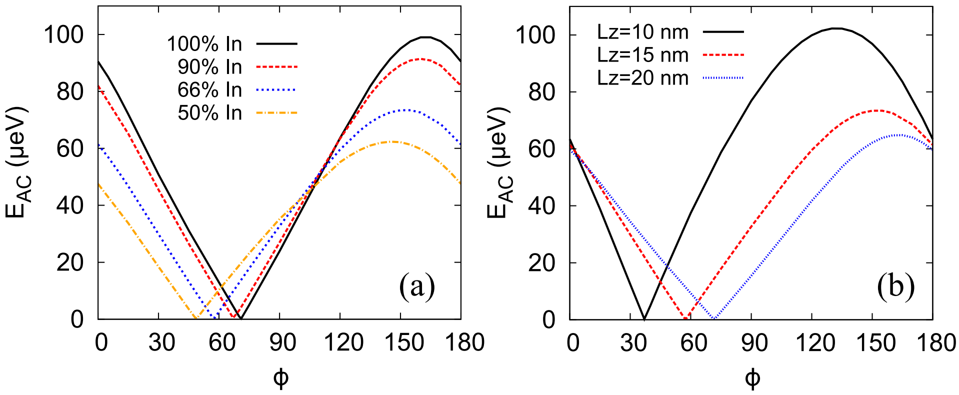

Figure 4.14: Anticrossing energy E_{AC} as a function of the magnetic field in-plane orientation for various (a) QD compositions and (b) QD heights. In panel (a) results for four QDs with different In content are shown: 100 % In (black solid line), 90 % In (red dashed line), 66 % In (blue dotted line), and 50 % In (orange dash-dotted line). Panel (b) presents the E_{AC} dependence for QDs with a height of 10 nm (black solid line), 15 nm (red dashed line), and 20 nm (blued dotted line).

L_z is found. Taller (shorter) dots give rise to smaller (larger) gaps and the cancellation angle is shifted towards larger (smaller) values. The effect of L_z can be explained if one analyzes the form of the SOI Hamiltonians. In the pyramidal QDs considered, the confinement along the z direction is stronger than in the xy plane, so that the dominant term in the DSOI Hamiltonian, equation (2.22), is $b_{41}^{CB} k_z^2 (\sigma_y k_y - \sigma_x k_x)$. Consequently, changes in the QD height modify the strength of DSOI approximately as $H_{BIA} \propto \langle k_z^2 \rangle \propto 1/L_z^2$, while the RSOI Hamiltonian, equation (2.24), remains unaltered. Therefore, an increase in L_z weakens the DSOI while RSOI remains roughly the same, thus leading to smaller anticrossing gaps and the zero SOI angle is shifted towards the RSOI limit, $\phi = 90$.

4.6 Summary

In this chapter we have studied the spin relaxation of electrons and holes, paying special attention to the SOI as a source of spin admixture, which allows the energy relaxation in the phonon bath. To this end, we have developed truly 3D models, going beyond the commonly employed quasi-2D simplified descriptions. Both semianalytic integration of Hamiltonians with harmonic confining potential, appropriate to describe ellipsoids of arbitrary shapes, and highly accurated numerical integration of Hamiltonians for pyramidal or cuboidal QDs have been carried out. Our numerical results reveal the need of including all three spatial dimensions for a proper description of the studied phenomena, since the physics of 3D systems, e.g. typical self-assembled dots or core-shell nanocrystals, cannot be inferred from that of flat systems modeled with quasi-2D simplified Hamiltonians. With our model we have been able to describe the highly anisotropic character of the spin relaxation with respect to the QD aspect ratio and the orientation of external magnetic fields for various crystal growth directions, the high sensitivity to alignment in QD molecules, etc., so that some apparent, previously reported, contradictory results have been harmonized and experimental results theoretically rationalized.

CHAPTER 5

Strain and piezoelectricity in wurtzite and polytype QDs

In the previous chapter, we have seen the crucial role of strain and piezoelectricity as the main carrier-phonon coupling mechanism in spin scattering processes induced by SOI in QDs. Nevertheless, the influence of these phenomena is not restricted to the field of spin dynamics. Indeed, both strain and piezoelectricity can lead to important changes in the electronic and optical properties of confined systems. Thus, understanding and controlling their effects is critical for the fabrication of novel QD-based devices.

Strain in semiconductor nanostructures is caused by the mismatch of the lattice constants of the constituent materials. In most applications strain is undesirable since it may originate interface defects that reduce PL efficiency.[149, 150] However, it also offers the opportunity to tailor the system properties by means of strain engineering. For instance, strain can be used to modify the CB and VB energies in order to induce changes in the band alignment of the materials, such as an indirect-to-direct band gap transition in germanium,[151] or from a type-I to a type-II heterostructure in CdTe/ZnSe QDs.[152] In addition, strain has also been used to change the VB ground state character between lh and hh in excitons.[153] As for the strain-induced piezoelectric fields, they are known to impact the spatial separation between electrons and holes in colloidal QDs which, in turn, may affect the exciton lifetimes,[154, 155] e-h exchange interaction,[156] and other properties relevant for opto-electronic devices.[1]

Piezoelectricity emerges in non-centrosymmetric crystals, e.g. ZB and WZ, when the structure is under strain or stress. Due to symmetry considerations, ZB presents quadrupole piezoelectric polarization, while WZ presents a stronger dipolar polarization.[157] Moreover, WZ crystals have an additional contribution to the total polarization, the so-called spontaneous polarization, P_{sp}. As a consequence, piezoelectric effects are, in general, far more important in WZ QDs than in ZB ones. In fact, typical piezoelectric fields in WZ materials are larger than 10^6 V/cm, an order of magnitude stronger than in ZB.[158]

The spontaneous polarization in heterostructures is stronger when the constituent materials have very different P_{sp} parameters. Hence, this phenomenon is expected to be especially relevant in polytype QDs. Such novel semiconductor structures are synthesized by growing alternate segments of WZ and ZB phases, i.e. alternating regions where spontaneous polarization is present with others where it is absent. As a result of the abrupt changes in P_{sp} at the WZ/ZB and ZB/WZ interfaces, one expects polytype systems to exhibit strong polarizations that give rise to important built-in electric fields. In spite of this, most theoretical works dealing with polytype QDs have neglected this effect,[20, 159, 160] so that further studies are required in order to gain a deeper understanding.

In light of the above, we investigate the role of strain and piezoelectricity, including P_{sp}, in WZ and polytype QDs. In particular, we focus on the behavior of excitons in colloidal CdSe/CdS nanocrystals and GaAs polytype QDs. We find out that piezoelectricity in core-shell colloidal structures and spontaneous polarization in polytype QDs are efficient mechanisms of charge separation for large enough systems. The spatial separation of electrons and holes governs the e-h overlap and, in turn, the exciton lifetime, thus representing a new degree of freedom for engineering nanodevices with the desired properties. The contents of the present chapter are based on the results of two articles, which can be consulted in pages 235 and 245.

5.1 Piezoelectric control of exciton wave function in wurtzite QDs

Excitons are bound states composed of an electron and a hole that are attracted to each other by the electrostatic Coulomb interaction. Consequently, the spatial separation between electrons and holes strongly affects many exciton properties, e.g. exciton emission lifetime,[154] Auger recombination rate,[161, 162] and e-h exchange interaction,[156] to name a few.

In colloidal core-shell nanocrystals the localization of the carriers has been typically tailored by means of band gap engineering. That is, electrons and holes can be confined into the core or the shell by properly combining materials with different band gap. Depending on the material combination we can have both carriers in the core (type-I band alignment), both in the shell (inverted type-I), one in the core and the other in the shell (type-II), and also one in the core and the other delocalized over both core and shell (quasi-type-II).

Additionally, in systems with large lattice mismatch strain has also been proposed as a mechanism to control carriers separation. In such a case, strain produces shifts of different magnitude in the band edges of core and shell materials, leading to transitions from one band alignment to another. This control mechanism has been investigated in CdTe/ZnSe,[152] CdSe/CdTe,[163] and ZnSe/ZnTe nanocrystals,[164] among others. However, it cannot be efficiently employed in CdSe/CdS QDs owing to their weak strain, hence the e-h separation in such structures has been traditionally controlled by quantum confinement. This is unfortunate because this system is particularly of interest due to their monodispersity, narrow emission linewidth, reduced blinking and high PL quantum yield.[165, 166] Nevertheless, a recent experiment in a "giant" CdSe/CdS rod-in-rod system has reported extremely long exciton lifetimes as a consequence of a relatively strong strain-induced piezoelectric field.[155] One then wonders if piezoelectricity may be also important in other CdSe/CdS systems and, if so, under which circumstances.

In this section, we explore how strain and piezoelectricity[1] affect the exciton wave function in 3D dot-in-dot WZ CdSe/CdS nanocrystals. We describe electrons and holes using a 2- and 6-band k·p Hamiltonian, respectively, taking into account strain and piezoelectricity within the continuous elastic theory, as discussed in section 2.4. The position-dependent Hamiltonian for electrons reads:

$$H_e = \mathbf{p}\frac{1}{2m^*}\mathbf{p} + V_{QD} + H^{WZ}_{\epsilon,CB} + H_{pz}, \tag{5.1}$$

where m^* is the electron effective mass, $\mathbf{p} = -i\hbar\boldsymbol{\nabla}$ and V_{QD} stands for the confining potential. $H^{WZ}_{\epsilon,CB}$ represents the strain Hamiltonian for the WZ CB, equation (C.4), and H_{pz} represents the diagonal piezoelectric potential, equation (2.41). The Hamiltonian for holes is as follows:

$$H_h = H_{WZ} + V_{QD} + H^{WZ}_{\epsilon,VB} + H_{pz}. \tag{5.2}$$

Here, H_{WZ} is the six-band Hamiltonian describing the WZ VB, equation (A.4). $H^{WZ}_{\epsilon,VB}$ denotes the WZ strain Hamiltonian for holes, equation (C.5), while H_{pz} is the same as for electrons, but using hole's charge.

[1]For simplicity, the contribution of the spontaneous polarization is disregarded since preliminary results show that it does not change the qualitative trends.

The Coulomb interaction between electrons and holes is taken into account by iteratively solving the Schrödinger-Poisson equation. First, we solve the independent single-particle problem for the CB. Next, the calculation is carried out for the VB including the electron charge density from the previous step via the Poisson equation, equation (2.36). Then, equation (5.1) for electrons is solved again, but now incorporating the calculated hole charge density. Lastly, this procedure of alternately solving electrons and holes considering the charge density of the other carrier from the previous step is repeated until convergence is reached.

Hamiltonians (5.1) and (5.2), and the Poisson equation are solved using the commercial software Comsol 4.2, which employs the finite elements method in a 3D mesh. Material parameters are given in the Supplementary Material of the article, page 245.

5.1.1 Spheroidal dot-in-dot systems

We start investigating systems of spheroidal shape in which CdSe core and CdS shell are equally elongated. Three different structures are considered: spherical, figure 5.1(a), prolate, figure 5.1(b), and oblate, figure 5.1(c).

Analyzing the form of the polarization vector for WZ materials, equation (2.40), it can be seen that the usually larger diagonal strain components appear only in the P_z component. Thus, one expects polarization effects to be more important along the c-axis. Because of this, we study the potential profiles along the growth direction z, figures 5.1(d-f). Black dashed lines indicate CB and VB confining potentials for reference. The total potential $V^{tot} = V_{QD} + V_{str} + V_{pz}$ for each subband is also depicted as solid lines of different colors.

In general, we find a similar behavior for the three geometries. For the CB, orange curve, we observe that the core potential well becomes shallower and the core bottom develops a built-in electric field of approximately 15 mV/nm. The potential of the shell is increased by V_{str} and V_{pz} at one side of the well, while it is decreased at the other one. Remarkably, the potential minima, indicated by red arrows in the plots, are lower in energy than the core bottom, thus favoring the leakage of electrons into the shell. As for the VB, subbands A, B and C are represented as red, green and blue curves, respectively. In this case, the core bottom is moved upwards, originating a deeper well. A built-in electric field similar to that in the CB is also present. Holes are pushed towards the contrary direction compared to electrons provided their opposite charge sign, thus favoring e-h separation.

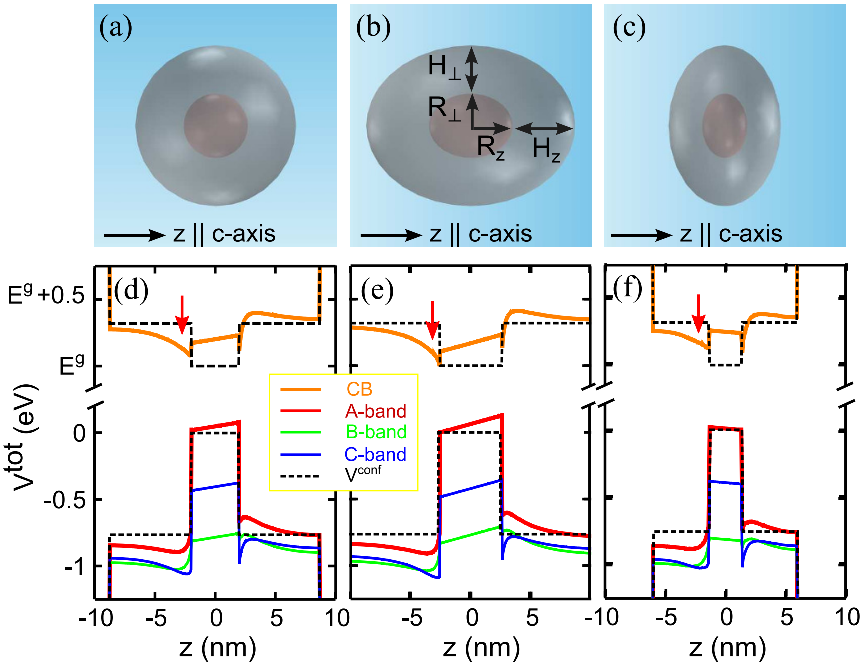

Figure 5.1: Schematic drawing of (a) spherical, (b) prolate, and (c) oblate CdSe/CdS core-shell nanocrystals. The c-axis is indicated together with the core radii $R_{(\perp,z)}$ and shell thicknesses $H_{(\perp,z)}$. (a) $R_\perp = R_z = 2\,\text{nm}$ and $H_\perp = H_z = 7\,\text{nm}$. (b) Same as (a) in the in-plane direction and $R_z = 1.3R_\perp$ and $H_z = 1.3H_\perp$. (c) Same but with $R_z = 0.7R_\perp$ and $H_z = 0.7H_\perp$. Panels (d) to (f) show the CB and VB potential profiles along the z direction for the (d) spherical, (e) prolate, and (f) oblate systems. The plots include the confining potential (black dashed line), and the total potential for the CB (orange line), A-band (red line), B-band (green line), and C-band (blue line).

The potentials in the shell are also similar to those in the CB, but now the potential well remains deep enough to guarantee the localization of the holes inside the core.

In order to understand the origin of this behavior we show in figure 5.2 the individual effect of strain and piezoelectricity. The potentials shown correspond to the CB, but are also extensive to the VB. We see that strain V_{str}, figure 5.2(a-c), increases the energy inside the core, while in the shell it decreases the energy in a small region next to the interface. This explains the shallower well found for the CB. The piezoelectric potential V_{pz}, figure 5.2(d-f), forms a dipole due to the accumulation of charges of opposite sign on each CdSe/CdS interface, and a linear built-in electric field in the

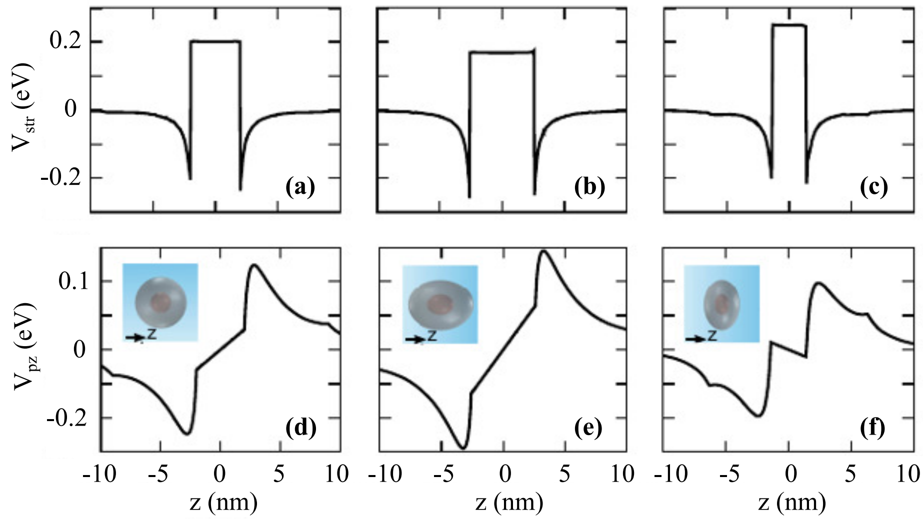

Figure 5.2: (a-c) V_{str} and (d-f) V_{pz} along the c-axis of the WZ structure. Results for spheric (left column), prolate (central column), and oblate (right column) are presented.

core. Obviously, the potential created in the shell by these charges has opposite sign at each side of the core, and its magnitude is large enough to compensate the CB core well depth, allowing electron delocalization. It is also interesting to notice that the core electric field is larger (smaller) in prolate (oblate) systems. Indeed, in oblate QDs the electric field can even change sign, as can be observed in figure 5.2(f).

The dependence of the polarization field on the QD geometry can be justified by analyzing the axial and in-plane strain components ϵ_z and $\epsilon_\perp$, respectively. Figure 5.3 illustrates the values of ϵ_z and $\epsilon_\perp$ in the cut plane xz for the three geometries. The polarization along the c-axis is given by $P_z = e_{31}(\epsilon_{xx} + \epsilon_{yy}) + e_{33}\,\epsilon_{zz}$. Since $e_{33} \approx -2e_{31}$, the sign of the polarization is determined by the relative magnitude of $\epsilon_\perp$ and ϵ_{zz}. In figures 5.3(a) and 5.3(d), spheric system, the compressive strain in the core is slightly anisotropic with $|\epsilon_{zz}| > |\epsilon_\perp|$, which yields a small negative P_z. In prolate nanocrystals, figures 5.3(b) and 5.3(e), the strain ϵ_{zz} increases further, explaining the strongest P_z and V_{pz}. Finally, in oblate systems, figures 5.3(c) and 5.3(f), ϵ_{zz} in the core decreases while $\epsilon_\perp$ increases. In fact we have $|\epsilon_{zz}| < |\epsilon_\perp|$, yielding a positive polarization P_z that justifies the sign reversal in figure 5.2(f).

If we focus now on the strain components in the shell, it can be seen that

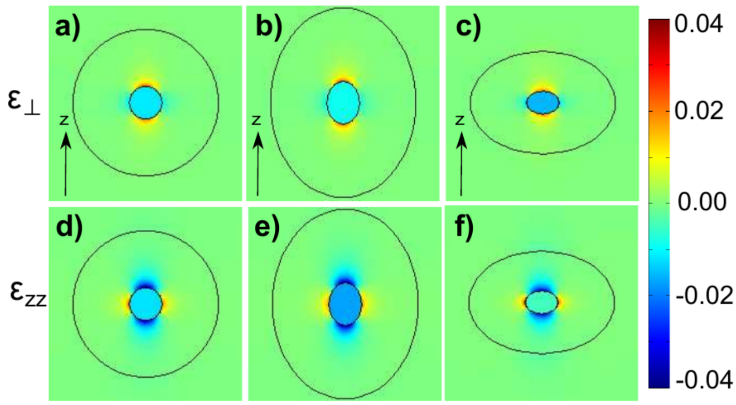

Figure 5.3: Diagonal strain along the c-axis ϵ_{zz} (top row) and in the xy plane $\epsilon_{\perp} = 1/2(\epsilon_{xx} + \epsilon_{yy})$ (bottom row). Left column corresponds to spherical QDs, central column to prolate QDs, and right column to oblate QDs.

the anisotropy is much more important. In the z direction, $\epsilon_{\perp}$ is tensile, $|\epsilon_{\perp}| > 0$, while ϵ_{zz} is compressive, $|\epsilon_{zz}| < 0$. This originates a strong V_{pz} in the shell with an abrupt change at the interface, as seen in figure 5.2(d-f).

Now that we know the form of strain and piezoelectric potentials, we investigate the carriers localization in CdSe/CdS dot-in-dots for various core radii R and shell thicknesses H. We have seen in figure 5.1 that the piezoelectric field pushes electrons towards the shell, but we need to explore if this is strong enough to surpass the Coulomb interaction. Figure 5.4 depicts the charge density of electrons, panels (a-d), and holes, panels (e-h). Overall, we find that the electron charge density can be localized in the core or the shell depending on the system dimensions, while holes are localized into the core in all cases.

For small radius and thin shell, figures 5.4(a) and 5.4(e), both electron and hole are localized in the CdSe core, although the electron density penetrates a little into the shell due to the shallower potential well. When the shell is enlarged, figures 5.4(b) and 5.4(f), the core is more compressed and, thus, the strongest polarization makes the electron to leak partially into the shell. Contrarily, the deeper potential well of the VB prevents the hole delocalization. If we increase the core radius and maintain a thin shell instead, figures 5.4(c) and 5.4(g), both carriers remain inside the core but electron and hole are pushed downwards and upwards, respectively, in spite of the Coulomb interaction. Interestingly, in a large core with a giant shell, fig-

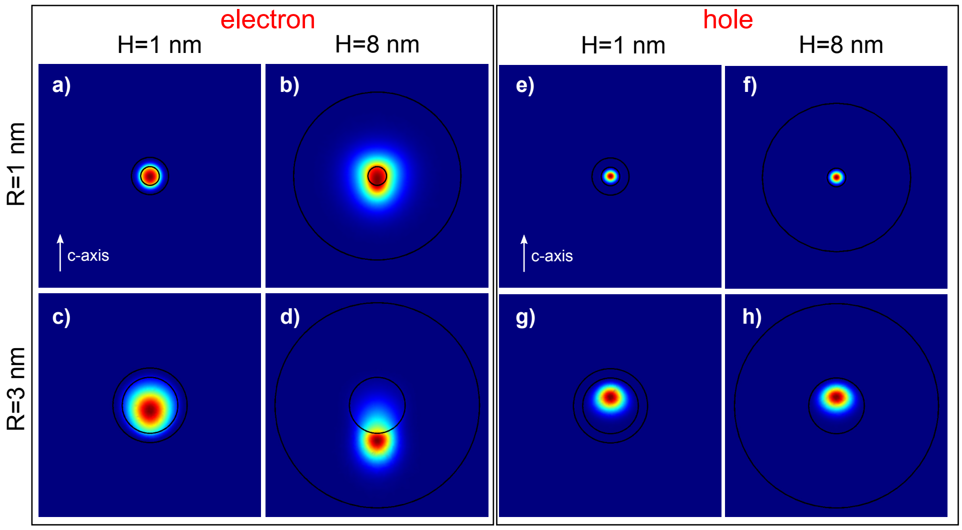

Figure 5.4: (a-d) Electron charge density in spheric core-shell QDs of various radii and shell thicknesses, as indicated in the plot. (e-h) Same for the hole charge density.

ures 5.4(d) and 5.4(h), the electron density is mainly localized in the shell near the interface while the hole remains in the core. This demonstrates that piezoelectricity is capable of originating an evident charge separation in WZ dot-in-dot systems as a consequence of the transition from type-I to type-II band alignment when growing larger shells.

In order to systematically study the dependence of carriers separation on core-shell QD dimensions we compute the e-h overlap integral squared $S_{eh}^2 = \langle \Psi_e | \Psi_h \rangle^2$ as a function of R and H. The results are summarized in figure 5.5 for $V_{str} = 0$ and $V_{pz} = 0$, panel (a), $V_{str} \neq 0$ and $V_{pz} = 0$, panel (b), and $V_{str} \neq 0$ and $V_{pz} \neq 0$, panel (c). In general, by comparing the three series of calculations we observe an important reduction in S_{eh}^2 as strain and piezoelectricity are included in the simulations.

When only quantum confinement effects and Coulomb interaction are considered, figure 5.5(a), we obtain high e-h overlaps for moderate and large cores independently of the shell thickness. For small CdSe core radius, $R \approx 1 - 1.5\,\mathrm{nm}$, the overlap is strong for thin shells but decreases substantially as the shell becomes thicker. In systems of these dimensions, i.e. small R and large H, the band alignment is quasi-type-II explaining the small value of S_{eh}^2, see the marked regions in figure 5.5(a). Here, electron density penetrates into the shell as a result of the high kinetic energy in small QDs

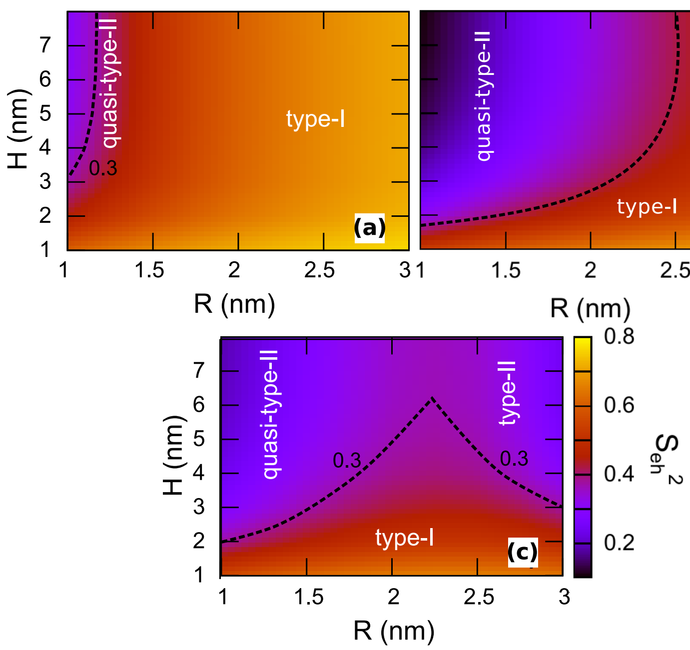

Figure 5.5: Map of the squared e-h overlap S_{eh}^2 as a function of R and H for excitons in spherical CdSe/CdS dot-in-dot systems. Calculations are carried out without considering strain and piezoelectricity, panel (a), including only strain, panel (b), and also considering both of them, panel (c).

and the shallow potential well. Figure 5.5(b) shows the exciton overlap squared when strain is included. One can see that the region with quasi-type-II regime is extended to larger cores. This is because strain lessens the potential well depth, so that weaker kinetic energies suffice to produce electron delocalization. Lastly, the results when both effects are taken into account are depicted in figure 5.5(c). For moderately small core radius, $R < 2.5$ nm, the results are similar to those with only strain. However, for larger dots piezoelectricity starts playing a role and we see the emergence of a type-II region for large enough shells. This behavior corresponds to figures 5.4(d) and 5.4(h) where electrons are localized in the shell while holes stay inside the core.

It is worth noting that the exciton overlap behavior is robust against small elongations of the system as seen in calculations for the same prolate and oblate structures of figures 5.1(b) and 5.1(c), respectively. The corresponding results are not included here for brevity, but can be found in figure S5 of the publication's Supplementary Material, page 245.

All the above results have been confirmed experimentally in a series of giant-shell CdSe/CdS dot-in-dot structures. In those experiments, time-resolved PL measurements reveal longer exciton lifetimes with increasing core radius, in agreement with the smaller exciton overlap predicted theoretically. The experiments were carried out by A. Polovitsyn and I. Moreels from the *Istituto Italiano di Tecnologia* in Genova (Italy) in a collaboration with our group. The experimental results and the details of the synthesis and measurement methods can be found in the published article, page 245.

5.1.2 Other CdSe/CdS core-shell structures

For the sake of completeness, we also explore the influence of strain and piezoelectricity on the e-h overlap in nanostructures with other geometries, namely dot-in-rods, dot-in-plates and rod-in-rods. Such systems are modeled as highly elongated ellipsoids in either the z or the in-plane direction.

Figure 5.6 shows the electron and hole charge densities for such structures with various core and shell dimensions. In general, we find that piezoelectricity is an efficient mechanism of charge separation in all the studied wurtzite CdSe/CdS core-shell structures as long as both core and shell are large. This is clearly seen in rod-in-rods with large cores and giant shells, figure 5.6(d), which goes along with the extremely long exciton lifetimes reported for this system.[155] It is worth stressing that a thick shell is necessary not only in the growth direction, where the polarization field emerges, but also in the lateral one. For example, in systems with thin shells in one direction such as dot-in-rods, figure 5.6(a), and dot-in-plates, figure 5.6(c), of typical dimensions, carriers are localized inside the core since the shell cannot compress much the core, thus yielding a weak core strain and in turn a weak polarization field. This becomes evident in figure 5.6(b) (5.6(e)) where carriers separation is enhanced (suppressed) when the lateral confinement is weakeaned (strengthened). Therefore, it can be concluded that the e-h overlap induced by piezoelectricity can be modulated in all the structures investigated by properly controlling their shell lateral confinement.

5.2 Spontaneous polarization in GaAs polytype QDs

Polytype QDs are a new type of semiconductor nanostructures that have been successfully synthesized in the past few years.[20, 21] They consist of

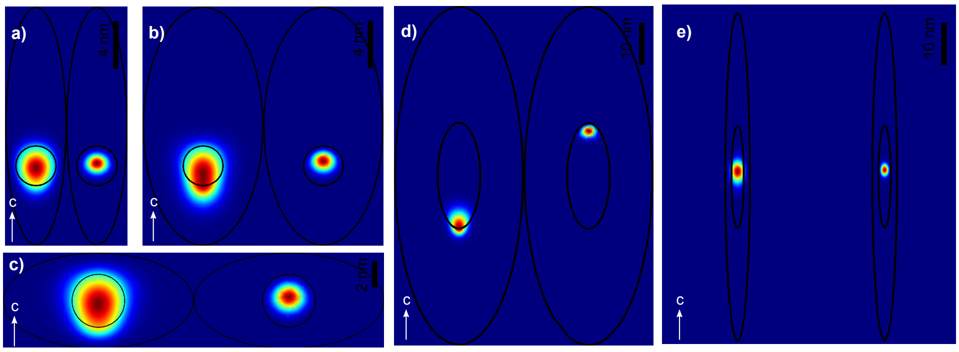

Figure 5.6: Excitonic charge density in various wurtzite CdSe/CdS nanocrystals: (a) dot-in-rod with standard dimensions; (b) dot-in-rod with enlarged lateral shell; (c) dot-in-plate; (d) rod-in-rod with large core and giant shell; (e) rod-in-rod with core and shell of small lateral size. In each panel, electrons are represented on the left and holes on the right side.

a nanowire system in which ZB and WZ crystal structures of the same material coexist, i.e. the system presents alternate segments of both crystal phases. These two phases have somewhat different band gaps, hence band offsets are formed and carriers can be confined originating QDs.[167] Since all regions are composed of the same atoms with the only difference being their spatial arrangement, these dots present negligible strain and atomically sharp interfaces.[168, 169] This offers the opportunity to control the geometry with a single atomic layer precision, which is a great advantage compared to self-assembled QDs where strain and alloying effects limit the optoelectronic performance. Consequently, polytype QDs are expected to have excellent optical properties, which makes them promising for future applications.

Recent advances in the synthesis techniques have allowed the fabrication of single crystal phase QDs with good control on their dimensions. In particular, Vainorius *et al.* [159] have reported the synthesis of GaAs polytype QDs with exact control on the dot thickness, while Loitsch *et al.* [170] have grown samples of the same system with various nanowire diameters down to 7 nm. Together, these experimental works show that precise tailoring of the QD geometry and, thus, of the energy structure is possible, which represents the first step towards the development of real devices.

From a theoretical point of view, however, crystal phase QDs have not been extensively investigated yet and the influence of several factors is still unclear. Among them, here we pay special attention to the role of quantum

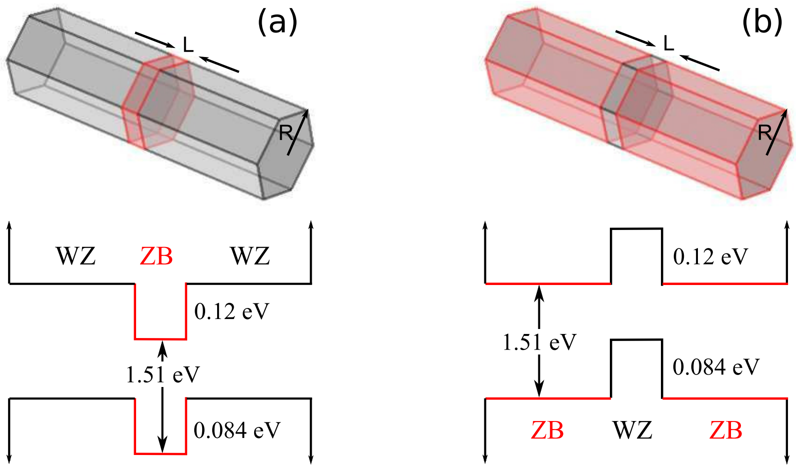

Figure 5.7: Schematic drawings of the hexagonal polytype structures and the potential profiles along the growth direction for (a) ZB QD in a WZ wire and (b) WZ QD in a ZB wire. Band offsets, band gaps and parameters defining the structure size are also indicated.

confinement, spontaneous polarization, VB mixing and exciton Coulomb interaction. Polytype QDs often present a type-II band alignment, e.g. in GaAs [159] and InP [169], giving rise to effective e-h separation. Nevertheless, the band offsets between WZ and ZB are commonly small and the high kinetic energy in small systems may lead to significant electron and hole wave function leakage into each other's phase. Additionally, as seen in the preceding section, polarization fields and Coulomb interaction strongly affect carrier localization and, hence, they may drastically change the exciton properties. Lastly, to date the role of VB mixing is poorly understood and further assessment to determine the dominant subband for different size regimes is needed.

Particularly, in the present section we focus on GaAs polytype QDs within the confinement ranges reported by Vainorius *et al.* [159] and Loitsch *et al.* [170]. We study hexagonal nanowires with variable dot thickness L and radius R, as illustrated in figure 5.7. Since GaAs ZB/WZ structures have type-II band alignment, electrons and holes are localized in different regions of the system. Thus, we investigate excitons considering the two possibilities of defining a single polytype QD, namely a ZB QD embedded in a WZ nanowire, figure 5.7(a), and a WZ QD embedded in a ZB wire, figure 5.7(b). Such polytypical structures are modeled using the k·p method as explained in section 2.1.5.

Electrons are described using a single-band Hamiltonian. This is justified in ZB structures where the lowest subband is well separated from other remote bands. However, the situation is different in WZ GaAs where Γ_{8c} and Γ_{7c} bands are close to each other. In spite of this, the lack of mass parameters does not allow to model both bands simultaneously. Instead, we use a single-band Hamiltonian of hybrid character: Γ_{8c} masses but optically bright as Γ_{7c} band.[171, 172] The polytype CB Hamiltonian reads

$$H_e = \mathbf{p}\frac{1}{2m^*}\mathbf{p} + V_{QD} + H_{pz}, \tag{5.3}$$

where $\mathbf{p} = -i\hbar\boldsymbol{\nabla}$, V_{QD} is the confining potential defined by the ZB/WZ band offset, and H_{pz} stands for the total polarization field potential, equation (2.41).

Holes are described employing a six-band position-dependent Hamiltonian spanned on the same basis of Bloch functions in both crystal structures. The specific basis set used here is that of lower symmetry, i.e. the one for WZ materials given in equation (2.16). The VB Hamiltonian is as follows:

$$H_h = H^{BF}_{ZB/WZ} + \left(V_{QD} + H_{pz} - \frac{\Delta_{so}}{3}Y_{ZB}\right)\mathcal{I}_{6x6}, \tag{5.4}$$

with $H^{BF}_{ZB/WZ}$ denoting the VB polytype Hamiltonian given in equation (A.6). As in the CB, equation (5.3), V_{QD} and H_{pz} are the confining and polarization field potentials, respectively. Last term in (5.4) corrects the Hamiltonian when using ZB parameters by subtracting $\Delta_{so}/3$ in all diagonal elements. Then, Y_{ZB} is a heaviside function which takes $Y_{ZB} = 0$ in WZ and $Y_{ZB} = 1$ in ZB crystal phase.

As already discussed in section 2.1.5, polytype QDs are formed by segments of ZB phase grown along the [111] crystal direction and segments of WZ phase grown along [0001]. These two crystal phases are constituted by the same atoms and only differ in the stacking order of the layers. Furthermore, the atoms have the same tetrahedral coordination in both crystal structures. As a result, the lattice mismatch at the ZB/WZ interface is insignificant and strain effects can be safely disregarded in equations (5.3) and (5.4). This is in agreement with experimental works that have synthesized defect-free dots.[159, 170]

If strain is negligible, so is the strain-induced piezoelectric polarization. Therefore, spontaneous polarization is the only significant source of polarization in these systems. Relevantly, such phenomenon is expected to be particularly strong in polytype QDs owing to the alternation of phases where the spontaneous polarization is absent (ZB) with others where symmetry allows its presence (WZ). The abrupt change in P_{sp} at the interfaces should result in a substantial overall polarization field. Nonetheless, WZ GaAs presents one order of magnitude weaker P_{sp} in comparison to other materials, so its effect might be limited.

Finally, neutral excitons are described by the following Hamiltonian

$$H_X = H_e + H_h^{1B} + V_{eh}, \tag{5.5}$$

where V_{eh} is the e-h Coulomb interaction. For the sake of simplicity, we use here a single-band model for the VB, H_h^{1B}, obtained after decoupling the F band from the rest of the matrix in Hamiltonian (5.4), which is justified under certain conditions,[2] as will be shown in section 5.2.2. Please note that in this section we refer to the WZ A, B and C hole subbands as F, G and λ, respectively, which is an alternative notation commonly used in literature. The resulting one-band Hamiltonian is

$$H_h^{1B} = \Delta_1 + \Delta_2 + \mathbf{p}_\perp \frac{1}{2m_\perp^*}\mathbf{p}_\perp + \mathbf{p}_z \frac{1}{2m_z^*}\mathbf{p}_z + V_{QD} + H_{pz} - \frac{\Delta_{so}}{3} Y_{ZB} \tag{5.6}$$

Equation (5.5) is solved by taking into account V_{eh} using exactly the same procedure introduced in the previous section, in which Hamiltonians (5.3) and (5.4), and the Poisson equation are iteratively solved until convergence.

Simulations are carried out considering the nanowire to be surrounded by an insulating material by setting in this region $|V_{QD}| = 5\,\mathrm{eV}$ and the relative dielectric constant $\varepsilon_r = 4$. We use Comsol 4.2 software in the calculations, which employs a finite elements scheme on a 3D adaptive mesh. The GaAs parameters used to model the ZB and WZ materials can be found in the corresponding publication, page 235.

5.2.1 Electrons in GaAs WZ/ZB/WZ polytype QDs

We first investigate a single electron confined in a ZB QD as the one represented in figure 5.7(a). We consider a nanowire with radius $R = 50\,\mathrm{nm}$, and calculate the electron energy as a function of the dot thickness L. Figure 5.8(a) compares the results for two values of the GaAs spontaneous polarization: the one reported in literature $P_{sp} = 2.3 \times 10^{-3}\,\mathrm{C\,m^{-2}}$ (solid line) and a value weakened artificially one order of magnitude $P_{sp} = 2.3 \times 10^{-4}\,\mathrm{C\,m^{-2}}$

[2] In WZ holes, the uppermost F band is separated by the spin-orbit ($\Delta_{so} = 3\Delta_2$) and crystal field splittings ($\Delta_{cr} = \Delta_1$). In ZB, instead, hh and lh subbands are degenerate but they are split by the action of quantum confinement.

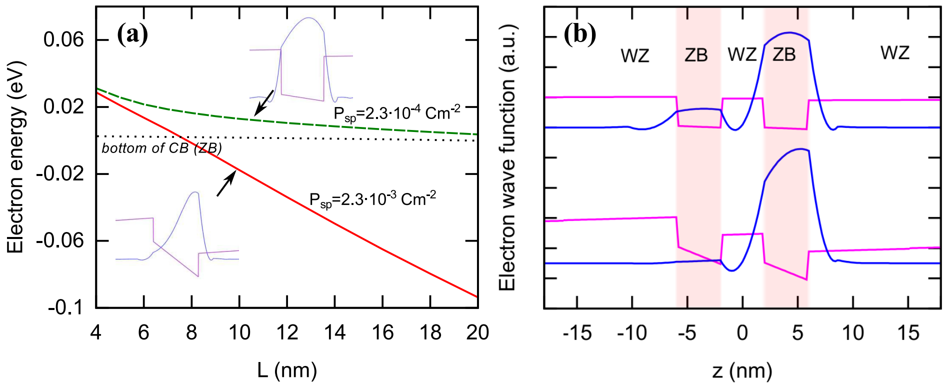

Figure 5.8: (a) Electron ground state energy for varying QD thickness in a ZB QD with fixed radius $R = 50\,\text{nm}$. Calculations for realistic (solid line) and weakened (dashed line) GaAs spontaneous polarization are presented. The bottom of the QD CB is indicated as a dotted line for reference. The insets show the localization of the wave function in both cases studied. (b) Wave function and confining potential cut line along the growth direction for a vertically symmetric GaAs ZB DQD. Results for weakened (top) and full P_{sp} (bottom) are shown. Both QDs have $L = 4\,\text{nm}$.

(dashed line). By comparing the two curves, one can see the big influence of spontaneous polarization on the ground state energy, specially for large dot thickness. This clearly points out that P_{sp} cannot be disregarded in moderately large systems. In the case of a realistic P_{sp}, the curve presents a linear dependence with L that stabilizes the ground state well below the bottom of the CB as a consequence of the built-in electric field. The wave function is then pushed towards the upper ZB/WZ interface partially leaking into the WZ phase, see the corresponding inset in figure 5.8(a). Contrarily, when the spontaneous polarization is reduced we find a quadratic regime for $L < 10\,\text{nm}$, governed by quantum confinement, that becomes linear for larger L. In such a case, the energy stabilization is much less pronounced and the wave function is mainly localized inside the ZB dot, see inset.

Similarly to traditional heterostructures where quantum confinement is originated by growing regions of different materials, polytypes can also be used to build systems of coupled QDs. In fact, the exact control in the synthesis of atomically sharp interfaces opens the possibility to produce homonuclear molecular states by fabricating perfectly symmetric pairs of QDs. Oppositely to self-assembled DQDs, polytype DQDs would not require the help of external electric fields to get states with homonuclear character. However, as seen in the insets of figure 5.8(a), the polarization fields originate a significant distortion of the wave function that implies the breaking of its symmetry. Indeed, this fact is confirmed in figure 5.8(b), where the wave function along the z direction is depicted for the same P_{sp} values of figure 5.8(a). It can be observed that, even when the spontaneous polarization is reduced, the wave function is mainly localized in the upper dot, thus confirming P_{sp} as a factor to be accounted for in the fabrication of polytype DQDs with homonuclear molecular states.

5.2.2 Holes in GaAs ZB/WZ/ZB polytype QDs

Holes are confined in the WZ phase in GaAs polytype structures. Thus, we study the VB of WZ QDs embedded in a ZB nanowire, see figure 5.7(b) for a schematic representation. The behavior of the hole energy under the effect of spontaneous polarization is similar to that of electrons, so we do not include the corresponding results here. Instead, we focus on the VB mixing and, more specifically, on determining the subband that contributes the most to the ground state.

The VB wave function is a six-component spinor of the form: $\Psi_h = \sum_{i=1}^{6} f_i(\mathbf{r})\,|u_i\rangle$, with $f_i(\mathbf{r})$ standing for the envelope function and $|u_i\rangle$ for the associated Bloch function. Previous works have assumed a ground state with dominating well-defined hh character.[159, 160, 170] In Hamiltonian (5.4) the hh corresponds to the F subbands, i.e. the first ($|u_1\rangle$) and the fourth ($|u_4\rangle$) components which denote spin-up ($F_z = +3/2$) and spin-down ($F_z = -3/2$), respectively. In order to disentangle these two components, a small Zeeman splitting is added, $\Delta_z = B_z \mu_B\, g\, \mathbb{J}_z$, with $B_z = 1\,\mathrm{T}$ and $g = 4/3$.

Figure 5.9(a) presents the weight of the subbands with hh character, $(|f_1|^2 + |f_4|^2)/\sum |f_i|^2$, for varying R and L in a system with spontaneous polarization. The F subbands are clearly dominant for moderate and large QD radii, $R > 5\,\mathrm{nm}$, while the thickness does not substantially affect the VB mixing in the range of L under study. The inset of figure 5.9(a) shows that this abrupt change in the hole composition for radii under 5 nm is due to a transition from a F band (hh) to a λ band (so). In large systems, the F band dominates because the bulk spin-orbit Δ_{so} and crystal-field Δ_{cr} splittings stabilize this subband. Nevertheless, in small enough dots the high kinetic energy may take over and the character of the ground state is then determined by the effective masses of the subbands. In this case, we have $m_\perp^F = m_\perp^G = 1/(A_2 + A_4) = -0.13$ and $m_\perp^\lambda = 1/A_2 = -0.617$. Therefore, the lighter mass of the λ band in the in-plane direction ,$|m_\perp^F| < |m_\perp^\lambda|$,

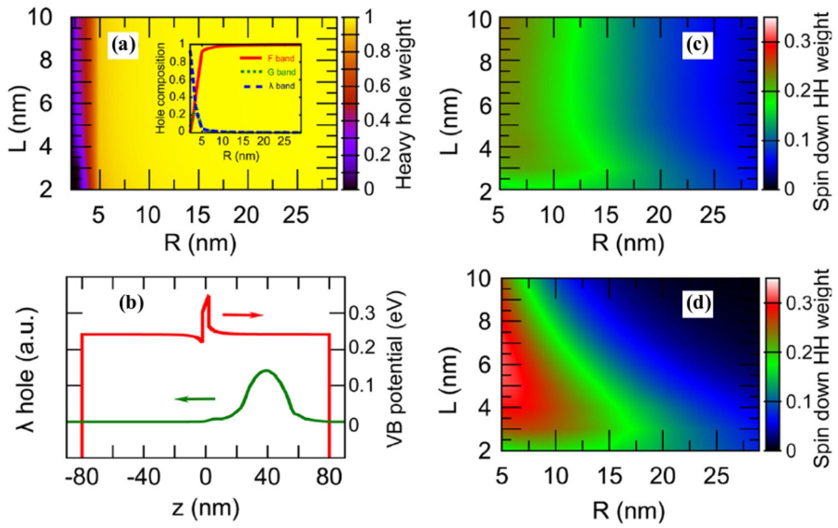

Figure 5.9: (a) Contour map showing the weight of the F band in the ground state as a function of the QD thickness L and radius R. Inset: same but for only varying R ($L = 4\,\text{nm}$) and including also the G and λ bands in the plot. (b) Confining potential (red) and λ hole wave function (green) along the nanowire growth direction in a QD with $R = 2.5\,\text{nm}$ and $L = 4\,\text{nm}$. (c-d) Weight of the envelope function f_4, spin-down hh, in the (c) presence and (d) absence of P_{sp}.

makes such band more stable than the hh one in QDs with strong lateral confinement. The effective mass of the λ band is even lighter in the z direction, $m_z^\lambda = 1/A_1 = -0.05$, thus causing the wave function to mainly localize outside the WZ QD, see figure 5.9(b).

We next explore the spin purity of the ground state by calculating the weight of the spin-down F subband, $|f_4|^2/\sum|f_i|^2$. Calculations with P_{sp}, figure 5.9(c), and without P_{sp}, figure 5.9(d), are compared. In general, we observe an insignificant contribution of the spin-down hh in large systems that increases as the size of the QD is reduced. The inclusion of spontaneous polarization in the model does not remarkably modify this trend and only smoothens the regions of maximum and minimum weight in figure 5.9(d). It is worth mentioning that the coupling between Zeeman-split hh bands is not direct and takes place solely at second order through the coupling with intermediate G and λ subbands, see equation (A.6). Interestingly, in spite of this fact, the contribution of these intermediate subbands to the hole ground state is nearly zero, as seen in figure 5.9(a).

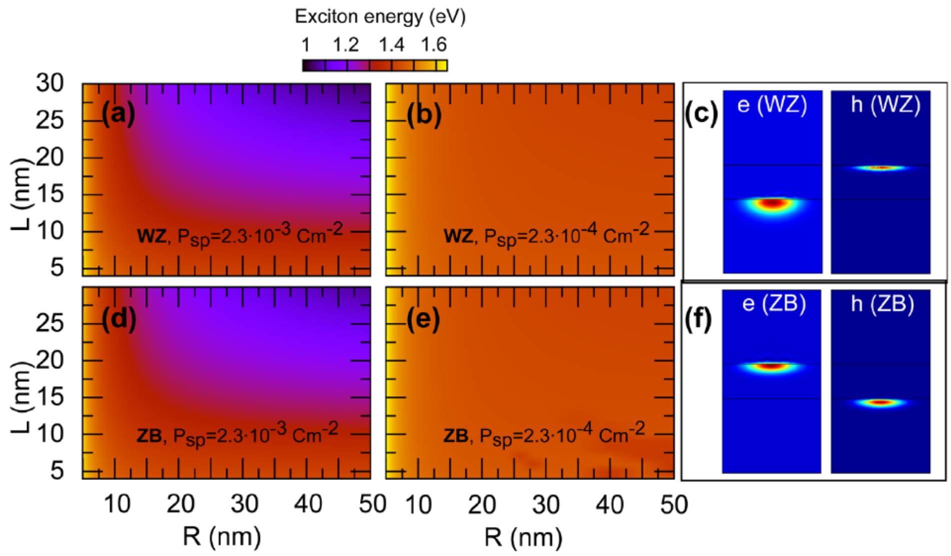

Figure 5.10: (a-b) Exciton energy versus WZ QD radius R and thickness L in a ZB/WZ/ZB system. The energy is computed considering (a) full and (b) weakened P_{sp}. (c) Electron (left) and hole (right) wave functions in a WZ QD with $R = 50\,\text{nm}$ and $L = 30\,\text{nm}$. Full P_{sp} used in the simulations. (d-f) Same but for a ZB QD.

Finally, we stress that using a single-band hh model is justified except for polytype QDs with small radius, where the ground state switches from being mainly a F band to a λ band. This change in the hole ground state character should be found in the thin polytype nanowires synthesized by Loitsch *et al.* [170], e.g. by analyzing the polarization of interband optical transitions.

5.2.3 Excitons in GaAs WZ/ZB/WZ and ZB/WZ/ZB polytype structures

Lastly, the behavior of excitons in polytype QDs is investigated. We restrict to dots with $R > 5\,\text{nm}$, so that a single-band model including only one hh subband, equation (5.5), is enough to describe the VB states satisfactorily. The two possibilities of defining a QD in a system with type-II band alignment are taken into account, namely ZB QDs embedded in a WZ nanowire and vice versa.

First, we analize the exciton energy as a function of the system dimensions. For a WZ QD in the presence of P_{sp}, figure 5.10(a), a striking

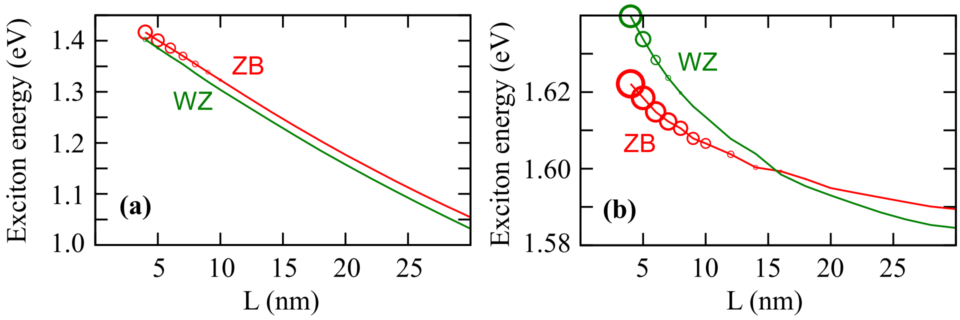

Figure 5.11: Calculated exciton energy in WZ (green line) and ZB (red line) QDs for varying dot thickness L. Two different nanowire radii are considered: (a) $R = 50\,\mathrm{nm}$ and (b) $R = 5\,\mathrm{nm}$. The size of the circles indicates the relative magnitude of the e-h overlap.

tunability of the exciton energy is found from $E_X \approx 1\,\mathrm{eV}$ (near infrared) in large dots to $E_X \approx 1.6\,\mathrm{eV}$ (visible) in small ones. When the spontaneous polarization is weakened, figure 5.10(b), such tunability is strongly reduced, evidencing again the importance of this phenomenon in polytype structures. For excitons in ZB QDs, bottom row in figure 5.10, we find exactly the same results as for WZ QDs.

We next investigate the e-h overlap behavior in the presence of full P_{sp}. Figures 5.10(c) and 5.10(f) illustrate the electron and hole wave functions for large QDs , i.e. $R = 50\,\mathrm{nm}$ and $L = 30\,\mathrm{nm}$. In both WZ and ZB dots, carriers are separated despite the attractive Coulomb interaction, yielding weak e-h overlaps and, hence, dark character to the excitons. This demonstrates that spontaneous polarization is capable of inducing e-h separation in large enough polytypical structures.

In order to assess the differences between ZB and WZ QDs, in figure 5.11 we directly compare the exciton energy of both systems by plotting E_X versus the dot thickness. Simulations for two representative size regimes are carried out: typical QDs with large radius $R = 50\,\mathrm{nm}$ in figure 5.11(a), and QDs with strong lateral confinement $R = 5\,\mathrm{nm}$ in figure 5.11(b). A comparison between both plots shows that in QDs with large radius the excitonic energy scales linearly with L while the dependence is quadratic for small radius. In dots with weak lateral confinement the thickness dependence is linear due to the built-in electric field induced by P_{sp}, which prevails over Coulomb interactions. In strongly confined dots, instead, the high kinetic energy makes the quantum confinement to take over and the dependence becomes quadratic. If we compare now the curves of both crystal phases, we also observe a remarkable distinct behavior: for large R excitons in WZ QDs haver lower energy than those in ZB QDs regardless of L, while the curves cross at $L \approx 15\,\text{nm}$ for small R. These results can be understood taking into account the effective masses m_z of the confined carriers. Electrons in ZB have lighter mass than holes in WZ, causing excitons in ZB to have higher energy as can be seen in figure 5.11(a). This reasoning is also valid in figure 5.11(b) for large dot thickness, but for $L < 15\,\text{nm}$ the high kinetic energy of electrons allows them to escape into the WZ phase, becoming more delocalized, i.e. more stable. In contrast, the heavier mass of holes limits their penetration outside the WZs QD and the exciton energy rapidly increases with decreasing dot thickness.

We turn now our attention to the e-h overlap, represented in figure 5.11 by circles of different size. It can be seen that the overlap is substantially enhanced in QDs with small R, which is also connected with the delocalization of the confined carriers due to their higher kinetic energy. This points out that a transition from the usual type-II band alignment in GaAs polytype QDs to a type-I one is produced by the interplay of the spatial confinement and the P_{sp}-induced polarization. Therefore, the QD thickness can be used as a mechanism to control the e-h overlap and also related properties such as the intensity of absorption processes and exciton lifetimes.

To close this section, we briefly compare the results of figure 5.11 with the experimental observations reported by recent works that investigate GaAs polytype QDs of similar size to ours. On one hand, Vainorius *et al.* [159] investigated the PL of both ZB and WZ QDs with large radii, $R = 45 - 60\,\text{nm}$, and variable dot thickness. They obtained a WZ emission redshifted with respect to ZB one by a few tens of meV. This is consistent with the higher energy found for ZB dots in figure 5.11(a), which corresponds to the same size regime of the samples. However, in the experiments the change in the emission energy with L is much less pronounced, about one order of magnitude, than the calculated one in figure 5.11(a). In fact, such variation is found when disregarding the effect of spontaneous polarization and only quantum confinement is included in the model (results not shown). This fact suggests that the spontaneous polarization is somehow suppressed in the experimental setup. On the other hand, Loitsch *et al.* [170] studied the PL energy of GaAs polytype structures as a function of the dot radii. They found an exciton energy up to $1.610\,\text{eV}$ for WZ QDs, presenting a blueshift as large as $100\,\text{meV}$ with respect to bulk GaAs for the thinnest nanowires investigated, $R \approx 5\,\text{nm}$. In figure 5.11(b) we have seen that this blueshift could be even larger for WZ QDs with small L (the GaAs bulk band gap is $1.51\,\text{eV}$). Another work of the same authors studying the same system has also reported fast radiative lifetimes (below $1\,\text{ns}$) in very thin nanowires,[160] in contrast to the commonly long lifetimes ($> 3\,\mathrm{ns}$) exhibited by typical large-diameter structures. In their work, the fastest exciton decay for small R was ascribed to a transition from type-II to type-I band alignment, which goes along with our prediction in figure 5.11(b).

CHAPTER 6

Edge states in monolayer MoS_2 nanostructures

Over the last few years the emergence of atomically thin materials has revolutionized the fields of solid-state physics and material science, chiefly because they exhibit dramatically different, and often superior, properties compared to their bulk counterparts. The main reason for this dissimilarity lies in their distinct dimensionality. The first truly 2D system was graphene. It was discovered by Novoselov *et al.* [22] in 2004 and, since then, many groups have dedicated big efforts to investigate these novel systems. As a result, nowadays several new 2D materials have been prepared.[173, 174]

Particularly, in this work we focus on monolayer TMDCs[1]. Among the rich variety of TMDCs, we investigate those with semiconducting behavior, specifically MoS_2. Unlike graphene, MoS_2 and other TMDCs present a finite band gap which is indirect in bulk form but becomes direct in the monolayer limit.[175] The direct band gap makes single-layer TMDCs especially attractive for electronic and optoelectronic applications.[176–178]

Similarly to traditional 3D bulk semiconductors, single-layer materials also offer the possibility of fabricating nanostructures with lower dimensionality, e.g. nanoribbons (1D) and QDs (0D). To date, these finite structures have not been extensively investigated yet and a more detailed understanding of their electronic structure is needed for the development of possible

[1] The 2D form of TMDC materials (MX_2) is commonly called monolayer, but it is actually composed by three layers of atoms (X-M-X): i.e. one layer of metal atoms sandwiched between two layers of chalcogenide atoms. The atoms in each layer are arranged as a triangular lattice.

devices. Several works have reported the existence of edge states in finite MoS_2 systems under different conditions.[179–182] The presence of these edge states is very relevant since they form 1D metallic channels along the edges, thus affecting transport and optical properties.

In this chapter, we deal with the electronic structure of monolayer MoS_2 nanostructures, namely nanoribbons and QDs. Special attention is paid to the origin of edge states in these finite systems and its connection with topological insulators. Topological insulators have been intensely discussed in recent literature due to their unique properties.[183, 184] They are materials with insulating behavior in the bulk, but present gapless conducting states at the edges/surfaces of the system.[185, 186] Surface states may originate from different sources, e.g. dangling bonds or polar discontinuities [187, 188], but what makes topological insulators special is that metallic states are protected by time-reversal symmetry. Therefore, they are robust against backscattering and in the presence of non-magnetic perturbations.

The contents of the present chapter are based on an article published in collaboration with professor Sergio E. Ulloa from Ohio University (USA) and are the result of a research short stay in his group. The full version of the publication can be found in page 267.

6.1 Effective Hamiltonian

Apart from their dimensionality, monolayer TMDCs and the traditional semiconductors studied in the previous chapters present more structural differences. In monolayer MoS_2 the metal atoms have trigonal prismatic coordination with the chalcogenide ones, and the direct gap of the band structure is situated at the two nonequivalent points K and K' of the Brillouin zone. Contrarily, WZ and ZB semiconductors present tetrahedral coordination and the direct gap is at the center of the Brillouin zone (Γ point). As a consequence, the Hamiltonians introduced in chapter 2 are not valid and several authors have derived effective k·p models to study the low-energy physics of TMDC monolayers.[189–192] Since we deal with edge states in the gap, we should employ a Hamiltonian including both CB and VB. A simple two-band model describing such bands up to second order in k suffices for our exploratory purposes. It can be written as:

$$H = \begin{pmatrix} \varepsilon_v + \alpha k^2 & \tau\gamma k_- \\ \tau\gamma k_+ & \varepsilon_c + \beta k^2 \end{pmatrix}, \tag{6.1}$$

where $k_\pm = k_x \pm i\tau k_y$, and $\varepsilon_c = \Delta/2$ and $\varepsilon_v = -\Delta/2$ are the band-edge energies with $\Delta = 1.9\,\text{eV}$ standing for the material band gap; $\mathbf{k}$ is the momentum relative to the K/K' points. The constants α, β and γ are material parameters, while τ identifies the valley K ($\tau = 1$) or K' ($\tau = -1$). In literature, different authors report different values for these parameters. We use in all calculations presented here the ones suggested in reference [191] unless otherwise specified. These parameters are $\alpha = 1.72\,\mathrm{eV\AA^2}$, $\beta = -0.13\,\mathrm{eV\AA^2}$ and $\gamma = 3.82\,\mathrm{eV\AA}$, as fitted from density functional theory calculations.

Hamiltonian (6.1) takes into account the electron-hole symmetry breaking observed in first-principles simulations by using unlike values for α and β. However, for the sake of simplicity, trigonal warping and other minor contributions have been disregarded as they do not change the qualitative results. Additionally, hard-wall boundary conditions are employed to describe the edges of the nanostructures. These boundary conditions do not produce coupling between valleys or spins, so each valley/spin can be discussed independently and a two-band model can be used. Such situation is also expected of zigzag edges, although further investigations are required to confirm the equivalence of both conditions.

6.2 Results and discussion

In this section we apply the above presented model to study the electronic behavior of MoS_2 nanoribbons and QDs. All simulations are carried out using COMSOL utilities, a commercial software that uses the numerical finite element method.

6.2.1 MoS_2 nanoribbons

Nanoribbons are structures of finite width where particles are confined in one direction of space and move freely in the perpendicular one. We define the nanoribbons in our calculations to be translational invariant along the y direction, so that the momentum k_y is a good quantum number and the two-component wave function can be written as $\psi(x,y) = e^{ik_y y}\phi(x)$, where ψ and ϕ have components over the conduction c and valence v basis. Substituting $\psi(x,y)$ into Hamiltonian (6.1) results in a two coupled second-order differential equation system in one dimension that can be numerically solved for a given k_y.

The band dispersion obtained for a 10 nm-width MoS_2 nanoribbon is shown in figure 6.1(b). Interestingly, we find two states inside the band

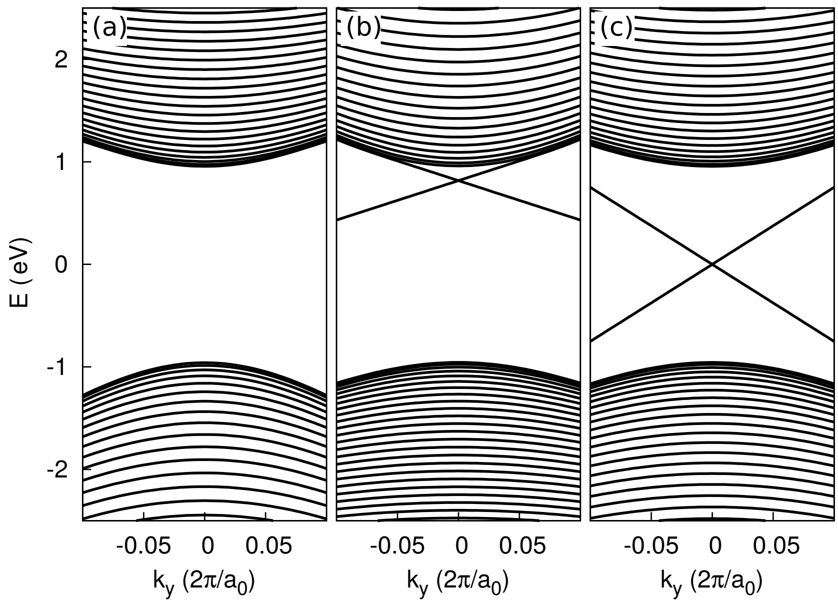

Figure 6.1: Energy-band dispersion for MoS_2 nanoribbons considering different values of α and β: (a) $\alpha = -1.72\,\mathrm{eV\AA^2}$ and $\beta = 0.13\,\mathrm{eV\AA^2}$, (b) $\alpha = 1.72\,\mathrm{eV\AA^2}$ and $\beta = -0.13\,\mathrm{eV\AA^2}$, and (c) $\alpha = 1.72\,\mathrm{eV\AA^2}$ and $\beta = -1.72\,\mathrm{eV\AA^2}$. The edges are parallel to the y direction, and the wave vector k_y is measured with respect to the K valley, where $a_0 = 3.193\,\mathrm{\AA}$ is the lattice constant.

gap with a nearly linear dispersion. These levels cross at $k_y = 0$ and $E = 0.816\,\mathrm{eV}$, and have energies very close to the CB edge. In fact, they disperse upwards in energy coming very close to the CB for not large k_y, and soon admix with the band states, becoming indistinguishable from them. The states of lower energy, instead, remain far from the VB and are not hybridized in the range of k_y considered.

In order to study the origin of these states, we repeat the same calculations but for other sets of parameters. We only tune α and β since γ does not affect the presence of midgap states. First, the sign of both α and β is changed: $\alpha = -1.72\,\mathrm{eV\AA^2}$ and $\beta = 0.13\,\mathrm{eV\AA^2}$. Figure. 6.1(a) shows that the states lying inside the gap are now absent. Subsequently, in figure. 6.1(c) we keep the signs unaltered to those in panel (b) but modify β to have the same absolute value of α: $\alpha = 1.72\,\mathrm{eV\AA^2}$ and $\beta = -1.72\,\mathrm{eV\AA^2}$. In this case, the two states inside the gap are still present but they have lower energies compared to figure 6.1(b). The dispersion bands now cross exactly at $k_y = 0$ and $E = 0$. This is as expected from symmetry considerations

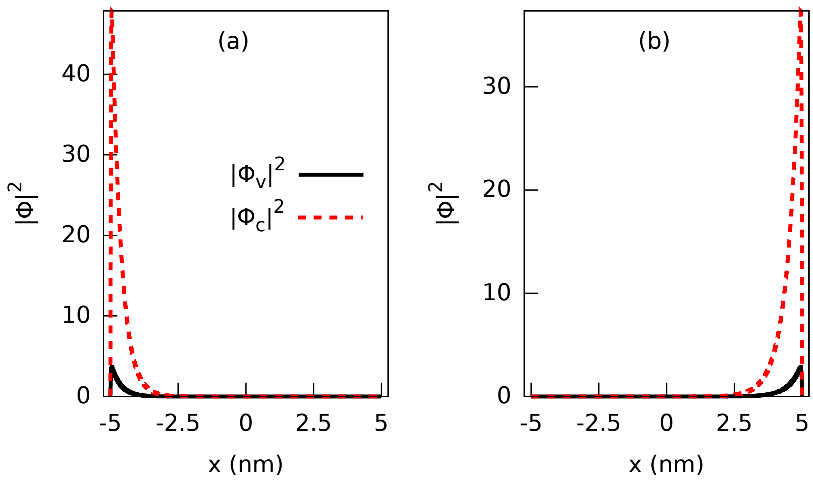

Figure 6.2: Squared modulus $|\phi|^2$ of the two components of the wave function for the two states with energies lying in the band gap in figure 6.1(b). The states correspond to $k_y = 0.01 \times 2\pi/a_0$ and have the following energies: (a) $E = 0.778\,\text{eV}$, and (b) $E = 0.855\,\text{eV}$. Black solid lines represent the VB component ϕ_v and red dashed lines the CB component ϕ_c.

because $\alpha = \beta$ confers electron-hole symmetry to the Hamiltonian. We also stress that a situation with α and β having the same sign is not taken into account since in such a case there is not a real gap separating the bands.

From the analysis of the results for the three sets of parameters in figure 6.1, it is clear that the presence/absence of midgap states is determined by the sign of α and β. It can be inferred that they exist if $\alpha > 0$ and $\beta < 0$, and are absent if $\alpha < 0$ and $\beta > 0$. The energy and, therefore, the position of the states inside the gap is determined by the relative value of the two parameters. When $|\alpha| > |\beta|$ the states are closer to the CB as in figure 6.1(b), and when $|\alpha| < |\beta|$ they become closer to the VB.

Midgap states are typically associated to states localized at the edge of finite structures, the so-called edge states. Thus, to further explore their nature we examine the form of the wave functions. As an example, we represent in figure 6.2 the midgap states corresponding to $k_y = 0.01 \times 2\pi/a_0$ in figure 6.1(b). We choose this value of k_y to avoid problems derived from degeneracies and mixing with the CB. Figure 6.2(a) illustrates the wave function squared modulus of the lower state at $E = 0.778\,\text{eV}$ and figure 6.2(b) of the higher one at $E = 0.855\,\text{eV}$. We clearly observe that both states are localized at opposite edges of the MoS_2 nanoribbon, thus confirming that they are in effect edge states. Figure 6.2 also reveals that the width of the nanoribbon is large enough to ensure decoupled states on both edges.

By comparing the height of the components in figure 6.2, it is also evident that the CB component (red dashed line) is the main contribution to the wave function in both states. The calculation of the relative weight of the two components yields $w(\phi_c) = 93\%$ and $w(\phi_v) = 7\%$ for the conduction- and valence-components, respectively. These values can be directly obtained from the parameters α and β using the expressions $w(\phi_c) = |\beta|/(|\alpha| + |\beta|)$ and $w(\phi_v) = |\alpha|/(|\alpha| + |\beta|)$. These expressions hold as long as the edge states are relatively far from the bulk bands. Moreover, it can be seen that the wave functions of the two states are slightly different, e.g. by comparing the maximum value of $|\phi_c|^2$ or the x extension. This asymmetry is due to the different proximity of the CB. The edge state in panel (b) is closer to the CB and, thus, it is slightly more admixed with the bulk states and its wave function is somewhat more delocalized.

The results summarized in figure 6.1 and figure 6.2 can be related to those coming from the model proposed by Bernevig, Hughes, and Zhang (BHZ).[193] In this model, the observation of the quantum spin Hall effect (QSHE) was predicted in HgTe quantum wells larger than a critical thickness, due to a band inversion, i.e. a change in Δ's sign. In that work, for $\Delta < 0$ bands are inverted and the system shows topological behavior. This means that edge states will form when a transition between two distinct topological phases takes place, as predicted by the principle of bulk-edge correspondence.[185] In our system we have $\Delta > 0$, which is apparently trivial, but the sign of the band curvatures ($\alpha > 0$ and $\beta < 0$) yields also a situation with inverted bands[2] similar to the BHZ model, so that the origin of the edge states can be analyzed in terms of the topological character of Hamiltonian (6.1).

In order to make the above reasoning clear, we perform calculations of the energy spectrum as a function of Δ. Results are shown in figure 6.3. We fix $k_y = 0$ and consider two sets of band curvatures: $\alpha = 1.72\,\mathrm{eV\AA^2}$ and $\beta = -0.13\,\mathrm{eV\AA^2}$ in figure 6.3(a), and $\alpha = 1.72\,\mathrm{eV\AA^2}$ and $\beta = -1.72\,\mathrm{eV\AA^2}$ in figure 6.3(b). Two red dashed lines showing the limits of the band gap have been added in each plot to improve the readability. In both cases, a trivial situation with no states in the gap is observed at large negative Δ. As Δ increases and changes sign two degenerate edge states appear with energies

[2] The "bare" effective masses for the VB and CB are determined by the α and β coefficients, respectively. A negative β, corresponding to a negative mass $\approx 1/\beta$, is "inverted", and that symmetry is present in the states even after the mixing due to γ.

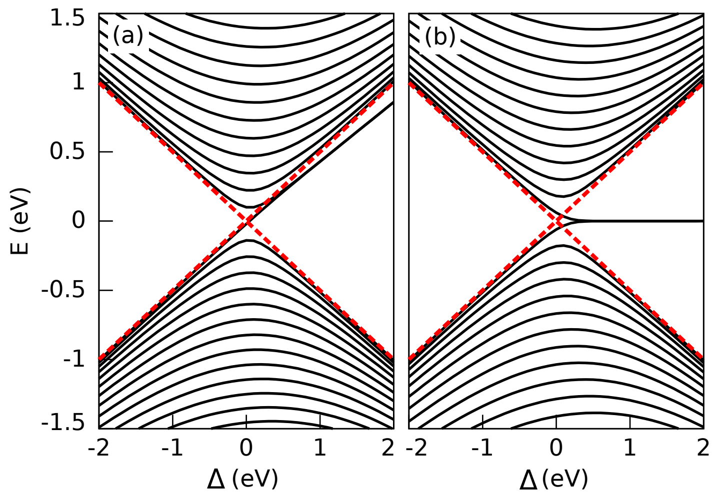

Figure 6.3: Energy spectrum of a MoS_2 nanoribbon as a function of the band gap Δ, for $k_y = 0$. Two sets of parameters are considered: (a) $\alpha = 1.72\,\text{eV}\text{Å}^2$ and $\beta = -0.13\,\text{eV}\text{Å}^2$, and (b) $\alpha = 1.72\,\text{eV}\text{Å}^2 = -\beta$. Red dashed lines indicate the edges of the band gap.

clearly lying in the gap. This behavior confirms the connection between edge states and band inversion as in the BHZ model. As already discussed in figure 6.1, midgap states are closer to the CB when $|\alpha| > |\beta|$, panel (a), and become perfectly equidistant from the CB and VB for $|\alpha| = |\beta|$ due to electron-hole symmetry, panel (b).

To explore the topological behavior further, we analyze the results with the help of the Chern number associated with the occupied band. The Chern number is a topological invariant (its value cannot change under smooth deformations of the Hamiltonian parameters) that characterizes a state as trivial ($c = 0$) or nontrivial ($c \neq 0$). For a two-level Hamiltonian like that in equation (6.1), once we rewrite it in the form $H(\mathbf{k}) = \mathbf{g}(\mathbf{k})\cdot\boldsymbol{\sigma}$, where $\boldsymbol{\sigma}$ is a vector with the Pauli matrices as components, the Chern number is given by[185]

$$c = \frac{1}{4\pi}\int d^2k(\partial_{k_x}\hat{\mathbf{g}} \times \partial_{k_y}\hat{\mathbf{g}})\cdot\hat{\mathbf{g}}\,, \tag{6.2}$$

where $\hat{\mathbf{g}} = \mathbf{g}/|\mathbf{g}|$ and the integral is computed over the entire Brillouin zone. For Hamiltonian (6.1), equation (6.2) yields $c = \tau/2\big[\text{sgn}(\Delta) + \text{sgn}(\alpha - \beta)\big]$. Then, for $\Delta > 0$ one obtains $c = 0$ if $\alpha < \beta$ and $c = \tau$ if $\alpha > \beta$. When $\alpha = 1.72\,\text{eV}\text{Å}^2$ and $\beta = -0.13\,\text{eV}\text{Å}^2$ we have $c \neq 0$, denoting the non-trivial character of the MoS_2 Hamiltonian. As a consequence, gapless states must be present at the domain wall separating the nanoribbon (non-trivial) and the vacuum (trivial), according to the bulk-edge correspondence. This goes along with the previous discussion based on band inversion arguments.

It is important to note, however, that the contribution of the valleys K and K' to the topological invariant has opposite signs, originating an overall $c = 0$. Therefore, strictly speaking multivalley materials such as graphene or MoS_2 are topologically trivial. In spite of this, the origin of edge states in gapped and bilayer graphene has been discussed in terms of the marginal topological properties of the single-valley Hamiltonians.[194, 195] This analysis is possible owing to the close analogy between graphene systems and 2D topological insulators, and can also be applied to monolayer MoS_2. Nevertheless, this analogy has important limitations. Since c per valley is not a well-defined topological invariant, $c \neq 0$ does not guarantee the existence of edge states at the boundaries with the vacuum. Furthermore, they are not topologically protected against backscattering and can then be affected by any mechanism of disorder or valley coupling. All the same, edge states in bilayer graphene have been shown to be robust under moderate disorder,[196] and to exhibit pure valley currents, as indicated by the local valley Berry curvature.[197]

6.2.2 MoS_2 triangular QDs

We next investigate the electronic structure of monolayer MoS_2 QDs formed by finite-size flakes. The flakes are modeled as equilateral triangles since it is the most common shape obtained in the laboratory.[198–200] The side length of the QDs is 10 nm in all calculations. As for the material parameters, we employ the same ones as in figure 6.2(b) of previous section: $\alpha = 1.72\,\mathrm{eV\AA^2}$ and $\beta = -0.13\,\mathrm{eV\AA^2}$.

Similarly to MoS_2 nanoribbons, midgap states also emerge for this set of parameters. However, several states with energies lying in the band gap are found for MoS_2 QDs, in contrast to only one state per edge found for nanoribbons. This difference can be understood considering the finite size of the edges in QDs. The edge states are then confined along each border, thus originating the discretization of this band and the corresponding energy quantization.

To illustrate this, we show in figure 6.4 the squared modulus of the wave function for a selection of states with energy close to the CB ($E \approx 0.95\,\mathrm{eV}$). We choose this range of energies because we know that for these parameters the edge states are closer to the CB. Besides, it offers the possibility to compare the "bulk" and edge states in the flake. In figure. 6.4 the states

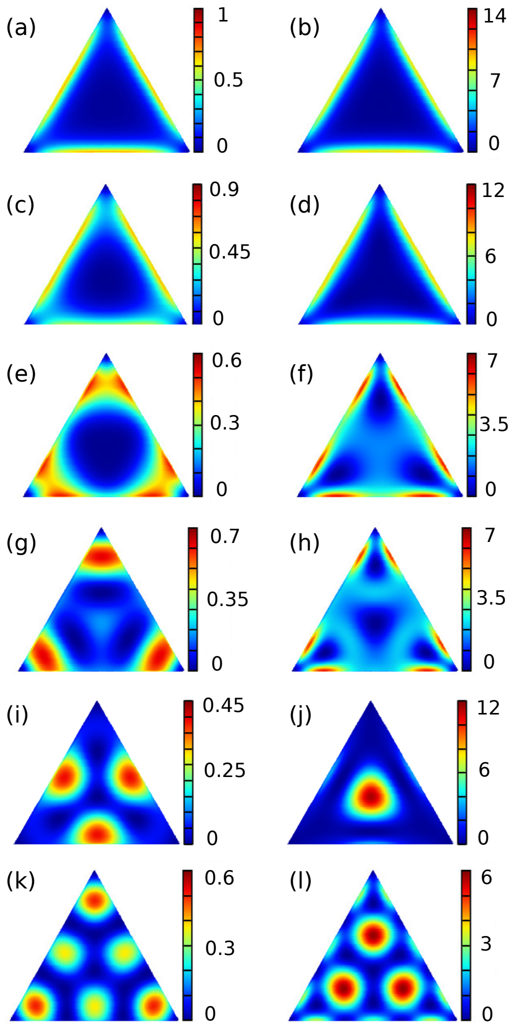

Figure 6.4: Wave-function squared modulus of a selection of states close to the CB edge energy. Left and right columns illustrate the VB, $|\phi_v|^2$, and CB, $|\phi_c|^2$, components, respectively. Different states are arranged in rows with increasing energy: (a)-(b) $E = 0.907\,\mathrm{eV}$, (c)-(d) $E = 0.962\,\mathrm{eV}$, (e)-(f) $E = 1.015\,\mathrm{eV}$, (g)-(h) $E = 1.022\,\mathrm{eV}$, (i)-(j) $E = 1.057\,\mathrm{eV}$ and (k)-(l) $E = 1.100\,\mathrm{eV}$.

are presented in order of increasing energy. Each row corresponds to a different state, with $|\phi_v|^2$ and $|\phi_c|^2$ components depicted on the left and right column, respectively. The first two states shown, panels (a)-(d), are clearly edge states with their wave functions localized near the triangle border. Next two states in energy, figure 6.4(e)-(h), also show their wave functions mainly near the edges, but noticeably more delocalized than the previous two. This suggests that they are partially admixed with the CB states due to their energy proximity. Finally, figure 6.4(i)-(l) show two conduction states with the wave function completely delocalized over the entire QD. A representation of the real and imaginary parts of the wave functions (not shown) allows one to see the wave function nodes more clearly. It is seen that the number of nodes increases with the energy of the states, a typical signature of quantization.

It is worth mentioning that calculations using other sets of parameters have also been carried out for MoS_2 QDs. The corresponding results show exactly the same dependence between the presence/absence of edge states and the curvature parameters as in the case of nanoribbons. Therefore, one can also invoke the marginal topological character of the Hamiltonian as the origin of edge states in these zero-dimensional nanostructures.

In summary, MoS_2 nanoribbons and QDs exhibit edge states spatially localized on the edges with energies lying in the band gap. Such states originate from the CB and VB curvatures and are related to the marginal topological properties of the MoS_2 single-valley Hamiltonian.

CHAPTER 7

Conclusions

The aim of this Thesis is to theoretically determine the effect of externally applied fields and the interaction with the environment on the optical and electronic properties of QDs with possible technological interest. To this end, we have employed effective k·p models within the EMA and the EFA, which offer satisfactory results for the electronic structure at a reasonable computational cost. In order to account for the various phenomena investigated, namely external electric and magnetic fields, SOI, strain and piezoelectricity, the k·p Hamiltonians have been supplemented with the corresponding additional terms. We outline next the main obtained results.

First, we have derived a six-band position-dependent Hamiltonian in cylindrical coordinates to study the VB of ZB GaN/AlN QDs. Using this model we have found a high spin purity in QDs of typical dimensions, i.e. with small aspect ratio, which is reduced in taller dots. In fact, the symmetry of the hole ground state can be switched in dots with aspect ratio approximately unity by applying external magnetic fields of different intensity, thus providing an easy way to modulate the optical answer of this aspect ratio systems.

The effect of axially applied external magnetic fields has also been investigated in hexagonal QRs. Similarly to circular ones, the AB effect emerge in such doubly-connected structures as a consequence of the topology, but some distinct symmetry-related features are found in this particular case. On one hand, in large hexagonal rings populated with six electrons in a regime of low electronic density, the typical AB oscillations are completely suppressed and the magnetization profile becomes flat. This behavior is due to an anticrossing between the multi-particle ground state and a highly excited state of the same symmetry. In other words, symmetry overpasses topology in this case. We have also demonstrated in nanowires presenting a hexagonal ring in their cross section and pierced by weak magnetic fields, that the AB-like magnetoconductance oscillations can disappear or resurface by varying the voltage strength in both gate-all-around and back-gate device configurations. In addition, in the high-magnetic-field regime we have shown that several field-induced transitions take place due to the electron distribution relocalization and to the complete electron depletion of excited bands. Signatures of such transitions should be observed in magnetoconductance experiments as a steplike behavior.

We have also addressed another topology-related problem: the emergence of edge states in monolayer MoS_2 nanoribbons and QDs. We have shown that these atomically thin nanostructures exhibit states spatially localized on the borders and with energies lying in the band gap. The origin of such edge states has been related to the marginal topological character of the single-valley MoS_2 Hamiltonian, which is governed in turn by the curvature of conduction and valence bands.

We have next turned our attention to the relaxation processes of the spin degree of freedom confined in QDs. The spin-orbit-induced spin relaxation is calculated for electrons and holes employing fully 3D models, going beyond the common quasi-2D ones. By using this more realistic description the important role of cubic DSOI becomes evident even in moderately short dots. It has also been found that the spin relaxation presents a remarkable anisotropy with the orientation of external fields and with anisotropies in the QD shape. Such behavior has been observed for both CB and VB in several structures of different materials, shapes, and grown along various crystallographic orientations, thus opening the possibility to enhance or suppress the spin lifetimes in these systems by properly designing them. Furthermore, for the VB we have provided insight into the dominant contribution of the various spin-mixing mechanisms. In particular, SOI or lh-hh couplings prevail depending on the dot aspect ratio. Additionally, we have shown that the spin lifetime of holes exceeds that of electrons in flat enough QDs. Moreover, spin relaxation has also been explored in vertical DQDs under axial electric fields. Maximum hole spin lifetimes are obtained for molecular states, but they rapidly decrease when the symmetry of the system is lowered by misalignment of the dots, non-resonant fields or inclusion of DSOI.

Finally, we have dealt with the influence of the environment on the QD properties, specifically how strain and piezoelectricity affect carriers spatial separation and, thus, exciton performance. Particularly, in WZ core-shell nanocrystals, strong built-in piezoelectric fields along the growth direction are found in dot-in-dot structures when cores and shells are large, leading to effective e-h separation in spite of the attractive Coulomb interaction. The same is true for other systems such as dot-in-rods, dot-in-plates and rod-in-rods as long as the core is large and the shell thick. Surprisingly enough, a thick shell is needed not only in the axial direction but also in the lateral one. This is because thin shells reduce the overall system strain independently of the direction, thus yielding weak polarization fields. This explains why piezoelectricity has not been reported yet as a feasible control mechanism in experiments studying dot-in-dot and dot-in-rod systems. The effect of polarization fields on excitons is also explored in polytype QDs, where strain and piezoelectricity are negligible, and spontaneous polarization is dominant. In such a system, the exciton energy has been proved to be very sensitive to the QD dimensions in the presence of spontaneous polarization, confirming its important action. Remarkably, radial confinement induces a gradual transition from type-II to type-I band alignment that results in a substantial modulation of the e-h overlap. For both crystal structures it can be concluded that a wide exciton wavelength and lifetime tunability is possible thanks to the emergence of strong polarizations when growing QDs with the appropriate dimensions.

APPENDIX **A**

Valence band Hamiltonians

A.1 Zinc-blende crystal structure

A.1.1 Four-band Luttinger-Kohn Hamiltonian

The Hamiltonian proposed by Luttinger and Kohn [122] in 1955 is one of the most commonly used to describe systems with constant mass. The matrix form reads:

$$H_{ZB}^{LK} = - \begin{array}{c} \begin{array}{cccc} \left|\tfrac{3}{2}\,\tfrac{+3}{2}\right\rangle & \left|\tfrac{3}{2}\,\tfrac{+1}{2}\right\rangle & \left|\tfrac{3}{2}\,\tfrac{-1}{2}\right\rangle & \left|\tfrac{3}{2}\,\tfrac{-3}{2}\right\rangle \end{array} \\ \begin{pmatrix} P+Q & -S & R & 0 \\ -S^{\dagger} & P-Q & 0 & R \\ R^{\dagger} & 0 & P-Q & S \\ 0 & R^{\dagger} & S^{\dagger} & P+Q \end{pmatrix} \end{array}, \tag{A.1}$$

with

$$\begin{aligned} P &= \frac{\hbar^2}{2\,m_0}\gamma_1\,\left(k_x^2+k_y^2+k_z^2\right), \\ Q &= \frac{\hbar^2}{2\,m_0}\gamma_2\,\left(k_x^2+k_y^2-2k_z^2\right), \\ R &= \frac{\hbar^2}{2\,m_0}\left[-\sqrt{3}\,\gamma_2\,(k_x^2-k_y^2)+2\,i\,\sqrt{3}\,\gamma_3\,k_x\,k_y\right], \\ S &= \frac{\hbar^2}{m_0}\sqrt{3}\,\gamma_3\,(k_x-i\,k_y)\,k_z. \end{aligned}$$

Here m_0 is the free electron mass and γ_i are the Luttinger parameters.

A.1.2 Six-band Burt-Foreman Hamiltonian

The position-dependent Hamiltonian derived by Foreman[40, 41] using Burt's formalism[37–39] to investigate the VB of ZB materials reads

$$H_{ZB}^{BF} = - \begin{array}{c} \begin{array}{cccccc} \left|\frac{3}{2},\frac{3}{2}\right\rangle & \left|\frac{3}{2},\frac{1}{2}\right\rangle & \left|\frac{3}{2},\frac{-1}{2}\right\rangle & \left|\frac{3}{2},\frac{-3}{2}\right\rangle & \left|\frac{1}{2},\frac{1}{2}\right\rangle & \left|\frac{1}{2},\frac{-1}{2}\right\rangle \end{array} \\ \begin{pmatrix} P' & S_- & -R & 0 & -\frac{1}{\sqrt{2}}S_- & -\sqrt{2}R \\ S_-^\dagger & P'' & -C & R & -\sqrt{2}Q & -\sqrt{\frac{3}{2}}\Sigma_- \\ -R^\dagger & -C^\dagger & P''^* & S_+^\dagger & \sqrt{\frac{3}{2}}\Sigma_+ & -\sqrt{2}Q^* \\ 0 & R^\dagger & S_+ & P'^* & \sqrt{2}R^\dagger & -\frac{1}{\sqrt{2}}S_+ \\ -\frac{1}{\sqrt{2}}S_-^\dagger & -\sqrt{2}Q^\dagger & \sqrt{\frac{3}{2}}\Sigma_+^\dagger & \sqrt{2}R & P''' - \Delta_{so} & C \\ -\sqrt{2}R^\dagger & -\sqrt{\frac{3}{2}}\Sigma_-^\dagger & -\sqrt{2}Q^* & -\frac{1}{\sqrt{2}}S_+^\dagger & C^\dagger & P'''^* - \Delta_{so} \end{pmatrix} \end{array}, \tag{A.2}$$

with

$$\begin{aligned}
P' =& \frac{1}{2}\{k_x(L+M)k_x + k_y(L+M)k_y + k_z 2M k_z\} \\
&+ \frac{i}{2}\{k_x(F-G-H_1+H_2)k_y - k_y(F-G-H_1+H_2)k_x\}, \\
P'' =& \frac{1}{6}\{k_x(L+5M)k_x + k_y(L+5M)k_y + 2k_z(2L+M)k_z\} \\
&+ \frac{i}{6}\{k_x(F-G-H_1+H_2)k_y - k_y(F-G-H_1+H_2)k_x\}, \\
P''' =& \frac{1}{3}\{k_x(L+2M)k_x + k_y(L+2M)k_y + k_z(L+2M)k_z\} \\
&+ \frac{i}{3}\{k_x(F-G-H_1+H_2)k_y - k_y(F-G-H_1+H_2)k_x\}, \\
Q =& -\frac{1}{6}\{k_x(L-M)k_x + k_y(L-M)k_y - 2k_z(L-M)k_z \\
&+ i[k_x(F-G-H_1+H_2)k_y - k_y(F-G-H_1+H_2)k_x]\}, \\
R =& \frac{1}{2\sqrt{3}}\{k_x(L-M)k_x - k_y(L-M)k_y - i[k_x N k_y + k_y N k_x]\}, \\
S_\pm =& -\frac{1}{\sqrt{3}}\{k_\pm(F-G)k_z + k_z(H_1-H_2)k_\pm\}, \\
C =& -\frac{1}{3}\{k_z(F-G-H_1+H_2)k_- - k_-(F-G-H_1+H_2)k_z\}, \\
\Sigma_\pm =& -\frac{1}{3\sqrt{3}}\{k_\pm(F-G+2H_1-2H_2)k_z + k_z(2F-2G+H_1-H_2)k_\pm\}.
\end{aligned}$$

where L, M, F, G, H_1 and H_2 are mass parameters and Δ_{so} is the spin-orbit energy. This set of parameters can be re-expressed in terms of the well-known Luttinger parameters if necessary.

A.1.3 Six-band Burt-Foreman Hamiltonian in cylindrical coordinates

The position-dependent Hamiltonian in cylindrical coordinates has been derived from (A.2) in the present work, since the six-band version was not available in literature. In order to do this, all Cartesian differential operators are replaced by their cylindrical counterparts. Then, the axial approximation $\tilde{\gamma} = \frac{1}{2}(\gamma_2 + \gamma_3)$[77, 78] is taken into account (only the R terms of (A.2) are changed) and the resulting Hamiltonian reads

$$H_{BF}^{ZB}(F_z) = \frac{\hbar^2}{2m_0} M_{6x6}, \tag{A.3}$$

with

$$\begin{aligned}
M_{11} &= \frac{\partial}{\partial\rho}(\gamma_1+\gamma_2)\frac{\partial}{\partial\rho} + \frac{(\gamma_1+\gamma_2)}{\rho}\frac{\partial}{\partial\rho} + \frac{\partial}{\partial z}(\gamma_1-2\gamma_2)\frac{\partial}{\partial z} - \frac{\left(F_z-\frac{3}{2}\right)^2}{\rho^2}(\gamma_1+\gamma_2) \\
&\quad + \frac{\left(F_z-\frac{3}{2}\right)}{2\rho}\left[\frac{\partial}{\partial\rho}(c_1+c_2) - (c_1+c_2)\frac{\partial}{\partial\rho}\right], \\
M_{12} &= \frac{1}{\sqrt{3}}\left\{\frac{\partial}{\partial\rho}c_1\frac{\partial}{\partial z} - \frac{\partial}{\partial z}c_2\frac{\partial}{\partial\rho} + \frac{\left(F_z-\frac{1}{2}\right)}{\rho}\left[c_1\frac{\partial}{\partial z} - \frac{\partial}{\partial z}c_2\right]\right\}, \\
M_{13} &= -\sqrt{3}\left\{\frac{\partial}{\partial\rho}\tilde{\gamma}\frac{\partial}{\partial\rho} + \frac{\left(F_z+\frac{1}{2}\right)}{\rho}\frac{\partial}{\partial\rho}\tilde{\gamma} + \frac{\left(F_z-\frac{1}{2}\right)}{\rho}\tilde{\gamma}\frac{\partial}{\partial\rho} + \frac{\left(F_z-\frac{3}{2}\right)\left(F_z+\frac{1}{2}\right)}{\rho^2}\tilde{\gamma}\right\}, \\
M_{14} &= 0, \\
M_{15} &= -\frac{1}{\sqrt{6}}\left\{\frac{\partial}{\partial\rho}c_1\frac{\partial}{\partial z} - \frac{\partial}{\partial z}c_2\frac{\partial}{\partial\rho} + \frac{\left(F_z-\frac{1}{2}\right)}{\rho}\left[c_1\frac{\partial}{\partial z} - \frac{\partial}{\partial z}c_2\right]\right\}, \\
M_{16} &= -\sqrt{6}\left\{\frac{\partial}{\partial\rho}\tilde{\gamma}\frac{\partial}{\partial\rho} + \frac{\left(F_z+\frac{1}{2}\right)}{\rho}\frac{\partial}{\partial\rho}\tilde{\gamma} + \frac{\left(F_z-\frac{1}{2}\right)}{\rho}\tilde{\gamma}\frac{\partial}{\partial\rho} + \frac{\left(F_z-\frac{3}{2}\right)\left(F_z+\frac{1}{2}\right)}{\rho^2}\tilde{\gamma}\right\}, \\
M_{21} &= \frac{1}{\sqrt{3}}\left\{\frac{\partial}{\partial z}c_1\frac{\partial}{\partial\rho} - \frac{\partial}{\partial\rho}c_2\frac{\partial}{\partial z} + \frac{\left(F_z-\frac{3}{2}\right)}{\rho}\left[c_2\frac{\partial}{\partial z} - \frac{\partial}{\partial z}c_1\right]\right\}, \\
M_{22} &= \frac{\partial}{\partial\rho}(\gamma_1-\gamma_2)\frac{\partial}{\partial\rho} + \frac{(\gamma_1-\gamma_2)}{\rho}\frac{\partial}{\partial\rho} + \frac{\partial}{\partial z}(\gamma_1+2\gamma_2)\frac{\partial}{\partial z} - \frac{\left(F_z-\frac{1}{2}\right)^2}{\rho^2}(\gamma_1-\gamma_2) \\
&\quad + \frac{\left(F_z-\frac{1}{2}\right)}{6\rho}\left[\frac{\partial}{\partial\rho}(c_1+c_2) - (c_1+c_2)\frac{\partial}{\partial\rho}\right], \\
M_{23} &= \frac{1}{3}\left\{\frac{\partial}{\partial\rho}(c_1+c_2)\frac{\partial}{\partial z} - \frac{\partial}{\partial z}(c_1+c_2)\frac{\partial}{\partial\rho}\right. \\
&\quad \left. + \frac{\left(F_z+\frac{1}{2}\right)}{\rho}\left[(c_1+c_2)\frac{\partial}{\partial z} - \frac{\partial}{\partial z}(c_1+c_2)\right]\right\},
\end{aligned}$$

$$M_{24} = \sqrt{3}\left\{\frac{\partial}{\partial\rho}\tilde{\gamma}\frac{\partial}{\partial\rho} + \frac{\left(F_z+\frac{3}{2}\right)}{\rho}\frac{\partial}{\partial\rho}\tilde{\gamma} + \frac{\left(F_z+\frac{1}{2}\right)}{\rho}\tilde{\gamma}\frac{\partial}{\partial\rho} + \frac{\left(F_z+\frac{3}{2}\right)\left(F_z-\frac{1}{2}\right)}{\rho^2}\tilde{\gamma}\right\},$$

$$M_{25} = \sqrt{2}\left\{\frac{\partial}{\partial\rho}\gamma_2\frac{\partial}{\partial\rho} - 2\frac{\partial}{\partial z}\gamma_2\frac{\partial}{\partial z} + \frac{\gamma_2}{\rho}\frac{\partial}{\partial\rho} - \frac{\left(F_z-\frac{1}{2}\right)^2}{\rho^2}\gamma_2 \right.$$
$$\left. + \frac{\left(F_z-\frac{1}{2}\right)}{6\rho}\left[\frac{\partial}{\partial\rho}(c_1+c_2) - (c_1+c_2)\frac{\partial}{\partial\rho}\right]\right\},$$

$$M_{26} = -\frac{1}{3\sqrt{2}}\left\{\frac{\partial}{\partial\rho}(c_1-2c_2)\frac{\partial}{\partial z} + \frac{\partial}{\partial z}(2c_1-c_2)\frac{\partial}{\partial\rho}\right.$$
$$\left. + \frac{\left(F_z+\frac{1}{2}\right)}{\rho}\left[(c_1-2c_2)\frac{\partial}{\partial z} + \frac{\partial}{\partial z}(2c_1-c_2)\right]\right\},$$

$$M_{31} = -\sqrt{3}\left\{\frac{\partial}{\partial\rho}\tilde{\gamma}\frac{\partial}{\partial\rho} - \frac{\left(F_z-\frac{3}{2}\right)}{\rho}\frac{\partial}{\partial\rho}\tilde{\gamma} - \frac{\left(F_z-\frac{1}{2}\right)}{\rho}\tilde{\gamma}\frac{\partial}{\partial\rho} + \frac{\left(F_z-\frac{3}{2}\right)\left(F_z+\frac{1}{2}\right)}{\rho^2}\tilde{\gamma}\right\},$$

$$M_{32} = \frac{1}{3}\left\{\frac{\partial}{\partial z}(c_1+c_2)\frac{\partial}{\partial\rho} - \frac{\partial}{\partial\rho}(c_1+c_2)\frac{\partial}{\partial z}\right.$$
$$\left. + \frac{\left(F_z-\frac{1}{2}\right)}{\rho}\left[(c_1+c_2)\frac{\partial}{\partial z} - \frac{\partial}{\partial z}(c_1+c_2)\right]\right\},$$

$$M_{33} = \frac{\partial}{\partial\rho}(\gamma_1-\gamma_2)\frac{\partial}{\partial\rho} + \frac{(\gamma_1-\gamma_2)}{\rho}\frac{\partial}{\partial\rho} + \frac{\partial}{\partial z}(\gamma_1+2\gamma_2)\frac{\partial}{\partial z}$$
$$- \frac{\left(F_z+\frac{1}{2}\right)^2}{\rho^2}(\gamma_1-\gamma_2) - \frac{\left(F_z+\frac{1}{2}\right)}{6\rho}\left[\frac{\partial}{\partial\rho}(c_1+c_2) - (c_1+c_2)\frac{\partial}{\partial\rho}\right],$$

$$M_{34} = \frac{1}{\sqrt{3}}\left\{\frac{\partial}{\partial z}c_1\frac{\partial}{\partial\rho} - \frac{\partial}{\partial\rho}c_2\frac{\partial}{\partial z} - \frac{\left(F_z+\frac{3}{2}\right)}{\rho}\left[c_2\frac{\partial}{\partial z} - \frac{\partial}{\partial z}c_1\right]\right\},$$

$$M_{35} = \frac{1}{3\sqrt{2}}\left\{\frac{\partial}{\partial\rho}(c_1-2c_2)\frac{\partial}{\partial z} + \frac{\partial}{\partial z}(2c_1-c_2)\frac{\partial}{\partial\rho}\right.$$
$$\left. - \frac{\left(F_z-\frac{1}{2}\right)}{\rho}\left[(c_1-2c_2)\frac{\partial}{\partial z} + \frac{\partial}{\partial z}(2c_1-c_2)\right]\right\},$$

$$M_{36} = \sqrt{2}\left\{\frac{\partial}{\partial\rho}\gamma_2\frac{\partial}{\partial\rho} - 2\frac{\partial}{\partial z}\gamma_2\frac{\partial}{\partial z} + \frac{\gamma_2}{\rho}\frac{\partial}{\partial\rho} - \frac{\left(F_z+\frac{1}{2}\right)^2}{\rho^2}\gamma_2 \right.$$
$$\left. - \frac{\left(F_z+\frac{1}{2}\right)}{6\rho}\left[\frac{\partial}{\partial\rho}(c_1+c_2) - (c_1+c_2)\frac{\partial}{\partial\rho}\right]\right\},$$

$$M_{41} = 0,$$

$$M_{42} = \sqrt{3}\left\{\frac{\partial}{\partial\rho}\tilde{\gamma}\frac{\partial}{\partial\rho} - \frac{\left(F_z-\frac{1}{2}\right)}{\rho}\frac{\partial}{\partial\rho}\tilde{\gamma} - \frac{\left(F_z+\frac{1}{2}\right)}{\rho}\tilde{\gamma}\frac{\partial}{\partial\rho} + \frac{\left(F_z+\frac{3}{2}\right)\left(F_z-\frac{1}{2}\right)}{\rho^2}\tilde{\gamma}\right\},$$

$$M_{43} = \frac{1}{\sqrt{3}}\left\{\frac{\partial}{\partial\rho}c_1\frac{\partial}{\partial z} - \frac{\partial}{\partial z}c_2\frac{\partial}{\partial\rho} - \frac{\left(F_z+\frac{1}{2}\right)}{\rho}\left[c_1\frac{\partial}{\partial z} - \frac{\partial}{\partial z}c_2\right]\right\},$$

$$M_{44} = \frac{\partial}{\partial\rho}(\gamma_1+\gamma_2)\frac{\partial}{\partial\rho} + \frac{(\gamma_1+\gamma_2)}{\rho}\frac{\partial}{\partial\rho} + \frac{\partial}{\partial z}(\gamma_1-2\gamma_2)\frac{\partial}{\partial z} - \frac{\left(F_z+\frac{3}{2}\right)^2}{\rho^2}(\gamma_1+\gamma_2)$$
$$- \frac{\left(F_z+\frac{3}{2}\right)}{2\rho}\left[\frac{\partial}{\partial\rho}(c_1+c_2) - (c_1+c_2)\frac{\partial}{\partial\rho}\right],$$

$$M_{45} = \sqrt{6}\left\{\frac{\partial}{\partial\rho}\tilde{\gamma}\frac{\partial}{\partial\rho} - \frac{\left(F_z-\frac{1}{2}\right)}{\rho}\frac{\partial}{\partial\rho}\tilde{\gamma} - \frac{\left(F_z+\frac{1}{2}\right)}{\rho}\tilde{\gamma}\frac{\partial}{\partial\rho} + \frac{\left(F_z+\frac{3}{2}\right)\left(F_z-\frac{1}{2}\right)}{\rho^2}\tilde{\gamma}\right\},$$

$$M_{46} = -\frac{1}{\sqrt{6}}\left\{\frac{\partial}{\partial\rho}c_1\frac{\partial}{\partial z} - \frac{\partial}{\partial z}c_2\frac{\partial}{\partial\rho} - \frac{\left(F_z+\frac{1}{2}\right)}{\rho}\left[c_1\frac{\partial}{\partial z} - \frac{\partial}{\partial z}c_2\right]\right\},$$

$$M_{51} = -\frac{1}{\sqrt{6}}\left\{\frac{\partial}{\partial z}c_1\frac{\partial}{\partial\rho} - \frac{\partial}{\partial\rho}c_2\frac{\partial}{\partial z} + \frac{\left(F_z-\frac{3}{2}\right)}{\rho}\left[c_2\frac{\partial}{\partial z} - \frac{\partial}{\partial z}c_1\right]\right\},$$

$$M_{52} = \sqrt{2}\left\{\frac{\partial}{\partial\rho}\gamma_2\frac{\partial}{\partial\rho} - 2\frac{\partial}{\partial z}\gamma_2\frac{\partial}{\partial z} + \frac{\gamma_2}{\rho}\frac{\partial}{\partial\rho} - \frac{\left(F_z-\frac{1}{2}\right)^2}{\rho^2}\gamma_2\right.$$
$$\left.+ \frac{\left(F_z-\frac{1}{2}\right)}{6\rho}\left[\frac{\partial}{\partial\rho}(c_1+c_2) - (c_1+c_2)\frac{\partial}{\partial\rho}\right]\right\},$$

$$M_{53} = \frac{1}{3\sqrt{2}}\left\{\frac{\partial}{\partial\rho}(2c_1-c_2)\frac{\partial}{\partial z} + \frac{\partial}{\partial z}(c_1-2c_2)\frac{\partial}{\partial\rho}\right.$$
$$\left.+ \frac{\left(F_z+\frac{1}{2}\right)}{\rho}\left[(2c_1-c_2)\frac{\partial}{\partial z} + \frac{\partial}{\partial z}(c_1-2c_2)\right]\right\},$$

$$M_{54} = \sqrt{6}\left\{\frac{\partial}{\partial\rho}\tilde{\gamma}\frac{\partial}{\partial\rho} + \frac{\left(F_z+\frac{3}{2}\right)}{\rho}\frac{\partial}{\partial\rho}\tilde{\gamma} + \frac{\left(F_z+\frac{1}{2}\right)}{\rho}\tilde{\gamma}\frac{\partial}{\partial\rho} + \frac{\left(F_z+\frac{3}{2}\right)\left(F_z-\frac{1}{2}\right)}{\rho^2}\tilde{\gamma}\right\},$$

$$M_{55} = \frac{\partial}{\partial\rho}\gamma_1\frac{\partial}{\partial\rho} + \frac{\partial}{\partial z}\gamma_1\frac{\partial}{\partial z} + \frac{\gamma_1}{\rho}\frac{\partial}{\partial\rho} - \frac{\left(F_z-\frac{1}{2}\right)^2}{\rho^2}\gamma_1$$
$$+ \frac{\left(F_z-\frac{1}{2}\right)}{3\rho}\left[\frac{\partial}{\partial\rho}(c_1+c_2) - (c_1+c_2)\frac{\partial}{\partial\rho}\right] - 2\Delta_{so},$$

$$M_{56} = -\frac{1}{3}\left\{\frac{\partial}{\partial\rho}(c_1+c_2)\frac{\partial}{\partial z} - \frac{\partial}{\partial z}(c_1+c_2)\frac{\partial}{\partial\rho}\right.$$
$$\left.+ \frac{\left(F_z+\frac{1}{2}\right)}{\rho}\left[(c_1+c_2)\frac{\partial}{\partial z} - \frac{\partial}{\partial z}(c_1+c_2)\right]\right\},$$

$$M_{61} = -\sqrt{6}\left\{\frac{\partial}{\partial\rho}\tilde{\gamma}\frac{\partial}{\partial\rho} - \frac{\left(F_z-\frac{3}{2}\right)}{\rho}\frac{\partial}{\partial\rho}\tilde{\gamma} - \frac{\left(F_z-\frac{1}{2}\right)}{\rho}\tilde{\gamma}\frac{\partial}{\partial\rho}\right.$$
$$\left.+ \frac{\left(F_z-\frac{3}{2}\right)\left(F_z+\frac{1}{2}\right)}{\rho^2}\tilde{\gamma}\right\},$$

$$
\begin{aligned}
M_{62} &= -\frac{1}{3\sqrt{2}}\left\{\frac{\partial}{\partial\rho}(2c_1-c_2)\frac{\partial}{\partial z}+\frac{\partial}{\partial z}(c_1-2c_2)\frac{\partial}{\partial\rho}\right.\\
&\quad\left.-\frac{\left(F_z-\frac{1}{2}\right)}{\rho}\left[(2c_1-c_2)\frac{\partial}{\partial z}+\frac{\partial}{\partial z}(c_1-2c_2)\right]\right\},\\
M_{63} &= \sqrt{2}\left\{\frac{\partial}{\partial\rho}\gamma_2\frac{\partial}{\partial\rho}-2\frac{\partial}{\partial z}\gamma_2\frac{\partial}{\partial z}+\frac{\gamma_2}{\rho}\frac{\partial}{\partial\rho}-\frac{\left(F_z+\frac{1}{2}\right)^2}{\rho^2}\gamma_2\right.\\
&\quad\left.-\frac{\left(F_z+\frac{1}{2}\right)}{6\rho}\left[\frac{\partial}{\partial\rho}(c_1+c_2)-(c_1+c_2)\frac{\partial}{\partial\rho}\right]\right\},\\
M_{64} &= -\frac{1}{\sqrt{6}}\left\{\frac{\partial}{\partial z}c_1\frac{\partial}{\partial\rho}-\frac{\partial}{\partial\rho}c_2\frac{\partial}{\partial z}-\frac{\left(F_z+\frac{3}{2}\right)}{\rho}\left[c_2\frac{\partial}{\partial z}-\frac{\partial}{\partial z}c_1\right]\right\},\\
M_{65} &= -\frac{1}{3}\left\{\frac{\partial}{\partial z}(c_1+c_2)\frac{\partial}{\partial\rho}-\frac{\partial}{\partial\rho}(c_1+c_2)\frac{\partial}{\partial z}\right.\\
&\quad\left.+\frac{\left(F_z-\frac{1}{2}\right)}{\rho}\left[(c_1+c_2)\frac{\partial}{\partial z}-\frac{\partial}{\partial z}(c_1+c_2)\right]\right\},\\
M_{66} &= \frac{\partial}{\partial\rho}\gamma_1\frac{\partial}{\partial\rho}+\frac{\partial}{\partial z}\gamma_1\frac{\partial}{\partial z}+\frac{\gamma_1}{\rho}\frac{\partial}{\partial\rho}-\frac{\left(F_z+\frac{1}{2}\right)^2}{\rho^2}\gamma_1\\
&\quad-\frac{\left(F_z+\frac{1}{2}\right)}{3\rho}\left[\frac{\partial}{\partial\rho}(c_1+c_2)-(c_1+c_2)\frac{\partial}{\partial\rho}\right]-2\Delta_{so}.
\end{aligned}
$$

where γ_1, γ_2 and $\tilde{\gamma}$ are the Luttinger mass parameters, Δ_{so} is the spin-orbit splitting and F_z stands for the total angular momentum.

A.2 Wurtzite crystal structure

The position-dependent Hamiltonian for the VB of WZ materials derived with Burt-Foreman operator ordering is:[45]

$$H_{WZ} = - \begin{array}{c} \begin{array}{cccccc} |u_1\rangle & |u_2\rangle & |u_3\rangle & |u_4\rangle & |u_5\rangle & |u_6\rangle \end{array} \\ \begin{bmatrix} F-\rho & \kappa & \xi^* & 0 & 0 & 0 \\ \kappa^* & G+\rho & -\xi & 0 & 0 & \sqrt{2}\Delta_3 \\ \eta & -\eta^* & \lambda & 0 & \sqrt{2}\Delta_3 & 0 \\ 0 & 0 & 0 & F+\rho & \kappa^* & -\xi \\ 0 & 0 & \sqrt{2}\Delta_3 & \kappa & G-\rho & \xi^* \\ 0 & \sqrt{2}\Delta_3 & 0 & -\eta^* & \eta & \lambda \end{bmatrix} \end{array}, \tag{A.4}$$

where

$$\begin{aligned} F &= \Delta_1 + \Delta_2 + \lambda + \theta, \\ G &= \Delta_1 - \Delta_2 + \lambda + \theta, \\ \lambda &= \frac{\hbar^2}{2m_0} \left[k_z A_1 k_z + k_x A_2 k_x + k_y A_2 k_y\right], \\ \theta &= \frac{\hbar^2}{2m_0} \left[k_z A_3 k_z + k_x A_4 k_x + k_y A_4 k_y\right], \\ \kappa &= \frac{\hbar^2}{2m_0} \left[-k_x A_5 k_x + k_y A_5 k_y + i\,(k_x A_5 k_y + k_y A_5 k_x)\right], \\ \eta &= \frac{\hbar^2}{2m_0} \left[-k_z A_6^{(+)} k_+ - k_+ A_6^{(-)} k_z\right], \\ \xi &= \frac{\hbar^2}{2m_0} \left[-k_z A_6^{(-)} k_+ - k_+ A_6^{(+)} k_z\right], \\ \rho &= \frac{\hbar^2}{2m_0} \left[i\,k_y\,(A_5^{(+)} - A_5^{(-)}) k_x - i\,k_x\,(A_5^{(+)} - A_5^{(-)}) k_y\right]. \end{aligned}$$

Here, m_0 is the free electron mass and A_i are material mass parameters, with $A_5 = A_5^{(+)} + A_5^{(-)}$ and $A_6 = A_6^{(+)} + A_6^{(-)}$. In addition, the crystal-field splitting is denoted by $\Delta_1 = \Delta_{cr}$, and Δ_2 and Δ_3 are the spin-orbit terms. In the so-called cubic approximation we have $\Delta_2 = \Delta_3 = \Delta_{so}/3$.

It should be stressed that coefficients $A_5^{(\pm)}$ and $A_6^{(\pm)}$ are not generally available in literature. Here we take the complete asymmetric operator order, i.e. $A_i^{(+)} = A_i$ and $A_i^{(-)} = 0$, following the criteria suggested by Veprek *et al.* [201, 202]. In their works it is shown that the emergence of spurious solutions within the k·p method comes from the non-ellipticity of the coupled differential equation system. After analyzing various sets of mass parameters for several materials, they found that taking $A_i^{(-)} = 0$ grants the ellipticity of the Hamiltonian, thus avoiding non-physical solutions. We have reached the same result for the materials studied in this work.

A.3 Polytypes

A.3.1 Constant-mass Hamiltonian

The six-band Hamiltonian for studying the VB of ZB/WZ polytypes is as follows:[46]

$$H_{ZB/WZ} = - \begin{array}{c} \begin{array}{cccccc} |u_1\rangle & |u_2\rangle & |u_3\rangle & |u_4\rangle & |u_5\rangle & |u_6\rangle \end{array} \\ \begin{bmatrix} F & -K^* & -H^* & 0 & 0 & 0 \\ -K & G & H & 0 & 0 & \sqrt{2}\Delta_3 \\ -H & H^* & \lambda & 0 & \sqrt{2}\Delta_3 & 0 \\ 0 & 0 & 0 & F & -K & H \\ 0 & 0 & \sqrt{2}\Delta_3 & -K^* & G & -H^* \\ 0 & \sqrt{2}\Delta_3 & 0 & H^* & -H & \lambda \end{bmatrix} \end{array}, \tag{A.5}$$

where

$$\begin{aligned} F &= \Delta_1 + \Delta_2 + \lambda + \theta, \\ G &= \Delta_1 - \Delta_2 + \lambda + \theta, \\ \lambda &= \frac{\hbar^2}{2m_0}[A_1 k_z^2 + A_2 k_\perp^2], \\ \theta &= \frac{\hbar^2}{2m_0}[A_3 k_z^2 + A_4 k_\perp^2], \\ K &= \frac{\hbar^2}{2m_0} A_5 k_+^2 + \Delta K, \\ H &= \frac{\hbar^2}{2m_0} A_6 k_+ k_z + \Delta H, \\ \Delta K &= 2\sqrt{2}\,\frac{\hbar^2}{2m_0} A_z k_- k_z, \\ \Delta H &= \frac{\hbar^2}{2m_0} A_z k_-^2. \end{aligned}$$

Here, m_0 is the free electron mass, A_i are effective mass parameters, $k_\perp = k_x^2 + k_y^2$, $k_\pm = k_x \pm i k_y$, Δ_1 is the crystal field splitting, and Δ_2 and Δ_3 are spin-orbit matrix elements.

A.3.2 Variable mass Hamiltonian

The position-dependent Burt-Foreman version of Hamiltonian (A.5) reads:

$$H^{BF}_{ZB/WZ} = - \begin{array}{c} \begin{array}{cccccc} |u_1\rangle & |u_2\rangle & |u_3\rangle & |u_4\rangle & |u_5\rangle & |u_6\rangle \end{array} \\ \begin{bmatrix} F-\rho & \kappa & \xi^* & 0 & 0 & 0 \\ \kappa^* & G+\rho & -\xi & 0 & 0 & \sqrt{2}\Delta_3 \\ \eta & -\eta^* & \lambda & 0 & \sqrt{2}\Delta_3 & 0 \\ 0 & 0 & 0 & F+\rho & \kappa^* & -\xi \\ 0 & 0 & \sqrt{2}\Delta_3 & \kappa & G-\rho & \xi^* \\ 0 & \sqrt{2}\Delta_3 & 0 & -\eta^* & \eta & \lambda \end{bmatrix} \end{array}, \tag{A.6}$$

where

$$\begin{aligned}
F &= \Delta_1 + \Delta_2 + \lambda + \theta, \\
G &= \Delta_1 - \Delta_2 + \lambda + \theta, \\
\lambda &= \frac{\hbar^2}{2m_0}\left[k_z A_1 k_z + k_x A_2 k_x + k_y A_2 k_y\right], \\
\theta &= \frac{\hbar^2}{2m_0}\left[k_z A_3 k_z + k_x A_4 k_x + k_y A_4 k_y\right], \\
\kappa &= \frac{\hbar^2}{2m_0}\left[-k_x A_5 k_x + k_y A_5 k_y + i\left(k_x A_5 k_y + k_y A_5 k_x\right)\right] + \Delta\kappa, \\
\eta &= \frac{\hbar^2}{2m_0}\left[-k_z A_6^{(+)} k_+ - k_+ A_6^{(-)} k_z\right] + \Delta\eta, \\
\xi &= \frac{\hbar^2}{2m_0}\left[-k_z A_6^{(-)} k_+ - k_+ A_6^{(+)} k_z\right] + \Delta\xi, \\
\rho &= \frac{\hbar^2}{2m_0}\left[i\, k_y \left(A_5^{(+)} - A_5^{(-)}\right) k_x - i\, k_x \left(A_5^{(+)} - A_5^{(-)}\right) k_y\right], \\
\Delta\xi &= \frac{\hbar^2}{2m_0}\left[-(k_x - i\, k_y) A_z (k_x - i\, k_y)\right], \\
\Delta\eta &= \Delta\xi, \\
\Delta\kappa &= -2\sqrt{2}\,\frac{\hbar^2}{2m_0}\left[(k_x + i\, k_y)\, A_z^{(+)}\, k_z + k_z\, A_z^{(-)}\,(k_x + i\, k_y)\right].
\end{aligned}$$

Here, m_0 is the free electron mass, A_i are material mass parameters, $A_5 = A_5^{(+)} + A_5^{(-)}$, $A_6 = A_6^{(+)} + A_6^{(-)}$, $\Delta_1 = \Delta_{cr}$ the crystal-field splitting and $\Delta_2 = \Delta_3 = \Delta_{so}/3$ the spin-orbit energy terms within the quasi-cubic approximation.

Following the same reasoning as for the WZ VB Hamiltonian in section A.2, we also take complete asymmetric operator ordering ($A_i^{(+)} = A_i$ and $A_i^{(-)} = 0$) in order to ensure equation system ellipticity.[201, 202]

APPENDIX **B**

Spin-orbit Hamiltonians in matrix form

This appendix collects the explicit matrix form of the SOI Hamiltonians introduced in section 2.3.

B.1 Dresselhaus SOI

B.1.1 Conduction band DSOI Hamiltonian

The DSOI Hamiltonian accounting for the spin-up and spin-down bands of the CB is:

$$H_{BIA}^{CB} = b_{41}^{CB} \begin{pmatrix} \frac{1}{2}\left\{k_+^2 + k_-^2, k_z\right\} & \frac{1}{4}\left\{k_+^2 - k_-^2, k_-\right\} - \left\{k_z^2, k_+\right\} \\ \frac{1}{4}\left\{k_-^2 - k_+^2, k_+\right\} - \left\{k_z^2, k_-\right\} & -\frac{1}{2}\left\{k_+^2 + k_-^2, k_z\right\} \end{pmatrix}, \tag{B.1}$$

where $k_\pm = k_x \pm i\, k_y$.

B.1.2 Valence band DSOI Hamiltonian

Matrix form of the four-band DSOI Hamiltonian in Cartesian coordinates:

$$H_{BIA}^{VB} = H_{C_k} + H_{b_{41}} + H_{b_{42}} + H_{b_{51}} + H_{b_{52}}, \tag{B.2}$$

where:

$$H_{C_k} = C_k \begin{pmatrix} 0 & -\frac{k_-}{2} & k_z & -\frac{\sqrt{3}\,k_-}{2} \\ -\frac{k_+}{2} & 0 & \frac{\sqrt{3}\,k_+}{2} & -k_z \\ k_z & \frac{\sqrt{3}\,k_-}{2} & 0 & -\frac{k_-}{2} \\ -\frac{\sqrt{3}\,k_+}{2} & -k_z & -\frac{k_+}{2} & 0 \end{pmatrix}, \tag{B.3}$$

with $k_\pm = k_x \pm i\,k_y$.

$$H_{b_{41}} = b_{41}^{VB} \begin{pmatrix} \frac{3}{2}\,P_{41} & \frac{\sqrt{3}}{2}\,L_{41} & 0 & 0 \\ \frac{\sqrt{3}}{2}\,L_{41}^\dagger & \frac{1}{2}\,P_{41} & L_{41} & 0 \\ 0 & L_{41}^\dagger & -\frac{1}{2}\,P_{41} & \frac{\sqrt{3}}{2}\,L_{41} \\ 0 & 0 & \frac{\sqrt{3}}{2}\,L_{41}^\dagger & -\frac{3}{2}\,P_{41} \end{pmatrix}, \tag{B.4}$$

where $P_{41} = (k_x^2 - k_y^2)\,k_z$ and $L_{41} = i\,k_-\,k_x\,k_y - k_+\,k_z^2$.

$$H_{b_{42}} = b_{42} \begin{pmatrix} \frac{27}{8}\,P_{41} & \frac{7\sqrt{3}}{8}\,L_{41} & 0 & -\frac{3}{4}\,L_{42} \\ \frac{7\sqrt{3}}{8}\,L_{41}^\dagger & \frac{1}{8}\,P_{41} & \frac{5}{2}\,L_{41} & 0 \\ 0 & \frac{5}{2}\,L_{41}^\dagger & -\frac{1}{8}\,P_{41} & \frac{7\sqrt{3}}{8}\,L_{41} \\ \frac{3}{4}\,L_{42}^\dagger & 0 & \frac{7\sqrt{3}}{8}\,L_{41}^\dagger & -\frac{27}{8}\,P_{41} \end{pmatrix}, \tag{B.5}$$

where $L_{42} = i\,k_+\,k_x\,k_y + k_-\,k_z^2$.

$$H_{b_{51}} = b_{51} \begin{pmatrix} 0 & -\frac{\sqrt{3}}{4}\,K_+ & \frac{\sqrt{3}}{2}\,K_z & -\frac{3}{4}\,K_- \\ -\frac{\sqrt{3}}{4}\,K_- & 0 & \frac{3}{4}\,K_+ & -\frac{\sqrt{3}}{2}\,K_z \\ \frac{\sqrt{3}}{2}\,K_z & \frac{3}{4}\,K_- & 0 & -\frac{\sqrt{3}}{4}\,K_+ \\ -\frac{3}{4}\,K_+ & -\frac{\sqrt{3}}{2}\,K_z & -\frac{\sqrt{3}}{4}\,K_- & 0 \end{pmatrix}, \tag{B.6}$$

where $K_+ = K_x + i\,K_y$, $K_- = K_x - i\,K_y$, $K_x = k_x\,(k_y^2 + k_z^2)$, $K_y = k_y\,(k_x^2 + k_z^2)$, and $K_z = k_z\,(k_x^2 + k_y^2)$.

$$H_{b_{52}} = b_{52} \begin{pmatrix} 0 & -\frac{\sqrt{3}}{4}\,M_+ & \frac{\sqrt{3}}{2}\,k_z^3 & -\frac{3}{4}\,M_- \\ -\frac{\sqrt{3}}{4}\,M_- & 0 & \frac{3}{4}\,M_+ & -\frac{\sqrt{3}}{2}\,k_z^3 \\ \frac{\sqrt{3}}{2}\,k_z^3 & \frac{3}{4}\,M_- & 0 & -\frac{\sqrt{3}}{4}\,M_+ \\ -\frac{3}{4}\,M_+ & -\frac{\sqrt{3}}{2}\,k_z^3 & -\frac{\sqrt{3}}{4}\,M_- & 0 \end{pmatrix}, \tag{B.7}$$

where $M_+ = k_x^3 + i\,k_y^3$ and $M_- = k_x^3 - i\,k_y^3$.

B.2 Rashba SOI

B.2.1 Conduction band RSOI Hamiltonian

The electron RSOI Hamiltonian reads:

$$H_{SIA}^{CB} = r_{41} \begin{pmatrix} -F_x k_y + F_y k_x & -(iF_x + F_y)k_z + iF_z k_- \\ (iF_x + F_y)k_z - iF_z k_+ & F_x k_y - F_y k_x \end{pmatrix}, \tag{B.8}$$

where F_i are the components of the external electric field $\mathbf{F}$ and $k_\pm = k_x \pm i\, k_y$.

APPENDIX C

Strain Hamiltonians

The implementation of strain into the k·p models is carried out following Bir and Pikus [32]. In this appendix we present the strain Hamiltonians for the crystal structures studied throughout the Thesis.

C.1 Zinc-blende QDs

C.1.1 Conduction band

The one-band electron Hamiltonian of equation (2.14) has to be supplemented with

$$H_{\epsilon}^{ZB} = a_c(\epsilon_{xx} + \epsilon_{yy} + \epsilon_{zz}), \tag{C.1}$$

with a_c standing for the CB deformation potential.

C.1.2 Valence band

The four-band VB strain Hamiltonian is derived from Hamiltonian (A.1) after performing the following substitutions:

$$\frac{\hbar^2}{2m_0}\gamma_1 \rightarrow -a_v, \tag{C.2a}$$

$$\frac{\hbar^2}{2m_0}\gamma_2 \rightarrow -\frac{b}{2}, \tag{C.2b}$$

$$\frac{\hbar^2}{2m_0}\gamma_3 \rightarrow -\frac{d}{2\sqrt{3}}. \tag{C.2c}$$

Here, a_v is the hydrostatic VB deformation potential, and b and d are shear VB deformation potentials. The strain Hamiltonian is as follows:

$$H_\epsilon^{ZB} = - \begin{array}{c} \begin{array}{cccc} \left|\frac{3}{2}\ \frac{+3}{2}\right\rangle & \left|\frac{3}{2}\ \frac{+1}{2}\right\rangle & \left|\frac{3}{2}\ \frac{-1}{2}\right\rangle & \left|\frac{3}{2}\ \frac{-3}{2}\right\rangle \end{array} \\ \begin{pmatrix} P_\epsilon + Q_\epsilon & -S_\epsilon & R_\epsilon & 0 \\ -S_\epsilon^\dagger & P_\epsilon - Q_\epsilon & 0 & R_\epsilon \\ R_\epsilon^\dagger & 0 & P_\epsilon - Q_\epsilon & S_\epsilon \\ 0 & R_\epsilon^\dagger & S_\epsilon^\dagger & P_\epsilon + Q_\epsilon \end{pmatrix} \end{array}, \tag{C.3}$$

with

$$\begin{aligned} P_\epsilon &= -a_v(\epsilon_{xx} + \epsilon_{yy} + \epsilon_{zz}), \\ Q_\epsilon &= -\frac{b}{2}(\epsilon_{xx} + \epsilon_{yy} - 2\epsilon_{zz}), \\ R_\epsilon &= \frac{\sqrt{3}}{2} b(\epsilon_{xx} - \epsilon_{yy}) - id\epsilon_{xy}, \\ S_\epsilon &= -d(\epsilon_{zx} - i\epsilon_{yz}). \end{aligned}$$

C.2 Wurtzite QDs

C.2.1 Conduction band

WZ crystals are hexagonal, so they have different lattice parameters in the axial and in-plane directions. Therefore, the strain is clearly anisotropic and this is also reflected in the strain Hamiltonian

$$H_\epsilon^{WZ} = a_c^\perp(\epsilon_{xx} + \epsilon_{yy}) + a_c^z \epsilon_{zz}, \tag{C.4}$$

where $a_c^\perp$ and a_c^z are the CB deformation potentials for the in-plane and growth directions, respectively.

C.2.2 Valence band

The hole Hamiltonian for strained WZ systems is obtained by substituting the effective mass parameters $\frac{\hbar^2}{2m_0}A_i$ by the deformation potentials D_i in equation (A.4). The resulting strain Hamiltonian reads:

$$H_\epsilon^{WZ} = \begin{array}{c} \begin{array}{cccccc} |u_1\rangle & |u_2\rangle & |u_3\rangle & |u_4\rangle & |u_5\rangle & |u_6\rangle \end{array} \\ \begin{bmatrix} F_\epsilon & \kappa_\epsilon & \xi_\epsilon^* & 0 & 0 & 0 \\ \kappa_\epsilon^* & F_\epsilon & -\xi_\epsilon & 0 & 0 & 0 \\ \xi_\epsilon & -\xi_\epsilon^* & \lambda_\epsilon & 0 & 0 & 0 \\ 0 & 0 & 0 & F_\epsilon & \kappa_\epsilon^* & -\xi_\epsilon \\ 0 & 0 & 0 & \kappa_\epsilon & F_\epsilon & \xi_\epsilon^* \\ 0 & 0 & 0 & -\xi_\epsilon^* & \xi_\epsilon & \lambda_\epsilon \end{bmatrix} \end{array}, \tag{C.5}$$

where

$$\begin{aligned} F_\epsilon &= (D_1 + D_3)\epsilon_{zz} + (D_2 + D_4)(\epsilon_{xx} + \epsilon_{yy}), \\ \lambda_\epsilon &= D_1\epsilon_{zz} + D_2(\epsilon_{xx} + \epsilon_{yy}), \\ \kappa_\epsilon &= D_5(-\epsilon_{xx} + \epsilon_{yy} + 2i\,\epsilon_{xy}), \\ \xi_\epsilon &= -D_6(\epsilon_{xz} + i\,\epsilon_{yz}). \end{aligned}$$

APPENDIX D

Carrier-phonon interaction Hamiltonians

This appendix outlines the derivation and contains complete expressions for the deformation-potential and piezoelectric Hamiltonians, equation (4.1), in terms of the phonon normal modes of vibration. Only ZB semiconductors are considered since spin scattering phenomena in WZ are not investigated in the present Thesis.

The origin of these interaction potentials lies in the displacement of lattice atoms from their equilibrium positions, producing strain and this strain yielding piezoelectricity. Therefore, we can use the expressions introduced for the strain and piezoelectricity in section 2.4.1, which depend on the strain tensor components ϵ_{ij}, and then relate them to the normal modes of vibration.

First, we write the displacement of crystal atoms $\mathbf{u}_\lambda(\mathbf{r})$ in terms of the phonon creation and annihilation operators, $a^\dagger_{\mathbf{q}}$ and $a_{\mathbf{q}}$, respectively:[203]

$$\mathbf{u}_\lambda(\mathbf{r}) = \sum_{\mathbf{q}} \eta_\lambda(\mathbf{q}) \sqrt{\frac{\hbar}{2MN\omega_{q\lambda}}} \left(a_{\mathbf{q}}\, e^{i\mathbf{q}\mathbf{r}} + a^\dagger_{\mathbf{q}}\, e^{-i\mathbf{q}\mathbf{r}} \right), \tag{D.1}$$

where M and N are the mass and number of atoms in the crystal, $\mathbf{q}$ is the wave vector, and λ indicates the phonon branch: longitudinal ($\lambda = l$) or transversal ($\lambda = t_1, t_2$). $\eta_\lambda(\mathbf{q})$ stands for the polarization vector. Here we use:[118]

$$\eta_l(\mathbf{q}) = \frac{1}{q}\begin{pmatrix} q_x \\ q_y \\ q_z \end{pmatrix}, \quad \eta_{t_1}(\mathbf{q}) = \frac{1}{q\, q_\perp}\begin{pmatrix} q_x\, q_z \\ q_y\, q_z \\ -q_\perp^2 \end{pmatrix}, \quad \eta_{t_2}(\mathbf{q}) = \frac{1}{q_\perp}\begin{pmatrix} q_y \\ -q_x \\ 0 \end{pmatrix}, \tag{D.2}$$

with $q_\perp = \sqrt{q_x^2 + q_y^2}$.

Taking into account equation (D.2) and the definition of the strain tensor in terms of displacements, equation (2.25), after some algebra one obtains:

$$\epsilon_{ij}^\lambda = -\frac{i}{2} \sum_{\mathbf{q}} U^\lambda(q) \left(\eta_\lambda^i(\mathbf{q})\, q_j + \eta_\lambda^j(\mathbf{q})\, q_i \right) F(\mathbf{q}, \mathbf{r}), \tag{D.3}$$

where $F(\mathbf{q}, \mathbf{r}) = a_{\mathbf{q}}^\dagger\, e^{-i\mathbf{qr}}$ and $U^\lambda(q) = \sqrt{\hbar/(2\,\rho\, V\, \omega_{q\,\lambda})}$. Here, the annihilation operator term has been dropped since we have assumed zero temperature, i.e. no emission processes, and $MN = \rho V$, with ρ and V standing for the crystal density and volume.

Equation (D.3) is the general form of the strain components. The specific expressions for the six independent strain components and three phonon branches can be easily obtained from the general one. Thus, we show here the case of ϵ_{xx}^l as an example and omit the others for brevity. After substituting the polarization vector $\eta_l(\mathbf{q})$ given in equation (D.2) into (D.3), one obtains:

$$\epsilon_{xx}^l = -i \sum_{\mathbf{q}} U^\lambda(q) \left(\frac{q_x^2}{q} \right) F(\mathbf{q}, \mathbf{r}). \tag{D.4}$$

Following a similar procedure one can calculate the remaining strain components, which will be further substituted in the strain and piezoelectric Hamiltonians as shown below.

D.1 Piezoelectric potential

The piezoelectric potential is given by:[204]

$$\phi_{pz}^\lambda = -\sum_{\mathbf{q}} \frac{4\pi\, i}{\varepsilon_r\, q^2}\, h_{14} \left(q_x\, \epsilon_{yz}^\lambda + q_y\, \epsilon_{xz}^\lambda + q_z\, \epsilon_{xy}^\lambda \right). \tag{D.5}$$

where ε_r is the relative dielectric constant and h_{14} is the piezoelectric constant. The corresponding expressions for the different phonon branches are

$$\phi_{pz}^l = -\frac{12\,\pi\, h_{14}}{\epsilon_r}\, U^l(q) \sum_{\mathbf{q}} \frac{q_x q_y q_z}{q^3}\, F(\mathbf{q}, \mathbf{r}), \tag{D.6a}$$

$$\phi_{pz}^{t_1} = -\frac{4\,\pi\, h_{14}}{\epsilon_r}\, U^t(q) \sum_{\mathbf{q}} \frac{q_x q_y\, (2q_z^2 - q_\perp^2)}{q^3\, q_\perp}\, F(\mathbf{q}, \mathbf{r}), \tag{D.6b}$$

$$\phi_{pz}^{t_2} = -\frac{4\,\pi\,h_{14}}{\epsilon_r}\,U^t(q)\sum_{\mathbf{q}}\frac{q_z\,(q_y^2 - q_x^2)}{q^2\,q_\perp}\,F(\mathbf{q},\mathbf{r}), \tag{D.6c}$$

It is worth noting that ϕ_{pz} is a potential diagonal term and the expressions in (D.6) are valid for both electrons and holes.

D.2 Deformation potential

The carrier-phonon interaction Hamiltonian for the deformation-potential relaxation mechanism, H_{dp}^{λ}, is derived by simply substituting the strain components calculated above into the corresponding strain Hamiltonians presented in appendix C.

D.2.1 Conduction band

For electrons, only longitudinal phonon modes contribute to the deformation-potential scattering. After carrying out the aforementioned substitution into equation C.1 one gets

$$H_{dp}^{l} = -i\,a_c\,U^l(q)\sum_{\mathbf{q}} q\,F(\mathbf{q},\mathbf{r}) \tag{D.7}$$

with a_c denoting the CB deformation potential.

D.2.2 Valence band

The deformation potential term is given by the four-band Bir-Pikus strain Hamiltonian, equation (C.2). The strain operators for the three branches become

$$p^l = i\,a_v\,U^l(q)\sum_{\mathbf{q}} q\;F(\mathbf{q},\mathbf{r}), \tag{D.8a}$$

$$q^l = i\,\frac{b}{2}\,U^l(q)\sum_{\mathbf{q}}\left(q - 3\,\frac{q_z^2}{q}\right)\,F(\mathbf{q},\mathbf{r}), \tag{D.8b}$$

$$r^l = -i\,U^l(q)\sum_{\mathbf{q}}\left(\frac{\sqrt{3}}{2}b\,\frac{q_x^2 - q_y^2}{q} - i\,d\,\frac{q_x\,q_y}{q}\right)\,F(\mathbf{q},\mathbf{r}), \tag{D.8c}$$

$$s^l = i\,d\,U^l(q)\sum_{\mathbf{q}}\frac{q_z\,(q_x - i\,q_y)}{q}\,F(\mathbf{q},\mathbf{r}), \tag{D.8d}$$

for longitudinal phonons,

$$p^{t_1} = 0, \tag{D.9a}$$

$$q^{t_1} = i\,\frac{b}{2}\,U^t(q)\sum_{\mathbf{q}}\left(\frac{3\,q_z\,q_\perp}{q}\right)\,F(\mathbf{q},\mathbf{r}), \tag{D.9b}$$

$$r^{t_1} = -i\,U^t(q)\sum_{\mathbf{q}}\left(\frac{\sqrt{3}}{2}b\,\frac{q_z\,(q_x^2-q_y^2)}{q\,q_\perp} - i\,d\,\frac{q_x\,q_y\,q_z}{q\,q_\perp}\right)\,F(\mathbf{q},\mathbf{r}), \tag{D.9c}$$

$$s^{t_1} = i\,\frac{d}{2}\,U^t(q)\sum_{\mathbf{q}}\frac{(q_z^2-q_\perp^2)\,(q_x-i\,q_y)}{q_\perp\,q}\,F(\mathbf{q},\mathbf{r}), \tag{D.9d}$$

for transversal t_1 phonons, and

$$p^{t_2} = 0, \tag{D.10a}$$

$$q^{t_2} = 0, \tag{D.10b}$$

$$r^{t_2} = -i\,U^t(q)\sum_{\mathbf{q}}\left(\sqrt{3}b\,\frac{q_x\,q_y}{q_\perp} - i\frac{d}{2}\,\frac{q_y^2-q_x^2}{q_\perp}\right)\,F(\mathbf{q},\mathbf{r}), \tag{D.10c}$$

$$s^{t_2} = -\frac{d}{2}\,U^t(q)\sum_{\mathbf{q}}\frac{q_z\,(q_x-i\,q_y)}{q_\perp}\,F(\mathbf{q},\mathbf{r}), \tag{D.10d}$$

for transversal t_2 phonons. Parameters a_v, b and d stand for the VB deformation potential.

Resum

El treball presentat en aquesta Tesi doctoral s'emmarca dintre del camp de la nanotecnologia, és a dir, estudia les propietats de sistemes amb grandàries en escala nanomètrica. Aquesta escala propicia l'aparició de fenòmens quàntics perquè quan els portadors de càrrega, tant electrons com forats, es troben confinats en un espai de dimensions del mateix ordre o inferior a la seua longitud d'ona de *de Broglie*, es comporten seguint les lleis de la mecànica quàntica, de manera que una descripció clàssica deixa de ser vàlida. Aquest fet dóna lloc a una sèrie de propietats no habituals en sistems tradicionals que fan que aquestes nanoestructures siguen especialment prometedores per al desenvolupament de nombroses aplicacions tecnològiques en camps tan diversos com medicina, electrònica, cèl·lules solars, computació, etc.[1, 4–8]

Entre la gran diversitat de sistemes nanoscòpics, nosaltres ens centrem principalment en nanoestructures semiconductores de baixa dimensionalitat, concretament en aquelles que confinen els portadors de càrrega en les tres direccions de l'espai, anomenades normalment punts quàntics o *quantum dots* (QDs). Aquestes estructures es caracteritzen per presentar un espectre d'energia discret paregut al dels àtoms, pel que de vegades se les coneix també com àtoms artificials.[2] A més, els punts quàntics presenten l'avantatge de poder ser sintetitzats en una gran varietat de formes, grandàries, materials i de ser poblats de forma controlada amb un nombre de portadors determinat.[10, 11] Aquesta gran flexibilitat permet el disseny de punts quàntics molt diversos, podent decidir en cada cas quin sistema és el més adient per a la finalitat que ha de complir.

Els mètodes de fabricació més importants són bàsicament tres: tècniques litogràfiques,[13, 14] creixement auto-ordenat[16, 17] i tècniques de química humida.[18] Cadascun d'ells proporciona punts quàntics amb unes característiques diferents. Els més estudiats en aquesta memòria són els obtinguts a partir de les dues darreres tècniques per motiu de la seua tridimensionalitat. Els punts quàntics auto-ordenats solen presentar forma piramidal, de

piràmide truncada, lents planes o anells, amb alçades de l'ordre de 25 nm i bases de 20 nm d'amplada. Pel que fa als nanocristalls col·loïdals fabricats per via humida, solen ser pràcticament esfèrics amb radis menuts (d'aproximadament 1.2-10 nm). Quant als materials emprats, els punts quàntics típics estan compostos per semiconductors binaris amb estructura cristallina zinc-blenda (ZB) o wurtzita (WZ), però recentment també s'ha aconseguit sintetitzar punts quàntics politípics, en els que coexisteixen ambdues fases cristal·lines d'un mateix material. A més a més, en els darrers anys també ha sigut possible obtenir punts quàntics a partir de materials purament bidimensionals, com per exemple grafé o d'altres més recents com ara el MoS_2 monocapa.

Per tal de poder implementar satisfactòriament els punts quàntics en dispositius tecnològics que algun dia arriben a comercialitzar-se, és fonamental entendre en profunditat les seues propietats, tant des d'un punt de vista teòric com experimental. A aquest respecte, cal tindre present que no es tracta de sistemes aïllats del seu voltant i que la interacció amb el medi exterior pot provocar canvis substàncials en el seu comportament. Per aquest motiu, un dels principals objectius d'aquesta Tesi és investigar l'efecte que el medi que envolta als punts quàntics té sobre la seua estructura electrònica. En particular, estudiem la influència de les tensions que sorgeixen en la interfase entre dos materials com a conseqüència de tenir constants de xarxa diferents, així com dels camps piezoelèctrics derivats d'aquestes forces de tensió. Aquests dos factors poden donar lloc a canvis en l'estructura electrònica, separació d'electrons i forats en excitons, i són també els principals mecanismes de relaxació d'espín. D'altra banda, tant important com entendre les propietats electròniques i òptiques dels punts quàntics, ho és també disposar dels mitjans per a manipular-les externament de forma reversible i així poder controlar fàcilment la seua resposta. Açò sol fer-se mitjançant camps elèctrics i magnètics externament aplicats, de forma que esdevé de vital importància conèixer com afecten aquests a l'estructura electrònica i a la resposta dels punts quàntics.

L'objectiu principal d'aquesta Tesi és estudiar teòricament l'estructura electrònica de punts quàntics semiconductors sota la influència de camps externament aplicats i del medi que els envolta. La metodologia emprada és bàsicament el mètode $k{\cdot}p$ en el marc de les aproximacions de massa efectiva (EMA) i funció envolupant (EFA).[1] El mètode $k{\cdot}p$ és un model continu basat en la teoria de pertorbacions que té en compte les simetries dels cristalls per descriure l'estructura electrònica en funció d'un reduït

[1] Altres formalismes s'han utilitzat en l'estudi de sistemes correlacionats però només de forma puntual.

nombre de paràmetres empírics, que es determinen experimentalment o a partir de càlculs *ab initio*. Malgrat la seua senzillesa, aquest model permet estimar satisfactòriament les propietats d'electrons i forats amb una exigència computacional raonable. Adicionalment, el mètode k·p permet estudiar amb relativa facilitat camps magnètics i elèctrics aplicats externament, la interacció espín-òrbita, les forces de tensió i deformació, i també la piezoelectricitat, que són els fenòmens analitzats en aquesta Tesi. Pel que fa als dos factors enumerats en darrer lloc, els camps que aquests originen i que després entren en els Hamiltonians, es calculen utilitzant la teoria contínua de l'elasticitat.

La metodologia emprada consisteix en la modelització teòrica de les propietats de les nanoestructures mitjançant el desenvolupament de codis computacionals fent ús dels programes FORTRAN i MATLAB. Per a la integració numèrica dels Hamiltonians utilitzem els mètodes de diferències finites o elements finits. Adicionalment, també s'ha usat el programari comercial *Comsol Multiphysics* en alguns treballs, específicament en aquells que investiguen les forces de tensió i la piezoelectricitat.

En primer lloc, estudiem els efectes resultants de l'aplicació de camps magnètics externs en dos sistemes diferents. D'una banda, explorem l'estructura electrònica de la banda de valència de punts quàntics de GaN/AlN amb estructura cristal·lina zinc-blenda. Aquests materials tenen la banda de *split-off* (so) molt pròxima a les de forat pesat (hh) i lleuger (lh), de forma que és d'esperar que hi haja una interacció no rebutjable de les bandes esmentades, fet pel qual esdevé necessari l'ús d'un model de sis bandes. Com els punts considerats presenten simetria axial i els paràmetres màssics dels dos materials són prou diferents, construïm un Hamiltonià de massa variable en coordenades cilíndriques, de manera que el problema es redueix de tres a dues dimensions. Els resultats obtinguts ens indiquen que la puresa de espín de punts quàntics de GaN/AlN de dimensions típiques és extraordinàriament gran. Fins i tot major que la de punts quàntics de InGaAs/GaAs. Resultat aquest sorprenent atesa la massa efectiva més gran del GaN que origina una major densitats d'estats i la menor interacció espín-òrbita que implica una major proximitat de la banda de *split-off*. La justificació la trobem en el valor petit del paràmetre de mescla $\tilde{\gamma}$ que apareix en els termes extradiagonals de l'Hamiltonià. Un segon resultat remarcable és la possibilitat de creuament entre un estat fonamental hh i un excitat lh quan la proporció alçada/diàmetre és aproximadament la unitat, creuament originat per l'acció d'un camp magnètic extern axialment aplicat. Aquest fet significa que és possible controlar magnèticament les propietats òptiques, com ara la polarització d'emissió excitònica.

Tot seguit, analitzem el paper d'un camp magnètic axialment aplicat en anells quàntics de forma hexagonal poblats amb un nombre reduït d'electrons. És ben conegut que l'acció d'un camp magnètic aplicat axialment sobre un sistema anular origina l'anomenat efecte Aharonov-Bohm. Aquest efecte, que és conseqüència de la topologia doblement connexa del sistema, dóna lloc a un espectre energètic que es repeteix periòdicament amb el flux magnètic. Aquest fenòmen ha sigut àmpliament estudiat en anells amb simetria circular però les conseqüències d'una reducció de simetria han estat poc o gens explorades. Realitzem una sèrie de càlculs canviant el nombre d'electrons que poblen l'anell des d'un fins a set i analitzem la forma dels espectres d'energia. El resultat més llamatiu és la completa supressió de les oscil·lacions típiques associades a l'efecte Aharonov-Bohm en el cas del sistema poblat amb sis electrons. Aquest fet és conseqüència directa de la simetria hexagonal dels anells i s'ha comprovat que només pot ocórrer en el cas de sis electrons, i sempre que el sistema estiga en un règim de baixa densitat electrònica. Estudiem també la influència d'un camp magnètic axial en nanofils hexagonals multi-capa, la secció dels quals origina un pou de potencial en forma d'anell hexagonal. Els resultats mostren senyals característiques de la simetria hexagonal, així com un patró típic d'oscil·lacions d'Aharonov-Bohm. A camps febles aquestes oscil·lacions poden desaparèixer o ressorgir en funció de la intensitat dels camps aplicats, independentment de la configuració dels electròdes en el dispositiu. Aquests resultats permeten entendre les observacions experimentals de treballs recents on es realitzen experiments de magneto-conductància en nanofils similars. Quan els camps són més forts sorgeixen diverses transicions en l'espectre d'energia que són induïdes pel camp magnètic. El seu origen són tant els canvis en la distribució electrònica com el buidatge o despoblament electrònic de bandes excitades. Des d'un punt de vista experimental, aquestes transicions haurien d'observar-se en mesures de magneto-conductància com a corbes amb forma d'escaló.

Realitzem un segon estudi on la topologia juga un paper clau: l'existència o no d'estats localitzats en la frontera física del sistema, amb energies situades en la zona prohibida (*band gap*), en el cas de nanocintes i punts quàntics fabricats a partir de monocapes de MoS_2. Aquest material pertany a la familia dels dicalcogenurs de metalls de transició i en la seua forma purament bidimensional es comporta com un semiconductor de *gap* directe. En el cas de les nanocintes mostrem que aquestes estructures finites efectivament presenten estats espacialment localitzats a les vores o frontera física del sistema amb energies situades dintre de la banda prohibida. L'origen d'aquests estats localitzats s'ha pogut relacionar amb el caràcter topològic marginal de l'Hamiltonià del MoS_2. Aquesta topologia està directament determinada per la curvatura de les bandes de conducció i valència. Pel que fa a punts quàntics, el comportament observat és qualitativament el mateix però ara les bandes dels estats de vora es troben quantitzades, de forma que hi ha un nombre discret d'estats a la banda prohibida.

Investiguem també els processos de relaxació d'espín en punts quàntics. En particular, tenim en compte transicions entre els subnivells d'espín contrari en què es desdobla l'estat fonamental per l'acció de l'efecte Zeeman en presència d'un camp magnètic. Com la separació energètica entre els estats implicats és d'uns pocs meV, el principal mecanisme de relaxació és la interacció amb fonons acústics. Adicionalment, per a que la relaxació tinga lloc fa falta una font de mescla d'espín que permeta la transició. En els sistemes abordats ací, aquesta mescla ve originada per la interacció espín-òrbita. Tradicionalment, els treballs que han estudiat els efectes de la interacció espín-òrbita en la literatura han considerat models bidimensionals, els quals descriuen correctament punts quàntics electrostàtics. Tanmateix, en punts auto-ordenats i nanocristalls l'alçada de les estructures pot arribar a ser important i, per tant, s'espera que aquests models simplificats comencen a fallar. Per aquest motiu, nosaltres estudiem l'efecte de la tridimensionalitat en la relaxació d'espín, prestant especial atenció a la seua anisotropia. Primer, examinem com afecta la forma del confinament espacial a la relaxació d'espín fent ús d'un model de punts quàntics de forma esferoïdal. Trobem, tant en la banda de conducció com en la de valència, que la tridimensionalitat dels punts és rellevant, evidenciant que els models bidimensionals utilitzats fins ara no són suficient per estudiar aquests sistemes de forma rigorosa. A més, observem una gran anisotropia en la relaxació quan es canvia la forma dels punts com a conseqüència de la gran influència de la simetria del sistema en els Hamiltonians d'espín-òrbita, fet que determina el grau de mescla d'espín i, per tant, l'eficiència dels mecanismes de relaxació. Tot seguit, passem a explorar punts quàntics més realistes on la tridimensionalitat és a priori important, com per exemple punts quàntics piramidals o molècules de dos punts quàntics acoblats verticalment. En aquests casos observem també una gran anisotropia de la relaxació d'espín quan es rota l'orientació de camps aplicats externament, evidenciant que és possible maximitzar o minimitzar els processos de relaxació orientant els camps en la direcció adequada. Aquest comportament anisotropic és, en general, robust davant de canvis en la geometria i en la orientació cristal·logràfica dels sistemes considerats. En particular, observem que, en molècules de punts quàntics, el temps de vida mitjana és màxim quan la funció d'ona forma estats moleculars homonuclears, però es redueix ràpidament en presència de qualsevol factor que minve la seua simetria.

Seguidament analitzem els efectes que té el medi que envolta als punts quàntics sobre les seues propietats. En concret, ens centrem en les forces de tensió i la piezoelectricitat que s'originen en la diferència entre les constants de xarxa del material del punt i el de la matriu que l'envolta. Incloem també la polarització espontània quan és rellevant. Simulem el comportament d'electrons i forats formant excitons en dos sistemes amb estructura crital·lina diferent. Per un costat, en nanocristalls esfèrics de CdSe/CdS amb estructura wurtzita amb cor i capa exterior grans[2] (*dot-in-dot*) sorgeixen forts camps piezoelèctrics dipolars en la direcció de creixement, mentre que la polarització espontània és menyspreable. Aquests forts camps de polarització produeixen una clara separació d'electrons i forats malgrat el potencial atractiu de Coulomb que actua en sentit contrari. La separació de les dues partícules origina que el solapament de les funcions d'ona siga feble i, per tant, els temps de vida mitjana de l'excitó llargs. Es troben resultats semblants quan estudiem altres geometries sempre que tant cor com capa externa siguen el suficientment grans. Les diverses estructures considerades s'obtenen elongant el cor, la capa exterior o tots dos al mateix temps, de manera que representen de forma aproximada sistemes anomenats en anglès *dot-in-rod*, *dot-in-plate* i *rod-in-rod*. Cal destacar que per obtenir excitons amb temps de vida mitjana llargs, cal que la capa exterior siga gran en la direcció axial, tal com podem esperar, però sorprenentment cal que siga també gran en la direcció lateral, ja que aquesta capa afecta a la magnitud global de les forces de tensió. Explorem també el paper d'aquests efectes en punts quàntics politípics de GaAs. Aquestes estructures estan formades per segments amb estructura crital·lina zinc-blenda en la direcció [111] que s'alternen amb altres que presenten estructura wurtzita [0001]. Degut a la gran similitud d'ambdues estructures cristal·lines i al fet d'estar formades pel mateix material, les forces de tensió i la piezoelectricitat són rebutjables. En canvi, la polarització espontània s'espera que siga molt important ja que en les interfases es passa d'una regió on la polarització espontània és zero a una altra on no ho és, cosa que pot originar forts camps de polarització en la direcció de creixement. En estudiar aquest fenòmen comprovem que efectivament la polarització espontània no és menyspreable i afecta notablement al comportament dels excitons. D'una banda, l'energia de l'excitó és molt sensible a canvis en les dimensions dels punts quàntics. D'altra banda, controlant el confinament lateral es pot induir una transició gradual entre excitons directes i indirectes, fet que influeix en gran mesura a la separació d'electrons i forats i, per extensió, a les propietats òptiques dels punts politípics.

[2] Utilitzem "cor" i "capa exterior" per referir-nos a *core* i *external shell*.

Tots els continguts presentats en la present Tesi doctoral es basen en els onze articles d'investigació en què l'autor ha particitat durant els darrers quatre anys. Tots ells estan publicats en revistes especialitzades de reconegut prestigi internacional. Una còpia d'aquests es recull al final d'aquesta memòria.

1. C. Segarra, J. I. Climente, and J. Planelles, *Valence band mixing of cubic GaN/AlN quantum dots*, J. Phys.: Condens. Matter **24**, 115801 (2012)
2. J. Planelles, J. I. Climente, and C. Segarra, *Electron spin relaxation in 3D quantum dots: geometrical suppression of Dresselhaus and Rashba spin-orbit interaction*, J. Phys. Chem. C **116**, 25143 (2012)
3. J. I. Climente, C. Segarra, and J. Planelles, *Spin-orbit-induced hole spin relaxation in InAs and GaAs quantum dots*, New J. Phys. **15**, 093009 (2013)
4. A. Ballester, C. Segarra, A. Bertoni, and J. Planelles, *Suppression of the Aharonov-Bohm effect in hexagonal quantum rings*, EPL **104**, 67004 (2013)
5. M. Royo, C. Segarra, A. Bertoni, G. Goldoni, and J. Planelles, *Aharonov-Bohm oscillations and electron gas transitions in hexagonal core-shell nanowires with an axial magnetic field*, Phys. Rev. B **91**, 115440 (2015)
6. C. Segarra, J. Planelles, and J. I. Climente, *Control of electron spin-orbit anisotropy in pyramidal InAs quantum dots*, Physica E **66**, 234 (2015)
7. C. Segarra, J. Planelles, J. I. Climente, and F. Rajadell, *Anisotropy of spin-orbit induced electron spin relaxation in [001] and [111] grown GaAs quantum dots*, New J. Phys. **17**, 033014 (2015)
8. C. Segarra, J. I. Climente, F. Rajadell, and J. Planelles, *Hole spin relaxation in InAs/GaAs quantum dot molecules*, J. Phys.: Condens. Matter **27**, 415301 (2015)
9. C. Segarra, J. Planelles, and S. E. Ulloa, *Edge states in dichalcogenide nanoribbons and triangular quantum dots*, Phys. Rev. B **93**, 085312 (2016)
10. J. I. Climente, C. Segarra, F. Rajadell, and J. Planelles, *Electrons, holes, and excitons in GaAs polytype quantum dots*, J. Appl. Phys. **119**, 125705 (2016)
11. C. Segarra, J. I. Climente, A. Polovitsyn, F. Rajadell, I. Moreels, and J. Planelles, *Piezoelectric control of the exciton wave function in colloidal CdSe/CdS nanocrystals*, J. Phys. Chem. Lett. **7**, 2182 (2016)

Publications

IOP Publishing — Journal of Physics: Condensed Matter

J. Phys.: Condens. Matter **24** (2012) 115801 (8pp) doi:10.1088/0953-8984/24/11/115801

Valence band mixing of cubic GaN/AlN quantum dots

C Segarra, J I Climente and J Planelles

Departament de Química Física i Analítica, Universitat Jaume I, E-12080 Castelló, Spain

E-mail: climente@uji.es

Received 6 December 2011, in final form 30 January 2012
Published 21 February 2012
Online at stacks.iop.org/JPhysCM/24/115801

Abstract
We study the spin purity of the hole ground state in nearly axially symmetric GaN/AlN quantum dots (QDs). To this end, we develop a six-band Burt–Foreman Hamiltonian describing the valence band structure of zinc blende nanostructures with cylindrical symmetry and calculate the effects of eccentricity variationally. We show that the aspect ratio is a key factor for spin purity. In typical QDs with small aspect ratio the ground state is essentially a heavy hole (HH) whose spin purity is even higher than that of InGaAs QDs of similar sizes. When the aspect ratio increases, mixing with light-hole (LH) and split-off (SO) subbands becomes important and, additionally, the ground state becomes sensitive to QD anisotropy, which further enhances the mixing. We finally show that, despite the large GaN hole effective mass, an efficient magnetic modulation is feasible in QDs with aspect ratio $\sim$1, which can be used to modify the ground state symmetry and hence the optical spectrum properties.

(Some figures may appear in colour only in the online journal)

1. Introduction

GaN/AlN QDs are nanostructures of current interest for optoelectronic applications owing to their emission in the UV spectrum and their efficient optical activity up to room temperature [1]. The former property follows from the wide bandgap of GaN (3.4 eV), while the latter follows from the low dielectric constants, large effective masses and band offsets, which enable the unprecedented strength of exciton confinement. The wide bandgap is also responsible for weak spin–orbit interactions [2], which should translate into long exciton spin relaxation lifetimes. This is of interest for spintronic applications.

GaN QDs can be grown in hexagonal (wurtzite) or cubic (zinc blende) crystallographic phases [1, 3, 4]. Wurtzite QDs are characterized by the presence of strong built-in electric fields (of the order of MV cm^{-1}) due to spontaneous and piezoelectric polarization [1, 5]. This constitutes a critical factor in determining the optical response of the QDs [6, 5, 7], as well as the exciton spin lifetime, which turns out to be rather short—of the order of 200 ps at room temperature [8]. Built-in electric fields are, however, missing in GaN/AlN QDs with zinc blende structure [6]. Lagarde *et al* showed that, as a consequence, the optical orientation in cubic structures is robust even at room temperature, with exciton spin lifetimes exceeding 10 ns [9].

These results hold promise for both optoelectronic and spintronic applications of cubic GaN/AlN QDs and have triggered an increasing number of works investigating their properties [2, 10–13]. An important aspect to understand such properties is the valence band mixing, which is known to underlie the optical polarization [13, 14] and the exciton spin dynamics [13, 15, 16]. The valence band structure of GaN is complicated because the spin–orbit splitting is only 17 meV [17]. As a consequence, light-hole (LH) and split-off (SO) subbands may couple strongly and come close to the heavy-hole (HH) subband in the Brillouin zone center, as noted in GaN/AlN superlattices [18]. The situation could, however, be different in QDs because HH, LH and SO have different effective masses and hence feel quantum confinement differently [13]. Indeed, the long spin lifetimes observed by Lagarde *et al* suggest a ground state with weak valence band mixing. Understanding the relationship between QD confinement and valence band mixing is then desirable.

In this work we investigate how the size and shape of cubic GaN/AlN QDs influence the valence band admixture of the hole ground state. The QDs are assumed to be grown along the [001] axis [3, 4]. Because holes have strongly anisotropic masses, we find that flat QDs—where vertical confinement dominates over the lateral one—favor HH character and high spin purity. As a matter of fact, the spin purity is higher than that of more conventional materials such as InGaAs, which supports the suitability of these structures for optical spin storage. In contrast, high QDs with strong lateral confinement imply dominant LH character. When vertical and lateral confinements are comparable HH and LH states are close in energy. Then, the admixture becomes significant and very sensitive to in-plane anisotropy, as noted in recent experiments. In this case, we show that the different Zeeman splitting of states with dominant HH and LH components can be used to induce ground state transitions. This enables efficient magnetic manipulation of the optical spectrum in spite of the large effective mass of GaN.

2. Theory

An accurate description of holes in GaN/AlN QDs can be obtained using six-band k · p Hamiltonians including HH, LH and SO subbands [19]. This requires spanning the Hamiltonian on the basis of periodic Bloch functions $|J, J_z\rangle$:

$$\left|\frac{3}{2},+\frac{3}{2}\right\rangle = \frac{1}{\sqrt{2}}\,|(X+\mathrm{i}Y)\uparrow\rangle = |hh_+\rangle,$$
$$\left|\frac{3}{2},+\frac{1}{2}\right\rangle = \frac{1}{\sqrt{6}}\,|(X+\mathrm{i}Y)\downarrow\rangle - \sqrt{\frac{2}{3}}\,|Z\uparrow\rangle = |lh_+\rangle,$$
$$\left|\frac{3}{2},-\frac{1}{2}\right\rangle = -\frac{1}{\sqrt{6}}\,|(X-\mathrm{i}Y)\uparrow\rangle - \sqrt{\frac{2}{3}}\,|Z\downarrow\rangle = |lh_-\rangle,$$
$$\left|\frac{3}{2},-\frac{3}{2}\right\rangle = \frac{1}{\sqrt{2}}\,|(X-\mathrm{i}Y)\downarrow\rangle = |hh_-\rangle,$$
$$\left|\frac{1}{2},+\frac{1}{2}\right\rangle = \frac{1}{\sqrt{3}}\,|(X+\mathrm{i}Y)\downarrow\rangle + \sqrt{\frac{1}{3}}\,|Z\uparrow\rangle = |so_+\rangle,$$
$$\left|\frac{1}{2},-\frac{1}{2}\right\rangle = -\frac{1}{\sqrt{3}}\,|(X-\mathrm{i}Y)\uparrow\rangle + \sqrt{\frac{1}{3}}\,|Z\downarrow\rangle = |so_-\rangle.$$

The $|3/2, \pm 3/2\rangle$ components correspond to HH, the $|3/2, \pm 1/2\rangle$ to LH and the $|1/2, \pm 1/2\rangle$ to SO. One can see from the explicit $|J, J_z\rangle$ functions above that HH components have pure spin, while LH and SO components contain a spin admixture.

Since the Luttinger parameters of GaN and AlN are quite different, it is convenient to employ position-dependent effective mass parameters. Then, instead of the classical Luttinger Hamiltonian [20] one must use the Burt–Foreman one [21, 22]. A detailed description of this Hamiltonian can be found in [23], where the due expression in Cartesian coordinates is given[1]. For circular QDs it is, however, convenient to use cylindrical coordinates instead. We then convert the coordinate system from Cartesian to cylindrical. Additionally, we include a magnetic field along [001] by following the prescription of [24] i.e. by introducing the magnetic terms in the k · p Hamiltonian prior to applying the envelope function approximation. Note that this is in contrast to the traditional Luttinger formulation for bulk semiconductors and the usual formulations for nanostructures which implement the magnetic field after the envelope function approximation [25]. For multi-band studies of nanostructures, our formulation provides a more reliable description of the magnetic field [26, 27].

The resulting Hamiltonian is one of the important results of this work. It is a 6 × 6 matrix, $\mathcal{H}_6$, whose elements are given in the appendix. The QD is modeled as a quantum disc of radius R and height H. Since the disc has axial symmetry, the angular coordinate is integrated analytically. Then, within the axial approximation of the k·p Hamiltonian [28], the states can be labeled by their total angular momentum $F_z = m_z + J_z$, which is the sum of the envelope angular momentum m_z and the Bloch angular momentum J_z. The eigenfunctions of $\mathcal{H}_6$ are then six-component spinorial objects of the form

$$|F_z, n\rangle = \begin{pmatrix} f^{(1)}_{F_z-3/2}(\rho, z)\ |hh_+\rangle \\ f^{(2)}_{F_z-1/2}(\rho, z)\ |lh_+\rangle \\ f^{(3)}_{F_z+1/2}(\rho, z)\ |lh_-\rangle \\ f^{(4)}_{F_z+3/2}(\rho, z)\ |hh_-\rangle \\ f^{(5)}_{F_z-1/2}(\rho, z)\ |so_+\rangle \\ f^{(6)}_{F_z+1/2}(\rho, z)\ |so_-\rangle \end{pmatrix} \qquad (1)$$

where $n = 1, 2, 3, \ldots$ is the main quantum number and $f^{(i)}_{m_z}(\rho, z)$ is the envelope function of the ith component. For calculations in this work we use GaN and AlN material parameters [17]. The confining potential is zero inside the QD and V_0 outside, where $V_0 = 0.5$ eV is the valence band offset between GaN and AlN [29]. For InGaAs/GaAs QDs, which we also study for comparison, we take $In_{0.53}Ga_{0.47}As$ and GaAs parameters, with $V_0 = 0.4$ eV [17]. For simplicity, strain is disregarded. This leads to slightly overestimated subband mixing, but the trends we report should not be affected. The Hamiltonian is integrated with a finite differences scheme.

3. Results and discussion

In this section we investigate the composition of the hole ground state as a function of the QD geometry and external fields. The composition is given in terms of the weight of each component within the spinor (1). For example, the weight of the $|hh_+\rangle$ component is

$$c_{hh_+} = \frac{\langle f^{(1)}|f^{(1)}\rangle}{\sum_i \langle f^{(i)}|f^{(i)}\rangle}. \qquad (2)$$

3.1. Effect of the aspect ratio

Our starting point is a GaN QD with typical dimensions, radius $R = 6$ nm and height $H = 1.5$ nm [3, 9]. The

[1] Please note that table 12.4 in [23], where the information is included, contains a few typos. Thus, the Hamiltonian element (5, 4) must be $+\sqrt{2}R$ instead of $-\sqrt{2}R$, and the Hamiltonian element (6, 3) should be $-\sqrt{2}Q^*$ instead of $-\sqrt{2}Q$. Finally, in the definitions of Q, the third term in the sum reading $+2k_z(L-M)k_z$ must be $-2k_z(L-M)k_z$.

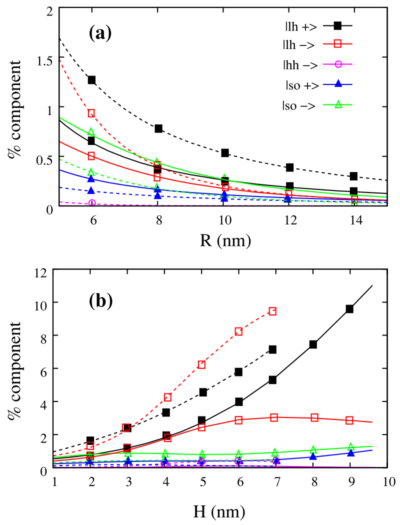

Figure 1. Minor components of the hole ground state in GaN/AlN QDs (solid lines) and InGaAs/GaAs QDs (dashed lines).
(a) Variable radius and fixed height $H = 1.5$ nm. (b) Variable height and fixed radius $R = 6$ nm.

ground state has $F_z = 3/2$ symmetry, with a largely dominant $|hh_+\rangle$ component[2]. Yet, the minor components are important in determining the optical polarization and the hole spin dynamics [13]. Thus, in figure 1(a) we analyze how the minor components vary with the QD radius (solid lines). For comparison, we also show the minor components in the better-known case of InGaAs/GaAs QDs (dashed lines), which is taken as a reference. One can see that in both GaN and InGaAs QDs the weight of the minor components decreases with R.

This result can be understood from the anisotropic effective masses of holes, which are summarized in table 1. In the QDs of figure 1(a), the vertical confinement is much stronger than the lateral one. If we disregard lateral confinement completely and pay attention to the effective masses along z ([001] axis) only, we can see that $m^z_{hh} > m^z_{lh} \sim m_{so}$. Thus, the kinetic energy of LH and SO states will be large and the coupling with HH weak. The smaller the aspect ratio (H/2R), the closer we are to this limit.

In figure 1(b) we plot the variation of the minor components with the QD height. Here the behavior is the opposite. As H increases the vertical confinement becomes weaker. Then, the lateral confinement becomes more relevant and the ground state gains LH character because $m^\perp_{lh} > m^\perp_{hh}$. As a result, the $|lh_+\rangle$ component weight may now exceed 10% for large H. As a matter of fact, when H is large enough the ground state symmetry changes from $F_z = \pm 3/2$ (dominant HH component) to $F_z = \pm 1/2$ (dominant LH component). This translates into a sharp enhancement of the

[2] The analysis is analogous for the Kramers-degenerate $Fz = -3/2$ state.

Table 1. Effective masses of HH, LH and SO (times m_0).

	m^z_{hh}	m^z_{lh}	$m^\perp_{hh}$	$m^\perp_{lh}$	m_{so}
GaN	0.85	0.24	0.29	0.52	0.37
InGaAs	0.38	0.05	0.07	0.15	0.09

LH character, which can be used to emit strongly linearly polarized light [30–32]. For InGaAs QDs the transition occurs at $H = 7$ nm (aspect ratio $\sim$0.6), while for GaN QDs it occurs at $H = 9.7$ nm (aspect ratio $\sim$0.8). For clarity of presentation, in figure 1 we have truncated the lines at the position of the transitions. State-of-the-art cubic GaN QDs are grown by self-assembly techniques and have small aspect ratio. Yet, the results in figure 1(b) stress the interest of potential developments in the synthesis of elongated QDs.

Figure 1 reveals that the valence band mixing of the ground state in GaN QDs is weaker than that in InGaAs QDs with equal sizes. This implies high spin purity, which is consistent with the long spin lifetimes observed by Lagarde *et al* [9]. The result is, however, surprising because the effective masses in GaN are much heavier than in InGaAs, so that the density of states is larger and one could expect stronger mixing. Also, the LH–SO coupling could, in principle, bring these subbands close to the HH one, as in higher-dimensional structures [18]. The underlying reason for the high purity of the ground state is twofold. First, the inter-subband coupling terms are weaker than those of InGaAs. For example, many coupling terms are proportional to $\tilde{\gamma}$ (see $\mathcal{H}_6$ terms in the appendix). For GaN $\tilde{\gamma} = 0.925$, which is about five times smaller than that of InGaAs, $\tilde{\gamma} = 4.51$. Second, according to equation (1), the spinor of the $F_z = 3/2$ ground state is

$$|3/2, 1\rangle = \begin{pmatrix} f_0^{(1)}(\rho, z)\ |hh_+\rangle \\ f_1^{(2)}(\rho, z)\ |lh_+\rangle \\ f_2^{(3)}(\rho, z)\ |lh_-\rangle \\ f_3^{(4)}(\rho, z)\ |hh_-\rangle \\ f_1^{(5)}(\rho, z)\ |so_+\rangle \\ f_2^{(6)}(\rho, z)\ |so_-\rangle \end{pmatrix}. \qquad (3)$$

Note that only the dominant $|hh_+\rangle$ component has envelope angular momentum $m_z = 0$. Other components have finite m_z and are then pushed high in energy by the lateral confinement. We stress that this makes valence band mixing in GaN QDs much weaker than in quantum wells [18].

3.2. Magnetic field modulation

The large effective mass of GaN hinders the use of magnetic fields to manipulate the electronic structure of typical QDs (aspect ratio $\sim$1/8). To circumvent this problem, consider a GaN QD with aspect ratio close to 1. In this case the kinetic energy of HH and LH is similar. As a consequence, spinors with dominant HH and LH character are close in energy and moderate Zeeman splittings suffice to modify the electronic structure. This opens the possibility of magnetic modulation in GaN QDs.

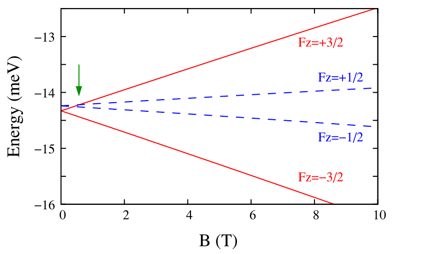

Figure 2. Magnetic field splitting of the lowest hole levels in a GaN/AlN QD with aspect ratio ∼1. The arrow points to the ground state transition at $B = 0.6$ T. Zero energy is the top of the valence band.

To illustrate this point, in figure 2 we show the energy structure of a QD with $R = 6$ nm and $H = 10$ nm. At zero magnetic field, the ground state is $|1/2, 1\rangle$ and the first excited one is $|3/2, 1\rangle$. The dominant components of these spinors are $|lh_+\rangle$ and $|hh_+\rangle$, respectively (i.e. the components with $m_z = 0$). The corresponding linear-in-B coefficients are $(\gamma_1 + \gamma_2)/2$ for $|hh_+\rangle$ and $(\gamma_1 - \gamma_2)/6$ for $|lh_+\rangle$—see $\mathcal{H}_6$ in the appendix. Thus, the orbital Zeeman splitting of $|3/2, 1\rangle$ is larger than that of $|1/2, 1\rangle$. As a result, with increasing B the ground state changes from $F_z = 1/2$ to $3/2$ (see the arrow in figure 2). Because $|3/2\rangle$ and $|1/2\rangle$ yield different optical polarizations, this can be used to modify the optical response of QDs at will.

3.3. Effect of QD anisotropy

The presence of anisotropy in QDs is often considered to be a source of HH–LH coupling, with due consequences on the optical polarization [33–35] and hole spin mixing [36]. To see how this affects GaN QDs, next we study how the ground state composition is influenced by an elongation of the QD.

We consider three reference geometries: a QD with typical dimensions $R = 6$ nm and $H = 1.5$ nm (QD1); a QD with large aspect ratio—similar to that of InAs QDs, $R = 15$ nm and $H = 1.5$ nm (QD2); a QD with aspect ratio ∼1, $R = 6$ nm and $H = 10$ nm (QD3). We start from circular QDs and let the eccentricity ε increase while keeping the basis area constant. The semi-major (semi-minor) axis R_a (R_b) of the elliptical QD is then

$$R_a = R/\left(1 - \varepsilon^2\right)^{1/4}, \tag{4}$$

$$R_b = R^2/R_a. \tag{5}$$

Note from the above expressions that, for small QD radius R, large eccentricities are required to provide significant anisotropy R_a/R_b. The hole states are calculated with a variational procedure, projecting the 3D anisotropic potential on a basis of circular QD eigenstates, as described in [36]. For simplicity, in this section the GaN effective mass in used all over the structure.

Figure 3 shows the composition of the ground state in each QD. In QD1 the dominant component is by far $|hh_+\rangle$, with the eccentricity having little effect up to $\varepsilon \sim 0.6$. At this point the semi-minor axis starts imposing a strong lateral confinement and the valence band mixing rapidly increases. For $\varepsilon \sim 0.8$ ($R_b = 4.6$ nm) the weight of $|hh_+\rangle$ has already decreased from 97% to 86%. Noteworthily, the largest of the minor components is not a LH but a SO instead—LHs are unfavored by the strong vertical confinement. In QD2 the dot radius is much larger. As a result, lateral confinement is weak even for strong eccentricities and the ground state composition is barely affected by the anisotropy. In QD3 the vertical confinement is weak, so the ground state is $|F_z = 1/2, n = 1\rangle$ with a dominant $|lh_+\rangle$ component. In this case, even small anisotropies induce severe HH–LH mixing.

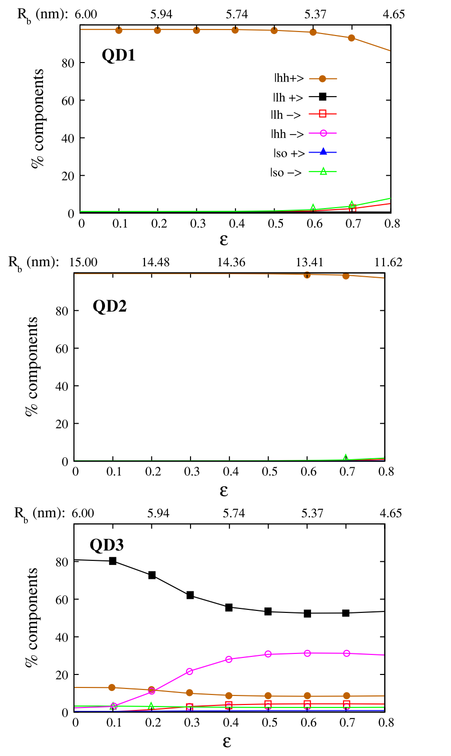

Figure 3. Components of the hole ground state as a function of the eccentricity in a typical QD (QD1), a QD with small (QD2) and large (QD3) aspect ratio. The upper axis indicates the length of the semi-minor axis.

Comparing QD1, QD2 and QD3 we conclude that the influence of elongations on the valence band mixing depends on the aspect ratio. When the aspect ratio is small (QD2) the influence is negligible, while when it is large (QD3) the influence becomes dramatic. This result is consistent with recent experiments in GaAs QDs, where severe HH–LH mixing was ascribed to dot elongations [35]. Such QDs turn out to have comparable lateral and vertical dimensions [37]. Typical cubic GaN/AlN QDs (QD1) have aspect ratio ∼1/8.

Owing to the dense energy spectrum this is enough to be sensitive to moderate anisotropies.

4. Conclusions

We have derived a six-band Burt–Foreman Hamiltonian in cylindrical coordinates for zinc blende nanostructures grown along the [001] axis. The Hamiltonian properly includes position-dependent Luttinger parameters and axial magnetic fields.

Using this Hamiltonian we have shown that HH mixing with LH and SO subbands in typical GaN/AlN QDs is weak provided the dot has good circular symmetry. Indeed, the mixing is weaker than that in GaAs/AlAs quantum wells or InAs/GaAs QDs of similar sizes. This makes the system suited for optical manipulation and storage of spins. Elongations of the QD do, however, introduce significant HH–SO and HH–LH mixing. The band mixing and the sensitivity to QD anisotropy can be enhanced (reduced) by growing QDs with small (large) aspect ratio.

We have also shown that in GaN QDs with large aspect ratio the small energy splitting between states with dominant HH and LH components, along with their different Zeeman splittings, can be used to switch the ground state symmetry with external magnetic fields. This is in spite of the large effective masses of GaN and allows us to modify the optical emission characteristics (energy, polarization, intensity).

Acknowledgments

We thank T Amand for useful discussions. Support from MICINN projects CTQ2008-03344 and CTQ2011-27324, UJI-Bancaixa project P1-1A2009-03 and the Ramon y Cajal program (JIC) is acknowledged.

Appendix . Six-band k · p Hamiltonian

In this appendix we provide the elements of the Burt–Foreman six-band Hamiltonian in cylindrical coordinates. An external magnetic field B along the growth axis is included following [24].

To describe the uniform axial magnetic field, a potential vector in the symmetric gauge $A = [-y, x, 0]B/2$ is considered. The presence of this potential vector turns the in-plane part of the kinetic energy operator from $p_\perp \frac{1}{2m_\perp} p_\perp$ into $(p_\perp - qA_\perp)\frac{1}{2m_\perp}(p_\perp - qA_\perp)$, where the charge $q = 1$ au for holes. In the presence of axial symmetry $m_\perp = m_\perp(\rho, z)$ and we have

$$\begin{aligned}\mathcal{H}(B) &= \mathcal{H}_0 - \frac{A_\perp}{m_\perp} p_\perp + \frac{A_\perp^2}{2m_\perp}\\ &= \mathcal{H}_0 + \frac{B}{2m_\perp} L_z + \frac{B^2\rho^2}{8m_\perp}\end{aligned} \tag{A.1}$$

where $\mathcal{H}_0$ is the Hamiltonian in the absence of a magnetic field. Now, we follow the procedure in [24, 27] to obtain the magnetic field contribution to the different matrix elements of the Burt–Foreman Hamiltonian. For example, the magnetic contribution to the (1, 1) matrix element is $\frac{1}{m_\perp}[\frac{F_z-1/2}{2}B + \frac{B^2\rho^2}{8}]$, with $m_\perp^{-1} = -(\gamma_1 + \gamma_2)$ being the mass factor corresponding to the $|\frac{3}{2}, \frac{3}{2}\rangle$ heavy-hole state.

As a result, the position-dependent six-band Hamiltonian, including an axial uniform magnetic field, in cylindrical coordinates is as follows:

$$\mathcal{H}_6 = \tfrac{1}{2}\mathcal{M} + V(\rho, z)\mathcal{I}, \tag{A.2}$$

where atomic units are used ($\hbar = q = m_0 = 1$), with m_0 as the free electron mass. $V(\rho, z)$ is the confining potential, $\mathcal{I}$ is the identity matrix and $\mathcal{M}$ is a rank-6 matrix with the following elements:

$$\begin{aligned}\mathcal{M}[1,1] &= \frac{\partial}{\partial\rho}(\gamma_1+\gamma_2)\frac{\partial}{\partial\rho} + \frac{(\gamma_1+\gamma_2)}{\rho}\frac{\partial}{\partial\rho}\\ &\quad + \frac{\partial}{\partial z}(\gamma_1 - 2\gamma_2)\frac{\partial}{\partial z} - \frac{(F_z-\frac{3}{2})^2}{\rho^2}(\gamma_1+\gamma_2)\\ &\quad + \frac{(F_z-\frac{3}{2})}{2\rho}\left[\frac{\partial}{\partial\rho}(C_1+C_2) - (C_1+C_2)\frac{\partial}{\partial\rho}\right]\\ &\quad - 2(\gamma_1+\gamma_2)\left[\frac{(F_z-\frac{1}{2})B}{2} + \frac{B^2\rho^2}{8}\right],\end{aligned}$$

$$\begin{aligned}\mathcal{M}[1,2] &= \frac{1}{\sqrt{3}}\left\{\frac{\partial}{\partial\rho}C_1\frac{\partial}{\partial z} - \frac{\partial}{\partial z}C_2\frac{\partial}{\partial\rho}\right.\\ &\quad \left. + \frac{(F_z-\frac{1}{2})}{\rho}\left[C_1\frac{\partial}{\partial z} - \frac{\partial}{\partial z}C_2\right]\right\},\end{aligned}$$

$$\begin{aligned}\mathcal{M}[1,3] &= -\sqrt{3}\left\{\frac{\partial}{\partial\rho}\tilde{\gamma}\frac{\partial}{\partial\rho} + \frac{(F_z+\frac{1}{2})}{\rho}\frac{\partial}{\partial\rho}\tilde{\gamma}\right.\\ &\quad \left. + \frac{(F_z-\frac{1}{2})}{\rho}\tilde{\gamma}\frac{\partial}{\partial\rho} + \frac{(F_z-\frac{3}{2})(F_z+\frac{1}{2})}{\rho^2}\tilde{\gamma}\right\},\end{aligned}$$

$$\mathcal{M}[1,4] = 0,$$

$$\begin{aligned}\mathcal{M}[1,5] &= -\frac{1}{\sqrt{6}}\left\{\frac{\partial}{\partial\rho}C_1\frac{\partial}{\partial z} - \frac{\partial}{\partial z}C_2\frac{\partial}{\partial\rho}\right.\\ &\quad \left. + \frac{(F_z-\frac{1}{2})}{\rho}\left[C_1\frac{\partial}{\partial z} - \frac{\partial}{\partial z}C_2\right]\right\},\end{aligned}$$

$$\begin{aligned}\mathcal{M}[1,6] &= -\sqrt{6}\left\{\frac{\partial}{\partial\rho}\tilde{\gamma}\frac{\partial}{\partial\rho} + \frac{(F_z+\frac{1}{2})}{\rho}\frac{\partial}{\partial\rho}\tilde{\gamma}\right.\\ &\quad \left. + \frac{(F_z-\frac{1}{2})}{\rho}\tilde{\gamma}\frac{\partial}{\partial\rho} + \frac{(F_z-\frac{3}{2})(F_z+\frac{1}{2})}{\rho^2}\tilde{\gamma}\right\},\end{aligned}$$

$$\begin{aligned}\mathcal{M}[2,1] &= \frac{1}{\sqrt{3}}\left\{\frac{\partial}{\partial z}C_1\frac{\partial}{\partial\rho} - \frac{\partial}{\partial\rho}C_2\frac{\partial}{\partial z} + \frac{(F_z-\frac{3}{2})}{\rho}\right.\\ &\quad \left. \times\left[C_2\frac{\partial}{\partial z} - \frac{\partial}{\partial z}C_1\right]\right\},\end{aligned}$$

$$\begin{aligned}\mathcal{M}[2,2] &= \frac{\partial}{\partial\rho}(\gamma_1-\gamma_2)\frac{\partial}{\partial\rho} + \frac{(\gamma_1-\gamma_2)}{\rho}\frac{\partial}{\partial\rho}\\ &\quad + \frac{\partial}{\partial z}(\gamma_1+2\gamma_2)\frac{\partial}{\partial z} - \frac{(F_z-\frac{1}{2})^2}{\rho^2}(\gamma_1-\gamma_2)\end{aligned}$$

$$+\frac{(F_z-\frac{1}{2})}{6\rho}\left[\frac{\partial}{\partial\rho}(C_1+C_2)-(C_1+C_2)\frac{\partial}{\partial\rho}\right]$$
$$-2(\gamma_1-\gamma_2)\left[\frac{(F_z-\frac{1}{6})B}{2}+\frac{B^2\rho^2}{8}\right],$$

$$\mathcal{M}[2,3]=\frac{1}{3}\left\{\frac{\partial}{\partial\rho}(C_1+C_2)\frac{\partial}{\partial z}-\frac{\partial}{\partial z}(C_1+C_2)\frac{\partial}{\partial\rho}\right.$$
$$\left.+\frac{(F_z+\frac{1}{2})}{\rho}\left[(C_1+C_2)\frac{\partial}{\partial z}-\frac{\partial}{\partial z}(C_1+C_2)\right]\right\},$$

$$\mathcal{M}[2,4]=\sqrt{3}\left\{\frac{\partial}{\partial\rho}\tilde{\gamma}\frac{\partial}{\partial\rho}+\frac{(F_z+\frac{3}{2})}{\rho}\frac{\partial}{\partial\rho}\tilde{\gamma}\right.$$
$$\left.+\frac{(F_z+\frac{1}{2})}{\rho}\tilde{\gamma}\frac{\partial}{\partial\rho}+\frac{(F_z+\frac{3}{2})(F_z-\frac{1}{2})}{\rho^2}\tilde{\gamma}\right\},$$

$$\mathcal{M}[2,5]=\sqrt{2}\left\{\frac{\partial}{\partial\rho}\gamma_2\frac{\partial}{\partial\rho}-2\frac{\partial}{\partial z}\gamma_2\frac{\partial}{\partial z}\right.$$
$$+\frac{\gamma_2}{\rho}\frac{\partial}{\partial\rho}-\frac{(F_z-\frac{1}{2})^2}{\rho^2}\gamma_2+\frac{(F_z-\frac{1}{2})}{6\rho}$$
$$\left.\times\left[\frac{\partial}{\partial\rho}(C_1+C_2)-(C_1+C_2)\frac{\partial}{\partial\rho}\right]\right\}-2\gamma_2\frac{B}{3},$$

$$\mathcal{M}[2,6]=-\frac{1}{3\sqrt{2}}\left\{\frac{\partial}{\partial\rho}(C_1-2C_2)\frac{\partial}{\partial z}\right.$$
$$+\frac{\partial}{\partial z}(2C_1-C_2)\frac{\partial}{\partial\rho}+\frac{(F_z+\frac{1}{2})}{\rho}$$
$$\left.\times\left[(C_1-2C_2)\frac{\partial}{\partial z}+\frac{\partial}{\partial z}(2C_1-C_2)\right]\right\},$$

$$\mathcal{M}[3,1]=-\sqrt{3}\left\{\frac{\partial}{\partial\rho}\tilde{\gamma}\frac{\partial}{\partial\rho}-\frac{(F_z-\frac{3}{2})}{\rho}\frac{\partial}{\partial\rho}\tilde{\gamma}\right.$$
$$\left.-\frac{(F_z-\frac{1}{2})}{\rho}\tilde{\gamma}\frac{\partial}{\partial\rho}+\frac{(F_z-\frac{3}{2})(F_z+\frac{1}{2})}{\rho^2}\tilde{\gamma}\right\},$$

$$\mathcal{M}[3,2]=\frac{1}{3}\left\{\frac{\partial}{\partial z}(C_1+C_2)\frac{\partial}{\partial\rho}-\frac{\partial}{\partial\rho}(C_1+C_2)\frac{\partial}{\partial z}\right.$$
$$\left.+\frac{(F_z-\frac{1}{2})}{\rho}\left[(C_1+C_2)\frac{\partial}{\partial z}-\frac{\partial}{\partial z}(C_1+C_2)\right]\right\},$$

$$\mathcal{M}[3,3]=\frac{\partial}{\partial\rho}(\gamma_1-\gamma_2)\frac{\partial}{\partial\rho}+\frac{(\gamma_1-\gamma_2)}{\rho}\frac{\partial}{\partial\rho}$$
$$+\frac{\partial}{\partial z}(\gamma_1+2\gamma_2)\frac{\partial}{\partial z}-\frac{(F_z+\frac{1}{2})^2}{\rho^2}(\gamma_1-\gamma_2)$$
$$-\frac{(F_z+\frac{1}{2})}{6\rho}\left[\frac{\partial}{\partial\rho}(C_1+C_2)-(C_1+C_2)\frac{\partial}{\partial\rho}\right]$$
$$-2(\gamma_1-\gamma_2)\left[\frac{(F_z+\frac{1}{6})B}{2}+\frac{B^2\rho^2}{8}\right],$$

$$\mathcal{M}[3,4]=\frac{1}{\sqrt{3}}\left\{\frac{\partial}{\partial z}C_1\frac{\partial}{\partial\rho}-\frac{\partial}{\partial\rho}C_2\frac{\partial}{\partial z}\right.$$
$$\left.-\frac{(F_z+\frac{3}{2})}{\rho}\left[C_2\frac{\partial}{\partial z}-\frac{\partial}{\partial z}C_1\right]\right\},$$

$$\mathcal{M}[3,5]=\frac{1}{3\sqrt{2}}\left\{\frac{\partial}{\partial\rho}(C_1-2C_2)\frac{\partial}{\partial z}+\frac{\partial}{\partial z}\right.$$
$$\times(2C_1-C_2)\frac{\partial}{\partial\rho}-\frac{(F_z-\frac{1}{2})}{\rho}$$
$$\left.\times\left[(C_1-2C_2)\frac{\partial}{\partial z}+\frac{\partial}{\partial z}(2C_1-C_2)\right]\right\},$$

$$\mathcal{M}[3,6]=\sqrt{2}\left\{\frac{\partial}{\partial\rho}\gamma_2\frac{\partial}{\partial\rho}-2\frac{\partial}{\partial z}\gamma_2\frac{\partial}{\partial z}+\frac{\gamma_2}{\rho}\frac{\partial}{\partial\rho}\right.$$
$$-\frac{(F_z+\frac{1}{2})^2}{\rho^2}\gamma_2-\frac{(F_z+\frac{1}{2})}{6\rho}$$
$$\left.\times\left[\frac{\partial}{\partial\rho}(C_1+C_2)-(C_1+C_2)\frac{\partial}{\partial\rho}\right]\right\}+2\gamma_2\frac{B}{3},$$

$$\mathcal{M}[4,1]=0,$$

$$\mathcal{M}[4,2]=\sqrt{3}\left\{\frac{\partial}{\partial\rho}\tilde{\gamma}\frac{\partial}{\partial\rho}-\frac{(F_z-\frac{1}{2})}{\rho}\frac{\partial}{\partial\rho}\tilde{\gamma}\right.$$
$$\left.-\frac{(F_z+\frac{1}{2})}{\rho}\tilde{\gamma}\frac{\partial}{\partial\rho}+\frac{(F_z+\frac{3}{2})(F_z-\frac{1}{2})}{\rho^2}\tilde{\gamma}\right\},$$

$$\mathcal{M}[4,3]=\frac{1}{\sqrt{3}}\left\{\frac{\partial}{\partial\rho}C_1\frac{\partial}{\partial z}-\frac{\partial}{\partial z}C_2\frac{\partial}{\partial\rho}\right.$$
$$\left.-\frac{(F_z+\frac{1}{2})}{\rho}\left[C_1\frac{\partial}{\partial z}-\frac{\partial}{\partial z}C_2\right]\right\},$$

$$\mathcal{M}[4,4]=\frac{\partial}{\partial\rho}(\gamma_1+\gamma_2)\frac{\partial}{\partial\rho}+\frac{(\gamma_1+\gamma_2)}{\rho}\frac{\partial}{\partial\rho}$$
$$+\frac{\partial}{\partial z}(\gamma_1-2\gamma_2)\frac{\partial}{\partial z}-\frac{(F_z+\frac{3}{2})^2}{\rho^2}$$
$$\times(\gamma_1+\gamma_2)-\frac{(F_z+\frac{3}{2})}{2\rho}$$
$$\times\left[\frac{\partial}{\partial\rho}(C_1+C_2)-(C_1+C_2)\frac{\partial}{\partial\rho}\right]$$
$$-2(\gamma_1+\gamma_2)\left[\frac{(F_z+\frac{1}{2})B}{2}+\frac{B^2\rho^2}{8}\right],$$

$$\mathcal{M}[4,5]=\sqrt{6}\left\{\frac{\partial}{\partial\rho}\tilde{\gamma}\frac{\partial}{\partial\rho}-\frac{(F_z-\frac{1}{2})}{\rho}\frac{\partial}{\partial\rho}\tilde{\gamma}\right.$$
$$\left.-\frac{(F_z+\frac{1}{2})}{\rho}\tilde{\gamma}\frac{\partial}{\partial\rho}+\frac{(F_z+\frac{3}{2})(F_z-\frac{1}{2})}{\rho^2}\tilde{\gamma}\right\},$$

$$\mathcal{M}[4,6]=-\frac{1}{\sqrt{6}}\left\{\frac{\partial}{\partial\rho}C_1\frac{\partial}{\partial z}-\frac{\partial}{\partial z}C_2\frac{\partial}{\partial\rho}\right.$$
$$\left.-\frac{(F_z+\frac{1}{2})}{\rho}\left[C_1\frac{\partial}{\partial z}-\frac{\partial}{\partial z}C_2\right]\right\},$$

$$\mathcal{M}[5,1]=-\frac{1}{\sqrt{6}}\left\{\frac{\partial}{\partial z}C_1\frac{\partial}{\partial\rho}-\frac{\partial}{\partial\rho}C_2\frac{\partial}{\partial z}\right.$$
$$\left.+\frac{(F_z-\frac{3}{2})}{\rho}\left[C_2\frac{\partial}{\partial z}-\frac{\partial}{\partial z}C_1\right]\right\},$$

$$\mathcal{M}[5,2] = \sqrt{2}\left\{\frac{\partial}{\partial\rho}\gamma_2\frac{\partial}{\partial\rho} - 2\frac{\partial}{\partial z}\gamma_2\frac{\partial}{\partial z} + \frac{\gamma_2}{\rho}\frac{\partial}{\partial\rho} - \frac{(F_z-\frac{1}{2})^2}{\rho^2}\gamma_2 + \frac{(F_z-\frac{1}{2})}{6\rho} \times \left[\frac{\partial}{\partial\rho}(C_1+C_2) - (C_1+C_2)\frac{\partial}{\partial\rho}\right]\right\} - 2\gamma_2\frac{B}{3},$$

$$\mathcal{M}[5,3] = \frac{1}{3\sqrt{2}}\left\{\frac{\partial}{\partial\rho}(2C_1-C_2)\frac{\partial}{\partial z} + \frac{\partial}{\partial z}(C_1-2C_2)\frac{\partial}{\partial\rho} + \frac{(F_z+\frac{1}{2})}{\rho} \times \left[(2C_1-C_2)\frac{\partial}{\partial z} + \frac{\partial}{\partial z}(C_1-2C_2)\right]\right\},$$

$$\mathcal{M}[5,4] = \sqrt{6}\left\{\frac{\partial}{\partial\rho}\tilde{\gamma}\frac{\partial}{\partial\rho} + \frac{(F_z+\frac{3}{2})}{\rho}\frac{\partial}{\partial\rho}\tilde{\gamma} + \frac{(F_z+\frac{1}{2})}{\rho}\tilde{\gamma}\frac{\partial}{\partial\rho} + \frac{(F_z+\frac{3}{2})(F_z-\frac{1}{2})}{\rho^2}\tilde{\gamma}\right\},$$

$$\mathcal{M}[5,5] = \frac{\partial}{\partial\rho}\gamma_1\frac{\partial}{\partial\rho} + \frac{\partial}{\partial z}\gamma_1\frac{\partial}{\partial z} + \frac{\gamma_1}{\rho}\frac{\partial}{\partial\rho} - \frac{(F_z-\frac{1}{2})^2}{\rho^2}\gamma_1 + \frac{(F_z-\frac{1}{2})}{3\rho} \times \left[\frac{\partial}{\partial\rho}(C_1+C_2) - (C_1+C_2)\frac{\partial}{\partial\rho}\right] - 2\gamma_1\left[\frac{(F_z+\frac{1}{6})B}{2} + \frac{B^2\rho^2}{8}\right] - 2\Delta_o(\rho,z),$$

$$\mathcal{M}[5,6] = -\frac{1}{3}\left\{\frac{\partial}{\partial\rho}(C_1+C_2)\frac{\partial}{\partial z} - \frac{\partial}{\partial z}(C_1+C_2)\frac{\partial}{\partial\rho} + \frac{(F_z+\frac{1}{2})}{\rho}\left[(C_1+C_2)\frac{\partial}{\partial z} - \frac{\partial}{\partial z}(C_1+C_2)\right]\right\},$$

$$\mathcal{M}[6,1] = -\sqrt{6}\left\{\frac{\partial}{\partial\rho}\tilde{\gamma}\frac{\partial}{\partial\rho} - \frac{(F_z-\frac{3}{2})}{\rho}\frac{\partial}{\partial\rho}\tilde{\gamma} - \frac{(F_z-\frac{1}{2})}{\rho}\tilde{\gamma}\frac{\partial}{\partial\rho} + \frac{(F_z-\frac{3}{2})(F_z+\frac{1}{2})}{\rho^2}\tilde{\gamma}\right\},$$

$$\mathcal{M}[6,2] = -\frac{1}{3\sqrt{2}}\left\{\frac{\partial}{\partial\rho}(2C_1-C_2)\frac{\partial}{\partial z} + \frac{\partial}{\partial z}(C_1-2C_2)\frac{\partial}{\partial\rho} - \frac{(F_z-\frac{1}{2})}{\rho} \times \left[(2C_1-C_2)\frac{\partial}{\partial z} + \frac{\partial}{\partial z}(C_1-2C_2)\right]\right\},$$

$$\mathcal{M}[6,3] = \sqrt{2}\left\{\frac{\partial}{\partial\rho}\gamma_2\frac{\partial}{\partial\rho} - 2\frac{\partial}{\partial z}\gamma_2\frac{\partial}{\partial z} + \frac{\gamma_2}{\rho}\frac{\partial}{\partial\rho} - \frac{(F_z+\frac{1}{2})^2}{\rho^2}\gamma_2 - \frac{(F_z+\frac{1}{2})}{6\rho} \times \left[\frac{\partial}{\partial\rho}(C_1+C_2) - (C_1+C_2)\frac{\partial}{\partial\rho}\right]\right\} + 2\gamma_2\frac{B}{3},$$

$$\mathcal{M}[6,4] = -\frac{1}{\sqrt{6}}\left\{\frac{\partial}{\partial z}C_1\frac{\partial}{\partial\rho} - \frac{\partial}{\partial\rho}C_2\frac{\partial}{\partial z} - \frac{(F_z+\frac{3}{2})}{\rho} \times \left[C_2\frac{\partial}{\partial z} - \frac{\partial}{\partial z}C_1\right]\right\},$$

$$\mathcal{M}[6,5] = -\frac{1}{3}\left\{\frac{\partial}{\partial z}(C_1+C_2)\frac{\partial}{\partial\rho} - \frac{\partial}{\partial\rho}(C_1+C_2)\frac{\partial}{\partial z} + \frac{(F_z-\frac{1}{2})}{\rho}\left[(C_1+C_2)\frac{\partial}{\partial z} - \frac{\partial}{\partial z}(C_1+C_2)\right]\right\},$$

$$\mathcal{M}[6,6] = \frac{\partial}{\partial\rho}\gamma_1\frac{\partial}{\partial\rho} + \frac{\partial}{\partial z}\gamma_1\frac{\partial}{\partial z} + \frac{\gamma_1}{\rho}\frac{\partial}{\partial\rho} - \frac{(F_z+\frac{1}{2})^2}{\rho^2}\gamma_1 - \frac{(F_z+\frac{1}{2})}{3\rho}\left[\frac{\partial}{\partial\rho}(C_1+C_2) - (C_1+C_2)\frac{\partial}{\partial\rho}\right] - 2\gamma_1\left[\frac{(F_z-\frac{1}{6})B}{2} + \frac{B^2\rho^2}{8}\right] - 2\Delta_o(\rho,z).$$

Here γ_i are the position-dependent Luttinger parameters, $\tilde{\gamma} = (\gamma_2+\gamma_3)/2$, $C_1 = 1+\gamma_1-2\gamma_2-6\gamma_3$ and $C_2 = 1+\gamma_1-2\gamma_2$, F_z is the total angular momentum z projection and $\Delta_o(\rho,z)$ is the spin–orbit splitting.

References

[1] Lefebvre P and Gayral B 2008 *C. R. Phys.* **9** 816
[2] Weng M Q, Wang Y Y and Wu M W 2009 *Phys. Rev.* B **79** 155309
[3] Martinez-Guerrero E, Adelmann C, Chabuel F, Simon J, Pelekanos N T, Mula G, Daudin B, Feuillet G and Mariette H 2000 *Appl. Phys. Lett.* **77** 809
[4] Martinez-Guerrero E, Chabuel F, Daudin B, Rouviere J L and Mariette H 2002 *Appl. Phys. Lett.* **81** 5117
[5] Fonoberov V A and Balandin A A 2003 *J. Appl. Phys.* **94** 7178
[6] Simon J, Pelekanos N T, Adelmann C, Martinez-Guerrero E, André R, Daudin B, Dang L S and Mariette H 2003 *Phys. Rev.* B **68** 035312
[7] Shojaei S, Troiani F, Asgari A, Kalafi M and Goldoni G 2008 *Eur. Phys. J.* B **65** 505
[8] Nagahara S, Arita M and Arakawa Y 2006 *Appl. Phys. Lett.* **88** 083101
[9] Lagarde D, Balocchi A, Carrere H, Renucci P, Amand T, Marie X, Founta S and Mariette H 2008 *Phys. Rev.* B **77** 041304(R)
[10] Brimont C, Gallart M, Cregut O, Hoenerlage B, Gilliot P, Lagarde D, Balocchi A, Amand T, Marie X, Founta S and Mariette H 2009 *J. Appl. Phys.* **106** 053514
[11] Buss J H, Rudolph J, Schupp T, As D J, Lischka K and Haegele D 2010 *Appl. Phys. Lett.* **97** 062101
[12] Xia C, Zeng Z and Wei S 2011 *J. Lumin.* **131** 623
[13] Tong H and Wu M W 2011 *Phys. Rev.* B **83** 235323
[14] Chuang S L and Chang C S 1996 *Appl. Phys. Lett.* **68** 1657
[15] Liao Y H, Climente J I and Cheng S J 2011 *Phys. Rev.* B **83** 165317
[16] Tsitsishvili E and Kalt H 2010 *Phys. Rev.* B **82** 195315
[17] Vurgaftman I, Meyer J L and Ram-Mohan L R 2001 *J. Appl. Phys.* **89** 5815
[18] Rodrigues S C P, Scolfaro L M R, Leite J R and Sipahi G M 2000 *Appl. Phys. Lett.* **76** 1015
[19] Marquardt O, Mourad D, Schulz S, Hickel T, Czycholl G and Neugebauer J 2008 *Phys. Rev.* B **78** 235302
[20] Luttinger J M and Kohn W 1955 *Phys. Rev.* **97** 869
Luttinger J M 1956 *Phys. Rev.* **102** 1030

[21] Burt M G 1992 *J. Phys.: Condens. Matter* **4** 6651
Burt M G 1999 *J. Phys.: Condens. Matter* **11** R53

[22] Foreman B A 1993 *Phys. Rev.* B **48** 4964

[23] Voon L and Willatzen M 2009 *The k.p Method: Electronic Properties of Semiconductors* (Berlin: Springer)

[24] Planelles J and Jaskólski W 2003 *J. Phys.: Condens. Matter* **15** L67

[25] Mlinar V, Tadic M, Partoens B and Peeters F M 2005 *Phys. Rev.* B **71** 205305

[26] Climente J I, Planelles J and Jaskólski W 2003 *Phys. Rev.* B **68** 075307

[27] Planelles J, Climente J I, Rajadell F, Doty M F, Bracker A S and Gammon D 2010 *Phys. Rev.* B **82** 155307

[28] Sercel P C and Vahala K J 1990 *Phys. Rev.* B **42** 3690

[29] Mietze C, Landmann M, Rauls E, Machhadani H, Sakr S, Tchernycheva M, Julien F H, Schmidt W G, Lischka K and As D J 2011 *Phys. Rev.* B **83** 195301

[30] Hu J, Li L, Yang W, Manna L, Wang L and Alivisatos A 2001 *Science* **292** 2060

[31] Planelles J, Rajadell F and Climente J I 2010 *J. Phys. Chem.* C **114** 8337

[32] Baskoutas S and Bester G 2011 *J. Phys. Chem.* C **115** 15862
Baskoutas S and Bester G 2010 *J. Phys. Chem.* C **114** 94301

[33] Koudinov A V, Akimov I A, Kusrayev Y G and Henneberger F 2004 *Phys. Rev.* B **70** 241305

[34] Bardoux R, Guillet T, Gil B, Lefebvre P, Bretagnon T, Taliercio T, Rousset S and Semond F 2008 *Phys. Rev.* B **77** 235315

[35] Belhadj T, Amand T, Kunold A, Simon C M, Kuroda T, Abbarchi M, Mano T, Sakoda K, Kunz S, Marie X and Urbaszek B 2010 *Appl. Phys. Lett.* **97** 051111

[36] Doty M F, Climente J I, Greilich A, Yakes M, Bracker A S and Gammon D 2010 *Phys. Rev.* B **81** 035308

[37] Keizer J G, Bocquel J, Koenraad P M, Mano T, Noda T and Sakoda K 2010 *Appl. Phys. Lett.* **96** 062101

A LETTERS JOURNAL EXPLORING THE FRONTIERS OF PHYSICS

December 2013

EPL, **104** (2013) 67004 www.epljournal.org
doi: 10.1209/0295-5075/104/67004

Suppression of the Aharonov-Bohm effect in hexagonal quantum rings

A. BALLESTER[1], C. SEGARRA[1], A. BERTONI[2] and J. PLANELLES[1]

[1] *Departament de Química Física i Analítica, Universitat Jaume I - Castelló de la Plana, Spain*
[2] *Institute for Nanoscience, CNR NANO S3 - I-41125 Modena, Italy*

received 18 September 2013; accepted 16 December 2013
published online 13 January 2014

PACS 75.75.-c – Magnetic properties of nanostructures
PACS 73.21.Hb – Quantum wires
PACS 73.21.La – Quantum dots

Abstract – Few-electron states of AlAs-GaAs-AlAs hexagonal quantum rings pierced by an axial magnetic field are computed through full configuration interaction calculations. The quantum ring is in the low-density regime, populated with $N = 1$ up to $N = 7$ electrons. Similar to circular rings, the energy spectra of the hexagonal ones reflect an integer and fractional Aharonov-Bohm regular oscillation pattern for $N = 1$ and $N = 2, 3$, respectively. Deviations from the regular fractional period with increasing electron density become apparent for larger N. Remarkably, for $N = 6$ the Aharonov-Bohm effect is completely suppressed. This is a unique symmetry-related feature of hexagonal rings that only can emerge in the low-density regime.

Introduction. – Most III–V nanowires with a diameter less than about 400 nm have a very neat hexagonal section even after a few overcoating processes [1–7]. These core-multishell nanowires have an unconstrained longitudinal direction and different material composition along the orthogonal plane (radial direction), that eventually bound carriers on a prismatic tube surrounding the central core. With a proper material modulation along the growth axis, or just by cutting them, a strong confinement of carriers in the longitudinal direction can be introduced [8–11] leading to a hexagonal flat quantum ring (QR) where the free carriers are confined on a square-well–type potential in the radial direction [12]. These flat polygonal structures are much less studied than their circular counterparts, where evidences of the Aharanov-Bohm (AB) effect have given rise to a decade of intensive research [13–19]. One then wonders what differences can be expected from the different confinement symmetry of hexagonal rings.

In a recent paper [20] we presented a theoretical study of correlated multi-electron states of hexagonal semiconductor rings populated with $N = 1$ up to $N = 7$ electrons and found that charges get more localized in the corners as the number of electrons increases up to $N = 6$, where we found a maximum of localization. The result evidences the deficiency of a picture based on orbitals delocalized on the whole ring, *i.e.* electron correlation becomes crucial. In this letter we investigate the response of this N-electron system to an external axial magnetic field which brings AB physics into play. Specifically, we focus on the different response in comparison to circular QRs.

It is well known that an increase in the strength of an externally applied axial magnetic field in a circular QR leads to oscillations of the ground-state energy. The period and amplitude of the oscillations depends on the electron population and it is referred to as fractional AB effect [21]. The first unambiguous experimental evidence of this effect may be traced back to the work by Keyser [22]. Soon after, Emperador *et al.* [23] related this fractional response to a low kinetic energy and a phenomenon of electronic localization. Full configuration interaction (FCI) calculations by Niemelä *et al.* [24] of QRs populated up to four electrons revealed the crucial role of electron-electron interaction on the decrease of the period and amplitude of the ground-state energy and its fractional character. Liu *et al.* [25] extended the FCI calculation to QRs populated with $N = 5$ and $N = 6$ electrons as a function of the magnetic field and the QR radius, thus yielding a phase diagram with a rich variety of ground states. The fractional character of the AB effect was though fully explored earlier using the empirical Hubbard model [26], and it was concluded that fractional AB oscillations arise for small values of the factor $\alpha = Nt/(UL)$, where N is the number of electrons in the QR, t is the tunnelling integral, U is the repulsion integral, and L is the number of sites along the

QR where the single-particle functions are located. For α to be small, the ratio between the one-electron integral t and the two-electron integral U must be small, *i.e.*, a low kinetic energy and a strong electron-electron interaction are required. Also, since α is proportional to N, a low-density regime is needed. Additionally, L introduces the possible role of symmetry lowering: the larger L the sooner the Hubbard model reaches the fractional AB regime. But no other symmetry-related effect is reported.

In this work, we consider the same AlAs-GaAs-AlAs hexagonal QR studied in ref. [20], where all physical parameters, namely effective masses, conduction-band offset and dielectric constant can be found. We carry out calculations for $N = 2$ up to $N = 7$ interacting electrons in the low-density regime. We find that the low-energy spectrum of the hexagonal QR resembles that of circular ones. Like in circular QRs, the energy spectra of the hexagonal QRs analyzed here reflect an integer and regular AB oscillation pattern for $N = 1$, a fractional, also regular, AB oscillation pattern for $N = 2$ and $N = 3$, and deviations from the regular period with the increasing electron density. Specifically, $N = 4$ and $N = 5$ have not regular oscillation amplitude patterns, while $N = 7$ shows already an integer period, like that of $N = 1$. The most intriguing result is found for $N = 6$ electrons, where AB effect is completely suppressed, which translates into zero magnetization. We show this is a peculiar symmetry-related response of the $N = 6$ system in hexagonal QRs that only can emerge in the low-density regime.

Theory. – We perform an exact diagonalization of the multi-particle Schrödinger equation via a FCI procedure. As a first step, the single-particle orbitals ϕ_i and energies ϵ_i of the conduction band are computed through a real-space numerical solution of the eigenvalue equation of the effective-mass Hamiltonian,

$$h = \frac{1}{2}(\mathbf{p} + \mathbf{A})\frac{1}{m^*(\mathbf{r})}(\mathbf{p} + \mathbf{A}) + V(\mathbf{r}), \qquad (1)$$

where $\mathbf{r}$ is the 2D coordinate on the hexagonal domain, $m^*(\mathbf{r})$ is the isotropic material-dependent effective mass of electrons, $\mathbf{A}$ is the magnetic vector potential, and $V(\mathbf{r})$ is the confining potential, represented schematically in the inset of fig. 1. This equation is numerically integrated using the finite-elements method on a regular triangular mesh with hexagonal elements. The grid reproduces the symmetry of the system thus avoiding numerical artifacts originated by discretization asymmetries of the six domain boundaries, as would be the case, *e.g.*, using a rectangular grid. Unless otherwise indicated, the employed geometry is a regular hexagon domain with edges 66.5 nm long including a GaAs well 6.8 nm wide with uniform thickness all around the 37.3 nm AlAs core. The GaAs well is covered by a 13.5 nm AlAs capping layer (see inset in fig. 1).

Finally, we diagonalize the multi-particle Hamiltonian

$$H = \sum_{i\sigma} \epsilon_i e^\dagger_{i\sigma} e_{i\sigma} + \frac{1}{2}\sum_{ijkl}\sum_{\sigma\sigma'} U_{ijkl} e^\dagger_{i\sigma} e^\dagger_{j\sigma'} e_{k\sigma'} e_{j\sigma}, \qquad (2)$$

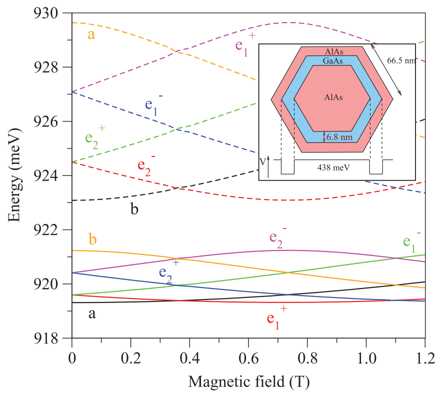

Fig. 1: (Colour on-line) Orbital energies *vs.* magnetic field, labelled according to the C_6 symmetry group. Two well-separated shells composed by 6 orbitals can be identified, with a 2 meV energy gap between them. Inset: schematics of the system. The GaAs ring is wrapped around a hexagonal AlAs core and capped by an additional AlAs shell. The free electrons are confined in the GaAs region.

where $e_{i\sigma}$ ($e^\dagger_{i\sigma}$) is the annihilation (creation) operator for an electron in the orbital state i and with spin σ. For all the calculations we use 24 spin-orbital single-particle states, giving $\binom{24}{N}$ Slater determinants, with N being the number of electrons.

Results and discussion. – In fig. 1 we show the low-lying part of the single-electron energy spectrum as a function of the magnetic field. Orbitals are labelled according to the C_6 symmetry group. Well separated with a 2 meV energy gap between them, we can identify two shells each composed by 6 orbitals. Namely, two groups of orbitals well separated in energy, having the same degeneracy pattern. The result, quite different from that of a circular QR, originates from the symmetry lowering when going from circular to hexagonal shape. In the first case we have an infinite number of irreducible representations (irreps) which associated orbitals can cross. By contrast, the hexagonal ring has only six irreps, so that anticrossings between orbitals with the same symmetry appear. This opens a gap between the shells. The states cross with increasing field only within the shell where states have different symmetry (see fig. 1). As a consequence of the shell splitting, we find that in a wide range of the low-lying N-electron states only the lowest 6 orbitals (spin-independent real space wave functions) have significant population.

In fig. 2 we summarize the behaviour of the energy of lowest-lying few-electron states *vs.* the magnetic field. The represented energies are relative to the N-electron ground-state energy in the absence of magnetic field (horizontal red line). The few-electron states are labelled according to the C_6 symmetry group and spin multiplicity of

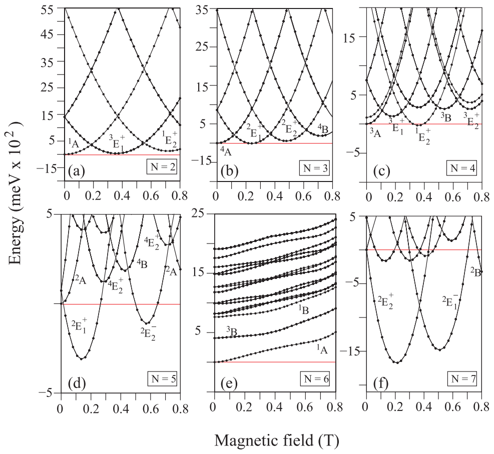

Fig. 2: (Colour on-line) Energy of low-lying few-electron states, labelled according to the C_6 symmetry group and spin multiplicity, *vs.* the magnetic field. The six panels show the cases of $N = 2$ to $N = 7$ electrons, as indicated. Zero energy, indicated by the straight reference line, corresponds to the ground-state energy without magnetic field.

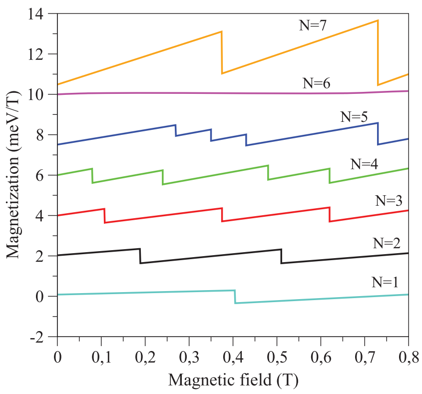

Fig. 3: (Colour on-line) Magnetization of the N-electron hexagonal QR *vs.* the applied magnetic field, for $N = 1$ (bottom) up to $N = 7$ (top). For the sake of clarity, the different magnetization profiles have been offset by 2 meV/T.

states. Figure 3 displays the corresponding magnetization in meV/T. We can see that for $N = 2$ and $N = 3$ a perfect fractional AB is observed. Thus, fig. 3 reveals that for $N = 2$ the AB period is halved as compared to the $N = 1$ case. Likewise, for $N = 3$ it is one third. Deviations of the regular fractional period become apparent for larger N. For $N = 4$ and especially for $N = 5$ the oscillation amplitude pattern is far from regular, and

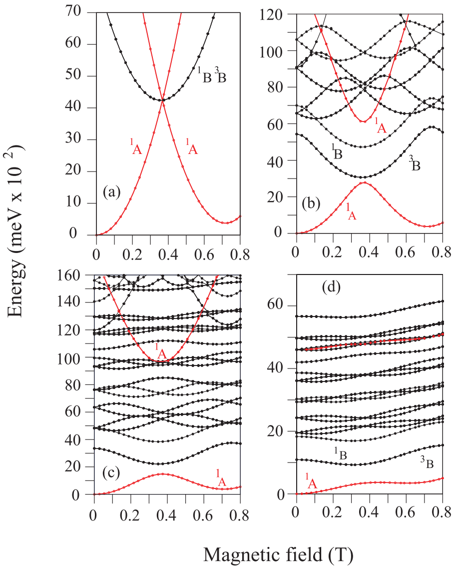

Fig. 4: (Colour on-line) Lowest-lying states for $N = 6$ for increasing Coulomb interaction. In the panels (a), (b), (c) and (d) the Coulomb repulsion is scaled down by a factor of 0, 0.1, 0.2 and 0.5, respectively. Red lines correspond to the states which anticrossing is responsible for the suppression of the AB effect and for the flat magnetization profile.

the $N = 7$ case already shows an integer period. The observed behaviour is consistent with the previous calculations on QRs [23–26]. In particular, the behaviour *vs.* N is consistent with an increasing α factor that prevents the fractional behaviour of the AB oscillations [26].

The most striking result in figs. 2 and 3 is found for $N = 6$. In this case a complete suppression of the AB oscillation that turns into a completely flat magnetization profile occurs.

In order to understand the peculiar behaviour of the $N = 6$ system, we repeated the set of FCI calculations but introducing a scaling factor f that multiplies the electron-electron interaction integrals. For $f = 0$ we obtain the non-interacting particle spectrum with a crossing, at about 1/2 of flux, of two different configurations, $a^2(e_1^+)^2(e_1^-)^2$ and $(e_1^+)^2a^2(e_2^+)^2$, corresponding to two different states ^1A with the same total symmetry and total spin (see panel (a) in fig. 4). We use the standard Schoenflies notation for the C_6 group, and lower-case and capital letters to refer to the C_6 symmetry of orbitals and N-electron states, respectively. The first configuration given above is the lowest one at $B = 0$, while the second represents a highly excited configuration at this magnetic field. The two configurations are essentially exchanged at about one unit of flux. When the electron-electron

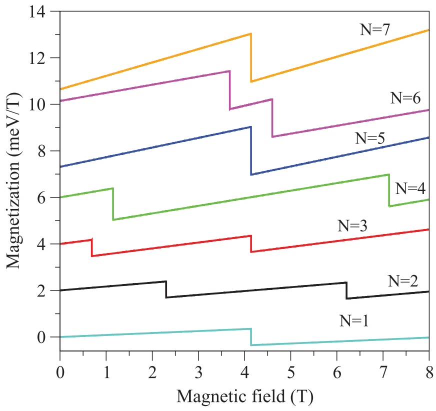

Fig. 5: (Colour on-line) Magnetization of the small hexagonal QR (three times smaller than in previous figures) for $N = 1$ (bottom) up to $N = 7$ (top). For the sake of clarity, the different magnetization profiles have been offset by $2\,\mathrm{meV/T}$.

repulsion is included the string of symmetry-labels of the orbitals cannot be used as good quantum numbers, since the configuration interaction takes place. Then, only the total symmetry and total spin are good labels. However we can still identify these configurations as dominant, with a large contribution in the case of small f factors. In the presence of Coulomb interactions, the two ${}^1A$ states having these leading configurations anticross, the anticrossing being larger as electron-electron interaction increases (see panels (b), (c) and (d) in fig. 4).

To further assess the role of the regime of density, we carried out calculations for an hexagonal QR three times smaller than the above sample. Simulations of magnetizations are reported in fig. 5. In this case, we can observe a neat fractional behaviour only for $N = 2$. As far as the $N = 6$ case is concerned, fig. 5 reveals that the AB suppression is no longer present. This is because in this density regime the magnitude of the anticrossing between the two ${}^1A$ states of the $N = 6$ system cannot overcome the relative stabilization of the triplet ${}^3B$ state coming from the exchange integrals (see fig. 4) so that ${}^3B$ emerges as the ground state in a narrow window around one half of flux, yielding an irregular discontinuity in the magnetization profile around this magnetic field, as reported in fig. 5.

Role of symmetry and conclusions. – To conclude, we explore whether or not the suppression of the AB effect may occur in QRs of symmetries other than C_6. To this end, we take into account the previous result relating the suppression of the AB effect to the anticrossing between the $B = 0$ ground state and an excited state of the same symmetry and total spin. In particular, the symmetry of the N-electron state can be calculated as the product of the irreps of the orbitals in the leading configuration. Furthermore, the orbital ordering can also be determined from that of a circular QR by considering the symmetry reduction $C_\infty \to C_n$. We give the mathematical details in the appendix. By considering the C_n symmetry groups with $n = 3$ up to $n = 10$ (*i.e.* from triangular to decagonal shape) we prove that, besides the $N = 6$ hexagonal QR, the smallest C_n group that may render a possible anticrossing is the $N = 10$ C_{10}-symmetry QR. On the one hand, C_{10} is not a geometry that can be realistically synthesized at the nanometric level, on the other hand, the relatively large number of electrons required, $N = 10$, and the need of a low-density regime points this regime as difficult to be experimentally achieved. Then, we may say that no other ground state anticrossing like that of the $N = 6$ case in hexagonal QRs can occur for the currently synthesized geometries.

In summary, we have shown that hexagonal QRs exhibit AB phenomena different from the well-known circular rings. The most remarkable finding is the complete suppression of the AB effect when the six-electron hexagonal QR system is in the high-correlation, low-density regime. The phenomenon originates in the anticrossing between the $B = 0$ ground state and an excited state of the same symmetry and total spin. We have demonstrated that this effect is exclusive of hexagonal structures and it implies the possibility of switching on and off the device magnetization by varying the number of confined carriers.

* * *

This work was partially supported by UJI-Bancaixa Project No. P1-1B2011-01, MCINN Project No. CTQ2011-27324, and FPI and FPU Grants (ABa and CS). ABe acknowledges the CINECA award under the ISCRA initiative for high-performance computing resources.

Appendix

A C_n group has n irreps labelled with $k = 0 \pm 1 \pm 2, \dots,$ up to the integer part of $n/2$. The $k = 0$ irrep is generally referred to as A and it is real and fully symmetric. The remaining irreps are complex and labelled $E_k^{\pm}$. For even n, $k = n/2$ and $k = -n/2$ correspond to the same real and fully antisymmetric irrep B. The character $\chi_{\pm k}(C_n^m)$ of the irrep k $(-k)$ corresponding to an angle $2\pi m/n$ around the rotation axis of the C_n group is

$$\chi_{\pm k}(C_n^m) = \exp\left[\pm i \frac{2\pi}{n} km\right]. \tag{A.1}$$

This expression allow us to write the character table of any C_n group. All the same, if $k = np + q$ with $q = 0, 1, \dots, (n-1)$ and $p = 0, 1, 2, \dots,$ the following identities,

$$\exp\left[\pm i \frac{2\pi}{n}(np+q)m\right] = \exp\left[\pm i \frac{2\pi}{n} qm\right], \tag{A.2}$$

$$\exp\left[\mp i \frac{2\pi}{n}(n-q)m\right] = \exp\left[\pm i \frac{2\pi}{n} qm\right], \tag{A.3}$$

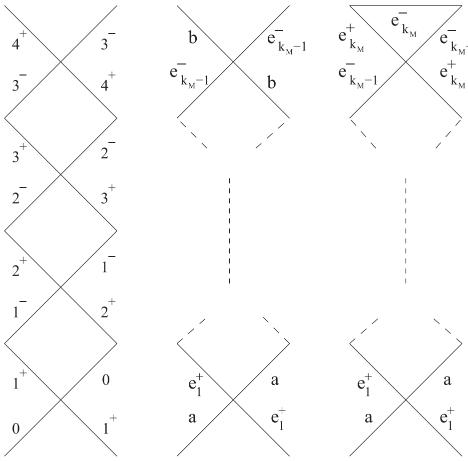

Fig. 6: Scheme of the orbital energies *vs.* the magnetic field. Left: low-lying part of the energy spectrum corresponding to a C_n symmetry with large n. The orbitals are labelled by $k = 0 \pm 1 \pm 2 \pm 3, \ldots$. Center: top and bottom of the orbital shell for even n. The notation for orbitals, $\{A, e_k^\pm\ (k = 1, 2, \ldots, k_{M-1}), B\}$, is that of the C_n irreps. Right: top and bottom of the orbital shell for odd n. The C_n notation $\{A, e_k^\pm\ (k = 1, 2, \ldots, k_M)\}$ is used.

allow us to conclude that

$$\chi_{\pm k}(C_n^m) = \begin{cases} \chi_{\pm q}(C_n^m); & q \leq k_M, \\ \chi_{\mp(n-q)}(C_n^m); & q > k_M, \end{cases} \tag{A.4}$$

where k_M is the integer part of $n/2$, *i.e.*, the largest value of k in the character table of C_n.

The last result allow us to determine the symmetry $C_\infty \to C_n$ reduction table. Thus, for even n, the C_∞ irreps labelled as $k = 0, 1, -1, 2, -2, \ldots$, correspond to A, E_1^+, E_1^-, E_2^+, $E_2^-, \ldots$, $E_{k_M-1}^+$, $E_{k_M-1}^-$, B, B, $E_{k_M-1}^-, \ldots$, E_1^-, E_1^+, A, A, E_1^+, $E_1^-, \ldots$. For odd n they correspond to A, E_1^+, $E_1^-, \ldots$, $E_{k_M}^+$, $E_{k_M}^-$, $E_{k_M}^-$, $E_{k_M}^+, \ldots$, E_1^-, E_1^+, A, A, E_1^+, $E_1^-, \ldots$. This symmetry reduction scheme helps to understand the evolution *vs.* the magnetic field of the single-particle orbitals of poligonal rings pierced by an axial magnetic field: sets of non-crossing shells containing n orbitals with different symmetry repeatedly crossing as the magnetic field increases (see, *e.g.*, fig. 1).

As for the product of irreps we have

$$\chi_{\pm k_1}(C_n^m)\chi_{\pm k_2}(C_n^m) = \exp\left[i\frac{2\pi}{n}\Big[(\pm k_1) + (\pm k_2)\Big]m\right]. \tag{A.5}$$

Then, the product of two irreps $\pm k_1$, $\pm k_2$ yields the irrep labelled with the sum $k = (\pm k_1) + (\pm k_2)$. In case the resulting k is larger than k_M, then we write $k = np + q$ with $q < n$ and identify k with q (with $-(n-q)$) if $q \leq k_M$ ($q > k_M$).

Table 1: Possible q values for the symmetry groups C_n from $n = 3$ up to $n = 10$ as a function of $m = 1, 2, \ldots, (n-1)$. The integer values are highlighted.

n \ k	0	1	2	3	4
3	$\frac{2}{3}m$				
4	$\frac{1}{2}m$	$\frac{3}{2}m$			
5	$\frac{2}{5}m$	$\frac{6}{5}m$			
6	$\frac{1}{3}m$	$\boxed{\mathbf{m}}$	$\frac{5}{3}m$		
7	$\frac{2}{7}m$	$\frac{6}{7}m$	$\frac{10}{7}m$		
8	$\frac{1}{4}m$	$\frac{3}{4}m$	$\frac{5}{4}m$	$\frac{7}{4}m$	
9	$\frac{2}{9}m$	$\frac{6}{9}m$	$\frac{10}{9}m$	$\frac{14}{9}m$	
10	$\frac{1}{5}m$	$\frac{3}{5}m$	$\boxed{\mathbf{m}}$	$\frac{7}{5}m$	$\frac{9}{5}m$

With this information we may address the problem of anticrossings. The scheme of orbital energies *vs.* the magnetic field is shown in fig. 6.

In order to have, at a given value of the magnetic field, an anticrossing between two N-electron states that are the ground state in either side of the avoided crossing, the dominant electronic configuration in either side of the monoelectronic crossing must be different yet it must yield the same symmetry and total spin for the N-electron state. This cannot occur for odd number N of electrons. For even N it can only occur if the square of the irreps Γ_{-k} and Γ_{k+1}, $k + 1 \leq k_M$ yield the same irrep, *i.e.*, if

$$\chi_{-k}(C_n^m)^2 = \chi_{k+1}(C_n^m)^2 \tag{A.6}$$

with

$$\chi_{-k}(C_n^m)^2 = \exp\left[-i\,\frac{4\pi}{n}\,km\right], \tag{A.7}$$

$$\chi_{k+1}(C_n^m)^2 = \exp\left[i\,\frac{4\pi}{n}\,(k+1)\,m\right]. \tag{A.8}$$

It obviously occurs for $m = 0$. It must be also true for $m = 1, 2, 3, \ldots, (n-1)$, *i.e.*, it must occur both that q be a natural number ($q \in N$) and the fulfilment of the identity:

$$\frac{4\pi}{n}(k+1)m = 2\pi q - \frac{4\pi}{n}km. \tag{A.9}$$

In other words,

$$k = \frac{1}{4}\Big(\frac{nq}{m} - 2\Big), \quad m = 1, 2, \ldots, (n-1) \text{ and } q \in N. \tag{A.10}$$

It clearly holds for ($k = 1$, $n = 6$), for we may just select $q = m$ in eq. (A.10). It cannot hold for $n = 3$. In this case we have three irreps $k = 0 \pm 1$. Then, $q = (2k+2)m/n$ must be a natural number for $k = 0$, $m = 0, 1$, which is not the case ($q = 2m/3 \notin N$ for $m = 0, 1$). In table 1 we enclose the possible q values for the symmetry groups C_n from $n = 3$ up to $n = 10$ as a function of m. Since for a given group C_n the irrep label k_M is equal to the integer part of $n/2$, we have then a single possible k for C_3, two of them for C_4 and C_5, three for C_6 and C_7, etc.

As we can see in table 1, up to the symmetry group C_{10}, no ground-state anticrossing occurs except for ($n = 6$, $k = 1$) and ($n = 10$, $k = 2$). In other words, for the currently synthesized geometries, only the hexagonal one presents the ground-state anticrossing when the number of electron just fills the e_2^+ with two electrons. As discussed in previous sections, this anticrossing has deep physical consequences if the system is the high-correlation low-density regime.

REFERENCES

[1] Noborisaka J., Motohisa J., Hara S. and Fuku T., *Appl. Phys. Lett.*, **87** (2005) 093109.
[2] Fontcuberta i Morral A., Spirkoska D., Arbiol J., Heigoldt M., Morante J. R. and Abstreiter G., *Small*, **4** (2008) 899.
[3] Algra R. E., Hocevar M., Verheijen M. A., Zardo I., Immink G. G. W., van Enckevort W. J. P., Abstreiter G., Kouwenhoven L. P., Vlieg E. and Bakkers E. P. A. M., *Nano Lett.*, **11** (2011) 1690.
[4] Keplinger T. M. M., Stangl J., Wintersberger E., Mandl B., Kriegner D., Hol V., Bauer G., Deppert K. and Samuelson L., *Nano Lett.*, **9** (2009) 1877.
[5] Rudolph D., Funk S., Döblinger M., Morkötter S., Hertenberger S., Schweickert L., Becker J., Matich S., Bichler M., Spirkoska D., Zardo I., Finley J. J., Abstreite G. and Koblmüller G., *Nano Lett.*, **13** (2013) 1522.
[6] Royo M., Bertoni A. and Goldoni G., *Phys. Rev. B* , **87** (2013) 115316.
[7] Funk S., Royo M., Zardo I., Rudolph D., Morkötter S., Mayer B., Becker J., Bechtold A., Matich S., Döblinger M., Bichler M., Koblmüller G., Finley J. J., Bertoni A., Goldoni G. and Abstreiter G., *Nano Lett.*, **13** (2013) 6189.
[8] Lauhon L. J., Gudiksen M. S., Wang D. and Lieber C. M., *Nature*, **420** (2002) 57.
[9] Shen G., Chen D., Bando Y. and Golberg D., *J. Mater. Sci. Technol.*, **24** (2008) 541.
[10] Shen G. and Chen D., *Sci. Adv. Mater.*, **1** (2009) 353.
[11] Heigoldt M., Arbiol J., Spirkoska D., Rebled J. M., Conesa-Boj S., Abstreiter G., Peir F., Morante J. R. and Fontcuberta i Morral A., *J. Mater. Chem.*, **19** (2009) 840.
[12] Hasen J., Pfeiffer L. N., Pinczuk A., He S., West K. W. and Dennis B. S., *Nature*, **390** (1997) 54; Fasth C., Fuhrer A., Björk M. T. and Samuelson L., *Nano Lett.*, **5** (2005) 1487; Tatebayashi J., Ota Y., Ishida S., Nishioka M., Iwamoto S. and Arakawa Y., *Appl. Phys. Lett.*, **100** (2012) 263101.
[13] Fuhrer A., Lscher S., Ihn T., Heinzel T., Ensslin K., Wegscheider W. and Bichler M., *Nature*, **413** (2001) 822.
[14] Lorke A., Luyken R. J., Govorov A. O., Kotthaus J., García J. M. and Petroff P. M., *Phys. Rev. Lett.*, **84** (2000) 2223.
[15] Viefers S., Koskinen P., Deo P. S. and Manninen M., *Physica E*, **21** (2004) 1.
[16] Filikhin I., Suslov V. M. and Vlahovic B., *Physica E*, **33** (2006) 349.
[17] Chakraborty T. and Pietilainen P., *Phys. Rev. B*, **50** (1994) 8460.
[18] Barticevic Z., Pacheco M. and Latg A., *Phys. Rev. B*, **62** (2000) 6963.
[19] Climente J. I., Planelles J. and Jaskolski W., *Phys. Rev. B*, **68** (2003) 075307; Climente J. I., Planelles J. and Movilla J. L., *Phys. Rev. B*, **70** (2004) 081301.
[20] Ballester A., Planelles J. and Bertoni A., *J. Appl. Phys.*, **112** (2012) 104317.
[21] Lipparini L. E., *Modern Many-Particle Physics* (World Scientific, Singapore) 2008.
[22] Keyser U. F., Fühner C., Borck S., Haug R. J., Bichler M., Abstreiter G. and Wegscheider W., *Phys. Rev. Lett.*, **90** (2003) 196601.
[23] Emperador A., Pederiva F. and Lipparini E., *Phys. Rev. B*, **68** (2003) 115312.
[24] Niemelä K., Pietiläinen P., Hyvönen P. and Chakraborty T., *Europhys. Lett.*, **36** (1996) 533.
[25] Liu Y. M., Huang G. M. and Shi T. Y., *Phys. Rev. B*, **77** (2008) 115311.
[26] Kusmartsev F. V., Weisz J. F., Kishore R. and Takahashi M., *Phys. Rev. B*, **49** (1994) 16234.

PHYSICAL REVIEW B **91**, 115440 (2015)

Aharonov-Bohm oscillations and electron gas transitions in hexagonal core-shell nanowires with an axial magnetic field

Miquel Royo,[1,2,*] Carlos Segarra,[1] Andrea Bertoni,[2] Guido Goldoni,[2,3] and Josep Planelles[1]
[1]*Departament de Química Física i Analítica, Universitat Jaume I, E-12080 Castelló, Spain*
[2]*CNR-NANO S3, Institute for Nanoscience, Via Campi 213/a, 41125 Modena, Italy*
[3]*Department of Physics, Informatics and Mathematics, University of Modena and Reggio Emilia, Italy*
(Received 27 January 2015; revised manuscript received 17 March 2015; published 30 March 2015)

We use spin-density-functional theory within an envelope function approach to calculate electronic states in a GaAs/InAs core-shell nanowire pierced by an axial magnetic field. Our fully three-dimensional quantum modeling includes explicitly a description of the realistic cross section and composition of the sample, and the electrostatic field induced by external gates in two different device geometries: gate-all-around and back-gate. At low magnetic fields, we investigate Aharonov-Bohm oscillations and signatures therein of the discrete symmetry of the electronic system, and we critically analyze recent magnetoconductance observations. At high magnetic fields, we find that several charge and spin transitions occur. We discuss the origin of these transitions in terms of different localization and Coulomb regimes, and we predict their signatures in magnetoconductance experiments.

DOI: 10.1103/PhysRevB.91.115440 PACS number(s): 62.23.Hj, 75.47.−m, 71.10.Hf, 81.05.Ea

I. INTRODUCTION

Gated semiconductor nanowire (NW) devices represent flexible test beds to study transport phenomena in the quasi-one-dimensional quantum regime. In this context, InAs-based NWs offer privileged properties derived, for instance, from the light InAs electron effective mass, which enables the experimental observation of the subband spectrum quantization even in NWs of a relatively large section, [1–3] or from its large spin-orbit interaction and Landé factor [4,5]. This boosts their prospective applications in spintronics [6], even at relatively high temperature [7]. Furthermore, in this narrow-gap material, the Fermi energy, E_F, is pinned by surface states above the conduction-band edge [8], leading to an accumulation of electrons at the NW surface and facilitating the fabrication of Ohmic contacts [1,9].

The resulting tubular shape of the conducting channel points toward interesting quantum phenomena under external magnetic fields [10]. In particular, an axial field may lead to Aharonov-Bohm (AB) field-periodic modulation of the electron energy spectrum [11] and, if the phase-coherent length exceeds the perimeter of the NW, the observation of magnetoconductance oscillations [12,13]. Indeed, several observations of AB-like oscillations in magnetotransport experiments performed on radial heterostructures have been reported [14–18]. Recently, Gül *et al.* [16] observed flux-periodic magnetoconductance oscillations in GaAs/InAs core-shell NWs. The oscillations persisted at different density regimes, modulated by a back-gate, exhibiting phase shifts as the back-gate voltage was gradually increased. A field-periodic magnetoconductance has also been observed in the same system with superconductor contacts [17] and, after removal of the GaAs core, in a hollow InAs shell [18].

The single-crystal NW-based heterostructures investigated in these experiments have a prismatic hexagonal cross section. However, the experimental observations were analyzed in terms of simplified cylindrical electronic systems, and the potential induced by the back-gate voltage, which also removes the cylindrical symmetry, was neglected. Likewise, theoretical calculations dealing with radial electronic systems with an axial magnetic field usually assume a cylindrical symmetry [5,12,13,19,20]. Ferrari *et al.* [10] investigated the effect of an axial magnetic field in prismatic systems, but the single-particle model adopted did not allow for a direct comparison with experiments.

Such approximations are particularly severe in radial heterostructures, where coupling between the discrete (hexagonal in InAs or GaAs) symmetry and many-electron interactions leads to strongly inhomogeneously distributed electron gas and, in turn, to the coexistence of one-dimensional (1D) and 2D channels at the corners and facets of the hexagonal heterointerfaces [21–23]. Strong anisotropy-induced effects are predicted in this case, such as negative magnetoresistance in a transverse magnetic field [24] and symmetry-induced cancellation of the AB effect in hexagonal quantum rings [25]. The inhomogeneous electron gas localization was crucially exposed in the recent observation of intra- and interband excitations [23,26].

In this paper, we study the electronic states and magnetoconductance in GaAs/InAs core-shell NWs with an axial magnetic field within a spin-density-functional theory (SDFT) approach. Our fully 3D modeling explicitly includes the description of the quantum states within an envelope function approach with a realistic cross section and composition of the sample, and it includes the electrostatic field induced by external gates in two different device geometries, namely gate-all-around and back-gate. At low magnetic fields, we investigate the nature of the magnetoconductance oscillations, as measured in Ref. [16], predicting specific signatures of the discrete symmetry of the electronic system in the AB magnetoconductance oscillations, and justifying the observation of AB oscillations despite the broken symmetry induced by the back-gate voltage. At high magnetic fields, we found that several charge and spin transitions occur. We discuss the origin of these transitions in terms of different magnetic-field-induced localization and Coulomb regimes, and we predict their signatures in magnetoconductance experiments.

*mroyo@qfa.uji.es

II. THEORETICAL MODEL

Within a parabolic single-band envelope-function description, the effective Kohn-Sham Hamiltonian under an external magnetic field reads

$$\hat{H} = \frac{1}{2}\left(\hat{\mathbf{P}} - e\,\mathbf{A}(\mathbf{R})\right)\frac{1}{m^*(\mathbf{R})}\left(\hat{\mathbf{P}} - e\,\mathbf{A}(\mathbf{R})\right) + V_{\rm conf}(\mathbf{R}) + V_Z^\sigma(\mathbf{R}) + V_H(\mathbf{R}) + V_{\rm XC}^\sigma(\mathbf{R}). \quad (1)$$

Here, $\mathbf{R} = (x,y,z)$, $\hat{\mathbf{P}}$ is the momentum operator, $\mathbf{A}(\mathbf{R})$ is the vector potential, e is the elementary charge, and $m^*(\mathbf{R})$ is the material-dependent electron effective mass. $V_{\rm conf}(\mathbf{R})$ is the spatial confinement potential induced by the heterostructure, and $V_H(\mathbf{R})$ is the Hartree potential energy. The Zeeman energy $V_Z^\sigma(\mathbf{R})$ and the exchange-correlation potential $V_{\rm XC}^\sigma(\mathbf{R})$ depend on the the spin index $\sigma = \uparrow, \downarrow$ of the electrons.

We consider an infinitely long NW extending along the z direction. To describe an axial magnetic field, we adopt the symmetric gauge $\mathbf{A}(\mathbf{R}) = B/2(-y,x,0)$ (see Fig. 1 for axis definition). The axial field does not break the spatial invariance along the z axis. Therefore, the single-particle eigenfunctions of (1) can be written as $\Psi_{n,k,\sigma}(\mathbf{R}) = e^{ikz}\phi_{n,\sigma}(\mathbf{r})$, with $\mathbf{r} \equiv (x,y)$, n the principal quantum number, and k the wave number along direction z. Substituting $\Psi_{n,k,\sigma}(\mathbf{R})$ and $\mathbf{A}(\mathbf{R})$ in (1), we obtain the spin-dependent Kohn-Sham equation

$$\left[-\frac{\hbar^2}{2}\nabla_{\mathbf{r}}\frac{1}{m^*(\mathbf{r})}\nabla_{\mathbf{r}} + \frac{e\,B}{2\,m^*(\mathbf{r})}\hat{L}_z + \frac{e^2\,B^2}{8\,m^*(\mathbf{r})}(x^2+y^2) + v_{\rm conf}(\mathbf{r}) + v_Z^\sigma(\mathbf{r}) + v_H(\mathbf{r}) + v_{\rm xc}^\sigma(\mathbf{r})\right]\phi_{n,\sigma}(\mathbf{r}) = \epsilon_{n,k,\sigma}\,\phi_{n,\sigma}(\mathbf{r}). \quad (2)$$

Here, $\epsilon_{n,k,\sigma} = \varepsilon_{n,\sigma} + \frac{\hbar^2 k^2}{2m_z^*}$ includes the 1D parabolic dispersion along the z axis, and $\hat{L}_z = -i\,\hbar(x\,\frac{\partial}{\partial y} - y\,\frac{\partial}{\partial x})$ is the azimuthal angular momentum operator. To obtain Eq. (2), it is necessary to assume that the z component of the effective mass, m_z^*, does not depend on $\mathbf{r}$, i.e., on the material. This approximation is expected to have a small effect [27] and enables us to decouple the electron motion in the longitudinal and transverse directions.

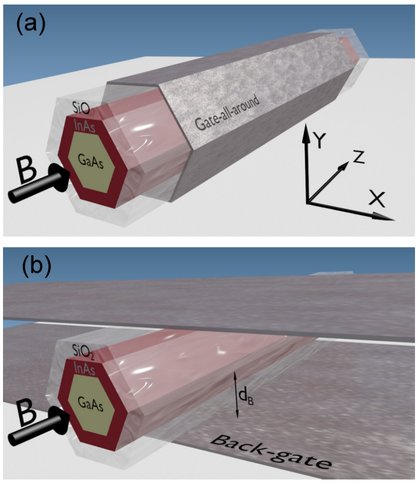

FIG. 1. (Color online) Schematics of a core-shell NW in the (a) gate-all-around and (b) back-gate device configurations.

The confinement potential $v_{\rm conf}(\mathbf{r})$ is set by the conduction-band offsets among the different materials that are radially modulated in the NW cross section. The Zeeman term is

$$v_Z^\sigma(\mathbf{r}) = g^*(\mathbf{r})\mu_B B\eta_\sigma, \quad (3)$$

where $g^*(\mathbf{r})$ is the material-dependent Landé factor, μ_B is the Bohr magneton, and $\eta_\sigma = +1/2(-1/2)$ for $\sigma = \uparrow (\downarrow)$.

The Hartree potential energy, $v_H(\mathbf{r})$, is calculated from the electrostatic potential, $v_H(\mathbf{r}) = -e\,\Phi(\mathbf{r})$, via the Poisson equation

$$\nabla\varepsilon(\mathbf{r})\nabla\Phi(\mathbf{r}) = \frac{1}{\varepsilon_0}e[n(\mathbf{r}) - n_D(\mathbf{r})]. \quad (4)$$

Here, $n(\mathbf{r}) = n_\uparrow(\mathbf{r}) + n_\downarrow(\mathbf{r})$ is the total free-electron charge density calculated, using the Kohn-Sham eigenstates obtained from Eq. (2), as

$$n_\sigma(\mathbf{r}) = \frac{1}{2\pi}\sum_n |\phi_{n,\sigma}(\mathbf{r})|^2\int_{-\infty}^{\infty} dk\, f(\epsilon_{n,k,\sigma} - E_F, T), \quad (5)$$

where

$$f(\epsilon_{n,k,\sigma} - E_F, T) = \frac{1}{1 + e^{(\epsilon_{n,k,\sigma} - E_F)/k_B T}} \quad (6)$$

is the Fermi occupation, with E_F, T, and k_B being, respectively, the Fermi energy, temperature, and Boltzmann constant. In Eq. (4), $n_D(\mathbf{r})$ is the density of static donors and $\varepsilon(\mathbf{r})$ is the material-dependent static dielectric constant.

The exchange and correlation potential, $v_{\rm xc}^\sigma(\mathbf{r})$, in the local-spin-density approximation (LSDA) [28] is given by the functional derivative

$$v_{\rm xc}^\sigma(\mathbf{r}) = \frac{\delta\varepsilon_{\rm xc}(n(\mathbf{r}),\zeta(\mathbf{r}))}{\delta n_\sigma(\mathbf{r})}, \quad (7)$$

where $\varepsilon_{\rm xc}(n(\mathbf{r}),\zeta(\mathbf{r}))$ is the exchange and correlation energy density, and

$$\zeta(\mathbf{r}) = \frac{n_\uparrow(\mathbf{r}) - n_\downarrow(\mathbf{r})}{n(\mathbf{r})} \quad (8)$$

is the local spin polarization. In the present paper, we use the correlation functional proposed by Perdew and Wang [29].

From the solutions of the Kohn-Sham equations, we also obtain the total free energy per unit length from [30]

$$E = \frac{1}{2\pi}\sum_{n,\sigma}\int_{-\infty}^{\infty} dk\,\epsilon_{n,k,\sigma}f_{n,k,\sigma} - \frac{1}{2}\int d\mathbf{r}\,v_H(\mathbf{r})n(\mathbf{r}) - \sum_\sigma\int d\mathbf{r}\,v_{\rm xc}^\sigma(\mathbf{r})n_\sigma(\mathbf{r}) + \int d\mathbf{r}\,\varepsilon_{\rm xc}(n(\mathbf{r}),\zeta(\mathbf{r})) + \frac{k_B T}{2\pi}\sum_{n,\sigma}\int_{-\infty}^{\infty} dk \times [f_{n,k,\sigma}\ln f_{n,k,\sigma} + (1 - f_{n,k,\sigma})\ln(1 - f_{n,k,\sigma})]. \quad (9)$$

Here, the second term on the right-hand side is the Hartree energy per unit length with the sign inverted, the fourth term is the exchange and correlation energy per unit length, and the last term is an entropy functional, where $f_{n,k,\sigma} = f(\epsilon_{n,k,\sigma} - E_F, T)$.

Equations (2)–(9) are solved iteratively until self-consistency is reached, which we consider to occur when two convergence criteria are simultaneously fulfilled in two consecutive iterations: first, the relative variation of the charge density is lower than 10^{-4} at any point of the discretization domain, and second, the relative variation in total free energy per unit length [Eq. (9)] is lower than 10^{-8}.

Equations (2) and (4) are numerically integrated in a real-space hexagonal domain. We use the same symmetry-preserving triangular grid with $\sim$1.14 points/nm^2 for both formulas, and we integrate Eqs. (2) and (4) with the methods of finite elements and finite volumes, respectively. Dirichlet boundary conditions are assumed in both cases, generally forcing the solutions to vanish at the boundaries. To simulate the effect of a gate-all-around [see Fig. 1(a)], the electrostatic potential in the Poisson equation is forced to take the gate voltage V_g at the domain boundaries. For a back-gate, we assume that the hexagonal domain is sandwiched by two flat infinite electrodes [see Fig. 1(b)] and the electrostatic potential is set at the gate voltage V_g at the bottom facet and zero at the top one. Accordingly, at the lateral boundaries the electrostatic potential is set to $F\,d_B(\mathbf{r})$, with F and $d_B(\mathbf{r})$ being, respectively, the electric field in the capacitor and the vertical distance from the boundary point to the bottom electrode [see Fig. 1(b)].

Finally, we also calculate the spin-projected free charge density per unit length,

$$\bar{n}_\sigma = \int n_\sigma(\mathbf{r}) d\mathbf{r}, \tag{10}$$

and the spin-projected ballistic conductance of the NW by means of the linear-response Landauer formula [31],

$$G^\sigma = \frac{e^2}{h} \sum_n \int_{\mathcal{B}_{n,\sigma}} -\frac{\partial f(E - E_F, T)}{\partial E}\, dE, \tag{11}$$

where the integral is performed along each energy spin-subband $\mathcal{B}_{n,\sigma}$. Note that the integrand makes a significant contribution only in the energy region close to the crossings of the subband with the Fermi energy E_F.

III. NUMERICAL RESULTS

We consider a GaAs/InAs core-shell hexagonal NW such as the one measured in Ref. [16] and outlined in Fig. 1. It is composed of a GaAs NW core with a minimal diameter of 100 nm and an InAs shell with a thickness of 25 nm. In addition, we include in the device an external 30-nm-thick layer of SiO_2 intended to simulate the insulating layer that separates the conducting channel from a back-gate in the experiment [16]. The GaAs core is doped with a homogeneous density of donors $n_D = 5 \times 10^{15}$ cm^{-3} (as in Ref. [16]). The material parameters used in the calculations are listed in Table I, where the conduction-band edge, E_{CB}, is obtained with the so-called 40:60 rule [32,33] from the band gap. Calculations have been conducted assuming a Fermi energy placed 75 meV above the InAs conduction-band edge (as in Ref. [16]), a temperature of 1.8 K, and the InAs effective mass as the constant mass factor

TABLE I. Material parameters used in the simulations; electron effective mass (m^*), dielectric constant (ε), effective Landé factor (g^*), and conduction-band edge (E_{CB}).

	GaAs	InAs	SiO_2
m^*	0.067	0.028	0.41
ε	13.18	15.5	3.9
g^*	− 0.484	− 14.3	2.0
E_{CB} (eV)	0.858	0.252	5.4

(m_z^*) arising in the parabolic dispersion of the 1D subbands [see Eq. (2)].

A. Low-magnetic-field regime: Magnetoconductance oscillations

In Fig. 2, we show the ground-state properties and magnetoconductance of the investigated core-shell NW at $V_g = 0$. The density distribution of conduction-band electrons [Fig. 2(b)] shows that charge is exclusively accumulated in the InAs shell and preferentially localized at the corners of the hexagonal section. As reported for several core-(multi)shell hexagonal NWs [21–23,34], such distribution is favored by Coulomb interactions, which tend to increase the interelectron distance. In Fig. 2(a), we show the energies of the spin-subband edges at different magnetic fields, hereafter referred to as magnetic spin-subbands (MSS), with spin up (↑-MSSs) and spin down (↓-MSSs). Due to the hexagonal symmetry of the self-consistent potential, the low-energy spectrum is at low fields formed out of groups of 12 MSSs arising from the six irreducible representations of the C_6 symmetry group. Each of these groups is further spin-split by the strong Zeeman effect

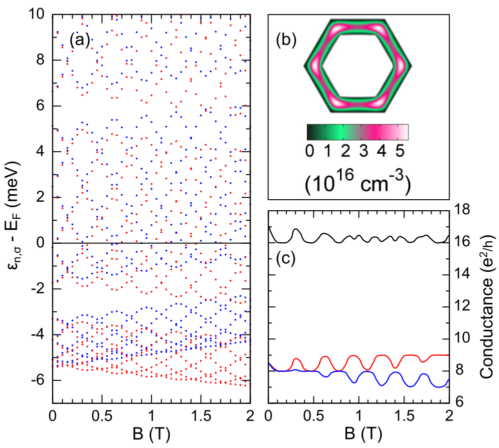

FIG. 2. (Color online) (a) Magnetic spin-subbands (MSS) in the low-field regime. Red and blue dots indicate ↓- MSSs and ↑-MSSs, respectively. The horizontal black line is set at E_F. (b) Self-consistent electron density distribution, $n(\mathbf{r})$, for the InAs/GaAs NW at $B = 0$. (c) Spin-projected magnetoconductances $G_\downarrow$ (red) and $G_\uparrow$ (blue), and total magnetoconductance (black).

forming two bunches, one of ↑-MSS and the other of ↓-MSSs, of six braided MSSs.

Within each group, the MSSs oscillate due to the AB effect, developing crossings with MSSs of their same group, which have different symmetry and/or different spin, and anticrossings with MSSs of neighboring groups with the same symmetry and spin. The oscillation period is $\sim$0.32 T. Since the calculated expectation value of the radial position, $\rho = \sqrt{x^2 + y^2}$, of the electron system is 66.36 nm, this periodicity corresponds fairly well to the periodicity of $\sim$0.30 T of the corresponding circular system.

In Fig. 2(c), we show the spin-projected magnetoconductances $G_\sigma(B)$ and the total magnetoconductance $G(B) = G_\uparrow(B) + G_\downarrow(B)$. Even though both $G_\sigma(B)$ exhibit regular flux-periodic oscillations, $G(B)$ only does so at very low fields. After the second oscillation cycle, the $G(B)$ periodicity is suppressed by the Zeeman effect, which breaks the periodicity of the MSS spectrum [12,13]. Apart from this, $G(B)$ does not differ qualitatively from that of an electron system in a cylindrical tube [12,13,16]. Indeed, in the present case, E_F lies within one group of braided MSSs, and the spectrum around E_F is similar to that of a cylindrical system. However, in an experiment E_F can be tuned by means of external gates. Therefore, we next study the system at different Fermi levels E_F or applied gate voltages V_g.

In Fig. 3, we show the effect of a gate-all-around voltage. This geometry tunes the position of the MSSs with respect to E_F, modulating the total density in the system while preserving the hexagonal symmetry. As shown in Fig. 3(a), the oscillatory behavior of the magnetoconductance due to the AB effect is absent at certain voltages. For instance, at $V_g = 80$ mV the magnetoconductance is flat. This is due to the positioning of E_F in the energy gap between the second and third group of MSSs, as shown in Fig. 3(c). Since E_F does not cross any MSS, the number of conducting channels is constant. Comparing Figs. 3(b) and 3(c), which correspond to $V_g = -60$ and 80 mV, respectively, we also observe that the gate voltage affects both the width of the MSSs groups and the gaps between them. In fact, V_g affects the total electron density and, hence, electron localization. As shown in the insets of Figs. 3(b) and 3(c), a $V_g > 0$ favors localization in the corners of the InAs shell, due to the larger electron-electron interaction. This, in turn, reduces the tunneling among states at the corners and, hence, the splittings within bunches of MSSs, while it increases the gaps between consecutive bunches [10]. Note that, since the latter gaps are a direct consequence of the discrete symmetry of the system, flat magnetoconductance is a direct signature of the hexagonal symmetry, which is more likely to be observed at positive gate voltages.

Observation of flat magnetoconductance when sweeping V_g has not been reported in the transport measurements performed hitherto on hexagonal NWs under axial magnetic fields [9,16–18]. However, in these works the electron density was normally modulated by a back-gate instead of a gate-all-around. The electrostatic field generated by a back-gate removes the hexagonal symmetry of the electronic system, and it could even destroy the doubly connected topology that originates the AB effect. Therefore, one may wonder why flux-periodic oscillations in the magnetoconductance are observed at all.

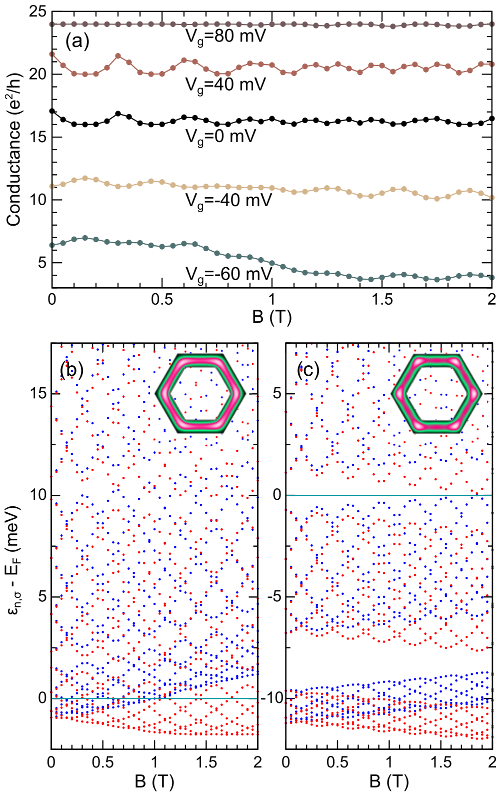

FIG. 3. (Color online) (a) Total magnetoconductance at selected gate-all-around voltages, V_g, as indicated by labels [the $V_g = 0$ curve is the same as the black line in Fig. 2(c)]. (b) MSSs at $V_g = -60$ mV. (c) MSSs at $V_g = 80$ mV. Insets in (b) and (c) show the corresponding $n(\mathbf{r})$.

To assess this point, in Fig. 4 we show the results of simulations performed at different back-gate voltages. As shown in the insets of Figs. 4(b) and 4(c), the applied voltage strongly reshapes the electron density distribution in the NW. At negative (positive) V_g the total density in the system is reduced (increased) and concentrated in the top (bottom) half of the InAs shell. However, whereas the doubly connected topology that results in AB oscillations is removed at sufficiently negative voltages (e.g., $V_g = -80$ mV), it is robust for $V_g > 0$. The origin of this difference can be appreciated from the corresponding MSSs [Figs. 4(b) and 4(c)]. The lowest-lying MSSs are strongly affected by the gate, losing the doubly connected topology and showing an almost linear dispersion with the magnetic field. Higher-energy MSSs, on the contrary, being more delocalized over the NW section, still show doubly connected topology. Since at $V_g = -80$ and -100 mV only low-lying MSSs are occupied [see Fig. 4(b)], the total electron density loses the doubly connected

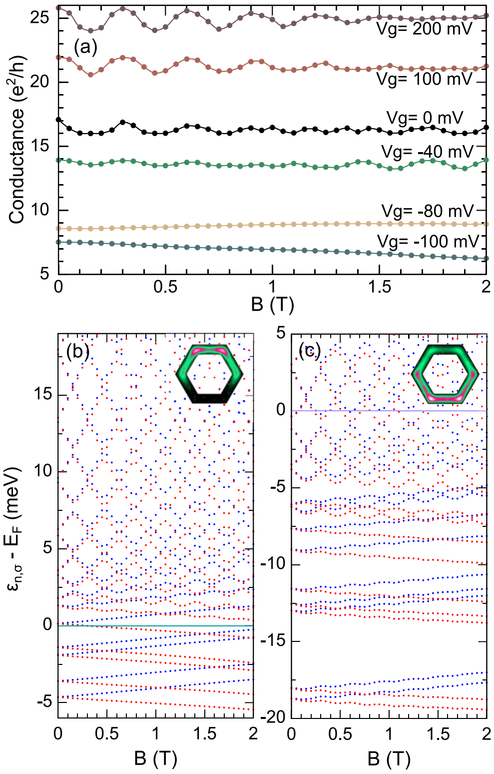

FIG. 4. (Color online) (a) Same as in Fig. 3 but for a back-gate device. (b) MSSs at $V_g = -80$ mV, (c) MSSs at $V_g = 200$ mV.

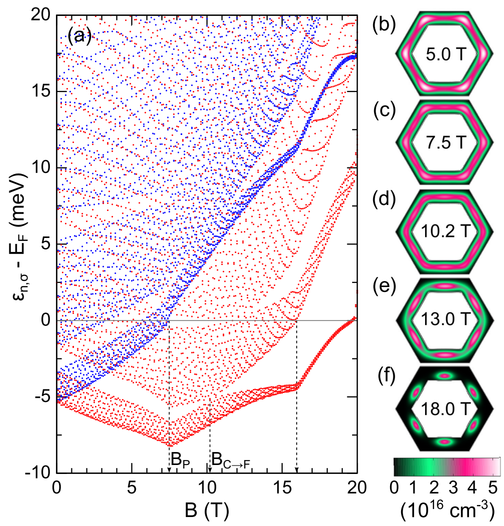

FIG. 5. (Color online) (a) MSSs up to complete charge depletion. Blue (red) dots are used for ↑-MSSs (↓-MSSs). The horizontal line indicates the position of E_F. Vertical dashed arrows indicate fields at which different spin/charge transitions occur (see text). (b)–(f) Self-consistent electron density distributions $n(\mathbf{r})$ at selected magnetic fields.

topology, and the corresponding magnetoconductance does not show AB oscillations. In contrast, at $V_g > 0$ several states with doubly connected topology are occupied, and the AB oscillations of the magnetoconductance persist [see Fig. 4(a)]. The latter is indeed the usual regime in magnetotransport experiments [16,17] where, therefore, periodic oscillations in the magnetoconductance are observed despite the symmetry reduction.

B. High-magnetic-field regime: Spin and charge transitions

We next study the high-magnetic-field regime, up to the limit of complete electron depletion, which occurs at $B \sim 20$ T in this sample. Figure 5 shows the MSSs and the self-consistent total electron density distributions at selected fields (spin-projected electron densities show only minor differences and are not shown here). All simulations in this section are performed at $V_g = 0$. The overall behavior of MSSs shows that, in addition to the diamagnetic shift, several transitions occur at discrete fields, as we discuss below.

The evolution of $n(\mathbf{r})$ in Figs. 5(b)–5(f) shows that the axial field induces a transition from an electron distribution localized at the corners [low field, Figs. 5(a) and 5(b)] to a distribution increasingly localized in the center of the facets [high field, Figs. 5(e) and 5(f)]. This charge reshaping is induced by the diamagnetic term [third term on the left-hand side of Eq. (2)], which constrains the electron density to adopt distributions with lower radius as the field is increased, counteracted by Coulomb interactions.

Such a corner-to-facet transition can be correlated with the evolution of the MSSs. In Fig. 5(a), the lowest-lying bunch of 12 MSSs at $B = 0$ corresponds to states localized at the corners, whereas the second set of states are localized at the facets for orthogonality. As the field is increased, Zeeman spin-splitting takes place and the two sets of six ↓-MSSs approach in energy, eventually overlapping at $B_{C\rightarrow F} \sim 10.2$ T. At this point, the 2D electron density integrated along the minimal (facet-to-facet) and maximal (corner-to-corner) diameter [22] is nearly the same [see Fig. 5(d)]. At $B > B_{C\rightarrow F}$, the six lowest ↓-MSSs are localized at the facets of the inner interface, while corner states are much higher in energy, corresponding to the third group of six ↓-MSS. The same transition occurs for ↑-MSS, however these states are already depopulated at the transition field.

Apart from this smooth spatial localization transition, two abrupt changes of slope appear in the calculated MSSs. The first one occurs at $B_P = 7.5$ T and corresponds to complete spin polarization, as demonstrated by the spin-projected electron densities $\bar{n}_\uparrow, \bar{n}_\downarrow$ shown in Fig. 6(a) and the corresponding spin polarization in Fig. 6(b), which marks a clear transition to a ferromagnetic state at B_P. Note that the total density

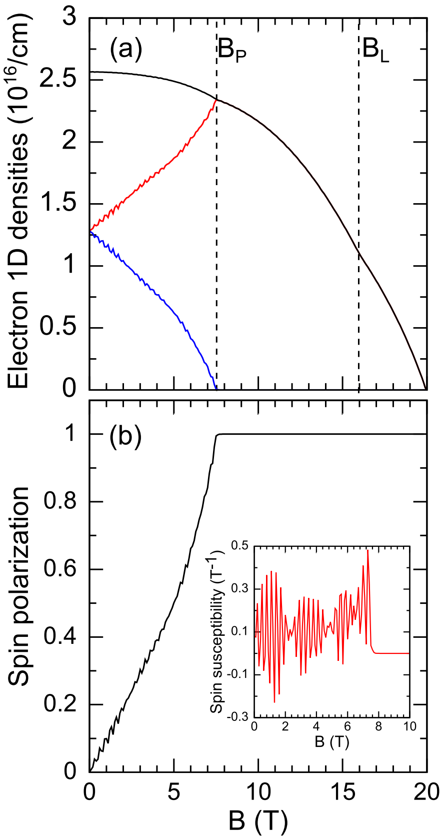

FIG. 6. (Color online) (a) Total density $\hat{n}$ (black lines) and spin-projected densities $\bar{n}_\uparrow$ (blue lines) and $\bar{n}_\downarrow$ (red lines) as a function of the field intensity B. Vertical dashed lines illustrate the transition fields in Fig. 5(a). (b) Spin polarization as a function of the magnetic field. Inset: spin susceptibility.

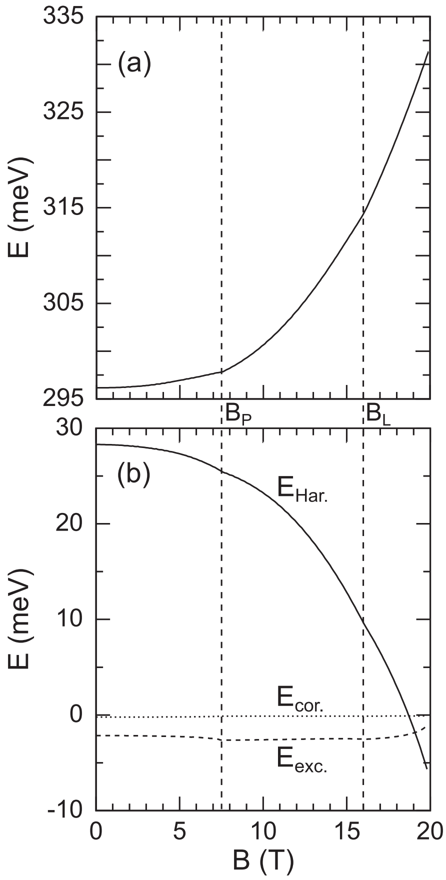

FIG. 7. (a) Total free energy per electron and (b) Hartree (solid), exchange (dashed), and correlation (dotted) energies per electron as a function of the field B. Vertical dashed lines indicate the transition fields in Fig. 5.

[black line in Fig. 6(a)] is reduced by the magnetic field with a roughly parabolic trend due to the depletion of successive, high-energy MSSs. However, the curve shows a change of slope at (B_P). At fields right after B_P, the rate at which the NW is depleted decreases momentarily. $\bar{n}_\downarrow$ passes abruptly from being increased to decreased at B_P, in agreement with the inversion of the $\downarrow$-MMSs slope exposed in Fig. 5(a).

The singular behavior of the spin polarization [Fig. 6(b)] is reminiscent of the first-order phase transition of a 2D electron gas with an in-plane magnetic field [35,36] (note that in our system, the Seitz radius $r_s \sim 0.07$ at zero field, which is a very weakly correlated regime), although it is difficult in our numerical treatment to establish whether it is a weakly first-order or continuous transition. The inset in Fig. 6(b) shows the spin susceptibility, i.e., the magnetic-field derivative of the spin polarization. This magnitude oscillates with the field as a consequence of the interplay between the AB effect and the Zeeman splitting, which produce short-period modulations of the spin densities.

At fields higher than B_P and $B_{C\to F}$, the MSSs shown in Fig. 5(a) rearrange in groups of six, which tend to form Landau-like bands. Finally, at a larger field $B_L = 16$ T the spectrum shows an additional transition. This corresponds to complete depletion of the incipient second Landau-like band. The transition is also marked by a weak but visible kink in $\bar{n}(B)$, as shown in Fig. 6(a), which, as for the ferromagnetic transition, indicates a sudden decrease in the depletion rate.

The free energy per electron and the many-electron energy contributions per electron are calculated dividing the corresponding magnitudes per unit length by the total electron density and plotted in Figs. 7(a) and 7(b), respectively. All energy contributions show weak kinks at B_P and B_L. The

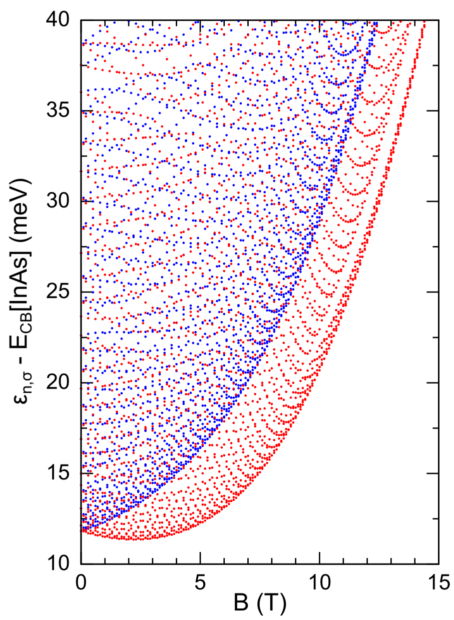

FIG. 8. (Color online) Noninteracting MSS edges with respect to the InAs conduction-band edge. Blue (red) dots are used for ↑-MSSs (↓-MSSs).

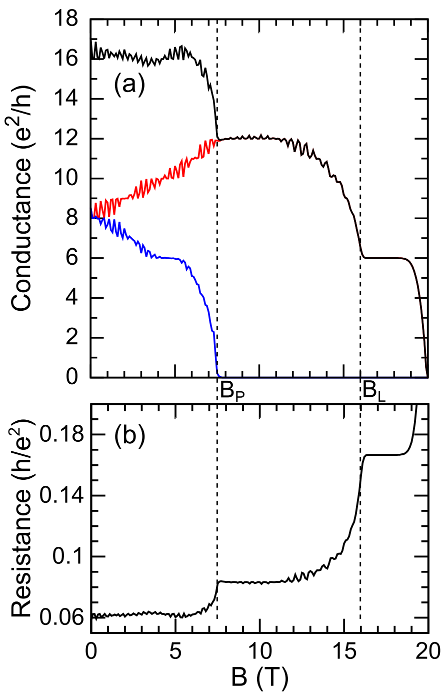

FIG. 9. (Color online) (a) Total magnetoconductance $G = G_\uparrow + G_\downarrow$ (black) and spin-resolved magnetoconductances, $G_\uparrow$ (blue) and $G_\downarrow$ (red). (b) Total magnetoresistance. Vertical dashed lines indicate the transition fields in Fig. 5.

free energy per electron increases with B due to the increase in magnetic confinement. However, the Hartree energy per electron [Fig. 7(b)] is reduced with B due to field-induced charge depopulation. At high magnetic fields, $B > 18.5$ T, the Hartree energy changes sign because the free-electron density is lower than the total density of static donors included in the simulation in the NW GaAs core. Note from Fig. 7(b) that the direct Hartree energy is one and two orders of magnitude larger than the exchange and correlation contributions, respectively, and therefore it will rule many-electron effects in the system.

To assess the role of many-electron contributions, in Fig. 8 we show the MSSs calculated in a noninteracting model, i.e., $v_H = 0$ and $v_{XC} = 0$. The MSSs follow in this case a smooth evolution with B, which evidences the many-electron origin of the two transitions at B_P and B_L in the SDFT calculation. We have also checked that such transitions persist when only $v_{XC} = 0$ (data not shown here), as was expected from the weak effect of the exchange and correlation contributions in the present system [see Fig. 7(b)].

Indeed, the transitions at B_P and B_L result from the balance between the two main energy contributions: the magnetic confinement, which increases the system energy with B, and the direct Coulomb or Hartree energy, which is reduced with B due to the charge depletion decreasing the system energy in this way. Thus, the first transition at B_P, which produces an inversion in the slope of the ↓-MSSs, can be understood as a transition between a regime, $B < B_P$, in which the reduction in Hartree energy dominates over the magnetic confinement, to another regime, $B > B_P$, in which the magnetic confinement dominates. The key difference before and after B_P is the magnitude of the Hartree energy that is lost per depleted state, which is larger at $B < B_P$. This is because when the system is not spin-polarized, the Hartree energy also arises from the interactions between electrons with antiparallel spin. The latter, which are absent in the ferromagnetic phase, are stronger than interactions between parallel spin electrons due to the lack of a Fermi hole.

The transition at B_L, which produces an abrupt increase of the MSSs, is also interpreted with similar arguments, i.e., the Hartree energy lost per depleted state is lower at $B > B_L$. This is due to the larger localization of the electron density at $B > B_L$ [cf. Figs. 5(e) and 5(f)], which entails a larger Fermi hole in the direct Coulomb interaction in this regime. Indeed, it has been proven that the conditional probability of finding an electron with a given spin when there is already another electron with the same spin nearby is lower when the former is localized [37].

The spin-projected magnetoconductances $G_\uparrow, G_\downarrow$ and the total magnetoconductance $G = G_\uparrow + G_\downarrow$ calculated from the SDFT modeling are shown in Fig. 9(a). Starting from low fields, the total magnetoconductance oscillates, due to oscillating MSSs crossing E_F, around an average value of 16

e^2/h up to a magnetic field $B \sim 6$ T. As the field approaches B_P, a sudden steplike reduction of four magnetoconductance units is caused by the sudden depletion of the lowest set of ↑-MSSs [see Fig. 5(a)] induced by the ferromagnetic transition.

At $B > B_P$, the magnetoconductance shows an almost flat plateau that lasts up to $B \sim 12$ T. This originates in the location of E_F in the symmetry-induced energy gap between the second and third group of six ↓-MSSs [see Fig. 5(a)]. As E_F merges in the second group of ↓-MSSs, the magnetoconductance starts to oscillate again, while reducing in average at an increasing rate approaching B_L. At $B > B_L$, E_F lies in the wide energy gap between the first and second Landau bands, hence G is constant.

Finally, $G(B)$ drops to zero when the first incipient Landau band crosses E_F and the conduction band gets completely depleted. In Fig. 9(b), we also plot the magnetoresistance $1/G(B)$ to illustrate the kink observed at B_P, which corresponds to that observed in experimental measures [38,39] of ferromagnetic transitions in flat *quasi*-2D electron systems under in-plane magnetic fields.

IV. SUMMARY AND CONCLUSIONS

We performed a SDFT study of the electronic structure and magnetoconductance of hexagonal core-shell NWs pierced by an axial magnetic field. Critically, our modeling goes beyond often employed cylindrical and/or single-particle approximations to simulate radial heterostructures, which neglect the strongly inhomogeneous, field-dependent distribution of the electron gas.

In the low-field regime ($B \lesssim 2$ T), we predict that AB magnetoconductance oscillations may disappear/resurface as a function of the gate-all-around voltage as a direct consequence of the presence of discrete symmetry-induced energy gaps. Our calculations also allowed us to critically analyze recent experiments [16,17] and justify the observation of AB oscillations in spite of the broken symmetry induced by the back-gate voltage.

In the high-magnetic-field regime, we found several field-induced transitions. First, the diamagnetic confinement induces a strong reshaping of the electron gas, which goes through a smooth transition from a low-field electron density distribution concentrated in the corners to a high-field distribution strongly localized in the facets of the radial heterojunction. Several experimental consequences of such reshaping are expected, for example in optical recombination experiments, due to the different localization of electrons and holes [26].

In addition, two abrupt transitions occur at discrete fields that are related to the depletion of higher MSSs. These depletions are either of the lowest antiparallel spin MSSs, leading to spin polarization, or of the second incipient Landau-like band with parallel spin. The origin of these transitions lies in the increase of the effective Fermi hole occurring at each transition, which affects the amount of Hartree energy that is lost per depleted state. As a consequence, such abrupt transitions are clearly marked in the calculated magnetoconductance by steplike behaviors.

ACKNOWLEDGMENTS

We acknowledge partial financial support from Universitat Jaume I, Projects No. P1-1B2011-01 and P1.1B2014-24, MINECO Project No. CTQ2011-27324, APOSTD/2013/052 Generalitat Valenciana Vali+d Grant (M.R.), and a MINECO FPU Grant (C.S.), from EU-FP7 Initial Training Network INDEX, and from Universitá di Modena e Reggio Emilia, through the Grant "Nano- and emerging materials and systems for sustainable technologies."

[1] S. Chuang, Q. Gao, R. Kapadia, A. C. Ford, J. Guo, and A. Javey, Nano Lett. **13**, 555 (2013).
[2] F. Vigneau, V. Prudkovkiy, I. Duchemin, W. Escoffier, P. Caroff, Y.-M. Niquet, R. Leturcq, M. Goiran, and B. Raquet, Phys. Rev. Lett. **112**, 076801 (2014).
[3] E. Halpern, A. Henning, H. Shtrikman, R. Rurali, X. Cartoixà, and Y. Rosenwaks, Nano Lett. **15**, 481 (2015).
[4] D. Liang and X. P. Gao, Nano Lett. **12**, 3263 (2012).
[5] A. Bringer and T. Schäpers, Phys. Rev. B **83**, 115305 (2011).
[6] S. Nadj-Perge, S. Frolov, E. Bakkers, and L. P. Kouwenhoven, Nature (London) **468**, 1084 (2010).
[7] F. Rossella, A. Bertoni, D. Ercolani, M. Rontani, L. Sorba, F. Beltram, and S. Roddaro, Nat. Nanotech. **9**, 997 (2014).
[8] H. Lüth, *Solid Surfaces, Interfaces and Thin Films*, 6 ed. (Springer-Verlag, Berlin, Heidelberg, 2015).
[9] C. Blomers, M. I. Lepsa, M. Luysberg, D. Grutzmacher, H. Luth, and T. Schapers, Nano Lett. **11**, 3550 (2011).
[10] G. Ferrari, G. Goldoni, A. Bertoni, G. Cuoghi, and E. Molinari, Nano Lett. **9**, 1631 (2009).
[11] J. Planelles, W. Jaskólski, and J. I. Aliaga, Phys. Rev. B **65**, 033306 (2001).
[12] Y. Tserkovnyak and B. I. Halperin, Phys. Rev. B **74**, 245327 (2006).
[13] T. O. Rosdahl, A. Manolescu, and V. Gudmundsson, Phys. Rev. B **90**, 035421 (2014).
[14] M. Jung, J. S. Lee, W. Song, Y. H. Kim, S. D. Lee, N. Kim, J. Park, M.-S. Choi, S. Katsumoto, H. Lee, and J. Kim, Nano Lett. **8**, 3189 (2008).
[15] T. Richter, C. Blömers, H. Lüth, R. Calarco, M. Indlekofer, M. Marso, and T. Schäpers, Nano Lett. **8**, 2834 (2008).
[16] Ö. Gül, N. Demarina, C. Blömers, T. Rieger, H. Lüth, M. I. Lepsa, D. Grützmacher, and T. Schäpers, Phys. Rev. B **89**, 045417 (2014).
[17] Ö. Gül, H. Y. Günel, H. Lüth, T. Rieger, T. Wenz, F. Haas, M. Lepsa, G. Panaitov, D. Grützmacher, and T. Schäpers, Nano Lett. **14**, 6269 (2014).
[18] T. Wenz, M. Rosien, F. Haas, T. Rieger, N. Demarina, M. I. Lepsa, H. Lüth, D. Grützmacher, and T. Schäpers, Appl. Phys. Lett. **105**, 113111 (2014).
[19] V. N. Gladilin, J. Tempere, J. T. Devreese, and P. M. Koenraad, Phys. Rev. B **87**, 165424 (2013).
[20] T. O. Rosdahl, A. Manolescu, and V. Gudmundsson, Nano Lett. **15**, 254 (2015).

[21] B. M. Wong, F. Léonard, Q. Li, and G. T. Wang, Nano Lett. **11**, 3074 (2011).

[22] A. Bertoni, M. Royo, F. Mahawish, and G. Goldoni, Phys. Rev. B **84**, 205323 (2011).

[23] S. Funk, M. Royo, I. Zardo, D. Rudolph, S. Morkötter, B. Mayer, J. Becker, A. Bechtold, S. Matich, M. Döblinger, M. Bichler, G. Koblmüller, J. J. Finley, A. Bertoni, G. Goldoni, and G. Abstreiter, Nano Lett. **13**, 6189 (2013).

[24] M. Royo, A. Bertoni, and G. Goldoni, Phys. Rev. B **87**, 115316 (2013).

[25] A. Ballester, C. Segarra, A. Bertoni, and J. Planelles, Europhys. Lett. **104**, 67004 (2013).

[26] J. Jadczak, P. Plochocka, A. Mitioglu, I. Breslavetz, M. Royo, A. Bertoni, G. Goldoni, T. Smolenski, P. Kossacki, A. Kretinin, H. Shtrikman, and D. K. Maude, Nano Lett. **14**, 2807 (2014).

[27] T. Ando, J. Phys. Soc. Jpn. **51**, 3893 (1982).

[28] The validity of the LSDA for the B values of interest was assessed in Ref. [40] by comparing the obtained results for a single QD with those given by current-spin-density-functional theory [41], which is better suited to study many-electron systems in magnetic fields.

[29] J. P. Perdew and Y. Wang, Phys. Rev. B **45**, 13244 (1992).

[30] K. Hirose, S.-S. Li, and N. S. Wingreen, Phys. Rev. B **63**, 033315 (2001).

[31] This formula assumes a fully ballistic regime, which is not exactly the experimentally attainable regime (although quasi-ballistic transmissions as large as 0.8 have been experimentally observed, even at room temperature, in InAs NW FETs [1]). We employ this simplified formula since it can surely yield a correct qualitative description of the magnetoconductance.

[32] S. Adachi (ed.), *Properties of Aluminum Gallium Arsenide, EMIS Datareviews Series No. 7* (INSPEC; The Institution of Electrical Engineers, London, 1993).

[33] N. Debbar, D. Biswas, and P. Bhattacharya, Phys. Rev. B **40**, 1058 (1989).

[34] G. Martínez-Criado, A. Homs, B. Alén, J. A. Sans, J. Segura-Ruiz, A. Molina-Sánchez, J. Susini, J. Yoo, and G.-C. Yi, Nano Lett. **12**, 5829 (2012).

[35] A. L. Subaşi and B. Tanatar, Phys. Rev. B **78**, 155304 (2008).

[36] Y. Zhang and S. Das Sarma, Phys. Rev. Lett. **96**, 196602 (2006).

[37] E. Matito, B. Silvi, M. Duran, and M. Solà, J. Chem. Phys. **125**, 024301 (2006).

[38] B. A. Piot, D. K. Maude, U. Gennser, A. Cavanna, and D. Mailly, Phys. Rev. B **80**, 115337 (2009).

[39] E. Tutuc, S. Melinte, E. P. De Poortere, M. Shayegan, and R. Winkler, Phys. Rev. B **67**, 241309 (2003).

[40] F. Ancilotto, D. G. Austing, M. Barranco, R. Mayol, K. Muraki, M. Pi, S. Sasaki, and S. Tarucha, Phys. Rev. B **67**, 205311 (2003).

[41] M. Ferconi and G. Vignale, Phys. Rev. B **50**, 14722 (1994).

Physica E 66 (2015) 234–237

Contents lists available at ScienceDirect

Physica E

journal homepage: www.elsevier.com/locate/physe

Control of electron spin–orbit anisotropy in pyramidal InAs quantum dots

C. Segarra, J. Planelles*, J.I. Climente[1]

Departament de Química Física i Analítica, Universitat Jaume I, E-12080 Castelló, Spain

HIGHLIGHTS

- We investigate the spin–orbit anisotropy of InGaAs pyramidal dots under in-plane magnetic fields.
- We show that the anisotropy found in dots like those of PRL 104, 246801 (2010) is due to the interplay between Rashba and Dresselhaus spin–orbit interaction.
- We show that controlling the QD height and (In,Ga) alloying provides a powerful tool to tailor the spin–orbit anisotropy.

ARTICLE INFO

Article history:
Received 18 July 2014
Received in revised form
17 October 2014
Accepted 21 October 2014
Available online 24 October 2014

Keywords:
Semiconductor
Nanostructure
Spin–orbit effect
Magnetic field

ABSTRACT

We investigate the electron spin–orbit interaction anisotropy of pyramidal InAs quantum dots using a fully three-dimensional Hamiltonian. The dependence of the spin–orbit interaction strength on the orientation of externally applied in-plane magnetic fields is consistent with recent experiments, and it can be explained from the interplay between Rashba and Dresselhaus spin–orbit terms in dots with asymmetric confinement. Based on this, we propose manipulating the dot composition and height as efficient means for controlling the spin–orbit anisotropy.

1. Introduction

In recent years, spin physics has become one of the most active branches in condensed matter physics due to its promising applications [1]. In particular, spin–orbit interaction (SOI) has been intensively investigated in semiconductor quantum dots (QDs) [2] in which confinement hinders many decoherence mechanisms and leads to long-lived spin states [3,4]. This makes these systems good candidates for spin-based technological applications in spintronics [5] and quantum information [6].

For electrons in zinc-blende semiconductor QDs, the most important mechanisms of SOI are known to be Rashba SOI [7], resulting from the structure inversion asymmetry, and Dresselhaus SOI [8], resulting from the bulk inversion asymmetry of the material itself. The Hamiltonians that describe both Rashba and Dresselhaus SOI present intrinsic anisotropy. A good understanding of such anisotropy is crucial to control and manipulate single electron spins via external electric or magnetic fields. One way to probe it is through examination of the spin anticrossings in the energy level spectrum, whose magnitude is proportional to the SOI intensity [9–11]. Taking profit of this, Takahashi and coworkers recently investigated SOI in self-assembled InAs QDs [12]. The choice of InAs is particularly interesting because of the strong SOI of this material, which makes it convenient for spin manipulation via external fields. Indeed, the possibility of controlling single spin-states in these systems has been demonstrated both electrically [13] and magnetically [12].

The experiment of Takahashi et al. showed that electrons in InAs QDs present pronounced in-plane SOI anisotropy. To this end, they used an in-plane magnetic field, whose direction was rotated over all possible azimuthal angles, ϕ. It was found that the angular dependence of the SOI strength fits the form of an absolute cosine function with an offset ϕ_0, $|\cos(\phi-\phi_0)|$. The origin of this dependence was tentatively ascribed to the QD elongated geometry along with the contribution of Rashba SOI [12]. Soon after, a theoretical work by Nowak et al. proposed an alternative explanation. They ascribed the origin of the offset to the combined action of Rashba and Dresselhaus SOI in elongated QDs [14]. This conclusion

* Corresponding author.
E-mail address: josep.planelles@uji.es (J. Planelles).
[1] *URL:* http://quimicaquantica.uji.es/ (J.I. Climente).

http://dx.doi.org/10.1016/j.physe.2014.10.030
1386-9477/

was based on a single-electron effective mass model where QDs are represented as simple cuboids and the confinement potential is separable, namely $V(r) = V_x(x) + V_y(y) + V_z(z)$. Because recent evidences have demonstrated that a realistic three-dimensional confinement is required for quantitative understanding of the SOI properties [15,16], one wonders to which extent this finding holds in the actual pyramidal-shaped QDs of the experiment.

In this work, we provide further insight on the SOI anisotropy of self-assembled InAs QDs. This is done by using fully three dimensional effective mass Hamiltonians, with inclusion of both Rashba and Dresselhaus SOI, electric and magnetic fields, and accurate modeling of pyramidal QD structures. We find that Rashba or Dresselhaus interaction alone does not explain the presence of the offset ϕ_0 in the angular magnetic field dependence even if the QD is anisotropic. Rather, it arises from the simultaneous presence of the two SOI terms. This confirms that the interpretation of Nowak and co-workers [14] holds in more realistic geometries. Knowing the origin of the SOI anisotropy, we set to explore the effect of the QD height and (In,Ga) composition. Since these two factors have a strong and selective influence on the strength of Dresselhaus and Rashba SOI, respectively, they can be used to tip the balance between the two SOI terms. As a result, we show that the magnitude of the angular offset ϕ_0 can be modulated over a wide range of values.

2. Theory

We study the conduction band electronic structure of semiconductor QDs within the effective mass and envelope function approximations. The three-dimensional single-electron Hamiltonian reads

$$H = \frac{\mathbf{p}^2}{2m^*} + V(\mathbf{r}) + \mathbf{Er} + H_Z + H_R + H_D \tag{1}$$

where m^* stands for the electron effective mass, $\mathbf{p} = -i\hbar\nabla + \mathbf{A}$ is the canonical momentum operator and $V(\mathbf{r})$ is the confining potential. Following the setup of Ref. [12], a magnetic field oriented in the xy plane and rotated an angle ϕ with respect to the x-axis is also included. Such a magnetic field has the form $\mathbf{B} = B(\cos\phi, \sin\phi, 0)$ and is described by the vector potential $\mathbf{A} = (zB\sin\phi, -zB\cos\phi, 0)$. The third term accounts for an externally applied electric field, which is directed along z in the experiments. Thus, $\mathbf{E} = (0, 0, E_z)$.

We also introduce the Zeeman term

$$H_Z = \frac{1}{2} g\mu_B \mathbf{B}\boldsymbol{\sigma} \tag{2}$$

where $\boldsymbol{\sigma}$ are the Pauli spin matrices, μ_B is the Bohr magneton and g is the electron g-factor.

The last two terms in Eq. (1) are additional terms resulting from the SOI [17]. The Rashba SOI is described by the Hamiltonian

$$H_R = \alpha_r E_z(\sigma_x p_y - \sigma_y p_x). \tag{3}$$

and the Dresselhaus SOI by the Hamiltonian

$$H_D = \beta_d[\sigma_x p_x(p_y^2 - p_z^2) + \sigma_y p_y(p_z^2 - p_x^2) + \sigma_z p_z(p_x^2 - p_y^2)] \tag{4}$$

Here, α_r and β_d are material-dependent coefficients determining the strength of the SOI in the conduction band [17].

The eigenvalue equation of Hamiltonian (1) is solved numerically using a finite-difference method on a three-dimensional grid.

3. Results and discussion

The system we consider is represented in Fig. 1. It consists of a pyramidal InAs QD similar to that used in Ref. [12]. The QD is grown on top of a GaAs wetting layer and is uncapped. Because the surface of uncapped QDs is usually oxidized, the tip can be considered as insulating and the QD is better described as a truncated pyramid [18]. The base of the QD is rectangular due to the electrostatic confinement induced by the side gates. We assume that the elongated direction (x-axis) is along the [100] crystallographic axis.

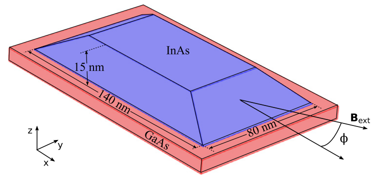

Fig. 1. Schematic representation of the uncapped InAs QD system. The dimensions of the QD considered in the simulations and the orientation of the magnetic field are also indicated. The upper base of the pyramid is 0.6 times the lower one.

Our first target is to understand the origin of the SOI angular dependence. Following Ref. [12] experiment, this is estimated from the magnitude of the spin anticrossing gap between the s-shell and the p-shell for different orientations of the magnetic field. The confining potential is defined by the conduction band offset between InAs and GaAs, $V_{\mathrm{InAs/GaAs}}$=0.69 eV [19], and the vacuum is treated by using a high potential barrier, V_{vacuum}=4 eV. A uniform composition of 66% In is assumed inside the QD, which takes into account the diffusion of Ga into the otherwise pure InAs material. Similar alloy compositions have been experimentally observed in other epitaxially grown InAs QDs [20,21]. The electron effective mass and the SOI coefficients are calculated using linear interpolation from the pure InAs and GaAs parameters [17,19]. The values used in the simulations are $m^* = 0.04m_0$ (m_0 is the free electron mass), α_r = 79.0 e Å^2 and β_d = 27.32 eV Å^3.

The magnitude of the electric field in the QD is roughly estimated to be $E_z = -15$ KV/cm [22], and we use this value in all our calculations. For the g-factor, we take the experimental value, $g = -4.1$, much smaller than the bulk value used in Ref. [14]. This shifts the spin anticrossing under study towards higher magnetic fields. Indeed, the dimensions and composition of the QD in Fig. 1 have been adjusted in order to match the magnetic field at which the anticrossing takes place in the experiment. Using the experimentally inferred g-factor is also consistent with recent work showing that the bulk g-factor is strongly reduced by quantum confinement [23].

3.1. SOI angular dependence

Fig. 2 illustrates the electron energy levels under an in-plane magnetic field oriented along the x direction ($\phi = 0$) in the absence of SOI. The labels near the lowest levels indicate the orbital symmetry at zero field (irreducible representation of the C_{2v} group) and the spin of each state. In this case, the lowest spin-down state ($|A_1\rangle|\downarrow\rangle$) and the first excited spin-up state ($|B_1\rangle|\uparrow\rangle$) can cross (see dashed rectangle). As mentioned above, the dimensions and composition of our QD are fitted to reproduce the experimental field of the anticrossing, $B_{AC} \approx 11.5$ T. On doing this, we also reproduce the experimental anticrossing field for B aligned along y ($\phi = 90$), which takes place at $B_{AC} \approx 10$ T due to the stronger confinement – not shown – [22].

When SOI is included, the intersection of the states we consider turns into an anticrossing. The inset of Fig. 2 shows the anticrossing formed in the presence of SOI. We define the anticrossing energy E_{AC} as the minimal separation between the two states at the avoided crossing. It is worth noting that such anticrossing has been well studied in circular QDs, where only Rashba SOI can

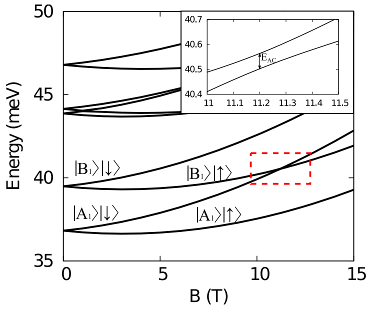

Fig. 2. Electron energy spectrum as a function of the magnetic field in the absence of SOI. The magnetic field is oriented in the x direction, $\phi = 0$. The crossing of electron states we examine is pointed out by the dashed red box. The labels denote the orbital and spin symmetry at zero field and zero SOI. Inset: avoided crossing when both Dresselhaus and Rashba SOI are present. (For interpretation of the references to color in this figure caption, the reader is referred to the web version of this paper.)

couple the two states [10,11,24–27]. As we shall see next, in pyramids the lower symmetry implies that Dresselhaus SOI can also contribute.

In Fig. 3, we show the magnitude of the anticrossing energy when Rashba and Dresselhaus SOI mechanisms are present individually and also simultaneously. In all three curves there is a clear dependency between E_{AC} and the magnetic field orientation revealing the SOI anisotropy. When only Rashba SOI is present, the anticrossing is maximum when **B** is oriented parallel to the x-axis ($\phi = 0$) and it decreases with the rotation of **B** until it cancels out at $\phi = 90$. For this orientation, the SOI quenches and the states cross. For Dresselhaus SOI the behavior is the opposite instead. E_{AC} is zero at $\phi = 0$ and it becomes maximum at $\phi = 90$. The results in Fig. 3 can be fitted well by the absolute value of a cosine (sine) function for the Rashba (Dresselhaus) SOI.

When both contributions are present at the same time, the anticrossing energy has a similar form compared with the single SOI cases, but the singular points are no longer found when **B** is aligned with the principal axes of the dot. In this case, the minimum appears at $\phi \approx 57$ and the maximum at $\phi \approx 147$. Note that the curve including both terms can be obtained qualitatively as the absolute value of the subtraction (addition) of the individual curves for $0 < \phi < 90$ ($90 < \phi < 180$). Then, the minimum takes place at $0 < \phi < 90$ when the two single SOI curves cross since the two terms cancel each other out. The results can be fitted by the absolute value of a cosine function with an offset ϕ_0, $E_{AC} \propto |\cos(\phi - \phi_0)|$. The extent of ϕ_0 is determined by the relative strength of the Rashba and Dresselhaus SOI contributions. In the limit of Rashba SOI only, $\phi_0 = 0$, and in the limit of Dresselhaus SOI only, $\phi_0 = 90$.

Fig. 3 shows that the finite value of ϕ_0 observed in experiments [12] can only occur when both SOI terms are present simultaneously. This result confirms that the explanation given by Nowak et al. [14] for cuboidal QDs holds also in more realistic geometries.

Determining the precise value of ϕ_0 in a QD thus depends on the balance between Rashba and Dresselhaus SOI terms. Obviously, knowledge on the angle where the spin–orbit coupling between two states cancels out is of interest for spin control and enhanced spin lifetimes [28]. Therefore, detailed understanding on the structural parameters affecting its value is desirable. One can see from Hamiltonians (3) and (4) that rotating the anisotropic confinement potential of the QD with respect to the crystallographic axes leads to changes in the weight of the SOI terms. This was shown to be an important control parameter of the SOI anisotropy in Ref. [14]. In what follows, we discuss two additional factors which are equally important, namely the diffusion of Ga into the InAs dot and the height of the dot.

3.2. Dependence on the QD composition

Self-assembled InAs/GaAs QDs experience substantial diffusion of Ga from the GaAs matrix into the InAs islands during the growth process, which leads to significant variations in the QD composition [20,21,29]. In this section we investigate how this affects the SOI anisotropy. Four InGaAs alloys with a uniform concentration, ranging from 50% In to 100% In, are considered. To this end, effective masses and SOI parameters α_r and β_d in Eq. (1) are linearly interpolated from their pure values [19]. The results including both Rashba and Dresselhaus SOI are summarized in Fig. 4. As can be seen, decreasing the In concentration not only visibly reduces the magnitude of the spin anticrossings gap E_{AC} but it also reduces the angle where the two SOI terms cancel out.

This result can be understood considering the value of Rashba and Dresselhaus parameters of the pure materials. InAs and GaAs parameters for Dresselhaus SOI are similar ($\beta_d^{InAs} = 27.18$ eV Å^3 and $\beta_d^{GaAs} = 27.58$ eV Å^3) [17]. Thus, the contribution of this term remains approximately the same for all InAs/GaAs alloys. By contrast, the parameters for Rashba SOI are very different ($\alpha_r^{InAs} = 117.1$ e Å^2 and $\alpha_r^{GaAs} = 5.026$ e Å^2) [17] so that the strength of the Rashba term decreases with decreasing In composition. As a

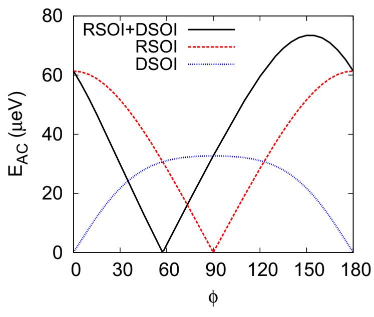

Fig. 3. Anticrossing energy E_{AC} as a function of the in-plane magnetic field orientation ϕ. Results including only Dresselhaus SOI (blue dotted line), only Rashba SOI (red dashed line) and both Dresselhaus and Rashba SOI (black solid line) are presented. (For interpretation of the references to color in this figure caption, the reader is referred to the web version of this paper.)

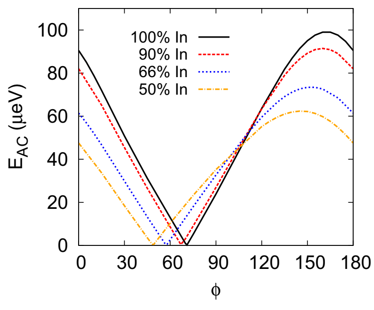

Fig. 4. Anticrossing energy vs. magnetic field orientation with both SOI contributions present. Results for different QD compositions are shown: 100% In (black solid line), 90% In (red dashed line), 66% In (blue dotted line) and 50% In (orange dash-dotted line). (For interpretation of the references to color in this figure caption, the reader is referred to the web version of this paper.)

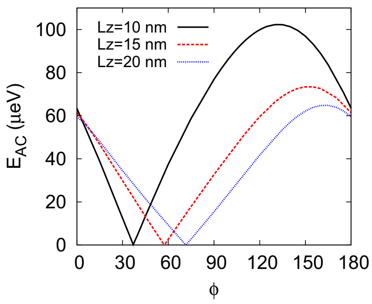

Fig. 5. Anticrossing energy as a function of the magnetic field orientation with both SOI. Results for a QD height of 20 nm (blue dotted line), 15 nm (red dashed line) and 10 nm (black solid line) are presented. (For interpretation of the references to color in this figure caption, the reader is referred to the web version of this paper.)

consequence, Ga diffusion shifts the zero SOI angle towards the Dresselhaus limit, $\phi = 0$.

3.3. *Effect of the QD height*

We next explore the influence of the QD height on the anticrossing gap. The results, summarized in Fig. 5, compare the SOI anisotropy of the QD studied so far (where the height is $L_z = 15$ nm), with a shorter ($L_z = 10$ nm) and a taller ($L_z = 20$ nm) QD. We can see in this figure that while the global shape of the SOI dependence on the magnetic field does not change with the height, the anticrossing gap and the zero SOI angle do change. In particular, with the increasing L_z the magnitude of E_{AC} decreases while the zero SOI angle increases.

This behavior can be qualitatively understood by considering the QD as a quasi-2D structure, where confinement along z is much stronger than that in the xy plane. One can then separate adiabatically the in-plane and vertical motions. By considering that only the lowest z state contributes to the low-energy spectrum, and integrating over this degree of freedom, the Dresselhaus Hamiltonian of Eq. (4) simplifies to

$$H_D = d^c \langle p_z^2 \rangle (\sigma_y p_y - \sigma_x p_x). \tag{5}$$

where we have assumed $\langle p_z \rangle = 0$ and neglected terms which do not involve $\langle p_z^2 \rangle$. Because $\langle p_z^2 \rangle \propto 1/L_z^2$, Eq. (5) reveals that the Dresselhaus SOI term tends to decrease with QD height. By contrast, the height barely affects the Rashba SOI term, see Eq. (3). As a result, increasing L_z reduces the overall SOI strength and shifts the zero SOI angle towards the Rashba SOI limit, $\phi = 90$.

It is worth pointing out that the results of Fig. 5 are obtained with a fully 3D, cubic Dresselhaus Hamiltonian, without the approximations of Eq. (5). This is important for a quantitative analysis, as the strong magnetic fields where spin anticrossings take place ($B \approx 10$ T) already imply comparable magnetic and spatial confinement in the growth direction. This has been found to affect the electron SOI anisotropy in related systems [28].

4. Conclusions

We have shown that the anisotropy of the SOI in InGaAs QDs subject to in-plane magnetic fields is severely affected by the QD height and the (In,Ga) alloying. This is because the anisotropy is determined by the interplay between Rashba and Dresselhaus SOI. In particular, the SOI between two electron states is suppressed for field angles where the coupling strength induced by the two SOI terms is balanced.

The amount of Ga diffusion into the self-assembled QDs provides direct control on the strength of the Rashba SOI, and it can be determined through the growth temperature [29]. In turn, the QD height provides direct control on the strength of the Dresselhaus SOI, and it can be determined using e.g. In flux techniques [30]. Therefore, we conclude that the two parameters offer an excellent control knob to tailor the SOI anisotropy of self-assembled QDs.

Acknowledgments

This work was supported by UJI-Bancaixa Project no. P1-1B2011-01, MINECO Project no. CTQ2011-27324, and FPU Grant (C. Segarra).

References

[1] D.D. Awschalom, D. Loss, N. Samarth, Semiconductor Spintronics and Quantum Computing, Springer, New York, 2002.
[2] R. Hanson, L. Kouwenhoven, J. Petta, S. Tarucha, L. Vandersypen, Rev. Mod. Phys. 79 (2007) 1217.
[3] A.V. Khaetskii, Y.V. Nazarov, Phys. Rev. B 64 (2001) 125316.
[4] M. Wu, J. Jiang, M. Weng, Phys. Rep. 493 (2010) 61.
[5] S. Datta, B. Das, Appl. Phys. Lett. 56 (1990) 665.
[6] D. Loss, D.P. DiVincenzo, Phys. Rev. A 57 (1998) 120.
[7] Y.A. Bychkov, E.I. Rashba, J. Phys. C: Solid State Phys. 17 (1984) 6039.
[8] G. Dresselhaus, Phys. Rev. 100 (1955) 580.
[9] O. Voskoboynikov, C. Lee, O. Tretyak, Phys. Rev. B 63 (2001) 165306.
[10] C. Destefani, S.E. Ulloa, G. Marques, Phys. Rev. B 69 (2004) 125302.
[11] D.V. Bulaev, D. Loss, Phys. Rev. B 71 (2005) 205324.
[12] S. Takahashi, R. Deacon, K. Yoshida, A. Oiwa, K. Shibata, K. Hirakawa, Y. Tokura, S. Tarucha, Phys. Rev. Lett. 104 (2010) 246801.
[13] A.J. Bennett, M.A. Pooley, Y. Cao, N. Sköld, I. Farrer, D.A. Ritchie, A.J. Shields, Nat. Commun. 4 (2013) 1522.
[14] M. Nowak, B. Szafran, F. Peeters, B. Partoens, W. Pasek, Phys. Rev. B 83 (2011) 245324.
[15] Y. Kanai, R. Deacon, S. Takahashi, A. Oiwa, K. Yoshida, K. Shibata, K. Hirakawa, Y. Tokura, S. Tarucha, Nat. Nanotechnol. 6 (2011) 511.
[16] S. Takahashi, R. Deacon, A. Oiwa, K. Shibata, K. Hirakawa, S. Tarucha, Phys. Rev. B 87 (2013) 161302.
[17] R. Winkler, Spin–Orbit Coupling Effects in Two-Dimensional Electron and Hole Systems, Springer, Berlin, 2003.
[18] T. Johal, R. Rinaldi, A. Passaseo, R. Cingolani, A. Vasanelli, R. Ferreira, G. Bastard, Phys. Rev. B 66 (2002) 075336.
[19] I. Vurgaftman, J. Meyer, L. Ram-Mohan, J. Appl. Phys. 89 (2001) 5815.
[20] M. Müller, A. Cerezo, G. Smith, L. Chang, S. Gerstl, Appl. Phys. Lett. 92 (2008) 233115.
[21] A. Giddings, J. Keizer, M. Hara, G. Hamhuis, H. Yuasa, H. Fukuzawa, P. Koenraad, Phys. Rev. B 83 (2011) 205308.
[22] S. Takahashi, R. Deacon, K. Yoshida, A. Oiwa, K. Shibata, K. Hirakawa, Y. Tokura, S. Tarucha, Phys. Rev. Lett. 104 (2010) 246801, See Supplemental Material.
[23] J. Van Bree, A.Y. Silov, P. Koenraad, M. Flatté, C. Pryor, Phys. Rev. B 85 (2012) 165323.
[24] T. Chakraborty, P. Pietiläinen, Phys. Rev. Lett. 95 (2005) 136603.
[25] P. Pietiläinen, T. Chakraborty, Phys. Rev. B 73 (2006) 155315.
[26] A. Manaselyan, T. Chakraborty, Europhys. Lett. 88 (2009) 17003.
[27] A. Manaselyan, A. Ghazaryan, T. Chakraborty, Europhys. Lett. 99 (2012) 17009.
[28] P. Stano, J. Fabian, Phys. Rev. Lett. 96 (2006) 186602.
[29] J. Garcıa, T. Mankad, P. Holtz, P. Wellman, P.M. Petroff, Appl. Phys. Lett. 72 (1998) 3172.
[30] Z. Wasilewski, S. Fafard, J. McCaffrey, J. Cryst. Growth 201 (1999) 1131.

THE JOURNAL OF PHYSICAL CHEMISTRY C
Article
pubs.acs.org/JPCC

Electron Spin Relaxation in 3D Quantum Dots: Geometrical Suppression of Dresselhaus and Rashba Spin–Orbit Interaction

Josep Planelles,* Juan I. Climente, and Carlos Segarra

Departament de Química Física i Analítica, Universitat Jaume I, Castelló de la Plana, Spain

Supporting Information

ABSTRACT: We investigate the electron spin relaxation between Zeeman sublevels of fully three-dimensional quantum dots. By going beyond the usual two-dimensional description of Rashba and Dresselhaus spin–orbit interactions (SOI), we provide a general overview of the effect of the quantum dot shape. It is shown that, in spherical quantum dots, the Dresselhaus SOI is severely suppressed, leading to slow relaxation rates and a strong (B^9) dependence on the magnetic field.

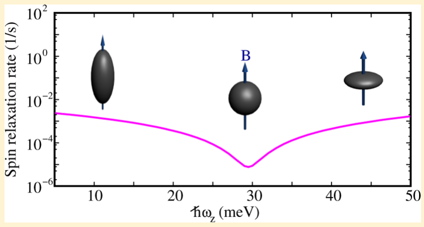

INTRODUCTION

A major issue for the development of spintronic, optical, and quantum information devices based on semiconductor nanostructures is to assess the effect of quantum confinement on the spin–orbit coupling.[1] Quantum confinement has a profound influence on the orbital motion of electrons, which is then felt by the spin degree of freedom through spin–orbit interactions (SOI). Thus, as observed soon after the fabrication of two-dimensional electron gases, tailoring the confinement provides unprecedented control on the electron spin, revealing new spin physics and spin-based applications.[2,3] Much of this knowledge has been transferred to the study of SOI effects in quasi-two-dimensional (electrostatic or self-assembled) quantum dots (QDs), enabling full control over individual spins.[4−6] This has opened perspectives of fundamental physics studies as well as several potential applications, ranging from single spin spintronic devices to solid-state quantum bits.[6−8]

While most previous studies of SOI effects in QDs have dealt with two-dimensional systems, where confinement in the growth direction is strong, recent experiments have started addressing the spin dynamics of colloidal QDs, where the fully three-dimensional quantum confinement can be tailored to form a variety of shapes, including spheres and elongated rods.[9−12] Spin relaxation in the presence of a magnetic field (be it external or effective internal, as that splitting dark and bright excitons) is generally driven by acoustic phonons and SOI.[6,13] Structural anisotropies are known to have important consequences on both of these factors.[6,14−17] Therefore, properly accounting for the 3D nature of SOI becomes essential to understand the properties and the possibilities of these systems.

In this work, we probe the effect of the vertical confinement on the electron spin relaxation between Zeeman sublevels of zinc-blende QDs. As compared to the well-established case of quasi-2D systems, the additional degree of freedom brings about qualitatively different behavior. This allows us to generalize the role of the interaction between quantum confinement and SOI in the spin dynamics. In particular, we determine the confinement anisotropy regimes that maximize and minimize the spin lifetime (T_1), as well as the dependence on external fields.

METHODS

The spin relaxation due to single-phonon emission is calculated from a Fermi golden rule as[6]

$$\frac{1}{T_1} = \frac{2\pi}{\hbar}\sum_{\lambda\mathbf{q}} |M_\lambda(\mathbf{q})\langle f|e^{-i\mathbf{qr}}|i\rangle|^2 \times \delta(\Delta_{fi} + E_q) \tag{1}$$

Here, $M_\lambda(\mathbf{q})$ is a measure of the electric field strength of a bulk acoustic phonon with wave vector $\mathbf{q}$ and electron–phonon interaction mechanism λ (see ref 17 for details). $|i\rangle$ and $|f\rangle$ are the initial and final electron states, Δ_{fi} is their energy splitting and E_q the phonon energy. For transitions between Zeeman sublevels, Δ_{fi} is small, and we are in the linear dispersion regime of phonons, where $E_q = \hbar c_\alpha q$ (c_α is velocity of sound for the phonon branch α). We describe the electron states in spheroidal QDs subject to a magnetic field along the z axis $\mathbf{B} = (0,0,B)$ and an electric field with arbitrary direction $\boldsymbol{\varepsilon}$. The Hamiltonian reads

$$H = \sum_{j=x,y,z} H_{HO}(j) + e\boldsymbol{\varepsilon}\mathbf{r} + \frac{1}{2}g\mu B\sigma_z + H_{SOI} \tag{2}$$

Here, $H_{HO}(j)$ is the harmonic oscillator Hamiltonian, $H_{HO}(j) = p_j^2/2m^* + 1/2m^*\omega_j^2 j^2$, where m^* stands for the effective mass and ω_j for the frequency of the confining parabola. The canonical momentum $p_j = k_j + eA_j$, where $k_j = -i\hbar d/dj$, e is the electron charge, and A is the vector potential in the symmetric

Received: September 21, 2012
Revised: October 31, 2012
Published: November 5, 2012

dx.doi.org/10.1021/jp309389p | J. Phys. Chem. C 2012, 116, 25143−25146

gauge, $A = B/2(-y,x,0)$. It is worth noting that the magnetic confinement leads to modified frequencies of the in-plane confining parabola, $\tilde{\omega}_j(B) = (\omega_j^2 + \omega_c^2)^{1/2}$, where $j = x,y$, and $\omega_c = eB/2m^*$ is the cyclotron frequency. The second term in eq 2 represents the electric field potential. The third term is the Zeeman splitting, with g standing for the Landé factor, μ for the Bohr magneton, and σ_z the spin projection on the direction of $\mathbf{B}$, $|\uparrow\rangle$ or $|\downarrow\rangle$. The fourth term accounts for the SOI, which mixes electron states with opposite spin projections. This term is essential for spin relaxation to take place, as phonons cannot couple states with opposite spin, i.e., $\langle\uparrow| e^{-i\mathbf{qr}} |\downarrow\rangle = 0$.

For electrons in zinc-blende semiconductors, the dominant SOI mechanisms are known to be the Dresselhaus spin−orbit interaction (DSOI), originating in the inversion asymmetry of the crystal cell, and the Rashba spin−orbit interaction (RSOI), originating in the structural asymmetry when subject to an electric field.[2] We then take $H_{\mathrm{SOI}} = H_{\mathrm{D}} + H_{\mathrm{R}}$, where

$$H_{\mathrm{D}} = d[\mathrm{p}_x(\mathrm{p}_y^{\ 2} - \mathrm{p}_z^{\ 2})\sigma_x + \mathrm{p}_y(\mathrm{p}_z^{\ 2} - \mathrm{p}_x^{\ 2})\sigma_y + \mathrm{p}_z(\mathrm{p}_x^{\ 2} - \mathrm{p}_y^{\ 2})\sigma_z] \tag{3}$$

$$H_{\mathrm{R}} = r\boldsymbol{\sigma}(\mathbf{p} \times \boldsymbol{\varepsilon}) \tag{4}$$

Here, d and r are material-specific prefactors determining the strength of SOI, and σ_j are the Pauli spin matrices.

Hamiltonian (eq 2) is solved by rewriting all derivatives and coordinates in terms of harmonic oscillator ladder operators and then projecting it onto a basis formed by oscillator eigenstates. The resulting electron states are of the form $|m\rangle = \sum_{s,\sigma_z} c^m_{s\sigma_z} |\nu_x,\nu_y,\nu_z\rangle|\sigma_z\rangle$, where $\nu_j = 0,1,2$, etc., is the quantum number of the 1D harmonic oscillator along the j direction, and s is the combined orbital quantum number, $s = (\nu_x,\nu_y,\nu_z)$. The phonon scattering matrix elements $G_{n,m} = \langle n|e^{-i\,q_j j}|m\rangle$ can be evaluated from the analytical expression $G_{0,0} = e^{(a/2)^2}$, where $a = iql_0$ and $l_0 = (\hbar/(m\tilde{\omega}_j))^{1/2}$ is the characteristic oscillator length in the j direction. The following recursive formulas are then used:

$$G_{n+1,m} = \frac{1}{\sqrt{n+1}} \times \left(\sqrt{m}\, G_{n,m-1} - \frac{a}{\sqrt{2}} G_{n,m}\right) \tag{5}$$

$$G_{n,m+1} = \frac{1}{\sqrt{m+1}} \times \left(-\frac{a}{\sqrt{2}} G_{n,m} + \sqrt{n}\, G_{n-1,m}\right) \tag{6}$$

For the calculations, we take In(Ga)As parameters.[18] The Rashba and Dresselhaus constants for this material are well-known from experiments in 2D systems.[2] Qualitatively similar results can be expected for other zinc-blende materials such as CdSe (often used in nanocrystals), albeit wider gaps would weaken SOI effects.

RESULTS AND DISCUSSION

Dresselhaus SOI. We start by investigating the influence of the vertical confinement, ω_z, in QDs subject to DSOI. Figure 1a shows the spin relaxation rate for QDs at $B = 1$ T. Different in-plane confinement strengths, $\omega_x = \omega_y = \omega_\perp$, are considered. It is known from the literature of quasi-2D systems that $1/T_1$ increases with vertical confinement.[2,6] This is precisely what we observe for the QD with $\hbar\omega_\perp = 5$ meV, as here $\omega_z > \omega_\perp$ (~2D QD) for all the range under study. However, the results for QDs with stronger in-plane confinement show that the general behavior is richer, displaying a profound spin relaxation

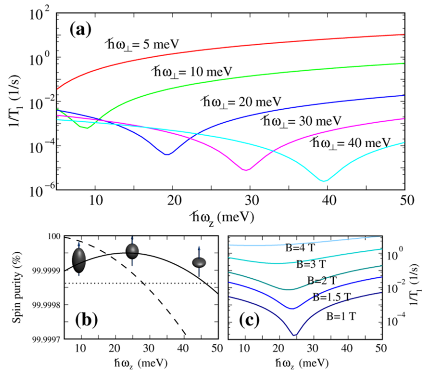

Figure 1. (a) Spin relaxation rate in QDs with DSOI as a function of the vertical confinement. (b) Spin purity of the ground state for QDs with $\hbar\omega_\perp = 25$ meV. Solid line, exact result; dashed line, linear approximation; dotted line, in-plane cubic approximation. In panels a and b, $B = 1$ T. (c) Same as that in panel a but for increasing magnetic fields and $\hbar\omega_\perp = 25$ meV.

minimum when $\omega_z = \omega_\perp$ (i.e., in spherical QDs) and rapidly increasing for any kind of confinement anisotropy.

To understand this behavior, we consider the factors contributing to $1/T_1$ in eq 1. The phonon density of states at the spin flip energy is constant because the Zeeman splitting, Δ_{fi}, does not depend on ω_z. Also, $\Delta_{fi} = 0.06$ meV, which implies phonon wavelengths $\lambda_{ph} \approx 350$ nm, much greater than the QD size. Thus, we are in the dipole limit where the QD size and shape have little effect on the efficiency of electron−phonon coupling.[6] It then follows that the ω_z dependence must ensue from the degree of spin admixing between the Zeeman sublevels. This is confirmed by the solid line in Figure 1b, which plots the spin purity of the ground state for $\hbar\omega_\perp = 25$ meV. Clearly, minimal admixture is observed at $\omega_z = \omega_\perp$ (spherical QDs), increasing for both oblate ($\omega_z > \omega_\perp$) and prolate ($\omega_z < \omega_\perp$) structures.

The spin admixture of the Zeeman sublevels can be explained from the σ_x and σ_y terms in H_{D} (σ_z does not flip spins). For qualitative reasoning, we can restrict the Hilbert space to that spanned by the lowest orbitals: $|0\rangle = |0,0,0\rangle$, $|x\rangle = |1,0,0\rangle$, $|y\rangle = |0,1,0\rangle$, and $|z\rangle = |0,0,1\rangle$. The spin mixing part of H_{D} is then approximated as[19]

$$H_{\mathrm{D}}^{\mathrm{mix}} = d[\mathrm{p}_x(\langle \mathrm{p}_y^{\ 2}\rangle - \langle \mathrm{p}_z^{\ 2}\rangle)\sigma_x + \mathrm{p}_y(\langle \mathrm{p}_z^{\ 2}\rangle - \langle \mathrm{p}_x^{\ 2}\rangle)\sigma_y] \tag{7}$$

Note in eq 7 that the Zeeman sublevels of $|0\rangle$ do not couple directly, but rather with the excited states $|x\rangle$ and $|y\rangle$. The strength of the coupling depends on (i) the energetic proximity of such states and (ii) the DSOI strength coefficients $d(\langle \mathrm{p}_y^2\rangle - \langle \mathrm{p}_z^2\rangle)$ and $d(\langle \mathrm{p}_z^2\rangle - \langle \mathrm{p}_x^2\rangle)$. While the former factor does not depend on ω_z, the latter does. Indeed, for a perfect sphere $\langle \mathrm{k}_x^2\rangle = \langle \mathrm{k}_y^2\rangle = \langle \mathrm{k}_z^2\rangle$. For $B \to 0$, this implies $\langle \mathrm{p}_z^2\rangle \approx \langle \mathrm{p}_\perp^2\rangle$, so that the DSOI strength coefficients tend to vanish. This explains the extremely slow spin relaxation of spherical QDs. Because the suppression originates in the SOI, the same behavior can be expected for two-phonon processes.

For oblate structures, $\langle \mathrm{k}_z^2\rangle > \langle \mathrm{k}_\perp^2\rangle$, and the DSOI strength coefficients increase. In the limit of $\langle \mathrm{k}_z^2\rangle \gg \langle \mathrm{k}_\perp^2\rangle$, $H_{\mathrm{D}}^{\mathrm{mix}} \to d\langle \mathrm{p}_z^2\rangle(\mathrm{p}_y\sigma_y - \mathrm{p}_x\sigma_x)$. This is the so-called linear approximation of DSOI, widely employed for quasi-2D QDs.[6] As can be seen in Figure 1b, dashed line, it provides a qualitatively correct estimate of the spin mixing for oblate QDs, albeit systematically overestimated. Likewise, for prolate structures, $\langle k_z^2\rangle < \langle k_\perp^2\rangle$, and the DSOI strength coefficients also increase. In the 1D limit, $\langle k_z^2\rangle \ll \langle k_\perp^2\rangle$, so that $H_D^{mix} \to d\langle p_\perp^2\rangle(p_x\sigma_x - p_y\sigma_y)$. This is the in-plane cubic approximation, which does not depend on ω_z and provides a saturation limit for quasi-1D QDs such as nanorods, see dotted line in Figure 1b. Clearly, for QDs with aspect ratio ~1 (nearly spherical), the spin admixture is not the sum of the linear and cubic approximations. The interplay between 3D degrees of freedom becomes important and the full H_D Hamiltonian must be considered.

The suppression of the DSOI strength coefficients for spherical QDs is maximal when $B \to 0$. As shown in Figure 1c, for increasing B, the spin relaxation minimum is gradually removed. The main reason is that with increasing Zeeman splitting, the dipole approximation to electron−phonon coupling starts failing. Phonon scattering becomes then very sensitive to the QD size,[6,17] and it supersedes the influence of SOI in determining $1/T_1$.

Rashba SOI. Next, we investigate QDs subject to RSOI. A number of recent works have pointed out that the confinement anisotropy gives rise to modulations of the RSOI strength in quasi-2D QDs.[20−22] Here, we extend the study to include the vertical confinement. One can easily show from eq 4 that spherical QDs under isotropic built-in electric fields will also have suppressed SOI. Yet, a rich manipulation of the spin dynamics can be obtained through externally applied (anisotropic) electric fields. We then consider spheroidal QDs with fixed $\omega_\perp$ subject to an axial field B and an external electric field $\boldsymbol{\varepsilon}$ applied at a polar angle θ. Figure 2a shows the

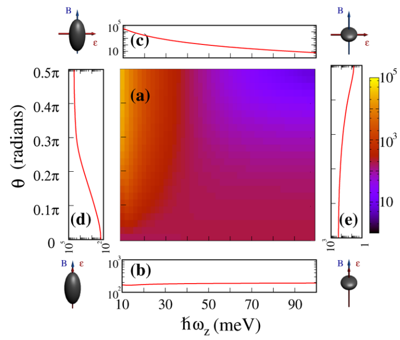

Figure 2. Spin relaxation rate $(1/s)$ in QDs with RSOI. (a) Contour plot as a function of the vertical confinement and electric field orientation. ε = 30 kV/cm, B = 5 T, $\hbar\omega_\perp$ = 50 meV. (b−e) Cross-sections: (b), $\theta = 0$; (c) $\theta = \pi/2$; (d) $\hbar\omega_z$ = 10 meV; (e) $\hbar\omega_z$ = 100 meV. The schematics near the corners illustrate the corresponding QD shape and the orientation of $\boldsymbol{\varepsilon}$ with respect to B.

spin relaxation rate for different ω_z and θ values. One can see that the fastest (slowest) spin relaxation occurs for $\boldsymbol{\varepsilon}$ perpendicular to the direction of weakest (strongest) confinement. More insight on the effect of RSOI is gained from the insets, which depict cross-sections of Figure 2a for limiting cases. Thus, for an axial electric field, panel b shows that ω_z has no influence, while, for an in-plane field, panel c shows that the influence is highest. However, increasing the polar angle has opposite effect for prolate QDs, panel d, and oblate QDs, panel e. This behavior is independent of the magnitudes of the external fields.

To understand the above results, we note that, as in the DSOI case, here, $1/T_1$ simply maps the degree of spin admixing. The spin mixing part of H_R reads

$$H_R^{mix} = r[\varepsilon_z(p_y\sigma_x - p_x\sigma_y) + \varepsilon_x p_z\sigma_y - \varepsilon_y p_z\sigma_x] \tag{8}$$

The first term in eq 8 applies for $\boldsymbol{\varepsilon}\|\mathbf{B}$. This is the only term considered in most studies of quasi-2D QDs, where $\boldsymbol{\varepsilon}$ is applied along the growth direction.[6] This term couples the ground state $|0\rangle$ with $|x\rangle$ and $|y\rangle$, similar to the case of DSOI. Notice that it is independent of ω_z, which explains the flat response in Figure 2b. The second and third terms of eq 8 show up when $\boldsymbol{\varepsilon}\angle\mathbf{B}$. They couple the ground state to $|z\rangle$, which implies that a correct description of the motion in the z direction can be essential for RSOI. As $\boldsymbol{\varepsilon}$ is tilted from $\mathbf{B}$, ω_z becomes increasingly important, which explains its strong effect in Figure 2c.

Equation 8 evidences that $|0\rangle$ couples to excited states with a node in the direction $\mathbf{j} \perp \boldsymbol{\varepsilon}$, e.g., to $|z\rangle$ for ε_y. The strength of this coupling scales with p_j. However, the energetic proximity scales with p_j^2. Therefore, with increasing confinement in the direction perpendicular to $\boldsymbol{\varepsilon}$, the RSOI admixture decreases. This is why the maximum (minimum) admixing takes place for prolate (oblate) QDs and in-plane ε in Figure 2a.

Magnetic Field Dependence. Last, we discuss the magnetic field dependence of $1/T_1$. In quasi-2D QDs, a B^5 power law is obeyed for both RSOI and DSOI, which is taken in experiments as a signature of SOI mediated relaxation.[6] We find that the same power law holds for RSOI for any shape and $\boldsymbol{\varepsilon}$ orientation. By contrast, the B dependence for DSOI is very sensitive to the shape. This is shown in Figure 3a−c, where dots represent the calculated values of $1/T_1$, and solid lines give the corresponding fits to B^n functions. While B^5 offers a correct description for oblate (quasi-2D) and prolate (quasi-1D) QDs, a severe deviation is observed for spherical QDs, where $1/T_1 \propto B^9$ (see panel b).

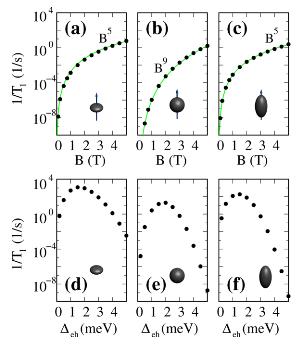

Figure 3. Spin relaxation rate in QDs with DSOI as a function of the magnetic field. (a−c) External magnetic field, $\hbar\omega_p$ = 50 meV and $\hbar\omega_z$ = 100 meV (a), $\hbar\omega_z$ = 50 meV (b), $\hbar\omega_z$ = 10 meV (c). (d,e) Same as that in panels a−c but as a function of the electron−hole exchange constant. The schematics represent the shape of the QD under study.

The influence of the shape on the B dependence can be traced back to that of the spin mixing given by H_R^{mix} (for RSOI) and H_D^{mix} (for DSOI). These Hamiltonians contain terms proportional to B^n, where $n = 0,1$ for H_R^{mix} and $n = 0-3$ for H_D^{mix}, coming from $p = k + eA$. For oblate/prolate QDs under moderate B, the B^0 term dominates, and both RSOI and DSOI show the same B dependence. For spherical QDs, B^0 is still dominant for RSOI, but it vanishes for DSOI (recall Figure 1). In such a case, B^2 and B^3 terms dominate, changing the B-dependence from B^5 to B^9, as observed in Figure 3b. An analytical derivation of the B power laws can be found in the Supporting Information.[23]

In Figure 3d–f, we study the effect of the effective magnetic field produced by the electron–hole exchange interaction splitting dark and bright excitons.[10−12] From the point of view of the electron, this is felt as a Zeeman-like term $H_{xc} = 1/2 \times \Delta_{eh}\sigma_z$,[13] where the exchange constant Δ_{eh} ranges from fractions of meV in self-assembled QDs to few meV in colloidal QDs. The main differences with respect to the external B studied before lies in the magnitude of the Zeeman splitting, which can be much larger. Thus, with increasing Δ_{eh}, the electron–phonon coupling departs from the dipole limit. The coupling strength is then known to become most efficient when λ_{ph} is comparable to the QD size, and it becomes again inefficient when λ_{ph} increases further.[6,17] This explains the maximum of $1/T_1$ observed in Figure 3d–f. It is worth stressing that, even in this regime of phonon energies, the reduced DSOI of spherical dots generally translates into slower relaxation (compare the maxima in panel e with that in panels d and f). Because spin relaxation in colloidal QDs is presumably induced by DSOI,[11] these results set principles for the design of QDs with either fast or slow relaxation between dark and bright excitons.

We close by noting that, in this work, we have assumed bulk phonons. This is an appropiate model for embedded QDs, such as self-assembled QDs, colloidal solids, and nanocrystals with thick shells. For suspended nanocrystals, however, phonon confinement may alter the phonon density and electron–phonon coupling efficiency. This would modify quantitative estimates of the spin relaxation rate, such as the B^9 power law, but the central message of this work,the geometrical suppression of SOI, persists.

■ CONCLUSIONS

We have studied the effect of the vertical confinement on the electron spin relaxation in QDs with DSOI and RSOI. The behavior of quasi-1D structures is similar to that of quasi-2D systems. By contrast, spherical QDs show a distinct behavior, which arises from a symmetry-induced quenching of the DSOI. This leads to longer T_1 values and a B^9 power law. We have shown that, for small (large) Zeeman splittings, $1/T_1$ is dominated by the efficiency of the SOI (electron–phonon) coupling. Our results allow to identify the geometrical conditions that maximize or minimize $1/T_1$ in zinc-blende QDs.

■ ASSOCIATED CONTENT

Ⓢ Supporting Information

Analytical derivation of the power laws in Figure 3. This material is available free of charge via the Internet at http://pubs.acs.org.

■ AUTHOR INFORMATION

Corresponding Author

*E-mail: josep.planelles@uji.es.

Notes

The authors declare no competing financial interest.

■ ACKNOWLEDGMENTS

Support from MICINN project CTQ2011-27324, UJI-Bancaixa project P1-1A2009-03, and the Ramon y Cajal program (JIC) is acknowledged.

■ REFERENCES

(1) Awschalom, D. D.; Loss, D.; Samarth, N., Eds. *Semiconductor Spintronics and Quantum Computing*; Springer: New York, 2002.
(2) Winkler, R. *Spin-Orbit Coupling Effects in Two-Dimensional Electron and Hole Systems*; Springer: Berlin, Germany, 2003.
(3) Wu, M. W.; Jiang, J. H.; Weng, M. Q. *Phys. Rep.* **2010**, *493*, 61–236.
(4) (a) Berezovsky, J.; Mikkelson, M. H.; Stoltz, N. G.; Coldren, L. A.; Awschalom, D. D. *Science* **2008**, *320*, 349–352. (b) Press, D.; Ladd, T. D.; Zhang, B.; Yamamoto, Y. *Nature* **2008**, *456*, 218–221.
(5) Nadj-Perge, S.; Frolov, S. M.; Bakkers, E. P. A. M.; Kouwenhoven, L. P. *Nature* **2010**, *468*, 1084–1087.
(6) Hanson, R.; Kouwenhoven, L. P.; Petta, J. R.; Tarucha, S.; Vandersypen, L. M. K. *Rev. Mod. Phys.* **2007**, *79*, 1217–1265.
(7) Vamivakas, A. N.; Lu, C. Y.; Matthiesen, C.; Zhao, Y.; Fält, S.; Badolato, A.; Atatüre, M. *Nature* **2010**, *467*, 297–300.
(8) Kanai, Y.; Deacon, R. S.; Takahasi, S.; Oiwa, A.; Yoshida, K.; Shibata, K.; Hirakawa, K.; Tokura, Y.; Tarucha, S. *Nat. Nanotechnol.* **2011**, *6*, 511–516.
(9) Scholes, G. D.; Kim, J.; Wong, C. Y.; Huxter, V. M.; Sreekumari Nair, P.; Fritz, K. P.; Kumar, S. *Nano Lett.* **2006**, *6*, 1765–1771.
(10) Biadala, L.; Louyer, Y.; Tamarat, P.; Lounis, B. *Phys. Rev. Lett.* **2010**, *105*, 157402.
(11) (a) Wong, C. Y.; Kim, J.; Sreekumari Nair, P.; Nagy, M. C.; Scholes, G. D. *J. Phys. Chem. C* **2009**, *113*, 795–811. (b) Huxter, V. M.; Kim, J.; Lo, S. S.; Lee, A.; Sreekumari Nair, P.; Scholes, G. D. *Chem. Phys. Lett.* **2010**, *491*, 187–192.
(12) Ma, H.; Jin, Z.; Zhang, Z.; Li, G.; Ma, G. *J. Phys. Chem. A* **2012**, *116*, 2018–2023.
(13) Liao, Y. H.; Climente, J. I.; Cheng, S. J. *Phys. Rev. B* **2011**, *83*, 165317.
(14) Stano, P.; Fabian, J. *Phys. Rev. Lett.* **2006**, *96*, 186602.
(15) Amasha, S.; MacLean, K.; Radu, I. P.; Zumbühl, D. M.; Kastner, M. A.; Hanson, M. P.; Gossard, A. C. *Phys. Rev. Lett.* **2008**, *100*, 046803.
(16) Olendski, O.; Shahbazyan, T. V. *Phys. Rev. B* **2007**, *75*, 041306(R).
(17) Climente, J. I.; Bertoni, A.; Goldoni, G.; Molinari, E. *Phys. Rev. B* **2006**, *74*, 035313.
(18) d = 25 eV·Å^3 and r = 100 e·Å^2;[3] g = −1.0; and all other parameters as in ref 13.
(19) Within this subspace, the operators $p_x p_y^2$ and $p_x\langle 0|p_y^2|0\rangle$ are equivalent (they have the same matrix representation). The same holds for the rest of the cubic operators.
(20) (a) Takahashi, S.; Deacon, R. S.; Yoshida, K.; Oiwa, A.; Shibata, K.; Hirakawa, K.; Tokura, Y.; Tarucha, S. *Phys. Rev. Lett.* **2010**, *104*, 246801. (b) Nadj-Perge, S.; Pribiag, V. S.; van den Berg, J. W. G.; Zuo, K.; Plissard, S. R.; Bakkers, E. P. A. M.; Frolov, S. M.; Kouwenhoven, L. P. *Phys. Rev. Lett.* **2012**, *108*, 166801.
(21) Destefani, C. F.; Ulloa, S. E. *Phys. Rev. B* **2005**, *72*, 115326.
(22) Avetisyan, S.; Pietiläinen, P.; Chakraborty, T. *Phys. Rev. B* **2012**, *85*, 153301.
(23) See Supporting Information.

Supplementary Information for the article: "Electron Spin Relaxation in 3D Quantum Dots: Geometrical Suppression of Dresselhaus and Rashba Spin-Orbit Interaction"

J. Planelles,* J.I. Climente, and C. Segarra

Departament de Química Física i Analítica, Universitat Jaume I, Castelló de la Plana, Spain

E-mail: josep.planelles@uji.es

*To whom correspondence should be addressed

These supplementary notes present a more detailed derivation of the B^5 and B^9 power laws observed for the electron spin relaxation rates in QDs with different shapes in the article "Electron Spin Relaxation in 3D Quantum Dots: Generalized Effect of Rashba and Dresselhaus Spin-Orbit Interaction".

The B dependence can be understood by analyzing the different terms contributing to the spin relaxation rate, Eq. (1) of the article:

$$\frac{1}{T_1} = \frac{2\pi}{\hbar} \sum_{\lambda\,\mathbf{q}} |M_\lambda(\mathbf{q}) \langle f\,| e^{-i\mathbf{qr}}\,| i\rangle|^2\, \delta(\Delta_{fi} + E_q). \tag{1}$$

The transition occurs between Zeeman sublevels, which are split by a small energy (typically fractions of meV). Under these conditions, the dominant electron-phonon scattering mechanism involves small phonon energies (large wavelengths) yielding a homogeneous strain which only can cause a piezoelectric interaction, $\lambda = pz$.[1] In this wavelength regime, the phonon dispersion relation is linear, $E_q = \hbar c q$, where c is the speed of propagation of the acoustic phonon.

Note from the sum and the delta function in Eq. (1) that we are considering all phonon modes with energy $E_q = -\Delta_{fi}$. The sum can be rewritten as an integral in spherical coordinates (q, θ_q, ϕ_q):

$$\frac{1}{T_1} \propto \int_{\theta_q} d\theta_q \int_{\phi_q} d\phi_q \int_q q^2\, dq\, |M_{pz}(\mathbf{q}) \langle f\,| e^{-i\mathbf{qr}}\,| i\rangle|^2\, \delta(\Delta_{fi} + \hbar c_\alpha q). \tag{2}$$

The delta function restricts the integral over the phonon momentum modulus q to the resonant value, $q_0 = -\Delta_{fi}/\hbar c$. We then obtain:

$$\frac{1}{T_1} \propto q_0^2 \int_{\theta_q} d\theta_q \int_{\phi_q} d\phi_q\, |M_{pz}(\mathbf{q}) \langle f\,| e^{-i\mathbf{qr}}\,| i\rangle|^2. \tag{3}$$

Eq. (3) shows that the phonon density of states at the resonant energy introduces a factor q_0^2 to $1/T_1$. Since the resonant energy is proportional to the magnetic field, $\Delta_{fi} = g\mu B$, this translates into a factor B^2. On the other hand, the electron-phonon scattering due to the piezoelectric field gives rise to $M_{pz}(\mathbf{q})$ terms with a $1/\sqrt{q_0}$ dependence.[1,2] When squared, this adds a $1/B$ factor.

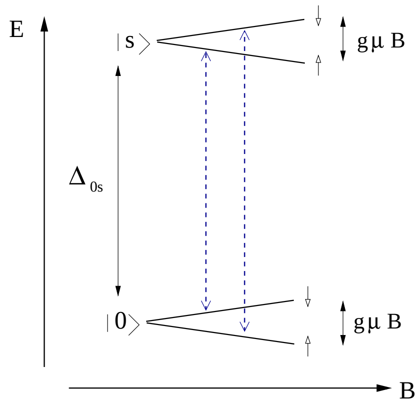

Figure 1: Electron energy levels participating in the admixture of the Zeeman sublevels $|i\rangle$ and $|f\rangle$. The dashed line indicates the levels coupled by SOI.

As for the matrix element $\langle i|e^{-i\mathbf{qr}}|f\rangle$, to lowest-order SOI perturbation we can approximate the electron states as:

$$|i\rangle = c_0^i|0\rangle|\downarrow\rangle + c_s^i|s\rangle|\uparrow\rangle, \tag{4}$$

$$|f\rangle = c_0^f|0\rangle|\uparrow\rangle + c_s^f|s\rangle|\downarrow\rangle, \tag{5}$$

where $|0\rangle$ is the lowest orbital and $|s\rangle$ is the orbital with the largest SOI admixture (see Fig. Figure 1). Since the phonon cannot couple states with different spin, we get:

$$|\langle i|e^{-i\mathbf{qr}}|f\rangle|^2 = |c_0^{i*}c_s^f\,\langle 0|e^{-i\mathbf{qr}}|s\rangle + c_s^{i*}c_0^f\,\langle s|e^{-i\mathbf{qr}}|0\rangle|^2. \tag{6}$$

Assuming that SOI is a small perturbation, we can take $c_0^i \approx 1$ and $c_0^f \approx 1$. The following simplified expression is then obtained:

$$|\langle i|e^{-i\mathbf{qr}}|f\rangle|^2 \approx |(c_s^f + c_s^{i*})\,\langle 0|e^{-i\mathbf{qr}}|s\rangle|^2. \tag{7}$$

In the dipole limit, $|\langle 0|e^{-i\mathbf{qr}}|s\rangle|^2 \propto q_0^2$, thus giving an additional B^2 factor to $1/T_1$. If we collect all the B powers so far, we obtain a B^3 dependence, which accounts for the phonon scattering terms. What is left is the SOI contribution, which comes into play via the $(c_s^f + c_s^{i*})$ coefficients in Eq. (7). From perturbation theory, the coefficients can be approximated as:

$$c_s^i = \frac{\langle\downarrow|\langle 0|H_{SOI}^{\text{mix}}|s\rangle|\uparrow\rangle}{\Delta_{0s} - g\mu B}, \tag{8}$$

$$c_s^f = \frac{\langle\uparrow|\langle 0|H_{SOI}^{\text{mix}}|s\rangle|\downarrow\rangle}{\Delta_{0s} + g\mu B}, \tag{9}$$

where H_{SOI}^{mix} is the spin mixing part of the Hamiltonian.

For DSOI, most of the mixing comes from H_D^{mix}:

$$H_D^{\text{mix}} = d\left[p_x(p_y^2 - p_z^2)\sigma_x + p_y(p_z^2 - p_x^2)\sigma_y\right], \tag{10}$$

which is cubic in $p_\perp$. When replacing the canonical momentum $\mathbf{p}$ by $\mathbf{k} - e\mathbf{A}$, since $\mathbf{A} = B/2\,(-y, x, 0)$, the matrix elements $\langle\downarrow|\langle 0|H_D^{\text{mix}}|s\rangle|\uparrow\rangle$ will contain terms of up to cubic order in B,

$$\langle\uparrow|\langle 0|H_D^{\text{mix}}|s\rangle|\downarrow\rangle = \sum_{j=0}^{3} a_j^s B^j. \tag{11}$$

In what follows we shall assume $|s\rangle = |1,0,0\rangle = |x\rangle$, although similar reasoning applies to $|s\rangle = |y\rangle$ and $|s\rangle = |x\rangle \pm i|y\rangle$. The coefficients a_j^x read:

$$a_0^x = d\left(\langle k_y^2\rangle - \langle k_z^2\rangle\right)\langle 0|k_x|x\rangle, \tag{12}$$

$$a_1^x = \frac{id}{2}\left(\langle k_z^2\rangle - \langle k_x^2\rangle\right)\langle 0|x|x\rangle, \tag{13}$$

$$a_2^x = \frac{d}{4}\langle x^2\rangle\langle 0|k_x|x\rangle, \tag{14}$$

$$a_3^x = \frac{-id}{8}\langle y^2\rangle\langle 0|x|x\rangle. \tag{15}$$

One can note from the above expressions that $(a_j^x)^* = -a_j^x$. On the other hand,

$$\langle \downarrow | \langle 0 | H_D^{\rm mix} | x \rangle | \uparrow \rangle = \sum_{j=0}^{3} (-1)^j a_j^x B^j. \quad (16)$$

due to the hermiticity of σ_y. The sum of coefficients can then be written as:

$$c_s^f + c_s^{i*} = \sum_{j=0}^{3} \left(\frac{a_j^x}{\Delta_{0s} + g\mu B} - \frac{(-1)^j a_j^x}{\Delta_{0s} - g\mu B} \right), \quad (17)$$

For oblate and prolate QDs under moderate magnetic fields, the B^0 term of the expansion is by far dominant. Therefore,

$$c_s^f + c_s^{i*} \approx a_0^x \left(\frac{1}{\Delta_{0s} + g\mu B} - \frac{1}{\Delta_{0s} - g\mu B} \right), \quad (18)$$

Since $\Delta_{0s} \gg g\mu B$, we can Taylor-expand the term in brackets and find that the lowest term is linear in B:

$$c_s^f + c_s^{i*} \approx -2 a_0^x g\mu B / \Delta_{0s}^2. \quad (19)$$

When squared, this gives a B^2 factor which, along with the phonon contribution B^3, sum up the B^5 power law observed in Fig. 3(a) and (c) of the article.

For spherical QDs, however, the B^0 and B^1 terms of Eq. (11) expansion vanish because $\langle k_x^2 \rangle = \langle k_y^2 \rangle = \langle k_z^2 \rangle$, which cancels the coefficients a_0^x and a_1^x (see Eqs. (12-13)). We are then left with the B^2 and B^3 terms of the expansion. The sum of coefficients now reads:

$$c_s^f + c_s^{i*} \approx a_2 B^2 \left(\frac{1}{\Delta_{0s} + g\mu B} - \frac{1}{\Delta_{0s} - g\mu B} \right) + a_3 B^3 \left(\frac{1}{\Delta_{0s} + g\mu B} + \frac{1}{\Delta_{0s} - g\mu B} \right),$$

The first (quadratic) term gives a B^2 factor from the numerator plus a B factor from the difference of the fractions. All in all, this yields a B^3 dependence. The second (cubic) term gives a B^3 factor from the numerator and a B^0 factor from the sum of the fractions, since $\Delta_{0s} \gg g\mu B$. Again, this yields a B^3 dependence. Thus, $(c_s^f + c_s^{i*})^2 \propto B^6$. Together with the phonon contribution B^3, this explains the B^9 power law observed in Fig. 3(b) of the article.

For RSOI, there is no symmetry-induced suppression of the B^0 term. Then, the reasoning is analogous to that of DSOI with non-spherical QDs and a B^5 power law follows.

References

(1) R. Hanson, L. P. Kouwenhoven, J. R. Petta, S. Tarucha, and L. M. K. Vandersypen, Rev. Mod. Phys. **79**, 1217 (2007).

(2) For the calculations presented in the article we have implemented $M_{pz}(\mathbf{q})$ with full consideration of its dependence on the components of **q**, see Eqs.(3)-(4) of Ref.17. Thus, we properly account for the anisotropy of electron-phonon coupling.

New Journal of Physics
The open access journal at the forefront of physics

Deutsche Physikalische Gesellschaft DPG
IOP Institute of Physics

Published in partnership with: Deutsche Physikalische Gesellschaft and the Institute of Physics

PAPER

Anisotropy of spin–orbit induced electron spin relaxation in [001] and [111] grown GaAs quantum dots

C Segarra, J Planelles, J I Climente and F Rajadell
Departament de Química Física i Analítica, Universitat Jaume I, Castelló de la Plana, Spain
E-mail: josep.planelles@uji.es

Keywords: spin–orbit interaction, spin relaxation, quantum dot, magnetic field

Abstract
We report a systematic study of the spin relaxation anisotropy between single electron Zeeman sublevels in three-dimensional cuboidal GaAs quantum dots (QDs). The QDs are subject to an in-plane magnetic field. As the field orientation varies, the relaxation rate oscillates periodically, showing ‘magic’ angles where the relaxation rate is suppressed by several orders of magnitude. This behavior is found in QDs with different shapes, heights, crystallographic orientations and external fields. The origin of these angles can be traced back to the symmetries of the spin admixing terms of the Hamiltonian. Our results evidence that cubic Dresselhaus terms play an important role in determining the spin relaxation anisotropy, which can induce deviations of the ‘magic’ angles from the crystallographic directions reported in recent experiments (P Scarlino *et al* 2014 Phys. Rev. Lett. **113** 256802).

1. Introduction

The electron spin confined in semiconductor quatum dots (QDs) is a promising candidate for the realization of quantum computing and the development of spin-based devices in spintronics [1, 2]. Using the spin of electrons as qubits was first proposed by Loss and DiVincenzo [3] and, since then, a lot of effort has been devoted to its accomplishment [4]. QDs offer the possibility of isolating single electron spins which exhibit longer lifetimes than in delocalized systems since quantum confinement suppresses the main bulk decoherence mechanisms [5]. Nevertheless, coupling between the electron spin and the surrounding environment cannot be avoided, resulting in spin relaxation and decoherence. Therefore, a good understanding of the relaxation mechanisms in QDs is needed for the development of spin-based applications.

The two main mechanisms of spin relaxation in III–V zinc-blende semiconductor QDs are the hyperfine coupling with the nuclear spins of the lattice and the spin–orbit interaction (SOI) [4]. The hyperfine interaction is generally important at relatively weak magnetic fields while for moderate and strong fields the phonon-mediated relaxation due to SOI predominates. In semiconductors without inversion symmetry, e.g. GaAs, SOI can be originated by the bulk inversion asymmetry of the material (Dresselhaus SOI) [6] and the structure inversion asymmetry of the confining potential (Rashba SOI) [7]. The Hamiltonians describing both SOI have different symmetries and exhibit an anisotropic behavior [8]. This anisotropy can be exploited to externally control and manipulate the electron spin by changing the orientation of applied magnetic or electric fields [9–11]. As a consequence, the anisotropy of the spin relaxation and its control via external means has been intensively studied [12–20].

Most previous theoretical works have dealt with two-dimensional (2D) circular QDs grown along the [001] crystal direction [4, 12–14, 21], where in-plane anisotropy arises from the interference between Rashba and Dresselhaus SOI. However, QDs are prone to deviate from the circular symmetry and there is gathering evidence that this has a primary influence on the spin relaxation anisotropy [15–18]. This fact has been confirmed in very recent experiments by Scarlino and co-workers [22]. Relevantly, all the studies analyzing the influence of non-circular confinement on the spin relaxation anisotropy of single QDs have so far missed the effect of cubic Dresselhaus SOI terms and that of three-dimensionality (3D). Cubic terms are expected to become particularly

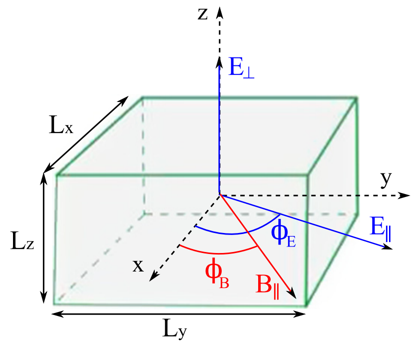

Figure 1. Schematic representation of the cuboidal QD system. The orientation of the external electric and magnetic fields is indicated.

important in tall QDs [23], which are increasingly available owing to recent progress in synthetic control [24, 25]. On the other hand, going beyond [001] grown QDs is also of interest, especially in view of the convenience of [111] grown QDs for optical spin preparation [26]. The effect of the crystallographic orientation on the spin dynamics has been well studied in quantum wells [27–29], but further work is needed in relation to fully localized spins, where studies are limited [18].

In this article, we study the anisotropy of the electron spin relaxation between Zeeman sublevels in cuboidal GaAs QDs. The anisotropy is monitored by varying the orientation of an externally applied in-plane magnetic field (ϕ_B). We consider QDs grown along both [001] and [111] crystal directions, including all linear and cubic terms of Rashba and Dresselhaus SOI in a fully 3D model. Different heights, base shapes, crystallographic orientations, magnetic field intensities and external electric fields are considered. The numerical results, together with perturbative interpretations, provide a wide overview on the effect of confinement asymmetry and 3D on the spin relaxation anisotropy.

We find that, in [001] grown QDs, the spin relaxation anisotropy is very different depending on the dominating spin–orbit mechanism, Rashba or Dresselhaus SOI. By contrast, in [111] grown QDs the anisotropy is the same for both terms. In all cases, the spin relaxation rate shows strong oscillations with ϕ_B. Interestingly, cubic Dresselhaus terms are shown to be critical in determining such anisotropic behavior. This occurs not only in tall QDs, but—contrary to common belief—also in quasi-2D QDs, provided the high symmetry directions of the dot are not aligned with the main crystallographic axes. In both squared and rectangular QDs we observe order-of-magnitude suppressions of the spin relaxation rate at certain 'magic' magnetic field angles ϕ_B, which can be understood from symmetry considerations. A 'magic' angle around [110] has actually been very recently reported in experiments with a single GaAs QD strongly elongated along one in-plane direction [22]. We generalize this study considering less elongated structures. We show that cubic Dresselhaus terms help explain the deviation from [110] observed in the experiment, and in less elongated structures they switch the 'magic' angle to $[\bar{1}10]$ or $[1\bar{1}0]$.

The paper is organized as follows. Section 2 presents the model we use to compute the electron spin relaxation, including the SOI Hamiltonians for QDs rotated with respect to the main crystallographic axes. In section 3 we show and discuss the numerical results for the cases under study. Finally, conclusions are given in section 4.

2. Theoretical model

We study the electron spin relaxation driven by SOI between Zeeman split sublevels of cuboidal GaAs QDs subject to externally applied electric **E** and magnetic **B** fields (see figure 1). The isotropy of the conduction band of III–V semiconductors leads to an isotropic kinetic energy term in the 3D one-electron Hamiltonian which reads

$$H = \frac{\mathbf{p}^2}{2m^*} + V_c + \mathbf{E}\mathbf{r} + H_Z + H_{\mathrm{SOI}}, \tag{1}$$

where m^* stands for the electron effective mass, V_c is the confinement potential, **E** is an external electric field and $\mathbf{p} = -i\hbar\nabla + \mathbf{A}$, where **A** is the vector potential. An in-plane magnetic field $\mathbf{B} = B\left(\cos\phi_B,\ \sin\phi_B,\ 0\right)$ rotated an angle ϕ_B with respect to the x axis of the dot is included. This field is described by the vector potential $\mathbf{A} = \left(zB \sin\phi_B, -zB\cos\phi_B, 0\right)$. The Zeeman term is $H_Z = \frac{1}{2} g\mu_B \mathbf{B}\boldsymbol{\sigma}$ with g, μ_B and $\boldsymbol{\sigma}$ standing for the electron g-factor, Bohr magneton and Pauli spin matrices, respectively.

The last term in (1) corresponds to the SOI, [8] $H_{\mathrm{SOI}} = H_R + H_D$, with H_R being the Rashba SOI

$$H_R^{[001]} = \alpha_r \boldsymbol{\sigma}(\mathbf{p}\times\mathbf{E}), \tag{2}$$

and H_D the Dresselhaus SOI

$$H_D^{[001]} = \beta_d\left[\sigma_x p_x\left(p_y^2 - p_z^2\right) + \sigma_y p_y\left(p_z^2 - p_x^2\right) + \sigma_z p_z\left(p_x^2 - p_y^2\right)\right]. \tag{3}$$

Here, α_r and β_d are material-dependent coefficients determining the strength of the SOI and the superscript [001] indicates de growth direction of the QD.

Equations (2) and (3) correspond to QDs grown along the [001] crystal direction. In order to consider other orientations of the QD with respect to the crystal host we maintain the confinement potential fixed in space and perform a rotation of the crystalline structure. Since the confining potential as well as the externally applied fields are kept while the crystalline structure is rotated, only the H_{SOI} part of the Hamiltonian is affected. In particular, the H_{SOI} Hamiltonian corresponding to an axially applied electric field and a crystalline structure subject to an in-plane rotation θ_z around the z axis reads:

$$H_R^{[001]}\left(\theta_z\right) = \alpha_r E_z\left(\sigma_x p_y - \sigma_y p_x\right), \tag{4}$$

and

$$\begin{aligned} H_D^{[001]}\left(\theta_z\right) = {}& \beta_d \cos 2\theta_z\left[\sigma_x p_x\left(p_y^2 - p_z^2\right) + \sigma_y p_y\left(p_z^2 - p_x^2\right) + \sigma_z p_z\left(p_x^2 - p_y^2\right)\right] \\ & + \beta_d \sin 2\theta_z\left[p_z^2\left(\sigma_y p_x + \sigma_x p_y\right) - 2\sigma_z p_x p_y p_z + \frac{1}{2}\left(p_x^2 - p_y^2\right)\left(\sigma_x p_y - \sigma_y p_x\right)\right]. \end{aligned} \tag{5}$$

Note that this particular case of an axially applied electric field yields a Rashba Hamiltonian (4) independent of θ_z.

We consider next QDs grown along the [111] direction. In particular, we consider the rotation $\chi = \arccos(1/\sqrt{3})$ around the straight line $y = -x$, that corresponds to the Euler angles $\theta = \arccos(1/\sqrt{3})$, $\phi = 45$ and $\alpha = -45$. The rotated SOI Hamiltonians have the form

$$H_R^{[111]} = \frac{\alpha_r E_z}{\sqrt{3}}\left[\sigma_z\left(p_y - p_x\right) - \sigma_y\left(p_x + p_z\right) + \sigma_x\left(p_y + p_z\right)\right], \tag{6}$$

and

$$\begin{aligned} H_D^{[111]} = \frac{\beta_d}{2\sqrt{3}}\Big[&\left(p_x^2 + p_y^2 - 4p_z^2\right)\left(p_x\sigma_y - p_y\sigma_x\right) + p_z\left(p_x^2 - p_y^2\right)\left(\sigma_x + \sigma_y\right) \\ & + 2p_x p_y p_z(\sigma_x - \sigma_y) - \sigma_z p_x^2\left(p_x + 3p_y\right) + \sigma_z p_y^2\left(p_y + 3p_x\right)\Big], \end{aligned} \tag{7}$$

where the electric field is aligned with the dot z axis.

The relaxation rate between the initial electron state $|\Psi_i\rangle$ and the final electron state $|\Psi_f\rangle$ is estimated by the Fermi golden rule

$$\frac{1}{T_1} = \frac{2\pi}{\hbar}\sum_{\lambda,\mathbf{q}}\left|M_\lambda(\mathbf{q})\right|^2\left|\left\langle\Psi_f\left|e^{-i\mathbf{q}\mathbf{r}}\right|\Psi_i\right\rangle\right|^2\delta\left(E_f - E_i - E_q\right). \tag{8}$$

Here, the sum is done over all possible decay channels and directions of the phonon wave vector $\mathbf{q}$. $M_\lambda(\mathbf{q})$ denotes the scattering matrix element corresponding to the electron–phonon interaction including the piezoelectric and deformation potentials [30]. The expressions for $M_\lambda(\mathbf{q})$ are derived considering the three phonon modes λ of the bulk zinc-blende crystals, one longitudinal and two transversals, as producing strain and this strain yielding piezoelectricity (see [31] for more details). We assume bulk phonons, which is an appropiate model for embedded QDs. As a consequence, the scattering matrix elements $M_\lambda(\mathbf{q})$ does not depend on the QD orientation. All calculations are carried out at zero temperature, thus only phonon emission processes are possible, i.e. those inducing transitions from the first excited to the ground electronic state. The splitting energy between Zeeman sublevels is small so that only acoustic phonons are important and the linear dispersion regime applies $E_q = \hbar c_\lambda q$, where c_λ is the velocity of the longitudinal or transversal phonon branch [32]. Note that phonons cannot couple states with opposite spin and the spin admixture caused by SOI is essential for relaxation to take place.

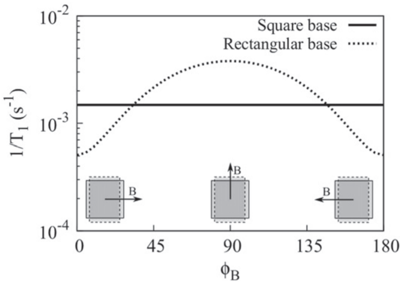

Figure 2. Electron spin relaxation rate as a function of the in-plane magnetic field orientation when only the Rashba SOI contribution is included. QDs of 10 nm height with rectangular (dotted line) and square base (solid line) are considered.

The eigenvalue problem is solved numerically using a finite difference method on a 3D grid. Accounting for SOI in the calculation of the energy spectra requires high numerical precision due to the small magnitude of this coupling and the presence of third-order derivatives. Accuracy in the derivatives in the finite difference method can be achieved by increasing the number of mesh nodes. However, the 3D character of the calculations is a serious hindrance, since the number of nodes increases as $n_x \cdot n_y \cdot n_z$, with n_i the discretization along the axis i. We can also improve accuracy by increasing the points of the discretization of derivatives. We have explored the performance of 5, 7 and 15-point central difference schemes and, after a series of convergence tests, found that a seven-point stencil central difference scheme and a number of 42875 mesh nodes discretizing the 3D system guarantees an appropiate description at a reasonable computational cost. In order to preserve the accuracy we model QDs as hard-wall cuboids fitting exact numbers of nodes, so that the potential energy term does not introduce any additional inaccuracy. This idealized geometry has been shown to capture the basic features of the spin–orbit anisotropy of realistic InAs/GaAs QDs [11], while enabling a simple interpretation in terms of symmetries, which is the goal of this work.

We use GaAs material parameters, particularly electron effective mass $m^* = 0.067$, density $\rho = 5310$ kg m^{-3} , dielectric constant $\epsilon_r = 12.9$, piezoelectric constant $h_{14} = 1.45 \times 10^9$ V m^{-1}, g-factor $g = -0.44$ and sound velocities $c_l = 4720$ m s^{-1} and $c_t = 3340$m s^{-1}. [33, 34] For the SOI constants, we take $\beta_d = 27.58 eV\,\text{Å}^3$ and $\alpha_r = 5.026 e\text{Å}^2$. [8] All simulations are carried out, unless otherwise stated, considering an axial electric field $E_z = 10$ kV cm^{-1} and an in-plane magnetic field $B_\parallel = 1\ T$.

3. Results and discussion

3.1. Geometry dependence

We investigate first the relaxation rate anisotropy for different dot geometries when applying an in-plane magnetic field at different orientations. The QDs considered have a base with square ($L_x = 80nm, L_y = 80$ nm) or rectangular ($L_x = 70$ nm, $L_y = 90$ nm) shape and various heights ranging from $L_z = 10$ nm to $L_z = 40$ nm.

Figure 2 shows the spin relaxation rate when only Rashba SOI is present. .[1] For QDs with square base the relaxation rate is constant for any ϕ_B. In contrast, in rectangular QDs it presents an anisotropic behavior, where the maximum (minimum) corresponds to a magnetic field oriented along the direction of weaker (stronger) confinement. In both cases, $1/T_1$ is independent of the QD height and, for the sake of clarity, only results for $L_z = 10nm$ are included in figure 2.

In figure 3(a), we analyze the spin relaxation in the only presence of Dresselhaus SOI for QDs with square base. The relaxation rate for short QDs ($L_z = 10$ nm) is almost isotropic with the orientation of the magnetic field. This is in sharp contrast with taller QDs, where strong quenchings are found at $\phi_B = 45$ and $\phi_B = 135$. On the other hand, when the QD base is rectangular, figure 3(b), only moderate modulations of $1/T_1$ are observed. Again, the dependence on ϕ_B is different depending on the dot height. When $B_\parallel$ is oriented along the direction of weaker confinement the relaxation is minimum for QDs with $L_z = 10$ nm, but it changes into a maximum for $L_z = 20, 30, 40$ nm.

[1] The relaxation is slower than in previous studies (e.g. [14, 21]) because in our cuboidal QDs there is no potential gradient, so the only source of inversion asymmetry contributing to equation (2) is the (relatively weak) external field **E**. The dependence on ϕ_B we describe below is however largely independent of the strength of the field

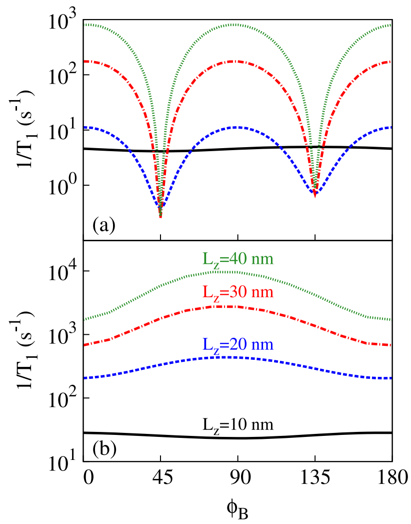

Figure 3. Calculated spin relaxation rate versus magnetic field orientation ϕ_B considering only Dresselhaus SOI in (a) square and (b) rectangular base QDs. Different dot heights are studied: $L_z = 10\ nm$ (solid black line), $L_z = 20\ nm$ (blue dashed line), $L_z = 30\ nm$ (red dash-dotted line) and $L_z = 40\ nm$ (green dotted line).

The preceding results reveal a strong sensitivity of the spin relaxation anisotropy to both the QD symmetry (squared or rectangular) and the QD height. Both factors can induce major, qualitative changes in the anisotropy. To understand such a behavior, we consider that the relaxation rate is proportional to the degree of spin admixture of the initial and final states of the transition, Ψ_i and Ψ_f in (8) [32]. These states can be approximated as:

$$\Psi_i \approx \psi_{000}\left|\downarrow\right\rangle + c_x^i\psi_{100}\mid\uparrow\rangle + c_y^i\psi_{010}\mid\uparrow\rangle$$
$$\Psi_f \approx \psi_{000}\mid\uparrow\rangle + c_x^f\psi_{100}\mid\downarrow\rangle + c_y^f\psi_{010}\mid\downarrow\rangle, \tag{9}$$

where ψ_{ijk} represents the electron orbital in the absence of SOI, with ijk the number of nodes in x, y and z, respectively, while $\mid\uparrow\rangle$ ($\mid\downarrow\rangle$) represents parallel (antiparallel) spin alignment along the direction of the magnetic field. For the analysis we can focus on Ψ_i (analogous reasoning is valid for Ψ_f). Ψ_i is mostly a spin down state, with a little SOI induced spin admixture with excited levels. Notice that $\psi_{000}\mid\uparrow\rangle$ does not contribute to the spin admixture of Ψ_i because the parity symmetry in x and y prevents direct SOI coupling with $\psi_{000}\mid\downarrow\rangle$. Thus, the degree of spin admixture is essentially captured by the coefficients c_x^i and c_y^i, which can be estimated perturbatively as:

$$c_x^i = -\frac{\langle\uparrow\mid\left\langle\psi_{100}\right|H_{\rm SOI}\left|\psi_{000}\right\rangle\mid\downarrow\rangle}{\varepsilon_{100\uparrow} - \varepsilon_{000\downarrow}}, \tag{10}$$

and

$$c_y^i = -\frac{\langle\uparrow\mid\left\langle\psi_{010}\right|H_{\rm SOI}\left|\psi_{000}\right\rangle\mid\downarrow\rangle}{\varepsilon_{010\uparrow} - \varepsilon_{000\downarrow}}. \tag{11}$$

The energy separations $\Delta\varepsilon_x = \varepsilon_{100\uparrow} - \varepsilon_{000\downarrow}$ and $\Delta\varepsilon_y = \varepsilon_{010\uparrow} - \varepsilon_{000\downarrow}$ do not vary with ϕ_B. Thus, the origin of the anisotropy must be sought in the SOI matrix elements.

We consider first Rashba SOI, i.e. $H_{\rm SOI} = H_R^{[001]}(0)$. From (4) and parity considerations, it follows that, for $\phi_B = 0$,

$$c_x^i = \alpha_r\, E_z\frac{\left\langle\uparrow\left|\sigma_y\right|\downarrow\right\rangle\left\langle\psi_{100}\right|p_x\left|\psi_{000}\right\rangle}{\Delta\varepsilon_x}, \qquad c_y^i = 0 \tag{12}$$

while for $\phi_B = 90$,

$$c_x^i = 0, \qquad c_y^i = \alpha_r\, E_z \frac{\left\langle \uparrow \left|\sigma_x\right| \downarrow \right\rangle \left\langle \psi_{010} \middle| p_y \middle| \psi_{000} \right\rangle}{\Delta\varepsilon_y}. \tag{13}$$

We see that depending on the orientation of the magnetic field the spin admixture is caused by the coupling to a different excited state. For QDs with square base $\Delta\varepsilon_x = \Delta\varepsilon_y$, and $\langle\psi_{100}|\ p_x\ |\psi_{000}\rangle = \langle\psi_{010}|\ p_y|\psi_{000}\rangle$. Consequently, the degree of spin mixing does not change at $\phi_B = 0$ and $\phi_B = 90$, in agreement with the isotropic $1/T_1$ observed in figure 2. Conversely, in rectangular QDs with stronger confinement in x, $\Delta\varepsilon_x > \Delta\varepsilon_y$. Then, the admixture coefficients at $\phi_B = 90$ are larger than at $\phi_B = 0$, which justifies the anisotropy observed in figure 2.

The anisotropy of Dresselhaus SOI induced spin relaxation, shown in figure 3, can be understood in similar terms. We split equation (3) as $H_D^{[001]} = H_z + H_{xy}$, where $H_z = \beta_d p_z^2\left(p_y\sigma_y - p_x\sigma_x\right)$ and $H_{xy} = H_x + H_y = \beta_d\left[p_x^2\left(p_z\sigma_z - p_y\sigma_y\right) + p_y^2\left(p_x\sigma_x - p_z\sigma_z\right)\right]$. Calculations using these Hamiltonians independently show that H_z dominates for $L_z = 10\ nm$, in agreement with the usual practice of approximating the Dresselhaus SOI by H_z in quasi-2D systems. If we perform a similar analysis for H_z as the one carried out for Rashba SOI, we find that coupling to ψ_{010} and ψ_{100} dominates at $\phi_B = 0$ and $\phi_B = 90$, respectively. This is exactly the opposite as for the Rashba SOI case, explaining the results obtained for $L_z = 10\ nm$ QDs (see figure 3(b)). As the QD height is increased, however, H_{xy} soon dominates over H_z. Indeed, for $L_z = 20\ nm$ it is already dominant. Considering individually H_x and H_y it can be shown that they present opposite behaviors with ϕ_B. H_x produces a maximum (minimum) relaxation for $\phi_B = 90$ ($\phi_B = 0$) and H_y for $\phi_B = 0$ ($\phi_B = 90$). This dependence does not change with the base shape and a stronger confinement in one direction only determines which term, H_x or H_y, prevails. In the rectangular dot of figure 3(b), $L_x < L_y$ so H_x is more important and we observe its angular dependence. Instead, when the dot base is squared H_x and H_y cancel each other out at $\phi_B = 45$ and $\phi_B = 135$, thus giving rise to the pronounced minima of $1/T_1$ observed in figure 3(a).

To summarize this section, the spin relaxation anisotropy of [001] grown GaAs QDs is determined by the spin admixture induced by SOI. This is qualitatively different in systems where Rashba or Dresselhaus SOI terms dominate. In the latter case, the anisotropy reflects whether H_z or H_{xy} prevails. It turns out that H_{xy} is already dominant for $L_z = 20\ nm$ (height-to-base aspect ratio of 1:4), which points out at the early relevance of cubic Dresselhaus terms in structures where 3D starts becoming important. In this case, the use of QDs with symmetric x–y confinement enables strong suppressions of the relaxation at certain magnetic field orientations.

3.1.1. The influence of strong magnetic fields

We study next the spin relaxation angular dependence in square QDs under strong magnetic fields. In such a case, the orbital effects of the magnetic field are expected to play an important role, especially in tall systems. We emphasize the need of a true 3D calculation to account for this effect, since it cannot be properly described using 2D models [14]. We calculate the relaxation rate for different values of the magnetic field up to $B_\parallel = 10T$ in QDs with $L_x = L_y = 80\ nm$ and $L_z = 20\ nm$.

The impact of the magnetic field strength on the angular dependence through the Rashba SOI is negligible and not shown. We enclose in figure 4 the spin relaxation yielded by the Dresselhaus SOI term only. Figure 4 shows that the minima of $1/T_1$ at $\phi_B = 45$ and $\phi_B = 135$ is gradually removed for strong magnetic fields. This behavior can be understood in terms of the differential contribution of H_{xy} and H_z, as pointed out previously. For QDs with $L_z = 20\ nm$ and $B_\parallel = 1T$, H_{xy} dominates and we observe two pronounced minima (see inset in figure 4). When $B_\parallel$ increases, H_z rises up and it becomes dominant at $B_\parallel = 10T$, this being responsible for the suppression of the minima. It is noteworthy to mention that an increase in the height of the dot enhances the effects of the magnetic field but also diminishes the contribution of H_z to the Hamiltonian. As a consequence, in taller QDs a balance of these two contributions will determine which term, H_{xy} or H_z, dominates and, therefore, the angular dependence of the spin relaxation.

3.2. In-plane confinement potential orientation

In this section, we investigate the impact of the QD orientation with respect to the crystal host on the spin relaxation. The rotation angle θ_z is defined as the angle between the [001] crystal direction and the x axis of the dot, see inset of figure 5(a) for a schematic representation. All calculations are carried out with the magnetic field $B_\parallel = 1T$ oriented along the x axis of the QD and an axial electric field $E_z = 10$ kV cm^{-1}.

In figure 5(a), we plot the relaxation rate in the presence of Rashba SOI only for QDs with $L_z = 10\ nm$ (results for $L_z = 20\ nm$ are identical and are omitted for clarity). We find that $1/T_1$ is not affected by changes in the dot orientation. This result is as expected since (4) does not depend on θ_z.

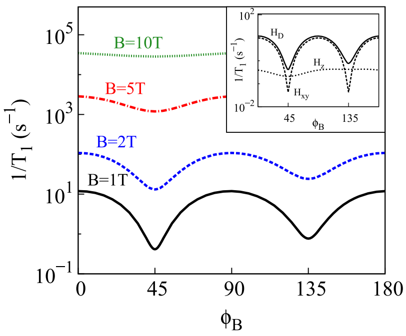

Figure 4. Spin dynamics of a square QD of $L_z = 20$ nm as a function of ϕ_B for different magnetic field intensities: $B_\parallel = 1T$ (black solid line), $B_\parallel = 2T$ (blue dashed line), $B_\parallel = 5T$ (red dash-dotted line) and $B_\parallel = 10T$ (green dotted line). Only the presence of Dresselhaus SOI is considered. The inset shows the spin relaxation for $B_\parallel = 1T$ when considering the full Dresselhaus Hamiltonian $H_D = H_{xy} + H_z$ (solid line), and also the partial contributions of H_{xy} (dashed line) and H_z (dotted line).

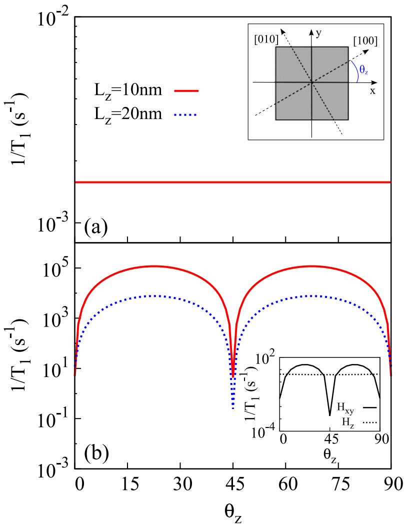

Figure 5. Spin relaxation rate as a function of the dot orientation θ_z for square base QDs with $L_z = 10$ nm (black solid curve) and $L_z = 20$ nm (blue dotted curve). Results are shown for (a) pure Rashba SOI and (b) pure Dresselhaus SOI. The in-plane magnetic field $B_\parallel = 1T$ is oriented along the dot x axis ($\phi_B = 0$). The inset in (a) illustrates a representation of the system and the definition of the rotation angle. The inset in (b) shows the relaxation due to H_{xy} and H_z in the $L_z = 10$ nm dot.

For the Dresselhaus SOI case instead, figure 5(b) shows a strong dependence of $1/T_1$ on the confinement potential rotation. In particular, one can see some specific rotation angles, $\theta_z = 0, 45, 90$, where the spin relaxation is reduced by 4–5 orders of magnitude as compared to others. This behavior can be understood from the form of the Hamiltonian in (5). The Dresselhaus SOI presents a $2\theta_z$ dependence, with half of the terms multiplied by $\sin 2\theta_z$ and the other half by $\cos 2\theta_z$. Therefore, the first part of (5) cancels for $\theta_z = 45$ and the second part for $\theta_z = 0$ and $\theta_z = 90$. This suppresses some of the SOI coupling channels, giving rise to slower relaxation rates than for intermediate angles.

It is noteworthy to mention that the dependence on θ_z originates in H_{xy}, with H_z remaining isotropic, see figure 5(b) inset. This highlights the important role of the cubic terms of the Dresselhaus SOI Hamiltonian in GaAs QDs. As a matter of fact, the inset shows that even in the shortest QDs ($L_z = 10$ nm), save for the vicinity of

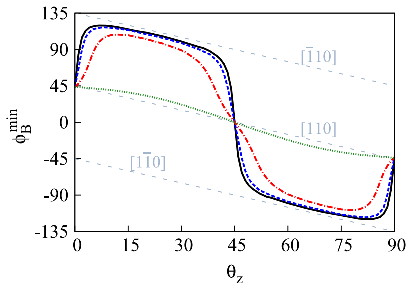

Figure 6. 'Magic' angle as a function of the dot orientation θ_z for a QD with $L_z = 10$ *nm*, $L_x = 80$ *nm* and various L_y: $L_y = 80$ *nm* (black solid line), $L_y = 90$ *nm* (blue dashed line), $L_y = 110$ *nm* (red dash-dotted line) and $L_y = 150$ *nm* (green dotted line). The grey dashed lines correspond to ϕ_B pointing along [110], [$\bar{1}$10] and [1$\bar{1}$0] direction for each θ_z.

the 'magic' rotation angles ($\theta_z = 0, 45, 90$) the main contribution to the relaxation rate does not come from H_z but from H_{xy}.

These results are robust against changes in the QD geometry, such as height and base shape, which do not modify the qualitative trend. In particular, the minimum at $\theta_z = 45$ remains unaltered while the minima at $\theta_z = 0$ and $\theta_z = 90$ are only slightly shifted in rectangular QDs.

Recent experiments by Scarlino and co-workers have also explored spin relaxation anisotropy of GaAs QDs. [22] For their specific QD, they observed a periodicity of 180 degrees in ϕ_B, with a 'magic' angle near [110]. Both the periodicity and the relaxation suppression were explained assuming Rashba and Dresselhaus SOI terms had roughly the same weight and the QD was strongly elongated in one direction. It was shown that the deviation from the [110] direction could arise from the values of θ_z and the Rashba to Dresselhaus SOI strength ratio, which are unknown for their sample. Here we generalize this study by considering QDs with different in-plane shape, from square (L_x=L_y) to strongly elongated ($L_x \ll L_y$), and include the cubic Dresselhaus terms which are missing in their analysis. We set Rashba SOI to be as strong as the linear (H_z) Dresselhaus term by setting $\alpha_r = \beta_d \langle p_z^2 \rangle / E_z$. The results are shown in figure 6.

One can see that for the strongly elongated QD, $L_y = 150nm$, the 'magic' angle $\phi_B^{\min}$ takes place when the magnetic field points approximately along [110] ($\phi_B^{\min} \simeq 45 - \theta_z$). This is consistent with the estimates of Scarlino *et al* (figure 4(a) in [22]). The small deviations from [110] (dashed grey line in figure 6) are atributed to the influence of the cubic Dresselhaus terms. As the QD elongation is reduced, the anisotropy evolves towards a completely different limit, which is reached for the square QD, $L_y = 80nm$. In this case, the magic angle remains at [110] for $\theta_z = 0, 45, 90$, but it rapidly deviates for any other θ_z. For $0 < \theta_z < 45$ it switches to [$\bar{1}$10] ($\phi_B^{\min} \simeq 135 - \theta_z$), while for $45 < \theta_z < 90$ it switches to [1$\bar{1}$0] ($\phi_B^{\min} \simeq -45 - \theta_z$). The origin of this distinct behavior is the same discussed in figure 5(b) inset. Namely, when the *x* axis of the dot does not coincide with [100], [110] or [010], Dresselhaus H_{xy} terms take over H_z ones. This breaks the balance between Rashba and H_z Dresselhaus SOI described in [22]. Because statistically QDs are likely to be tilted from $\theta_z = 0, 45, 90$, it follows that cubic Dresselhaus terms can induce severe deviations from the spin–orbit anisotropy described in the experiment if the QDs are not strongly elongated.

3.3. Effect of an additional in-plane electric field

We next explore the influence of applying an in-plane electric field on the spin relaxation anisotropy. We consider the squared QD of section 3.1 with $B_\parallel = 1T$ and $E_z = 10$ kV cm^{-1}, but now we add an additional electric field component $E_\parallel = 10kV\ cm^{-1}$. Calculations are performed rotating the in-plane electric field for some fixed magnetic field orientations.

In figures 7(a) and (b), we present the relaxation rate obtained for pure Rashba and pure Dresselhaus SOI, respectively, at four different ϕ_B values. The most remarkable finding is that $1/T_1$ is increased by several orders of magnitude in comparison with the case with only axial electric field (figures 2 and 3), although strong suppressions show up at some specific combinations of ϕ_B and ϕ_E. For Rashba SOI the combination is $\phi_B - \phi_E = 90, 270$ and for Dresselhaus SOI $\phi_B + \phi_E = 0, 180$. Changes in the QD geometry do not modify significantly the qualitative results shown in figure 7. Only small displacements of the cancellation angles and the moderation of some minima occur.

The influence of the in-plane electric field can be explained from the fact that $E_\parallel$ breaks the parity symmetry in the direction ϕ_E. This enables the otherwise forbidden SOI coupling between the Zeeman sublevels $\psi_{000}|\uparrow\rangle$

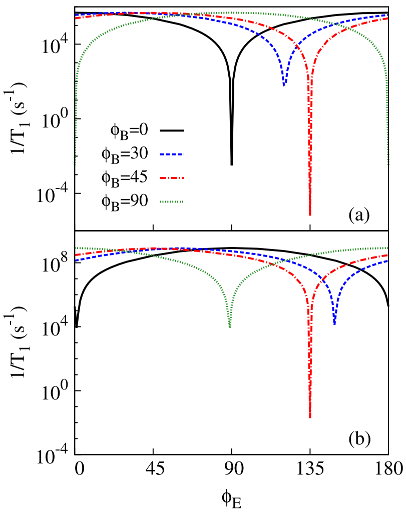

Figure 7. Electron spin relaxation as a function of the in-plane electric field orientation ϕ_E considering (a) only Rashba SOI and (b) only Dresselhaus SOI. The QDs studied have square base and $L_z = 10$ *nm*. Calculations with the magnetic field oriented at some fixed angles are presented: $\phi_B = 0$ (black solid line), $\phi_B = 30$ (blue dashed line), $\phi_B = 45$ (red dash-dotted line) and $\phi_B = 90$ (green dotted line).

and $\psi_{000}|\downarrow\rangle$ in Ψ_i and Ψ_f (recall section 3.1). Since these states are very close in energy, the ensuing spin admixture is important, which justifies the large enhancement of $1/T_1$. In order to understand the minima we carry out a similar perturbative analysis to that of section 3.1 but now focusing on the coupling between the two ψ_{000} sublevels. Let us consider first the Dresselhaus SOI term. Assuming $H_D^{[001]} \approx H_z$ (as is the case for quasi-2D QDs and $\theta_z = 0$), the $\phi_B = 0$ matrix element is:

$$\left\langle \psi_{000} \left\langle \uparrow \left| H_z \right| \psi_{000} \right| \downarrow \right\rangle = \beta_d \left\langle \downarrow \left| \sigma_y \right| \uparrow \right\rangle \left\langle \psi_{000} \left| p_z^2\ p_y \right| \psi_{000} \right\rangle. \tag{14}$$

The integral of the orbital part in (14) vanishes when $\phi_E = 0$ because of the odd parity along y, but other orientations of the electric field break the parity symmetry in the y direction and then $1/T_1$ increases, as seen in figure 7(b) (black line). Similar reasoning shows that for $\phi_B = 90$ the parity-induced minimum occurs at $\phi_E = 90$. For intermediate magnetic field angles, however, the minimum no longer takes place when $E_\parallel \parallel \mathbf{B}$. Indeed, for $\phi_B = 45$, the minimum is found at $\phi_E = 135$ ($E_\parallel \perp \mathbf{B}$). To explain this, it is convenient to rotate the coordinate system 45 degrees from (x,y) into (x', y') so that the x' axis is aligned with the direction of $\mathbf{B}$. As inferred from (5), the resulting SOI term is $H_z^{45} = \beta_d p_z^2 (\sigma_{y'} p_x' + \sigma_{x'} p_y')$ and the matrix element becomes:

$$\left\langle \psi_{000} \left\langle \uparrow \left| H_z^{45} \right| \psi_{000} \right| \downarrow \right\rangle = \beta_d \left\langle \downarrow \left| \sigma_{y'} \right| \uparrow \right\rangle \left\langle \psi_{000} \left| p_z^2\ p_y' \right| \psi_{000} \right\rangle. \tag{15}$$

This integral vanishes due to the odd parity in x' when $E_\parallel$ is parallel to the y' axis, i.e. when $\phi_E = 135$ in the initial coordinate frame, in agreement with figure 5(b).

The minima in the presence of Rashba SOI can be explained in similar terms, but because $H_R^{[001]}$ has rotational symmetry, see equation (4), it does not change when rotating the coordinate system. Then, the minima always take place for $E_\parallel \perp \mathbf{B}$.

To summarize this section, the presence of in-plane electric fields greatly enhances spin relaxation due to the lowered orbital symmetry, but the anisotropy of both Rashba and Dresselhaus SOI makes it possible to find relative angles between $E_\parallel$ and $\mathbf{B}$ such that the relaxation is severely reduced.

3.4. [111] Grown QDs

In figure 8 we plot the spin relaxation rate for the squared QD studied in section 3.1, but now considering the dot is grown along the [111] crystal direction. In general, faster relaxation rates are obtained for this orientation as compared to the [001] grown QDs. Interestingly, we observe the same angular dependence for both Rashba SOI (figure 8(a)) and Dresselhaus SOI (figure 8(b)). Both mechanisms show strong suppressions at $\phi_B = 135$ and $\phi_B = 315$. However, when increasing L_z Rashba and Dresselhaus SOI mechanisms show opposite behaviors and

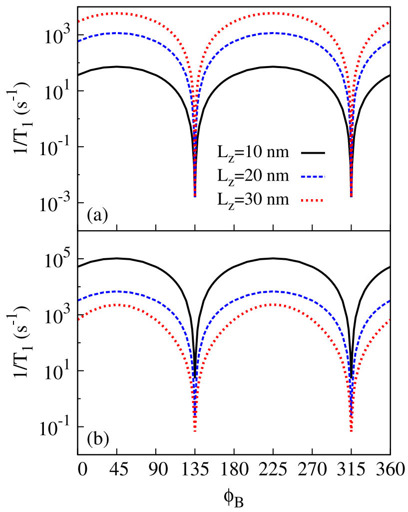

Figure 8. Electron spin dynamics of square QDs grown along the [111] crystallographic direction as a function of the magnetic field orientation. Simulations considering (a) the Rashba SOI and (b) the Dresselhaus SOI are included for three QD heights: $L_z = 10\ nm$ (black solid curve), $L_z = 20\ nm$ (blue dashed curve) and $L_z = 30\ nm$ (red dotted curve).

$1/T_1$ increases and decreases, respectively. Therefore, the dot height determines which of the coupling mechanisms dominates.

The cancellation angles of the relaxation in figure 8 can be justified noting that the canonical momenta $p_x = -i\hbar \mathrm{d}/\mathrm{d}_x + zB \sin\phi_B$ and $p_y = -i\hbar \mathrm{d}/\mathrm{d}_y - zB \cos\phi_B$ have exactly the same form for $\phi_B = 135$ and $\phi_B = 315$ since $L_x = L_y$. As a result, the first term in (6) and several terms in (7) cancel out, yielding two sharp minima in the scattering rate curve.

The identical anisotropy of Rashba and Dresselhaus SOI induced spin relaxation in [111] QDs revealed by figure 8, which is a consequence of the formal equivalences between $H_R^{[111]}$ and $H_D^{[111]}$, [35], facilitates in practice the simultaneous quenching of both mechanisms. For magnetic fields where hyperfine interaction is negligible and square dots, this should lead to spin lifetimes in the range of seconds. We have further checked that changes in the QD base shape do not modify the qualitative behavior reported above, the minima being only slightly shifted for rectangular dots under Dresselhaus SOI.

4. Conclusions

We have investigated systematically the electron spin scattering anisotropy in 3D cuboidal GaAs QDs grown along the [001] and [111] directions. We have shown that the relaxation rate can be controlled by several orders of magnitude by varying the in-plane orientation of external magnetic and electric fields.

In [001] grown QDs under an axial electric field, the spin relaxation in-plane anisotropy is strongly dependent on the QD geometry and the nature of the dominating SOI term. For Rashba SOI, the relaxation is isotropic or anisotropic when the base is squared and rectangular, respectively, and it is not affected by changes in the QD height. On the other hand, for Dresselhaus SOI, the relaxation presents a different behavior depending not only on the base shape, but also on the QD height. In fact, short and tall dots can even show contrary angular dependence, evidencing the important role of QD 3D. In addition, we have demonstrated that the isotropic/anisotropic behavior can be controlled by changing the magnetic field strength.

We have also shown that rotating the confinement potential in-plane with respect to the crystal structure causes an important modulation of the spin relaxation, that is severely suppressed when the high symmetry directions of the QD confinement match the main crystallographic axes. This modulation arises from the cubic Dresselhaus terms, which are important even for small heights. Such terms can explain the deviation of the slow spin relaxation direction of the magnetic field away from [110], as measured in very recent experiments [22], for strongly elongated QDs. For less elongated structures they can even switch it to $[1\bar{1}0]$ or $[\bar{1}10]$.

An additional in-plane electric field component causes a strong increase in the relaxation rate, but certain combinations of ϕ_B and ϕ_E lead to enhanced spin lifetimes. We find that these combinations are different for Rashba, $\phi_B - \phi_E = 90,\ 270$, and Dresselhaus SOI, $\phi_B + \phi_E = 0,\ 180$.

We have further studied QDs grown along the [111] direction. We have found that Rashba and Dresselhaus SOI present the same angular dependence with ϕ_B, with pronounced minima at certain magnetic field orientations. This enables simultaneous suppression of Rashba and Dresselhaus SOI induced spin relaxation, which is an advantadge as compared to more conventional [001] grown QDs.

Acknowledgments

This work was supported by UJI-Bancaixa Project No. P1-1B2011-01, MINECO Project No. CTQ2011-27324, and FPU Grant (C S).

References

[1] Awschalom D D, Loss D and Samarth N 2002 *Semiconductor Spintronics and Quantum Computation* (Berlin: Springer)
[2] Fabian J, Matos-Abiague A, Ertler C, Stano P and Žutić I 2007 *Acta Phys. Slovaca* **57** 565
[3] Loss D and DiVincenzo D P 1998 *Phys. Rev.* A **57** 120
[4] Hanson R, Kouwenhoven L P, Petta J R, Tarucha S and Vandersypen L M K 2007 *Rev. Mod. Phys.* **79** 1217
[5] Khaetskii A V and Nazarov Y V 2000 *Phys. Rev.* B **61** 12639
[6] Dresselhaus G 1955 *Phys. Rev.* **100** 580
[7] Bychkov Y A and Rashba E I 1984 *J. Phys.* C **17** 6039
[8] Winkler R 2003 *Spin-Orbit Coupling Effects in Two-Dimensional Electron and Hole Systems* (Berlin: Springer)
[9] Könemann J, Haug R J, Maude D K, Fal'ko V I and Altshuler B L 2005 *Phys. Rev. Lett.* **94** 226404
[10] Takahashi S, Deacon R S, Yoshida K, Oiwa A, Shibata K, Hirakawa K, Tokura Y and Tarucha S 2010 *Phys. Rev. Lett.* **104** 246801
[11] Nowak M P and Szafran B 2013 *Phys. Rev.* B **87** 205436
[12] Fal'ko V I, Altshuler B L and Tsyplyatyev O 2005 *Phys. Rev. Lett.* **95** 076603
[13] Destefani C F and Ulloa S E 2005 *Phys. Rev.* B **72** 115326
[14] Stano P and Fabian J 2006 *Phys. Rev. Lett.* **96** 186602
[15] Olendski O and Shahbazyan T V 2007 *Phys. Rev.* B **75** 041306
[16] Amasha S, MacLean K, Radu I P, Zumbühl D M, Kastner M A, Hanson M P and Gossard A C 2008 *Phys. Rev. Lett.* **100** 046803
[17] Prabhakar S, Melnik R and Bonilla L L 2013 *Phys. Rev.* B **87** 235202
[18] Stano P and Fabian J 2006 *Phys. Rev.* B **74** 045320
[19] Nowak M P, Szafran B, Peeters F M, Partoens B and Pasek W J 2011 *Phys. Rev.* B **83** 245324
[20] Stepanenko D, Rudner M, Halperin B I and Loss D 2012 *Phys. Rev.* B **85** 075416
[21] Golovach V N, Khaetskii A and Loss D 2004 *Phys. Rev. Lett.* **93** 016601
[22] Scarlino P, Kawakami E, Stano P, Shafiei M, Reichl C, Wegscheider W and Vandersypen L M K 2014 *Phys. Rev. Lett.* **113** 256802
[23] Planelles J, Climente J I and Segarra C 2012 *J. Phys. Chem.* C **116** 25143
[24] Dalacu D, Mnaymneh K, Wu X, Lapointe J, Aers G C, Poole P J and Williams R L 2011 *Appl. Phys. Lett.* **98** 251101
[25] Pfund A, Shorubalko I, Leturcq R and Ensslin K 2006 *Appl. Phys. Lett.* **89** 252106
[26] Mano T, Abbarchi M, Kuroda T, McSkimming B, Ohtake A, Mitsuishi K and Sakoda K 2010 *Appl. Phys. Express* **3** 065203 and references therein
[27] Vurgaftman I and Meyer J R 2005 *J. Appl. Phys.* **97** 053707
[28] Biermann K, Hernández-Mínguez A, Hey R and Santos P V 2012 *J. Appl. Phys.* **112** 083913
[29] Balocchi A, Amand T, Wang G, Liu B L, Renucci P, Duong Q H and Marie X 2013 *New J. Phys.* **15** 095016
[30] Climente J I, Bertoni A, Goldoni G and Molinari E 2006 *Phys. Rev.* B **74** 035313
[31] Climente J I, Segarra C and Planelles J 2013 *New J. Phys.* **15** 093009
[32] Khaetskii A V and Nazarov Y V 2001 *Phys. Rev.* B **64** 125316
[33] Vurgaftman I, Meyer J R and Ram-Mohan L R 2001 *J. Appl. Phys.* **89** 5815
[34] Madelung O (ed) 1982 *Semiconductors. Physics of Group IV Elements and III–V Compounds* (*Landolt–Börnstein* vol 17) (Berlin: Springer)
[35] Žutić I, Fabian J and Das Sarma S 2004 *Rev. Mod. Phys.* **76** 323

New Journal of Physics
The open access journal for physics

Spin–orbit-induced hole spin relaxation in InAs and GaAs quantum dots

J I Climente, C Segarra and J Planelles[1]
Departament de Química Física i Analítica, Universitat Jaume I, Box 224, E-12080 Castelló, Spain
E-mail: josep.planelles@qfa.uji.es

New Journal of Physics **15** (2013) 093009 (21pp)
Received 4 April 2013
Published 5 September 2013
Online at http://www.njp.org/
doi:10.1088/1367-2630/15/9/093009

Abstract. We study the effect of valence band spin–orbit interactions (SOI) on the acoustic phonon-assisted spin relaxation of holes confined in quantum dots (QDs). Heavy hole–light hole (hh–lh) mixing and all the spin–orbit terms arising from zinc-blende bulk inversion asymmetry (BIA) are considered on equal footing in a fully three-dimensional Hamiltonian. We show that hh–lh mixing and BIA have comparable contributions to the hole spin relaxation in self-assembled QDs, but BIA becomes dominant in gated QDs. Simultaneously accounting for both mechanisms is necessary for quantitatively correct results in quasi-two-dimensional QDs. The dependence of the hole spin relaxation on the QD geometry and spin splitting energy is drastically different from that of electrons, with a non-monotonic behavior which results from the interplay between SOI terms. Our results reconcile contradictory predictions of previous theoretical works and are consistent with experiments.

[1] Author to whom any correspondence should be addressed.

Contents

1. Introduction

Over the last few years, the spin of holes confined in III–V semiconductor quantum dots (QDs) has emerged as a promising building block for spintronic and spin-based quantum information devices [1]. As compared to electrons, the p-like nature of the hole orbitals leads to weaker hyperfine interaction with the lattice nuclei, resulting in coherence times which hold promise for applications [2–7]. As a matter of fact, demonstrations of hole spin manipulation in QDs have been recently reported [8–10] and theoretical proposals of control mechanisms are being proposed [11–14]. In this context, the study of hole spin relaxation has become a subject of interest. Hole spin relaxation is also important for optical applications because it is believed to rule the exciton spin dynamics in both dark-to-bright exciton transitions [15–18], which affect exciton storage times [19–21], and transitions within the bright doublet [22], which affect light depolarization [17].

Experimental observations in self-assembled InAs QDs point at hole spin lifetimes ranging from $T_1^{\mathrm{h}} \sim 10\,\mathrm{ps}$ to 1 ms [2, 23–26]. The large dispersion is partly attributed to the different relaxation mechanisms involved in different studies. When the energy splitting between orthogonal spin states is small, hyperfine interaction is the dominant relaxation channel [16, 27]. In this case, the lifetime is strongly dependent on the degree of hh–lh mixing. If the hole state is a pure hh, as in the ground state of flat (quasi-two-dimensional (2D)) QDs, the hyperfine interaction takes an Ising form and spin relaxation is slow, but it rapidly increases in non-flat QDs due to hh–lh mixing [1, 7]. On the other hand, when the energy splitting exceeds the nuclear magnetic field, the valence band spin–orbit interaction (SOI) takes over as the main source of relaxation [16, 27]. Long hole spin lifetimes have then been observed, reaching up to $T_1^{\mathrm{h}} \sim 0.25\,\mathrm{ms}$, which is only five to ten times shorter than electron spin lifetimes, T_1^{e} [26]. This result is encouraging for the use of holes in quantum information and optical applications, but it is surprising because the valence band SOI is known to be much stronger than that of the conduction band [28].

The above paradox has prompted a number of theoretical works trying to understand which factors determine the relaxation dynamics of single holes under magnetic fields [29–33] and that of holes forming excitons [15, 22, 34, 35] in quasi-2D InAs/GaAs QDs. For the relaxation to take place one needs a source of energy relaxation, which in these systems is provided by the acoustic phonon bath [23, 24], plus a source of spin admixture. Woods *et al* [29] and Lu *et al* [30] proposed that the latter is the coupling between hh and lh subbands. Other authors have suggested instead that the splitting between hh and lh subbands in flat QDs is large owing to confinement and strain, so that spin admixture must be due to other SOI mechanisms. It was then proposed that hole SOI should have an origin similar to that of conduction electrons, namely the bulk inversion asymmetry (BIA) of zinc-blende crystals, which gives rise to Dresselhaus SOI terms [28]. Bulaev and Loss assumed that the cubic-in-k Dresselhaus term is dominant and showed that T_1^{h} could then become comparable to T_1^{e} in flat QDs [31]. Other studies followed this assumption and succeeded in explaining some experimental observations [15, 26, 32]. By contrast, Tsitsishvili *et al* [35] suggested that if the lateral confinement is weak, it is the linear-in-k term that dominates the mixing. Last, Roszak *et al* [34] suggested that for holes forming excitons, it is the electron–hole (e–h) exchange interaction together with the strain that gives rise to hole spin admixture.

It is worth noting that all the previous works assumed a dominating SOI mechanism without actually comparing it with others. In addition, simplified models disregarding hh–lh mixing become highly parametric, and different parameters were needed to explain different experimental observations even in the same system [15, 26, 32]. The lack of a comprehensive study translates into many open questions which show that hole spin relaxation in QDs is still not fully understood. To name a few: (i) while Woods *et al* [29] predict that T_1^{h} decreases with the QD diameter, Lu *et al* [30] predict exactly the opposite behavior; (ii) Bulaev and Loss [31] predicted $T_1^{\mathrm{h}} > T_1^{\mathrm{e}}$ in the limit of 2D QDs, but experiments on self-assembled QDs have only shown $T_1^{\mathrm{e}}/T_1^{\mathrm{h}} = 5 - 10$ [26], so that one wonders if any realistic QD structure would actually permit holes relaxing slower than electrons; (iii) in excitons, the role of e–h exchange energy is not clear: while experiments with self-assembled QDs have shown negligible dependence of T_1^{h} [24], a strong dependence has been found in colloidal quantum rods [36].

In this work, we aim at covering the existing gap in the understanding of hole spin relaxation in QDs. We study the hole spin dynamics considering simultaneously the most relevant intrinsic SOI terms of III–V QDs, namely hh–lh mixing and all the different Dresselhaus SOI terms arising from the BIA of zinc-blende crystals, along with the hole–acoustic phonon coupling. All the terms are described within a four-band $k \cdot p$ formalism and three-dimensional (3D) Hamiltonians, which allows us to provide a general overview on the effect of the QD size and geometry dependence while relying on well-known bulk parameters only. In this way, we are able to establish the regime of validity of previous studies which assumed a single dominating SOI mechanism. Furthermore, we explore spheroidal QDs beyond the usual quasi-2D limit, thus providing theoretical assessment for developing experimental research with spherical and prolate QDs [18, 36].

We find that hh–lh is the main SOI channel in prolated or spherical QDs, but Dresselhaus SOI has a comparable contribution in oblated QDs (such as self-assembled dots), and it becomes dominant in quasi-2D QDs with very weak confinement (as in electrostatically confined dots). The competition between SOI coupling terms and the energy splitting between hh and lh leads to a non-monotonic dependence of T_1^{h} with the QD geometry, in sharp contrast with the well-known case of electrons. This explains the opposite trends reported by different theoretical studies in the literature. The dependence of T_1^{h} on the e–h exchange energy we predict is consistent with experiments on colloidal nanorods [36], but it suggests that two-phonon processes are relevant in self-assembled QDs. In prolate QDs, where the ground state is formed by lh, the spin relaxation is shown to take place in similar timescales as for transitions between hh states. However, the coupling to acoustic phonons is different, with deformation potential interaction being the main mechanism even for vanishing spin splitting energy.

2. Theoretical model

We study the spin relaxation of holes confined in zinc-blende QDs grown along the [001] direction. The hole spin states are considered split energetically, for example by the e–h exchange interaction in excitons or any other source that can be viewed as an effective axial magnetic field. Thus, similar results can be expected for transitions between Zeeman sublevels under moderate external magnetic fields.

2.1. Hamiltonian

The system Hamiltonian reads

$$H = H_{\mathrm{h}} + H_{\mathrm{ph}} + H_{\mathrm{h-ph}}. \tag{1}$$

In equation (1), H_{h} is the hole Hamiltonian

$$H_{\mathrm{h}} = H_{\mathrm{L}} + H_{\mathrm{BIA}} + V_{\mathrm{QD}}\,\mathcal{I} + H_Z, \tag{2}$$

where H_{L} is the four-band Luttinger Hamiltonian describing the coupled hh–lh bands [37]. It includes quadratic terms in k only:

$$H_{\mathrm{L}} = \frac{1}{m_0}\left[\left(\gamma_1 + \frac{5}{2}\gamma_2\right)\frac{k^2}{2} - \gamma_2(k_x^2 J_x^2 + k_y^2 J_y^2 + k_z^2 J_z^2)\right.$$
$$\left. -2\gamma_3(\{k_x, k_y\}\{J_x, J_y\} + \{k_y, k_z\}\{J_y, J_z\} + \{k_z, k_x\}\{J_z, J_x\})\right], \tag{3}$$

where m_0 is the free electron mass, γ_i are the Luttinger parameters, $k_j = -\mathrm{i}\hbar\,\partial_j$ the j component of the linear momentum, $\{A, B\} = \frac{1}{2}(AB + BA)$ and J_i is the ith component of the angular momentum corresponding to the quantum number $J = 3/2$. To obtain the matrix representation of this Hamiltonian we multiply the first term of equation (3) by the 4×4 unit matrix and employ the standard matrix representation of the $J = 3/2$ components of the angular momentum [38]. We finally obtain

$$H_{\mathrm{L}} = \begin{pmatrix} P+Q & -S & R & 0 \\ -S^\dagger & P-Q & 0 & R \\ R^\dagger & 0 & P-Q & S \\ 0 & R^\dagger & S^\dagger & P+Q \end{pmatrix} \tag{4}$$

with

$$P = \frac{1}{2\,m_0}\,\gamma_1\,\left(k_x^2 + k_y^2 + k_z^2\right), \tag{5}$$

$$Q = \frac{1}{2\,m_0}\,\gamma_2\,\left(k_x^2 + k_y^2 - 2k_z^2\right), \tag{6}$$

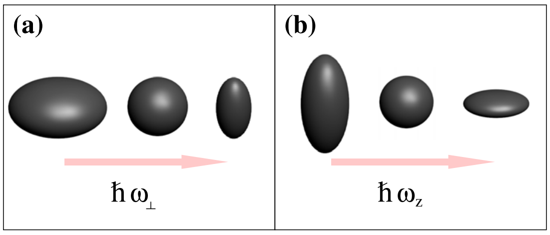

Figure 1. Geometry of QDs with varying lateral (a) and vertical (b) confinement frequency.

$$R = \frac{1}{2\,m_0}\left[-\sqrt{3}\,\gamma_2\,(k_x^2 - k_y^2) + 2\,\mathrm{i}\,\sqrt{3}\,\gamma_3\,k_x\,k_y\right], \tag{7}$$

$$S = \frac{1}{2\,m_0}\,2\,\sqrt{3}\,\gamma_3\,(k_x - \mathrm{i}\,k_y)\,k_z. \tag{8}$$

H_{BIA} includes the linear and the Dresselhaus SOI third order in k terms [28]:

$$H_{\mathrm{BIA}} = \frac{2}{\sqrt{3}}\,C_k\,[k_x\,\{J_x, J_y^2 - J_z^2\} + \mathrm{cp}] + b_{41}\,(\{k_x, k_y^2 - k_z^2\}\,J_x + \mathrm{cp}) + b_{42}\,(\{k_x, k_y^2 - k_z^2\}\,J_x^3 + \mathrm{cp})$$
$$+ b_{51}\,(\{k_x, k_y^2 + k_z^2\}\,\{J_x, J_y^2 - J_z^2\} + \mathrm{cp}) + b_{52}\,(k_x^3\,\{J_x, J_y^2 - J_z^2\} + \mathrm{cp}), \tag{9}$$

where C_k, b_{41}, b_{42}, b_{51} and b_{52} are material-dependent coefficients and cp stands for cyclic permutations of the preceding terms. The matrix form of the Hamiltonian terms above is given in the appendix. One can note that all BIA terms provide direct mixing between hh spin-up and spin-down ($J_z = +3/2$ and $-3/2$) components except for b_{41}, which requires the participation of the lh ($J_z = +1/2$ and $-1/2$) components. Rashba SOI is neglected in this study because it is an extrinsic effect, which depends on the details of the electric field felt by the system. Besides, for holes it couples energetically distant states so that, under moderate external fields, it is less efficient than Dresselhaus SOI [31]. V_{QD} describes the confining potential of the QD. We model QDs with parabolic confinement in the x, y and z directions:

$$V_{\mathrm{QD}} = -\tfrac{1}{2}\,\chi_\perp\,(x^2 + y^2) - \tfrac{1}{2}\,\chi_z z^2, \tag{10}$$

where $\chi_\perp$ and χ_z are the force constants perpendicular and parallel to the growth direction, respectively. Equation (10) allows us to simulate 3D spheroidal QDs with different aspect ratios, from flat (quasi-2D) to spherical or elongated (quasi-one-dimensional (1D)) structures, see figure 1. H_Z is the Hamiltonian modeling the splitting of the hole states by an effective axial magnetic field, three times larger for heavy ($|J_z| = 3/2$) than for light holes ($|J_z| = 1/2$). This field could originate, e.g. from the e–h exchange interaction [34] or a spin Zeeman effect. Then, we assume that

$$H_Z = \frac{1}{2}\begin{pmatrix} \Delta & 0 & 0 & 0 \\ 0 & \frac{1}{3}\,\Delta & 0 & 0 \\ 0 & 0 & -\frac{1}{3}\,\Delta & 0 \\ 0 & 0 & 0 & -\Delta \end{pmatrix}. \tag{11}$$

To calculate the hole states from H_h, we note that the diagonal terms correspond to harmonic oscillator Hamiltonians:

$$P + Q + V_\mathrm{QD} = T_{\mathrm{hh},\perp} - \tfrac{1}{2}\,\chi_\perp\,(x^2+y^2) + T_{\mathrm{hh},z} - \tfrac{1}{2}\,\chi_z\,z^2 \tag{12a}$$

and

$$P - Q + V_\mathrm{QD} = T_{lh,\perp} - \tfrac{1}{2}\,\chi_\perp\,(x^2+y^2) + T_{\mathrm{lh},z} - \tfrac{1}{2}\,\chi_z\,z^2, \tag{12b}$$

where $T_{i,j} = \frac{\hbar^2}{2m_j^i}\,k_j^2$, with $i = (\mathrm{hh},\ \mathrm{lh})$, $j = (\perp, z)$, $k_\perp = (k_x^2 + k_y^2)^{1/2}$, $m_\perp^\mathrm{hh} = m_0/(\gamma_1+\gamma_2)$, $m_z^\mathrm{hh} = m_0/(\gamma_1 - 2\gamma_2)$, $m_\perp^\mathrm{lh} = m_0/(\gamma_1-\gamma_2)$ and $m_z^\mathrm{lh} = m_0/(\gamma_1+2\gamma_2)$. This suggests rewriting all derivatives and coordinates of H_h in terms of harmonic oscillator ladder operators and then projecting it onto a basis formed by oscillator eigenstates. The problem is that equation (12*a*) has hh masses while equation (12*b*) has lh masses, and hence they have different oscillator frequency, $\omega_j^i = (\chi_j/m_j^i)^{1/2}$. Because the off-diagonal terms of H_L couple hh and lh components, it is convenient to use a single kind of oscillator state, e.g. hh state. This can be done by rewriting equation (12*b*) in terms of the hh harmonic oscillator Hamiltonians:

$$P - Q + V_\mathrm{QD} = \frac{\gamma_1-\gamma_2}{\gamma_1+\gamma_2}\,H_{\mathrm{hh},\perp} - \frac{\gamma_2}{\gamma_1+\gamma_2}\,\chi_\perp\,(x^2+y^2) + \frac{\gamma_1+2\gamma_2}{\gamma_1-2\gamma_2}\,H_{\mathrm{hh},z} + \frac{2\gamma_2}{\gamma_1-2\gamma_2}\,\chi_z\,z^2, \tag{13}$$

where $H_{\mathrm{hh},\perp} = T_{\mathrm{hh},\perp} - \chi_\perp\,(x^2+y^2)/2$ and $H_{\mathrm{hh},z} = T_{\mathrm{hh},z} - \chi_z\,(z^2)/2$. The resulting hole states are Luttinger spinors of the form

$$|\Psi_m^\mathrm{h}\rangle = \sum_{r,J_z} c_{r,J_z}^m |v_x,\, v_y,\, v_z\rangle\,|3/2,\, J_z\rangle, \tag{14}$$

where $v_j = 0, 1, 2\ldots$ is the quantum number of the 1D hh harmonic oscillator along the j direction, r is the combined orbital quantum number, $r = (v_x,\, v_y,\, v_z)$ and $|3/2,\, J_z\rangle$ the Bloch function.

H_ph in equation (1) is the Hamiltonian of acoustic phonons, given by $H_\mathrm{ph} = \sum_{\mathbf{q}\,\lambda}\hbar\,\omega_{q\,\lambda}\,a_{\mathbf{q}\,\lambda}^\dagger\,a_{\mathbf{q}\,\lambda}$, with $\omega_{q\,\lambda}$ standing for the phonon energy spectrum of branch λ ($\lambda = l$, t1, t2 for longitudinal and the two transversal phonon modes) and momentum $\mathbf{q}$. We restrict to low phonon energies, where the linear dispersion regime applies, $\omega_{q\lambda} = c_\lambda\,q$, with c_λ as the phonon velocity.

$H_\mathrm{h-ph}$ is the hole–phonon interaction

$$H_\mathrm{h-ph} = e\,\phi_\mathrm{pz}\,\mathcal{I} + H_\mathrm{dp}, \tag{15}$$

where e is the hole charge, ϕ_pz the piezoelectric potential and H_dp the deformation potential term. These are the two relevant scattering mechanisms at low temperatures [30]. The piezoelectric potential is given by [39]

$$\phi_\mathrm{pz} = \sum_\lambda \phi_\mathrm{pz}^\lambda = -\sum_{\lambda\,\mathbf{q}} \frac{4\pi\,\mathrm{i}}{\epsilon_\mathrm{r}\,q^2}\,h_{14}\,\left(q_x\,\varepsilon_{yz}^\lambda + q_y\,\varepsilon_{zx}^\lambda + q_z\,\varepsilon_{xy}^\lambda\right), \tag{16}$$

where ϵ_r is the relative dielectric constant, h_{14} is the piezoelectric constant and ε_{ij} is the strain tensor component. On the other hand, the deformation potential term is given by the Bir–Pikus strain Hamiltonian:

$$\mathcal{H}_{\rm dp} = \sum_{\lambda} \begin{pmatrix} p^\lambda + q^\lambda & -s^\lambda & r^\lambda & 0 \\ -(s^\lambda)^\dagger & p^\lambda - q^\lambda & 0 & r^\lambda \\ (r^\lambda)^\dagger & 0 & p^\lambda - q^\lambda & s \\ 0 & (r^\lambda)^\dagger & (s^\lambda)^\dagger & p^\lambda + q^\lambda \end{pmatrix}, \tag{17}$$

where

$$p^\lambda = -a\,(\varepsilon^\lambda_{xx} + \varepsilon^\lambda_{yy} + \varepsilon^\lambda_{zz}), \tag{18}$$

$$q^\lambda = -\frac{b}{2}\,(\varepsilon^\lambda_{xx} + \varepsilon^\lambda_{yy} - 2\varepsilon^\lambda_{zz}), \tag{19}$$

$$r^\lambda = \frac{\sqrt{3}}{2}\,b\,(\varepsilon^\lambda_{xx} - \varepsilon^\lambda_{yy}) - \mathrm{i}\,d\,\varepsilon^\lambda_{xy}, \tag{20}$$

$$s^\lambda = -d(\varepsilon^\lambda_{zx} - \mathrm{i}\,\varepsilon^\lambda_{yz}). \tag{21}$$

Here a, b and d are the valence band deformation potential constants.

The components of the strain tensor are rewritten using normal-modes coordinates [29]

$$\varepsilon^\lambda_{ij} = -\frac{\mathrm{i}}{2}\sum_{\mathbf{q}} U^\lambda(q)\,(\eta^i_\lambda(\mathbf{q})\,q_j + \eta^j_\lambda(\mathbf{q})\,q_i)\,F(\mathbf{q},\mathbf{r}), \tag{22}$$

where $F(\mathbf{q},\mathbf{r}) = (\mathrm{e}^{-\mathrm{i}\mathbf{qr}}\,a^+_q + \mathrm{e}^{\mathrm{i}\mathbf{qr}}\,a_q)$ and $U^\lambda(q) = \sqrt{\hbar/2\,\rho\,V\,\omega_{q\,\lambda}}$, with ρ and V standing for the crystal density and volume. $\eta_\lambda(\mathbf{q})$ are the phonon polarization vectors: $\boldsymbol{\eta}_l(\mathbf{q}) = (q_x,\ q_y,\ q_z)/q$, $\boldsymbol{\eta}_{t1}(\mathbf{q}) = (q_x\,q_z, q_y\,q_z, -q_\perp^2)/q\,q_\perp$ and $\boldsymbol{\eta}_{t2}(\mathbf{q}) = (q_y, -q_x, 0)/q_\perp$, with $q_\perp = \sqrt{q_x^2 + q_y^2}$. The piezoelectric potential now reads

$$\begin{aligned} \phi^{\rm l}_{\rm pz} &= -\frac{12\,\pi\,h_{14}}{\epsilon_{\rm r}}\,U^{\rm l}(q)\sum_{\mathbf{q}}\frac{q_x q_y q_z}{q^3}\,F(\mathbf{q},\mathbf{r}), \\ \phi^{\rm t1}_{\rm pz} &= -\frac{4\,\pi\,h_{14}}{\epsilon_{\rm r}}\,U^{\rm t}(q)\sum_{\mathbf{q}}\frac{q_x q_y\,(2q_z^2 - q_\perp^2)}{q^3\,q_\perp}\,F(\mathbf{q},\mathbf{r}), \\ \phi^{\rm t2}_{\rm pz} &= -\frac{4\,\pi\,h_{14}}{\epsilon_{\rm r}}\,U^{\rm t}(q)\sum_{\mathbf{q}}\frac{q_z\,(q_y^2 - q_x^2)}{q^2\,q_\perp}\,F(\mathbf{q},\mathbf{r}). \end{aligned} \tag{23}$$

In turn, the deformation potential operators become

$$\begin{aligned} p^{\rm l} &= \mathrm{i}\,a\,U^{\rm l}(q)\sum_{\mathbf{q}} q\ \ F(\mathbf{q},\mathbf{r}), \\ q^{\rm l} &= \mathrm{i}\,\frac{b}{2}\,U^{\rm l}(q)\sum_{\mathbf{q}}\left(q - 3\,\frac{q_z^2}{q}\right)F(\mathbf{q},\mathbf{r}), \\ r^{\rm l} &= -\mathrm{i}\,U^{\rm l}(q)\sum_{\mathbf{q}}\left(\frac{\sqrt{3}}{2}b\,\frac{q_x^2 - q_y^2}{q} - \mathrm{i}d\,\frac{q_x\,q_y}{q}\right)F(\mathbf{q},\mathbf{r}), \\ s^{\rm l} &= \mathrm{i}\,d\,U^{\rm l}(q)\sum_{\mathbf{q}}\frac{q_z\,(q_x - \mathrm{i}\,q_y)}{q}\,F(\mathbf{q},\mathbf{r}) \end{aligned} \tag{24}$$

for longitudinal phonons,

$$
\begin{aligned}
p^{\mathrm{t1}} &= 0,\\
q^{\mathrm{t1}} &= \mathrm{i}\,\frac{b}{2}\,U^{\mathrm{t}}(q)\sum_{\mathbf{q}}\left(\frac{3\,q_z\,q_\perp}{q}\right)F(\mathbf{q},\mathbf{r}),\\
r^{\mathrm{t1}} &= -\mathrm{i}\,U^{\mathrm{t}}(q)\sum_{\mathbf{q}}\left(\frac{\sqrt{3}}{2}b\,\frac{q_z\,(q_x^2-q_y^2)}{q\,q_\perp}-\mathrm{i}d\,\frac{q_x\,q_y\,q_z}{q\,q_\perp}\right)F(\mathbf{q},\mathbf{r}),\\
s^{\mathrm{t1}} &= \mathrm{i}\,\frac{d}{2}\,U^{\mathrm{t}}(q)\sum_{\mathbf{q}}\frac{(q_z^2-q_\perp^2)\,(q_x-\mathrm{i}\,q_y)}{q_\perp\,q}\,F(\mathbf{q},\mathbf{r})
\end{aligned}
\tag{25}
$$

for transversal t1 phonons and

$$
\begin{aligned}
p^{\mathrm{t2}} &= 0,\\
q^{\mathrm{t2}} &= 0,\\
r^{\mathrm{t2}} &= -\mathrm{i}\,U^{\mathrm{t}}(q)\sum_{\mathbf{q}}\left(\sqrt{3}b\,\frac{q_x\,q_y}{q_\perp}-\mathrm{i}\frac{d}{2}\,\frac{q_y^2-q_x^2}{q_\perp}\right)F(\mathbf{q},\mathbf{r}),\\
s^{\mathrm{t2}} &= -\frac{d}{2}\,U^{\mathrm{t}}(q)\sum_{\mathbf{q}}\frac{q_z\,(q_x-\mathrm{i}\,q_y)}{q_\perp}\,F(\mathbf{q},\mathbf{r})
\end{aligned}
\tag{26}
$$

for transversal t2 phonons.

2.2. Relaxation rate

We calculate the spin relaxation from an initial hole state $|\Psi_{\mathrm{i}}^{\mathrm{h}}\rangle$, with energy $E_{\mathrm{i}}^{\mathrm{h}}$, to a final hole state $|\Psi_{\mathrm{f}}^{\mathrm{h}}\rangle$, with energy $E_{\mathrm{f}}^{\mathrm{h}}$. The relaxation rate is estimated with a Fermi golden rule. We consider zero temperature, so that there is no phonon absorption. After integrating over phonon degrees of freedom, the rate is given by

$$
\tau_{\mathrm{i}\to\mathrm{f}}^{-1} = \frac{2\pi}{\hbar}\sum_{\lambda,\mathbf{q}}\left|\langle\Psi_{\mathrm{f}}^{\mathrm{h}}|\mathcal{H}_{\mathrm{h-ph}}^{\lambda q}\,|\Psi_{\mathrm{i}}^{\mathrm{h}}\rangle\right|^2\,\delta(\Delta E_{\mathrm{fi}}+\hbar c_\lambda q).
\tag{27}
$$

Here $\mathcal{H}_{\mathrm{h-ph}}^{\lambda q}$ is the hole–phonon interaction Hamiltonian, equation (15), but for a fixed phonon branch λ and momentum $\mathbf{q}$, and $\Delta E_{\mathrm{fi}} = E_{\mathrm{f}}^{\mathrm{h}} - E_{\mathrm{i}}^{\mathrm{h}}$. It can be seen from equations (23)–(26) that all the terms of $\mathcal{H}_{\mathrm{h-ph}}^{\lambda q}$ contain a factor which depends on $\mathbf{q}$ only and $F(\mathbf{q},\mathbf{r})$, which depends on spatial coordinates as well. Thus, when expanded, the matrix element $\langle\Psi_{\mathrm{f}}^{\mathrm{h}}|\mathcal{H}_{\mathrm{h-ph}}^{\lambda q}\,|\Psi_{\mathrm{i}}^{\mathrm{h}}\rangle$ takes the form

$$
\langle\Psi_{\mathrm{f}}^{\mathrm{h}}|\mathcal{H}_{\mathrm{h-ph}}^{\lambda q}\,|\Psi_{\mathrm{i}}^{\mathrm{h}}\rangle = \sum_{J_z',J_z,r',r}(c_{r',J_z'}^{\mathrm{f}})^*\,c_{r,J_z}^{\mathrm{i}}\,M_{J_z',J_z}^{\lambda}(\mathbf{q})\;G_{r',r}(\mathbf{q}),
\tag{28}
$$

where $G_{r,r'}(\mathbf{q}) = \langle r'|\,\mathrm{e}^{-\mathrm{i}\mathbf{q}\mathbf{r}}\,|r\rangle$ and $M_{J_z',J_z}^{\lambda}(\mathbf{q})$ gathers the $\mathbf{q}$-dependent factor of the $\mathcal{H}_{\mathrm{h-ph}}^{\lambda q}$ term coupling J_z and J_z'. $G_{r,r'}(\mathbf{q})$ is calculated analytically using iterative procedures as described in [40]. The sum over $\mathbf{q}$ in equation (27) is then carried out using numerical integration. To this

Table 1. Parameters used in the numerical calculations for InAs (left column) and GaAs (right column) QDs. GaAs parameters are used for the matrix in both cases. e^-, h^+ and ph stand for electron, hole and phonon.

Parameter	Symbol	InAs	GaAs	
e^- mass (m_0)	m_e	0.026	0.067	[41]
h^+ Luttinger param.	γ_1	20	6.98	[41]
h^+ Luttinger param.	γ_2	8.5	2.06	[41]
h^+ Luttinger param.	γ_3	9.2	2.93	[41]
e^- deformation pot. (eV)	a_c	−5.08	−7.17	[41]
h^+ deformation pot. (eV)	a	1.0	1.16	[41]
h^+ deformation pot. (eV)	b	−1.8	−2.0	[41]
h^+ deformation pot. (eV)	c	−3.6	−4.8	[41]
e^- BIA coeff. (eV Å^3)	b_{41}^c	27.18	27.58	[28]
h^+ BIA coeff. (eV Å)	C_k	−0.0112	−0.0034	[28]
h^+ BIA coeff. (eV Å^3)	b_{41}	−50.18	−81.93	[28]
h^+ BIA coeff. (eV Å^3)	b_{42}	1.26	1.47	[28]
h^+ BIA coeff. (eV Å^3)	b_{51}	0.42	0.49	[28]
h^+ BIA coeff. (eV Å^3)	b_{52}	−0.84	−0.98	[28]
Longitudinal ph speed (m s^{-1})	c_l	4720	4720	[41]
Transversal ph speed (m s^{-1})	c_t	3340	3340	[41]
Crystal density (kg m^{-3})	ρ	5310	5310	[41]
Piezoelectric coeff. (V cm^{-1})	h_{14}	3.5×10^6	1.45×10^7	[49]

end, it is convenient to use spherical coordinates, as the modulus q is fixed by the resonance condition and we are left with a 2D integral.

Calculations are carried out for InAs QDs embedded in a GaAs matrix. When differences are expected, we also calculate GaAs QD embedded in an $Al_xGa_{1-x}As$ matrix. Table 1 summarizes the parameters we use. The parameters correspond to the QD material, except for the crystal density and velocity of sound, which correspond to the matrix material because we assume bulk phonons (for simplicity, for $Al_xGa_{1-x}As$ we assume $x \to 0$ and use GaAs phonon parameters). For the dielectric constant, an average value of $\epsilon_r = 12.9$ is taken all over the structure. The basis used to solve Hamiltonian (1) contains all the hh oscillator eigenstates with the quantum numbers $v_x, v_y < 13$ and $v_z < 9$.

3. Numerical results and discussion

We shall start this section by describing the dependence of the hole spin lifetime on the QD geometry and the spin splitting magnitude (section 3.1). The influence of each parameter can be understood by analyzing the spin admixture mechanisms, as we show in section 3.2. Next, in section 3.3, we study the effect of the ground state changing from mainly hh character, which is the case addressed in most previous studies, to mainly lh character. This transition is observed in QDs with large aspect ratio [42–45]. Last, in section 3.4, we compare the role of deformation potential and piezoelectric potential interactions in determining the efficiency of hole–phonon coupling.

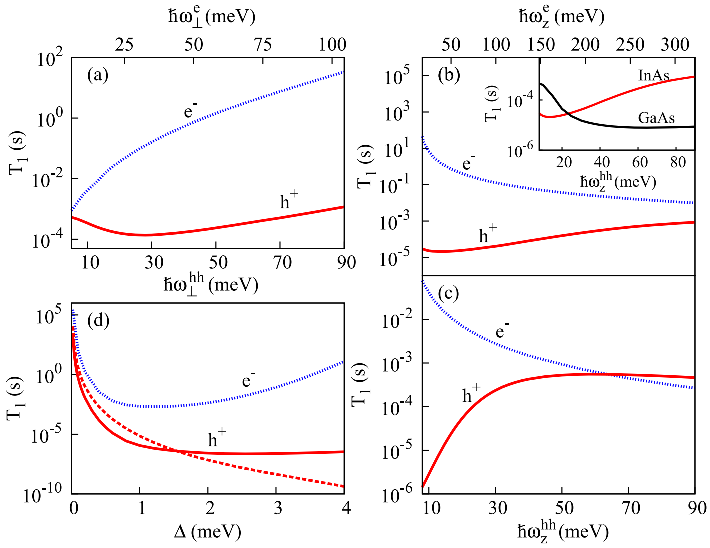

Figure 2. Hole (red solid line) and electron (blue dotted line) spin lifetime in InAs QDs, as a function of the lateral confinement (a), vertical confinement (b)–(c) and spin splitting energy (d). The inset in (b) compares T_1^{h} for InAs and GaAs. (a) $\hbar\omega_z^{\mathrm{hh}} = 50\,\mathrm{meV}$, $\hbar\omega_z^{\mathrm{e}} = 179\,\mathrm{meV}$, $\Delta = 0.4\,\mathrm{meV}$. (b) $\hbar\omega_\perp^{\mathrm{hh}} = 20\,\mathrm{meV}$, $\hbar\omega_\perp^{\mathrm{e}} = 23.2\,\mathrm{meV}$, $\Delta = 0.4\,\mathrm{meV}$. (c) $\hbar\omega_\perp^{\mathrm{hh}} = 5\,\mathrm{meV}$, $\hbar\omega_\perp^{\mathrm{e}} = 5.8\,\mathrm{meV}$, $\Delta = 0.4\,\mathrm{meV}$. (d) $\hbar\omega_\perp^{\mathrm{hh}} = 20\,\mathrm{meV}$ and $\hbar\omega_z^{\mathrm{hh}} = 50\,\mathrm{meV}$ (red solid line); $\hbar\omega_\perp^{\mathrm{e}} = 23.2\,\mathrm{meV}$ and $\hbar\omega_z^{\mathrm{e}} = 179\,\mathrm{meV}$ (blue dotted line); $\hbar\omega_\perp^{\mathrm{hh}} = 40\,\mathrm{meV}$ and $\hbar\omega_z^{\mathrm{hh}} = 5\,\mathrm{meV}$ (red dashed line).

3.1. Geometry and spin splitting dependence

Solid lines in figure 2 show the hole spin lifetime as a function of the QD geometry and the spin splitting energy of InAs QDs. For comparison, we also plot the electron spin lifetimes (dotted lines). The latter have been calculated using the same formalism as for holes but adapted for single-band conduction electrons [40]. Both electrons and holes are assumed to be confined in the same QD, hence they share the same force constants but have different confinement frequencies. One can see immediately in the figure that the behavior of holes differs drastically from the well-known case of electrons. Below we summarize the influence of each parameter.

Figure 2(a) shows the spin lifetime dependence on the lateral confinement in QDs with strong vertical confinement. T_1^{e} increases monotonically with $\omega_\perp$. This is because, as we approach the spherical confinement regime ($\omega_z^{\mathrm{e}} = \omega_\perp^{\mathrm{e}}$), the Dresselhaus SOI of electrons is gradually suppressed [40]. No such trend is however observed for holes, as H_{BIA} does not cancel out even if the confinement is isotropic. As a matter of fact, T_1^{h} shows an evident non-monotonic behavior, with a minimum at $\omega_\perp^{\mathrm{hh}} = 28\,\mathrm{meV}$ and increasing away from it. It is worth noting that a previous study by Woods *et al* [29] predicted T_1^{h} to decrease with the QD diameter, while a similar study by Lu *et al* [30] for somewhat larger QDs predicted the opposite trend. Figure 2(a) shows that both predictions are conciliable, corresponding to the right and left sides of the $T_1^{\rm h}$ minimum, respectively. The origin of the different trends will be discussed in section 3.2.

Figures 2(b) and (c) show the spin lifetime dependence on the vertical confinement in QDs with moderately strong and weak lateral confinement, respectively. These confinement strengths roughly correspond to self-assembled (panel (b)) [46, 47] and electrostatic (panel (c)) [48] QDs. As can be seen in figure 2(b), electrons and holes have opposite behaviors. $T_1^{\rm e}$ now decreases with $\omega_z^{\rm e}$ because the structure is becoming flatter (less isotropic). Instead, the behavior of $T_1^{\rm h}$ is similar to that observed for varying lateral confinement, with a shallow minimum at $\omega_z^{\rm hh} = 14$ meV. Previous studies have shown that $T_1^{\rm h}$ increases with the vertical confinement [30]. This is consistent with the right side of the $T_1^{\rm h}$ minimum in figure 2(b), but here we show that the opposite trend is also possible if the QD aspect ratio is large enough (left side of the minimum).

Figure 2(c) illustrates the case in which the lateral confinement is weak. The minimum of $T_1^{\rm h}$ is now shifted toward very small $\hbar\omega_z^{\rm hh}$ values so that only the right side behavior is seen in the range under study. Interestingly, here $T_1^{\rm h}$ shows a clear saturation with increasing vertical confinement ($\hbar\omega_z^{\rm hh} > 40$ meV), which has not been noticed before [30]. As we show in section 3.2, this saturation reflects the fact that $H_{\rm BIA}$ has replaced hh–lh mixing as the main source of SOI.

The inset in figure 2(b) compares $T_1^{\rm h}$ in InAs and GaAs QDs with moderate lateral confinement. As can be observed, the spin lifetime in InAs QDs is longer than that in GaAs QDs when $\omega_z^{\rm hh} > \omega_\perp^{\rm hh}$, which is, e.g. the case of self-assembled QDs. This is an unexpected result because in bulk the valence band SOI of InAs is stronger than that of GaAs (compare the split-off band splittings [41] or the γ_2 and γ_3 coefficients appearing in R and S terms of equation (4), which couple hh to lh). The underlying reason is that in confined structures, the cubic Dresselhaus SOI becomes important and it is stronger for GaAs (see b_{41} in table 1).

Figure 2(d) shows the spin-flip lifetime of electrons and holes in a self-assembled-like QD as a function of the spin splitting energy. For electrons, $T_1^{\rm e}$ is largely determined by the efficiency of the carrier–phonon coupling [40]. It is short when the phonon wavelength is of the same order as the carrier wavefunction extension, but it increases for large (small) Δ values because the phonon wavelength becomes too short (long), as $q \approx \Delta/\hbar c$. The same happens for holes (notice that $G_{r,r'}(\mathbf{q})$ in equation (28) vanishes in the limits of large and small phonon wavevector). However, figure 2(d) shows that $T_1^{\rm h}$ is only sensitive to Δ for small splittings, but then it reaches a plateau where $T_1^{\rm h} \sim \mu$s. The different behavior of holes and electrons is due to the different effective mass along the growth direction, m_z. For $\hbar\omega_z = 50$ meV, the characteristic length of the oscillator states in the growth direction, $l_z = \sqrt{\hbar/m_z\,\omega_z}$, is $l_z^{\rm e} = 4.5$ nm for electrons and $l_z^{\rm hh} = 2.4$ nm for holes, i.e. the hole confinement is stronger. As a result, larger values of Δ than those used in figure 2(d) are required for $T_1^{\rm h}$ to increase.

Experiments with excitons in self-assembled InGaAs QDs have revealed a negligible influence of e–h interactions on $T_1^{\rm h}$ [24]. Our results would be consistent with such an observation in the regime of large Δ. For self-assembled QDs, however, $\Delta \leqslant 0.5$ meV. Thus, the insensitivity noted in the experiment is inconsistent with the single-phonon processes we consider in figure 2. This suggests that two-phonon processes dominate in these systems [15, 32]. On the other hand, experiments with colloidal nanorods have shown a sizable increase of $T_1^{\rm h}$ when changing from type-I to type-II confinement, which modulates the e–h exchange energy from typical colloidal structure values (few meV) to type-II system values (fractions of meV) [36]. We have run simulations for a nanorod-like geometry (red dashed line in figure 2(d))

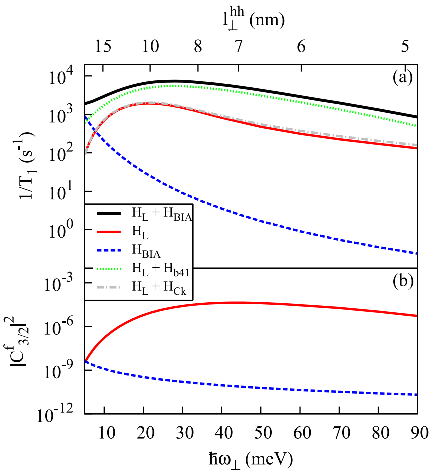

Figure 3. Hole spin relaxation (a) and weight of the minor hh component (b) as a function of the lateral confinement. Different SOI terms are considered. The system is the same as that of figure 2(a).

and find that the weak vertical confinement renders T_1^{h} sensitive to Δ for all the range under study, in agreement with the experiment. This indicates that the weak vertical confinement of rods renders single-phonon processes efficient.

To close this section, we notice that previous theoretical studies with simpler models had predicted that hole spin lifetimes can exceed those of electrons in very flat QDs [31]. Figure 2 confirms that this could actually be achieved in gated structures, where lateral confinement is very weak (see the crossing between T_1^{e} and T_1^{h} in panel (c)). However, for typical self-assembled InAs QDs, T_1^{e} is about one order of magnitude longer than T_1^{h} (see panel (b) for large $\hbar\omega_z$).[2] This is consistent with experimental measurements by Heiss *et al* [26].

3.2. Mechanism of spin admixture

Spin admixture is a requirement for spin-flip transitions to take place [50]. In this section, we compare the spin admixture resulting from all the SOI terms affecting the hole ground state. As we shall see, once the dominant SOI mechanism is determined, one can rationalize the geometry dependence of T_1^{h} described in the previous section. For convenience of the analysis, in what follows we plot and discuss relaxation rates, $1/T_1^{\mathrm{h}}$. Furthermore, we shall often drop the hh superscript when referring to the confinement frequency, $\omega_\perp^{\mathrm{hh}}$ or ω_z^{hh}.

Figure 3(a) shows the relaxation rate for the InAs QDs of figure 2(a), but now obtained by calculating hole states with the diagonal terms of H_{L} plus different SOI terms: off-diagonal H_{L} terms (hereafter hh–lh coupling), full Dresselhaus Hamiltonian (H_{BIA}), hh–lh coupling plus linear-in-k term ($H_{\mathrm{L}} + H_{C_k}$) and hh–lh coupling plus the dominant cubic-in-k Dresselhaus term

[2] The same conclusions, albeit with somewhat lower T_1^{e}, are obtained using larger electron masses to account, e.g. for Ga diffusion into the InAs QD.

($H_L + H_{b_{41}}$). The total rate, corresponding to $H_L + H_{BIA}$, is also shown (thick black line). One can see that H_L (red solid line) is more important than H_{BIA} (blue dashed line) for large $\omega_\perp$ values. However, as the lateral confinement is weakened and the system becomes flatter, H_{BIA} gains weight. For self-assembled QDs ($\hbar\omega_\perp \approx 10$–25 meV), H_{BIA} is already comparable to H_L and it becomes dominant for weakly confined (e.g. gated) QDs. Figure 3 also reveals that the linear-in-k BIA term (gray dot-dashed line) is but a secondary mechanism, which barely enhances the relaxation rate coming from H_L. This is inspite of the fact that it is a source of direct admixture between hh states with opposite spin, with no participation of lh states. For this reason, it had been proposed as the dominant SOI term in flat QDs with weak lateral confinement [35]. Instead, figure 3 shows that most of the H_{BIA} contribution comes from the cubic-in-k b_{41} term (see green dotted line).

This term relies on intermediate lh states in order to mix hh $J_z = +3/2$ and $-3/2$ components (see equation (A.3) in the appendix), which implies that a simultaneous description of hh and lh states is necessary for realistic modeling.

By comparing the total relaxation rate coming from $H_L + H_{BIA}$ with that coming from H_L and H_{BIA}, it is clear that the total rate is not just the sum of the two independent mechanisms. For example, at $\hbar\omega_\perp = 30\,\text{meV}$, adding H_{BIA} to H_L enhances $1/T_1^h$ about an order of magnitude, even though the contribution coming from H_{BIA} alone is about 100 times smaller than that coming from H_L. This can be understood by means of a perturbative reasoning: neither H_L, equation (4), nor $H_{b_{41}}$—the most relevant term of H_{BIA}—, equation (A.3), contribute to hh–lh mixing at first order. H_L contributes at second order, due to terms involving non-zero products like $H_L(1, 2)\, H_L(2, 4)$, while $H_{b_{41}}$ does not. It contributes at third order, due to non-zero products like $H_{b_{41}}(1, 2)\, H_{b_{41}}(2, 3)\, H_{b_{41}}(3, 4)$. However, the sum of the two Hamiltonians allows $H_{b_{41}}$ to contribute at second order. Thus, the effect of $H_{b_{41}}$ is clearly non-additive because it is enhanced by H_L. Simultaneously accounting for both SOI terms is then required for quantitative estimates.

For a qualitative understanding of the geometry dependence of $1/T_1^h$, we rewrite the hole states, equation (14), as $|\Psi_m^h\rangle = \sum_{J_z} c_{J_z}^m\, |\phi_{J_z}^m\rangle\, |3/2, J_z\rangle$, where $|\phi_{J_z}^m\rangle = \sum_r c_{J_z,r}^m\, |r\rangle$ is the envelope function associated with the periodic Bloch function $|3/2, J_z\rangle$. If we restrict to the diagonal components of H_{h-ph}, the matrix element determining the relaxation rate becomes

$$\langle\Psi_f^h|\mathcal{H}_{h-ph}^{\lambda q}\,|\Psi_i^h\rangle \approx \sum_{J_z} (c_{J_z}^f)^* c_{J_z}^i\, \langle\phi_{J_z}^f|\mathcal{H}_{h-ph}^{\lambda q}\,|\phi_{J_z}^i\rangle. \tag{29}$$

When the QD is oblated or spherical, the low-energy states are essentially hh states. Thus, the initial (final) state of the spin transition is mostly a pure spin-up (spin-down) hh state. Considering that $|c_{3/2}^i| \gg |c_{3/2}^f|$ ($|c_{-3/2}^f| \gg |c_{-3/2}^i|$), one can obtain an approximate expression

$$\frac{1}{T_1^h} \propto \left|\langle\Psi_f^h|\mathcal{H}_{h-ph}^{\lambda q}|\Psi_i^h\rangle\right|^2 \propto |c_{3/2}^f|^2\, \left|\langle\phi_{3/2}^f|\mathcal{H}_{h-ph}^{\lambda q}|\phi_{3/2}^i\rangle\right|^2. \tag{30}$$

In other words, the relaxation rate is proportional to the spin admixture of the ground state through the squared coefficient of the minor hh component (here spin-up, $J_z = 3/2$), and proportional to the efficiency of the hole–phonon coupling through the rightmost matrix element.

The geometry dependence of $1/T_1^h$ for a given SOI mechanism simply reflects the spin admixture variation. This can be seen in figure 3(b), which shows that, for H_L and H_{BIA}, $|c_{3/2}^f|^2$ has the same qualitative dependence on the geometry as the corresponding $1/T_1^h$ values in figure 3(a). This allows us to interpret the observed maximum as a function of $\omega_\perp$.

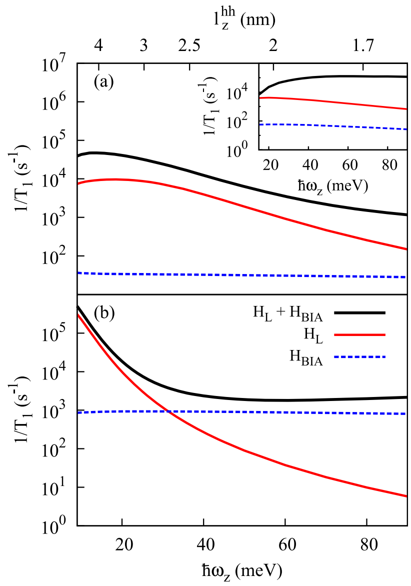

Figure 4. Hole spin relaxation as a function of the vertical confinement. Different SOI terms are considered. (a) Strong lateral confinement, $\hbar\omega_\perp = 20$ meV. (b) Weak lateral confinement, $\hbar\omega_\perp = 5$ meV. The inset in (a) is the corresponding result for GaAs. The system is the same as that of figures 2(b) and (c).

For H_L, the spin admixture between the hh spin-up and spin-down components takes place necessarily through the intermediate lh components (see equation (4)). The weight of the minor hh component is then related to the strength of the off-diagonal terms of H_L (R and S) and to the energy splitting between the hh and the lh states. For small $\omega_\perp$ values, the main effect of increasing the lateral confinement is to enhance the coupling terms, which are proportional to k_x and k_y (see equations (7) and (8)). As a result, the weight of the minor hh component $|c^f_{3/2}|$ increases, hence $1/T_1^h$ increases. For larger $\omega_\perp$ values, however, when the lateral and vertical confinements become comparable, the main effect of increasing the lateral confinement is to bring lh states closer to hh ones [44, 45]. When this happens, the lh states stop acting as intermediate states for the admixture between hh components and start participating in the admixture themselves. This is at the expense of reducing the weight of the minor hh component, hence $1/T_1^h$ decreases.

Next, we analyze the mechanisms involved in the spin relaxation with varying vertical confinement. Figure 4 shows $1/T_1^h$ for the same systems as in figures 2(b) and (c), but calculating the hole states with the diagonal terms of H_L plus hh–lh coupling (red solid line) or full H_{BIA} Hamiltonian (blue dashed line). Panel (a) corresponds to strong lateral confinement. The total rate has a maximum at $\hbar\omega_z = 14$ meV, whose origin is analogous to that described above for varying lateral confinement. Beyond the maximum, the total rate ($H_L + H_{BIA}$) decreases with the vertical confinement strength, in agreement with previous studies [30]. However, we also find that the decrease eventually saturates. This is evident for

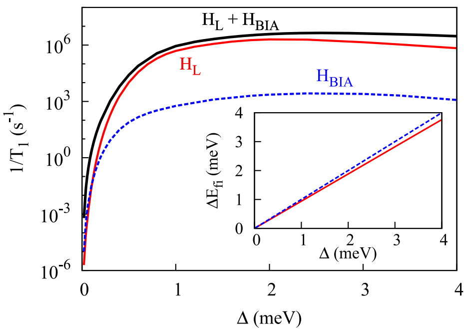

Figure 5. Hole spin relaxation as a function of the spin splitting energy in a QD with $\hbar\omega_\perp = 20\,\text{meV}$ and $\hbar\omega_z = 50\,\text{meV}$. Same legend as in figure 3 is used. The inset compares the energy splitting between the Kramer doublet for hh–lh coupling and Dresselhaus SOI.

InAs QDs with weak lateral confinement, as shown in figure 4(b), or GaAs QDs with strong lateral confinement, as in figure 4(a) inset. The origin of this saturation is the contribution of H_{BIA}, which provides a lower bound to $1/T_1^{\text{h}}$. In particular, $H_{b_{41}}$ introduces off-diagonal coupling terms which are quadratic in k_z (see operator L_{41} in the appendix), instead of the linear k_z terms of H_{L} (see S operator in equation (4)). Since the uncoupled hh and lh energies are also quadratic in k_z, a perturbational analysis easily shows that the two contributions compensate each other. For strong ω_z, when lateral confinement is negligible, the cancelation is exact and the relaxation rate does not depend on the vertical confinement.

The magnitude of the spin splitting also influences the dominant mechanism of spin admixture. This is illustrated in figure 5, which considers a self-assembled InAs QD with varying spin splitting energy. For large Δ, H_{L} has a dominant contribution to the relaxation rate, but H_{BIA} becomes equally important for small enough Δ. The relative enhancement of the role of H_{BIA} originates in its zero-field spin splitting, which leads to larger energy difference between the Kramers pair (ΔE_{fi}) than with Δ alone, as shown in the figure inset. When $\Delta \to 0$ and the phonon wavelength increases beyond the QD size, the extra energy coming from the zero-field spin splitting of H_{BIA} provides a significant contribution to preserve the hole–phonon coupling efficiency.

3.3. Light hole spin relaxation

When the aspect ratio increases and the QD shape becomes prolate, the hole ground state evolves from the eminent hh character discussed so far to lh character, as noted, e.g. in colloidal nanorods [42–45]. Here we investigate how the change of the ground state affects the relaxation between the two highest hole states. Figure 6(a) shows the hole energy levels in a QD with $\hbar\omega_\perp = 40\,\text{meV}$ as a function of $\hbar\omega_z$. In the limit of strong and weak vertical confinement, the two highest states are essentially hh and lh doublets, $J_z = \pm 3/2$ and $\pm 1/2$, respectively. In the intermediate regime, $\hbar\omega_z = 9$–$17\,\text{meV}$, the two doublets cross. This gives rise to pronounced changes in the relaxation rate, as shown in figure 6(b).

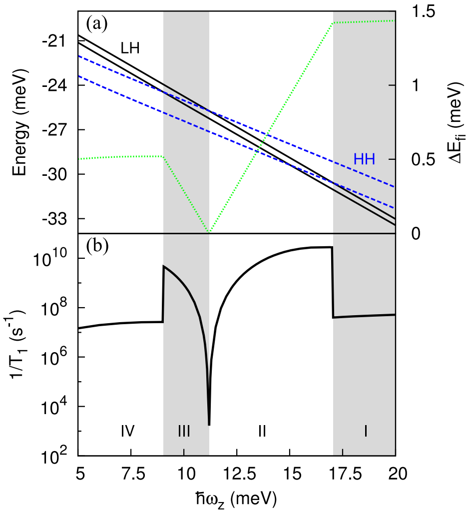

Figure 6. Hole energy levels (a) and spin relaxation rate (b) around the hh–lh crossing region. $\hbar\omega_\perp = 40$ meV and $\Delta = 2$ meV. In (a), solid and dashed lines are used for states with dominant lh and hh character, respectively. The dotted line gives the energy splitting. Shades are used to distinguish the regions with different kinds of states involved in the transition.

The changes can be understood as follows. In region I of the figure, the two highest states are the hh doublet. The relaxation is between states with opposite spin and roughly constant energy splitting (see ΔE_{fi}, dotted line in figure 6(a)). At $\hbar\omega_z = 17$ meV, when we enter region II, the excited hh state crosses with the first lh state. Now the relaxation is between an lh ($J_z = -1/2$) and an hh ($J_z = -3/2$). Since lh have mixed spin-up and spin-down projections, there is no need for spin flip. Then, the s^λ terms of the strain Hamiltonian, H_{dp}, provide direct coupling with hh and the resulting transition is much faster. This explains the abrupt increase of $1/T_1^{\mathrm{h}}$. However, the energy splitting between the hh and lh becomes smaller with decreasing ω_z because of their different masses. As a result, at $\hbar\omega_z = 11$ meV, the lh replaces the hh as the ground state. Near the degeneracy point, $\hbar\omega_z = 11.2$ meV, ΔE_{fi} is so small that hole–phonon coupling becomes inefficient and the relaxation is strongly suppressed, but it increases again in region III for the same reasons as in region II. Finally, at $\hbar\omega_z = 9$ meV, the excited lh state crosses with the highest hh state. We thus enter region IV, where the transition takes place between two lh states with orthogonal Bloch functions, $|3/2, \pm 1/2\rangle$. J_z admixture mechanisms are necessary and the relaxation becomes slow. As a matter of fact, the spin relaxation timescale for transitions between lh states is similar to that between hh states, in spite of the fact that their Bloch functions contain mixed spins.

3.4. Mechanism of hole–phonon coupling

Electron–acoustic phonon coupling in QDs is known to occur mainly through deformation potential interaction when the energy splitting is large ($\Delta E_{\mathrm{fi}} > 0.1$ meV) and through

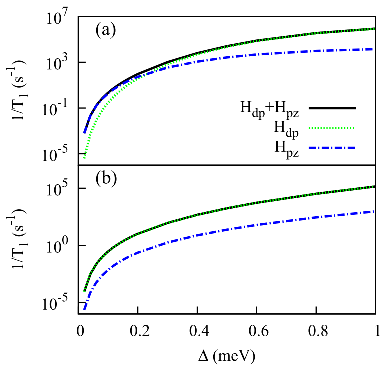

Figure 7. Hole spin relaxation as a function of the spin splitting energy. (a) Transition between hh states in a QD with $\hbar\omega_\perp = 20$ and $\hbar\omega_z = 50\,$meV. (b) Transition between lh states in a QD with $\hbar\omega_\perp = 40$ and $\hbar\omega_z = 5\,$meV.

piezoelectric potential when it is small [51]. In principle, for holes, the situation may differ because the deformation potential Hamiltonian, equation (17), is formally different from that of electrons. To investigate this point, in this section we compare the role of the two kinds of carrier–phonon coupling mechanism for holes subject to varying effective magnetic fields.

Figure 7(a) shows the spin relaxation rate in an oblate (quasi-2D) QD, where the highest states are hh, while figure 7(b) shows that in a prolate (quasi-1D) QD, where the highest states are lh. For the spin transition within the hh doublet, panel (a), the behavior is analogous to that of electrons. Deformation potential interaction (dotted line) provides the largest contribution to $1/T_1^{\mathrm{h}}$ except for very small Δ, when piezoelectric interaction (dashed-dotted line) takes over. This is because all the terms of $\mathcal{H}_{\mathrm{dp}}$ are proportional to the phonon momentum $\sqrt{q}$ (see equations (24)–(26)) while the piezoelectric potential is proportional to $1/\sqrt{q}$ (see equation (23)). With decreasing Δ, both mechanisms become inefficient, because for long phonon wavelength $\mathrm{e}^{\mathrm{i}\mathbf{qr}} \approx 1$. Then, in equation (28), the matrix element $G_{r,r'}(\mathbf{q}) \approx \langle r'|r\rangle$, i.e. it tends to the overlap between the envelope components of the initial and final states. For hh, these components have different symmetries, so the coupling vanishes. For example, in axially symmetric structures, the $J_z = +3/2$ component of the initial state has a well-defined azimuthal angular momentum $m_z = 0$, which couples through the s^λ operator of H_{dp} with the $J_z = +1/2$ component of the final state, for which $m_z = -2$.[3]

The situation for lh is quite different. As shown in figure 7(b), now deformation potential interaction is the dominant relaxation channel even for small Δ. The underlying reason is that, in contrast to the hh case, the off-diagonal terms of $\mathcal{H}_{\mathrm{dp}}$ couple envelope components with the same symmetry. For example, the $J_z = +3/2$ and $1/2$ components of the initial and final state

[3] In axially symmetric systems, the envelope functions of the Luttinger spinor have well-defined z-component of the orbital angular momentum, $m_z = F_z - J_z$. In oblate QDs, the highest doublet has $F_z = \pm 3/2$, and in prolate QDs it has $F_z = \pm 1/2$. See e.g. [45].

now have both $m_z = -1$, and hence are not orthogonal. As a consequence, $G_{r,r'}(\mathbf{q})$ does not vanish when $q \to 0$.

4. Summary

We have investigated hole spin relaxation in InAs and GaAs QDs using 3D four-band $k \cdot p$ Hamiltonians. We have shown that the hole spin lifetime has a non-monotonic dependence on the lateral and vertical confinement strength. This is due to the interplay between the energy splitting of hh and lh, which is set by their different masses, and the anisotropic hh–lh coupling terms. The resulting geometry dependence of hole spin relaxation is qualitatively different from that of electrons.

hh–lh coupling and Dresselhaus SOI have been found to have comparable contributions to the spin admixture of hole states in self-assembled QDs, with the former becoming dominant for prolate structures, such as nanorods, and the latter for strongly oblate ones, such as gated QDs. The cubic-in-k Dresselhaus term leads to an upper bound of T_1^{h} with increasing vertical confinement, which is missed when considering hh–lh coupling only.

We have also investigated the spin relaxation involving states with dominant lh character. Transitions between lh and hh states are very fast because lh have strong spin admixture. Instead, transitions between lh states with different Bloch angular momentum J_z are as slow as the transitions between hh states with opposite spin. There is, however, a difference in the dominating hole–phonon interaction mechanism. At small energy splittings, the relaxation is mainly due to deformation potential interaction, unlike for hh transitions, where it is due to piezoelectric interaction.

Acknowledgments

Support from MICINN project CTQ2011-27324, UJI-Bancaixa project P1-1B2011-01, the Ramon y Cajal program (JIC) and UJI fellowship (CS) is acknowledged.

Appendix. Dresselhaus Hamiltonian for holes

In this appendix, we write the explicit matrix forms of the different H_{BIA} terms in Cartesian coordinates. Separating the different invariants in equation (9) we obtain

$$H_{\mathrm{BIA}} = H_{C_k} + H_{b_{41}} + H_{b_{42}} + H_{b_{51}} + H_{b_{52}}, \tag{A.1}$$

where

$$H_{C_k} = C_k \begin{pmatrix} 0 & -\frac{k_-}{2} & k_z & -\frac{\sqrt{3}k_-}{2} \\ -\frac{k_+}{2} & 0 & \frac{\sqrt{3}k_+}{2} & -k_z \\ k_z & \frac{\sqrt{3}k_-}{2} & 0 & -\frac{k_-}{2} \\ -\frac{\sqrt{3}k_+}{2} & -k_z & -\frac{k_+}{2} & 0 \end{pmatrix} \tag{A.2}$$

with $k_\pm = k_x \pm \mathrm{i}\, k_y$:

$$H_{b_{41}} = b_{41} \begin{pmatrix} \frac{3}{2}\, P_{41} & \frac{\sqrt{3}}{2}\, L_{41} & 0 & 0 \\ \frac{\sqrt{3}}{2}\, L_{41}^\dagger & \frac{1}{2}\, P_{41} & L_{41} & 0 \\ 0 & L_{41}^\dagger & -\frac{1}{2}\, P_{41} & \frac{\sqrt{3}}{2}\, L_{41} \\ 0 & 0 & \frac{\sqrt{3}}{2}\, L_{41}^\dagger & -\frac{3}{2}\, P_{41} \end{pmatrix}, \tag{A.3}$$

where $P_{41} = (k_x^2 - k_y^2)\, k_z$ and $L_{41} = \mathrm{i}\, k_-\, k_x\, k_y - k_+\, k_z^2$:

$$H_{b_{42}} = b_{42} \begin{pmatrix} \frac{27}{8}\, P_{41} & \frac{7\sqrt{3}}{8}\, L_{41} & 0 & -\frac{3}{4}\, L_{42} \\ \frac{7\sqrt{3}}{8}\, L_{41}^\dagger & \frac{1}{8}\, P_{41} & \frac{5}{2}\, L_{41} & 0 \\ 0 & \frac{5}{2}\, L_{41}^\dagger & -\frac{1}{8}\, P_{41} & \frac{7\sqrt{3}}{8}\, L_{41} \\ -\frac{3}{4}\, L_{42}^\dagger & 0 & \frac{7\sqrt{3}}{8}\, L_{41}^\dagger & -\frac{27}{8}\, P_{41} \end{pmatrix}, \tag{A.4}$$

where $L_{42} = \mathrm{i}\, k_+\, k_x\, k_y + k_-\, k_z^2$:

$$H_{b_{51}} = b_{51} \begin{pmatrix} 0 & -\frac{\sqrt{3}}{4}\, K_+ & \frac{\sqrt{3}}{2}\, K_z & -\frac{3}{4}\, K_- \\ -\frac{\sqrt{3}}{4}\, K_- & 0 & \frac{3}{4}\, K_+ & -\frac{\sqrt{3}}{2}\, K_z \\ \frac{\sqrt{3}}{2}\, K_z & \frac{3}{4}\, K_- & 0 & -\frac{\sqrt{3}}{4}\, K_+ \\ -\frac{3}{4}\, K_+ & -\frac{\sqrt{3}}{2}\, K_z & -\frac{\sqrt{3}}{4}\, K_- & 0 \end{pmatrix}, \tag{A.5}$$

where $K_+ = K_x + \mathrm{i}\, K_y$, $K_- = K_x - \mathrm{i}\, K_y$, $K_x = k_x\, (k_y^2 + k_z^2)$, $K_y = k_y\, (k_x^2 + k_z^2)$ and $K_z = k_z\, (k_x^2 + k_y^2)$:

$$H_{b_{52}} = b_{52} \begin{pmatrix} 0 & -\frac{\sqrt{3}}{4}\, M_+ & \frac{\sqrt{3}}{2}\, k_z^3 & -\frac{3}{4}\, M_- \\ -\frac{\sqrt{3}}{4}\, M_- & 0 & \frac{3}{4}\, M_+ & -\frac{\sqrt{3}}{2}\, k_z^3 \\ \frac{\sqrt{3}}{2}\, k_z^3 & \frac{3}{4}\, M_- & 0 & -\frac{\sqrt{3}}{4}\, M_+ \\ -\frac{3}{4}\, M_+ & -\frac{\sqrt{3}}{2}\, k_z^3 & -\frac{\sqrt{3}}{4}\, M_- & 0 \end{pmatrix}, \tag{A.6}$$

where $M_+ = k_x^3 + \mathrm{i}\, k_y^3$ and $M_- = k_x^3 - \mathrm{i}\, k_y^3$.

References

[1] Fischer J, Trif M, Coish W A and Loss D 2009 *Solid State Commun.* **149** 1443

[2] Gerardot B D, Brunner D, Dalgarno P A, Öhberg P, Seidl S, Kroner M, Karrai K, Stoltz N G, Petroff P M and Warburton R J 2008 *Nature* **451** 441

[3] Brunner D, Gerardot B D, Dalgarno P A, Wüst G, Karrai K, Stoltz N G, Petroff P M and Warburton R J 2009 *Science* **325** 70

[4] Fallahi P, Yilmaz S T and Imamoglu A 2010 *Phys. Rev. Lett.* **105** 257402

[5] Chekhovich E A, Krysa A B, Skolnick M S and Tartakovskii A I 2011 *Phys. Rev. Lett.* **106** 027402
[6] Eble B, Testelin C, Desfonds P, Bernardot F, Balocchi A, Amand T, Miard A, Lemaitre A, Marie X and Chamarro M 2009 *Phys. Rev. Lett.* **102** 144601
[7] Testelin C, Bernardot F, Eble B and Chamarro M 2009 *Phys. Rev.* B **79** 195440
[8] De Greve K *et al* 2011 *Nature Phys.* **7** 872
[9] Godden T M, Quilter J H, Ramsay A J, Wu Y, Brereton P, Boyle S J, Luxmoore I J, Puebla-Nunez J, Fox A M and Skolnick M S 2012 *Phys. Rev. Lett.* **108** 017402
[10] Greilich A, Carter S G, Kim D, Bracker A S and Gammon D 2011 *Nature Photon.* **5** 703
[11] Szumniak P, Bednarek S, Partoens B and Peeters F M 2012 *Phys. Rev. Lett.* **109** 107201
[12] Hsieh C Y, Cheriton R, Korkusinski M and Hawrylak P 2009 *Phys. Rev.* B **80** 235320
[13] Budich J C, Rothe D G, Hankiewicz E M and Trauzettel B 2012 *Phys. Rev.* B **85** 205425
[14] Roloff R, Eissfeller T, Vogl P and Pötz W 2010 *New J. Phys.* **12** 093012
[15] Liao Y H, Climente J I and Cheng S J 2011 *Phys. Rev.* B **83** 165317
[16] Kurtze H, Yakovlev D R, Reuter D, Wieck A D and Bayer M 2012 *Phys. Rev.* B **85** 195303
[17] Kowalik K, Krebs O, Lemaitre A, Gaj J A and Voisin P 2008 *Phys. Rev.* B **77** 161305
[18] Huxter V M, Kim J, Lo S S, Lee A, Sreekumari Nair P and Scholes G D 2010 *Chem. Phys. Lett.* **491** 187
[19] Lundstrom T, Schoenfeld W, Lee H and Petroff P M 1999 *Science* **286** 2312
[20] Reischle M, Beirne G J, Rossbach R, Jetter M and Michler P 2008 *Phys. Rev. Lett.* **101** 146402
[21] Li S D, Fu Y J and Cheng C 2012 *Opt. Express* **20** 19850
[22] Tsitsishvili E and Kalt H 2010 *Phys. Rev.* B **82** 195315
[23] Gündogdu K, Hall K C, Koerperick E J, Pryor C E, Flatté M E and Boggess T F 2005 *Appl. Phys. Lett.* **86** 113111
[24] Hall K C, Koerperick E J, Boggess T F, Shchekin O B and Deppe D G 2007 *Appl. Phys. Lett.* **90** 053109
[25] Laurent S, Eble B, Krebs O, Lemaitre A, Urbaszek B, Marie X, Amand T and Voisin P 2005 *Phys. Rev. Lett.* **94** 147401
[26] Heiss D, Schaeck S, Huebl H, Bichler M, Abstreiter G, Finley J J, Bulaev D V and Loss D 2007 *Phys. Rev.* B **76** 241306
[27] Fras F, Eble B, Desfonds P, Bernardot F, Testelin C, Chamarro M, Miard A and Lemaitre A 2012 *Phys. Rev.* B **86** 045306
[28] Winkler R 2003 *Spin–Orbit Coupling Effects in Two-Dimensional Electron and Hole Systems* (Berlin: Springer)
[29] Woods L M, Reinecke T L and Kotlyar R 2004 *Phys. Rev.* B **69** 125330
[30] Lü C, Cheng J L and Wu M W 2005 *Phys. Rev.* B **71** 075308
[31] Bulaev D V and Loss D 2005 *Phys. Rev. Lett.* **95** 076805
[32] Trif M, Simon P and Loss D 2009 *Phys. Rev. Lett.* **103** 106601
[33] Wei H, Gong M, Guo G C and He L 2012 *Phys. Rev.* B **85** 045317
[34] Roszak K, Axt V M, Kuhn T and Machnikowski P 2007 *Phys. Rev.* B **76** 195324
[35] Tsitsishvili E, Baltz R V and Kalt H 2005 *Phys. Rev.* B **72** 155333
[36] He J, Zhong H and Scholes G D 2010 *Phys. Rev. Lett.* **105** 046601
[37] Luttinger J M 1956 *Phys. Rev.* **102** 1030
[38] Voon L C L Y and Willatzen M 2009 *The* $\mathbf{k}\cdot\mathbf{p}$ *Method* (Berlin: Springer) p 97
[39] Uenoyama T and Sham L J 1990 *Phys. Rev.* B **42** 7114
[40] Planelles J, Climente J I and Segarra C 2012 *J. Phys. Chem.* C **116** 25143
[41] Vurgaftman I, Meyer J R and Ram-Mohan L R 2001 *J. Appl. Phys.* **89** 5815
[42] Hu J, Li L S, Yang W, Manna L, Wang L W and Alivisatos A P 2001 *Science* **292** 2060
[43] Katz D, Wizansky T, Millo O, Rothenberg E, Mokari T and Banin U 2002 *Phys. Rev. Lett.* **89** 086801
[44] Voon L C L Y, Melnik R, Lassen B and Willatzen M 2004 *Nano Lett.* **4** 289
[45] Planelles J, Rajadell F and Climente J I 2010 *J. Phys. Chem.* C **114** 8337
[46] Blokland J H, Wijnen F J P, Christianen P C M, Zeitler U, Maan J C, Kailuweit P, Reuter D and Wieck A D 2007 *Phys. Rev.* B **75** 233305

[47] Warburton R J, Miller B T, Dürr C S, Bödefeld C, Karrai K, Kotthaus J P, Medeiros-Ribeiro G, Petroff P M and Huant S 1998 *Phys. Rev.* B **58** 16221

[48] Schinner G J, Repp J, Schubert E, Kotthaus J P, Rai A K, Reuter D, Wieck A D, Govorov A O and Holleitner A W 2012 Single exciton emission from gate-defined quantum dots arXiv:1204.3199

[49] Madelung O 2004 *Semiconductors: Data Handbook* (Berlin: Springer)

[50] Khaetskii A V and Nazarov Y V 2001 *Phys. Rev.* B **64** 125316

[51] Climente J I, Bertoni A, Goldoni G and Molinari E 2006 *Phys. Rev.* B **74** 035313

IOP Publishing Journal of Physics: Condensed Matter
J. Phys.: Condens. Matter **27** (2015) 415301 (8pp) doi:10.1088/0953-8984/27/41/415301

Hole spin relaxation in InAs/GaAs quantum dot molecules

C Segarra, J I Climente, F Rajadell and J Planelles

Departament de Química Física i Analítica, Universitat Jaume I, Castelló de la Plana, Spain

E-mail: josep.planelles@uji.es

Received 30 July 2015, revised 3 September 2015
Accepted for publication 8 September 2015
Published 29 September 2015

Abstract

We calculate the spin–orbit induced hole spin relaxation between Zeeman sublevels of vertically stacked InAs quantum dots. The widely used Luttinger–Kohn Hamiltonian, which considers coupling of heavy- and light-holes, reveals that hole spin lifetimes (T_1) of molecular states significantly exceed those of single quantum dot states. However, this effect can be overcome when cubic Dresselhaus spin–orbit interaction is strong. Misalignment of the dots along the stacking direction is also found to be an important source of spin relaxation.

Keywords: spin–orbit interaction, hole spin relaxation, quantum dot molecules

(Some figures may appear in colour only in the online journal)

1. Introduction

The spin of carriers confined in nanostructures has been intensively studied in recent years due to its promising applications in spintronics and spin-based quantum information processing [1, 2]. In particular, hole spins in quantum dots (QDs) have received great attention as a consequence of their long decoherence times and versatility. The confinement in heterostructures is responsible for the suppression of the main decoherence mechanisms present in bulk systems [3, 4]. Additionally, the p-type symmetry of the valence band orbitals causes a weak hyperfine interaction with the lattice nuclei, thus giving rise to decoherence times potentially longer than those of electron spins [5–11]. This has enabled successful hole spin initialization [12] and coherent control [10, 13]. Double quantum dots (DQDs) are a natural extension which should facilitate the use of independent optical transitions for spin preparation, manipulation and readout [14], as well as the scalability towards multiple qubit architectures [15]. Also, DQDs are more versatile than single QDs since the coupling between the two QDs offers an additional control mechanism, as the tunneling can be tuned by using externally applied electric fields [16–19].

Using the spin of holes in qubits requires control over the hole spin relaxation (T_1) and decoherence (T_2) times, the latter being related to the former at low temperatures [20]. In the presence of external magnetic fields, the main mechanism of spin relaxation for the valence band is usually phonon scattering mediated by spin–orbit interaction (SOI) [21, 22]. Indeed, the strong SOI of holes is responsible for some of its characteristic properties, e.g. the g-factor anisotropy or the origin of antisymmetric ground states in DQDs [23–26]. The three main SOI mechanisms are the light hole-heavy hole (LH-HH) mixing, the bulk inversion asymmetry (BIA or Dresselhaus SOI) [27] and the structural inversion asymmetry (SIA or Rashba SOI) [28]. Several works have theoretically addressed the hole spin relaxation in single QDs taking into account different SOI mechanisms and have showed that one or another prevail depending on the QD traits [20, 29–32]. By comparison, the spin relaxation of holes in DQDs is still poorly understood. This is inspite of their promising prospects for the development of quantum information architectures [10, 15, 19]. Understanding the hole spin dynamics in DQDs is also of relevance for recently proposed exciton spin based qubits [33], since hole relaxation usually determines the excitonic spin lifetime.

In the present work, we investigate the hole spin relaxation between Zeeman split sublevels in vertically coupled DQDs. We consider InAs/GaAs DQDs with various relative positions of the individual dots while maintaining their dimensions unaltered. In particular, we study the spin relaxation for different interdot barrier thicknesses and dots alignments. The hole states are simulated using three-dimensional (3D) Hamiltonians including not only quadratic-in-k LH-HH coupling present in the Luttinger–Kohn Hamiltonian, but also cubic Dresselhaus SOI, which was found to be potentially important in single InAs QDs [31]. Calculations are carried out for varying strength of an electric field applied along the DQD stacking direction. This makes possible to study the transition from atomic-like states confined in one of the constituent QDs to fully molecular-like states, which are obtained when the electric field tunes the energy of the upper and lower dots to be the same [19].

We show that T_1 of molecular spin–orbitals is often larger than that of holes localized in single QDs, with lifetime extensions reaching 600% in some cases, which is a result of the higher symmetry of the system under resonant electric fields. Dresselhaus SOI however plays an important role in the description of the hole spin dynamics. Its inclusion in the Hamiltonian provides new channels of spin admixture, decreasing T_1 up to one order of magnitude and reducing the differences between molecular and single QD states. Nevertheless, the most drastic factor reducing T_1 is misalignment between the QDs forming the DQD. The severe symmetry breaking enhances SOI, leading to pronounced shortenings of T_1, as well as to the appearance of spin anticrossings in the energy spectra, which constitute spin-hot spots with extremely fast relaxation.

The paper is organized as follows. In section 2 we present the details of the model we use to compute the hole states and the spin lifetimes. In section 3 we show and discuss the results of the calculations for a DQD system with strong and weak hole tunneling. Finally, conclusions are given in section 4.

2. Theoretical model

We investigate the spin relaxation of holes confined in vertically coupled DQDs grown along the [0 0 1] direction. The system is subject to external magnetic and electric fields applied along the growth direction. The Hamiltonian that describes the hole states reads

$$H_h = H_{\mathrm{L}} + H_{\mathrm{B}} + (V_{\mathrm{QD}} + eF_z z)\,\mathcal{I} + H_{\mathrm{BIA}} + H_{\mathrm{SIA}}, \quad (1)$$

where H_{L} is the Luttinger Hamiltonian [34] and H_{B} represents the terms coming from the implementation of the magnetic field. The next two terms in (1) are the 3D confining potential V_{QD} and the externally applied electric field $\mathbf{F} = (0, 0, F_z)$, with e standing for the hole charge and $\mathcal{I}$ the 4×4 identity matrix. Finally, H_{BIA} is the spin–orbit Hamiltonian corresponding to the Dresselhaus SOI. Rashba SOI is disregarded in this study because the system asymmetry in the growth direction is suppressed under resonant electric fields, which lead to the formation of molecular states with effective parity symmetry [23]. All the same, we have carried out a series of calculations (not shown) that confirm the negligible influence of Rashba SOI in the vicinity of the resonant field.

The Luttinger Hamiltonian H_{L} is a four-band Hamiltonian which includes the spin–orbit coupling between light-holes (LH) and heavy-holes (HH) subbands up to second order in k [34]. The matrix representation of H_{L} in terms of the Bloch basis functions $J_z = +3/2, +1/2, -1/2, -3/2$ is

$$H_{\mathrm{L}} = -\begin{pmatrix} P+Q & -S & R & 0 \\ -S^\dagger & P-Q & 0 & R \\ R^\dagger & 0 & P-Q & S \\ 0 & R^\dagger & S^\dagger & P+Q \end{pmatrix}, \quad (2)$$

with

$$P = \frac{1}{2\,m_0}\,\gamma_1\,(k_x^2 + k_y^2 + k_z^2), \quad (3)$$

$$Q = \frac{1}{2\,m_0}\,\gamma_2\,(k_x^2 + k_y^2 - 2k_z^2), \quad (4)$$

$$R = \frac{1}{2\,m_0}\left[-\sqrt{3}\,\gamma_2\,(k_x^2 - k_y^2) + 2\,\mathrm{i}\,\sqrt{3}\,\gamma_3\,k_x\,k_y\right] \quad (5)$$

$$S = \frac{1}{2\,m_0}\,2\,\sqrt{3}\,\gamma_3\,(k_x - \mathrm{i}\,k_y)\,k_z, \quad (6)$$

Here m_0 is the free electron mass and γ_i are the Luttinger mass parameters. For the sake of simplicity, we use constant Luttinger parameters throughout the entire nanostructure.

The uniform axial magnetic field is described by the vector potential in the symmetric gauge $\mathbf{A} = \frac{B}{2}(-y, x, 0)$. The implementation follows the procedure described in [35]. The resulting Hamiltonian H_{B} has the form

$$H_{\mathrm{B}} = -\left(\frac{B^2}{8m_0}(x^2 + y^2) + \frac{B}{2m_0}(xk_y - yk_x)\right)M - \kappa\mu_{\mathrm{B}}BJ_z \quad (7)$$

with M being the 4×4 diagonal matrix with elements $\{\gamma_1 + \gamma_2, \gamma_1 - \gamma_2, \gamma_1 - \gamma_2, \gamma_1 + \gamma_2\}$. The last term of (7) corresponds to the Zeeman splitting with κ standing for the hole g factor, μ_{B} the Bohr magneton and J_z the matrix representation of the third component of the angular momentum with quantum number $J = 3/2$.

The last two elements in (1), H_{BIA} and H_{SIA}, are additional terms describing the Dresselhaus and Rashba SOI, respectively [36]. As stated above, we disregard H_{SIA} due to its negligible influence under resonant electric fields. H_{BIA} includes linear and third order in k terms and is given by:

$$\begin{aligned} H_{\mathrm{BIA}} = {} & \frac{2}{\sqrt{3}}\,C_k\,[k_x\,\{J_x, J_y^2 - J_z^2\} + \mathrm{cp}] \\ & + b_{41}\,[\{k_x, k_y^2 - k_z^2\}\,J_x + \mathrm{cp}] \\ & + b_{42}\,[\{k_x, k_y^2 - k_z^2\}\,J_x^3 + \mathrm{cp}] \\ & + b_{51}\,[\{k_x, k_y^2 + k_z^2\}\,\{J_x, J_y^2 - J_z^2\} + \mathrm{cp}] \\ & + b_{52}\,[k_x^3\,\{J_x, J_y^2 - J_z^2\} + \mathrm{cp}] \end{aligned} \quad (8)$$

where C_k, b_{41}, b_{42}, b_{51} and b_{52} are material dependent coefficients, $\{A, B\} = \frac{1}{2}(AB + BA)$ and cp stands for cyclic permutations of the preceding terms. The matrix form of Hamiltonian (8) can be found in [31].

Since H_h is a four-band Hamiltonian, its eigenfunctions are four-component spinors of the form:

$$\Psi_n = \sum_{J_z=-3/2}^{3/2} f_{J_z}^{(n)}(\mathbf{r})\,|J_z\rangle, \tag{9}$$

where $f_{J_z}^{(n)}(\mathbf{r})$ and $|J_z\rangle$ are the envelope and Bloch parts of the J_z component.

We study the spin relaxation of hole states mediated by the phonon bath. The transitions considered involve the Zeeman split sublevels of lowest energy, i.e. from the first excited to the hole ground state. The energy splitting of these states is small and, thus, only long-wave acoustic phonons can participate and the linear dispersion regime holds, $E_{\lambda q} = \hbar c_\lambda q$. Here, c_λ is the phonon velocity of the longitudinal or two transversal phonon modes λ. The Hamiltonian that describes the coupling between holes and phonons is

$$H_{\mathrm{h-ph}} = e\,\phi_{\mathrm{pz}}\,\mathcal{I} + H_{\mathrm{dp}}, \tag{10}$$

where e is the hole charge, $\mathcal{I}$ is the 4×4 identity matrix, ϕ_{pz} the piezoelectric potential and H_{dp} the deformation potential term. These are the two scattering mechanisms that dominate the hole spin relaxation [30]. The deformation potential coupling H_{dp} is given by the strain Hamiltonian [37], formally identical to (2)–(6) with k_ik_j replaced by the strain component ε_{ij} and the mass coefficients by the deformation ones, and the piezoelectric interaction by the potential [38]

$$\phi_{\mathrm{pz}} = \sum_\lambda \phi_{\mathrm{pz}}^\lambda = -\sum_{\lambda\,\mathbf{q}} \frac{4\pi\,\mathrm{i}}{\epsilon_r\,q^2}\,h_{14}\,(q_x\,\varepsilon_{yz}^\lambda + q_y\,\varepsilon_{zx}^\lambda + q_z\,\varepsilon_{xy}^\lambda). \tag{11}$$

where ϵ_r stands for the relative dielectric constant, h_{14} is the piezoelectric constant and ε_{ij} is the strain tensor component. The complete expressions and derivation of the piezoelectric potential and the deformation potential operators for the three phonon branches is presented in [31].

The transition rate between the initial hole state $|\Psi_i^h\rangle$ and the final hole state $|\Psi_f^h\rangle$ is estimated using the Fermi golden rule

$$\frac{1}{T_1} = \frac{2\pi}{\hbar}\sum_{\lambda,\mathbf{q}} \left|\langle\Psi_f^h|\mathcal{H}_{\mathrm{h-ph}}^{\lambda q}\,|\Psi_i^h\rangle\right|^2 \delta(\Delta E_{fi} + \hbar c_\lambda q). \tag{12}$$

where $\mathcal{H}_{\mathrm{h-ph}}^{\lambda q}$ is the hole-phonon coupling Hamiltonian, equation (10), and $\Delta E_{fi} = E_f - E_i$. The sum is done over all directions of $\mathbf{q}$ and the three phonon branches of bulk zinc-blende crystals, one longitudinal and two transversal. All calculations are carried out at zero temperature, so that only phonon emission processes are possible.

The multi-band Hamiltonian (1) is of fully 3D nature, as in DQDs the vertical and lateral dimensions can be comparable, which prevents the adiabatic separation of variables usually employed for single QDs [1]. Besides, we are interested in analyzing the effect of misalignment between the QDs forming the DQD, which implies breaking the in-plane symmetry through V_{QD}. We then use Cartesian coordinates. It is also worth noting that H_h includes third-order derivatives through the H_{BIA} term. Since SOI is a fine effect, precise estimates of its influence require a very accurate description of such derivatives. To solve this challenging problem, we integrate H_h numerically using a finite differences scheme. In order to achieve the desired accuracy while maintaining a reasonable mesh, we have explored increasing the points of the derivatives discretization. After a series of convergence tests, we found that a 5-point stencil central difference scheme offers a good description at a reasonable computational cost. In addition, we consider QDs with cuboidal shape which are perfectly adjusted to the 3D regular mesh. This simplified geometry grants comparable accuracy in the estimate of potential and kinetic energy terms, while allowing us to study the influence of the basic features of DQDs on the spin dynamics, namely the effect of interdot barrier thickness and that of misalignment. The 3D discretization of (1) yields a huge sparse matrix that is diagonalized by means of the Arnoldi iterative method. The size of these matrices ranges from $73\,644\times73\,644$ for close aligned QDs up to $150\,326\times150\,326$ for distant misaligned QDs.

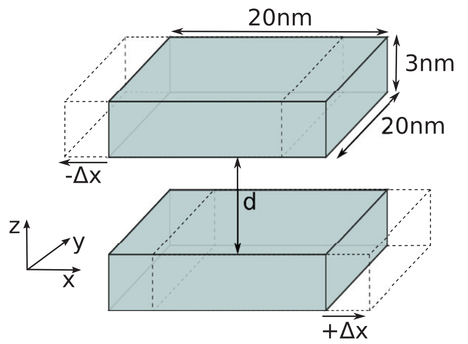

Figure 1. Schematic drawing of the InAs DQD cuboidal system. The dimensions of the QDs and the variable parameters d and Δ_x are indicated. The boxes with dashed lines represent the DQD with misalignment.

3. Numerical results and discussion

The system studied is a DQD of InAs embedded in a GaAs matrix as represented in figure 1. The QDs are identical with cuboidal shape ($L_x = 20$ nm, $L_y = 20$ nm and $L_z = 3$ nm) and are separated by a distance d. The parameters used in the calculations are summarized in table 1. They all correspond to the QD material InAs, except for the ones describing the phonons (c_l, c_t and ρ) which correspond to the matrix material GaAs as we assume bulk phonons. The confining potential V_{QD} is zero inside the QDs and V_0 outside, where $V_0 = -0.33$ eV is the valence band offset between InAs and GaAs [39]. Finally, we take $\kappa = 4/3$ for the hole g factor as suggested in [40].

We investigate the dependence of the hole spin lifetime on the external electric field F_z. We consider two different interdot barriers $d = 3$ nm and $d = 9$ nm as an example of a DQD system with strong and weak tunneling, respectively. In addition, for each d we study the possibility of the two QDs being perfectly aligned and also misaligned. The misalignment consists in a shift in x in opposite directions of the two

Table 1. Material parameters used in the numerical calculations.

Parameter	Symbol	InAs	Reference
Luttinger parameter	γ_1	20	[39]
Luttinger parameter	γ_2	8.5	[39]
Luttinger parameter	γ_3	9.2	[39]
Deformation potential (eV)	a	1.0	[39]
Deformation potential (eV)	b	−1.8	[39]
Deformation potential (eV)	c	−3.6	[39]
Dresselhaus coeff. (eV Å)	C_k	−0.0112	[36]
Dresselhaus coeff. (eV Å^3)	b_{41}	−50.18	[36]
Dresselhaus coeff. (eV Å^3)	b_{42}	1.26	[36]
Dresselhaus coeff. (eV Å^3)	b_{51}	0.42	[36]
Dresselhaus coeff. (eV Å^3)	b_{52}	−0.84	[36]
Longitudinal phonon speed (m s^{-1})	c_l	4720	[41]
Transversal phonon speed (m s^{-1})	c_t	3340	[41]
Crystal density (kg m^{-3})	ρ	5310	[41]
Piezoelectric constant (V cm^{-1})	h_{14}	3.5×10^6	[41]
Relative dielectric constant	ϵ_r	12.9	[41]

QDs by an offset $\Delta_x = 3.3$ nm as depicted in figure 1. This value corresponds to a DQD with large yet realistic lateral offset [42]. All calculations are carried out at a magnetic field $B = 2$ T. For this field, hole-phonon coupling via deformation potential prevails over piezoelectric coupling [31].

3.1. Strong tunneling regime

Figure 2 illustrates the energy spectra and hole spin lifetimes of a DQD with interdot distance $d = 3$ nm as a function of the external electric field F_z. An analysis of the low-energy hole states reveals that they have mainly HH character[1]. Thus, the transition between the Zeeman-split sublevels, indicated in figures 2(a) and (b) by orange arrows, is essentially a transition from a HH with $J_z = +3/2$ ($\Uparrow$ in figure 2) to a HH with $J_z = -3/2$ ($\Downarrow$).

Panels (a) and (c) of figure 2 show the energy spectrum and spin lifetime for a DQD with no misalignment. For a finite electric field the wave function tends to localize in one of the dots as represented in the insets of figure 2(a). The change of localization when varying F_z gives rise to a charge transfer anticrossing at $F_z = 0$, where hole states of both QDs are in resonance and the wave function forms delocalized molecular orbitals. Since the barrier thickness we consider is beyond the critical distance at which the hole ground state changes from bonding to antibonding character [23], the two states of the Zeeman doublet we consider are antibonding.

Calculations of the hole spin lifetime are shown in figure 2(c) for two different situations: considering only the LH-HH mixing derived from the standard Luttinger Hamiltonian H_{L} (black line) and considering the additional influence of H_{BIA} as well (dashed line). When only LH-HH mixing is taken into account, one can see that T_1 presents a maximum for molecular states ($F_z = 0$) that slowly decreases as we move toward localized, atomic-like states ($|F_z| > 10$ kV cm^{-1}). This remarkable result is reminiscent of the T_1 enhancement recently reported for single QDs at certain values of F_z [32]. The inclusion of H_{BIA}, however, reduces T_1 by one order of magnitude and moderates the longer lifetime of the molecular regime ($F_z \approx 0$).

Since spin lifetime is connected with SOI-induced spin admixture [1], in order to understand the above results we analyze the strength of the SOI, which can be qualitatively estimated from symmetry considerations. In general, a lowering in symmetry implies the activation of additional SOI mechanisms [36] and hence shorter T_1. In particular, this is specially relevant at $F_z = 0$, where the symmetry is highest. H_{L} in (1) has T_d symmetry, corresponding to the bulk zinc-blende point group. The confining potential that defines the aligned DQD system, V_{QD}, reduces the symmetry to D_{4h}. Then, the application of an external magnetic field in the axial direction further reduces it to C_{4h}. We can take this as the starting point, H_{L} at $F_z = 0$ in figure 2(b). Next we add other factors like external electric fields or additional SOI terms, which further reduce the symmetry and hence T_1. Thus, a finite electric field F_z lifts the parity symmetry in z, reducing the system symmetry to C_4, which explains the shorter T_1 for individual QDs as compared to the symmetric DQD in the H_{L} curve of figure 2(c). If we include H_{BIA} to the calculation instead, the reduction is more important, group C_2, and thus the decrease of T_1 is more pronounced. In this case, the introduction of an external electric field no longer reduces the symmetry and has negligible effect on T_1.

The results for a DQD with misalignment are illustrated in figures 2(b) and (d). Energetically, the main consequence of introducing a lateral offset to the QDs position is a reduction in the hole tunneling which, in turn, diminishes the magnitude of the charge anticrossing in the energy spectrum [42]. As for the hole spin lifetimes, by comparing with figure 2(c), figure 2(d) shows that misalignment of the QDs roughly preserves the shape of T_1 estimated from either H_{L} or H_{BIA}, but it causes an additional decrease in T_1 of one order of magnitude or more.

These results can be explained following the same reasoning as for a DQD with no misalignment. Now, the interplay of confinement potential V_{QD} and magnetic field removes all exact symmetry elements. Therefore, the hole spin lifetime is reduced in comparison to the aligned case. The symmetry breaking becomes even more efficient in the presence of an applied electric field, resulting in shorter lifetimes.

[1] Energies are negative because they are referred to the top of the valence band. By lowest energy we mean lowest absolute value.

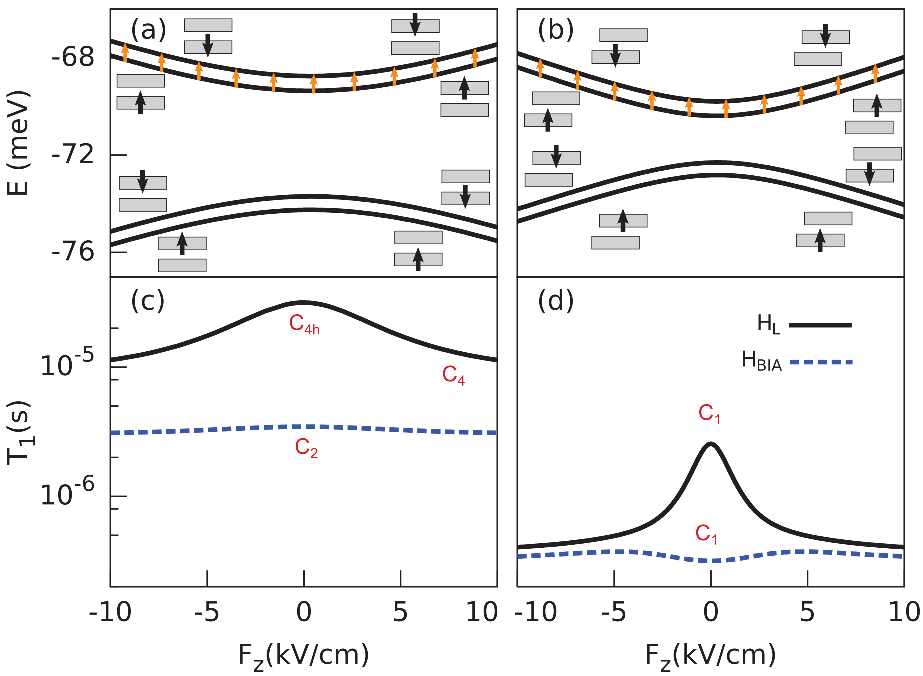

Figure 2. Hole energy spectra (a)–(b) and spin lifetime (c)–(d) as a function of the applied electric field for DQDs with interdot barrier $d = 3$ nm. Left panels: aligned QDs. Right panels: QDs with misalignment of $\Delta_x = 3.3$ nm. The energy spectra are obtained from H_h, (1). The hole spin lifetimes are calculated under different conditions: Luttinger Hamiltonian H_L only (black solid line) or $H_L + H_{BIA}$ (blue dashed line). The insets in (a)–(b) show the wave function localization and the dominant spinor component, $J_z = +3/2$ ($\Uparrow$) or $J_z = -3/2$ ($\Downarrow$). The orange arrows represent the transition studied. The labels in (c)–(d) give the point group of the system in different situations. $B = 2$ T in all calculations.

3.2. Weak tunneling regime

In this section we investigate the same situations as above but we consider now a DQD system with an interdot barrier $d = 9$ nm.

Figure 3(a) illustrates the energy spectrum when the QDs are aligned. A clear difference with the previous case, figure 2(a), is observed since now the $J_z = +3/2$ antibonding and $J_z = -3/2$ bonding states cross near the resonant field (see grey dotted boxes in figure 3). The inset of figure 3(a) contains a zoom of the crossing at $|F_z| \approx 0.5$ kV cm^{-1}. It shows that no spin anticrossing takes place in spite of including BIA spin–orbit terms in the calculations.

The absence of anticrossings can be understood analyzing the symmetry of the hole states. H_h belongs to the C_2 point group. The symmetry of its spinorial eigenstates Ψ_n, equation (9), is then obtained from the double group $\bar{C}_2$. As shown in the labels of figure 3(a), the two states crossing each other have $E_{3/2}$ and $E_{-3/2}$ symmetry, respectively (see appendix for more details). The different symmetry of the states justifies the absence of spin anticrossings in the spectrum.

The results for the spin lifetime are presented in figure 3(c). All calculations are also carried out considering the transition between the Zeeman split antibonding states (see orange arrows in figure 3). In general, we find similar lifetimes compared to the aligned DQD with strong tunneling. As in the strong tunneling case, H_L predicts the longest T_1 values for the molecular regime ($F_z = 0$), although the enhancement is now smaller and takes place for a narrower range of electric fields, which is a consequence of the weaker tunneling energy. Interestingly, in this case adding H_{BIA} preserves the T_1 maximum at zero electric field. This is because the dominant term of H_{BIA} (b_{41} in (8)) scales roughly proportional to $\langle k_z^2 \rangle$ [1]. In a DQD with thick interdot barrier a small electric field is enough to localize the wave function in one of the QDs, rapidly increasing $\langle k_z^2 \rangle$ and reducing T_1. In contrast, when the tunneling is important, stronger fields are needed to break the molecular character. As a consequence, in figure 2(c) $\langle k_z^2 \rangle$ did not change significantly in the range considered and the T_1 maximum was less pronounced.

Figure 3(b) illustrates the energy spectrum for a misaligned DQD. At first glance, no major differences with the aligned situation are observed, except for the smaller magnitude of the charge transfer anticrossings. However, the inset of figure 3(b) shows that now the states of different spin anticross. The size of this spin anticrossing is of the order of few μeV, particularly $\Delta_s \approx 6$ μeV for H_L and further increases to $\Delta_s \approx 20$

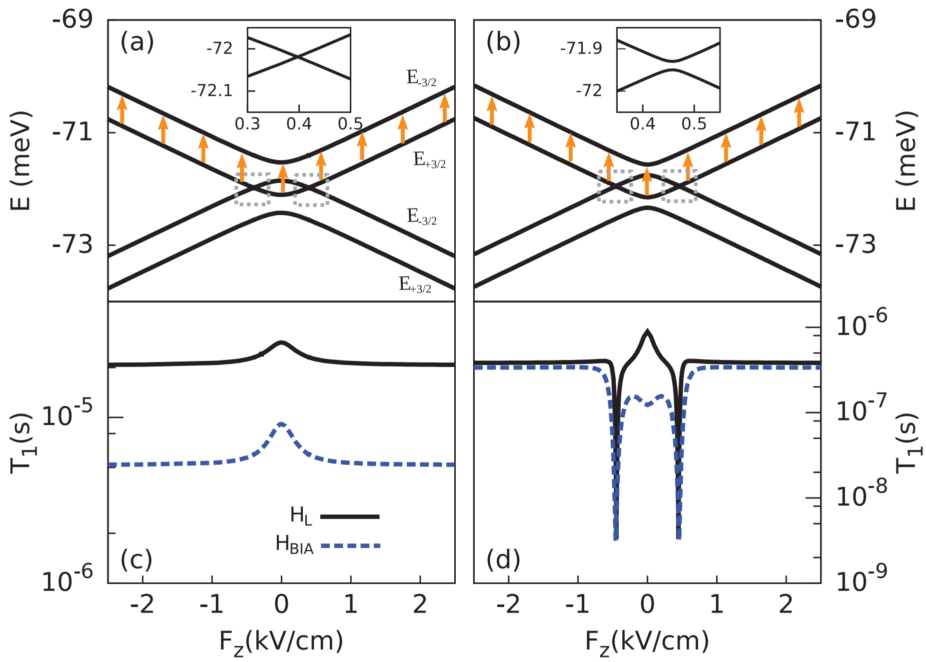

Figure 3. Same as figure 2 but for a DQD with barrier thickness $d = 9$ nm. The insets in (a)–(b) are a zoom of the squared region, showing the crossing/anticrossing between the hole states of different HH spin and localization at $F_z \approx 0.5$ kV cm^{-1}. $B = 2$ T in all calculations.

μeV when Dresselhaus SOI is included. The presence of a spin anticrossing implies the admixture of hole states with the same symmetry. The reason is that misalignment reduces the symmetry to the C_1 point group, and all the states belong to the totally symmetric irreducible representation.

The obtained lifetime results are summarized in figure 3(d). Similarly to the strong tunneling case, misalignment of the QDs reduces the spin lifetimes by one order of magnitude. The main difference with respect to the strong tunneling case (figure 2(d)) is the appearance of two sharp dips in the hole lifetime at $F_z \approx \pm 0.5$ kV cm^{-1}, where T_1 decreases by two orders of magnitude. These correspond to the spin anticrossings of figure 3(b). These anticrossings form so-called spin-hot spots (see, e.g. [43]), where spin mixing is maximized. While the strong spin mixing can be benefitial for spin control protocols [42], our calculatios show that it also leads to severely reduced T_1.

We have checked the robustness of the results in this section versus small changes in the model parameters (geometry, size and magnetic field). As discussed above, the qualitative trends are a consequence of the symmetry in the Hamiltonian rather than a specific set of parameters.

4. Conclusions

We have investigated the hole spin lifetime in InAs/GaAs DQDs as a function of the axial electric field strength. We have explored the effect of changing the QDs relative position (alignment and distance) and the introduction of Dresselhaus SOI.

The results reveal that severe changes in the distance d do not translate in large changes of the spin lifetime. A clear correlation between the symmetry of the system and T_1 is observed, which follows from the enhancement of SOI induced spin admixture with lowering symmetry. Thus, we show that the Luttinger Hamiltonian yields maximum T_1 for DQDs under resonant electric fields, but it decreases when the electric field pushes the wave function towards one of the QDs. This is a consequence of the higher symmetry of DQDs under resonant electric fields, when wave functions with parity symmetry are obtained.

Cubic Dresselhaus SOI lowers the symmetry to a C_2 point group, consequently reducing T_1 about one order of magnitude. In fact, a strong Dresselhaus SOI, as that found for DQDs in the strong tunneling regime, can even suppress the different behaviour between single QD and DQD states.

Misalignment of the QDs, which is often observed in DQDs, reduces the system symmetry to C_1. When severe, it can reduce of T_1 over one order of magnitude. It is also responsible for the appearance of spin anticrossings in the energy spectra, which are absent for aligned DQDs. These are spin-hot spots, where spin mixing is maximized and a drastic decrease of T_1 is observed.

In summary, while the increase of symmetry, reached by the formation of molecular orbitals induced by resonant electric fields, favors spin purity and long T_1 values, misalignment or defects as well as strong Dresselhaus spin–orbit interaction play in opposite direction and can eventually overcome the effects of the resonant field.

Appendix

The character table of the double group $\bar{C}_2$ we use is:

$\bar{C}_2$	E	C_2^1	C_2^2	C_2^3	basis ($e^{iM\phi}$)
A	1	1	1	1	$M = 0, \pm 2, \pm 4, k_x^2, k_y^2, k_z^2, k_x k_y$
B	1	-1	1	-1	$M = \pm 1, \pm 3, k_y k_z, k_x k_z$
$E_{-3/2}$	1	i	-1	$-$i	$M = 1/2, -3/2$
$E_{3/2}$	1	$-$i	-1	i	$M = -1/2, 3/2$

(A.1)

and the corresponding table of product of irreducible representations:

	A	B	$E_{-3/2}$	$E_{3/2}$
A	A	B	$E_{-3/2}$	$E_{3/2}$
B		A	$E_{3/2}$	$E_{-3/2}$
$E_{-3/2}$			B	A
$E_{3/2}$				B

(A.2)

Within this group, the four Bloch functions $|J_z\rangle$, with $J_z = 3/2$, $1/2$, $-1/2$, $-3/2$, form basis of the following irreducible representations:

$$\begin{pmatrix} E_{3/2} \\ E_{-3/2} \\ E_{3/2} \\ E_{-3/2} \end{pmatrix} \tag{A.3}$$

respectively.

As for the envelope parts, $f_{J_z}^n$, we consider that the symmetry of the matrix element operators in the 4-band Hamiltonian H_h, obtained with the help of (1), is:

$$\Gamma_{H_h} = \begin{pmatrix} A & B & A & B \\ B & A & B & A \\ A & B & A & B \\ B & A & B & A \end{pmatrix}. \tag{A.4}$$

Since the envelope eigenfunctions must have a definite symmetry within the C_2 group, the two possibilities compatible with (A.4) are:

$$\begin{pmatrix} A \\ B \\ A \\ B \end{pmatrix} \text{and} \begin{pmatrix} B \\ A \\ B \\ A \end{pmatrix}, \tag{A.5}$$

whose product with (A.3) gives total spinor symmetry $E_{3/2}$ and $E_{-3/2}$, respectively. For the ground state in figure 3(a), Ψ_1, since the main component is a totally symmetric spin down HH, $f_{-3/2}^{(1)}$ must have A symmetry and it follows that the spinor symmetry is $E_{-3/2}$. For the other Zeeman sublevel, Ψ_2, the dominant component is the spin up HH, so that $f_{3/2}^{(2)}$ has A symmetry and the spinor symmetry is $E_{3/2}$. A similar procedure is followed to obtain the symmetry of the remaining hole states in figure 3.

Acknowledgments

This work was supported by UJI Project No. P1.1B2014-24, MINECO Project No. CTQ2011-27324, and FPU Grant (C S).

References

[1] Hanson R, Kouwenhoven L P, Petta J R, Tarucha S and Vandersypen L M K 2007 *Rev. Mod. Phys.* **79** 1217
[2] Wu M W, Jiang J H and Weng M Q 2010 *Phys. Rep.* **493** 61
[3] Khaetskii A V and Nazarov Y V 2000 *Phys. Rev.* B **61** 12639
[4] Dyakonov M I(ed) 2008 *Spin Physics in Semiconductors* (Springer: Berlin)
[5] Gerardot B D, Brunner D, Dalgarno P A, Öhberg P, Seidl S, Kroner M, Karrai K, Stoltz N G, Petroff P M and Warburton R J 2008 *Nature* **451** 441
[6] Brunner D, Gerardot B D, Dalgarno P A, Wüst G, Karrai K, Stoltz N G, Petroff P M and Warburton R J 2009 *Science* **325** 70
[7] Fischer J, Trif M, Coish W A and Loss D 2009 *Solid State Commun.* **149** 1443
[8] Eble B, Testelin C, Desfonds P, Bernardot F, Balocchi A, Amand T, Miard A, Lemaitre A, Marie X and Chamarro M 2009 *Phys. Rev. Lett.* **102** 146601
[9] Fallahi P, Yilmaz S T and Imamoglu A 2010 *Phys. Rev. Lett.* **105** 257402
[10] De Greve K *et al* 2011 *Nat. Phys.* **7** 872
[11] Dahbashi R, Hübner J, Berski F, Pierz K and Oestreich M 2014 *Phys. Rev. Lett.* **112** 156601
[12] Godden T M, Quilter J H, Ramsay A J, Wu Y, Brereton P, Luxmoore I J, Puebla J, Fox A M and Skolnick M S 2012 *Phys. Rev.* B **85** 155310
[13] Godden T M, Quilter J H, Ramsay A J, Wu Y, Brereton P, Boyle S J, Luxmoore I J, Puebla-Nunez J, Fox A M and Skolnick M S 2012 *Phys. Rev. Lett.* **108** 017402
[14] Vamivakas A N, Lu C-Y, Matthiesen C, Zhao Y, Fält S, Badolato A and Atatüre M 2010 *Nature* **467** 297
[15] Economou S E, Climente J I, Badolato A, Bracker A S, Gammon D and Doty M F 2012 *Phys. Rev.* B **86** 085319
[16] Krenner H J, Sabathil M, Clark E C, Kress A, Schuh D, Bichler M, Abstreiter G and Finley J J 2005 *Phys. Rev. Lett.* **94** 057402
[17] Ortner G, Bayer M, Lyanda-Geller Y, Reinecke T L, Kress A, Reithmaier J P and Forchel A 2005 *Phys. Rev. Lett.* **94** 157401
[18] Petta J R, Johnson A C, Taylor J M, Laird E A, Yacoby A, Lukin M D, Marcus C M, Hanson M P and Gossard A C 2005 *Science* **309** 2180
[19] Stinaff E A, Scheibner M, Bracker A S, Ponomarev I V, Korenev V L, Ware M E, Doty M F, Reinecke T L and Gammon D 2006 *Science* **311** 636
[20] Bulaev D V and Loss D 2005 *Phys. Rev. Lett.* **95** 076805
[21] Heiss D, Schaeck S, Huebl H, Bichler M, Abstreiter G, Finley J J, Bulaev D V and Loss D 2007 *Phys. Rev.* B **76** 241306
[22] Trif M, Simon P and Loss D 2009 *Phys. Rev. Lett.* **103** 106601
[23] Climente J I, Korkusinski M, Goldoni G and Hawrylak P 2008 *Phys. Rev.* B **78** 115323
[24] Doty M F, Climente J I, Korkusinski M, Scheibner M, Bracker A S, Hawrylak P and Gammon D 2009 *Phys. Rev. Lett.* **102** 047401

[25] Andlauer T and Vogl P 2009 *Phys. Rev.* B **79** 045307
[26] Sheng W and Wang J 2010 *Phys. Rev.* B **82** 073308
[27] Dresselhaus G 1955 *Phys. Rev.* **100** 580
[28] Bychkov Y A and Rashba E I 1984 *J. Phys. C: Solid State Phys.* **17** 6039
[29] Woods L M, Reinecke T L and Kotlyar R 2004 *Phys. Rev.* B **69** 125330
[30] Lü C, Cheng J L and Wu M W 2005 *Phys. Rev.* B **71** 075308
[31] Climente J I, Segarra C and Planelles J 2013 *New J. Phys.* **15** 093009
[32] Wei H, Guo G-C and He L 2014 *J. Appl. Phys.* **116** 204304
[33] Schwartz I, Schmidgall E R, Gantz L, Cogan D, Bordo E, Don Y, Zielinski M and Gershoni D 2015 *Phys. Rev. X* **5** 011009
[34] Luttinger J M 1956 *Phys. Rev.* **102** 1030
[35] Planelles J and Climente J I 2013 *J. Phys.: Condens. Matter* **25** 485801
[36] Winkler R 2003 *Spin–Orbit Coupling Effects in Two-Dimensional Electron and Hole Systems* (Berlin: Springer)
[37] Bir G L and Pikus G E 1974 *Symmetry and Strain-Induced Effects in Semiconductors* (New York: Wiley)
[38] Uenoyama T and Sham L J 1990 *Phys. Rev.* B **42** 7114
[39] Vurgaftman I, Meyer J R and Ram-Mohan L R 2001 *J. Appl. Phys.* **89** 5815
[40] van Bree J, Silov A Y, Koenraad P M, Flatté M E and Pryor C E 2012 *Phys. Rev.* B **85** 165323
[41] Madelung O (ed) 1982 *Semiconductors. Physics of Group IV elements and III-V Compounds* (*Landolt-Börnstein* vol 17) (Berlin: Springer)
[42] Doty M F, Climente J I, Greilich A, Yakes M, Bracker A S and Gammon D 2010 *Phys. Rev.* B **81** 035308
[43] Stano P and Fabian J 2006 *Phys. Rev. Lett.* **96** 186602

JOURNAL OF APPLIED PHYSICS **119**, 125705 (2016)

Electrons, holes, and excitons in GaAs polytype quantum dots

Juan I. Climente, Carlos Segarra, Fernando Rajadell, and Josep Planelles[a)]
Departament de Química Física i Analítica, Universitat Jaume I, E-12080 Castelló, Spain

(Received 26 January 2016; accepted 20 March 2016; published online 31 March 2016)

Single and multi-band $k{\cdot}p$ Hamiltonians for GaAs crystal phase quantum dots are used to assess ongoing experimental activity on the role of such factors as quantum confinement, spontaneous polarization, valence band mixing, and exciton Coulomb interaction. Spontaneous polarization is found to be a dominating term. Together with the control of dot thickness [Vainorius *et al.*, Nano Lett. **15**, 2652 (2015)], it enables wide exciton wavelength and lifetime tunability. Several new phenomena are predicted for small diameter dots [Loitsch *et al.*, Adv. Mater. **27**, 2195 (2015)], including non-heavy hole ground state, strong hole spin admixture, and a type-II to type-I exciton transition, which can be used to improve the absorption strength and reduce the radiative lifetime of GaAs polytypes. [http://dx.doi.org/10.1063/1.4945112]

I. INTRODUCTION

Semiconductor quantum dots (QDs) have been widely studied since the 1990s because of their appealing electronic and photonic properties. However, standard fabrication methods involve a degree of dispersity which limits exact reproducibility within an ensemble of dots, from run-to-run and from lab-to-lab.[1–3] For example, in Stranski-Krastanov growth of InAs/GaAs QDs, the most widely employed technique to produce optically active III-V QDs, random diffusion of substrate material (GaAs) into the deposited material (InAs) leads to an ensemble of QDs with inhomogeneous composition, strain fields, and shapes.[3] This translates into an inhomogeneous distribution of energy levels, which poses a challenge for the scalability of many technological applications demonstrated at a single-dot level.[4,5]

Crystal phase (polytype) QDs[6] are likely to mitigate this problem. These structures exploit recent synthetic advances enabling control on the polytypical crystal structure of III-V nanowires, whereby one can grow alternating segments of wurtzite (WZ) grown along the [0001] direction and zinc-blende (ZB) grown along [111].[7] Because WZ and ZB phases have slightly different energy gaps at the Γ point, band offsets are formed and carriers confined in one of the phases.[8] One can then form QDs embedded in the wire, which turn out to have defect-free crystal structure, sharp interfaces, negligible strain and tapering, well defined shape, and homogeneous composition. Prospects have become especially promising with two studies published in the last months for GaAs polytype QDs. On the one hand, Vainorius *et al.* have reported exact control on the QD thickness, from bilayers to tens of nm.[9] On the other hand, Loitsch *et al.* have reported control of the wire diameter from typical values (∼100 nm) down to 7 nm.[10] Together, these studies pave the way towards full control of the QD confinement and, consequently, of the energy structure.

Progress in the synthesis of GaAs polytype QDs, however, has not been paralleled by theoretical understanding of the ensuing electronic and optoelectronic properties. As a result, several open questions remain which need to be clarified in order to eventually attain predictive design. To name a few: (i) the role of spontaneous polarization in WZ GaAs is not clear. The majority of experimental works simply neglect it,[8–12] but recent theoretical[13] and experimental[14] studies point to a value of $P_{sp} = 0.0023\,\mathrm{C/m^2}$, which Jahn *et al.* deemed influential at a single-particle level.[15] One then wonders if it is really important for Coulomb-bound excitons. (ii) The role of valence band (VB) coupling is also poorly understood. It is generally assumed that the hole ground state is a heavy hole (HH).[9–12] This is consistent with polarization measurements of large diameter nanowires.[16] However, radial confinement enhances valence band mixing.[17] Therefore, the validity should be tested at least in the small diameter regime enabled by the work of Loitsch *et al.*[10] (iii) The influence of electron-hole Coulomb interaction needs better assessment. Because WZ and ZB interfaces form a type-II band-alignment in GaAs,[8] previous simulations of optical transition energies in GaAs polytypes either tend to neglect it[9,15] or take it as a constant.[10] However, the band offsets are so small that both electron and hole wave functions are expected to penetrate into each other's phase, leading to non-vanishing electron-hole overlap.[12] What is more, strong Coulomb interactions could eventually overcome the band offsets and change the excitons from type-II to type-I. This is a possibility worth exploring.

In this work, we use a $k{\cdot}p$ model to study carriers confined in polytype QDs, which takes into account all the factors described above: spontaneous polarization, electron-hole Coulomb interaction, and valence band coupling of holes. The latter is included by building a 6-band Hamiltonian for ZB/WZ polytypes. We study polytype QDs within the confinement ranges made possible by the works of Vainorius[9] and Loitsch,[10] and evaluate the influence of the abovementioned factors on the energy structure of electrons, holes, and excitons. The results are discussed in view of the existing experiments.

II. $k{\cdot}p$ HAMILTONIANS FOR WZ/ZB QDs

In order to model polytypes, we use a $k{\cdot}p$ Hamiltonian spanned on the same Bloch functions in both crystal

a)josep.planelles@uji.es. URL: http://quimicaquantica.uji.es/

structures, the differences showing up in the parameters only. In this section, we describe such Hamiltonians for conduction band (CB) electrons, VB holes, and excitons.

A. Electrons

Low-energy electrons in ZB GaAs belong to the Γ_{6c} band, which is well separated from the valence band and the rest of CBs. This justifies the widely spread use of single-band models in the literature. In WZ GaAs, however, Γ_{8c} and Γ_{7c} bands are close to each other, and some band mixing can be expected.[18,19] Lacking effective mass parameters describing such a coupling, we model WZ electrons with a single-band Hamiltonian of hybrid character: Γ_{8c} masses but optically bright, like the Γ_{7c} band. This picture is consistent with the observations of different recent experiments[12,20,21] and suffices to assess the role of the physical factors we investigate. The polytype Hamiltonian then reads

$$H_e = -\frac{\hbar^2}{2}\sum_{i=x,y,z} k_i \frac{1}{m_i^*} k_i + V_c^{cb} + qV_{sp}. \tag{1}$$

Here, m_i^* is the effective mass along the i direction, which depends on the crystal phase, $k_i = -\nabla_i$, V_c^{cb} is the 3D confinement potential arising from the conduction band-offset potential between ZB and WZ phases, q is the electron charge, and V_{sp} is the electrostatic potential due to the spontaneous polarization P_{sp}.

The calculation of strain in polytype QDs deserves a short discussion. The initial strain in a heterostructure is given by the lattice mismatch. For a QD of a given material buried in a matrix of a different material with the same crystalline structure, it is zero in the matrix and $\epsilon_{ii}^0 = \frac{a_i^{(m)} - a_i^{(QD)}}{a_i^{(m)}}$ in the QD, where a_i^j is the lattice constant in the direction i for the medium j.[22] However, this expression cannot be employed in polytypes because QD and matrix have different crystalline structures. In our case, since we deal with ZB(111)/WZ(0001) interfaces, we may reason as follows. The ZB unit cell contains 9 anions and 9 cations, while the WZ unit cell has the same basis but different height and only 6 pairs of ions (see, e.g., Fig. 1 in Ref. 23). Then, three WZ unit cells contain the same number of ions as two ZB unit cells. If the ZB and WZ materials are the same (GaAs in or case) and under the assumption that the lattices are ideal, the basis surface of both unit cells is the same, and so is the height of three WZ unit cells vs. two ZB ones. Therefore, the strain is ideally zero. This is consistent with theoretical calculations[24] and experimental findings[9,10,24] pointing at negligible strain, as real lattice constants show but small deviations from ideal ones. One can then safely disregard it.

Since the strain is weak, so is the piezoelectric potential and its influence on the energy spectrum. By contrast, the spontaneous polarization potential V_{sp} can have a significant influence. There is no spontaneous polarization in the ZB phase for symmetry reasons, but it is present in WZ, where P_{sp} originates from the "eclipsed" dihedral conformation of layers N and $N+2$, yielding a non-ideal tetrahedral coordination and associated electric dipoles. Current estimates for GaAs are of $P_{sp} \approx 0.0023\,\mathrm{C\ m^{-2}}$,[13,14] about one order of magnitude weaker than in nitride materials. Since the change in P_{sp} is large at the ZB/WZ interface, it gives rise to an abrupt change in the built-in electric field, from zero in ZB up to an approximate constant value F in WZ given by $F = P_{sp}/\varepsilon$, with ε the dielectric constant, and back again to zero in ZB (see, e.g., Fig. 4 in Ref. 14). Then, the QD acts like a capacitor, with effective negative and positive charges accumulating at the ZB/WZ and WZ/ZB interfaces, and an almost linear potential in between (see, e.g., CB profile in the insets of Fig. 2).

B. Holes

1. Multi-band Hamiltonian

To study the effect of VB mixing, we use a multi-band k·p Hamiltonian. In order to compare [111]-grown ZB and [0001]-grown WZ structures systematically, we write the six-band Hamiltonian employing for both phases the same basis functions[23,25]

$$\begin{aligned}
|u_1\rangle &= -\frac{1}{\sqrt{2}}|(X+iY)\uparrow\rangle & |u_4\rangle &= \frac{1}{\sqrt{2}}|(X-iY)\downarrow\rangle \\
|u_2\rangle &= \frac{1}{\sqrt{2}}|(X-iY)\uparrow\rangle & |u_5\rangle &= -\frac{1}{\sqrt{2}}|(X+iY)\downarrow\rangle \\
|u_3\rangle &= |Z\uparrow\rangle & |u_6\rangle &= |Z\downarrow\rangle.
\end{aligned} \tag{2}$$

For [0001] WZ, the resulting Hamiltonian in this basis reads[26]

$$H_{6B} = \begin{bmatrix} F & -K^* & -H^* & 0 & 0 & 0 \\ -K & G & H & 0 & 0 & \sqrt{2}\Delta_3 \\ -H & H^* & \lambda & 0 & \sqrt{2}\Delta_3 & 0 \\ 0 & 0 & 0 & F & -K & H \\ 0 & 0 & \sqrt{2}\Delta_3 & -K^* & G & -H^* \\ 0 & \sqrt{2}\Delta_3 & 0 & H^* & -H & \lambda \end{bmatrix}, \tag{3}$$

where

$$\begin{aligned}
F &= \Delta_1 + \Delta_2 + \lambda + \theta, \\
G &= \Delta_1 - \Delta_2 + \lambda + \theta, \\
\lambda &= \frac{\hbar^2}{2m_e}\left[A_1 k_z^2 + A_2 k_\perp^2\right], \\
\theta &= \frac{\hbar^2}{2m_e}\left[A_3 k_z^2 + A_4 k_\perp^2\right], \\
K &= \frac{\hbar^2}{2m_e} A_5 k_+^2 + \Delta K, \\
H &= \frac{\hbar^2}{2m_e} A_6 k_+ k_z + \Delta H.
\end{aligned} \tag{4}$$

Here, m_e is the free electron mass, A_i is the effective mass parameters, $k_\perp = k_x^2 + k_y^2$, $k_\pm = k_x \pm ik_y$, Δ_1 is the crystal field splitting, Δ_2 and Δ_3 are the spin-orbit matrix elements, and $\Delta K = \Delta H = 0$.

For [111] ZB, according to Bir-Pikus,[27] the [001] ZB Hamiltonian—spanned on the basis of Eq. (2)—is first rotated 45° along the z axis, and then 54.7° along the new y'

axis. The resulting z' axis points along the [111] direction, while x' and y' do so along the $[11\bar{2}]$ and $[\bar{1}10]$ directions. The Hamiltonian obtained is formally identical to Eq. (3), but now

$$\Delta K = 2\sqrt{2}\,\frac{\hbar^2}{2m_e}\,A_z k_- k_z, \qquad \Delta H = \frac{\hbar^2}{2m_e}\,A_z k_-^2. \tag{5}$$

Additionally, the following relations emerge, which reduce the number of independent mass parameters to three, as expected for ZB:

$$\begin{aligned}
\Delta_1 &= 0,\\
\Delta_2 &= \Delta_3 = \Delta/3,\\
A_1 &= -\gamma_1 - 4\gamma_3,\\
A_2 &= -\gamma_1 + 2\gamma_3,\\
A_3 &= 6\gamma_3,\\
A_4 &= -3\gamma_3,\\
A_5 &= -\gamma_2 - 2\gamma_3,\\
A_6 &= -\sqrt{2}\,(2\gamma_2 + \gamma_3),\\
A_z &= \gamma_2 - \gamma_3,
\end{aligned} \tag{6}$$

where γ_1, γ_2, and γ_3 are the Luttinger mass parameters.

It is worth noting that H_{6B}—with ZB parameters, Eqs. (5) and (6)—actually shows all diagonal elements overstabilized by an amount $\Delta/3$. This is due to the term $\frac{1}{3}\Delta(\sigma \cdot \mathbf{J})$ in the sum of invariants defining H_{6B},[27] which is needed to yield the Hamiltonian extradiagonal elements H_{26}, H_{35}, H_{53}, and H_{62}. We recover the zero origin at the top of the HH band by subtracting $\Delta/3$ to all diagonal elements of H_{6B} in the ZB region.

The above considerations prompt us to obtain a Hamiltonian which is valid for both ZB and WZ regions, and hence open the possibility of dealing with polytypes. Since the parameters in the two phases are different, we should employ a variable mass Hamiltonian.[28–31] The use of bulk multiband Hamiltonian with different parameters in each phase leads to an abrupt change at the interface. The resulting matrix functions, though, must be considered to vary slowly on the scale of the lattice constant but rapidly on the scale of the envelope changes. Furthermore, the Hamiltonian must be modified to ensure Hermiticity. In the one-band model, this was overcome by the use of the Ben Daniel-Duke kinetic term.[32] The extension to multiband Hamiltonians was initially carried out by means the use of a symmetrization rule,[33] the operator ordering with respect to the band parameters reflecting the boundary conditions at the abrupt interface. We have checked that starting from a conventionally symmetrized [001] ZB Hamiltonian spanned on the above basis set, Eq. (2), and following the above-mentioned rotation prescription, we end up with symmetrized form of the [111] ZB Hamiltonian. All the same, an envelope function theory for nanostructures accounting for abrupt interfaces was later developed,[34–37] leading to a nonsymmetrized Hamiltonian.[38] Therefore, we implement here a nonsymmetrized or Burt-Foreman form of the Hamiltonian. Namely,

$$H_{6B}^{BF} = \begin{bmatrix} F-\rho & \kappa & \xi^* & 0 & 0 & 0\\ \kappa^* & G+\rho & -\xi & 0 & 0 & \sqrt{2}\Delta_3\\ \eta & -\eta^* & \lambda & 0 & \sqrt{2}\Delta_3 & 0\\ 0 & 0 & 0 & F+\rho & \kappa^* & -\xi\\ 0 & 0 & \sqrt{2}\Delta_3 & \kappa & G-\rho & \xi^*\\ 0 & \sqrt{2}\Delta_3 & 0 & -\eta^* & \eta & \lambda \end{bmatrix}, \tag{7}$$

where

$$\begin{aligned}
F &= \Delta_1 + \Delta_2 + \lambda + \theta,\\
G &= \Delta_1 - \Delta_2 + \lambda + \theta,\\
\lambda &= \frac{\hbar^2}{2m_e}[k_z A_1 k_z + k_x A_2 k_x + k_y A_2 k_y],\\
\theta &= \frac{\hbar^2}{2m_e}[k_z A_3 k_z + k_x A_4 k_x + k_y A_4 k_y],\\
\kappa &= \frac{\hbar^2}{2m_e}[-k_x A_5 k_x + k_y A_5 k_y + i(k_x A_5 k_y + k_y A_5 k_x)] + \Delta\kappa,\\
\eta &= \frac{\hbar^2}{2m_e}\left[-k_z A_6^{(+)} k_+ - k_+ A_6^{(-)} k_z\right] + \Delta\eta,\\
\xi &= \frac{\hbar^2}{2m_e}\left[-k_z A_6^{(-)} k_+ - k_+ A_6^{(+)} k_z\right] + \Delta\xi,\\
\rho &= \frac{\hbar^2}{2m_e}\left[ik_y\left(A_5^{(+)} - A_5^{(-)}\right)k_x - ik_x\left(A_5^{(+)} - A_5^{(-)}\right)k_y\right],\\
\Delta\xi &= \frac{\hbar^2}{2m_e}[-(k_x - ik_y)A_z(k_x - ik_y)],\\
\Delta\eta &= \Delta\xi,\\
\Delta\kappa &= -2\sqrt{2}\,\frac{\hbar^2}{2m_e}\left[(k_x + ik_y)\,A_z^{(+)}\,k_z + k_z\,A_z^{(-)}\,(k_x + ik_y)\right],
\end{aligned} \tag{8}$$

with $A_5 = A_5^{(+)} + A_5^{(-)}$, $A_6 = A_6^{(+)} + A_6^{(-)}$ and $A_z = A_z^{(+)} + A_z^{(-)}$. In the WZ region, $A_z^{(+)} = A_z^{(-)} = 0$. In the ZB region, Eqs. (6) still hold.

The practical hindrance for the use of this Hamiltonian, especially for studying polytypes, is the lack of available $A_i^{(\pm)}$ coefficients. At this regard, Veprek *et al*.[29] analyzed the spurious solution problem affecting the $k{\cdot}p$ envelope function method, which is related to the lack of ellipticity that the different sets of parameters confer to the Hamiltonian. They concluded by recommending the use of a complete asymmetric operator ordering ($A_i^{(+)} = A_i$, $A_i^{(-)} = 0$) for several ZB and WZ materials.[29,30,39] We have checked that this also applies to GaAs.

We are now in a condition to write the complete Hamiltonian for holes in polytype QDs

$$H_h^{6B} = H_{6B}^{BF} + \left(V_c^{vb} - qV_{sp} - \frac{\Delta}{3}Y_{ZB}\right)\mathbb{I}_{6\times 6}. \tag{9}$$

V_c^{vb} and V_{sp} are the confining and spontaneous polarization potentials, respectively, which we obtain as described for electrons. Y_{ZB} is a heaviside function, $Y_{ZB} = 0$ in the WZ phase and $Y_{ZB} = 1$ in the ZB one.

2. Single-band Hamiltonian

The use of single-band models for the hole ground state in GaAs polytypes is justified under certain conditions. In ZB, the degeneracy between heavy and light hole bands can be lifted by quantum confinement. In WZ, as can be seen in Eq. (3), the uppermost band (F) is split from the others (G, λ) by the spin-orbit (Δ_2) and crystal field (Δ_1) splittings, so degeneracy is lifted even at the Γ point. Thus, in order to get the single-band Hamiltonian, we decouple the diagonal elements corresponding to the F (heavy hole) band from the rest of the matrix in Eq. (9). This yields

$$H_h = \Delta_1 + \Delta_2 + \sum_{i=x,y,z} \frac{\hbar^2}{2} k_i \frac{1}{m_i^*} k_i + V_c^{vb} - qV_{sp} - \frac{\Delta}{3} Y_{ZB}, \tag{10}$$

where the parameters Δ_1, Δ_2, and m_i^* take different values in each crystal phase. In particular, for WZ, $m_z = 1/(A_1 + A_3)$ and $m_\perp = 1/(A_2 + A_4)$. For ZB, $m_z = -1/(\gamma_1 - 2\gamma_3)$ and $m_\perp = -1/(\gamma_1 + \gamma_3)$, $\Delta_1 = 0$, and $\Delta_2 = \Delta/3$.[40]

C. Excitons

We calculate neutral excitons using single-band Hamiltonians for both electron and hole

$$H_X = H_e + H_h + V_{eh}, \tag{11}$$

where V_{eh} is the electron-hole Coulomb interaction, which is obtained by integrating the Poisson equation in a dielectrically inhomogeneous environment.

D. System and parameters

We take ZB GaAs material parameters from Ref. 41. As for WZ GaAs, we take electron effective masses from Ref. 18, VB ones from Ref. 42, and the spontaneous polarization $P_{sp} = 0.0023\,\mathrm{C\,m^{-2}}$ from Ref. 13. Lacking more precise information for WZ, we use a dielectric constant $\varepsilon = 13.18$ for both phases.[43]

To define V_c^{cb} and V_c^{vb}, we consider either ZB QDs embedded in WZ nanowires, see Fig. 1(a), or WZ QDs embedded in ZB nanowires, see Fig. 1(b). The corresponding band offset values, represented in the figure, are taken from Ref. 8. The nanowires are assumed to be surrounded by an insulating material with $V_c^{cb} = -V_c^{vb} = 5\,\mathrm{eV}$ and $\varepsilon = 4$.

We use Comsol 4.2 to solve numerically the Hamiltonians described above. V_{sp} is obtained by calculating the polarization charge density $\rho = -\nabla \cdot P_{sp}$ and solving the Poisson equation, $\nabla \cdot [\varepsilon \nabla V] = \rho$. Next, Hamiltonians H_e, H_h^{6B}, and H_h are integrated using finite elements. As for H_X, converged interacting electron and hole states are obtained by using an iterative Schrödinger-Poisson scheme.

III. RESULTS

A. Electrons

We start by investigating the ground state of a single electron in a ZB QD, like that in Fig. 1(a). The QD is hexagonal, with a typical radius of the circumscribed circle, $R = 50\,\mathrm{nm}$, and variable thickness L. The results are plotted

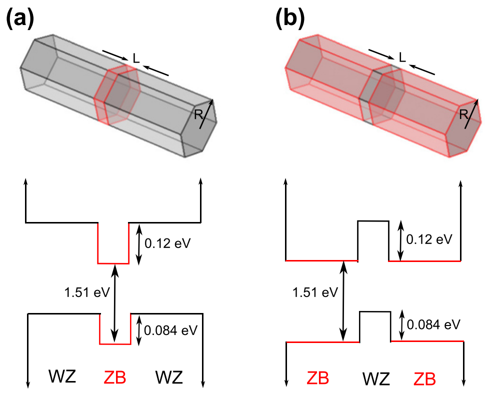

FIG. 1. (a) Sketch of ZB QD embedded in WZ wire and corresponding band-offset profile. (b) Same but for WZ QD embedded in ZB wire.

in Fig. 2, where we compare calculations with the expected spontaneous polarization of GaAs, $P_{sp} = 2.3 \times 10^{-3}\,\mathrm{C\,m^{-2}}$ (solid line), and calculations with an artificially weakened polarization, $P_{sp} = 2.3 \times 10^{-4}\,\mathrm{C\,m^{-2}}$ (dashed line). It is clear from the figure that, except for thin dots ($L < 5\,\mathrm{nm}$), P_{sp} plays a critical role in determining the electron energy. Under full polarization, the energy shows a linear dependence with L, determined by the capacitor-like built-in electric field. By contrast, under weakened polarization, the linear regime is preceded by a quadratic one (up to $L \lesssim 10\,\mathrm{nm}$), which is determined by quantum confinement. The magnitude of the energy stabilization is also very different. In fact, for $P_{sp} = 2.3 \times 10^{-3}\,\mathrm{C\,m^{-2}}$ and large L, the electric field leads to energies well below the CB bottom of bulk ZB.

These results are qualitatively similar to those obtained by Jahn and co-workers using a simpler 1D model with zinc-blende masses[15] and confirm that the spontaneous polarization in GaAs polytypes cannot be neglected, at least at a single particle level. As we shall see below, in Section III C, the same is true for excitons in spite of the electron-hole attraction.

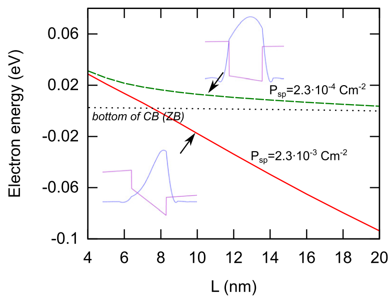

FIG. 2. Energy of the electron ground state in a ZB QD with realistic (solid line) and weakened (dashed line) spontaneous polarization, as a function of the dot thickness. Note the strong influence. The insets show the wave functions and band profiles for $L = 10\,\mathrm{nm}$.

The insets in Fig. 2 show the electron wave function and band profile for the full and weakened polarization values. Notice that P_{sp} pushes the electron towards the ZB/WZ interface and induces substantial spreading into the WZ phase.

The precise control of the thickness in GaAs polytype QD, recently achieved by Vainorius *et al.*,[9] suggests such structures could be used to build perfectly symmetric pairs of QDs. In principle, this could enable the formation of QD molecules with homonuclear character, unlike in self-assembled InAs/GaAs structures where the inherent structural asymmetries can only be overcome with external fields.[44] Symmetric molecules can be of interest for applications like optical qubits[45] or the development of superlattices with maximized coherent tunneling for solar cell devices.[46] However, the results of Fig. 2 suggest that the strong influence of P_{sp} can introduce significant asymmetries in the band profile of symmetric molecules. This is confirmed in Fig. 3, where one can see that for two identical ZB QDs separated by a thin WZ barrier, the electron wave function localizes mostly in one of the dots. This effect is already noticeable if the system has weakened P_{sp} (upper plot), and it becomes dramatic for full P_{sp} (lower plot), when tunneling is almost nearly suppressed.

B. Holes

The energetics of holes in WZ QDs is qualitatively similar to that of electrons in ZB dots. In this section, we focus on the role of VB mixing instead. In particular, we assess the validity of the usual assumption that the ground state has a well defined, single-band, HH character.[9–12]

The eigenfunctions of Hamiltonian H_h^{6B} are six-component spinors of the form: $\Psi_h^{6B} = \sum_{i=1}^{6} f_i(\mathbf{r})|u_i\rangle$, where $f_i(\mathbf{r})$ is the envelope function associated with the $|u_i\rangle$ Bloch function. The weight of an individual component is computed as $|f_i|^2$. As can be seen in Eq. (2), HH character corresponds to Bloch functions $|u_1\rangle$ (spin up) and $|u_4\rangle$ (spin down), i.e., the F band of Hamiltonian H_{6B}^{BF}. To disentangle spin up and down components, a small Zeeman-like term is included in Eq. (9), $\Delta_z = B\mu_B g \mathbb{J}_z$, where $B = 1\,\mathrm{T}$ is the longitudinal magnetic field, μ_B is the Bohr magneton, $g = 4/3$ is

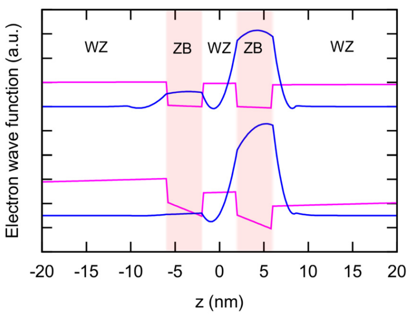

FIG. 3. Electron wave function and band profile in a ZB-WZ-ZB molecule with weakened and full P_{sp}. Both ZB QDs and the WZ barrier have thickness $L = 4\,\mathrm{nm}$.

the hole g-factor, and $\mathbb{J}_z$ is the angular momentum z-component diagonal matrix (with elements $\pm 3/2$, $\pm 1/2$).

We first estimate the total HH character from $(|f_1|^2 + |f_4|^2)$. Fig. 4(a) shows the normalized HH weight for the ground state of WZ QDs. The QDs structure is that of Fig. 1(b), with the radius R and thickness L varying within a parameter space enabled by state-of-the-art fabrication, which includes the regime of quantum confinement in the radial direction.[9,10] One can see that the ground state has almost exclusive HH character except for very thin radii, $R < 5\,\mathrm{nm}$. In this region, the ground state rapidly switches from mainly F band (HH) to mainly λ band character, as shown in Fig. 4(a) inset. The origin of the ground state change can be understood as follows. In the bulk limit, the F band of wurtzite is stabilized with respect to G and λ bands by the crystal field and spin-orbit splittings. However, the radial mass of F-band holes in WZ is $m_\perp^F = 1/(A_2 + A_4) = -0.13$, much lighter than that of λ-band holes, $m_\perp^\lambda = 1/A_2 = -0.617$. Therefore, with increasing radial confinement, the latter become more stable. It is worth noting that λ holes are very light in the [0001] direction, $m_z^\lambda = 1/A_1 = -0.05$. As a consequence, their kinetic energy exceeds the small band offset of the WZ/ZB interface, and the wave function tends to localize outside the QD, as shown in Fig. 4(b). This result is a consequence of the radial confinement, and it is also found when the spontaneous polarization is neglected (not shown).

The change of ground state character we report here should be observable in the narrowest wires synthesized by Loitsch *et al.*[10,11] Since the symmetry of the λ band Bloch functions ($|u_3\rangle$ and $|u_6\rangle$ in Eq. (2)) is different from that of HHs, it should be seen in experiments as a change in the polarization of interband optical transitions.

Next, we analyze the HH spin admixture by representing the ratio between the weight of spin up and down HH, $|f_1|^2/|f_4|^2$. This is done for QDs in the presence and absence of P_{sp}, Figs. 4(c) and 4(d), respectively. A remarkable observation is that moderate radial or vertical confinement leads to significant spin mixing between the Zeeman split levels. This is because the off-diagonal elements of Hamiltonian (7) scale with $k_\perp$ and k_z. Note that, in the presence of P_{sp}, the spin mixing takes place even for large L, because the vertical electrostatic confinement does not vanish with the dot thickness. Interestingly, the confinement leads to admixture between spin up and down F-band holes but coupling with G and λ bands remains negligible (recall Fig. 4(a) inset).

The spin mixing of HHs has influence on the magnetic properties of WZ/ZB QDs. For example, the values of the effective g-factors are often determined as $g = (E_+(B) - E_-(B))/\mu_B B$, where $E_\pm(B)$ is the energy of opposite spin projections under a magnetic field B. We have calculated the g factor at $B = 1\,\mathrm{T}$ switching on and off the spin-orbit term Δ in Hamiltonian (7). This leads to g factors with enabled (g^{so}) and suppressed (g^0) spin mixing. In Fig. 5, we plot the ratio g^{so}/g^0 in two instances: QDs with (a) and without (b) spontaneous polarization. One can see that for strong confinement, band mixing can enhance g factor values up to a factor of 2–3. Unlike in other QD systems, where the confinement symmetry plays a critical role in determining the spin admixture strength,[47] the mixing in polytypes is robust against

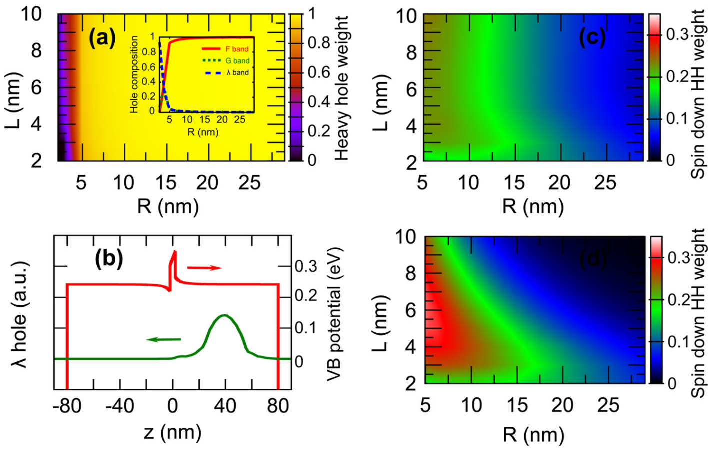

FIG. 4. (a) Weight of the HH (F band) component in the hole ground state, $(|f_1|^2+|f_4|^2)/\sum|f_i|^2$, as a function of dot radius and thickness in a WZ QD. The inset shows the weight of each subband for $L=4$ nm. The ground state changes from F band (HH) to λ band for radii under 5 nm. (b) Confining potential (red) and λ hole envelope wave function (green) along the z axis for a QD with $L=4$ nm and $R=2.5$ nm. The λ hole is not confined owing to its small mass. (c) and (d) Weight of spin down HH component, $|f_4|^2/\sum|f_i|^2$, with and without P_{sp}, respectively.

symmetry changes, as similar numbers are obtained if one replaces hexagonal wires by triangular[48] (Figs. 5(c) and 5(d)) or cylindrical (Figs. 5(e) and 5(f)) ones.

Recent experiments with GaAs polytype QDs revealed strong dispersion of the measured excitonic g-factors depending on the confinement strength.[12] As Fig. 5 shows, due to the VB mixing, the hole g-factor value can fluctuate substantially for different QD dimensions. This may partially explain the experimental observation.

One concludes from this section that the HH description of the ground state is valid except for small diameter wires, when a λ-band ground state is formed. However, in the presence of magnetic fields, one should be aware that VB mixing can strongly couple spin up and down HH states. We stress that such a spin mixing is mediated by excited (light-hole like) G and λ states, although they barely couple to the ground state themselves. In fact, as we show in the Appendix, the mixing cannot be described with effective two-band Hamiltonians. It is an intrinsic many-band coupling effect.

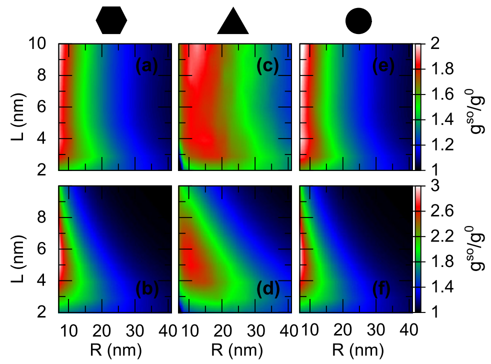

FIG. 5. Ratio of hole g-factors calculated with and without VB mixing, g^{so}/g^0. (a) and (b) Hexagonal QDs in the presence and absence of P_{sp}, respectively. (c) and (d) Same but for triangular QDs. (e) and (f) Same but for cylindrical QDs. For the sake of comparison, the nominal radius refers to the circumscribed circle of the triangle. For hexagons and cylinders, the actual radius is scaled so as to preserve the same area as the triangle.

C. Excitons

In what follows, we investigate the influence of confinement and spontaneous polarization on the properties of the ground state exciton. In order to compare with available experiments, we restrict to radii $R\geq 5$ nm, where the single-band HH description is valid. The exciton state is thus calculated with Eq. (11), which fully accounts for electron-hole Coulomb interaction.

Figure 6 shows the exciton energy in WZ QDs embedded in ZB wires, panels (a) and (b), and ZB QDs embedded in WZ wires, panels (d) and (e). The left column corresponds to full spontaneous polarization, $P_{sp}=2.3\times10^{-3}$ C m^{-2}, and the right one to artificially weakened polarization, $P_{sp}=2.3\times10^{-4}$ C m^{-2}.[49] One can see that for the realistic value of P_{sp}, the exciton energy has a very strong dependence on both the QD radius and thickness. The wavelength tunability is actually remarkable, as the energy can be tuned by over 700 meV, well above and below the bulk band gap (1.51 eV), from 1.65 eV (visible) to 1.0 eV (near infrared). For weak P_{sp}, instead, the tunability is reduced. Radial quantum confinement still plays a role, enabling exciton emission up to 1.65 eV for the narrowest wires. By contrast, the influence of the dot thickness is largely suppressed, as in the single-particle case we saw in Fig. 2. Consequently, the lowerbound exciton emission is only 1.41 eV, roughly the indirect band gap between the bottom of the ZB CB and the top of the WZ VB, see Fig. 1, which is the smallest possible energy allowed by quantum confinement alone.

It is worth noting that for large thicknesses, the electron-hole overlap decreases. This effect is especially pronounced in the presence of full P_{sp}, as shown in Figs. 6(c) and 6(f), where it can be seen that the exciton electron and hole wave functions localize at opposite interfaces. For this reason, the exciton becomes gradually dark, and optical experiments may not be able to observe low energy states.

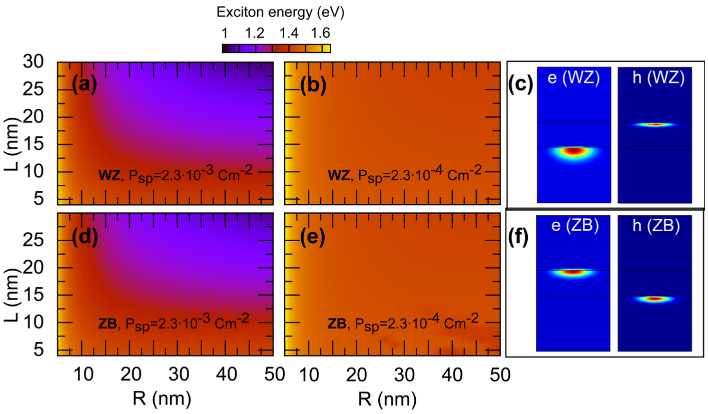

FIG. 6. Exciton energy as a function of radius and thickness in WZ QDs with full P_{sp} (a) or weakened P_{sp} (b). (c) Excitonic electron and hole wave functions for a WZ QD with $(R, L) = (50, 30)$ nm and full P_{sp}. (d)–(f) Same but for ZB QDs.

To better compare the optical properties of WZ QDs and ZB QDs, in Fig. 7, we plot the exciton energy as a function of the dot thickness. Two representative cases are considered. In Fig. 7(a), we study typical QDs, with large radius, $R = 50$ nm and full P_{sp}. In this case, the thickness dependence is linear for both WZ and ZB, owing to the large built-in electric field coming from P_{sp}, as already noted for electrons in Fig. 2. It follows that the spontaneous polarization prevails over Coulomb interactions in GaAs polytypes. This validates similar theoretical predictions obtained for ZB QDs at a single-particle level,[15] which here we extend to WZ QDs. Besides, we find that excitons in WZ QDs (green line) have lower energy than those in ZB QDs (red line), regardless of L. This is due to the smaller kinetic energy of the confined carrier, as for holes in WZ $m_z = 0.89$, while for electrons in ZB $m_z = 0.067$. For the same reason, holes leak out of the QD to a lesser extent than electrons. Consequently, the electron-hole overlap—proportional to the size of dots in Fig. 7—is also weaker for WZ QDs.

Interestingly, the behavior described above changes drastically when one switches to QDs with strong radial confinement. This can be seen in Fig. 7(b), which corresponds to QDs with $R = 5$ nm. First, the thickness dependence becomes quadratic in spite of P_{sp}. This is because the radial confinement provides enough energy for the carriers to escape from the electrostatic potential wells. The resulting wave functions are no longer localized near the WZ/ZB interface, but rather all over the QD, see Fig. 7(c). Hence, they become sensitive to the quantum confinement in the growth direction. Second, ZB becomes the lowest emitting structure for thin dots ($L < 15$ nm). The origin of this inversion can be inferred from Fig. 7(c) as well. The electron in the ZB QD can compensate for the strong radial confinement by penetrating into the WZ region, but the hole in the WZ QD cannot. This is again due to the relative masses m_z of the confined carrier. Third, the electron-hole overlap is enhanced with respect to that of large diameter QDs, for both WZ and ZB (compare the size of the circles in Figs. 7(a) and 7(b)). This is also connected with the confined carrier delocalizing all over the QD and penetrating into the wire crystal phase, which reduces the separation from the outer carrier. In other words, the radial confinement induces a gradual transition

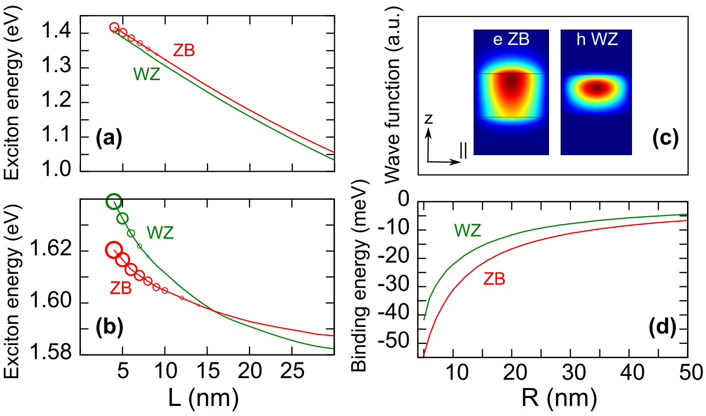

FIG. 7. (a) Exciton energy vs thickness in WZ (green) and ZB (red) QDs with $R = 50$ nm. (b) Same but with $R = 5$ nm. Note the qualitative change in behavior between the two radii. The size of the circles is proportional to the electron-hole envelope function overlap. (c) Wave function of exciton's electron in a ZB QD (left) and hole in a WZ QD (right), both with $(R, L) = (5, 5)$ nm. (d) Exciton Coulomb energy vs QD radius, with $L = 4$ nm.

from the usual type-II behavior of GaAs polytype QDs to a type-I one. One then concludes that reverse reaction growth[10] can be used for structural designs which improve the absorption strength and reduce the radiative lifetime of GaAs polytypes, as previously proposed for other (spontaneous polarization free) materials.[50]

We note that the type-II to type-I transition is partially stimulated by Coulomb interaction. As shown in Fig. 7(d), the exciton binding energy scales up with radial confinement. For small radii, it reaches several tens of meV, the same order of magnitude as the ZB/WZ band offsets. As a result, it helps bring electron and hole closer together in the growth direction.

Before closing this section, we briefly discuss the relation of the results in Fig. 7 with those of available experiments. Vainorius and co-workers recently measured the pholuminescence of WZ and ZB QDs with variable thickness and large radii, $R \approx 45$–$60\,\mathrm{nm}$.[9] They found that WZ emission is redshifted with respect to ZB one by a few tens of meV, in agreement with our Fig. 7(a). However, in their experiments, the emission energy was less sensitive to L. From $L = 5\,\mathrm{nm}$ to $30\,\mathrm{nm}$, the exciton emission in ZB QDs redshifted by about 60 meV, one order of magnitude less than we predict. They noted that a similar redshift could be obtained in theory if one considers quantum confinement only. We have confirmed this with our model, by considering excitons under weakened polarization (not shown).[51] The question then arises of whether the experimental system had, for some reason, suppressed spontaneous polarization at the ZB/WZ GaAs interface. Lacking more precise information about the system, at present we can only speculate for possible reasons. In some InAs polytypes, interface charges originating in spontaneous polarization were found to be concealed by dopant carriers.[52] Even in undoped wires, unintentional doping or migrating surface charges may play such a role.[53] Certainly, GaAs has a wider band gap and stronger spontaneous polarization than InAs[13] but, having uncapped wires, the authors of Ref. 9 mentioned that surface charges were possibly present in their samples, inducing fluctuations of tens of meV among QDs of the same thickness but different diameter. Therefore, dopant compensation of P_{sp} charges may be taking place. New experiments with capped GaAs/AlGaAs wires could study the linear or quadratic dependence on L to confirm the presence of spontaneous polarization. An alternative explanation could be related to the emission brightness. In the presence of full P_{sp}, we expect the ground state electron-hole overlap to decrease with L, see Fig. 7(a). For thick QDs, the overlap is so small that the ground state should be optically dark. If this is the case in Ref. 9, the measured photoluminescence may be arising not from the ground state but from higher energy exciton states, whose brightness is increasingly larger. This would be consistent with the fact that the experiments did not observe any systematic effect of the QD thickness on the photoluminescence intensity,[54] even though one would expect fading intensity as the ground state becomes darker. At this regard, we note that, even for weakened $P_{sp} = 2.3 \times 10^{-4}\,\mathrm{C\ m}^{-2}$, when the calculated redshift is similar to the experimental one, we find an order of magnitude decrease in the ground state electron-hole overlap with L, which should be visible experimentally.

As for the radius dependence, the experiments of Loitsch *et al.*[10,11] reported exciton emission up to 1.610 eV for WZ QDs with $R \approx 6.5\,\mathrm{nm}$ and random thickness, which is blueshifted by 100 meV with respect to bulk GaAs. According to our estimates in Fig. 7(b), for thin dots, one could reach even stronger blueshifts. In addition, the experiments measured excitonic lifetimes ranging between 0.5 and 0.8 ns, roughly one order of magnitude shorter than the values observed in large radius QDs (3–8 ns).[8] This was taken as being indicative of a type-II to type-I transition, which is actually consistent with our prediction for increasing radial confinement. For a more quantitative comparison, we consider that the exciton lifetime (τ) relates to the electron-hole overlap S_{eh} as $\tau \propto 1/S_{eh}^2$. We take a WZ QD with $R = 7\,\mathrm{nm}$ and another with $R = 50\,\mathrm{nm}$. As can be seen in Fig. 7, the overlap is sensitive to the exact dot thickness L. Experimentally, we only know that in Refs. 10 and 11 L takes unknown values from the twin plane limit up to $\sim 10\,\mathrm{nm}$.[55] Assuming an average $L = 5\,\mathrm{nm}$, the calculated exciton lifetime is 3.5 times shorter in the $R = 7\,\mathrm{nm}$ QD. The ratio increases to 30 if one considers $R = 5\,\mathrm{nm}$ instead, because the stronger radial confinement further promotes the type-I behavior. It also increases to 10 assuming QDs with $L = 10\,\mathrm{nm}$, because the spontaneous polarization enhances the type-II character, especially in the QD with weak radial confinement. All these values are close to the experimental range.

New experiments systematically comparing ZB and WZ dots with small diameter would be useful to confirm the other new phenomena we predict in this regime, namely, the change of the VB forming the hole ground state under $R = 5\,\mathrm{nm}$ (λ band), and the fact that ZB QDs emit at lower energies than WZ ones for short L.

IV. CONCLUSION

We have developed a k·p model to investigate WZ/ZB polytype QDs, including 3D confinement, spontaneous polarization effects, VB coupling through a Burt-Foreman six-band Hamiltonian, and electron-hole Coulomb interaction for excitons. When applied to GaAs QDs, we find a number of relevant observations:

(i) Contrary to what is often assumed, the spontaneous polarization in GaAs is not negligible; it should dominate the electronic structure for QDs with thickness above $\sim 5\,\mathrm{nm}$.

(ii) The hole ground state has nearly pure HH character except for the narrowest wires, $R < 5\,\mathrm{nm}$, when it switches to λ band.

(iii) When subject to a magnetic field, the HH ground states experience a strong spin mixing, mediated by excited valence bands.

(iv) The strong radial confinement brings about a transition from indirect (type-II) to direct (type-I) excitons and partially masks spontaneous polarization effects. Besides, ZB QDs start emitting at lower energies than WZ QDs.

Further experiments are called for to confirm the above points, which should help improve current understanding of the behavior and opportunities of these promising structures.

ACKNOWLEDGMENTS

We are grateful to P. Caroff, M. E. Pistol, and B. Loitsch for useful discussions. Support from UJI Project No. P1-1B2014-24, MINECO Project No. CTQ2014-60178-P, and a FPU grant (C.S.) is acknowledged.

APPENDIX: THE EFFECTIVE HAMILTONIAN

The spin mixing observed in Section II B basically involves the energetically close HH up $|u_1\rangle$ and down $|u_4\rangle$ states. It originates from the spin-orbit interaction term $\Delta_{so} = \sqrt{2}\Delta_3$, as no mixing occurs if we set $\Delta_{so} = 0$, due to the resulting block form of Hamiltonian (3), thus preventing the interaction between spin up and spin down states. Also, it is the result of a complex multiband interaction that cannot be reduced to an effective two band model. We can show it by reordering and splitting the basis vectors as follows, $\{\{|u_1\rangle, |u_4\rangle\}, \{|u_2\rangle, |u_3\rangle, |u_5\rangle, |u_6\rangle\}\}$, that turns the Hamiltonian (3) into:

$$\left[\begin{array}{cc|cccc} F & 0 & -K^* & -H^* & 0 & 0 \\ 0 & F' & 0 & 0 & -K & H \\ \hline -K & 0 & G & H & 0 & \Delta_{so} \\ -H & 0 & H^* & \lambda & \Delta_{so} & 0 \\ 0 & -K^* & 0 & \Delta_{so} & G' & -H^* \\ 0 & H^* & \Delta_{so} & 0 & -H & \lambda' \end{array}\right] \equiv \left[\begin{array}{c|c} H^{AA} & H^{AB} \\ \hline H^{BA} & H^{BB} \end{array}\right], \tag{A1}$$

where $X = F, G, \lambda$ differs from X' in a small $\kappa\mu_B B \mathbb{J}_z$ Zeeman term.

The 2×2 effective Hamiltonian $H^{eff} = H^{AA} + H^{AB}(I^{BB}E - H^{BB})^{-1}H^{BA}$, with I^{BB} the 4×4 identity matrix, is usually approximated by setting $(H^{BB})_{ij} \approx E_i^{BB}\delta_{ij}$ that allows an straightforward calculation of the inverse involved in the effective Hamiltonian, so that

$$(H^{eff})_{ij} = (H^{AA})_{ij} - \sum_{k\in B} \frac{H_{ik}^{AB} H_{kj}^{BA}}{E_k^{BB} - E}. \tag{A2}$$

However, the particular form of H^{AB} and H^{BA} leads to zero extradiagonal elements for this approximate effective Hamiltonian.

A more elaborate, but still simple, approximate effective Hamiltonian is obtained by setting $H \approx 0$, $G \approx G'$, and $\lambda \approx \lambda'$ in H^{BB}, thus yielding a twofold (cross-like) diagonal matrix. Its inverse $M = (I^{BB}E - H^{BB})^{-1}$ is still a twofold cross-like diagonal matrix, and the product $H^{AB}MH^{BA}$ is diagonal again.

Similar results are obtained by employing the Lowdin perturbation theory to account for the action of $\{|u_2\rangle, |u_3\rangle, |u_5\rangle, |u_6\rangle\}$ on the Hamiltonian expanded in the $\{|u_1\rangle, |u_4\rangle\}$ basis set.

A multi-band Hamiltonian is needed to enable strong interaction between two states corresponding to the basis i and j despite $H_{ij} = 0$. One of the simpler Hamiltonians illustrating this point would involve the basis set $\{|u_1\rangle, |u_2\rangle, |u_3\rangle\}$

$$\begin{bmatrix} F & 0 & \Delta_1 \\ 0 & F' & \Delta_2 \\ \Delta_1 & \delta_2 & X \end{bmatrix}. \tag{A3}$$

$|u_1\rangle - |u_3\rangle$ mixing occurs at first order, $c_{13}^{(1)} = \frac{H_{31}}{\Delta E_{13}}$, while $|u_1\rangle - |u_2\rangle$ interaction holds at second order, $c_{12}^{(2)} = \frac{H_{23}H_{31}}{\Delta E_{12}\Delta E_{13}} = c_{13}^{(1)}\frac{H_{23}}{\Delta E_{12}} = \frac{\Delta_2}{F-F'}$. However, for a small Zeeman splitting, $|F - F'| \ll \Delta_2$. Then, $c_{13}^{(1)} \ll c_{12}^{(2)}$.

[1]D. M. Talapin and Y. Yin, J. Mater. Chem. **21**, 11454 (2011).
[2]W. J. Baumgardner, Z. Quan, J. Fang, and T. Hanrath, Nanoscale **4**, 3625 (2012).
[3]J. J. Finley, M. Sabathil, P. Vogl, G. Abstreiter, R. Oulton, A. I. Tartakovskii, D. J. Mowbray, M. S. Skolnick, S. L. Liew, A. G. Cullis, and M. Hopkinson, Phys. Rev. B **70**, 201308(R) (2004).
[4]S. E. Economou, J. I. Climente, A. Badolato, A. S. Bracker, D. Gammon, and M. F. Doty, Phys. Rev. B **86**, 085319 (2012).
[5]H. Kim, S. M. Thon, P. M. Petroff, and D. Bouwmeester, Appl. Phys. Lett. **95**, 243107 (2009).
[6]N. Akopian, G. Patriarche, L. Liu, J.-C. Harmand, and V. Zwiller, Nano Lett. **10**, 1198 (2010).
[7]P. Caroff, J. Bolinsson, and J. Johansson, IEEE J. Sel. Top. Quantum Electron. **17**, 829 (2011).
[8]D. Spirkoska, J. Arbiol, A. Gustafsson, S. Conesa-Boj, F. Glas, I. Zardo, M. Heigoldt, M. H. Gass, A. L. Bleloch, S. Estrade, M. Kaniber, J. Rossler, F. Peiro, J. R. Morante, G. Abstreiter, L. Samuelson, and A. Fontcuberta i Morral, Phys. Rev. B **80**, 245325 (2009).
[9]N. Vainorius, S. Lehmann, D. Jacobsson, L. Samuelson, K. A. Dick, and M.-E. Pistol, Nano Lett. **15**, 2652 (2015).
[10]B. Loitsch, D. Rudolph, S. Morkötter, M. Döblinger, G. Grimaldi, L. Hanschke, S. Matich, E. Parzinger, U. Wurstbauer, G. Abstreiter, J. J. Finley, and G. Kolbmüller, Adv. Mater. **27**, 2195 (2015).
[11]B. Loitsch, J. Winnerl, G. Grimaldi, J. Wierzbowski, D. Rudolph, S. Morkötter, M. Döblinger, G. Abstreiter, G. Kolbmüller, and J. J. Finley, Nano Lett. **15**, 7544 (2015).
[12]P. Corfdir, B. V. Hattem, E. Uccelli, S. Conesa-Boj, P. Lefebvre, A. Fontcuberta i Morral, and R. T. Phillips, Nano Lett. **13**, 5303 (2013).
[13]A. Belabbes, J. Furthmüller, and F. Bechstedt, Phys. Rev. B **87**, 035305 (2013).
[14]B. Bauer, J. Hubmann, M. Lohr, E. Reiger, D. Bougeard, and J. Zweckb, Appl. Phys. Lett. **104**, 211902 (2014).
[15]U. Jahn, J. Lähnemann, C. Pfüller, O. Brandt, S. Breuer, B. Jenichen, M. Ramsteiner, L. Geelhaar, and H. Riechert, Phys. Rev. B **85**, 045323 (2012).
[16]D. Spirkoska, Al. L. Efros, W. R. L. Lambrecht, T. Cheiwchanchamnangij, A. Fontcuberta i Morral, and G. Abstreiter, Phys. Rev. B **85**, 045309 (2012).
[17]Al. L. Efros and W. R. L. Lambrecht, Phys. Rev. B **89**, 035304 (2014).
[18]A. De and C. E. Pryor, Phys. Rev. B **81**, 155210 (2010).
[19]F. Bechstedt and A. Belabbes, J. Phys.: Condens. Matter **25**, 273201 (2013).
[20]G. Signorello, E. Lörtscher, P. A. Khomyakov, S. Karg, D. L. Dheeraj, B. Gotsmann, H. Weman, and H. Riel, Nat. Commun. **5**, 3655 (2014).
[21]A. M. Graham, P. Corfdir, M. Heiss, S. Conesa-Boj, E. Uccelli, A. Fontcuberta i Morral, and R. T. Phillips, Phys. Rev. B **87**, 125304 (2013).
[22]F. Rajadell, M. Royo, and J. Planelles, J. Appl. Phys. **111**, 014303 (2012) (see supplementary material).
[23]P. E. Faria Junior and G. M. Sipahi, J. Appl. Phys. **112**, 103716 (2012).
[24]J. Lähnemann, O. Brandt, U. Jahn, C. Pfüller, C. Roder, P. Dogan, F. Grosse, A. Belabbes, F. Bechstedt, A. Trampert, and L. Geelhaar, Phys. Rev. B **86**, 081302(R) (2012).
[25]S.-H. Park and S.-L. Chuang, J. Appl. Phys. **87**, 353 (2000).
[26]S. L. Chuang and C. S. Chang, Phys. Rev. B **54**, 2491 (1996).
[27]G. L. Bir and G. E. Pikus, *Symmetry and Strain-Induced Effects in Semiconductors* (Wiley, New York, 1974).
[28]F. Mireles and S. Ulloa, Phys. Rev. B **62**, 2562 (2000).
[29]R. G. Veprek, S. Steiger, and B. Witzigmann, Phys. Rev. B **76**, 165320 (2007).

[30]R. G. Veprek, S. Steiger, and B. Witzigmann, Opt. Quantum Electron. **40**, 1169 (2008).
[31]M. F. Schubert, Phys. Rev. B **81**, 035303 (2010).
[32]D. J. Ben Daniel and C. B. Duke, Phys. Rev. **152**, 683 (1966).
[33]R. Eppenga, M. F. H. Schuurmans, and S. Colak, Phys. Rev. B **36**, 1554 (1987).
[34]M. G. Burt, J. Phys.: Condens. Matter **4**, 6651 (1992); **11**, 53 (1999).
[35]B. A. Foreman, Phys. Rev. Lett. **80**, 3823 (1998); Phys. Rev. B **48**, 4964(R) (1993); **56**, R12748 (1997).
[36]P. N. Stavrinou and R. van Dalen, Phys. Rev. B **55**, 15456 (1997).
[37]E. P. Pokatilov, V. A. Fonoberov, V. M. Fomin, and J. T. Devreese, Phys. Rev. B **64**, 245328 (2001).
[38]Further research has been developed to improve the asymmetric or Burt-Foreman Hamiltonian, which brought about additional interface terms, see e.g. B. A. Foreman, Phys. Rev. B **72**, 165345 (2005); J. Phys.: Condens. Matter **18**, 1335 (2006); Phys. Rev. B **75**, 235331 (2007). In Hamiltonian (7), we disregard them. In fact, we have checked that even using a symmetrized Hamiltonian the band coupling we observe is qualitatively consistent with that of Fig. 4.
[39]X. Zhou, F. Bertazzi, M. Goano, G. Ghione, and E. Bellotti, J. Appl. Phys. **116**, 033709 (2014).
[40]One could improve H_h, Eq. (10) by including the influence of decoupled bands on the HH effective mass. This can be done, e.g., by fitting independently the WZ and ZB one-band mass parameters from a series of 6-band vs. one-band calculations. For the QDs we simulate, we have checked this leads to minor corrections. Since our study is of qualitative character, we have disregarded them.
[41]I. Vurgaftman, J. R. Meyer, and L. R. Ram-Mohan, J. Appl. Phys. **89**, 5815 (2001).
[42]T. Cheiwchanchamnangij and W. R. L. Lambrecht, Phys. Rev. B **84**, 035203 (2011).
[43]S. Adachi, J. Appl. Phys. **58**, R1 (1985).
[44]A. S. Bracker, M. Scheibner, M. F. Doty, E. A. Stinaff, I. V. Ponomarev, J. C. Kim, L. J. Whitman, T. L. Reinecke, and D. Gammon, Appl. Phys. Lett. **89**, 233110 (2006).
[45]M. Bayer, P. Hawrylak, K. Hinzer, S. Fafard, M. Korkusinski, Z. R. Wasilewski, O. Stern, and A. Forchel, Science **291**, 451 (2001).
[46]S. Tomic, T. S. Jones, and N. M. Harrison, Appl. Phys. Lett. **93**, 263105 (2008).
[47]J. Planelles, F. Rajadell, and J. I. Climente, Phys. Rev. B **92**, 041302(R) (2015).
[48]J. Zou, M. Paladugu, H. Wang, G. J. Auchterloine, Y.-N. Guo, Y. Kim, Q. Gao, H. J. Joyce, H. H. Tan, and C. Jagadish, Small **3**, 389 (2007).
[49]Using weakened P_{sp} instead of null P_{sp} allows us to calculate single particle states confined in the wire phase, which form near the WZ/ZB interface. These states would otherwise spread all over the wire and form a poor starting point for the exciton self-consistent calculation.
[50]L. Zhang, J.-W. Luo, A. Zunger, N. Akopian, V. Zwiller, and J.-C. Harmand, Nano Lett. **10**, 4055 (2010).
[51]Unlike the calculations of Ref. 9, we consider Coulomb interaction and different masses for each crystal phase.
[52]C. Thelander, P. Caroff, S. Plissard, A. W. Dey, and K. Dick, Nano Lett. **11**, 2424 (2011).
[53]M. Hjort, S. Lehmann, J. Knutsson, A. A. Zakharov, Y. A. Du, S. Sakong, R. Timm, G. Nylund, E. Lundgren, P. Kratzer, K. A. Dick, and A. Mikkelsen, ACS Nano **8**, 12346 (2014).
[54]M. E. Pistol, private communication (2015).
[55]B. Loitsch, private communication (2015).

The Journal of Physical Chemistry Letters

Letter

pubs.acs.org/JPCL

Piezoelectric Control of the Exciton Wave Function in Colloidal CdSe/CdS Nanocrystals

Carlos Segarra,[†] Juan I. Climente,[†] Anatolii Polovitsyn,[‡] Fernando Rajadell,[†] Iwan Moreels,[‡] and Josep Planelles*[,†]

[†]Departament de Química Física i Analítica, Universitat Jaume I, E-12080 Castelló de la Plana, Spain

[‡]Istituto Italiano di Tecnologia, Via Morego 30, IT-16163 Genova, Italy

Supporting Information

ABSTRACT: Using multiband $k \cdot p$ calculations, we show that strain-engineered piezoelectricity is a powerful tool to modulate the electron−hole spatial separation in a wide class of wurtzite CdSe/CdS nanocrystals. The inherent anisotropy of the hexagonal crystal structure leads to anisotropic strain and, consequently, to a pronounced piezoelectric field along the *c* axis, which can be amplified or quenched through a proper design of the core−shell structure. The use of large cores and thick shells promotes a gradual departure from quantum confined nanocrystals to a regime dominated by piezoelectric confinement. This allows excitons to evolve from the usual type-I and quasi-type-II behavior to a type-II behavior in dot-in-dots, dot-in-rods, rod-in-rods, and dot-in-plates. Piezoelectric fields explain experimental observations for giant-shell nanocrystals, whose time-resolved photoluminescence reveals long exciton lifetimes for large cores, contrary to the expectations of standard quantum confinement models. They also explain the large differences in exciton lifetimes reported for different classes of CdSe/CdS nanocrystals.

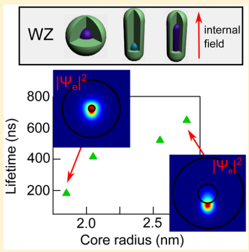

The spatial separation between electrons and holes in colloidal semiconductor nanocrystals (NCs) is a critical parameter that impacts the exciton emission lifetime,[1] Auger recombination rate,[2−4] electron−hole exchange interaction,[5] charge separation time,[6] and other properties of interest for optoelectronic devices such as LEDs, lasers, photovoltaic cells, or photocatalysts.[7] Control of the electron−hole separation is usually achieved by means of band gap engineering in core/shell hetero-NCs. An additional control mechanism was proposed for CdTe/ZnSe NCs, which exploited the epitaxial strain arising from the large lattice mismatch between the two materials (13.4%).[8] The growth of a thick compressive shell around the core shifts the core band edges via the deformation potential, leading to a gradual transition from (unstrained) type-I band alignment to a (fully strained) type-II one. Subsequently, the influence of strain on the band structure and electron−hole wave functions was investigated in other core/shell structures including CdSe/CdTe (6.7% lattice mismatch),[6,9] ZnSe/ZnTe (7%),[10,11] and CdS/ZnS (7%).[12−14]

In materials with a smaller lattice mismatch, strain-driven localization of carriers is less efficient, as the band edges are shifted only moderately. This is unfortunate because weakly strained NCs are less prone to interfacial defects and, hence, are preferred for their higher photoluminescence quantum yields.[15] This is the case of CdSe/CdS NCs,[16] (4.4% for zinc-blende (ZB), 4% and 3.8% along the *a* and *c* axes in wurtzite (WZ)), which are structures of particular interest owing to their monodispersity, reduced blinking, narrow emission line width and high quantum yield.[17,18] Several types of core−shell CdSe/CdS heterostructures have been synthesized in the past decade: dot-in-dots (DiDs),[2,15,17−21] dot-in-rods (DiRs),[22−25] dot-in-plates (DiPs),[26] rod-in-rods (RiRs),[27,28] tetrapods,[29,30] and octapods.[31] Carrier localization in these systems is generally assumed to be set by quantum confinement. The smaller gap of CdSe favors localization of both electron and hole inside the core (type-I exciton), but as the core size decreases, the electron kinetic energy allows it to overcome the CB offset barrier, delocalizing over both core and shell (quasi-type-II exciton).[2,5,24,32] Note, however, that the spatial separation between electron and hole is typically restricted to small core systems and is ultimately limited by Coulomb interaction, which binds the electron to the vicinity of the hole.[32,33]

Very recently, a study on CdSe/CdS RiRs with giant core and shell reported extremely long exciton lifetimes (up to 4400 ns).[28] This is 1 order of magnitude longer than any reported values for giant-shell CdSe/CdS DiDs[5,18] and two longer than those of DiR or core-only NCs,[24,28] which reflects a truly type-II behavior with well separated electrons and holes. It was shown that such exotic properties followed from the strain-induced piezoelectric (PZ) charges arising at the CdSe/CdS interfaces along the WZ *c* axis. Strain-induced PZ fields have been shown to be important in several epitaxial structures, including CdSe/CdS superlattices and III−V quantum dots.[34−36] This raises the question of how disruptive they can be in colloidal structures, if they are only important in large RiRs due to the anisotropic shape and weak longitudinal

Received: March 18, 2016
Accepted: May 25, 2016

DOI: 10.1021/acs.jpclett.6b00622
J. Phys. Chem. Lett. 2016, 7, 2182−2188

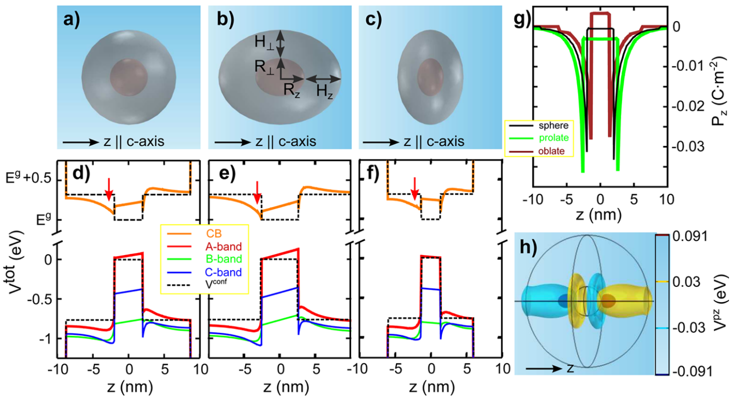

Figure 1. (a)−(c) schematic of spherical, prolate, and oblate DiDs. (d)−(f) CB and VB confining and total potential for a spherical DiD with core radius R = 2 nm and shell thickness H = 7 nm (d), prolate DiD with aspect ratio 1.3:1 ($R_z = 1.3R_\perp$ and $H_z = 1.3H_\perp$) (e) and oblate DiD with aspect ratio 0.7:1 (f). (g) strain-induced polarization along the c-axis for the three kinds of DiD. (h) isosurface representation of the piezoelectric potential for the spherical DiD. In (d)−(f), E^g is the bulk band gap.

confinement or if it is possible to use them as an efficient charge separation mechanism in other kinds of WZ NCs, with smaller core dimensions and different shapes. Potential signatures of PZ fields have been observed in CdSe/CdS DiDs[37,38] and DiRs,[37] but it has been mostly overlooked because calculations for a few particular structures deemed it a minor effect.[16,37,39] In this Letter, we show that with appropiate structural design, piezoelectricity indeed becomes a major factor determining the electron−hole separation in most kinds of WZ CdSe/CdS NCs.

We consider excitons in CdSe/CdS NCs where both core and shell present WZ structure. A few theoretical considerations are useful for the discussion of the results. The excitonic electron and hole Hamiltonians read

$$H_j = H_j^{\mathrm{kin}} + V_j^{\mathrm{conf}} + V_j^{\mathrm{str}} + V_j^{\mathrm{pz}} + V_j^{\mathrm{e-h}} \qquad (1)$$

where $j = e$ or h stands for electron or hole, H_j^{kin} is the kinetic energy term, V_j^{conf} the confining potential defined by the band offsets between bulk CdSe and CdS, V_j^{str} the strain induced deformation potential, V_j^{pz} the strain induced PZ potential and $V_j^{\mathrm{e-h}}$ is Coulomb attraction exerted upon carrier j by the other carrier. Special attention will be paid to the PZ potential term. In WZ, strain shifts the atomic nuclei inducing a PZ polarization vector

$$\mathbf{P} = \begin{pmatrix} e_{15}\epsilon_{xz} \\ e_{15}\epsilon_{yz} \\ e_{31}(\epsilon_{xx} + \epsilon_{yy}) + e_{33}\epsilon_{zz} \end{pmatrix} \qquad (2)$$

where e_{rs} are PZ coefficients and ϵ_{ij} strain tensor components. Notice that the polarization along the c-axis, P_z, is particularly important because it involves diagonal strain components, which are larger than the off-diagonal (shear) ones. Because $e_{33} \approx -2e_{31}$, sizable polarization P_z is expected when strain is anisotropic, that is, $(\epsilon_{xx} + \epsilon_{yy})/2 \neq \epsilon_{zz}$. The polarization is different in core and shell materials, as they experience different strain forces and have different piezoelectric coefficients. As a consequence, PZ charges $\rho(\mathbf{r}) = -\nabla\mathbf{P}$ arise near the interface. Again, these are especially important along the c axis. The PZ charges give rise to a PZ field according to the Poisson equation, $\nabla\epsilon(\mathbf{r})\nabla\phi^{\mathrm{pz}}(\mathbf{r}) = -4\pi\rho(\mathbf{r})$, and the PZ potential is finally obtained as $V_j^{\mathrm{pz}} = \pm\, q\phi^{\mathrm{pz}}$, where plus and minus sign apply to $j = e$ and $j = h$, respectively, and q is the electron charge.

We start by investigating spheroidal DiDs like those illustrated in Figure 1a−c. Consider first a fully spherical DiD. Figure 1(d) shows the CB and VB potential profiles. Dashed lines represent the confinement potential V^{conf}, whereas solid lines represent the total single-particle potential, including strain-induced deformation potential and PZ terms, $V^{\mathrm{tot}} = V^{\mathrm{conf}} + V^{\mathrm{str}} + V^{\mathrm{pz}}$. By inspecting the CB potential, orange line, one can see that the inclusion of $V^{\mathrm{str}} + V^{\mathrm{pz}}$ has three important effects. First, the core potential is shallower. This is a consequence of V^{str} (see Figure S1 in the Supporting Information (SI) or ref 16). Second, the core bottom develops a built-in PZ field of 15 mV/nm. This is a consequence of the PZ term, V^{pz} (see Figure S1 in SI or ref 16). Third, and most important, because the CB potential is shallow, the positive PZ charges accumulating at the bottom CdSe/CdS interface form a potential well in the shell where electrons can be trapped (red arrow in Figure 1d).

For holes the situation is different. We have three subbands: A-, B- and C-band. All three subbands are shifted upward by V^{str}. Contrary to electrons, this now results in a slightly deeper confinement. The effect of V^{pz} in the core is the same as for electrons, but owing to the different charge sign, holes will be pushed to the upper CdSe/CdS interface, thus favoring electron−hole separation. On the other hand, because the A-band confinement potential V^{conf} is very deep (see dashed lines), the negative PZ charges accumulating at the top CdSe/CdS interface do not suffice to localize the hole ground state outside the core.

Considering a prolate DiD instead of spherical, the PZ field increases (up to 23 mV/nm in Figure 1e). Conversely, for an oblate DiD the field is reduced and eventually the sign is even reversed, see Figure 1f.

The presence of a significant PZ field in the spherically symmetric DiD implies that even for structures with isotropic confinement, the inherent anisotropy of the WZ lattice leads

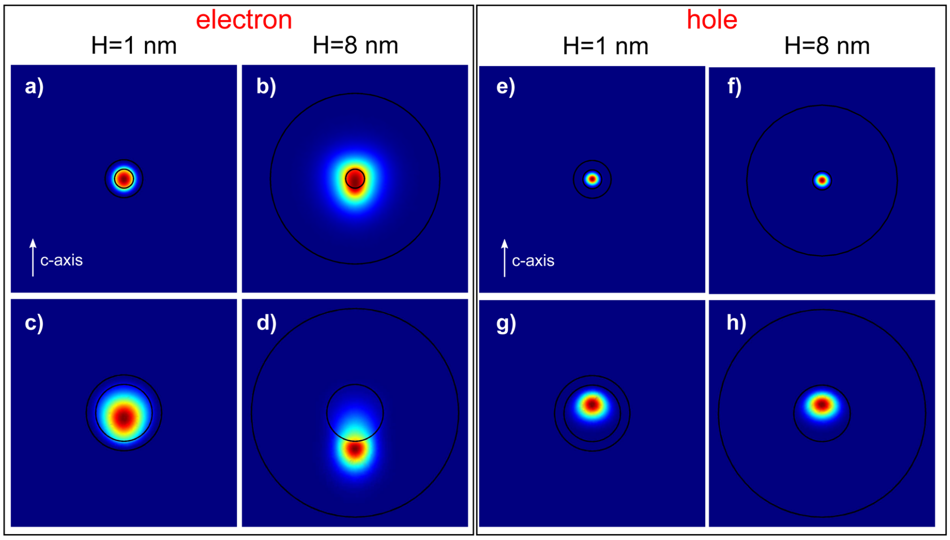

Figure 2. (a)−(d) Excitonic electron charge density in spherical DiDs with different core radius R and shell thickness H. (e−h) Same for excitonic hole. The electron moves into the shell for large cores and thick shells, panel d.

pronounced polarization near the CdSe/CdS interface, see black line in Figure 1g and notice the different weight of ϵ_{zz} and $\epsilon_\perp = (\epsilon_{xx} + \epsilon_{yy})/2$ in Figure S2 of the SI. This leads to a mostly dipolar PZ potential, as shown in Figure 1h. The strain anisotropy can be conveniently manipulated by using anisotropic geometries. Prolate structures favor $|\epsilon_{zz}| > |\epsilon_\perp|$ in the core, whereas oblate ones do the opposite, see Figure S2 in SI. This translates into more negative (positive) P_z values, see green (brown) line in Figure 1g. We then conclude that the shape of core/shell structures can be used to enhance, cancel or reverse PZ fields.

The next question is whether the magnitude of the attainable PZ fields is enough to influence excitonic wave functions in realistic DiDs. In Figure 2, we compare the exciton electron (a−d) and hole (e−h) charge densities for spherical DiDs with different dimensions. For small cores and thin shells (R = 1 nm, H = 1 nm), both electron (Figure 2a) and hole (Figure 2e) are centered in the core. Growing a giant shell (H = 8 nm) instead increases the core compression. As a result, V^{str} reduces the CB confinement barrier (recall Figure 1d) and the electron wave function starts leaking into the shell in spite of the Coulomb attraction, Figure 2b. The hole, by contrast, remains in the core because of the high confinement barrier, Figure 2f.

If the core is large enough (R = 3 nm) but the shell is thin (H = 1 nm), electron and hole are pushed toward opposite sides of the core along the c-axis by the PZ field, Figure 2c,g, but the resulting overlap is still substantial. The most remarkable effect of piezoelectricity takes place when a large core is surrounded by a giant shell. As can be seen in Figure 2d, in this case the electron escapes from the core and localizes in the shell near the CdSe/CdS interface. The electron is actually taking advantage of the potential minimum originated in the positive PZ interface charge, red arrow in Figure 1d. Because the hole remains in the core, Figure 2h, the spatial separation between the two carriers becomes large. In other words, by using large CdSe cores and growing giant CdS shells around, a gradual transition from type-I to type-II exciton driven by PZ is feasible.

For a comprehensive view of the effect of PZ on the exciton wave function of DiDs, we compute the electron−hole overlap integral squared, $S_{eh}^2 = \langle\Psi_e|\Psi_h\rangle^2$, which is directly proportional to the radiative exciton decay rate.[1] In Figure 3, we compare the overlap (a) excluding and (b) including strain and PZ effects (V^{str} and V^{pz}). The first case corresponds to DiDs governed by quantum confinement and Coulomb interactions only, which is the scenario assumed so far in the literature. The results are

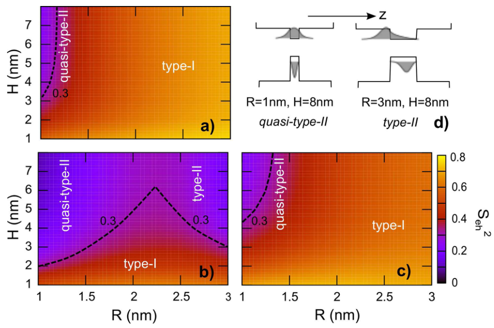

Figure 3. Electron−hole overlap squared for excitons confined in spherical WZ DiDs without (a) and with (b) strain and piezoelectric effects. The inclusion of strain and PZ reduces overlaps (compare the (dashed) isoline for S_{eh}^2 = 0.3 in the two panels) and introduces a type-II regime for large cores and thick shells. (c) Electron (top) and hole (bottom) charge densities along the c axis for two DiDs of panel (b), evidencing quasi-type-II (R = 1 nm) and type-II (R = 3 nm) exciton character. (d) Same as (a) and (b) but for strained ZB DiDs. The absence of PZ in this case translates into absence of type-II regime.

essentially the same as described, for example, in Figure 1f of ref 2. For core radii R = 1−1.5 nm, increasing the shell thickness H leads into a quasi-type-II regime, where the electron leaks into the shell due to the high kinetic energy in the core. For larger R, the electron stays inside the core no matter how thick the shell, and a type-I exciton is obtained with strong overlap values, similar to core-only samples.

The behavior changes drastically when strain and PZ effects are taken into account, Figure 3b. For thick shells, the quasi-type-II regime extends toward larger core radii ($R \lesssim 2$ nm). This is a consequence of strain making CB confinement shallower (see also S^2_{eh} for $V^{str} \neq 0$ and $V^{pz} = 0$ in Figure.S4 of SI). Moreover, with further increasing core radius ($R \gtrsim 2.5$ nm), instead of retrieving a type-I behavior the overlap decreases again. This is a consequence of the formation of PZ induced type-II excitons, as shown in Figure 2d,h. We stress that the nature of the reduced S_{eh} values is different on both sides of the figure. For small R (quasi-type-II regime), it is driven by the strong core confinement. For large R (type-II regime), it is driven by strain-induced PZ. The different localization of electron and hole charge densities in each case is clearly seen in Figure 3c. For comparison, in Figure 3d we also represent S^2_{eh} for ZB core/ZB shell CdSe/CdS DiDs. Strain is still present in such structures, but the dipolar PZ potential is quenched because of the cubic lattice symmetry. The resulting behavior is similar to that of unstrained WZ NCs, Figure 3a, and it is qualitatively different from that of realistic WZ DiDs, Figure 3b. We shall see below that this difference between WZ and ZB DiDs is fully consistent with experimental data.

The PZ control of the electron−hole overlap of WZ DiDs we report in Figure 3b, which should have important consequences on exciton lifetimes, electron−hole exchange integrals, and so forth, is robust against deviations from sphericity (Figure S5 in SI). Since the actual value of the CB offset is often discussed,[32] we have also studied the effect of changing from 0.32 eV (the value used in Figure 3) to a lower estimate of 0.20 eV. The results are qualitatively unchanged, but the overlap values in the type-II regime become manifestly lower than those in the quasi-type-II one, see Figure S6 in SI. It is also worth noting that although the PZ field is very efficient in separating carriers, its influence on the energy is modest. The exciton energy with and without strain differs at most in few tens of millielectronvolts (see Figure S7 in SI and ref 16).

To test the above predictions, we synthesized two series of giant-shell WZ DiDs with variable CdSe core radii and CdS shell thickness of about 20 and 15 ML, respectively (Figure 4a, see table S2 in SI for structural and optical properties). The resulting PL peak position varies between 648 and 663 nm and the time-resolved PL traces show a nonexponential decay (see Figure 4b,c for the 20 ML shell thickness series or Figure S10 in SI for the 15 ML one). Figure 4c shows that as the core size increases, we observe a slower decay. Note however that previous measurements[18] suggested the opposite, and the series with 15 ML shell thickness does not reveal a clear trend; hence, further work remains needed to firmly establish this behavior. Corresponding lifetimes for both 20 and 15 ML shell DiDs are plotted in Figure 4d using solid and open symbols, respectively. The values are calculated either from the time when the PL signal has decayed to $1/e$ (dots) or $1/e^2$ (triangles) of its initial value, or from a multiexponential fit (diamonds) to the decay trace (see SI for the analysis and summary of all components). Regardless of the core size dependence, the long lifetimes, especially for the large-core samples, are in clear contrast to

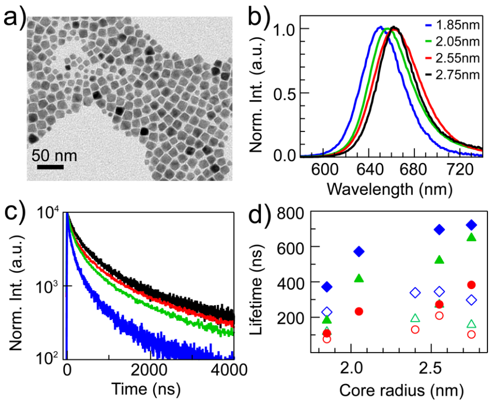

Figure 4. (a) Typical transmission electron microscope image of giant-shell DiDs (core radius 2.05 nm, 20 ML shell). (b) PL spectra for four different DiDs with 20 ML shell. (c) Corresponding PL decay traces. (d) Resulting effective lifetimes determined from the $1/e$ decay time (dots), $1/e^2$ decay time (triangles), and from a fit to the decay traces using a multiexponential function (diamonds, see SI for details). Solid (open) symbols are used for the 20 ML (15 ML) shell thickness series. The thinner shell gives shorter lifetimes. In general, lifetimes largely exceed those of giant-shell ZB DiDs.

expectations from the usual confinement picture for CdSe/CdS, where electron and hole states are expected to become localized into the core, approaching lifetimes of core-only CdSe NCs (ca. 15−20 ns). Such long lifetimes are indicative of a type-II regime, and they support the theory of PZ fields as an efficient mechanism of charge separation. Our values also exceed measurements of fluorescence lifetimes in ZB CdSe/CdS DiDs with moderately large cores ($R \approx 1.5$ nm) and thick shells ($H \approx 5.5$ nm) which have yielded values of about 30 ns.[21] This is again consistent with the theoretical predictions of Figure 3, which showed that PZ in thick-shell WZ DiDs leads to reduced electron−hole overlap as compared to ZB ones. Moreover, the strong differences in PL lifetime between the two samples series studied here highlight the sensitivity of the final lifetime to the shell thickness, even when it is grown to a regime where strong quantum confinement no longer influences the optical properties. This provides extra confirmation on PZ playing a significant role in giant-shell NCs with WZ crystal structure.

Having confirmed the influence of PZ fields in DiDs, we next probe other WZ CdSe/CdS structures such as DiRs, DiPs and RiRs, which we model as ellipsoids with different degrees of anisotropy and different orientation of the c axis. Let us consider first DiRs. Experiments available in the literature are generally consistent with a quantum confinement model, with a type-I band alignment and conduction band offsets between 0.1 and 0.3 eV. With decreasing core size, the excitons change from type-I to quasi-type-II behavior,[24,32] yielding room temperature lifetimes between 8 and 40 ns.[24,25,40] The absence of apparent PZ effects can be understood from two factors. First, typical cores for DiRs are small ($R \lesssim 2$ nm). The PZ dipole moment is then weak and, as noticed above (Figure 2 and Figure 3), V^{pz} has a minor influence. Second, the shell surrounding the core is thin on the lateral sides (usually 1 nm or less). As compared to the giant shells of DiDs, the thin lateral shell of DiRs allows the

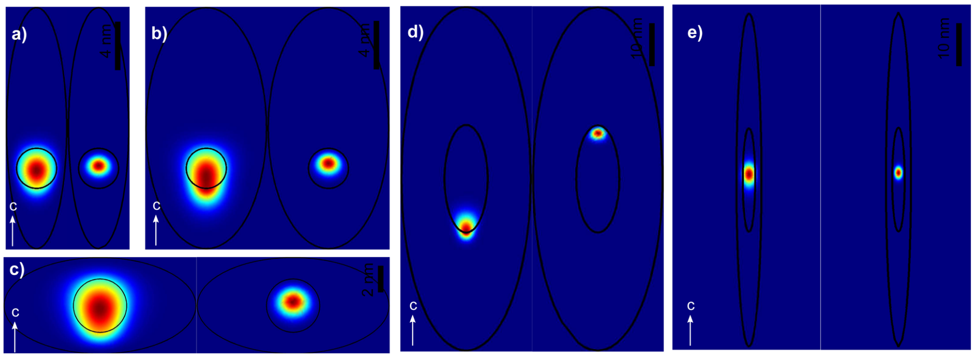

Figure 5. Excitonic charge density in different types of CdSe/CdS NCs. In each structure, the left (right) panel shows the electron (hole) density. (a) DiR with standard dimensions. (b) DiR with thicker lateral shell. The electron starts moving into the shell. (c) DiP with standard dimensions. (d) RiR with large core and giant shell. The charge separation is extremely efficient. (h) RiR with thinner core and shell. The charge separation is suppressed.

core to dilate, relaxing the strain in orthogonal directions. Consequently, the strain near the CdSe/CdS interfaces along the *c* axis, which is chiefly responsible for P_z, is reduced, see for example, Figure 4 in ref 41. The overall result is that PZ effects in DiRs are weak. This is precisely what we see in Figure 5a, where we plot the exciton electron and hole charge densities in a DiR: the carriers are well confined inside the core in spite of the relatively large size we have assumed ($R = 2$ nm). We note, however, that the picture would change if thicker shells could be grown, increasing the strain of the system. As shown in Figure 5b, keeping the same rod length as before but increasing $H_\perp$, the electron already starts moving toward the CdS shell, reducing the electron−hole overlap. We note that the enhancement of PZ fields with radial shell thickness explains recent experiments of Coropceanu et al.,[42] where the exciton lifetime of DiRs steadily increased from 20 to 60 ns with increasing shell thickness. For very thick shells, we predict a complete migration of the electron into the shell (Figure S8a in SI), so even longer lifetimes should be expected.

DiPs differ from DiRs mainly in that the shell is nearly two-dimensional, with the *c* axis pointing along the strong confinement direction.[26] Yet, their behavior in terms of PZ-induced electron delocalization (Figure 5c) is partly analogous to that of DiR: the thin shells along the *c* axis weaken the strain. This in turn leads to weak PZ effects and carriers localized inside the core. As in the case of DiRs, electron−hole distance could be readily increased if thicker shells were grown (Figure S8b).

The most favorable condition to maximize PZ effects is however achieved in recently synthesized RiRs.[28] The giant shell grants strong strain. The prolate shape makes strain highly anisotropic. The long core allows for huge dipole moments, and longitudinal quantum confinement is too weak to compete. The result, as plotted in Figure 5d, is that electron and hole are separated toward opposite CdSe/CdS interfaces along the *c* axis, which explains the record exciton lifetimes measured in these structures.[28] It is worth stressing that the giant shell plays a decisive role in RiRs too. RiRs with smaller core and shell width were previously synthesized by Sitt and co-workers, but long exciton lifetimes were not reported in such a case.[27] We simulate RiRs with similar dimensions to theirs in Figure 5e. As can be seen, in spite of the high aspect ratio and the weak longitudinal confinement, charge separation is completely suppressed, with both electron and hole localizing inside the core. The underlying reason is again the weaker strain of the system, which results in a PZ field unable to compete against electron−hole Coulomb interaction.

An important conclusion from Figure 5 is that PZ successfully rationalizes the very different exciton lifetimes reported for different kinds of WZ CdSe/CdS NCs. In RiRs,[28] lifetimes can be 1 order of magnitude longer than those in giant-shell DiDs (ref 18 and Figure 4), and these in turn are about 1 order of magnitude longer than those in DiRs.[24] This result cannot be interpreted in terms of quantum confinement because all structures have voluminous shells, but it is perfectly consistent with the different degrees of PZ-induced electron−hole separation we calculate.

To summarize, we have elucidated the conditions where strain-induced piezoelectricity becomes a practical mechanism for electron−hole spatial separation in several kinds of WZ CdSe/CdS NCs. The PZ field requires anisotropic strain, which is present even in spherical heterostructures due to the anistropy of the WZ lattice. PZ charges thus accumulate on the CdSe/CdS interfaces, forming a dipole and a sizable built-in field along the *c* axis, which enables directional charge separation. The magnitude of the PZ field can be enhanced using thick shells all around the core, which increase the strain in and around it, and using prolate cores, which reinforce the inherent strain anisotropy. The influence of PZ potential on the exciton wave function scales with the core size, as so does the PZ dipole moment, and on the shell thickness, as it provides space for the electron to escape from the core.

We have then shown that significant PZ effects are present not only in RiRs, as recently reported in ref 28 but also in giant-shell DiDs and, to a lesser extent, in DiRs. In fact, the different strength of PZ fields in each kind of structure interprets the large variations of radiative lifetime reported in the literature. The present results show that, with appropiate design, band alignment can be engineered all the way from type-I or quasi-type-II to a fully type-II one in any kind of CdSe/CdS NC, thus providing an efficient tool for tailoring electron−hole separation.

ASSOCIATED CONTENT

Supporting Information

The Supporting Information is available free of charge on the ACS Publications website at DOI: 10.1021/acs.jpclett.6b00622.

Details of methods, supporting calculations of strain maps, band-edge structure, wave functions, electron−hole overlap under different conditions, a list of the material parameters employed and further experimental data. (PDF)

AUTHOR INFORMATION

Corresponding Author

*E-mail: josep.planelles@uji.es.

Notes

The authors declare no competing financial interest.

ACKNOWLEDGMENTS

Support from MINECO project CTQ2014-60178-P, UJI project P1-1B2014-24 and a FPU grant (C.S.) is acknowledged. The present publication is further realized with the support of the Ministero degli Affari Esteri e della Cooperazione Internazionale (IONX-NC4SOL, I.M.).

REFERENCES

(1) Delerue, C.; Lannoo, M. *Nanostructures: Theory and Modelling*; Springer: Berlin, 2004.
(2) Garcia-Santamaria, F.; Chen, Y.; Vela, J.; Schaller, R. D.; Hollingsworth, J. A.; Klimov, V. I. Suppressed Auger Recombination in "Giant" Nanocrystals Boosts Optical Gain Performance. *Nano Lett.* **2009**, *9*, 3482−3488.
(3) Cragg, G. E.; Efros, A. L. Suppression of Auger Processes in Confined Structures. *Nano Lett.* **2010**, *10*, 313−317.
(4) Climente, J. I.; Movilla, J. L.; Planelles, J. Auger Recombination Suppression in Nanocrystals with Asymmetric Electron-Hole Confinement. *Small* **2012**, *8*, 754−759.
(5) Brovelli, S.; Schaller, R. D.; Crooker, S. A.; Garcia-Santamaria, F.; Chen, Y.; Viswanatha, R.; Hollingsworth, J. A.; Htoon, H.; Klimov, V. I. Nano-engineered Electronhole Exchange Interaction Controls Exciton Dynamics in CoreShell Semiconductor Nanocrystals. *Nat. Commun.* **2011**, *2*, 280.
(6) McDaniel, H.; Pelton, M.; Oh, N.; Shim, M. Effects of Lattice Strain and Band Offset on Electron Transfer Rates in Type-II Nanorod Heterostructures. *J. Phys. Chem. Lett.* **2012**, *3*, 1094−1098.
(7) Kovalenko, M.; Manna, L.; Cabot, A.; Hens, Z.; Talapin, D. V.; Kagan, Ch. R.; Klimov, V. I.; Rogach, A. L.; Reiss, P.; Milliron, D. J.; et al. Prospects of Nanoscience with Nanocrystals. *ACS Nano* **2015**, *9*, 1012−1057.
(8) Smith, A. M.; Mohs, A. M.; Nie, S. Tuning the Optical and Electronic Properties of Colloidal Nanocrystals by Lattice Strain. *Nat. Nanotechnol.* **2009**, *4*, 56−63.
(9) Yang, S.; Prendergast, D.; Neaton, J. B. Strain-Induced Band Gap Modification in Coherent Core/Shell Nanostructures. *Nano Lett.* **2010**, *10*, 3156−3162.
(10) Fairclough, S. M.; Tyrrell, E. J.; Graham, D. M.; Lunt, P. J. B.; Hardman, S. J. O.; Pietzsch, A.; Hennies, F.; Moghal, J.; Flavell, W. R.; Watt, A. A. R.; Smith, J. M. Growth and Characterization of Strained and Alloyed Type-II ZnTe/ZnSe Core-Shell Nanocrystals. *J. Phys. Chem. C* **2012**, *116*, 26898−26907.
(11) Yadav, S. K.; Sharma, V.; Ramprasad, R. Controlling Electronic Structure Through Epitaxial Strain in ZnSe/ZnTe Nano-Heterostructures. *J. Appl. Phys.* **2015**, *118*, 015701.
(12) Khoo, K. H.; Arantes, J. T.; Chelikowsky, J. R.; Dalpian, G. M. First-Principles Calculations of Lattice-Strained Core-Shell Nanocrystals. *Phys. Rev. B: Condens. Matter Mater. Phys.* **2011**, *84*, 075311.
(13) Phadnis, C.; Sonawane, K. G.; Hazarika, A.; Mahamuni, S. Strain-Induced Hierarchy of Energy Levels in CdS/ZnS Nanocrystals. *J. Phys. Chem. C* **2015**, *119*, 24165−24173.
(14) Pahomi, T. E.; Cheche, T. O. Strain Influence on Optical Absorption of Giant Semiconductor Colloidal Quantum Dots. *Chem. Phys. Lett.* **2014**, *612*, 33−38.
(15) Cirillo, M.; Aubert, T.; Gomes, R.; Deun, R. V.; Emplit, P.; Biermann, A.; Lange, H.; Thomsen, C.; Brainis, E.; Hens, Z. Flash" Synthesis of CdSe/CdS Core-Shell Quantum Dots. *Chem. Mater.* **2014**, *26*, 1154−1160.
(16) Park, S. H.; Cho, Y. H. Characteristics of Built-in Polarization Potentials in Vertically and Laterally Arranged InGaN/GaN Quantum Dots. *J. Appl. Phys.* **2011**, *109*, 113103.
(17) Chen, O.; Zhao, J.; Chauhan, V. P.; Cui, J.; Wong, C.; Harris, D. K.; Wei, H.; Han, H. S.; Fukumura, D.; Jain, R. K.; Bawendi, M. G. Compact High-Quality CdSe/CdS Core/Shell Nanocrystals with Narrow Emission Linewidths and Suppressed Blinking. *Nat. Mater.* **2013**, *12*, 445−451.
(18) Christodoulou, S.; Vaccaro, G.; Pinchetti, V.; De Donato, F.; Grim, J. Q.; Casu, A.; Genovese, A.; Vicidomini, G.; Diaspro, A.; Brovelli, S.; et al. Synthesis of Highly Luminescent Wurtzite CdSe/CdS Giant-shell Nanocrystals Using a Fast Continuous Injection Route. *J. Mater. Chem. C* **2014**, *2*, 3439−3447.
(19) Mahler, B.; Lequeux, N.; Dubertret, B. Ligand-Controlled Polytypism of Thick-Shell CdSe/CdS Nanocrystals. *J. Am. Chem. Soc.* **2010**, *132*, 953−959.
(20) van Embden, J.; Jasieniak, J.; Mulvaney, P. Mapping the Optical Properties of CdSe/CdS Heterostructure Nanocrystals: The Effects of Core Size and Shell Thickness. *J. Am. Chem. Soc.* **2009**, *131*, 14299−14309.
(21) Qin, H.; Niu, Y.; Meng, R.; Lin, X.; Lai, R.; Fang, W.; Peng, X. Single-Dot Spectroscopy of Zinc-Blende CdSe/CdS Core/Shell Nanocrystals: Nonblinking and Correlation with Ensemble Measurements. *J. Am. Chem. Soc.* **2014**, *136*, 179−187.
(22) Carbone, L.; Nobile, C.; De Giorgi, M.; Della Sala, F.; Morello, G.; Pompa, P.; Hytch, M.; Snoeck, E.; Fiore, A.; Franchini, I. R.; et al. Synthesis and Micrometer-Scale Assembly of Colloidal CdSe/CdS Nanorods Prepared by a Seeded Growth Approach. *Nano Lett.* **2007**, *7*, 2942−2950.
(23) Sitt, A.; Hadar, I.; Banin, U. Band-Gap Engineering, Optoelectronic Properties and Applications of Colloidal Heterostructured Semiconductor Nanorods. *Nano Today* **2013**, *8*, 494−513.
(24) Raino, G.; Stoferle, T.; Moreels, I.; Gomes, R.; Kamal, J. S.; Hens, Z.; Mahrt, R. F. Probing the Wave Function Delocalization in CdSe/CdS Dot-in-Rod Nanocrystals by Time- and Temperature-Resolved Spectroscopy. *ACS Nano* **2011**, *5*, 4031−4036.
(25) Wu, K.; Rodriguez-Cordoba, W. E.; Liu, Z.; Zhu, H.; Lian, T. Beyond Band Alignment: Hole Localization Driven Formation of Three Spatially Separated Long-Lived Exciton States in CdSe/CdS Nanorods. *ACS Nano* **2013**, *7*, 7173−7185.
(26) Cassette, E.; Mahler, B.; Guigner, J. M.; Patriarche, G.; Dubertret, B.; Pons, T. Colloidal CdSe/CdS Dot-in-Plate Nanocrystals with 2D-Polarized Emission. *ACS Nano* **2012**, *6*, 6741−6750.
(27) Sitt, A.; Salant, A.; Menagen, G.; Banin, U. Highly Emissive Nano Rod-in-Rod Heterostructures with Strong Linear Polarization. *Nano Lett.* **2011**, *11*, 2054−2060.
(28) Christodoulou, S.; Rajadell, F.; Casu, A.; Vaccaro, G.; Grim, J.; Genovese, A.; Manna, L.; Climente, J. I.; Meinardi, F.; Raino, G.; et al. Band Structure Engineering via Piezoelectric Fields in Strained Anisotropic CdSe/CdS Nanocrystals. *Nat. Commun.* **2015**, *6*, 7905.
(29) Talapin, D. V.; Nelson, J. H.; Shevchenko, E. V.; Aloni, S.; Sadtler, B.; Alivisatos, A. P. Seeded Growth of Highly Luminescent CdSe/CdS Nanoheterostructures with Rod and Tetrapod Morphologies. *Nano Lett.* **2007**, *7*, 2951−2959.
(30) Fiore, A.; Mastria, R.; Lupo, M. G.; Lanzani, G.; Giannini, C.; Carlino, E.; Morello, G.; De Giorgi, M.; Li, Y.; Cingolani, R.; Manna, L. Tetrapod-Shaped Colloidal Nanocrystals of II-VI Semiconductors Prepared by Seeded Growth. *J. Am. Chem. Soc.* **2009**, *131*, 2274−2282.

(31) Deka, S.; Miszta, K.; Dorfs, D.; Genovese, A.; Bertoni, G.; Manna, L. Octapod-Shaped Colloidal Nanocrystals of Cadmium Chalcogenides via "One-Pot" Cation Exchange and Seeded Growth. *Nano Lett.* **2010**, *10*, 3770−3776.

(32) Eshet, H.; Grünwald, M.; Rabani, E. The Electronic Structure of CdSe/CdS Core/Shell Seeded Nanorods: Type-I or Quasi-Type-II? *Nano Lett.* **2013**, *13*, 5880−5885.

(33) Shabaev, A.; Rodina, A. V.; Efros, A. L. Fine Structure of the Band-Edge Excitons and Trions in CdSe/CdS Core/Shell Nanocrystals. *Phys. Rev. B: Condens. Matter Mater. Phys.* **2012**, *86*, 205311.

(34) Langbein, W.; Hetterich, M.; Grun, M.; Klingshirn, C.; Kalt, H. Picosecond Luminescence Dynamics in CdS/CdSe Stark Superlattices. *Appl. Phys. Lett.* **1994**, *65*, 2466−2468.

(35) Andreev, A. D.; O'Reilly, E. P. Theory of the Electronic Structure of GaN/AlN Hexagonal Quantum Dots. *Phys. Rev. B: Condens. Matter Mater. Phys.* **2000**, *62*, 15851−15870.

(36) Seguin, R.; Schliwa, A.; Rodt, S.; Potschke, K.; Pohl, U. W.; Bimberg, D. Size-dependent Fine-Structure Splitting in Self-Organized InAs/GaAs Quantum Dots. *Phys. Rev. Lett.* **2005**, *95*, 257402.

(37) Morello, G.; Della Sala, F.; Carbone, L.; Manna, L.; Maruccio, G.; Cingolani, R.; De Giorgi, M. Intrinsic Optical Nonlinearity in Colloidal Seeded Grown CdSe/CdS Nanostructures: Photoinduced Screening of the Internal Electric Field. *Phys. Rev. B: Condens. Matter Mater. Phys.* **2008**, *78*, 195313.

(38) Zhu, B. H.; Zhang, H. C.; Zhang, Z. Y.; Cui, Y. P.; Zhang, J. Y. Effect of Shell Thickness on Two-Photon Absorption and Refraction of Colloidal CdSe/CdS Core/Shell Nanocrystals. *Appl. Phys. Lett.* **2011**, *99*, 231903.

(39) Luo, Y.; Wang, L. W. Electronic Structures of the CdSe/CdS Core-Shell Nanorods. *ACS Nano* **2010**, *4*, 91−98.

(40) Muller, J.; Lupton, J. M.; Lagoudakis, P. G.; Schindler, F.; Koeppe, R.; Rogach, A. L.; Feldmann, J.; Talapin, D. V.; Weller, H. Wave Function Engineering in Elongated Semiconductor Nanocrystals with Heterogeneous Carrier Confinement. *Nano Lett.* **2005**, *5*, 2044−2049.

(41) Rajadell, F.; Royo, M.; Planelles, J. Strain in Free Standing CdSe/CdS Core-Shell Nanorods. *J. Appl. Phys.* **2012**, *111*, 014303.

(42) Coropceanu, I.; Rossinelli, A.; Caram, J. R.; Freyria, F. S.; Bawendi, M. G. Slow-Injection Growth of Seeded CdSe/CdS Nanorods with Unity Fluorescence Quantum Yield and Complete Shell to Core Energy Transfer. *ACS Nano* **2016**, *10*, 3295−3301.

Supplemental Material for “Piezoelectric control of the exciton wave function in colloidal CdSe/CdS nanocrystals"

Carlos Segarra,† Juan I. Climente,† Anatolii Polovitsyn,‡ Fernando Rajadell,† Iwan Moreels,‡ and Josep Planelles*,†

Departament de Química Física i Analítica, Universitat Jaume I, E-12080, Castelló de la Plana, Spain, and Istituto Italiano di Tecnologia, Via Morego 30, IT-16163 Genova, Italy

E-mail: josep.planelles@uji.es

*To whom correspondence should be addressed

†Departament de Química Física i Analítica, Universitat Jaume I, E-12080, Castelló de la Plana, Spain

‡Istituto Italiano di Tecnologia, Via Morego 30, IT-16163 Genova, Italy

Theoretical method

Strain maps are calculated in the continuous medium model by minimizing the elastic energy. The boundary conditions are zero normal stress for the free surface.[1] The strain tensor elements $\varepsilon_{ij}(\mathbf{r})$, ensuing PZ polarization vector **P** and potential V^{pz} are obtained using the multiphysics mode of Comsol 4.2 software. Electron ($j = e$) and hole ($j = h$) states of the ground-state exciton are calculated with Hamiltonian (1) of the main text. For electrons, H_e^{kin} is a 3D single-band (actually two uncoupled bands including spin) effective mass Hamiltonian. H_h^{kin} is a 3D six-band Hamiltonian for wurtzite including A-band, B-band and C-band with spin-orbit interaction. The same Hamiltonian is used for [111]-grown zinc-blende structures by employing due parameters. See Ref.[2] for details of the Hamiltonian. The strain-induced deformation potential term, V^{str} is isomorphic to the kinetic energy term and V^{pz} is diagonal (see e.g. Ref.[3]) The Coulomb interaction term V^{e-h} takes into account the dielectric mismatch with the dielectric surroundings of the NC. Interacting electron and hole states are obtained by iterative resolution of the Schrodinger-Poisson equation.

Experimental method

CdSe core nanocrystals where synthesized according to the procedure of Carbone et al.[4] For all samples, the CdSe core diameter and concentration in solution were determined using the sizing curve of Jasieniak et al.[5] The shell was grown using the procedure described in Ref.[6] After synthesis, the nanocrystals were purified and finally dispersed in toluene.

Bright-field transmission electron microscopy was used to determine the final NC diameter (using ca. 50 NCs), from which the shell thickness could be calculated (see also table S2, note that the histogram reveals a minor contribution from sub-10 nm NCs which are likely CdS NCs that nucleated separately, these were not taken into account in the calculation of the final diameter). Steady-state and time-resolved luminescence spectra were measured using a FLS920 Edinburgh Instruments spectrofluorometer. We dispersed the DiDs in chloroform for all measurements, and excited the samples at 400 nm with a Xenon lamp to collect the PL spectra. The PL quantum efficiency was determined with an integrating sphere (2-measurement method[7]), exciting the samples at 550 nm. A 405 nm, 50 ps pulsed laser was used to collect the PL decay via time-correlate single photon counting. The time between pulses was adjusted to 10 μs to ensure full decay between subsequent excitations. As the decay is nonexponential, we determined 3 different effective lifetimes to compare between the different sizes. The first focuses on the initial decay, and considers the time τ_1 for the signal to decay to $1/e$ of its maximal value. The second evaluates time delay τ_2 until the decay reaches $1/e^2$, yielding an effective $\tau_2 = \Delta t/2$. Finally, we fitted the traces to a sum of four exponentials, from which an area-weighted average lifetime τ_3 can be determined (see table S3).

Supporting calculations

Role of each potential term in the single-particle Hamiltonian

As seen in Figure S1, for all DiD geometries (spherical, prolate and oblate), the band-offset confining potential V^{conf} forms a confining well in the core region. By contrast, the strain-induced deformation potential V^{str} forms a barrier. When considered together, V^{str} greatly reduces the well depth one would expect with a confinement-only model. This stimulates electron leakage into the shell. The piezoelectric (PZ) potential V^{pz} is similar to that reported by Park and Cho.[3] Charges of opposite sign accumulate on each CdSe/CdS interface forming a dipole and a nearly linear (capacitor-like) built-in field in the core. Notice that using prolate cores (ellipsoid is elongated along the *c*-axis) instead of spherical ones increases the field. In turn, using oblate cores reduces the field and can even revert the sign (that is the case we plot in the right column). As for the total potential V^{tot}, notice that in all cases a well is formed by the bottom CdSe/CdS interface where electrons can localize. This is because the positive PZ charges can compensate for the low conduction band offset of CdSe/CdS.

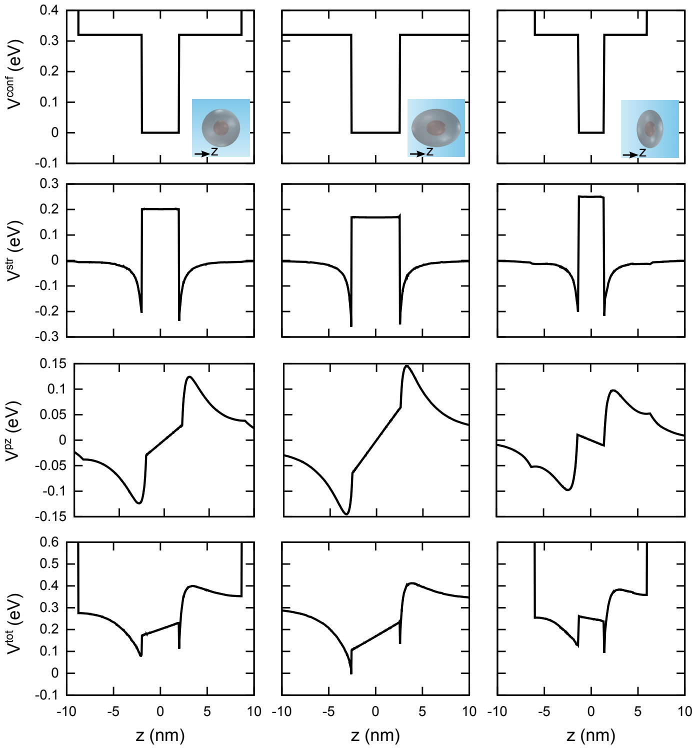

Figure S1: Top to bottom: V^{conf}, V^{str}, V^{pz} and $V^{tot} = V^{conf} + V^{str} + V^{pz}$ along the c-axis of a dot-in-dot (DiD). Left column: spherical geometry –core radius $R = 2$ nm and shell thickness $H = 7$ nm–. Middle column: prolate geometry –$R_\perp = R$, $R_z = 1.3R$, $H_\perp = H$ and $H_z = 1.3H$–. Right column: oblate geometry –$R_\perp = R$, $R_z = 0.7R$, $H_\perp = H$ and $H_z = 0.7H$–.

Effect of shape on the strain map

In CdSe/CdS NCs, the CdSe core is compressed because of its larger natural lattice constant (negative strain in the figure). In spherical cores, panels (a) and (d), the core strain is slightly anistropic as $|\varepsilon_{zz}| \gtrsim |\varepsilon_\perp|$. Since $P_z = e_{31}(\varepsilon_{xx} + \varepsilon_{yy}) + e_{33}\varepsilon_{zz}$ and $e_{33} \approx -2e_{31}$, this leads to a small but finite negative PZ polarization P_z inside the core, which can be seen in Fig.1(g) of the paper. In prolate cores, panels (b) and (e), ε_{zz} becomes visibly more compressive (darker blue) and the strain anisotropy increases. This explains the more negative values of P_z in Fig.1(g). The opposite occurs for oblate cores, panels (c) and (f). This explains the sign reversal of P_z for oblate cores in Fig.1(g).

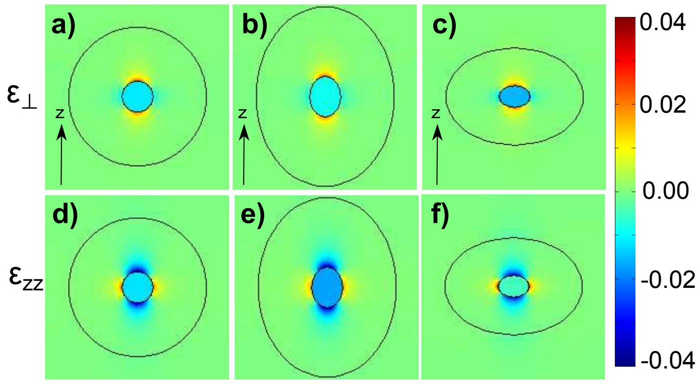

Figure S2: Diagonal strain along the c-axis (ε_{zz}) and the orthogonal direction ($\varepsilon_{\perp} = 1/2(\varepsilon_{xx} + \varepsilon_{yy})$. Left column: spherical geometry. Middle column: prolate geometry. Right column: oblate geometry (same dimensions as in Figure S1).

The strain anisotropy becomes much more pronounced in the shell surrounding the core. Along the c axis (vertical direction in the figure), ε_{zz} remains compressive (negative) but $\varepsilon_{\perp}$ becomes tensile (positive). This explains the drastic change of P_z at the interface (see Fig.1(g) of the main paper). Since PZ charges are proportional to the P_z gradient, $\rho(\mathbf{r}) = -\nabla\mathbf{P}$, significant PZ charges build up at the heterointerface.

Influence of each potential term on the exciton's electron wave function

To understand the origin of the electron localization in the shell reported in Fig.2(d) of the main paper, in Figure S3 we show the electron charge density calculated under different circumstances. When only the band-offset confinement is considered, Figure S3(a), the electron is well localized in the center of the core. Further adding the strain induced deformation potential, Figure S3(b), enhances leakage into the shell owing the overall shallower confining potential (recall Figure S1). It is the inclusion of the PZ field, Figure S3(c), that moves the electron to one of the core-shell interfaces. Adding Coulomb interaction with the hole –which remains in the core– moves the electron charge density partially back into the core, Figure S3(d). This is however a relatively minor effect because Coulomb interaction in a type-II system is weak.

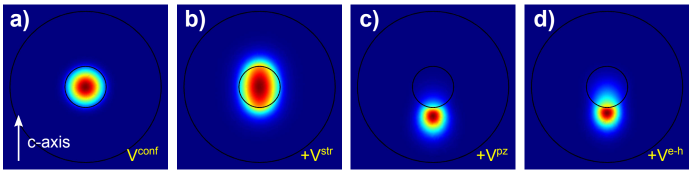

Figure S3: Electron charge density corresponding to the ground state exciton in a spherical DiD with $R = 3$ nm core and $H = 8$ nm shell, under different potential terms. (a) Confinement potential only, $H_e = H_e^{kin} + V_e^{conf}$. (b) Adding strain deformation potential, $H_e = H_e^{kin} + V_e^{conf} + V_e^{str}$. (c) Adding PZ potential, $H_e = H_e^{kin} + V_e^{conf} + V_e^{str} + V_e^{pz}$. (d) Adding Coulomb interaction with hole in core, $H_e = H_e^{kin} + V_e^{conf} + V_e^{str} + V_e^{pz} + V_e^{e-h}$.

Exciton overlap and energy in dot-in-dots

Figure S4 shows the electron-hole overlap squared, $S_{eh}^2 = |\langle \Psi_e | \Psi_h \rangle|^2$, calculated for the ground state exciton in spherical DiDs. Unlike in Fig. 3 of the main text, we keep V^{str} but set $V^{pz} = 0$. One can see that the quasi-type-II (purple) region extends to larger core sizes than in the case neglecting strain (Fig.3(a)), owing to the shallower confinement. On the other hand, lacking PZ terms, there is no type-II exciton region for the largest core sizes, unlike in Fig. 3(b).

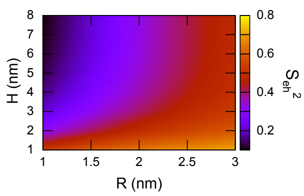

Figure S4: Electron-hole overlap squared, $|\langle \Psi_e | \Psi_h \rangle|^2$, in spherical DiDs with different core radius R and shell thickness H. Defomation potential is considered but PZ potential is neglected.

Figure S5 illustrates the overlap for spherical, prolate and oblate DiDs considering the full Hamiltonian. Note that in all cases, small overlaps are expected for large cores ($R_\perp > 2.5$ nm). It follows that the PZ induced charge separation is generally robust against shape deformations.

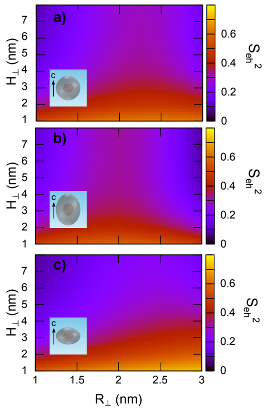

Figure S5: Electron-hole overlap squared, $|\langle\Psi_e|\Psi_h\rangle|^2$, in spherical (a), prolate (b) and oblate (c) DiDs with different lateral core radius $R_\perp$ and shell thickness $H_\perp$. For prolate dots, $R_z = 1.3R_\perp$. For oblate ones, $R_z = 0.7R_\perp$.

Figure S6 shows that the behavior reported in Fig. 3 of the paper is also robust against changes in the conduction band offset, a parameter whose exact value is often debated. Here we use a band offset of 0.20 eV instead of the bulk value of 0.32 eV, to account for experiments suggesting a flatter core-shell alignment.[8] The results are qualitatively consistent with Fig.3, but the lower band offset gives rise to a type-II regime (large R and H in panel (b)) with much more efficient charge separation than in the quasi-type-II one (small R). For $H = 8$ nm, the overlap squared of $R = 3$ nm is 5 times smaller than that of $R = 1$ nm.

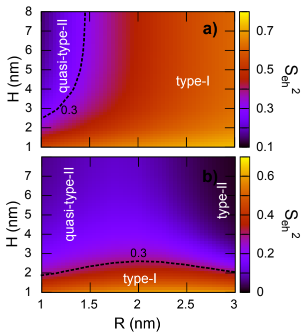

Figure S6: Same as Fig. 3 in the main text but considering a conduction band offset of 0.20 eV instead of 0.32 eV. The dashed line is the $S_{eh}^2 = 0.3$ isoline.

Figure S7 shows the exciton energy for spherical DiDs without (a) and with (b) strain and PZ effects. The results are similar, with a predominant influence of the core radius in both cases. The energy differences between the two cases are of few tens of meV at most, with a maximum of 80 meV for $R = 1$ nm and $H = 8$ nm. One concludes that, while PZ has important effects on the exciton wave function, its influence on the energy is relatively weak.

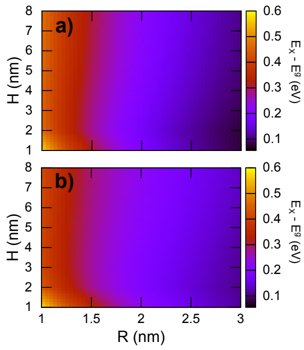

Figure S7: Exciton energy in spherical DiDs with $V^{str} = V^{pz} = 0$ (a), and $V^{str} \neq 0$, $V^{pz} \neq 0$ (b). E^g is the bulk band gap.

Towards type-II dot-in-rods and dot-in-plates

Typical dot-in-rods (DiRs) have weak strain and PZ effects because of the thin shell in the direction orthogonal to the c-axis, $H_\perp \lesssim 1$ nm. Figure S8(a) shows that electron migration into the shell becomes feasible if one combines large cores with considerably thicker shells ($H_\perp = 5$ nm in the figure). Similarly, typical dot-in-plates (DiPs) have thin shells along the c axis. Figure S8(b) shows that growing thicker shells again triggers electron migration.

Material Parameters

Below we summarize the material parameters used in the calculations. m_0 is the free electron mass and ε_0 the vacuum permitivitty. A relative dielectric constant of 3 and confining potential of 5 eV is taken outside the NC to account for the dielectric environment. See Ref.[2] for the Burt-Foreman

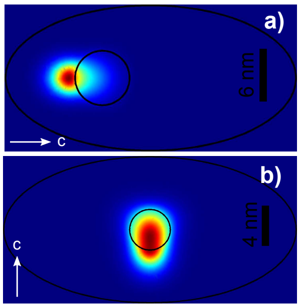

Figure S8: (a) Excitonic electron charge density in a DiR with large core and thick lateral shell (orthogonal to *c* axis). As compared with the DiRs in Fig.5a,b of the main text, the electron is more delocalized. (b) Same but in a DiP with thick shell along *c* axis. As compared with the DiP in Fig.5c of the main text, the electron is more delocalized.

kinetic energy term of Hamiltonian (to avoid spurious solutions, the hole mass parameters we use follow the complete asymmetric operator ordering, i.e. $A_i^{(+)} = A_i$ and $A_i^{(-)} = 0$), and see Ref.[3] for the strain terms.

Description	**Symbol**	**CdSe value**	**CdS value**	**Units**	**Ref.**
Elastic modulus tensor	C_{11}	$74.1 \cdot 10^9$	$86.5 \cdot 10^9$	Pa	9
Elastic modulus tensor	C_{12}	$45.2 \cdot 10^9$	$54.0 \cdot 10^9$	Pa	9
Elastic modulus tensor	C_{13}	$38.9 \cdot 10^9$	$47.3 \cdot 10^9$	Pa	9
Elastic modulus tensor	C_{33}	$84.3 \cdot 10^9$	$94.4 \cdot 10^9$	Pa	9
Elastic modulus tensor	C_{44}	$13.4 \cdot 10^9$	$15.0 \cdot 10^9$	Pa	9
Piezoelectric constant	e_{31}	-0.16	-0.24	C·m^2	10
Piezoelectric constant	e_{33}	0.347	0.44	C·m^2	10
Piezoelectric constant	e_{15}	-0.138	-0.21	C·m^2	10
Dielectric constant	$\varepsilon_\perp$	9.29	8.28	ε_0	10
Dielectric constant	ε_z	10.16	8.73	ε_0	10
Lattice constant $\parallel$ *c* axis	c	7.01	6.749	Å	10
Lattice constant $\perp$ *c* axis	a	4.30	4.135	Å	10
Conduction band offset	cbo	0.0	0.32	eV	11

Valence band offset	vbo	0.0	-0.40	eV	[11]
Crystal field splitting	Δ_1	0.039	0.027	eV	[12]
Spin-orbit matrix element	Δ_2	0.416	0.065	eV	[12]
Spin-orbit matrix element	Δ_3	0.416	0.065	eV	[12]
Electron mass	m^*	0.11	0.21	m_0	[10]
Hole mass parameter	A_1	-5.06	-4.53	$1/m_0$	[12]
Hole mass parameter	A_2	-0.43	-0.39	$1/m_0$	[12]
Hole mass parameter	A_3	4.5	4.02	$1/m_0$	[12]
Hole mass parameter	A_4	-1.29	-1.92	$1/m_0$	[12]
Hole mass parameter	A_5	-1.29	-1.92	$1/m_0$	[12]
Hole mass parameter	A_6	-0.47	-2.59	$1/m_0$	[12]
CB Deformation pot. $\parallel c$ axis	a_c^z	-1.76	-4.5	eV	[3]
CB Deformation pot. $\perp c$ axis	$a_c^\perp$	-7.8	-8.2	eV	[3]
VB Deformation pot.	D_1	-0.76	-2.8	eV	[13]
VB Deformation pot.	D_2	-3.7	-4.5	eV	[13]
VB Deformation pot.	D_3	-4.0	-1.3	eV	[13]
VB Deformation pot.	D_4	2.2	2.9	eV	[13]
VB Deformation pot.	D_5	-1.2	1.5	eV	[13]
VB Deformation pot.	D_6	-1.5	-1.2	eV	[13]

Table S1: Wurtzite CdSe and CdS parameters used in the calculations.

For calculations of zinc-blende phase, we take the material parameters given in Ref.,[9] except for the conduction deformation potential[13] and the band-offsets.[11]

Structural and optical data of experimental DID samples

Below we provide a few representative transmission electron microscopy (TEM) images of DID samples under investigation, as well as the corresponding histograms of total (core plus shell) size distribution.

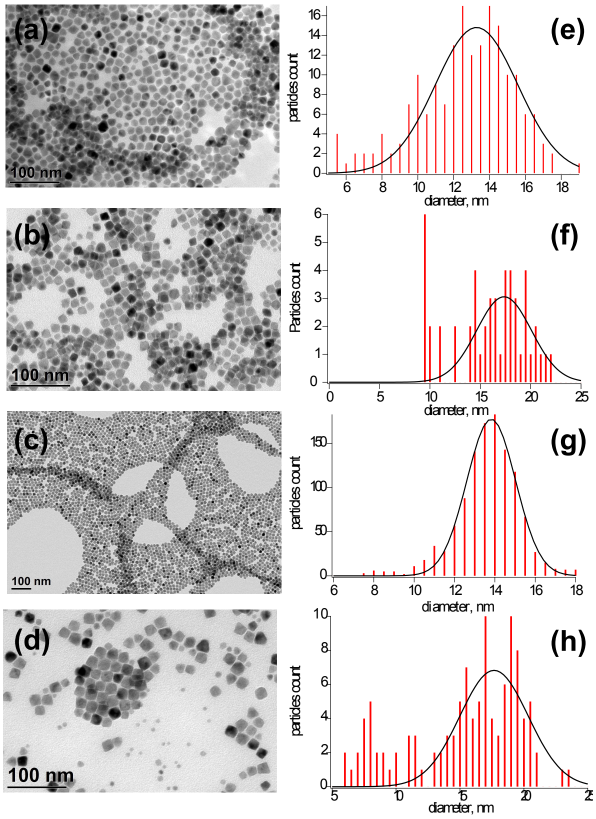

Figure S9: (a-d) TEM images of DiD samples 5, 1, 7 and 3 of table S1 (from top to bottom). (e-h) Corresponding histograms showing the final size distribution.

The complete structural data resulting from the TEM analysis is summarized in Table S2, along with the corresponding emission wavelength and measured quantum efficiency (see Methods). Samples 1-4 (5-8) have 20 ML (15 ML) nominal shell thickness.

Figure S10 shows PL spectra and corresponding decay traces for the 15ML shell thickness

Table S2: Structural and optical data for the different DiD samples.

Sample	Core radius (nm)	Final radius (nm)	Shell thickness (nm)	Emission wavelength nm	PL QE. %
1	1.85	8.7	6.9	651	31
2	2.05	7.95	5.9	657	58
3	2.55	8.85	6.3	663	60
4	2.75	9.5	6.8	663	43
5	1.85	6.65	4.8	648	56
6	2.40	6.1	3.7	656	54
7	2.55	6.9	4.4	661	66
8	2.75	8.0	5.3	664	51

DiDs (samples 5 to 8). The figure is analogous to that of the 20ML shell thickness samples shown in Fig. 4(b,c) of the paper.

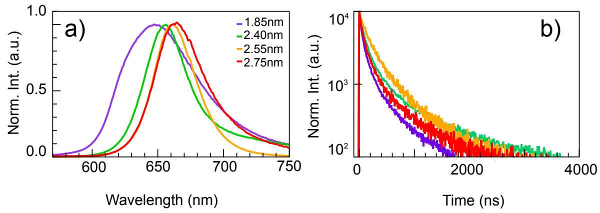

Figure S10: (a) PL spectra for DiD samples 5 to 8. (c) Corresponding PL decay traces.

Exciton lifetimes

Table S3: An accurate fit to the PL decay traces requires a sum of four exponentials. The last decay component has a considerably longer lifetime, and can be attributed to delayed emission.[14] The first three are used to calculate a weighted average lifetime. Weights w_i are determined from the respective amplitudes and lifetimes: $w_i = A_i \tau_i / \sum_{k=1}^{3} (A_k \tau_k)$.

Sample	**Core radius (nm)**	τ_1 **(ns)**	$\mathbf{w_1}$	τ_2 **(ns)**	$\mathbf{w_2}$	τ_3 **(ns)**	$\mathbf{w_3}$	τ_{avg} **(ns)**	$\tau_{delayed}$ **(ns)**
1	1.85	24	0.04	113	0.35	539	0.61	378	3988
2	2.05	49	0.04	189	0.29	773	0.67	572	4325
3	2.55	62	0.06	246	0.27	936	0.67	696	4719
4	2.75	88	0.05	288	0.29	961	0.66	722	4869
5	1.85	31	0.12	106	0.41	388	0.47	229	1673
6	2.40	33	0.07	125	0.40	545	0.53	339	3650
7	2.55	33	0.01	160	0.39	473	0.60	345	1821
8	2.75	41	0.11	139	0.42	505	0.46	298	2479

References

1. Rajadell F.; Royo M.; Planelles J. Strain in Free Standing CdSe/CdS Core-Shell Nanorods. *J. Appl. Phys.* **2012**, *111*, 014303.

2. Climente J.I.; Segarra C.; Rajadell F.; Planelles J. Electrons, Holes, and Excitons in GaAs Polytype Quantum Dots. *J. Appl. Phys.* **2016**, *119*, 125705.

3. Park S.H.; Cho Y.H. Characteristics of Built-in Polarization Potentials in Vertically and Laterally Arranged InGaN/GaN Quantum Dots. *J. Appl. Phys.* **2011**, *109*, 113103.

4. Carbone L.; Nobile C.; De Giorgi M.; Della Sala F.; Morello G.; Pompa P.; Hytch M.; Snoeck E.; Fiore A.; Franchini I.R.; *et al.* Synthesis and Micrometer-Scale Assembly of Colloidal CdSe/CdS Nanorods Prepared by a Seeded Growth Approach. *Nano Lett* **2007**, *7*, 2942-2950.

5. Jaseniak J.; Smith L.; van Embden J.; Mulvaney P.; Califano M. Re-examination of the Size-Dependent Absorption Properties of CdSe Quantum Dots. *J. Phys. Chem. C* **2009**, *113*, 19468.

6. Christodoulou S.; Vaccaro G.; Pinchetti V.; De Donato F.; Grim J.Q.; Casu A.; Genovese A.; Vicidomini G.; Diaspro A.; Brovelli S.; *et al.* Synthesis of Highly Luminescent Wurtzite CdSe/CdS Giant-shell Nanocrystals Using a Fast Continuous Injection Route. *J. Mater. Chem. C* **2014**, *2*, 3439-3447.

7. Leyre S.; Coutino-Gonzalez E.; Joos J.J.; Ryckaert J.; Meuret Y.; Poelman D.; Smet P.F.; Durinck G.; Hofkens J.; Deconinck G.; Hanselaer P. Absolute Determination of Photoluminescence Quantum Efficiency Using an Integrating Sphere Setup. *Rev. Sci. Instrum.* **2014**, *85*, 123115.

8. Eshet H.; Grünwald M.; Rabani E. The Electronic Structure of CdSe/CdS Core/Shell Seeded Nanorods: Type-I or Quasi-Type-II? *Nano Lett.* **2013**, *13*, 5880-5885 (and references therein).

9. Sadao, A. *Handbook of Physical Properties of Semiconductors*; Kluwert Academic Group, 2004.

10. Madelung, O. *Semiconductors: Data Handbook*; Springer, Berlin, 2004.

11. Wei S.H.; Zhang S. B.; Zunger A. First-principles Calculation of Band Offsets, Optical Bowings, and Defects in CdS, CdSe, CdTe, and Their Alloys. *J. Appl. Phys.* **2000**, *87*, 1304âĂŞ1311.

12. Jeon J.B.; Sirenko Y.M.; Kim K. W.; Littlejohn M.A.; Stroscio M.A. Valence Band Parameters of Wurtzite Materials. *Solid State Communications* **1996**, *99*, 423âĂŞ426.

13. Madelung O.; Rössler U.; Schulz M. *II-VI and I-VII Compounds; Semimagnetic Compounds. Volume 41B*; Springer Materials, 1999.

14. Rabouw F.T.; Kamp M.; van Dijk-Moes R.J.A.; Gamelin D.R.; Femius Koenderink A.; Meijerink, A.; Vanmaekelbergh D. Delayed Exciton Emission and Its Relation to Blinking in CdSe Quantum Dots. *Nano Lett.* **2015**, *15*, 7718-7725.

PHYSICAL REVIEW B **93**, 085312 (2016)

Edge states in dichalcogenide nanoribbons and triangular quantum dots

C. Segarra,[1,2] J. Planelles,[1] and S. E. Ulloa[2,*]

[1]*Departament de Química Física i Analítica, Universitat Jaume I, Avenida de Vicent Sos Baynat, s/n, 12071 Castelló de la Plana, Spain*

[2]*Department of Physics and Astronomy and Nanoscale and Quantum Phenomena Institute, Ohio University, Athens, Ohio 45701-2979, USA*

(Received 30 October 2015; revised manuscript received 25 January 2016; published 23 February 2016)

The electronic structure of monolayer MoS_2 nanoribbons and quantum dots has been investigated by means of an effective $\mathbf{k} \cdot \mathbf{p}$ two-band model. Both systems with borders exhibit states spatially localized on the edges and with energies lying in the band gap. We show that the conduction- and valence-band curvatures determine the presence/absence of these states the origin of which has been related to the marginal topological properties of the MoS_2 single-valley Hamiltonian.

DOI: 10.1103/PhysRevB.93.085312

I. INTRODUCTION

Since the discovery of graphene [1], atomically thin layered structures have attracted growing interest and several new two-dimensional (2D) materials have been prepared [2], including hexagonal BN and several transition metal dichalcogenides (TMDCs) [3,4]. There is a great variety of TMDCs, as many metal and chalcogen atoms can be combined to produce materials with properties that include metallic, semiconducting, and even superconducting behavior; the natural diversity of these materials with different properties makes them particularly promising for electronic and optical applications [5,6]. Unlike graphene, TMDCs such as MoS_2 and WS_2 have a finite band gap in the visible frequency range, which is indirect when in bulk (many layer) form, but becomes direct in the single 2D (trilayer) limit—where two S layers are separated by a layer of Mo or W metal atoms [7,8]. The direct gap in many of these single trilayer TMDCs makes them especially attractive candidates for optoelectronic and electronic applications [9–12], such as field-effect transistors [13–15], or photoaddressable sensors [5].

Although we know a great deal about the electronic states in single trilayers, it is important to gain a detailed understanding of the electronic structure of finite size systems such as nanoribbons and quantum dots, in order to fully and reliably tailor the properties of different TMDC materials and possible devices. Several works [16–21] have reported the existence of edge states in the gap of finite MoS_2 systems under different conditions. More recently, consideration of polar discontinuity effects in these and stronger polar materials has predicted the appearance of charged metallic edge states in free-standing ribbons [22,23]. The presence of metallic (dispersive) edge states in TMDCs nanostructures is especially relevant as new device geometries and interfaces become available; they would be expected to strongly affect transport and optical properties of nanoribbons and 2D interfaces [24,25].

Edge or surface states also emerge in topological insulators, as has been intensely discussed in recent literature [26,27]. In those systems, it has been well established that the presence of edge states is a direct consequence of the principle of bulk-edge correspondence [26,28]: gapless states must be present at the domain wall separating two regions with different topological invariants. Although pristine graphene is not a topological insulator due to its weak intrinsic spin-orbit interaction, the origin and character of edge states in gapped and bilayer graphene have been analyzed in terms of the topological properties of the Hamiltonians for individual valleys [29,30]. This analysis is made possible by the close analogy between graphene systems and 2D topological insulators. The details of this analogy and its limitations have been discussed in the literature, but allow one to understand the appearance and characteristics of symmetry allowed states at the edges of finite-size systems [31]. In light of the similar hexagonal structure of graphene and TMDCs, one may wonder if edge states in TMDCs single trilayers could be also analyzed in terms of the topological character imparted by the structure.

In this work, we use a two-band effective $\mathbf{k} \cdot \mathbf{p}$ model to investigate the electronic properties of MoS_2 nanoribbons and small triangular crystallites ("quantum dots") as those appearing naturally in growth chambers. We find the generic appearance of midgap states with wave functions strongly localized near the edges of the structure, which can be clearly identified as edge states. Calculations for various sets of model parameters show that the appearance and characteristics of edge states are controlled by the curvature of the 2D "bulk" band structure. In particular, the sign of the band curvature parameters near the edge of the valence and conduction bands is found to be responsible for whether the edge states exist or not, and the relative magnitude of the effective masses determines the location of the states in the gap. As in graphene systems [31], all of these results can be understood as arising from the marginal topological properties of the MoS_2 single-valley Hamiltonians. In particular, we demonstrate that the Chern number per inequivalent valley is nonvanishing in this structure, which suggests the system may sustain edge states (and yet the system is topological trivial, with overall vanishing Chern number).

We should comment that microscopic details such as bond saturation and/or reconstruction of edges in finite-size systems do affect the appearance and details of edge states. However, the lattice-symmetry "protection" that gives rise to the existence of edge states, as we discuss here, will strengthen the occurrence of such states under the effect of diverse microscopic details.

The remainder of the paper is organized as follows. Section II presents the Hamiltonian used to describe the MoS_2 trilayers. Then, in Sec. III, we show and discuss typical numerical results for the two different systems under study: MoS_2 nanoribbons (Sec. III A) and MoS_2 quantum

*ulloa@ohio.edu

dots (Sec. III B), as defined by triangular crystallites. Finally, conclusions are given in Sec. IV.

II. THEORETICAL MODEL

As mentioned above, single trilayers of TMDC materials such as MoS_2 are composed by a layer of Mo atoms sandwiched between two layers of S atoms. The metal atoms in this structure present trigonal prismatic coordination with the S atoms. The electronic structure of the single trilayer has a direct gap at two nonequivalent points K and K' of the Brillouin zone. Several works have derived an effective $\mathbf{k}\cdot\mathbf{p}$ model in the vicinity of these points in order to study the low-energy physics of TMDC monolayers [32–35]. The proposed two-band Hamiltonian describing the valence and conduction bands up to second order in k can be written as

$$H = \begin{pmatrix} \varepsilon_v + \alpha k^2 & \tau\gamma k_- \\ \tau\gamma k_+ & \varepsilon_c + \beta k^2 \end{pmatrix}, \qquad (1)$$

where $k_\pm = k_x \pm i\tau k_y$, and $\varepsilon_c = \Delta/2$ and $\varepsilon_v = -\Delta/2$ are the band-edge energies with $\Delta = 1.9\,\text{eV}$ standing for the material band gap; $\mathbf{k}$ is the momentum relative to the K/K' points. The constants α, β, and γ are material parameters, while τ identifies the valley K ($\tau = 1$) or K' ($\tau = -1$).

For the sake of simplicity, trigonal warping and other minor modifications present in the original model are neglected, although their inclusion would not qualitatively alter the main conclusions of the work presented here. Hamiltonian (1) takes into account the electron-hole symmetry breaking obtained from first-principles calculations by using unlike parameters α and β. Although different authors report different values of these parameters, some dependent on the details of the calculations, we employ here $\alpha = 1.72\,\text{eV\AA}^2$, $\beta = -0.13\,\text{eV\AA}^2$, and $\gamma = 3.82\,\text{eV\AA}$, as fitted from density functional theory calculations [33], unless noted otherwise.

Notice that Eq. (1) ignores the spin degree of freedom for clarity of presentation. Consideration of spin-orbit coupling in these materials results in effectively producing two valence-band edges, as a spin-dependent gap appears, with corresponding spin-valley coupling in the valence band. The conduction band in MoS_2 has a sizable but relatively weaker spin-orbit splitting [36,37]. Spin-orbit interactions will then result in a doubling of the states we discuss here. We revisit this issue in the discussion section below. We also notice that the edges of the nanostructures are defined by hard-wall boundary conditions in all simulations, and are assumed to result in no intervalley coupling—as expected of zigzag edges, although the full equivalence of these conditions would require further investigations, especially as detailed comparisons with experiments develop [21].

III. NUMERICAL RESULTS AND DISCUSSION

We study the electronic properties of two different types of 2D nanostructures: *nanoribbons*, where particles are confined in one direction, and *quantum dots*, where they are confined to triangular nanocrystallites. The calculations are carried out using COMSOL utilities over a fine grid (the finest default), and converged until the desired accuracy (typically 10^{-12} in the eigenvalues).

A. Nanoribbons

The nanoribbons are defined over a finite width along the direction x in our calculations, while maintaining translational invariance along the y direction. As such, the momentum k_y is a good quantum number and the two-component spinor wave function of Hamiltonian (1) can be written in the form $\psi(x,y) = e^{ik_y y}\phi(x)$, where ψ and ϕ have components over the c,v basis. As a consequence, the eigenvalue equation of this 2D Hamiltonian turns into a set of two coupled second-order differential equations in one dimension that depend on the quantum number k_y. We solve numerically these equations for an MoS_2 nanoribbon of 10-nm width, wide enough to allow decoupled states on both edges, as we will see. The results obtained are summarized in Fig. 1.

Figure 1(b) shows the calculated sub-band dispersion. Notice that the finite width of the ribbon has only slightly opened the gap, as the effective masses near the band edges, m_v and m_c, are both ≈ 0.5, and the size quantization is only a few meV. Most importantly, we find two states inside the band gap, with a nearly linear dispersion. The levels cross at $k_y = 0$ and $E = 0.816\,\text{eV}$, relatively close to the edge of the conduction band. These midgap states disperse upwards in energy, close to the conduction band for not large k_y values [$k_y \approx \pm 0.05(2\pi/a_0)$, see Fig. 1(b)], and soon admix with the band states, becoming indistinguishable from them. For lower energies, however, the midgap states remain well defined and exhibit increasing edge localization, as we will see below.

In order to study the origin of these states, and dependence on band-structure features, we carry out the same calculations but for other sets of parameters than those in Ref. [33]. We only tune the α and β values since γ does not qualitatively affect the results. In Fig. 1(a) we exchange the signs of both α and β ($\alpha = -1.72\,\text{eV\AA}^2$ and $\beta = 0.13\,\text{eV\AA}^2$) and observe that the states lying inside the gap disappear. In Fig. 1(c) we keep the signs unaltered to those in panel (b) but modify β to have the same absolute value of α ($\alpha = 1.72\,\text{eV\AA}^2$ and $\beta = -1.72\,\text{eV\AA}^2$).

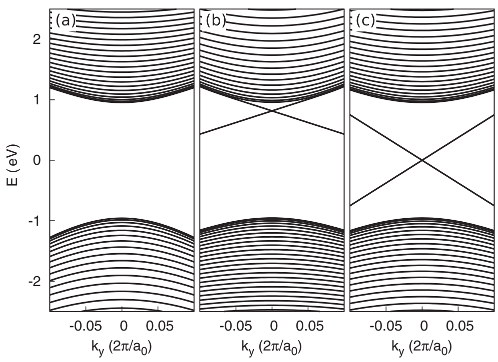

FIG. 1. Energy-band dispersion for MoS_2 nanoribbons considering different values of α and β: (a) $\alpha = -1.72\,\text{eV\AA}^2$ and $\beta = 0.13\,\text{eV\AA}^2$, (b) $\alpha = 1.72\,\text{eV\AA}^2$ and $\beta = -0.13\,\text{eV\AA}^2$, and (c) $\alpha = 1.72\,\text{eV\AA}^2$ and $\beta = -1.72\,\text{eV\AA}^2$. The edges are parallel to the y direction, and the wave vector k_y is measured with respect to the K valley, where $a_0 = 3.193$ Å is the lattice constant.

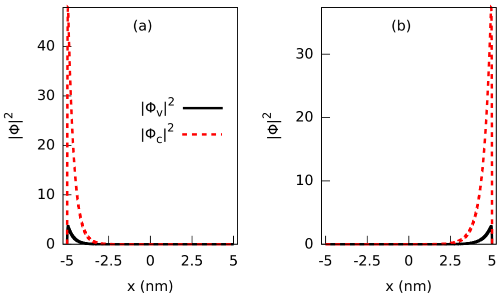

FIG. 2. Wave-function squared modulus $|\phi|^2$ of the two states at $k_y = 0.01 \times 2\pi/a_0$, with energies lying in the band gap (a) $E = 0.778$ eV and (b) $E = 0.855$ eV. Black solid lines correspond to the valence-band component and red dashed lines correspond to the conduction band.

In this case, the two states inside the gap are still present but they have lower energies compared to Fig. 1(b). As expected from symmetry, the dispersion bands now cross at $k_y = 0$ and $E = 0$, since $\alpha = \beta$ confers electron-hole symmetry to the Hamiltonian.

By comparing the results in Fig. 1 for the three sets of parameters, it is clear that the presence or absence of states inside the gap is determined by the sign of both α and β curvatures. Midgap states exist if $\alpha > 0$ and $\beta < 0$ and are absent if $\alpha < 0$ and $\beta > 0$ [38]. Furthermore, changes in the relative value of these two parameters affect the energy of the states inside the gap. When $|\alpha| > |\beta|$ the states are closer to the conduction band as in Fig. 1(b), and when $|\alpha| < |\beta|$ they become closer to the valence band.

One can qualitatively analyze this behavior in terms of the "bare" effective masses for valence and conduction bands, as determined by the α and β coefficients. A negative β (and corresponding negative mass $\simeq 1/\beta$) in the conduction band is "inverted," and that symmetry is contained in the states even after the mixing due to γ. The inverse effective masses for the full Hamiltonian (1) near the edges are, however, given by $2(\beta + \gamma^2/\Delta)/\hbar^2$ for the conduction band, and by $2(\alpha - \gamma^2/\Delta)/\hbar^2$ for the valence band, and therefore dominated by the large value of γ.

To further explore the nature of the states inside the gap, we analyze the wave functions in Fig. 2. As an example, we choose the states for $k_y = 0.01 \times 2\pi/a_0$ in Fig. 1(b), which are slightly away from the degeneracy point, and well away from the conduction band states. Figure 2(a) corresponds to the lower state at $E = 0.778$ eV and Fig. 2(b) corresponds to the higher one at $E = 0.855$ eV. We clearly observe that both states are localized at opposite edges of the MoS_2 nanoribbon—and have opposite dispersion, as expected of independent edge states. We see that the conduction-band component (red dashed line) is the dominant contribution to the wave function. Calculation of the relative weight of the two components yields $w(\phi_c) = 93\%$ and $w(\phi_v) = 7\%$ for the conduction- and valence-band components, respectively. These values can be directly obtained from the parameters α and β using the expressions $w(\phi_c) = |\beta|/(|\alpha| + |\beta|)$ and $w(\phi_v) = |\alpha|/(|\alpha| + |\beta|)$. These expressions hold as long as the edge states are relatively far from the bulk bands. Notice also the asymmetry in the wave functions as seen, for instance, in the different maximum value of $|\phi_c|^2$, and their different x extension. This asymmetry is due to the proximity of the conduction band. The higher-energy edge state is slightly more admixed with the bulk states and, thus, its wave-function results somewhat more delocalized. The asymmetry in the states continues to grow as k_y increases further.

The results summarized in Figs. 1 and 2 can be related to those coming from the model proposed by Bernevig, Hughes, and Zhang [39], in connection with the observation of the quantum spin Hall effect (QSHE). In that work, the QSHE was predicted in HgTe quantum wells larger than a critical thickness, due to a band inversion in the low-energy effective Hamiltonian. For $\Delta < 0$, bands are inverted and the system shows topological behavior. One consequence is that edge states will form when a transition between two distinct topological phases takes place, as predicted by the principle of bulk-edge correspondence [26]. In our system, Eq. (1), we have $\Delta > 0$, which is apparently trivial, although the sign of the bare band curvatures ($\alpha > 0$ and $\beta < 0$) yields also a situation with inverted bands. As such, the origin of the edge states here can be analyzed in terms of the topological character of the model in Eq. (1).

To explore this relationship further, Fig. 3 shows the energy spectrum as a function of Δ, for a given set of α and β parameters. The spectra shown are for $k_y = 0$ and band curvatures $\alpha = 1.72$ eVÅ^2 and $\beta = -0.13$ eVÅ^2 in Fig. 3(a), and $\alpha = 1.72$ eVÅ^2 and $\beta = -1.72$ eVÅ^2 in Fig. 3(b). Two red dashed lines in each panel show the limits of the band gap, for reference. In both cases shown, we see that a trivial situation develops, with no states in the gap, for negative Δ values. As Δ increases and changes to positive values, the conduction and valence bands seem to be similar, except for the appearance of a pair (for $k_y = 0$) of degenerate edge states with energies clearly in the gap. Notice that the edge states separate from the conduction band for larger Δ values in Fig. 3(a), but remain

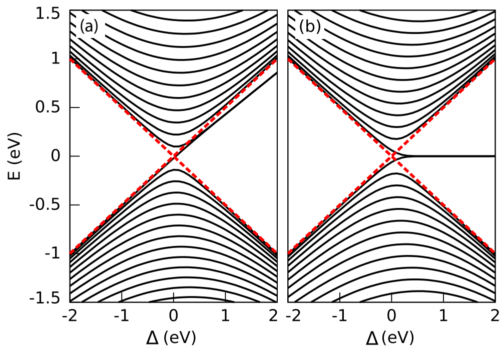

FIG. 3. Energy spectrum of a MoS_2 nanoribbon as in Fig. 1, shown as a function of the band gap Δ, for $k_y = 0$. Two sets of parameters are considered: (a) $\alpha = 1.72$ eVÅ^2 and $\beta = -0.13$ eVÅ^2 and (b) $\alpha = 1.72$ eVÅ$^2 = -\beta$. Red dashed lines indicate the edges of the band gap. Midgap edge states appear for $\Delta > 0$ in both cases.

exactly equidistant from both bands for $|\alpha| = |\beta|$ in Fig. 3(b), as expected, appearing closer to the conduction band for more asymmetric $|\alpha| > |\beta|$ values.

Next, we look at these results with the help of the Chern number associated with the occupied band (topological invariant). For a two-level Hamiltonian written in the form $H(\mathbf{k}) = \mathbf{g}(\mathbf{k}) \cdot \boldsymbol{\sigma}$, where $\boldsymbol{\sigma}$ is a vector with the Pauli matrices as components, the Chern number is given by [26]

$$c = \frac{1}{4\pi} \int d^2k(\partial_{k_x} \hat{\mathbf{g}} \times \partial_{k_y} \hat{\mathbf{g}}) \cdot \hat{\mathbf{g}} , \tag{2}$$

where $\hat{\mathbf{g}} = \mathbf{g}/|\mathbf{g}|$ and the integral is computed over the entire Brillouin zone. For the Hamiltonian in Eq. (1), one obtains $c = \tau/2[\mathrm{sgn}\,(\Delta) + \mathrm{sgn}\,(\alpha - \beta)]$, fully independent of the value of γ. That means that for $\Delta > 0$ one obtains $c = 0$ for $\alpha < \beta$, while $c = \tau$ for $\alpha > \beta$. A nonzero value of c suggests that a topological invariant is present, and this goes along with the previous discussion based on band inversion arguments. It is important to note, however, that the contribution of the K and K' valleys to the topological invariant has opposite signs, which produces an overall $c = 0$. As a result, one can strictly state that multivalley materials such as graphene or MoS_2 are topologically trivial.

In spite of the strict trivial topology of Eq. (1), a nonvanishing c for a single valley can be associated with marginal topological properties, in analogy with topological insulators [31]. This analogy has, however, important limitations. Since c per valley is not a well-defined topological invariant, $c \neq 0$ does not guarantee the existence of edge states at the boundaries with the vacuum. Furthermore, and perhaps most important, is the fact that if edge states are present they are not topologically protected against backscattering and can then be affected by any type of disorder and/or valley coupling. Nevertheless, it is the case that edge states in bilayer graphene have been shown to be robust under moderate disorder [29], and to exhibit pure valley currents, as indicated by the local valley Berry curvature and associated Chern number [40,41].

We should also comment that although, for simplicity, we have suppressed the spin degree of freedom in these calculations its role can be easily established. The presence of spin clearly results in *two* edge states per border of the structure, instead of the single state presented above [see Fig. 1(b)]. As the spin-orbit interaction in the valence band is large (yet much smaller than the band gap, and diagonal, pinning the spin projection to each of the valleys), the two edge states on the same border but different spin projection appear slightly shifted in energy and with minimally different dispersion (not shown). This simple duplication of edge states with different spins and energies would of course be strongly affected if the edges couple valleys, something that will depend on the border terminations and corresponding boundary conditions [18,21].

B. MoS_2 triangular quantum dots

We next investigate the electronic properties of MoS_2 quantum dots formed by finite-size flakes, using our Hamiltonian model and appropriate boundary conditions. Similar structures have also been studied by different approaches in the small-crystallite regime [42,43]. The flakes are equilateral triangles, as it is a commonly synthesized shape [44–47]. In this case, carriers are confined in the two directions of space and we must numerically solve the coupled differential equations in two variables in order to find eigenvalues and eigenfunctions of the Hamiltonian. In the results that follow, Fig. 4, the quantum dot side length is 10 nm, and we employ the same parameters as in the previous section [see Fig. 1(b)].

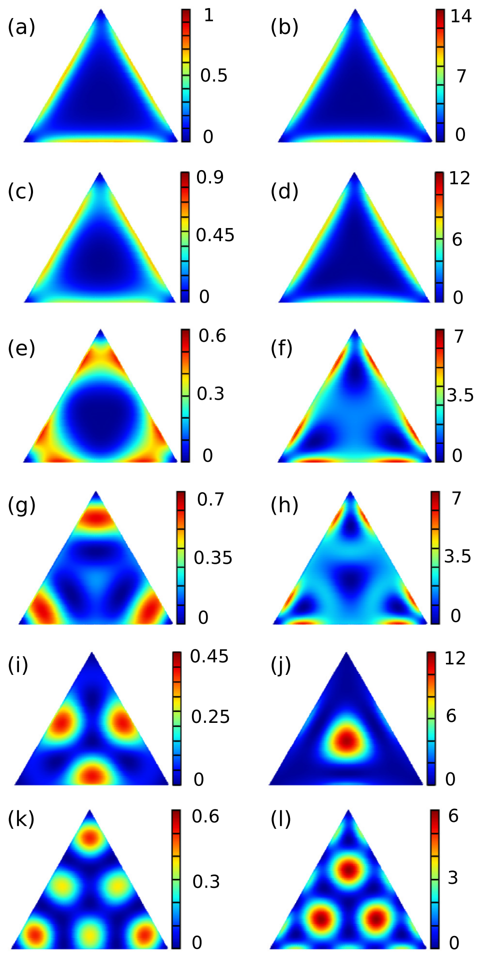

FIG. 4. Wave-function squared modulus of selected states with energies close to the conduction band. Left and right columns illustrate the valence-band $|\phi_v|^2$ and conduction-band $|\phi_c|^2$ components, respectively. Different states are arranged in rows with increasing energy: (a, b) $E = 0.907$ eV, (c, d) $E = 0.962$ eV, (e, f) $E = 1.015$ eV, (g, h) $E = 1.022$ eV, (i, j) $E = 1.057$ eV, and (k, l) $E = 1.100$ eV. As before, $|\phi_c|^2$ components are generally larger for these states, close to the conduction band.

The results obtained for this system show the presence of several states with energies in the gap. They can be seen as the result of the discretization of the edge states along each border, which are then hybridized near the corners of the flake. We illustrate this behavior in Fig. 4, where the squared modulus of the wave function for a selection of states with energy close to the conduction band ($E \approx 0.95$ eV) is shown. We choose this range of energies because we know that for $\alpha = 1.72\,\mathrm{eV\AA^2}$ and $\beta = -0.13\,\mathrm{eV\AA^2}$ [33] the edge states are closer to the conduction band. By gradually increasing energy, we also get to compare the clearly "bulk" and edge states in the flake. In Figs. 4(a)–4(d) we can see that the first two states are clearly edge states with wave functions localized near the triangle border, with similar appearance to that shown in Fig. 2 near each of the edges. The next two states in energy, Figs. 4(e)–4(h), also show wave functions mainly near the edges, but noticeably more delocalized than the previous two. This suggests that the edge states are partially admixed with the bulk conduction band, due to their energy proximity. Finally, Figs. 4(i)–4(l) show two conduction states with wave functions completely delocalized over the entire triangular quantum dot. A representation of the real and imaginary parts of the wave functions (not shown) allows one to see the wave-function nodes more easily, and see that their number increases with the energy of the states, an expected signature of quantization.

We should emphasize that we have also found the same pattern of edge states appearing for the curvature parameters as in the case of nanoribbons. As such, one can also invoke the marginal topological character of the Hamiltonian as the origin of edge states in these zero-dimensional nanostructures.

IV. CONCLUSIONS

The low-energy electronic structure of monolayer MoS_2 nanoribbons and quantum dots has been investigated using an effective two-band $\mathbf{k} \cdot \mathbf{p}$ model. We have shown that both systems present edge states with energies in the gap. Nanoribbons exhibit only one state per edge at a given value of the quantum number k_y, while in quantum dots, due to full confinement, the edge states appear distinctly away from the states that would form the sub-band continuum in a large triangular flake. As the energy of the edge states increases, for both nanoribbons and quantum dots, the edge states hybridize with the "bulk" and cease to be so well localized near the edges of the structure.

We have also found that the curvature of the bands, represented by parameters α and β, determines the presence ($\alpha > 0$ and $\beta < 0$) or absence ($\alpha < 0$ and $\beta > 0$) of edge states as well as their energy. This behavior is reminiscent of the marginal topological properties of materials such as MoS_2, as the Chern number per valley is indeed nonzero, reflecting a finite Berry curvature in each valley. Similar results are of course expected for other TMDC nanostructures, as long as the relative band curvature parameter signs are similar to those presented here.

We should emphasize that first-principles calculations are typically used to determine continuum model parameters. As the former may depend on functionals and other details of the calculations, the latter may indeed vary among different implementations and/or authors. In fact, some fittings result in values of α and β that are indeed substantially different, and for which the edge states we discuss here are not apparent [33]. It is also clear that tight-binding parametrizations may similarly allow for the presence of edge states, as explicitly seen in the literature [19]. These edge states, however, are found to be rather robust and to exist over a wide range of parameters. Similar conclusions have been reached in a recent preprint [48].

We draw the attention of the reader to the issue of atomic reconstructions and bondings in real crystallites. Such microscopic effects would surely modify the detailed edge state dispersions and characteristics of the states we have discussed here. Polarization and charge compensation may even result in interesting charged edge states, unlike those we have discussed [22,23]. It would be interesting to explore both theoretically and experimentally how truly robust these edge states are in nanoribbons and other natural structures with edges, and understand how the different effects compete. Exploring what observable consequences they have on the effective trapping of photoactivated carriers and excitons, or how they modulate the interaction between adsorbed/embedded impurity atoms, may provide further insights into the appearance of edge states in these systems.

ACKNOWLEDGMENTS

This work was supported by a Spanish FPU Grant (C.S.). Support from NSF Grant No. DMR-1508325 (S.E.U.), UJI Project No. P1.1B2014-24, and MINECO Project No. CTQ2014-60178-P (J.P.) is acknowledged.

[1] K. S. Novoselov, A. K. Geim, S. V. Morozov, D. Jiang, Y. Zhang, S. V. Dubonos, I. V. Grigorieva, and A. A. Firsov, Science **306**, 666 (2004).

[2] K. S. Novoselov, D. Jiang, F. Schedin, T. J. Booth, V. V. Khotkevich, S. V. Morozov, and A. K. Geim, Proc. Natl. Acad. Sci. USA **102**, 10451 (2005).

[3] P. Miró, M. Audiffred, and T. Heine, Chem. Soc. Rev. **43**, 6537 (2014).

[4] S. Z. Butler, S. M. Hollen, L. Cao, Y. Cui, J. A. Gupta, H. R. Gutiérrez, T. F. Heinz, S. S. Hong, J. Huang, A. F. Ismach, E. Johnston-Halperin, M. Kuno, V. V. Plashnitsa, R. D. Robinson, R. S. Ruoff, S. Salahuddin, J. Shan, L. Shi, M. G. Spencer, M. Terrones, W. Windl, and J. E. Goldberger, ACS Nano **7**, 2898 (2013).

[5] Q. H. Wang, K. Kalantar-Zadeh, A. Kis, J. N. Coleman, and M. S. Strano, Nat. Nanotechnol. **7**, 699 (2012).

[6] Z. M. Wang, *MoS_2: Materials, Physics, and Devices* (Springer, Switzerland, 2014).

[7] K. F. Mak, C. Lee, J. Hone, J. Shan, and T. F. Heinz, Phys. Rev. Lett. **105**, 136805 (2010).

[8] A. Splendiani, L. Sun, Y. Zhang, T. Li, J. Kim, C. Y. Chim, G. Galli, and F. Wang, Nano Lett. **10**, 1271 (2010).

[9] L. Britnell, R. M. Ribeiro, A. Eckmann, R. Jalil, B. D. Belle, A. Mishchenko, Y.-J. Kim, R. V. Gorbachev, T. Georgiou, S. V. Morozov, A. N. Grigorenko, A. K. Geim, C. Casiraghi, A. H. Castro Neto, and K. S. Novoselov, Science **340**, 1311 (2013).
[10] A. Pospischil, M. M. Furchi, and T. Mueller, Nat. Nanotechnol. **9**, 257 (2014).
[11] J. S. Ross, P. Klement, A. M. Jones, N. J. Ghimire, J. Yan, D. G. Mandrus, T. Taniguchi, K. Watanabe, K. Kitamura, W. Yao, D. H. Cobden, and X. Xu, Nat. Nanotechnol. **9**, 268 (2014).
[12] B. W. H. Baugher, H. O. H. Churchill, Y. Yang, and P. Jarillo-Herrero, Nat. Nanotechnol. **9**, 262 (2014).
[13] B. Radisavljevic, A. Radenovic, J. Brivio, V. Giacometti, and A. Kis, Nat. Nanotechnol. **6**, 147 (2011).
[14] D. Lembke and A. Kis, ACS Nano **6**, 10070 (2012).
[15] H. Wang, L. Yu, Y.-H. Lee, Y. Shi, A. Hsu, M. L. Chin, L.-J. Li, M. Dubey, J. Kong, and T. Palacios, Nano Lett. **12**, 4674 (2012).
[16] M. V. Bollinger, J. V. Lauritsen, K. W. Jacobsen, J. K. Nørskov, S. Helveg, and F. Besenbacher, Phys. Rev. Lett. **87**, 196803 (2001).
[17] H. Pan and Y.-W. Zhang, J. Mater. Chem. **22**, 7280 (2012).
[18] E. Erdogan, I. H. Popov, A. N. Enyashin, and G. Seifert, Eur. Phys. J. B **85**, 33 (2012).
[19] S. Pavlović and F. M. Peeters, Phys. Rev. B **91**, 155410 (2015).
[20] D. Davelou, G. Kopidakis, G. Kioseoglou, and I. N. Remediakis, Solid State Commun. **192**, 42 (2014).
[21] C. G. Péterfalvi, A. Kormányos, and G. Burkard, Phys. Rev. B **92**, 245443 (2015).
[22] F. Güller, A. M. Llois, J. Goniakowski, and C. Noguera, Phys. Rev. B **87**, 205423 (2013).
[23] M. Gibertini and N. Marzari, Nano Lett. **15**, 6229 (2015).
[24] Y. Gong, J. Lin, X. Wang, G. Shi, S. Lei, Z. Lin, X. Zou, G. Ye, R. Vajtai, B. I. Yakobson, H. Terrones, M. Terrones, B. K. Tay, J. Lou, S. T. Pantelides, Z. Liu, W. Zhou, and P. M. Ajayan, Nat. Mater. **13**, 1135 (2014).
[25] K. Chen, X. Wan, J. Wen, W. Xie, Z. Kang, X. Zeng, H. Chen, and J.-B. Xu, ACS Nano **9**, 9868 (2015).
[26] M. Z. Hasan and C. L. Kane, Rev. Mod. Phys. **82**, 3045 (2010).
[27] Special topic on topological insulators, APL Mat. **3**, issue 8 (2015).
[28] J. C. Y. Teo and C. L. Kane, Phys. Rev. B **82**, 115120 (2010).
[29] J. Li, I. Martin, M. Büttiker, and A. F. Morpurgo, Nat. Phys. **7**, 38 (2011).
[30] W. Yao, S. A. Yang, and Q. Niu, Phys. Rev. Lett. **102**, 096801 (2009).
[31] J. Li, A. F. Morpurgo, M. Büttiker, and I. Martin, Phys. Rev. B **82**, 245404 (2010).
[32] G. B. Liu, W. Y. Shan, Y. Yao, W. Yao, and D. Xiao, Phys. Rev. B **88**, 085433 (2013).
[33] A. Kormányos, V. Zólyomi, N. D. Drummond, P. Rakyta, G. Burkard, and V. I. Fal'ko, Phys. Rev. B **88**, 045416 (2013).
[34] H. Rostami, A. G. Moghaddam, and R. Asgari, Phys. Rev. B **88**, 085440 (2013).
[35] A. Kormányos, G. Burkard, M. Gmitra, J. Fabian, V. Zólyomi, N. D. Drummond, and V. Fal'ko, 2D Mater. **2**, 022001 (2015).
[36] K. Kośmider, J. W. González, and J. Fernández-Rossier, Phys. Rev. B **88**, 245436 (2013).
[37] A. Kormányos, V. Zólyomi, N. D. Drummond, and G. Burkard, Phys. Rev. X **4**, 011034 (2014).
[38] We do not consider parameters α and β with the same sign since in these cases there is not a real gap separating the bands.
[39] B. A. Bernevig, T. L. Hughes, and S.-C. Zhang, Science **314**, 1757 (2006).
[40] R. V. Gorbachev, J. C. W. Song, G. L. Yu, A. V. Kretinin, F. Withers, Y. Cao, A. Mishchenko, I. V. Grigorieva, K. S. Novoselov, L. S. Levitov, and A. K. Geim, Science **346**, 448 (2014).
[41] Y. Shimazaki, M. Yamamoto, I. V. Borzenets, K. Watanabe, T. Taniguchi, and S. Tarucha, Nat. Phys. **11**, 1032 (2015).
[42] H. Schweiger, P. Raybaud, G. Kresse, and H. Toulhoat, J. Catal. **207**, 76 (2002).
[43] T. Li and G. Galli, J. Phys. Chem. C **111**, 16192 (2007).
[44] X. Duan, C. Wang, J. C. Shaw, R. Cheng, Y. Chen, H. Li, X. Wu, Y. Tang, Q. Zhang, A. Pan, J. Jiang, R. Yu, Y. Huang, and X. Duan, Nat. Nanotechnol. **9**, 1024 (2014).
[45] M. S. J. Marshall and M. R. Castell, Chem. Soc. Rev. **43**, 2226 (2014).
[46] Z. Liu, M. Amani, S. Najmaei, Q. Xu, X. Zou, W. Zhou, T. Yu, C. Qiu, A. G. Birdwell, F. J. Crowne, R. Vajtai, B. I. Yakobson, Z. Xia, M. Dubey, P. M. Ajayan, and J. Lou, Nat. Commun. **5**, 5246 (2014).
[47] W. Bao, N. J. Borys, C. Ko, J. Suh, W. Fan, A. Thron, Y. Zhang, A. Buyanin, J. Zhang, S. Cabrini, P. D. Ashby, A. Weber-Bargioni, S. Tongay, S. Aloni, D. F. Ogletree, J. Wu, M. B. Salmeron, and P. J. Schuck, Nat. Commun. **6**, 7993 (2015).
[48] A preprint submitted after ours describes the appearance of edge states in monolayer MoS_2 using tight-binding and low-energy Hamiltonians. They reach very similar conclusions to ours, and emphasize the topological protection of the edge modes. See H. Rostami, R. Asgari, and F. Guinea, arXiv:1511.07003.

Bibliography

[1] M. V. Kovalenko, L. Manna, A. Cabot, Z. Hens, D. V. Talapin, C. R. Kagan, V. I. Klimov, A. L. Rogach, P. Reiss, D. J. Milliron, P. Guyot-Sionnnest, G. Konstantatos, W. J. Parak, T. Hyeon, B. A. Korgel, C. B. Murray, and W. Heiss, *Prospects of nanoscience with nanocrystals*, ACS Nano **9**, 1012 (2015).

[2] M. A. Kastner, *Artificial atoms*, Phys. Today **46**, 24 (1993).

[3] D. J. Norris, *Measurement and assignment of the size-dependent optical spectrum in cadmium selenide (CdSe) quantum dots*, Ph.D. thesis, Massachusetts Institute of Technology (1995).

[4] P. V. Kamat, *Quantum dot solar cells. Semiconductor nanocrystals as light harvesters*, J. Phys. Chem. C **112**, 18737 (2008).

[5] W. R. Algar, A. J. Tavares, and U. J. Krull, *Beyond labels: A review of the application of quantum dots as integrated components of assays, bioprobes, and biosensors utilizing optical transduction*, Anal. Chim. Acta **673**, 1 (2010).

[6] D. D. Awschalom, D. Loss, and N. Samarth, eds., *Semiconductor spintronics and quantum computation* (Springer, Berlin, 2002).

[7] V. Wood and V. Bulović, *Colloidal quantum dot light-emitting devices*, Nano Rev. **1**, 5202 (2010).

[8] T.-H. Kim, K.-S. Cho, E. K. Lee, S. J. Lee, J. Chae, J. W. Kim, D. H. Kim, J.-Y. Kwon, G. Amaratunga, S. Y. Lee, B. L. Choi, Y. Kuk, J. M. Kim, and K. Kim, *Full-colour quantum dot displays fabricated by transfer printing*, Nat. Photonics **5**, 176 (2011).

[9] E. Jang, S. Jun, H. Jang, J. Lim, B. Kim, and Y. Kim, *White-light-emitting diodes with quantum dot color converters for display backlights*, Adv. Mater. **22**, 3076 (2010).

[10] L. Jacak, P. Hawrylak, and A. Wójs, *Quantum dots* (Springer, Berlin, 1998).

[11] D. Bimberg, M. Grundmann, and N. N. Ledentsov, *Quantum dot heterostructures* (Wiley, Chichester, U.K., 1999).

[12] M. A. Reed, R. T. Bate, K. Bradshaw, W. M. Duncan, W. R. Frensley, J. W. Lee, and H. D. Shih, *Spatial quantization in GaAs-AlGaAs multiple quantum dots*, J. Vac. Sci. Technol. B **4**, 358 (1986).

[13] B. J. van Wees, L. P. Kouwenhoven, C. J. P. M. Harmans, J. G. Williamson, C. E. Timmering, M. E. I. Broekaart, C. T. Foxon, and J. J. Harris, *Observation of zero-dimensional states in a one-dimensional electron interferometer*, Phys. Rev. Lett. **62**, 2523 (1989).

[14] U. Meirav, M. A. Kastner, and S. J. Wind, *Single-electron charging and periodic conductance resonances in GaAs nanostructures*, Phys. Rev. Lett. **65**, 771 (1990).

[15] C. G. Smith, M. Pepper, H. Ahmed, J. E. F. Frost, D. G. Hasko, D. C. Peacock, D. A. Ritchie, and G. A. C. Jones, *The transition from one- to zero-dimensional ballistic transport*, J. Phys. C Solid State **21**, 893 (1988).

[16] L. Goldstein, F. Glas, J. Y. Marzin, M. N. Charasse, and G. Le Roux, *Growth by molecular beam epitaxy and characterization of InAs/GaAs strained-layer superlattices*, Appl. Phys. Lett. **47**, 1099 (1985).

[17] P. M. Petroff and S. P. DenBaars, *MBE and MOCVD growth and properties of self-assembling quantum dot arrays in III-V semiconductor structures*, Superlattices Microst. **15**, 15 (1994).

[18] C. B. Murray, C. R. Kagan, and M. G. Bawendi, *Synthesis and characterization of monodisperse nanocrystals and close-packed nanocrystal assembles*, Annu. Rev. Mater. Sci. **30**, 545 (2000).

[19] A. I. Ekimov, A. L. Efros, and A. A. Onushchenko, *Quantum size effect in semiconductor microcrystals*, Solid State Commun. **56**, 921 (1985).

[20] D. Spirkoska, J. Arbiol, A. Gustafsson, S. Conesa-Boj, F. Glas, I. Zardo, M. Heigoldt, M. H. Gass, A. L. Bleloch, S. Estrade, M. Kaniber, J. Rossler, F. Peiro, J. R. Morante, G. Abstreiter, L. Samuelson, and A. Fontcuberta i Morral, *Structural and optical properties of high quality zinc-blende/wurtzite GaAs nanowire heterostructures*, Phys. Rev. B **80**, 245325 (2009).

[21] N. Akopian, G. Patriarche, L. Liu, J.-C. Harmand, and V. Zwiller, *Crystal phase quantum dots*, Nano Lett. **10**, 1198 (2010).

[22] K. S. Novoselov, A. K. Geim, S. V. Morozov, D. Jiang, Y. Zhang, S. V. Dubonos, I. V. Grigorieva, and A. A. Firsov, *Electric field effect in atomically thin carbon films*, Science **306**, 666 (2004).

[23] A. D. Güçlü, P. Potasz, M. Korkusinski, and P. Hawrylak, *Graphene quantum dots* (Springer, Berlin, 2014).

[24] P. Recher and B. Trauzettel, *Quantum dots and spin qubits in graphene*, Nanotechnology **21**, 302001 (2010).

[25] J. Shen, Y. Zhu, X. Yang, and C. Li, *Graphene quantum dots: emergent nanolights for bioimaging, sensors, catalysis and photovoltaic devices*, Chem. Commun. **48**, 3686 (2012).

[26] X.-X. Song, D. Liu, V. Mosallanejad, J. You, T.-Y. Han, D.-T. Chen, H.-O. Li, G. Cao, M. Xiao, G.-C. Guo, and G.-P. Guo, *A gate defined quantum dot on the two-dimensional transition metal dichalcogenide semiconductor* WSe_2, Nanoscale **7**, 16867 (2015).

[27] W. Qiao, S. Yan, X. Song, X. Zhang, Y. Sun, X. Chen, W. Zhong, and Y. Du, *Monolayer* MoS_2 *quantum dots as catalysts for efficient hydrogen evolution*, RSC Adv. **5**, 97696 (2015).

[28] A. Srivastava, M. Sidler, A. V. Allain, D. S. Lembke, A. Kis, and A. Imamoğlu, *Optically active quantum dots in monolayer* WSe_2, Nat. Nanotechnol. **10**, 491 (2015).

[29] E. C. Le Ru, P. Howe, T. S. Jones, and R. Murray, *Strain-engineered InAs/GaAs quantum dots for long-wavelength emission*, Phys. Rev. B **67**, 165303 (2003).

[30] J. Zhang, Y. Huo, A. Rastelli, M. Zopf, B. Höfer, Y. Chen, F. Ding, and O. G. Schmidt, *Single photons on-demand from light-hole excitons in strain-engineered quantum dots*, Nano Lett. **15**, 422 (2015).

[31] L. C. Lew Yan Voon and M. Willatzen, *The* $k{\cdot}p$ *method* (Springer, Berlin, 2009).

[32] G. L. Bir and G. E. Pikus, *Symmetry and strain-induced effects in semiconductors* (Wiley, New York, 1974).

[33] R. Winkler, *Spin-orbit coupling effects in two-dimensional electron and hole systems* (Springer, Berlin, 2003).

[34] P.-O. Löwdin, *A note on the quantum-mechanical perturbation theory*, J. Chem. Phys. **19**, 1396 (1951).

[35] G. Bastard, *Wave mechanics applied to semiconductor heterostructures* (Les éditions de physique, Les Ulis, France, 1988).

[36] D. J. BenDaniel and C. B. Duke, *Space-charge effects on electron tunneling*, Phys. Rev. **152**, 683 (1966).

[37] M. G. Burt, *A new effective-mass equation for microstructures*, Semicond. Sci. Technol. **3**, 1224 (1988).

[38] M. G. Burt, *The justification for applying the effective-mass approximation to microstructures*, J. Phys.: Condens. Matter **4**, 6651 (1992).

[39] M. G. Burt, *Fundamentals of envelope function theory for electronic states and photonic modes in nanostructures*, J. Phys.: Condens. Matter **11**, 53 (1999).

[40] B. A. Foreman, *Effective-mass Hamiltonian and boundary conditions for the valence bands of semiconductor microstructures*, Phys. Rev. B **48**, 4964 (1993).

[41] B. A. Foreman, *Elimination of spurious solutions from eight-band k·p theory*, Phys. Rev. B **56**, R12748 (1997).

[42] A. De and C. E. Pryor, *Predicted band structures of III-V semiconductors in the wurtzite phase*, Phys. Rev. B **81**, 155210 (2010).

[43] S. L. Chuang and C. S. Chang, *k·p method for strained wurtzite semiconductors*, Phys. Rev. B **54**, 2491 (1996).

[44] Y. M. Sirenko, J.-B. Jeon, K. W. Kim, M. A. Littlejohn, and M. A. Stroscio, *Envelope-function formalism for valence bands in wurtzite quantum wells*, Phys. Rev. B **53**, 1997 (1996).

[45] M. F. Schubert, *Interband tunnel junctions for wurtzite III-nitride semiconductors based on heterointerface polarization charges*, Phys. Rev. B **81**, 035303 (2010).

[46] P. E. Faria Junior and G. M. Sipahi, *Band structure calculations of InP wurtzite/zinc-blende quantum wells*, J. Appl. Phys. **112**, 103716 (2012).

[47] S.-H. Park and S.-L. Chuang, *Comparison of zinc-blende and wurtzite GaN semiconductors with spontaneous polarization and piezoelectric field effects*, J. Appl. Phys. **87**, 353 (2000).

[48] J. M. Luttinger, *Quantum theory of cyclotron resonance in semiconductors: general theory*, Phys. Rev. **102**, 1030 (1956).

[49] J. I. Climente, J. Planelles, and W. Jaskólski, *Magneto-optical transitions in nanoscopic rings*, Phys. Rev. B **68**, 075307 (2003).

[50] J. Planelles and W. Jaskólski, *k·p Hamiltonians for quantum dots in a magnetic field*, J. Phys.: Condens. Matter **15**, L67 (2003).

[51] J. Planelles and J. I. Climente, *Magnetic field implementation in multiband k·p hamiltonians of holes in semiconductor heterostructures*, J. Phys.: Condens. Matter **25**, 485801 (2013).

[52] C. E. Pryor and M. E. Flatté, *Landé g factors and orbital momentum quenching in semiconductor quantum dots*, Phys. Rev. Lett. **96**, 026804 (2006).

[53] J. van Bree, A. Y. Silov, P. M. Koenraad, M. E. Flatté, and C. E. Pryor, *g factors and diamagnetic coefficients of electrons, holes, and excitons in InAs/InP quantum dots*, Phys. Rev. B **85**, 165323 (2012).

[54] R. Hanson, L. P. Kouwenhoven, J. R. Petta, S. Tarucha, and L. M. K. Vandersypen, *Spins in few-electron quantum dots*, Rev. Mod. Phys. **79**, 1217 (2007).

[55] J. Fabian, A. Matos-Abiague, C. Ertler, P. Stano, and I. Žutić, *Semiconductor spintronics*, Acta Phys. Slovaca **57**, 565 (2007).

[56] M. W. Wu, J. H. Jiang, and M. Q. Weng, *Spin dynamics in semiconductors*, Phys. Rep. **493**, 61 (2010).

[57] G. Dresselhaus, *Spin-orbit coupling effects in zinc blende structures*, Phys. Rev. **100**, 580 (1955).

[58] Y. A. Bychkov and E. I. Rashba, *Oscillatory effects and the magnetic susceptibility of carriers in inversion layers*, J. Phys. C: Solid State Phys. **17**, 6039 (1984).

[59] L. D. Landau and E. M. Lifshitz, *Theory of elasticity* (Pergamon, Oxford, 1986).

[60] K. H. Yoo, J. D. Albrecht, and L. R. Ram-Mohan, *Strain in layered zinc blende and wurtzite semiconductor structures grown along arbitrary crystallographic directions*, Am. J. Phys. **78**, 589 (2010).

[61] J. F. Nye, *Physical properties of crystals: Their representation by tensors and matrices* (Oxford, New York, 1985).

[62] S. Schulz, M. A. Caro, E. P. O'Reilly, and O. Marquardt, *Symmetry-adapted calculations of strain and polarization fields in (111)-oriented zinc-blende quantum dots*, Phys. Rev. B **84**, 125312 (2011).

[63] J. Bardeen and W. Shockley, *Deformation potentials and mobilities in non-polar crystals*, Phys. Rev. **80**, 72 (1950).

[64] C. Herring and E. Vogt, *Transport and deformation-potential theory for many-valley semiconductors with anisotropic scattering*, Phys. Rev. **101**, 944 (1956).

[65] T. Chakraborty, *Quantum dots: A survey of the properties of artificial atoms* (Elsevier, Amsterdam, 1999).

[66] Y. Aharonov and D. Bohm, *Significance of electromagnetic potentials in the quantum theory*, Phys. Rev. **115**, 485 (1959).

[67] R. G. Chambers, *Shift of an electron interference pattern by enclosed magnetic flux*, Phys. Rev. Lett. **5**, 3 (1960).

[68] H. Batelaan and A. Tonomura, *The Aharonov-Bohm effects: Variations on a subtle theme*, Phys. Today **62**, 38 (2009).

[69] V. M. Fomin, ed., *Physics of quantum rings* (Springer, Berlin, 2014).

[70] I. Vurgaftman and J. R. Meyer, *Band parameters for nitrogen-containing semiconductors*, J. Appl. Phys. **94**, 3675 (2003).

[71] S. Nakamura, S. Pearton, and G. Fasol, *The blue laser diode* (Springer, Berlin, 2000).

[72] S. Nakamura, T. Mukai, and M. Senoh, *Candela-class high-brightness InGaN/AlGaN double-heterostructure blue-light-emitting diodes*, Appl. Phys. Lett. **64**, 1687 (1994).

[73] P. Lefebvre and B. Gayral, *Optical properties of GaN/AlN quantum dots*, C. R. Phys. **9**, 816 (2008).

[74] D. Lagarde, A. Balocchi, H. Carrère, P. Renucci, T. Amand, X. Marie, S. Founta, and H. Mariette, *Room-temperature optical orientation of the exciton spin in cubic GaN/AlN quantum dots*, Phys. Rev. B **77**, 041304 (2008).

[75] Y.-H. Liao, J. I. Climente, and S.-J. Cheng, *Dominant channels of exciton spin relaxation in photoexcited self-assembled (In,Ga)As quantum dots*, Phys. Rev. B **83**, 165317 (2011).

[76] H. Tong and M. W. Wu, *Theory of excitons in cubic III-V semiconductor GaAs, InAs and GaN quantum dots: Fine structure and spin relaxation*, Phys. Rev. B **83**, 235323 (2011).

[77] N. O. Lipari and M. Altarelli, *A new method in the theory of indirect excitons in semiconductors*, Solid State Commun. **18**, 951 (1976).

[78] U. Ekenberg and M. Altarelli, *Subbands and Landau levels in the two-dimensional hole gas at the GaAs-$Al_xGa_{1-x}As$ interface*, Phys. Rev. B **32**, 3712 (1985).

[79] E. Martinez-Guerrero, C. Adelmann, F. Chabuel, J. Simon, N. T. Pelekanos, G. Mula, B. Daudin, G. Feuillet, and H. Mariette, *Self-assembled zinc blende GaN quantum dots grown by molecular-beam epitaxy*, Appl. Phys. Lett. **77**, 809 (2000).

[80] J. Hu, L.-S. Li, W. Yang, L. Manna, L.-W. Wang, and A. P. Alivisatos, *Linearly polarized emission from colloidal semiconductor quantum rods*, Science **292**, 2060 (2001).

[81] J. Noborisaka, J. Motohisa, S. Hara, and T. Fukui, *Fabrication and characterization of freestanding GaAs/AlGaAs core-shell nanowires and AlGaAs nanotubes by using selective-area metalorganic vapor phase epitaxy*, Appl. Phys. Lett. **87**, 093109 (2005).

[82] A. Fontcuberta i Morral, D. Spirkoska, J. Arbiol, M. Heigoldt, J. R. Morante, and G. Abstreiter, *Prismatic quantum heterostructures syn-*

thesized on molecular-beam epitaxy GaAs nanowires, Small **4**, 899 (2008).

[83] M. Keplinger, T. Mårtensson, J. Stangl, E. Wintersberger, B. Mandl, D. Kriegner, V. Holý, G. Bauer, K. Deppert, and L. Samuelson, *Structural investigations of core-shell nanowires using grazing incidence X-ray diffraction*, Nano Lett. **9**, 1877 (2009).

[84] R. E. Algra, M. Hocevar, M. A. Verheijen, I. Zardo, G. G. W. Immink, W. J. P. van Enckevort, G. Abstreiter, L. P. Kouwenhoven, E. Vlieg, and E. P. A. M. Bakkers, *Crystal structure transfer in core/shell nanowires*, Nano Lett. **11**, 1690 (2011).

[85] D. Rudolph, S. Funk, M. Döblinger, S. Morkötter, S. Hertenberger, L. Schweickert, J. Becker, S. Matich, M. Bichler, D. Spirkoska, I. Zardo, J. J. Finley, G. Abstreiter, and G. Koblmüller, *Spontaneous alloy composition ordering in GaAs-AlGaAs core-shell nanowires*, Nano Lett. **13**, 1522 (2013).

[86] L. J. Lauhon, M. S. Gudiksen, D. Wang, and C. M. Lieber, *Epitaxial core-shell and core-multishell nanowire heterostructures*, Nature **420**, 57 (2002).

[87] M. Heigoldt, J. Arbiol, D. Spirkoska, J. M. Rebled, S. Conesa-Boj, G. Abstreiter, F. Peiró, J. R. Morante, and A. Fontcuberta i Morral, *Long range epitaxial growth of prismatic heterostructures on the facets of catalyst-free GaAs nanowires*, J. Mater. Chem. **19**, 840 (2009).

[88] J. Hasen, L. N. Pfeiffer, A. Pinczuk, S. He, K. W. West, and B. S. Dennis, *Metamorphosis of a quantum wire into quantum dots*, Nature **390**, 54 (1997).

[89] C. Fasth, A. Fuhrer, M. T. Björk, and L. Samuelson, *Tunable double quantum dots in InAs nanowires defined by local gate electrodes*, Nano Lett. **5**, 1487 (2005).

[90] B. M. Wong, F. Léonard, Q. Li, and G. T. Wang, *Nanoscale effects on heterojunction electron gases in GaN/AlGaN core/shell nanowires*, Nano Lett. **11**, 3074 (2011).

[91] A. Bertoni, M. Royo, F. Mahawish, and G. Goldoni, *Electron and hole gas in modulation-doped GaAs/*$Al_{1-x}Ga_xAs$ *radial heterojunctions*, Phys. Rev. B **84**, 205323 (2011).

[92] A. Ballester, J. Planelles, and A. Bertoni, *Multi-particle states of semiconductor hexagonal rings: Artificial benzene*, J. Appl. Phys. **112**, 104317 (2012).

[93] T. Chakraborty and P. Pietiläinen, *Electron-electron interaction and*

the persistent current in a quantum ring, Phys. Rev. B **50**, 8460 (1994).

[94] A. Lorke, R. Johannes Luyken, A. O. Govorov, J. P. Kotthaus, J. M. Garcia, and P. M. Petroff, *Spectroscopy of nanoscopic semiconductor rings*, Phys. Rev. Lett. **84**, 2223 (2000).

[95] M. Jung, J. S. Lee, W. Song, Y. H. Kim, S. D. Lee, N. Kim, J. Park, M.-S. Choi, S. Katsumoto, H. Lee, and J. Kim, *Quantum interference in radial heterostructure nanowires*, Nano Lett. **8**, 3189 (2008).

[96] Ö. Gül, N. Demarina, C. Blömers, T. Rieger, H. Lüth, M. I. Lepsa, D. Grützmacher, and Th. Schäpers, *Flux periodic magnetoconductance oscillations in GaAs/InAs core/shell nanowires*, Phys. Rev. B **89**, 045417 (2014).

[97] Ö. Gül, H. Y. Günel, H. Lüth, T. Rieger, T. Wenz, F. Haas, M. Lepsa, G. Panaitov, D. Grützmacher, and Th. Schäpers, *Giant magnetoconductance oscillations in hybrid superconductor-semiconductor core/shell nanowire devices*, Nano Lett. **14**, 6269 (2014).

[98] A. Szabo and N. S. Ostlund, *Modern quantum chemistry* (Dover, New York, 1996).

[99] K. Niemelä, P. Pietiläinen, P. Hyvönen, and T. Chakraborty, *Fractional oscillations of electronic states in a quantum ring*, Europhys. Lett. **36**, 533 (1996).

[100] U. F. Keyser, C. Fühner, S. Borck, R. J. Haug, M. Bichler, G. Abstreiter, and W. Wegscheider, *Kondo effect in a few-electron quantum ring*, Phys. Rev. Lett. **90**, 196601 (2003).

[101] A. Emperador, F. Pederiva, and E. Lipparini, *Spin- and localization-induced fractional Aharonov-Bohm effect*, Phys. Rev. B **68**, 115312 (2003).

[102] L. E. Lipparini, *Modern many-particle physics* (World Scientific, Singapore, 2008).

[103] F. V. Kusmartsev, J. F. Weisz, R. Kishore, and M. Takahashi, *Strong correlations versus U-center pairing and fractional Aharonov-Bohm effect*, Phys. Rev. B **49**, 16234 (1994).

[104] J. P. Perdew and Y. Wang, *Accurate and simple analytic representation of the electron-gas correlation energy*, Phys. Rev. B **45**, 13244 (1992).

[105] S. Das Sarma, J. Fabian, X. Hu, and I. Žutić, *Spin electronics and spin computation*, Solid State Commun. **119**, 207 (2001).

[106] S. Datta and B. Das, *Electronic analog of the electro-optic modulator*, Appl. Phys. Lett. **56**, 665 (1990).

[107] D. Loss and D. P. DiVincenzo, *Quantum computation with quantum dots*, Phys. Rev. A **57**, 120 (1998).

[108] D. P. DiVincenzo, *Topics in quantum computers*, in *Mesoscopic electron transport*, edited by L. L. Sohn, L. P. Kouwenhoven, and G. Schön (Springer, 1997) pp. 657–677.

[109] L. Chirolli and G. Burkard, *Decoherence in solid-state qubits*, Adv. Phys. **57**, 225 (2008).

[110] J. Fischer, M. Trif, W. A. Coish, and D. Loss, *Spin interactions, relaxation and decoherence in quantum dots*, Solid State Commun. **149**, 1443 (2009).

[111] A. V. Khaetskii and Y. V. Nazarov, *Spin relaxation in semiconductor quantum dots*, Phys. Rev. B **61**, 12639 (2000).

[112] M. I. Dyakonov, ed., *Spin physics in semiconductors* (Springer, Berlin, 2008).

[113] C. Lü, J. L. Cheng, and M. W. Wu, *Hole spin relaxation in semiconductor quantum dots*, Phys. Rev. B **71**, 075308 (2005).

[114] A. V. Khaetskii and Y. V. Nazarov, *Spin-flip transitions between Zeeman sublevels in semiconductor quantum dots*, Phys. Rev. B **64**, 125316 (2001).

[115] C. F. Destefani and S. E. Ulloa, *Oscillatory spin relaxation rates in quantum dots*, Phys. Rev. B **72**, 115326 (2005).

[116] S. Takahashi, R. S. Deacon, K. Yoshida, A. Oiwa, K. Shibata, K. Hirakawa, Y. Tokura, and S. Tarucha, *Large anisotropy of the spin-orbit interaction in a single InAs self-assembled quantum dot*, Phys. Rev. Lett. **104**, 246801 (2010).

[117] S. Avetisyan, P. Pietiläinen, and T. Chakraborty, *Strong enhancement of Rashba spin-orbit coupling with increasing anisotropy in the Fock-Darwin states of a quantum dot*, Phys. Rev. B **85**, 153301 (2012).

[118] L. M. Woods, T. L. Reinecke, and R. Kotlyar, *Hole spin relaxation in quantum dots*, Phys. Rev. B **69**, 125330 (2004).

[119] D. V. Bulaev and D. Loss, *Spin relaxation and decoherence of holes in quantum dots*, Phys. Rev. Lett. **95**, 076805 (2005).

[120] E. Tsitsishvili, R. v. Baltz, and H. Kalt, *Exciton-spin relaxation in quantum dots due to spin-orbit interaction*, Phys. Rev. B **72**, 155333 (2005).

[121] K. Roszak, V. M. Axt, T. Kuhn, and P. Machnikowski, *Exciton spin decay in quantum dots to bright and dark states*, Phys. Rev. B **76**, 195324 (2007).

[122] J. M. Luttinger and W. Kohn, *Motion of electrons and holes in perturbed periodic fields*, Phys. Rev. **97**, 869 (1955).

[123] D. Heiss, S. Schaeck, H. Huebl, M. Bichler, G. Abstreiter, J. J. Finley, D. V. Bulaev, and D. Loss, *Observation of extremely slow hole spin relaxation in self-assembled quantum dots*, Phys. Rev. B **76**, 241306 (2007).

[124] V. N. Golovach, A. Khaetskii, and D. Loss, *Phonon-induced decay of the electron spin in quantum dots*, Phys. Rev. Lett. **93**, 016601 (2004).

[125] P. Stano and J. Fabian, *Orbital and spin relaxation in single and coupled quantum dots*, Phys. Rev. B **74**, 045320 (2006).

[126] P. Scarlino, E. Kawakami, P. Stano, M. Shafiei, C. Reichl, W. Wegscheider, and L. M. K. Vandersypen, *Spin-relaxation anisotropy in a GaAs quantum dot*, Phys. Rev. Lett. **113**, 256802 (2014).

[127] O. Olendski and T. V. Shahbazyan, *Theory of anisotropic spin relaxation in quantum dots*, Phys. Rev. B **75**, 041306 (2007).

[128] S. Amasha, K. MacLean, I. P. Radu, D. M. Zumbühl, M. A. Kastner, M. P. Hanson, and A. C. Gossard, *Electrical control of spin relaxation in a quantum dot*, Phys. Rev. Lett. **100**, 046803 (2008).

[129] S. Prabhakar, R. Melnik, and L. L. Bonilla, *Electrical control of phonon-mediated spin relaxation rate in semiconductor quantum dots: Rashba versus Dresselhaus spin-orbit coupling*, Phys. Rev. B **87**, 235202 (2013).

[130] T. Mano, M. Abbarchi, T. Kuroda, B. McSkimming, A. Ohtake, K. Mitsuishi, and K. Sakoda, *Self-assembly of symmetric GaAs quantum dots on (111)A substrates: Suppression of fine-structure splitting*, Appl. Phys. Express **3**, 065203 (2010).

[131] I. Vurgaftman and J. R. Meyer, *Spin-relaxation suppression by compensation of bulk and structural inversion asymmetries in [111]-oriented quantum wells*, J. Appl. Phys. **97**, 053707 (2005).

[132] K. Biermann, A. Hernández-Mínguez, R. Hey, and P. V. Santos, *Electrically tunable electron spin lifetimes in GaAs(111)B quantum wells*, J. Appl. Phys. **112**, 083913 (2012).

[133] A. Balocchi, T. Amand, G. Wang, B. L. Liu, P. Renucci, Q. H. Duong, and X. Marie, *Electric field dependence of the spin relaxation*

anisotropy in (111) GaAs/AlGaAs quantum wells, New J. Phys. **15**, 095016 (2013).

[134] I. Žutić, J. Fabian, and S. Das Sarma, *Spintronics: Fundamentals and applications*, Rev. Mod. Phys. **76**, 323 (2004).

[135] H. J. Krenner, M. Sabathil, E. C. Clark, A. Kress, D. Schuh, M. Bichler, G. Abstreiter, and J. J. Finley, *Direct observation of controlled coupling in an individual quantum dot molecule*, Phys. Rev. Lett. **94**, 057402 (2005).

[136] G. Ortner, M. Bayer, Y. Lyanda-Geller, T. L. Reinecke, A. Kress, J. P. Reithmaier, and A. Forchel, *Control of vertically coupled InGaAs/GaAs quantum dots with electric fields*, Phys. Rev. Lett. **94**, 157401 (2005).

[137] J. R. Petta, A. C. Johnson, J. M. Taylor, E. A. Laird, A. Yacoby, M. D. Lukin, C. M. Marcus, M. P. Hanson, and A. C. Gossard, *Coherent manipulation of coupled electron spins in semiconductor quantum dots*, Science **309**, 2180 (2005).

[138] E. A. Stinaff, M. Scheibner, A. S. Bracker, I. V. Ponomarev, V. L. Korenev, M. E. Ware, M. F. Doty, T. L. Reinecke, and D. Gammon, *Optical signatures of coupled quantum dots*, Science **311**, 636 (2006).

[139] A. N. Vamivakas, C.-Y. Lu, C. Matthiesen, Y. Zhao, S. Fält, A. Badolato, and M. Atatüre, *Observation of spin-dependent quantum jumps via quantum dot resonance fluorescence*, Nature **467**, 297 (2010).

[140] S. E. Economou, J. I. Climente, A. Badolato, A. S. Bracker, D. Gammon, and M. F. Doty, *Scalable qubit architecture based on holes in quantum dot molecules*, Phys. Rev. B **86**, 085319 (2012).

[141] M. F. Doty, J. I. Climente, A. Greilich, M. Yakes, A. S. Bracker, and D. Gammon, *Hole-spin mixing in InAs quantum dot molecules*, Phys. Rev. B **81**, 035308 (2010).

[142] O. Voskoboynikov, C. P. Lee, and O. Tretyak, *Spin-orbit splitting in semiconductor quantum dots with a parabolic confinement potential*, Phys. Rev. B **63**, 165306 (2001).

[143] C. F. Destefani, S. E. Ulloa, and G. E. Marques, *Spin-orbit coupling and intrinsic spin mixing in quantum dots*, Phys. Rev. B **69**, 125302 (2004).

[144] D. V. Bulaev and D. Loss, *Spin relaxation and anticrossing in quantum dots: Rashba versus Dresselhaus spin-orbit coupling*, Phys. Rev. B **71**, 205324 (2005).

[145] M. P. Nowak, B. Szafran, F. M. Peeters, B. Partoens, and W. J. Pasek, *Tuning of the spin-orbit interaction in a quantum dot by an in-plane magnetic field*, Phys. Rev. B **83**, 245324 (2011).

[146] T. K. Johal, R. Rinaldi, A. Passaseo, R. Cingolani, A. Vasanelli, R. Ferreira, and G. Bastard, *Imaging of the electronic states of self-assembled* $\mathrm{In}_x\mathrm{Ga}_{1-x}\mathrm{As}$ *quantum dots by scanning tunneling spectroscopy*, Phys. Rev. B **66**, 075336 (2002).

[147] M. Müller, A. Cerezo, G. D. W. Smith, L. Chang, and S. S. A. Gerstl, *Atomic scale characterization of buried $In_xGa_{1-x}As$ quantum dots using pulsed laser atom probe tomography*, Appl. Phys. Lett. **92**, 233115 (2008).

[148] A. D. Giddings, J. G. Keizer, M. Hara, G. J. Hamhuis, H. Yuasa, H. Fukuzawa, and P. M. Koenraad, *Composition profiling of InAs quantum dots and wetting layers by atom probe tomography and cross-sectional scanning tunneling microscopy*, Phys. Rev. B **83**, 205308 (2011).

[149] B. Mahler, P. Spinicelli, S. Buil, X. Quelin, J.-P. Hermier, and B. Dubertret, *Towards non-blinking colloidal quantum dots*, Nat. Mater. **7**, 659 (2008).

[150] Y. Chen, J. Vela, H. Htoon, J. L. Casson, D. J. Werder, D. A. Bussian, V. I. Klimov, and J. A. Hollingsworth, *"Giant" multishell CdSe nanocrystal quantum dots with suppressed blinking*, J. Am. Chem. Soc. **130**, 5026 (2008).

[151] F. Zhang, V. H. Crespi, and P. Zhang, *Prediction that uniaxial tension along $\langle 111 \rangle$ produces a direct band gap in germanium*, Phys. Rev. Lett. **102**, 156401 (2009).

[152] A. M. Smith, A. M. Mohs, and S. Nie, *Tuning the optical and electronic properties of colloidal nanocrystals by lattice strain*, Nat. Nanotechnol. **4**, 56 (2009).

[153] Y. H. Huo, B. J. Witek, S. Kumar, J. R. Cardenas, J. X. Zhang, N. Akopian, R. Singh, E. Zallo, R. Grifone, D. Kriegner, R. Trotta, F. Ding, J. Stangl, V. Zwiller, G. Bester, A. Rastelli, and O. G. Schmidt, *A light-hole exciton in a quantum dot*, Nat. Phys. **10**, 46 (2013).

[154] C. Delerue and M. Lannoo, *Nanostructures: Theory and modelling* (Springer, Berlin, 2004).

[155] S. Christodoulou, F. Rajadell, A. Casu, G. Vaccaro, J. Q. Grim, A. Genovese, L. Manna, J. I. Climente, F. Meinardi, G. Rainò, T. Stöferle, R. F. Mahrt, J. Planelles, S. Brovelli, and I. Moreels, *Band*

structure engineering via piezoelectric fields in strained anisotropic CdSe/CdS nanocrystals, Nat. Commun. **6**, 7905 (2015).

[156] S. Brovelli, R. D. Schaller, S. A. Crooker, F. García-Santamaría, Y. Chen, R. Viswanatha, J. A. Hollingsworth, H. Htoon, and V. I. Klimov, *Nano-engineered electron-hole exchange interaction controls exciton dynamics in core-shell semiconductor nanocrystals*, Nat. Commun. **2**, 280 (2011).

[157] M. Grundmann, O. Stier, and D. Bimberg, *InAs/GaAs pyramidal quantum dots: Strain distribution, optical phonons, and electronic structure*, Phys. Rev. B **52**, 11969 (1995).

[158] J. Simon, N. T. Pelekanos, C. Adelmann, E. Martinez-Guerrero, R. André, B. Daudin, L. S. Dang, and H. Mariette, *Direct comparison of recombination dynamics in cubic and hexagonal GaN/AlN quantum dots*, Phys. Rev. B **68**, 035312 (2003).

[159] N. Vainorius, S. Lehmann, D. Jacobsson, L. Samuelson, K. A. Dick, and M.-E. Pistol, *Confinement in thickness-controlled GaAs polytype nanodots*, Nano Lett. **15**, 2652 (2015).

[160] B. Loitsch, J. Winnerl, G. Grimaldi, J. Wierzbowski, D. Rudolph, S. Morkötter, M. Döblinger, G. Abstreiter, G. Koblmüller, and J. J. Finley, *Crystal phase quantum dots in the ultrathin core of GaAs-AlGaAs core-shell nanowires*, Nano Lett. **15**, 7544 (2015).

[161] F. García-Santamaría, Y. Chen, J. Vela, R. D. Schaller, J. A. Hollingsworth, and V. I. Klimov, *Suppressed Auger recombination in "giant" nanocrystals boosts optical gain performance*, Nano Lett. **9**, 3482 (2009).

[162] J. I. Climente, J. L. Movilla, and J. Planelles, *Auger recombination suppression in nanocrystals with asymmetric electron-hole confinement*, Small **8**, 754 (2012).

[163] H. McDaniel, M. Pelton, N. Oh, and M. Shim, *Effects of lattice strain and band offset on electron transfer rates in type-II nanorod heterostructures*, J. Phys. Chem. Lett. **3**, 1094 (2012).

[164] S. M. Fairclough, E. J. Tyrrell, D. M. Graham, P. J. B. Lunt, S. J. O. Hardman, A. Pietzsch, F. Hennies, J. Moghal, W. R. Flavell, A. A. R. Watt, and J. M. Smith, *Growth and characterization of strained and alloyed type-II ZnTe/ZnSe core-shell nanocrystals*, J. Phys. Chem. C **116**, 26898 (2012).

[165] O. Chen, J. Zhao, V. P. Chauhan, J. Cui, C. Wong, D. K. Harris, H. Wei, H.-S. Han, D. Fukumura, R. K. Jain, and M. G. Bawendi, *Compact high-quality CdSe-CdS core-shell nanocrystals with narrow*

emission linewidths and suppressed blinking, Nat. Mater. **12**, 445 (2013).

[166] S. Christodoulou, G. Vaccaro, V. Pinchetti, F. De Donato, J. Q. Grim, A. Casu, A. Genovese, G. Vicidomini, A. Diaspro, S. Brovelli, L. Manna, and I. Moreels, *Synthesis of highly luminescent wurtzite CdSe/CdS giant-shell nanocrystals using a fast continuous injection route*, J. Mater. Chem. C **2**, 3439 (2014).

[167] S. Assali, L. Gagliano, D. S. Oliveira, M. A. Verheijen, S. R. Plissard, L. F. Feiner, and E. P. A. M. Bakkers, *Exploring crystal phase switching in GaP nanowires*, Nano Lett. **15**, 8062 (2015).

[168] K. A. Dick, C. Thelander, L. Samuelson, and P. Caroff, *Crystal phase engineering in single InAs nanowires*, Nano Lett. **10**, 3494 (2010).

[169] M. Bouwes Bavinck, K. D. Jöns, M. Zieliński, G. Patriarche, J.-C. Harmand, N. Akopian, and V. Zwiller, *Photon cascade from a single crystal phase nanowire quantum dot*, Nano Lett. **16**, 1081 (2016).

[170] B. Loitsch, D. Rudolph, S. Morkötter, M. Döblinger, G. Grimaldi, L. Hanschke, S. Matich, E. Parzinger, U. Wurstbauer, G. Abstreiter, J. J. Finley, and G. Koblmüller, *Tunable quantum confinement in ultrathin, optically active semiconductor nanowires via reverse-reaction growth*, Adv. Mater. **27**, 2195 (2015).

[171] A. M. Graham, P. Corfdir, M. Heiss, S. Conesa-Boj, E. Uccelli, A. Fontcuberta i Morral, and R. T. Phillips, *Exciton localization mechanisms in wurtzite/zinc-blende GaAs nanowires*, Phys. Rev. B **87**, 125304 (2013).

[172] P. Corfdir, B. Van Hattem, E. Uccelli, S. Conesa-Boj, P. Lefebvre, A. Fontcuberta i Morral, and R. T. Phillips, *Three-dimensional magneto-photoluminescence as a probe of the electronic properties of crystal-phase quantum disks in GaAs nanowires*, Nano Lett. **13**, 5303 (2013).

[173] K. S. Novoselov, D. Jiang, F. Schedin, T. J. Booth, V. V. Khotkevich, S. V. Morozov, and A. K. Geim, *Two-dimensional atomic crystals*, Proc. Natl. Acad. Sci. U.S.A. **102**, 10451 (2005).

[174] P. Miró, M. Audiffred, and T. Heine, *An atlas of two-dimensional materials*, Chem. Soc. Rev. **43**, 6537 (2014).

[175] Z. M. Wang, ed., *MoS_2: Materials, physics, and devices* (Springer International, Switzerland, 2014).

[176] L. Britnell, R. M. Ribeiro, A. Eckmann, R. Jalil, B. D. Belle, A. Mishchenko, Y.-J. Kim, R. V. Gorbachev, T. Georgiou, S. V. Morozov, A. N. Grigorenko, A. K. Geim, C. Casiraghi, A. H. Castro Neto,

and K. S. Novoselov, *Strong light-matter interactions in heterostructures of atomically thin films*, Science **340**, 1311 (2013).

[177] A. Pospischil, M. M. Furchi, and T. Mueller, *Solar-energy conversion and light emission in an atomic monolayer p-n diode*, Nat. Nanotechnol. **9**, 257 (2014).

[178] J. S. Ross, P. Klement, A. M. Jones, N. J. Ghimire, J. Yan, D. G. Mandrus, T. Taniguchi, K. Watanabe, K. Kitamura, W. Yao, D. H. Cobden, and X. Xu, *Electrically tunable excitonic light-emitting diodes based on monolayer* WSe_2 *p-n junctions*, Nat. Nanotechnol. **9**, 268 (2014).

[179] M. V. Bollinger, J. V. Lauritsen, K. W. Jacobsen, J. K. Nørskov, S. Helveg, and F. Besenbacher, *One-dimensional metallic edge states in* MoS_2, Phys. Rev. Lett. **87**, 196803 (2001).

[180] D. Davelou, G. Kopidakis, G. Kioseoglou, and I. N. Remediakis, MoS_2 *nanostructures: Semiconductors with metallic edges*, Solid State Commun. **192**, 42 (2014).

[181] E. Erdogan, I. H. Popov, A. N. Enyashin, and G. Seifert, *Transport properties of* MoS_2 *nanoribbons: edge priority*, Eur. Phys. J. B **85**, 33 (2012).

[182] S. Pavlović and F. M. Peeters, *Electronic properties of triangular and hexagonal* MoS_2 *quantum dots*, Phys. Rev. B **91**, 155410 (2015).

[183] *Special topic: topological insulators*, APL Mat. **3**, issue 8 (2015).

[184] S. Zhang, *Topological field theory and the discovery of topological materials*, Phys. Scr. **T146**, 014022 (2012).

[185] M. Z. Hasan and C. L. Kane, *Colloquium: Topological insulators*, Rev. Mod. Phys. **82**, 3045 (2010).

[186] M. Z. Hasan and J. E. Moore, *Three-dimensional topological insulators*, Annu. Rev. Condens. Matter Phys. **2**, 55 (2011).

[187] F. Güller, A. M. Llois, J. Goniakowski, and C. Noguera, *Polarity effects in unsupported polar nanoribbons*, Phys. Rev. B **87**, 205423 (2013).

[188] M. Gibertini and N. Marzari, *Emergence of one-dimensional wires of free carriers in transition-metal-dichalcogenide nanostructures*, Nano Lett. **15**, 6229 (2015).

[189] H. Rostami, A. G. Moghaddam, and R. Asgari, *Effective lattice Hamiltonian for monolayer* MoS_2*: Tailoring electronic structure with perpendicular electric and magnetic fields*, Phys. Rev. B **88**, 085440 (2013).

[190] G.-B. Liu, W.-Y. Shan, Y. Yao, W. Yao, and D. Xiao, *Three-band tight-binding model for monolayers of group-VIB transition metal dichalcogenides*, Phys. Rev. B **88**, 085433 (2013).

[191] A. Kormányos, V. Zólyomi, N. D. Drummond, P. Rakyta, G. Burkard, and V. I. Fal'ko, *Monolayer MoS_2: Trigonal warping, the Γ valley, and spin-orbit coupling effects*, Phys. Rev. B **88**, 045416 (2013).

[192] A. Kormányos, G. Burkard, M. Gmitra, J. Fabian, V. Zólyomi, N. D. Drummond, and V. Fal'ko, *$k{\cdot}p$ theory for two-dimensional transition metal dichalcogenide semiconductors*, 2D Mater. **2**, 022001 (2015).

[193] B. A. Bernevig, T. L. Hughes, and S.-C. Zhang, *Quantum spin Hall effect and topological phase transition in HgTe quantum wells*, Science **314**, 1757 (2006).

[194] J. Li, A. F. Morpurgo, M. Büttiker, and I. Martin, *Marginality of bulk-edge correspondence for single-valley Hamiltonians*, Phys. Rev. B **82**, 245404 (2010).

[195] W. Yao, S. A. Yang, and Q. Niu, *Edge states in graphene: From gapped flat-band to gapless chiral modes*, Phys. Rev. Lett. **102**, 096801 (2009).

[196] J. Li, I. Martin, M. Büttiker, and A. F. Morpurgo, *Topological origin of subgap conductance in insulating bilayer graphene*, Nat. Phys. **7**, 38 (2011).

[197] Y. Shimazaki, M. Yamamoto, I. V. Borzenets, K. Watanabe, T. Taniguchi, and S. Tarucha, *Generation and detection of pure valley current by electrically induced Berry curvature in bilayer graphene*, Nat. Phys. **11**, 1032 (2015).

[198] X. Duan, C. Wang, J. C. Shaw, R. Cheng, Y. Chen, H. Li, X. Wu, Y. Tang, Q. Zhang, A. Pan, J. Jiang, R. Yu, Y. Huang, and X. Duan, *Lateral epitaxial growth of two-dimensional layered semiconductor heterojunctions.*, Nat. Nanotechnol. **9**, 1024 (2014).

[199] M. S. J. Marshall and M. R. Castell, *Scanning tunnelling microscopy of epitaxial nanostructures.*, Chem. Soc. Rev. **43**, 2226 (2014).

[200] W. Bao, N. J. Borys, C. Ko, J. Suh, W. Fan, A. Thron, Y. Zhang, A. Buyanin, J. Zhang, S. Cabrini, P. D. Ashby, A. Weber-Bargioni, S. Tongay, S. Aloni, D. F. Ogletree, J. Wu, M. B. Salmeron, and P. J. Schuck, *Visualizing nanoscale excitonic relaxation properties of disordered edges and grain boundaries in monolayer molybdenum disulfide*, Nat. Commun. **6**, 7993 (2015).

[201] R. G. Veprek, S. Steiger, and B. Witzigmann, *Ellipticity and the*

spurious solution problem of k·p envelope equations, Phys. Rev. B **76**, 165320 (2007).

[202] R. G. Veprek, S. Steiger, and B. Witzigmann, *Operator ordering, ellipticity and spurious solutions in k·p calculations of III-nitride nanostructures*, Opt. Quantum Electron. **40**, 1169 (2008).

[203] M. A. Stroscio and M. Dutta, *Phonons in nanostructures* (Cambridge University Press, Cambridge, 2001).

[204] T. Uenoyama and L. J. Sham, *Carrier relaxation and luminescence polarization in quantum wells*, Phys. Rev. B **42**, 7114 (1990).